The Disks and Accretion Behavior of Young Stellar Objects

Min Fang
Max-Planck-Institut für Astronomie

Heidelberg 2010

Dissertation in Astronomy
submitted to the
Combined Faculties of the Natural Sciences and Mathematics
of the Ruperto-Carola-University of Heidelberg, Germany,
for the degree of
Doctor of Natural Sciences

Put forward by
Min Fang
born in Jiangsu, China

Oral examination: 02.02.11

The Disks and Accretion Behavior of Young Stellar Objects

Referees: **Prof. Dr. Thomas Henning**
Prof. Dr. Andreas Quirrenbach

To my family

Abstract

Circumstellar disks play an essential role in the star formation process and are thought to be the sites where new planetary systems come into being. Knowledge of the evolution of these objects is pivotal to our understanding of star and planet formation. In this thesis, I present three studies aimed at characterizing the properties of newly formed stars and their circumstellar accretion disks in three qualitatively different environments: the sparse stellar association ϵ Cha, the L1630 and L1641 regions of clustered and distributed star formation in Orion, and the massive cluster Pismis 24. I combined infrared observations, taken from the ground and with the Spitzer Space Telescope, with optical imaging and spectroscopy obtained with various ground-based facilities. I characterized the disk geometry and evolutionary state using the infrared data, and from the optical data I determined the stellar properties as well as the rate at which disk material is accreted onto the central stars. Two important insights gained through my studies are: (1) the disk lifetimes for stars formed in isolation or sparse stellar associations are longer than those of stars formed in relatively dense clusters, whereas the disk lifetimes in clusters harboring very massive stars with spectral types earlier than ~O5 are shorter than those in otherwise similar clusters that lack such very massive stars; (2) the accretion rates show a steeper dependence on the stellar mass in the sub-solar mass regime than in the solar or intermediate mass regime.

Zusammenfassung

Zirkumstellare Scheiben spielen eine entscheidende Rolle im Prozess der Sternentstehung und gelten darüberhinaus als die Geburtsstätten neuer Planetensysteme. Notwendig zum Verständnis der Planeten- und Sternentstehung ist daher das Wissen um die Entwicklung zirkumstellarer Akkretionsscheiben in Abhängigkeit von der stellaren Umgebung. In dieser Arbeit lege ich drei Studien vor zur Charakterisierung der Eigenschaften von Sternen und Scheiben in unterschiedlichen Sternentstehungsgebieten: im lockeren Sternenverband ϵ Cha, in den Außenregionen des Orion-Nebels (L1630-North und L1641) und im massereichen Haufen Pismis 24. Dazu wurden Infrarotdaten aus bodengebundenen Durchmusterungen und des *Spitzer* Weltraumteleskops kombiniert mit optischen Bildern und Spektroskopie verschiedener bodengebundener Teleskope. Anhand der Infrarotbeobachtungen charakterisierte ich die Scheibengeometrie. Desweiteren verwende ich die optischen spektralen und photometrischen Daten zur Bestimmung der Akkretionsraten sowie zur Ermittlung der Eigenschaften der Zentralgestirne. Meine Untersuchungen zeigen, daß die Lebensdauer zirkumstellarer Scheiben in Isolation oder lockeren Sternverbänden sehr viel länger als in relativ dichten Sternhaufen ist. Dabei fällt die Lebensdauer in großen Haufen, die auch extrem massenreichen Sterne (Spektraltyp O5 und früher) enthalten, sehr viel geringer aus als in Haufen, in denen solche extrem massenreichen Sterne fehlen. Desweiteren zeigt die Akkretionsrate im Massenbereich der sub-solaren Sterne eine stärkere Abhängigkeit von der Zentralsternmasse als im Falle von solaren oder mittelschweren Sternen.

Contents

Chapter 1

Introduction

1.1 Star formation

Star formation occurs in cold and dense interstellar clouds of molecular gas and refractory material collectively referred to as "dust". Initially, such "molecular clouds" are supported against collapse under their own gravity by magnetic fields and turbulence. The densest regions inside the molecular clouds may develop into self-gravitating cores, which become denser and denser and can eventually no longer be sustained by magnetic and turbulent support. Thus, they become unstable to gravitational collapse in "inside-out" fashion (Shu et al. 1987). The cores have finite angular momentum which is conserved during collapse, preventing a substantial fraction of the infalling material to fall directly to the core center. Instead, this material builds a flattened structure around the forming central object, through which material may be further transported inwards while angular momentum is carried away. Through these *accretion disks* a substantial fraction of the final stellar mass is fed onto the stellar embryo.

The formation of low-mass stars, such as our own Sun, has been divided into four phases, with the corresponding objects being referred to as Class 0, I, II, and III sources (Lada 1987; Andre et al. 2000). While this division is primary empirical and based on the appearance of the Spectral Energy Distribution (SED) of a forming stellar object, it reflects to some extent also how the formation of a young star is driven by various physical mechanisms in successive phases. The extremely young Class 0 objects show SEDs that closely resemble a cold blackbody spectrum peaking at far-infrared wavelengths, and have a typical timelife of $\sim 10^5$ yr (Evans et al. 2009). During this phase, energetic outflows can develop that start to clear out material along the rotational poles of the protostellar systems. This causes the object to evolve into a less embedded class I source, with a well developed, optically thick disk of hundreds of astronomical units in diameter. The lifetime of class I objects is $\sim 5 \times 10^5$ yr (Evans et al. 2009) and such objects typically drive strong outflows that help further clearing of envelope material. The rate at which material is accreted onto the central star through the disk remains high and the disks are fed with

fresh material that is infalling from the envelope. When most of the envelope is dissipated and the supply of fresh material to the disk is halted, a longer pre-main sequence phase ensues during which the stars typically become visible at optical wavelengths while accretion continues at a strongly reduced rate. This so-called Class II phase lasts several million years, and is thought to be the main planet formation phase. Through still not fully understood mechanisms, the disks are dissipated on timescales of a few Myrs, and after some 10 Myr a young star may be left with an optically thin, gas-deprived "debris disk" which may co-exist and interact with a newly formed planetary system. During this last phase of the star formation process the young stars and whatever circumstellar material is left are referred to as "Class III" sources. The stars are still contracting until at some point the pressures and temperatures in their centers are high enough to ignite Hydrogen fusion. The young object has reached the zero-age main sequence and will remain stable, with only a modest and very gradual increase in luminosity, for billions of years. A star like our sun will remain on the main sequence for approximately 10 billion years.

In this thesis I present studies of a large number of young stars in various environments, with the goal of improving the observational characterization of the forming stars and their disks. My studies include sources in the latter three phases in the Lada classification, with a particular emphasis on sources in the Class II phase and the evolution of these into Class III objects.

1.2 Disk evolution

It is more than five decades ago that T Tauri stars (TTSs) were identified as being "special" (Joy 1945), and were recognized as pre-main sequence objects (Ambartsumian 1947). Later TTSs were found to often show strong excess emission over the expected photospheric level at near-infrared and longer wavelengths (Mendoza 1966, 1968). A significant fraction of nearby known TTSs have been detected at far-infrared to millimeter wavelengths (Rucinski 1985; Harris et al. 1988; Weintraub et al. 1989; Beckwith et al. 1990). The observed spectral energy distributions of TTSs can be naturally explained if these stars are surrounding by circumstellar disks (Lynden-Bell & Pringle 1974; Adams et al. 1987).

Circumstellar disks are formed as a result of angular momentum conservation during the protostellar core collapse (Shu 1977). These disks have potential to form the planets and are thus also referred to as *protoplanetary* disks. The disk dissipation process has been constrained observationally by investigating what fraction of young stars (still) shows strong excess emission from disk material at infrared wavelengths, in clusters with a range of ages. Near-infrared imaging surveys, which are sensitive to hot disk material very close to the central star, have indicated that the inner disk frequency is >50% at ages of 1-2 Myr but dramatically decreases to ~10% at ages of 5-10 Myr, indicating that the lifetime of inner disks is a few Myr (Strom et al. 1989; Haisch et al.

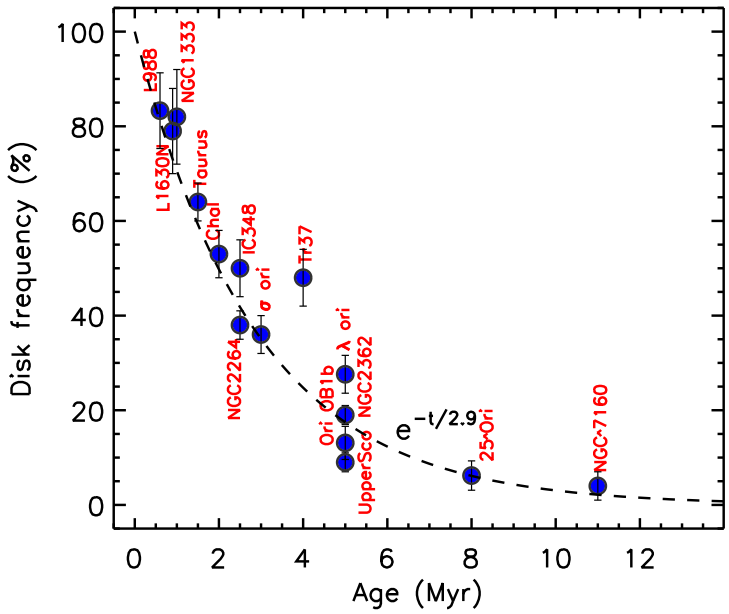

Figure 1.1: The disk frequencies vs. ages for different clusters/SFRs. The dashed line is the fit to disk frequencies of the clusters/SFRs, which is f_{disk}=e$^{-t/2.9}$. Here t is in the unit of Myr.

2001; Hillenbrand 2002). This has been confirmed by recent surveys performed with the Spitzer Space Telescope (e.g. Gutermuth et al. 2004; Young et al. 2004; Hartmann et al. 2005; Megeath et al. 2005b; Lada et al. 2006; Sicilia-Aguilar et al. 2006a, 2008; Hernández et al. 2006; Dahm & Hillenbrand 2007; Hernández et al. 2007b; Flaherty & Muzerolle 2008). Fig. 1.1 shows the (inner) disk frequency vs. age diagram for the various young clusters and star-forming regions collected from the literature. Overall, the data points in this diagram can be well represented by an exponential decay of the form $f_{\rm disk}$=exp(-t/τ_0), yielding a typical timescale τ_0 ~2.9 Myr for the dissipation of at least the hot inner parts of circumstellar disks (Fedele et al. 2010).

A number of different physical mechanisms have been proposed to drive the evolution and dissipation of a circumstellar disk, such as disk accretion (Hartmann et al. 1998), stellar encounters (Pfalzner et al. 2006), photoevaporation by the central stars and/or nearby massive stars (Johnstone et al. 1998; Clarke et al. 2001; Alexander et al. 2006), planet formation (Rice et al. 2003; Quillen et al. 2004), and stellar binarity (Artymowicz & Lubow 1994). The individual mechanisms are briefly described as follows:

Accretion: Turbulence and magnetic fields can transport disk angular momentum outward, allowing the disk material to move inward and eventually be accreted onto the central star. The timescale for viscous dispersal of the disk depends on the disks radius (Hartmann et al. 1998). Due to the conservation of angular momentum the outer disk will expand, and the viscous timescale in the outer disk becomes longer. Thus, viscous evolution may be only important

in the dissipation of the inner parts of disks (Hollenbach et al. 2000).

Stellar encounters: The stellar encounter mechanism involves a circumstellar disk and a nearby passing star. Mutual gravitational interaction can induce a significant exchange of angular momentum and lead to disruption of material from the outer disk regions or strongly enhanced accretion rates, both accelerating the dissipation of the circumstellar disk (Clarke & Pringle 1993; Pfalzner et al. 2006; Olczak et al. 2006; Pfalzner & Olczak 2007; Olczak et al. 2010).

Photoevaporation: UV photons emitted by the central star or by nearby massive stars can heat the gas in the disk surface layers to such high temperatures that the sound speed exceeds the local escape velocity from the gravitational potential well of the system. The gas will then flow freely into interstellar space in a photo-evaporative flow and the disk is slowly eroded (Johnstone et al. 1998; Störzer & Hollenbach 1999; Richling & Yorke 2000; Hollenbach et al. 2000; Clarke et al. 2001; Armitage et al. 2003; Alexander et al. 2006).

Planet formation: When the planets are forming deep in the disk interior they may substantially affect the structure of the disk through gravitational interaction with the disk gas. Giant gas planets may become massive enough open a gap in the disk, strongly hindering further transport of outer disk material across the gap to the inner disk regions. The inner disk regions will further accrete onto the central star but, no longer being supplied by fresh material from larger radii, are quickly dissipated. Thus these systems can evolve into "Transition Disks" with inner holes (Rice et al. 2003; Quillen et al. 2004).

Binarity: In a young binary system we distinguish two types of disks that may be present: a circumstellar disk that surrounds one of the components (both system members may have such a disk), and a "circum-binary" disk that surrounds the whole binary pair. Circumstellar disks may be truncated on the outside by gravitational interaction with the binary companion, which is in some scene a special case of the previously discussed "stellar encounters" scenario (Artymowicz & Lubow 1994). In the inner region of a disk surrounding a binary pair a gap will quickly form (Lin & Papaloizou 1993). Potentially present circumstellar disks will be dynamically isolated from the much larger circumbinary disk, and both will evolve independently.

1.3 Dust processing in protoplanetary disks

The dust in protoplanetary disks originates in the interstellar medium (ISM). It consists of silicates with olivine and pyroxene stoichiometry and carbonaceous material (Henning et al. 2004; Henning 2010). The silicate grains in the ISM have typical sizes of $\lesssim 0.25\,\mu$m and appear to be present essentially exclusively in amorphous form, as derived from an analysis of the "$10\,\mu$m silicate feature" seen in absorption through lines of sight with large interstellar extinction (Kemper

et al. 2004). Towards young stars, e.g. Herbig Ae/Be stars and T Tauri stars, the 10 μm feature is usually in emission (Cohen & Witteborn 1985; Natta et al. 2000b; Bouwman et al. 2001, 2003; van Boekel et al. 2004, 2005). The emission features arise in the optically thin disk atmosphere that "blankets" the optically thick disk interior (Chiang & Goldreich 1997; Henning & Meeus 2009; Henning 2010). Since in the whole disk, with the exception of the innermost regions of strongly accreting sources, the main energy source of the disk material is irradiation from the outside by the central object, the disk atmosphere is warmer than the disk interior. Thus, it is easily understood why peaks in the opacity curve of the disk material result in emission features in the spectrum.

Analysis of the 10 μm silicate feature in protoplanetary disk spectra revealed a large variety of grain properties. The disk atmospheres contain dust grains that in many, but not all, cases are substantially larger than their ISM counterparts, typically several microns. Also, often a substantial fraction of the disk silicates are present in a crystalline form (Bouwman et al. 2001, 2003; van Boekel et al. 2003, 2005; Bouwman et al. 2008; Juhász et al. 2010). The observed differences between the ISM and disk silicates indicates that physical mechanisms are at work in the disks that alter the properties of the dust. These processes may include thermal annealing at $T \gtrsim 800$ K close to the central star or also in the colder disk regions further out in brief "flash" heating events induced by shocks, evaporation and recondensation at $T \gtrsim 1200$ K, and grain growth. In addition, transport mechanisms such as turbulent mixing may move processed material through the disk, and we may observe it in a different location from where the dust processing originally took place (Henning & Meeus 2009; Henning 2010).

1.4 Outline of this work

In this section, I will outline this thesis. First, I will describe the scientific goals I have pursued, and then explain the observational methods that I used to do so. Finally, I will briefly introduce the star-forming regions that I have studied.

1.4.1 Scientific motivation

Over the past decades our understanding of star formation, disk evolution, and planet formation processes has advanced dramatically. This was to a large extent due to the advent of a new generation of ground- and space-based observatories that were vastly more powerful than anything that preceded. In parallel theoretical models of forming stars, disks, and planets have developed spectacularly, much helped by the dramatic increases in the power and availability of computing

facilities. Yet, there are still many important open questions out there, waiting to be answered, some of which I will address in this thesis. I will focus on the following main questions:

- What is the primary physical mechanism responsible for disk dissipation?
- How do the disk properties (geometry, accretion) depend on the properties of the central star, and the (close) stellar environment?
- How are the properties of the dust in disks related to the global properties of the disks and their central stars?

1.4.2 Observational approach

(1) Characterizing disks

The excess emission at infrared or longer wavelengths from young stars has been well understood in terms explained circumstellar material in the form of a disk (Lynden-Bell & Pringle 1974; Adams et al. 1987). The disk material may span a large range in temperature and density, from the hot regions at less an AU from the central star to the elusive cold outer regions at radii of 100 AU or more. This is reflected in the SED, which may show excess emission over the stellar photospheric level over many decades in frequency, from the near-infrared where the hot inner disk dominates, through the mid-infrared where the warm disk atmosphere contributes most, to far-infrared and (sub-) mm wavelengths where we see ever deeper into the disk, and are sensitive to an ever increasing fraction of the disk mass and ever cooler material. Fig. 1.2 shows a typical SED from a TTS with a flared disk (Dullemond et al. 2007), qualitatively illustrating how the various disk regions contribute to the SED. At mm wavelengths the disks are normally optically thin and the emission is dominated by the the cool disk interior where most of the mass resides. The infrared excess emission is almost exclusively thermal emission from dust grains, except in some cases at ~cm or longer wavelengths (not shown in Fig. 1.2) where it may be dominated by non-thermal (free-free) emission from a stellar wind.

The Spitzer Space Telescope featured two imaging cameras: the Infrared Array Camera (IRAC, Fazio et al. 2004) and the Multiband Imaging Photometer (MIPS, Rieke et al. 2004). These provide broad-band images with exquisite sensitivity at wavelengths from 3.6 μm to 24 μm and were used to do large area mapping of the infrared sky. Numerous star-forming regions and clusters with ages from 1 Myr to tens of Myrs were observed (e.g. Chapter 3; Gutermuth et al. 2004; Young et al. 2004; Hartmann et al. 2005; Megeath et al. 2005b; Lada et al. 2006; Sicilia-Aguilar et al. 2006a, 2008; Hernández et al. 2006; Dahm & Hillenbrand 2007; Hernández et al. 2007b; Flaherty & Muzerolle 2008), yielding well observed samples of many thousands of young

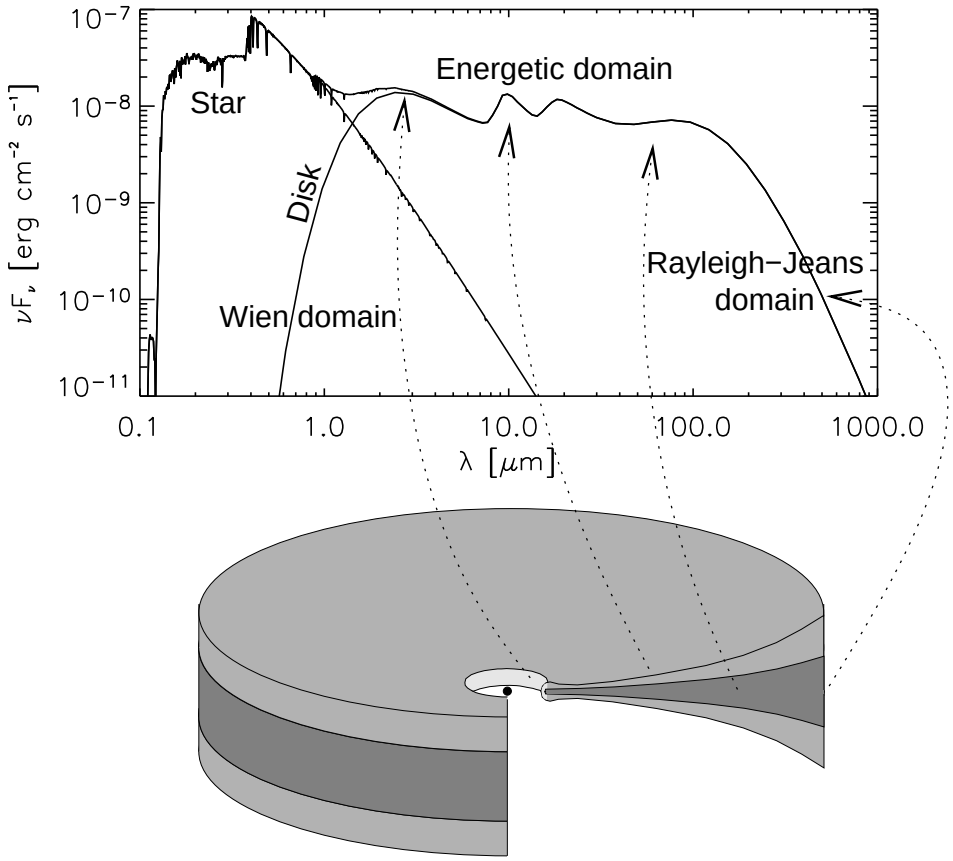

Figure 1.2: A sketch of construction of the SED from a young star with a flaring disk. Different part of the disk can have contributions in the SED at different wavelengths: (1)the near-infrared and mid-infrared emission come from the inner disk, (2) far-infrared emission is from the outer disk, and (3) the (sub-)millimeter emission mostly originates from the mid-plane of outer disk. The figure is taken from Dullemond et al. (2007)

stars down to very low masses. Combining the Spitzer data with existing ground based near-infrared data from e.g. the 2MASS and DENIS surveys, we can construct SEDs of the individual young stars in these star-forming clouds. This allows characterization of their disks from the innermost regions out to a radius that, depending on the luminosity of the central star, may be several to several tens of astronomical units.

(2) Characterizing dust properties of protoplanetary disks

The properties of dust grains in circumstellar environments in general, and protoplanetary disks in particular, have been studied mostly studied using infrared spectroscopy. In particular silicate dust shows many spectral features at infrared wavelengths whose presence, shape, strength,

and exact wavelength depend on the chemical composition, grain size and structure (compact or porous), and solid state lattice structure (amorphous or crystalline), and therefore provides a wealth of information about the nature of the dust. Spitzer Infrared Spectrograph (IRS) spectra are ideally suited for a mineralogical analysis of the dust in protoplanetary disks (e.g. Henning & Meeus 2009; Henning 2010). In Figs. 1.3(a), (b), (c), and (d) we show the mass mass absorption coefcients of amorphous silicates (with olivine and pyroxene stoichiometry), forsterite, and enstatite with grain sizes of 0.1 μm, 1.5 μm, and 6.0 μm (Dorschner et al. 1995; Servoin & Piriou 1973; Jaeger et al. 1998). The mass absorption coefficients of the various dust species are calculated from their optical constants (complex refractive indices) using classical Mie theory for the amorphous dust and a distribution of hollow spheres (DHS) approach for the crystalline dust (Min et al. 2007; Juhász et al. 2009). Laboratory measurements provided the needed measurements of the optical constants (Servoin & Piriou 1973; Preibisch et al. 1993; Dorschner et al. 1995; Henning & Mutschke 1997; Jaeger et al. 1998). The different dust species or different grain sizes generally show very different spectral signatures, and can therefore be distinguished from one-another in a mineralogical de-composition.

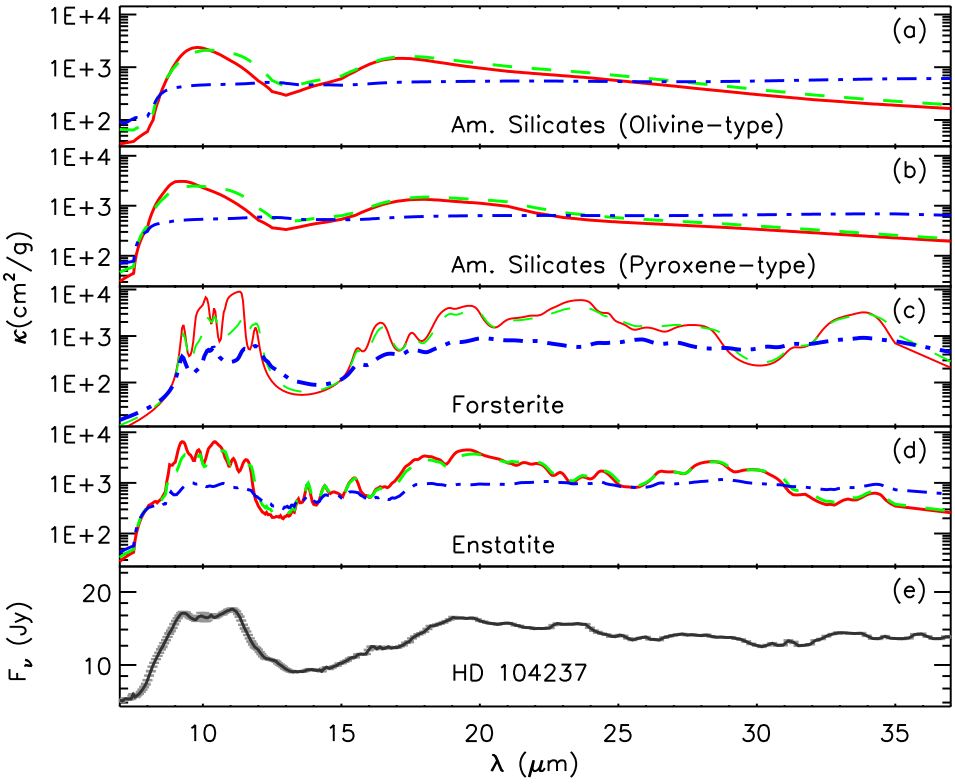

Figure 1.3: Panels (a), (b), (c), and (d): The mass mass absorption coefficients of amorphous silicates (with olivine and forsterite stoichiometry), forsterite, and enstatite with grain sizes of 0.1 μm(solid lines), 1.5 μm(dashed lines), and 6.0 μm(dash-dotted lines). Panel (e): The Spitzer IRS spectrum of Herbig Ae star HD 104237.

The Spitzer IRS covers the wavelength range from 5.3 to 38 μm with spectral resolutions R≈90 and 600 (Houck et al. 2004). In this wavelength domain there are many silicate features due to to Si-O stretching and O-Si-O bending vibrations in the solid state lattice (Henning 2010). Fig. 1.3(e) shows the IRS spectrum of HD 104237, the optically brightest Herbig Ae star. A first glance at this spectrum directly shows that it cannot be explained using silicate grains as found in the ISM that are typically much smaller than a micron and almost fully amorphous (Kemper et al. 2004) and whose opacity curve closely resembles the red curve in Fig. 1.3(a). Instead, larger grains and a substantial amount of crystalline material are required. A combination of the opacities shown in Fig. 1.3(a-d) can provide a good match to the observed spectrum. In this thesis I will use the Two Layer Temperature Distribution (TLTD) spectral decomposition routines developed by Juhász et al. (2009, 2010) in order to fit the Spitzer IRS spectra of a number of young stars. In this method the abundances of the individual dust species (i.e. multiplication factors of their respective opacity curves in the model spectrum) are fit parameters which are varied, along with several parameters that describe the disk structure and temperature in a simplified fashion, until the residuals between the observed and model spectra are minimized. Thus, IRS spectra provide a powerful way to constrain the relative abundances of the various dust species. We must keep in mind, though, that the IRS spectra are sensitive only to the surface layers of the disk and probe only a minor fraction of the total dust mass. Conclusions on the bulk composition of the dust based on IRS spectra rely on the *assumption* that the dust in the disk surface is representative of the whole disk.

(3) Measuring accretion rates

The process of mass accretion onto the central star is key to understanding the evolution and dissipation of circumstellar disks, and therefore also to understand the process of planet formation. Theoretical and observational studies of classical T Tauri stars (CTTS) have favored the magnetospheric accretion model for mass transfer from the circumstellar disk onto the young star (Calvet & Hartmann 1992; Hartmann et al. 1994; Muzerolle et al. 1998b, 2001). In this model, the stellar magnetosphere truncates the disk at a few stellar radii. Gas from the disk is lifted out of the disk midplane by magnetic pressure and is funneled onto the star along the magnetic field lines. It hits the stellar surface at approximately the free-fall velocity, causing a strong "accretion shock" and the associated hot-spots on the stellar surface. Various emission lines, such as the hydrogen Balmer series, He I λ=5876, and Brγ, are formed in the infalling magnetospheric flow. Optical/ultraviolet excess continuum emission is produced in the accretion shocks. Fig. 1.4 illustrates the magnetospheric accretion model (Hartmann 2005a).

The most robust estimates of the accretion rate can be obtained from measurements of the luminosity of UV excess emission which veils the photospheric spectrum of a young star (Calvet & Hartmann 1992; Calvet & Gullbring 1998). The excess emission arises as the gravitational

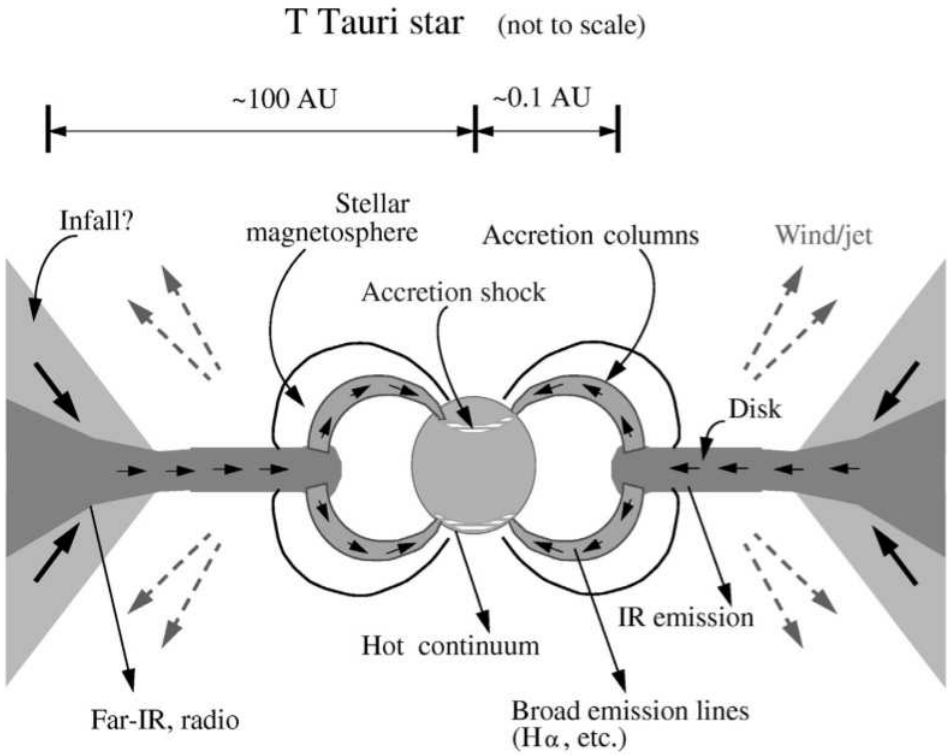

Figure 1.4: A sketch of the magnetospheric accretion model. The figure is taken from Hartmann (2005a).

energy of the infalling material is radiated away in the accretion shock and it thus forms a very direct measure of the accretion rate (Muzerolle et al. 1998b). In practice, however, the UV excess is measurable only in sources that suffer low extinction, and only if the accretion luminosity is a substantial fraction of that of the stellar photosphere. This limits the use of the UV-excess method to sources with accretion rates above $\sim 10^{-10}\ M_{\odot}\mathrm{yr}^{-1}$.

Emission lines in optical or near-infrared spectra provide a much more easily accessible tracer for the accretion rate. Observational studies have shown that the emission line luminosities are strongly correlated with the accretion luminosities and therefore with the rates, however generally with individual sources showing a large scatter about the average relation (Chapter 3; Herczeg & Hillenbrand 2008; Dahm 2008). This scatter may be in part be due to the fact that accretion in young stars can be a strongly time-variable process, and the emission lines and accretion rates (UV-excess) were not measured simultaneously. For optically thick lines, the viewing geometry also affects the observed line luminosity. In particular the Hα line is a very sensitive and easily accessible accretion tracer (Natta et al. 2004; Muzerolle et al. 2001), that does however show one of the largest scatters in the line luminosity versus accretion rate relation. The full width at 10% of the peak intensity of the Hα line shows a tighter relation with the accretion

rate (Natta et al. 2004), but also here the scatter is still substantial and individual sources can lie off the average relation by as much as an order of magnitude. Also here, the observed scatter is may in part be explained by time-variability of the accretion (the Hα profiles and accretion rates were not measured simultaneously), and in part be due to differences in viewing geometry (the Hα line normally has the highest optical depht of all lines used to trace the accretion). In practice, this means that the Hα lines may not be a very accurate quantitative measure of the accretion rate for individual objects, but is well suited to study the accretion properties of an ensemble of young stars in a statistical sense.

The luminosities of the Hβ and He I λ=5876 emission lines are well correlated with the accretion luminosity, as shown using simultaneous observations of the line fluxes and optical optical/UV excesses (Chapter 3; Herczeg & Hillenbrand 2008; Dahm 2008). The accretion rates can be derived from the accretion luminosities once the stellar mass and radius are known. The latter can be estimated from the effective temperatures and bolometric luminosities of the stars as derived from a combination of optical and near-infrared spectroscopy and photometry, by comparison to theoretical pre-main sequence evolutionary tracks. Thus, the Hβ and He I λ=5876 emission lines are also good tracers of the accretion rate, in addition to the UV-veiling. In this thesis, the Hα, Hβ, and He I λ=5876 emission lines are used to estimate the accretion rates of T Tauri stars.

1.4.3 Regions studied in this thesis

In this thesis, I will study three star-forming regions, representing a range of different environments in which new stars can form: the sparse association ϵ Cha, the extended regions of star formation in small clusters and aggregates and also medium-sized clusters in the outskirts of Orion (the Lynds 1630-North and Lynds L1641 clouds), and a massive, dense young OB association Pismis 24. The ϵ Cha association contains two intermediate mass stars and a number of lower-mass objects, down to the sub-stellar regime. Any star is typically a long way from its nearest neighbor. In the L1641 cloud stars are formed both in relative isolation as well as in small clusters that are substantially more "crowded" than the ϵ Cha. Most of the young stars in the L1630N cloud are formed in either of the two clusters that dominate this region. Pismis 24 is by far the most "violent" environment that I studied, having the highest number density of stars and several early-O type causing an intense interstellar UV radiation field. A comparison of the disk properties in these very different environment offers a great chance for studying and understanding disk evolution in different environments.

(1) The ϵ Cha association

The ϵ Cha association, located at a distance of ~114 pc, was firstly discovered by Feigelson et al.

(2003), and named after the most massive member ϵ Chamaeleontis AB. The initial catalog of members in ϵ Cha consisted of 9 sources (Feigelson et al. 2003). A spectroscopic survey covering a region of $0.^{\circ}5$ in radius centered on ϵ Cha AB was performed by Luhman (2004b), identifying 3 possible new members. At an age of (3-5 Myr) the disks in the ϵ Cha association are expected to be in a very interesting evolutionary stage in terms of their dissipation (Feigelson et al. 2003). Studying the ϵ Cha associations offers great prospects to understand disk evolution, and thus to provide fundamental observational constraints on the timescale of planet formation.

(2) L1630N and L1641

The L1630 and L1641 clouds are located in the Orion molecular cloud complex at distances between 400 and 500 pc (Anthony-Twarog 1982; Hirota et al. 2007). L1630 lies in the northern part of the Orion complex (Orion B), and L1641 is located in the southern part (Orion A). Toward L1630, near-infrared surveys show that most young stars are found in four clusters, i.e. NGC 2023, NGC 2024, NGC 2068, and NGC 2071, rather than being uniformly distributed (Lada et al. 1991; Li et al. 1997). The clusters NGC 2068/2071 are located in the northern part of L1630 and named L1630N hereafter. In contrast to the L1630 region, the L1641 cloud harbors a large population of young stars existing in relative isolation, in addition to a population of stars in a number of clusters or aggregates (Strom et al. 1993; Allen 1995). Thus, a comparative study of disks around young stars in L1630 and L1641 offers the opportunity to study the effect of a clustered or isolated environment on the disk evolution.

(3) The massive cluster Pismis 24

Pismis 24 is located in the Sagittarius spiral arm and contains dozens of massive OB-type stars, with two extremely luminous members: Pis 24-1 and Pis 24-17 (O3.5 III) (Massey et al. 2001). Pis 24-1 is a triple system consisting of Pis 24-1 NE (unresolved spectroscopic binary) and Pis 24-1 SW (Maíz Apellániz et al. 2007). Pis 24-1 NE and Pis 24-1 SW have an estimated mass of around 100 $M_{\odot}$ each. The distance to Pismis 24 has been estimated in different ways, and ranges from ∼1-3 kpc (Wilson et al. 1970; Neckel 1978; Massey et al. 2001). A total of 779 X-ray sources have been found in the Pismis 24 region, of which 616 sources have associated optical or infrared counterparts (Wang et al. 2007). With an estimated age of ∼1 Myr (Massey et al. 2001) Pismis 24 is an extremely interesting laboratory for investigating the circumstellar disk evolution in the harsh environments in the vicinity of extremely massive stars. The similarly old and similarly dense Orion Nebula Cluster serves a and extremely well studied local reference.

Overview of this thesis

I have organized this thesis as follows:

- In Chapter 2 I investigate the disk properties of the members in the ϵ Cha association, and characterize the dust properties using Spitzer IRS spectra.
- In Chapter 3 I analyze our own observations and archive data of the L1630-North and L1641 star-forming clouds. The data include the photometric data in 13 bands between $\sim$0.4 μm and $\sim$24 μm, and optical spectroscopy performed with VLT/VIMOS. I use the data at $\lambda \lesssim 1.5$ μm to derive the properties of the central stars (mass, age) and the accretion rates, and the longer wavelength data to establish the presence and evolutionary state of the disks. I investigate relations between the stellar, disk, and accretion properties.
- In Chapter 4 I investigate the star-formimg region NGC 6357 with a special focus on the central cluster Pismis 24. I includes X-ray data from the literature, optical photometry and spectroscopy performed with VLT/VIMOS, HST archival data, infrared data from the literature as well as our own Spitzer imaging of the central cluster, and millimeter data. I study the global star formation in NGC 6357, and the stellar and disk properties of the central cluster Pismis 24.
- In Chapter 5 I summarize the results of my thesis work, and look ahead to research I wish to perform in the future.

Chapter 2

Disk properties in the ϵ Cha association

M. Fang, R. van Boekel, J. Bouwman, Th. Henning, W. A. Lawson, and A. Sicilia-Aguilar
to be submitted to A&A

The observational characterization of the structure and evolution of circumstellar disks is key to our understanding of the disk dissipation and planet formation processes. Nearby pre-main sequence (PMS) associations are well suited for detailed investigations of young stars and their disks, since their members can be observed with high signal-to-noise throughout the electromagnetic spectrum. Several PMS associations have been studied with the Spitzer Space Telescope, e.g. MBM 12, ϵ Cha, and η Cha (Meeus et al. 2009; Megeath et al. 2005b; Bouwman et al. 2006; Sicilia-Aguilar et al. 2009), using the IRAC (Fazio et al. 2004) and MIPS (Rieke et al. 2004) cameras, and the Infrared Spectrograph (IRS, Houck et al. 2004). The Spitzer data allow characterization of the disks around low-mass stars up to radii of ∼10 AU. The observed disk frequencies in the MBM 12 and η Cha associations suggest that disk dissipation proceeds more slowly in these sparse PMS associations compared to denser environments. MBM 12 has a disk frequency of ≈90% at an age of 2 Myr (Meeus et al. 2009) and in the 8 Myr old (Megeath et al. 2005b; Sicilia-Aguilar et al. 2009) η Cha association 40-50% of the stars still retain a disk. In the latter cluster, binarity was shown to play an important role in protoplanetary disk evolution (Bouwman et al. 2006).

Silicates are an important dust component in protoplanetary disks. The most convincing evidence that silicates are present in the protoplanetary disks is the strong "10 μm feature" in mid-infrared spectra of Herbig Ae/Be stars and T Tauri stars (Cohen & Witteborn 1985; Natta et al. 2000b; Bouwman et al. 2001, 2003; van Boekel et al. 2004, 2005). This feature is emitted by silicate grains with the sizes of up to several microns that reside in the optically thin surface layers of the disk (Chiang & Goldreich 1997). The shape and the strength of the 10 μm silicate feature were found to be correlated and this was interpreted as evidence for grain growth in disks (van Boekel et al. 2005; Kessler-Silacci et al. 2006; Bouwman et al. 2008). The Spitzer IRS Spectrograph has provided spectra of many young objects covering the wavelength range from 5.3 to 38 μm. Analysis of the spectral features in the Spitzer IRS spectra provides constraints on the chemical composition and grain sizes (see e.g. Henning 2010for a recent review). The dust properties derived from Spitzer IRS spectra of the members of the MBM 12 and η Cha associations suggest

that dust processing in the disks occurs very early, and that radial mixing is not efficient (Meeus et al. 2009; Sicilia-Aguilar et al. 2009).

Because the η Cha association is much younger than MBM 12 it is highly desirable to study an association an intermediate age in order to draw a more complete picture of disk evolution in sparse stellar associations. With an estimated age of 3-5 Myr (Feigelson et al. 2003), the ϵ Cha association well suited for this purpose. Located at a distance of ~114 pc, the ϵ Cha association was discovered by Feigelson et al. (2003) who identified 9 members. The most massive member, ϵ Cha AB, has a spectral type of B9. Luhman (2004b) have found 3 new members of ϵ Cha from a survey covering a region with a radius of $0\overset{\circ}{.}5$ around ϵ Cha AB. At 3-5 Myr the ϵ Cha association is younger than the η Cha group (5-10 Myr, Mamajek et al. 1999; Luhman & Steeghs 2004). Lawson et al. (2009) provide a model-independent way to rank the ages of the nearest PMS associations employing gravity-sensitive spectral features in optical spectra. They confirmed that the ϵ Cha association is younger than the η Cha and TW Hya associations.

In this Chapter we will investigate the disks surrounding the ϵ Cha members in terms of overall (geometry) evolution and dust mineralogy. We arrange this Chapter as follows. In section 4.1 we describe the observations and data reduction. In section 4.2 we present our results which are then discussed. We summarize our efforts in section 4.4.

2.1 Observations, data reduction and analysis

2.1.1 Targets

There are 12 stars reported as the members of ϵ Cha in the literature (Feigelson et al. 2003; Luhman 2004b). We collected the photometric and spectroscopic data of these stars that are available in the literature and list these in Tables 2.1, 2.2, and 2.3. For the 10 stars whose spectral types have been estimated we performed SED fits in the optical and near-infrared spectral range to derive the luminosity of each star and its line-of-sight extinction, using the method described in Chapter 3. We take a model atmosphere spectrum with a fixed effective temperature corresponding to the observed spectral type, and generate synthetic photometry with two free parameters: the visual extinction $A_{\rm V}$ and the stellar angular diameter θ. Both fit parameters are fine-tuned as to minimize the residuals between synthetic and observed optical and near-infrared photometry. We adopt a standard extinction law (Cardelli et al. 1989) with a total to selective extinction ratio of $R = 3.1$. We used all the available optical photometry and the near-infrared J- and H-bands. The bolometric luminosity of each star is then obtained by integrating the de-reddened model spectrum and adopting a distance of 114 pc. For the ϵ Cha AB, which is a double

system, we estimate the luminosity of the A component from its V-band magnitude (5.34 mag, Torres et al. 2008) which has corrected for duplicity. The resulting extinctions and luminosities are listed in Table 2.3.

Table 2.1: Optical and near-infrared photometry for members of the ϵ Cha association. Column 5: the B-band photometry of member ID#2,5 come from the Tycho-2 Catalogue (Høg et al. 2000); the B-band photometry for members ID#10,11,12 are calculated from B-I colors derived from low-resolution spectra by Lyo et al. (2008) and I-band photometry from the DENIS survey (Epchtein et al. 1997). Column 6: the V-band photometry of members ID#1,6,7,8,9 is taken from Feigelson et al. (2003); the V-band photometry of members ID#2,5 are from the Tycho-2 Catalogue (Høg et al. 2000); the V-band photometry of members ID#10,11,12 are derived using the V-I colors by Lyo et al. (2008) and DENIS I-band magnitudes. Column 7: the R-band photometry of members ID#1,6,7,8,9 is adopted from Feigelson et al. (2003), whereas the R-band photometry of members ID#10,11,12 are obtained using R-I colors from Lyo et al. (2008). Column 8: the I-band photometry for members ID#1,6,7,8,9 was obtained by Feigelson et al. (2003), whereas the I-band photometry for members ID#10,11,12 was taken from the DENIS survey (Epchtein et al. 1997). Column (9)(10)(11): the photometry for members ID#3,4,6,7 are for the J, H, and K bands and are teken from Grady et al. (2004). The photometry for other members comes from the 2MASS survey (Skrutskie et al. 2006).

(1)	(2)	(3)	(4)	(5)	(6)	(7)	(8)	(9)	(10)	(11)
		RA	DEC	B	V	R	I	J	H	K_s
ID	Name	(J2000)	(J2000)	(mag)	(mag)	(mag)	(mag)	(mag)	(mag)	(mag)
1	CXOU J115908.2-781232	11:59:07.98	-78:12:32.2	···	16.99	15.57[a]	13.83	12.01	11.45	11.17
2	ϵ Cha AB	11:59:37.53	-78:13:18.9	4.86[b]	4.91	···	···	5.02	5.04	4.98
3	HD 104237C	12:00:03.89	-78:11:31.0	···	···	···	···	15.28[c]	14.85[c]	14.48[c]
4	HD 104237B	12:00:04.76	-78:11:34.8	···	···	···	···	11.43[c]	10.27[c]	9.52[c]
5	HD 104237A	12:00:05.21	-78:11:34.4	6.86[b]	6.62[b]	···	···	5.81	5.25	4.59
6	HD 104237D	12:00:08.39	-78:11:39.2	···	14.28[a]	13.09	11.62	10.53[c]	9.73[c]	9.67[c]
7	HD 104237E	12:00:09.43	-78:11:42.2	···	12.08[a]	11.25	10.28	9.10[c]	8.05[c]	7.70[c]
8	USNO-B120144.7-781926	12:01:44.42	-78:19:26.8	···	17.18[a]	15.61	13.72	11.68	11.12	10.78
9	CXOU J120152.8-781840	12:01:52.52	-78:18:41.4	···	16.78[a]	15.29	13.52	11.63	11.04	10.77
10	2MASS J12005517-7820296	12:00:55.17	-78:20:29.7	19.61[d]	17.85[d]	16.08	14.00	11.96	11.40	11.01
11	2MASS J12014343-7835472	12:01:43.43	-78:35:47.2	20.17[d]	18.55[d]	17.15	15.96	14.36	13.38	12.81
12	2MASS J12074597-7816064	12:07:45.98	-78:16:06.5	17.68[d]	16.08[d]	14.74	13.11	11.55	10.98	10.67

Table 2.2: Infrared photometry for members in the ϵ Cha association. Column 4,5,6: taken from Grady et al. (2004). Column 7: taken from Luhman et al. (2010). Column 8,9,10,11,12,13: taken from the AKARI IRC Point Source Catalogue and FIS Bright Source Catalogue (Ishihara et al. 2010; Yamamura et al. 2010).

(1)	(2)	(3)	(4)	(5)	(6)	(7)	(8)	(9)	(10)	(11)	(12)	(13)
	RA	DEC	L'	M	11.9 μm	[24]	S9W	L18W	N60	WIDE-S	WIDE-L	N160
ID	(J2000)	(J2000)	(mJy)	(mJy)	(mJy)	(mJy)	(mJy)	(mJy)	(mJy)	(mJy)	(mJy)	(mJy)
2	11:59:37.53	-78:13:18.9	···	···	···	73.7	561.4	···	···	···	···	···
5	12:00:05.12	-78:11:34.7	9795.	9091.	14167.	···	13479.7	13000.1	10036.2	8600.1	5116.1	4531.8
6	12:00:08.30	-78:11:39.6	45.	···	···	···	···	···	···	···	···	···
7	12:00:09.32	-78:11:42.5	481.	329.	498.	1055.2	···	···	···	···	···	···
8	12:01:44.42	-78:19:26.8	···	···	···	15.4	···	···	···	···	···	···
9	12:01:52.52	-78:18:41.4	···	···	···	0.8	···	···	···	···	···	···
10	12:00:55.17	-78:20:29.7	···	···	···	15.5	···	···	···	···	···	···
11	12:01:43.43	-78:35:47.2	···	···	···	55.4	···	···	···	···	···	···
12	12:07:45.98	-78:16:06.5	···	···	···	0.9	···	···	···	···	···	···

Table 2.3: Stellar parameters for members in the ϵ Cha association. Column 4,5: taken from Luhman (2004b). Column 10: The EWs of Hα line for ID#1,2,5,6,7,8,9 come from Feigelson et al. (2003). The equivalent widths (EWs) of Hα line for ID#10,11,12 are estimated from the optial spectra presented in Lyo et al. (2008). Negative values indicate emission lines. Column 11: W for weak T-Tauri star, C for classical T-Tauri star, and H for Herbig Ae/Be star.

(1)	(2)	(3)	(4)	(5)	(6)	(7)	(8)	(9)	(10)	(11)	(12)	(13)	(14)	(15)	(16)
	RA	DEC		$T_{\rm eff}$	$L_{\rm bol}$	$A_{\rm v}$	mass	age	EW(Hα)		$\dot{M}_{\rm acc}$		$\mu_\alpha cos(\delta)$	μ_δ	
ID	(J2000)	(J2000)	Spt	(K)	($L_\odot$)	(mag)	($M_\odot$)	(Myr)	(Å)	Class	($M_\odot$ yr^{-1})	Disk	(mas/yr)	(mas/yr)	Member
1	11:59:07.98	-78:12:32.2	M4.75	3161	0.027	0	0.17	9.6	-6.2	W	···	N	-35.7±13.6	-5.8±13.6	Y
2A	11:59:37.53	-78:13:18.9	B9	10500	99.7	0	2.87	2.7	+13	···	···	N	-35.1±1.5	4.0±1.9	Y
3	12:00:03.60	-78:11:31.0	···	···	···	···	0.015	5	···	···	···	···	···	···	Y
4	12:00:04.00	-78:11:37.0	···	···	···	4.5	0.42	4	···	···	···	Y	···	···	Y
5	12:00:05.12	-78:11:34.7	A7.75	7648	42.8	0.91	2.53	3.2	-20	H	4.17E-07	Y	-36.9±1.4	-5.6±1.8	Y
6	12:00:08.30	-78:11:39.6	M3.5	3342	0.12	0	0.29	3.0	-3.9	W	···	N	···	···	Y
7	12:00:09.32	-78:11:42.5	K5.5	4278	0.92	1.0	0.90	2.1	-4.5	C	8.59E-10	Y	···	···	Y
8	12:01:44.42	-78:19:26.8	M5	3125	0.036	0	0.16	5.1	-23	C	1.49E-11	Y	-31.5±7.7	0.5±7.7	Y
9	12:01:52.52	-78:18:41.4	M4.75	3161	0.039	0	0.18	5.9	-7.8	W	···	N	-28±7.7	-34±7.7	?
10	12:00:55.17	-78:20:29.7	M5.75	3024	0.029	0	0.11	3.1	-23.7	C	1.05E-11	Y	-33.6±7.7	-2.2±7.7	Y
11	12:01:43.43	-78:35:47.2	M2.25	3524	0.0038	0	0.27	4	-192.4	C	···	Y	-43.1±8.8	-6.5±8.8	Y
12	12:07:45.98	-78:16:06.5	M3.75	3306	0.042	0	0.27	12.5	-7.9	W	···	N	-68.7±7.8	-17.9±7.7	?

2.1.2 VISIR imaging

We observed the HD 104237 system with VLT/VISIR on the night starting 2006 March 17 through the SiC filter, which transmits radiation between ~10.7 and ~12.9 μm. We employed standard chopping and nodding techniques to eliminate the high instrumental and atmospheric background emission, with a chop throw of 8″in the N-S direction and a nod throw of 8″in the E-W direction. We assessed the quality of the individual chop half-cycles (here referred to as ”frames”) by fitting a 2D Gaussian to the A component, which is detected at high SNR in each frame. We find that the quality of most frames is good, meaning the image of the A component is sharp and round. The median $FWHM$ of the 75% best frames is 0.″33 and we shift-and-add these into our final image with sub-pixel accuracy, using shifts determined by cross-correlation.

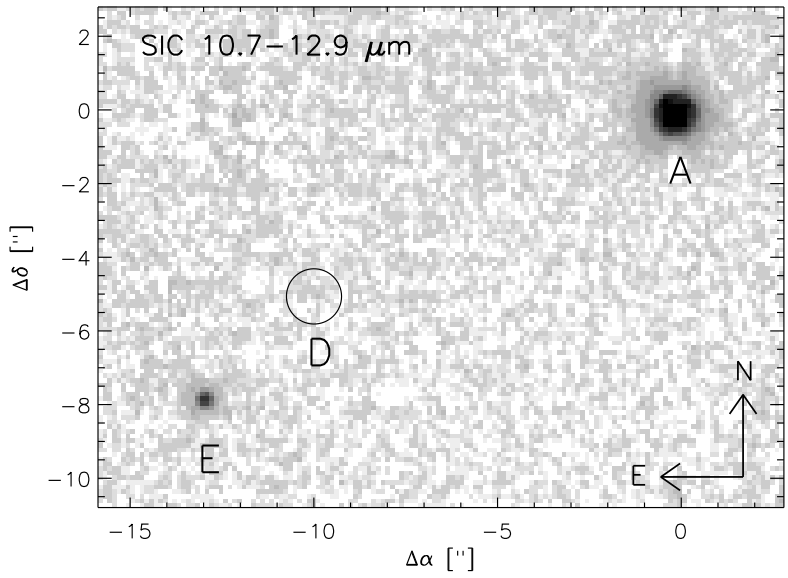

Figure 2.1: VLT/VISIR image of the HD 104237 region taken through the SIC filter, on a square root scaling from -0.1% to +6.5% of the peak flux of the HD 104237A component. The position of the HD 104237D component is indicated with a circle but there is no significant detection of this source. Coordinates are offsets in arcseconds with respect to HD 104237A.

In Fig. 2.1 we show our final VISIR image of the HD 104237 system. The A and E components, corresponding to sources 3 and 6 in Grady et al. (2004), respectively, are clearly detected. No sources are seen at the positions of the C and D components (source numbers 1 and 5 in Grady et al.). We have not attempted an absolute flux calibration of our VISIR data, but instead have performed PSF photometry on the D component, using the A component as the reference star. We find an A/E flux ratio of 23.4±0.4. To set the absolute flux scale we integrated the Spitzer spectrum of the A component over the transmission curve of the SIC filter. Assuming that the

spectrum of the E component is iso-photonic one obtains a flux of 551±10 mJy at 12 μm for this source. At the position of the D component we do not detect a source with confidence, and derive a 3σ upper limit of 18 mJy at 12 μm, again assuming an iso-photonic spectrum.

2.1.3 Spitzer IRS spectroscopy

The ϵ Cha members have been observed with Spitzer Space Telescope as a part of a larger programme aimed at studying the evolution of circumstellar disks in nearby associations (GO proposal 20691, PI: Bouwman). We obtained 7-35 μm low-resolution (R=60-120) spectra with the Infrared Spectrograph (IRS, Houck et al. 2004). The extracted spectra are based on the droopres products processed through the S18.7.0 version of the Spitzer data pipeline. Partially based on the SMART software package (Higdon et al. 2004), our data were further processed using spectral extraction tools developed by the "Formation and Evolution of Planetary Systems" (FEPS) Spitzer science legacy team (see also Bouwman et al. 2008). The spectra were extracted using a 6.0 pixel and 5.0 pixel fixed-width aperture in the spatial dimension for the observations with the first order of the short- (7.5-14 μm) and the long-wavelength (14-35 μm) modules, respectively. The background was subtracted using associated pairs of imaged spectra from the two nod positions along the slit, also eliminating stray light contamination and anomalous dark currents. Pixels tagged by the data pipeline as being "bad" were replaced with a value interpolated from an 8 pixel perimeter surrounding the errant pixel. Low-level fringing at wavelengths >20 μm was removed using the IRSFINGE package (Lahuis & Boogert 2003). To remove any effect of pointing offsets, we matched orders based on the point-spread function of the IRS instrument, thereby correcting for possible flux losses. The spectra are calibrated using a spectral response function derived from multiple IRS spectra of the calibration star 1 Doradus and a MARCS stellar model provided by the Spitzer Science Centre. The spectra of the calibration target were extracted in the same way as our science targets. The relative errors between spectral channels within one order are dominated by the noise in each channel and not by the calibration. We estimate the relative flux calibration within a spectral order to be good to ≈1% and the absolute calibration between different orders to be accurate to ≈3%, the uncertainty being dominated by mainly due to uncertainties in the scaling of the MARCS model.

We use the Two Layer Temperature Distribution (TLTD) spectral decomposition routines developed by Juhász et al. (2009, 2010) to investigate derive the mineralogical composition of the dust from the observed IRS spectra. The spectrum emitted by the optically thin surface layers of the disk is approximated by the following expression:

$$F_\nu = F_{\nu,\mathrm{cont}} + \sum_{i=1}^{N}\sum_{j=1}^{M} D_{i,j}\kappa_{\mathrm{i,j}} \int_{T_{\mathrm{a,max}}}^{T_{\mathrm{a,min}}} \frac{2\pi}{d^2} B_\nu(T) T^{\frac{2-qa}{qa}} dT \qquad (2.1)$$

where the different dust species in the model are denoted with subscripts *i* and for each species we include three different grain sizes, indicated with *j* subscripts. $\kappa_{\rm i,j}$ denotes the mass absorption coefficient of dust species *i* with grain size *j*. The abundances of each dust component are indicated by $D_{\rm i,j}$, $B_\nu(T)$ denotes the Plank function, and *qa* represents the exponent of the adopted power law temperature distribution. The disk atmosphere has a range of temperatures between the integration boundaries $T_{\rm a}$, and *d* denotes the distance between the star and Earth. $F_{\nu,\rm cont}$ denotes the continuum flux from the optically thick disk interior and is approximated by

$$F_{\nu,\rm cont} = D_0 \frac{\pi R_\star^2}{d^2} B_\nu(T_\star) + D1 \int_{T_{\rm r,max}}^{T_{\rm r,min}} \frac{2\pi}{d^2} B_\nu(T) T^{\frac{2-qr}{qr}} dT + D2 \int_{T_{\rm m,max}}^{T_{\rm m,min}} \frac{2\pi}{d^2} B_\nu(T) T^{\frac{2-qm}{qm}} dT \quad (2.2)$$

Here $R_\star$ and $T_\star$ are the radius and effective temperature of the star. The optically thick inner rim and midplane of the disk are assumed to have power law temperature distributions between the $T_{\rm r}$ and $T_{\rm m}$ boundaries, with exponents denoted by *qr* and *qm*. The D_0, D_1 and D_2 parameters denote scaling factors for the emission from the stellar photosphere, the hot inner rim, and the disk midplane, respectively.

Our dust model includes amorphous silicates with olivine and pyroxene stoichiometry, crystalline silicates forsterite, enstatite, and amorphous silica. For each species we include three grain sizes with radii of 0.1, 1.5, and 6.0 μm. We calculated the opacity curves for the amorphous species using MIE theory and those of the crystalline species using a Distribution of Hollow Spheres (DHS) approximation. The optical constants were taken from Servoin & Piriou (1973), Dorschner et al. (1995), Henning & Mutschke (1997), and Jaeger et al. (1998). To estimate the uncertainties in the derived abundances we apply a simple and well established Monte Carlo technique. We add normally distributed noise to the observed spectra with an amplitude given by the flux uncertainty in each spectral channel, and so generate 100 versions of each spectrum that are all consistent with the data. For each of these spectra we then perform the same compositional fit as described above, yielding 100 values for each fit parameter. The mean is then adopted as the best-fit value for each parameter and the standard deviation in the positive and negative directions yields the 1 σ uncertainty on each parameter. The fit results will be presented and discussed in Section 2.2.2(5).

2.2 Results and discussion

2.2.1 Stellar properties

In this section, we will first confirm the memberships of ϵ Cha using proper motion data, and then estimate the masses and ages of the members.

(1) Proper motions

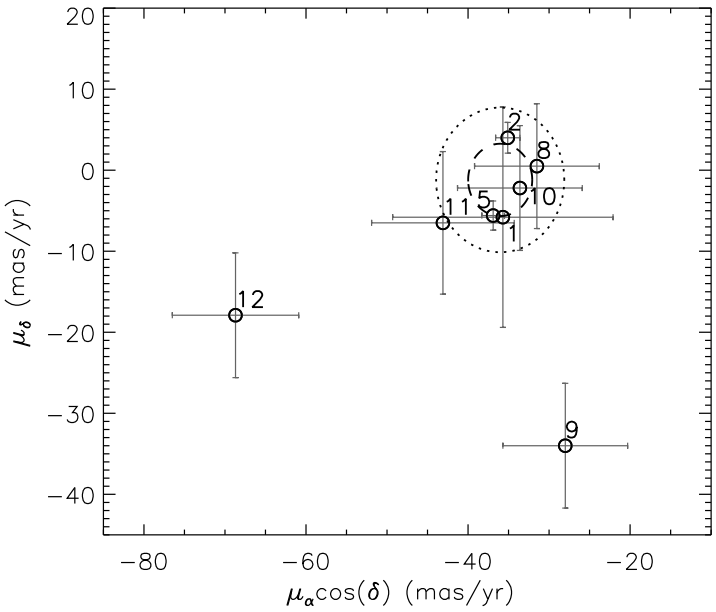

Figure 2.2: Proper motions of known stars in the ϵ Cha association taken from the catalogue by Roeser et al. (2010). The mean proper motions of the members and the 1 and 2 σ ellipses of the standard deviation of the distribution are shown with dashed-line and dotted-line curves, respectively.

Proper motions provide kinematic information of stars, which is often a very useful discriminant to separate members of a cluster or stellar association from unrelated field objects (see e.g. Rochau et al. 2010). Recently, Roeser et al. (2010) presented a new catalog of proper motions based in the International Celestial Reference System (ICRS) using a combination of USNO-B1.0 and 2MASS astrometry. This catalog provides proper motions of 8 ϵ Cha members, which are shown in Fig. 2.2 and listed in Table 2.3. It is clear that most stars have very similar proper motions, with the exception of the stars ID#9 and 12, which move in different directions. We calculate the weighted mean of the proper motions of the group members, excluding the latter

two sources, and find an average proper motion of μ_α=-36.0 mas/yr and μ_δ=-1.2 mas/yr, for the ϵ Cha association, corresponding to a projected linear velocity of ~19.5 km/s. The 1 and 2 σ error ellipses are also shown in Fig. 2.2. Since the stars with ID# 9 and 12 have proper motions that both differ $\gtrsim$3 sigma from the average group value, casting doubt on their membership of the ϵ Cha association. No proper motion estimates are available for the sources with ID# 3, 4, 6, and 7. Since these sources show X-ray emission and are spatially associated with HD 104237A, it is highly likely that they are ϵ Cha members. In summary, we confirm ten of previously identified members as the members of ϵ Cha, and challenge two stars, ID#9, 12 as the members of the association. The refined memberships of ϵ Cha are also listed in Table 2.3. We must stress that we cannot absolutely exclude ID#9, 12 as the ϵ Cha members. Both sources may be in the binary systemswhere their orbit motions can alter their proper motions. Moreover, the optical spectra of ID#9, 12 show strong Li absorption line, and present Na I and K I strengths, which are intermediate between those of dwarfs and giants (Luhman 2004b). And ID#9 is an X-ray emitter (Feigelson et al. 2003). All these suggest that both ID#9 and 12 are pre-main sequence stars. If ID#9 and 12 are unrelated with ϵ Cha, they could be the foreground pre-main sequence stars with ages older than ϵ Cha.

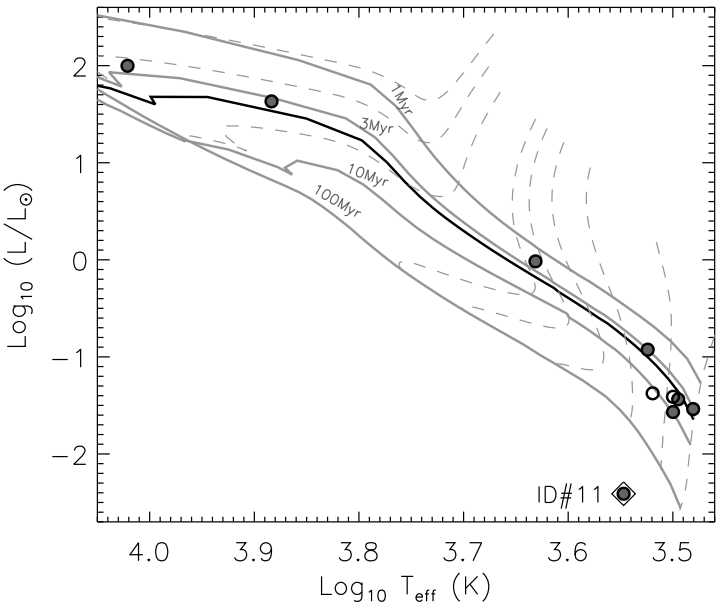

Figure 2.3: HR diagram of members (filled circles) of ϵ Cha. The open diamond marks the underluminous object ID#11. The grey lines are PMS isochrones of 1, 3, 10, and 100 Myr, and the dark line is the PMS isochrone of 4 Myr (Dotter et al. 2008). The dashed lines are the PMS evolutionary tracks for individual masses. The open circles are for stars ID#9 and 12, which have proper motions that deviate from the other stars and whose membership is less certain.

(2) The masses and ages of the ϵ Cha members

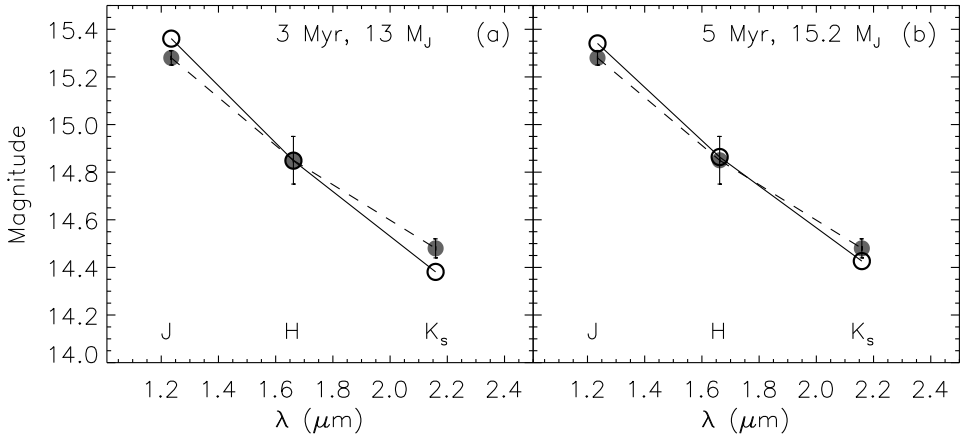

Figure 2.4: The observed photometry (filled circles) and model photometry (open circles) for HD 104237C in the J, H, and K_s bands. Panel (a) shows model photometry for a 13 M_{Jup} brown dwarf with an age of 3 Myr, panel (b) shows a model of a 15.2 M_{Jup} object of 5 Myr. The model photometry was adopted from Chabrier et al. (2000).

Fig. 4.8 shows the HR diagram of the sources in the ϵ Cha association, where the temperatures were adopted from the observed spectral types (Kenyon & Hartmann 1995; Luhman et al. 2003), and the luminosity was determined as described in Section 2.1.1. The masses and ages were then deduced by comparing the location of each object in the HR diagram with theoretical pre-main sequence evolutionary tracks (Dotter et al. 2008). For the probable non-members ID#9 and 12 were estimated assuming that they are at the same distance as the ϵ Cha association, but we note that if these objects are really unrelated, as we will further assume here, this not very meaningful

The resulting ages and masses for all stars are listed in Table 2.3. The ages of all the assumed members, with the exception of CXOU J115908.2-781232, are around 3-5 Myr, which is consistent with the previous estimate (Feigelson et al. 2003). The source ID#11 appears sub-luminous by a factor ~30 with respect to objects of similar spectral type placing it below the ZAMS and inhibiting a mass and age estimate through placement in the HR diagram. We estimated its mass from its spectral type (M2.25) by assuming an age of 4 Myr. For source HD 104237B (ID#4) there is no estimate of its spectral type. We estimated its mass from its position in the J vs. J-H color-magnitude diagram, assuming an age of 4 Myr and using model J and H magnitudes from Dotter et al. (2008). The results are listed in Table 2.3.

HD 104237C, located ~5.″3 to the North-West of HD 104237A, is a source of X-ray emission seen by Chandra (Feigelson et al. 2003) with a near-infrared counterpart (Grady et al. 2004). At a distance 116 pc, the projected distance between HD 104237C and HD 104237A is ~612 AU. Fig. 2.4 shows the observed photometry for HD 104237C in the J, H, and K_s bands from Grady

et al. (2004). Since no spectral type estimate is available for HD 104237C we estimate its mass by comparing the observed near-infrared photometry to model photometry for young brown dwarfs at ages of 3 and 5 Myr Chabrier et al. (2000). The best-fit masses for the assumed ages, and the assumed distance of 116 pc, are 13.0 and 15.2 Jupiter masses, respectively. We will adopt these numbers as the mass range for HD 104237C, putting this object at the boundary between a very low mass brown dwarf and a "free-floating planet". Of the currently known members of the ϵ Cha association, HD 104237C has by far the lowest mass.

2.2.2 Disk properties

In this section we will first estimate the rates at which material is accreted onto the central stars in the ϵ Cha member systems, and then characterize their disks in terms of evolutionary state. Finally, we will derive the dust properties of those protoplanetary disks that show emission from silicate dust in their IRS spectra, and compare them with the dust properties found for protoplanetary disks in other sparse stellar associations or clusters.

(1) Accretion

We estimated the accretion rates from the observed Hα emission-line luminosity using the empirical relation between the latter quantity and the accretion luminosity derived in Chapter 3:

$$log(L_{\rm acc}/L_{\odot}) = (2.27 \pm 0.23) + (1.25 \pm 0.07) \times log(L_{\rm H\alpha}/L_{\odot}) \quad (2.3)$$

The inferred accretion luminosities are then converted into mass accretion rates using the following relation:

$$\dot{M}_{\rm acc} = \frac{L_{\rm acc} R_{\star}}{G M_{\star} (1 - \frac{R_{\star}}{R_{\rm in}})}, \quad (2.4)$$

where $R_{\rm in}$ denotes the truncation radius of the disk, which is taken to be 5 $R_{\star}$ (Gullbring et al. 1998). G is the gravitational constant, $M_{\star}$ is the stellar mass as estimated from the location of each star in the HR diagram, and $R_{\star}$ is the stellar radius derived using the SED fitting procedure described in Section 2.1.1. There are four sources in ϵ Cha showing signs of active accretion and their accretion rates are listed in Table 2.3.

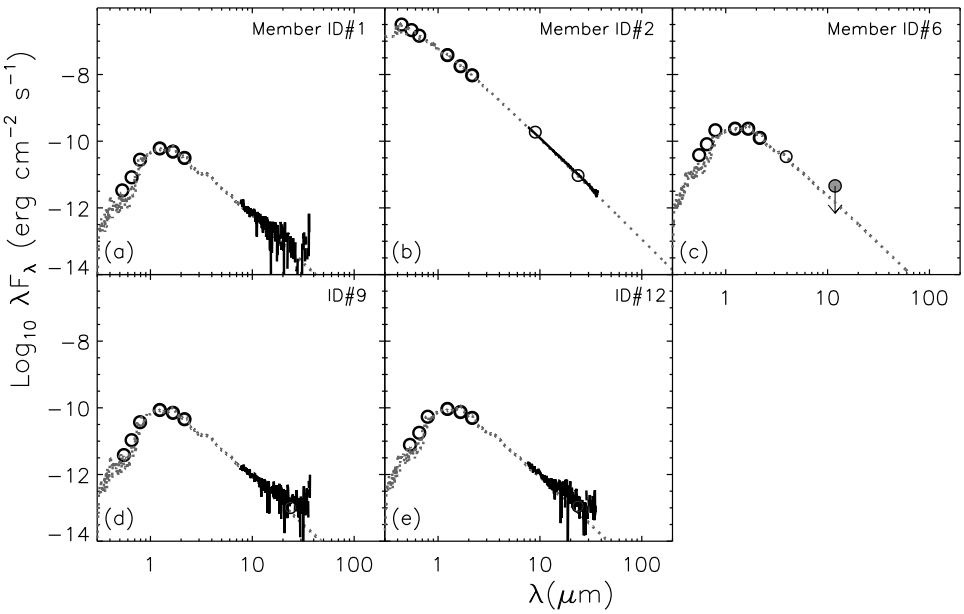

Figure 2.5: SEDs of apparently diskless stars. The photospheric emission level is indicated with a grey dotted curve in each panel. The circles show the photometry in different bands. The filled circle show the upper limit derived from our VLT/VISIR imaging for ID#6. The thick solid lines in panels a), b), d) and e) show the Spitzer IRS spectra.

(2) Demographics of disk population in ϵ Cha

In Figs. 2.5, 2.6, and 2.7(b), we show the spectral energy distributions (SEDs) of the 10 sources for which spectral types are available, together with the best-fit stellar model atmospheres (see Sect 2.1.1). In total we have detected 9 sources with the Spitzer IRS. Among these, 7 were confirmed as members of the ϵ Cha based on common proper motion in Section 2.2.1(1). Two of the members, CXOU J115908.2 (ID#1) and ϵ Cha AB (ID#2), do not show significant excess emission over the stellar photosphere in the IRS spectral range. Also both stars whose memberships were challenged based on their proper motions, ID#9 and 12, do not show infrared excess emission in the IRS spectra, strongly suggesting that they do not (any longer) harbor circumstellar disks. For the sources that were not detected with the IRS we characterized their disks based on infrared photometric data only. The source HD 104237D (ID#6) cannot be spatially separated from HD 104237A with the IRS and MIPS instruments due to the comparatively poor spatial resolution of the Spitzer Space telescope at long wavelengths. In our VISIR imaging at 12 μm HD 104237D is not detected and we derived a 3σ upper limit of $\sim$18 mJy for its flux at this wavelength. This upper limit is just above the expected photospheric emission level as extrapolated from shorter wavelengths and shown in Fig. 2.5, indicating that HD 104237D has no disk any longer, though the possibility of an evolved disk with a large inner hole that would be

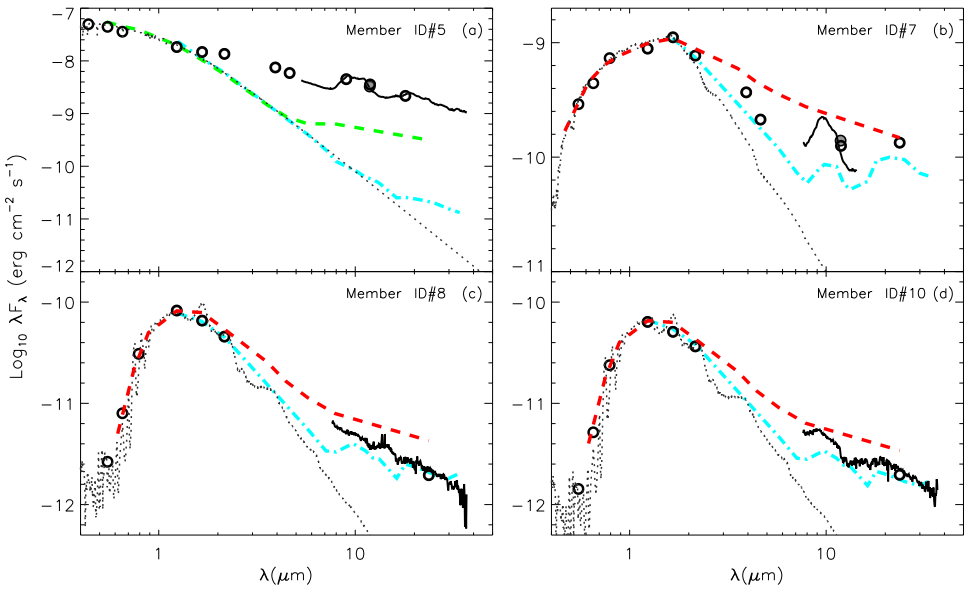

Figure 2.6: SEDs of the disk population in ϵ Cha. The photospheric emission levels are indicated with a grey dotted curves in each panel. The circles show the photometry in various bands. The filled circles show the photometry from our VLT/VISIR imaging. The solid lines show the IRS spectra in each panel. In panel(a), the dashed line represents the median SED of the disk population around stars with A-F spectral types in IC 348(2-3 Myr) (Lada et al. 2006). The dashed lines in other panels show the median SEDs of the disk population around stars with spectral types of b) K6-M0, c) M1-M4, and d) M5-M6 in L1641 (~1 Myr, distributed population, see Chapter 3). The dash-dotted lines show the median SEDs of the disk population with spectral types a) B9-A9, b) K5-M2, c) and d) M3-M5 in upper Scorpius (~5 Myr) (Dahm & Carpenter 2009a).

observable only at longer wavelengths cannot be excluded based on the currently available data. The underluminous object 2MASS J12014343 (ID#11) shows a very flat SED, which is similar to the SEDs of similarly underluminous objects discovered in other star formation regions (see Chapter 3). For sources HD 104237B (ID#4) and HD 104237C (ID#3), we only have photometry in JHK$_s$ bands. The [J-H] vs. [H-K$_s$] color-color diagram shows only HD 104237B to still have near-infrared excess emission indicative of a hot, optically thick inner disk (Grady et al. 2004).

In Fig. 2.6(a) we show the SED of HD 104237A, which exhibits strong excess emission at wavelengths beyond ~2 μm. HD 104237A therefore shows clear evidence for a hot, optically thick inner disk. For comparison we also show the median SEDs of disk population for early spectral type stars in IC 348 and upper Scorpius (Dahm & Carpenter 2009a; Lada et al. 2006) in Fig. 2.6(a). HD 104237A (~3 Myr) may be slightly younger than upper Scorpius (~5 Myr) and slightly older than IC 348 (~2-3 Myr). However, the SED of HD 104237A is very different from

the median SED of both aforementioned regions. The average object in IC 348 shows excess emission at wavelengths of $>\sim 5\,\mu$m, suggesting that an inner hole has been formed in its disk. A similar behavior is seen in upper Scorpius but with the excess emission starting only at $\sim 20\,\mu$m, indicative of larger inner holes. Even though HD 104237A is not of substantially different in age than IC 348, its SED shows much stronger excess emission starting from a much shorter wavelength. Since HD 104237A is the only early-type star in the ϵ Cha association, drawing any firm conclusions from this observation is premature. Still, what we see indicates that the disk surrounding HD 104237A evolved more slowly than the disks around early type stars in IC 348. This is consistent with the notion that disk dissipation due to stellar encounters, which is predicted to be particularly effective for early type stars (Pfalzner et al. 2006), has been important in IC 348 but not in the ϵ Cha group, due to the very different space number densities of stars in both environments.

In Figs. 2.6(b), (c) and (d), we show the SEDs of group members HD 104237E (ID#7), USNO-B120144.7 (ID#8), and 2MASS J12005517 (ID#10), as well as the median SEDs of objects with similar spectral types in L1641 ($\sim$1 Myr, Chapter 3) and upper Scorpius ($\sim$5 Myr, Dahm & Carpenter 2009a). Overall the is a clearly decreasing trend in the level of infrared excess emission with increasing age, from L641 to ϵ Cha to upper Scorpius. It can also be seen that the excess emission in the MIPS 24 μm band of source ID#7 (spectral type K5.5) is similar to the median SED of L1641 whereas its infrared excess at shorter wavelengths is substantially lower and intermediate between the median SEDs of L1641 and upper Scorpius. This indicates that source ID#7 has started to dissipate its inner disk while its outer disk remains relatively intact. In contrast to object ID#7, the very low-mass objects ID#8 and 10 show a fairly uniform depletion of the SED, with an infrared excess emission level that has been reduced by a similar factor across the whole IRS spectral range compared with the median SED of L1641.

Spitzer observations of clusters with ages of several Myrs, such as IC348, NGC2362, and η Cha, suggest that, qualitatively, two evolutionary paths exist for going from a primordial to a debris disk configuration (Lada et al. 2006; Currie & Kenyon 2009; Currie et al. 2009; Sicilia-Aguilar et al. 2009; Currie 2010). Each path shows a characteristic behavior of the SED: (1) some objects show little or no excess emission in the shorter IRAC bands and strong excess emission at $24\,\mu$m, suggesting that disks are dissipated in an inside out fashion; (2) some objects show infrared excess of an approximately uniformly reduced magnitude compared to primordial disks over all wavelengths out to 24 μm, suggesting a reduction of the effective disk height, i.e. the height above the disk midplane where the disk becomes optically thick to the stellar radiation. A reduced disk height causes a smaller fraction of the energy produced by the star to be absorbed and reprocessed by the disk, and thereby yields an infrared excess of reduced magnitude. This may occur if dust coagulation takes place in the disk, causing the grains to couple somewhat less well to the gas and allowing them to settle towards the midplane. How effective this is depends

also on the level of turbulence in the disk, in a disk with low turbulence grains settle more easily. In ϵ Cha, source ID#7 shows an SED reminiscent of the first type of disk evolution, whereas sources ID#8 and 10 show an SED corresponding to the second scenario. Both latter sources show strong evidence of dust growth, which seems to have progressed particularly far in source ID#8 judging from the absence of silicate features at ~10 and 20 μm, indicating that there is no substantial population of dust grains with sizes of $\lesssim$10 μm left in the atmosphere of this disk. It is interesting to note that source ID#7, showing evidence for an inside-out disk clearing, has a silicate feature emitted by predominantly small, sub-micron sized grains.

(3) 2MASS J12014343: a disk system with high inclination?

When inspecting the HR diagram of the ϵ Cha sample (Fig. 4.8) one object stands out in the sense that it lies well *below* the ZAMS. Compared to ~4 Myr old stars with the same spectral type, 2MASS J12014343-7835472 (ID#11) appears underluminous by a factor of ~30. Since evidence of group membership is strong (X-ray emission, optical emission lines, infrared excess, and in particular a proper motion in agreement with the ϵ Cha group, see Section 2.2.1(1)) its underluminosity cannot be simply explained as ID#11 being a background star. To understand its nature we should resort to other explanations. In Fig. 2.7(a), we show the optical spectrum of ID#11, on which Balmer emission lines and forbidden oxygen emission lines with very high equivalent widths are seen. Source ID#11 also shows a particularly strong infrared excess (Fig. 2.7(b)). Objects with these characteristics have been found in other star forming regions, e.g. Lupus 3 dark cloud, Taurus, L1630, and L1641 (Comerón et al. 2003; White & Hillenbrand 2004; Chapter 3). One possible explanation for this phenomenon is that these sources are systems harboring flared disks with moderately high inclinations where the stellar photospheric light is largely absorbed by the material in the cold, flared outer disk. We still receive photospheric light but at least a large fraction of the light we see is scattered off the disk surface and has a much reduced total flux. The optical emission lines of large equivalent width may arise in an outflow or disk wind. They need not intrinsically be brighter than in similar objects with "normal" apparent luminosities; it the reduced strength of the continuum flux, not the intrinsic line strength, that causes the *equivalent widths* to be high. This scenario only works if the line forming region is much larger than the central star, such that at least part of the line flux reaches us relatively unhindered while the photospheric continuum is strongly absorbed. In particular, this scenario also explains why some of these apparently underluminous objects show some emission lines like He I 5876Å, and the Ca II near-infrared triplet (8498, 8542, and 8662 Å) with equivalent widths that appear *not* enhanced (see Comerón et al. 2003; Chapter 3): these lines are mainly formed in the magnetospheric infall flows (Muzerolle et al. 1998a), which are close to the stellar surface and should be as much occulted as the photospheric continuum.

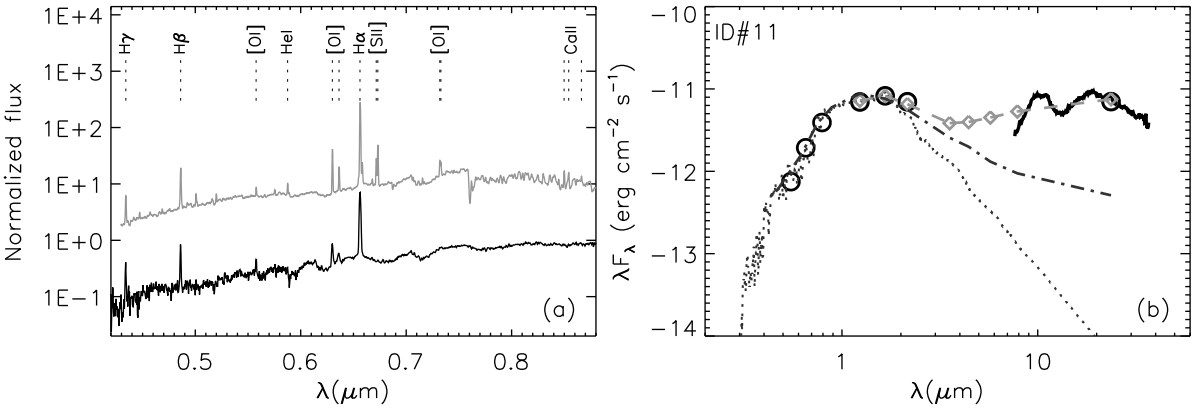

Figure 2.7: The optical spectrum and SED of 2MASS J12014343 (ID#11). (a) the optical spectrum of source ID#11 (black) and of a similarly underluminous object in L1641 (L1641-ID#122, Chapter 3). (b) The SED source ID#11. The photospheric emission level is indicated with a grey dotted curve. The open circles show the broad band photometry of ID#11, and the IRS spectrum of this source is shown in black. The photometry of underluminous source L1641-ID#122 is shown with the grey diamonds and dashed line for comparison and shows striking resemblance to that of ID#11. The dash-dotted line presents the median SED of the distributed disk population in L1641 (Chapter 3).

In Fig. 2.7 we also compare the optical spectrum and SED of source ID%11 with an object that shows very similar characteristics, that was recently found in the Lynds 1641 cloud in Orion (ID#122, named L1641#122 hereafter, see Chapter 3). L1641#122 is also apparently underluminous compared to stars of similar spectral type in the same cloud by a factor of ∼30, similar to ID#11. But, contrary to ID#11 it shows the He I 5876Å, [S II] and Ca II near-infrared triplet (8498, 8542, and 8662 Å) in emission, indicating active accretion. The optical spectrum of ID%11 did not show signs of active accretion at the time of observation. In Fig. 2.7(b), we compare the median SED of the distributed disk population in L1641 (L1641D) and that of L1641#122 (Chapter 3) with the SED of ID#11. From this comparison we can see that the infrared SEDs of ID#11 and L1641#122 are remarkably similar, and both underluminous objects show much stronger mid-infrared excesses than the average source in L1641, even though the L1641D population is much younger (∼1 Myr) than ϵ Cha.

(4) The disk and accretor frequencies in ϵ Cha

In order to estimate the disk frequency in ϵ Cha, i.e. the fraction of sources that shows evidence for a circumstellar disk in the form of infrared excess emission, one needs to identify all members of the ϵ Cha association and characterize their infrared SEDs. This is a challenging task since the

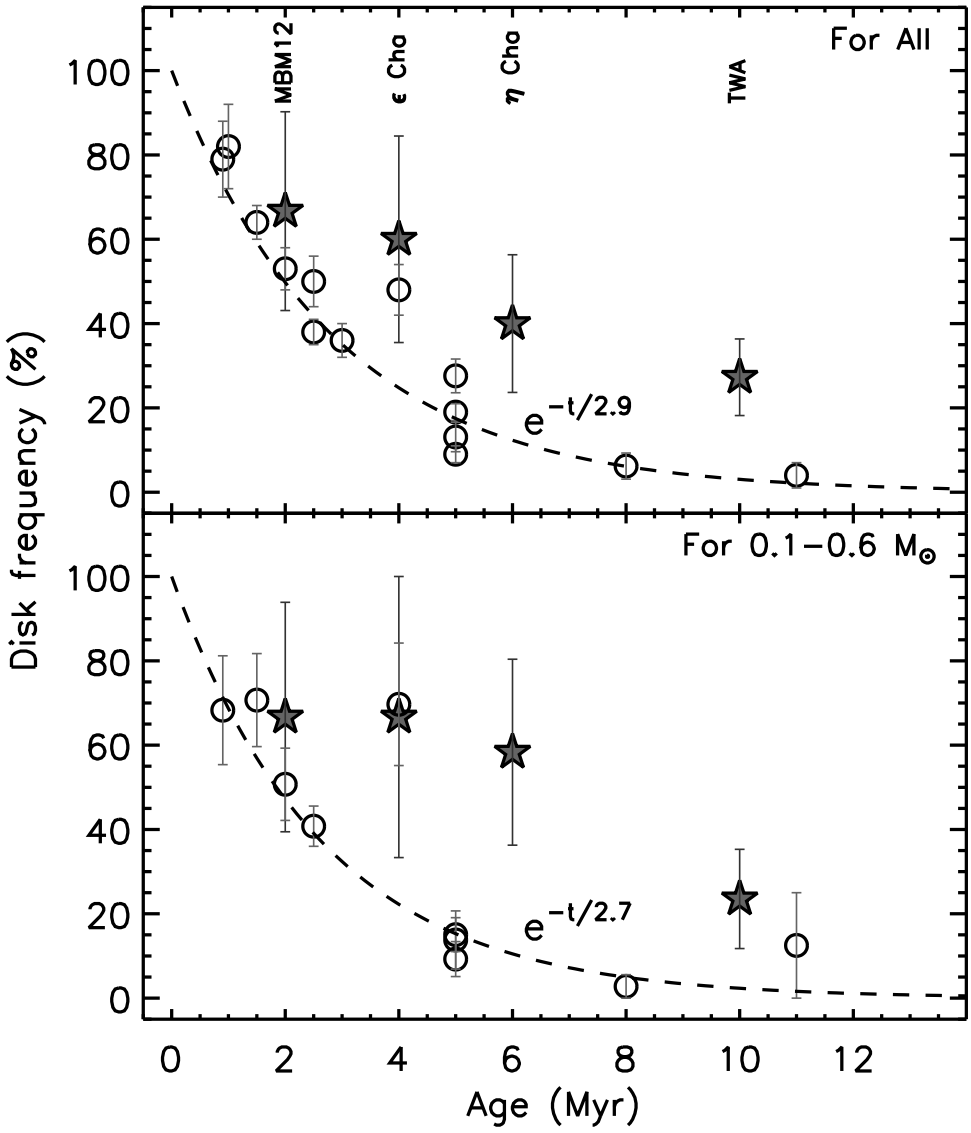

Figure 2.8: The disk frequencies for different clusters/star-forming regions (SFRs) plotted as a function of their ages. In panel (a) we plot the disk frequency among all known members, in panel (b) we show only the low-mass (0.1-0.6 $M_{\odot}$) population. The filled pentagram represent the sparse stellar associations MBM 12, ϵ Cha, η Cha, and TW Hya. The open circles show the disk frequencies in other clusters/SFRs (see Appendix (1) for a detailed description). In each panel, the dashed line represents the best fit exponential decay for all regions, excluding the four sparse associations. We find best fits of the form $f_{\rm d}$=e$^{-t/2.9}$ in panel (a), and $f_{\rm d}$=e$^{-t/2.7}$ in panel (b), where t is in units of Myr.

ϵ Cha association is spread over a large area of the sky, and a full inventory is beyond the scope of the current work. Instead, we restrict ourselves to the region within a radius of 0°.5 of ϵ Cha AB. This part of the sky has been surveyed by Luhman (2004b) and our knowledge of the association can be considered to be essentially complete here. As discussed in Section 2.2.1(1), there are 10 members in this region confirmed by proper motion. In Figs. 2.5, 2.6, and 2.7, we show the spectral energy distribution of 8 members with published spectral types. Among these, 5 objects show excess emission at near- or mid-infrared wavelengths and thus are harboring circumstellar disks. We include also HD 104237C, which shows excess emission at K_S bands according to Grady et al. (2004), and obtain a disk frequency among the 10 members of ϵ Cha association of 60±24% (6/10). This is quite high for a 3-5 Myr old population, though this value is clearly subject to low-number statistics and it is premature to conclude that the disk frequency in ϵ Cha is high based on these data alone. However, as we will see later in this section, the three other sparse associations of which we estimated the disk frequencies, MBM 12, η Cha, and TW hya, show a similar trend, and the ensemble of data provides strong evidence that disk lifetimes in sparse associations are longer than those in more crowded environments.

In Fig. 2.8 we illustrate this by showing the estimated disk frequencies in the aforementioned sparse associations and a number of other star-forming regions, as a function of their age (see Appendix (1) for a detailed description). Figure 2.8 also shows a fit to the observed disk frequencies of all regions, *except* the four sparse associations, of the form $f_{\rm disk}$=exp(-t/τ_0). We find a value of $\tau_0 = 2.9$ Myr to yield a very good fit to the overall distribution. This agrees well with the value of ∼2.9 Myr found by Fedele et al. (2010) in an earlier, similar study. Because the disk lifetime in any given environment may depend on the mass of the central star (e.g. Kennedy & Kenyon 2009) it is useful to investigate the low-mass population separately. In Fig. 2.8(b) we show the disk frequency among stars with estimated masses in the 0.1−0.6 $M_\odot$ range, for the same star forming regions as shown in Fig. 2.8 but including only those for which the low-mass population has been characterized. We find essentially the same typical disk dispersal time as for the whole mass range ($\tau_0 = 2.7$ Myr), and again the sparse associations are deviant in the sense that they show systematically higher disk frequencies.

To estimate the accretor frequency, i.e. the fraction of members that shows signs of active accretion, we turn to the Hα line as a diagnostic. Estimates of the Hα equivalent width are available for 8 of the ϵ Cha members, of which 5 are classified as accretors according the criteria in Chapter 3. This brings our estimate of the accretor frequency in ϵ Cha to 63±28%, again obviously subject to low-number statistics. Fedele et al. (2010) investigated the age-dependency of accretor frequency, and derive an empirical relation $f_{\rm acc}$=$e^{-t/2.3}$, where t is in units of Myrs, by fitting an exponential profile to the observed accretor frequencies of a number of star forming regions. For ϵ Cha, aged 3-5 Myr, the empirical relation predicts an accretor frequency of 27-11%, substantially below the observed value.

In conclusion, we can state that the disks around stars in sparse associations evolve more slowly than those in denser environments.

(5) The dust properties of disks

We have used the Two Layer Temperature Distribution (TLTD) spectral decomposition method developed by Juhász et al. (2009) to analyze our IRS spectra of the ϵ Cha members. In this section, we will first present the derived dust properties of the protoplanetary disks in ϵ Cha. Then, we will join the ϵ Cha sample with a collection of cool T Tauri stars in the MBM 12 and η Cha associations and the Coronet cluster, for which IRS spectra have been previously analyzed using identical methods. The combined data set is then used to do a statistical study on the dust properties of protoplanetary disks around the cool stars.

(a) The IRS spectra of the ϵ Cha disks

There are five ϵ Cha members for which we have IRS spectra that show evidence for a protoplanetary disk. Four of these show the well known silicate feature between 8 and 13 μm in emission (ID#5,7,10,11, see Fig. 2.9). Before using the TLTD routines to derive the dust composition we divide the IRS spectra into a "short" (7-17 μm) and a "long" (17-37 μm) wavelength regime, which are analyzed independently. Since the short wavelength part of the spectrum is dominated by warm disk regions closer to the central star than the cooler regions that dominate long wavelength data, we can thus search for radial gradients in the dust properties.

The derived dust properties are listed in Tables 2.4 and 2.5. In Table 2.4, we list the outcome of the fits in terms of mass abundances of the different species. In Table 2.5, we give the mass-averaged grain sizes of the amorphous and crystalline silicates, and fractional contribution of the crystalline species to the total dust mass present in the optically thin disk atmosphere. As shown in Table 2.5, the crystalline fractions of the objects in ϵ Cha are comparable to the those of the young stars with similar spectral type in the literature (Sicilia-Aguilar et al. 2008, 2009; Meeus et al. 2009; Juhász et al. 2010), with the exception of source ID#10 whose spectrum is best reproduced with exceptionally highly crystalline dust. Also, in the warm disk regions, the dust grains of our objects typically show typical larger sizes than those in interstellar medium (ISM), suggesting dust growth in these regions.

We will now briefly describe the individual objects:

HD 104237A (ID#5) Juhász et al. (2010) fitted the IRS spectrum of this object using amorphous dust with olivine and pyroxene stoichiometries, and silica, with grain sizes of 0.1, 2.0, 5.0 μm, with crystalline species forsterite and enstatite with grain sizes of 0.1 and 2.0 μm, and with

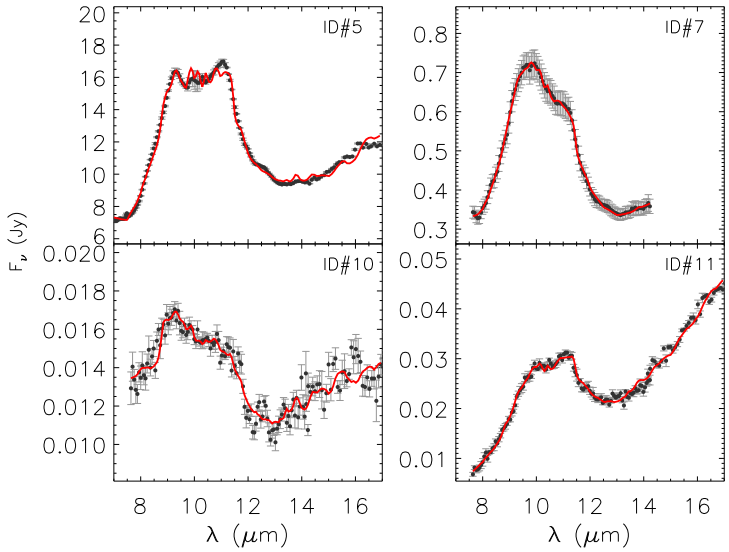

Figure 2.9: The 10 μm Silicate features fitted using the Two Layer Temperature Distribution method (solid red lines). The observed spectra are represented as filled circles with the errors in gray.

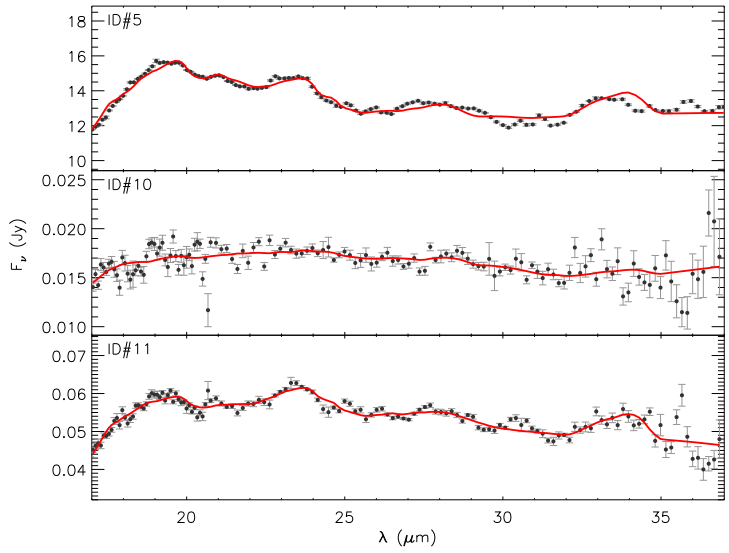

Figure 2.10: IRS spectra in the 17-37 μm range and spectral fits using the Two Layer Temperature Distribution method. The observed spectra are represented as filled circles with the errors in gray whereas the fits are shown in red.

Polycyclic Aromatic Hydrocarbons (PAHs). They divided the IRS spectrum into two sections: 5-17 μm and 17-35 μm, which are similar to those we use. From the short wavelength part they derived mass-averaged grain sizes of the amorphous and crystalline silicates, which are 4.6 μm and 1.4 μm, respectively, and a mass fraction of 9.5% in crystalline silicates. In the long wavelength part of the spectrum they find 0.1 μmand 0.4 μm for the mass-averaged grain size and 7.1% for the crystallinity. Even though we use a slightly different set of grain sizes in our fit, our results agree well with those derived by Juhász et al. (2010), with the exception of the mass-averaged grain size of the amorphous silicates derived from the long wavelength channel where we find a somewhat higher value. This may be due to the fact that the mass absorption coefficients of amorphous silicates with sizes of 0.1 and 1.5 μm are very similar in the 17-37 μm spectral range.

2MASS J12005517 (ID#10) We find that the spectrum of this object is best reproduced using an extraordinarily high mass fraction of crystalline silicates of ~82%. This may be a contrast effect: because of the very low luminosity of ID#10 its 10 μm silicate feature arises mainly in the inner ~0.5 AU of the disk. The central regions of disk can be highly crystalline (van Boekel et al. 2004), possibly leading to very high apparent crystallinities if only the very central disk regions contribute to the part of the spectrum used in the mineralogical analysis (see also Apai et al. 2005). In Fig. 2.11 we compare the IRS spectrum of ID#10 in the 7.8-14.3 μm spectral range with the mass absorption coefcients of enstatite and amorphous silicates with different grain sizes. The spectral signature of enstatite is clearly present in the spectrum of ID#10.

2MASS J12014343 (ID#11) As discussed in Section 2.2.2(3), source (ID#11) may be harboring a disk with a high inclination. Therefore, the IRS spectrum of ID#11 can be moderately reddened by the cold outer disk. In order to deredden the spectrum we would need to know the magnitude of the extinction and the proper extinction law at the mid-infrared wavelengths, both of which are not well known. We therefore applied no reddening correction, took the observed spectrum at face value, and fed it to the TLTD routines. Since the TLTD routines only work properly for low-extinction sources our results for source ID#11 should be regarded as tentative.

USNO-B120144.7 (ID#8) The luminosity and spectral type of this source are similar to those of ID#10. Both sources also show similar accretion activity (see Table 2.3), and show similar SEDs (see Fig. 2.6). However, in contrast to ID#10 the IRS spectrum of ID#8 does not show a silicate feature around 10 μm (see Fig. 2.11). This suggests that the silicates in the warm disk atmosphere of ID#8 have grown to larger sizes than those ID#10's disk. In the IRS spectrum of ID#8 we clearly detect the C_2H_2 rovibrational band at ~13.7 μm, but do not find the HCN rovibrational band at ~14.0 μm (see Fig. 2.11). This is consistent with what Pascucci et al. (2009) discovered in Spitzer spectra of other other cool stars, namely that the C_2H_2/HCN ux ratios from cool star disks are large with a median of ~3.8, which is an order of magnitude higher than the median C_2H_2/HCN ux ratio in spectra of disks surrounding sun-like stars (~0.34).

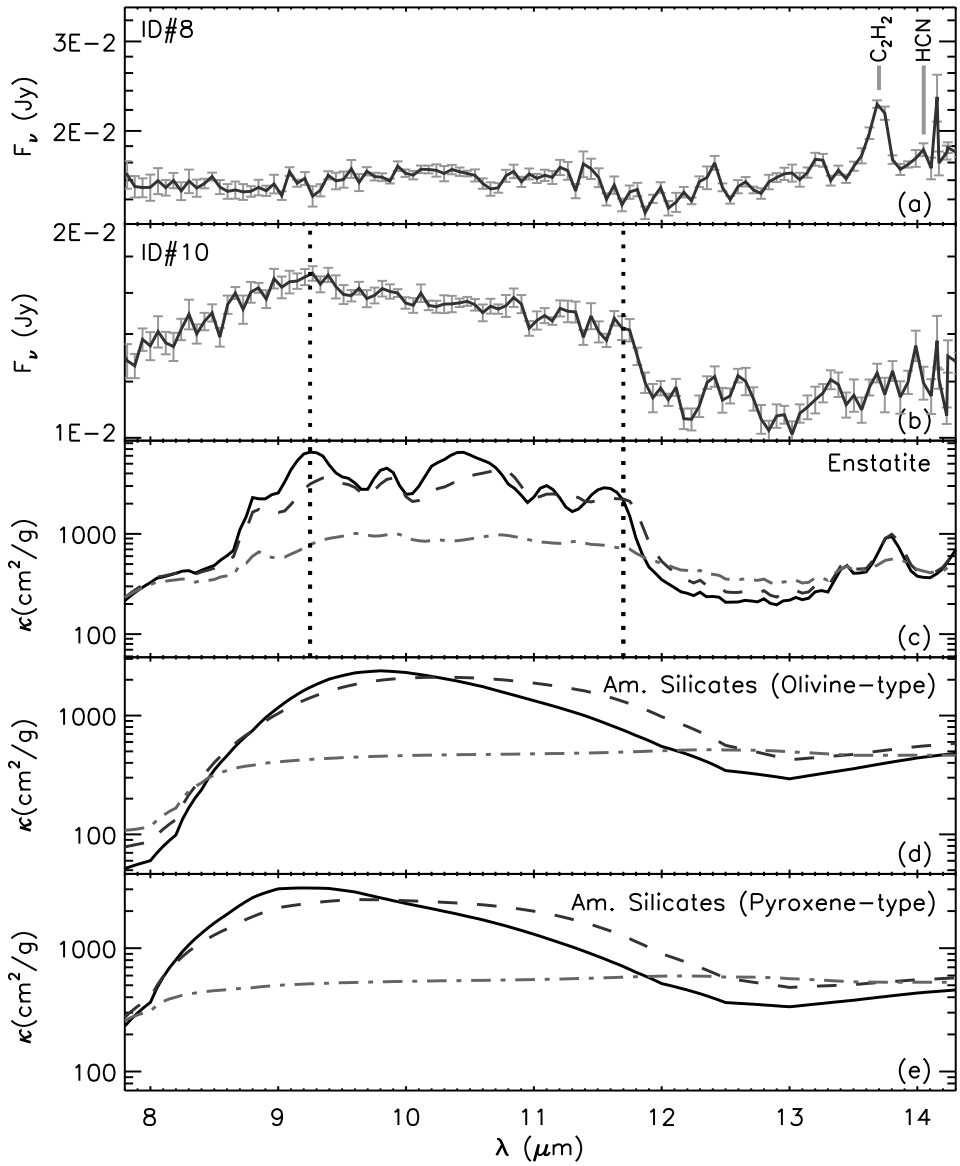

Figure 2.11: (a)The IRS spectrum of source ID#8. The positions of the C_2H_2 and HCN rovibrational bands are marked. (b)The IRS spectrum of the source ID#10. The dashed lines mark the features of enstatite. c), d) and e): The mass absorption coefcients of enstatite and amorphous silicates (with olivine and pyroxene stoichiometry) with grain sizes of 0.1 μm(solid lines), 1.5 μm(dashed lines), and 6.0 μm(dash-dotted lines). The dotted lines in panels (b) and (c) are identical.

Table 2.4: Silicate dust compositions deduced from the IRS spectra of ϵ Cha members, using the Two Layer Temperature Distribution spectral decomposition method.

		Am. (Olivine-type)			Am. (Pyroxene-type)			Forsterite			Enstatite			Silica		
ID	χ^2	0.1 μm	1.5 μm	6.0 μm	0.1 μm	1.5 μm	6.0 μm	0.1 μm	1.5 μm	6.0 μm	0.1 μm	1.5 μm	6.0 μm	0.1 μm	1.5 μm	6.0 μm
Short wavelength																
5	141.2	...	$0.1^{+0.3}_{-0.1}$	$28.9^{+2.5}_{-2.9}$	...	$18.1^{+1.4}_{-1.3}$	$39.7^{+1.8}_{-1.9}$	$2.8^{+0.3}_{-0.3}$	...	$0.6^{+0.9}_{-0.5}$	$0.1^{+0.2}_{-0.1}$	$6.4^{+0.9}_{-0.9}$	$0.5^{+1.6}_{-0.5}$	$1.2^{+0.1}_{-0.1}$	$0.1^{+0.1}_{-0.1}$	$1.3^{+1.3}_{-1.2}$
7	1.3	$27.7^{+6.1}_{-6.3}$	$0.2^{+3.0}_{-0.2}$	$14.7^{+15.8}_{-13.4}$	$5.1^{+6.6}_{-4.0}$	$30.1^{+13.1}_{-11.6}$	$5.6^{+22.3}_{-5.6}$	$2.8^{+1.0}_{-0.7}$	$0.3^{+1.2}_{-0.3}$	$0.1^{+5.8}_{-0.1}$	$0.6^{+1.2}_{-0.6}$	$2.3^{+3.1}_{-1.7}$	$4.9^{+9.1}_{-4.7}$	$0.1^{+0.3}_{-0.1}$	$1.8^{+1.9}_{-1.1}$	$3.8^{+5.4}_{-3.4}$
10	3.7	...	...	$2.3^{+10.7}_{-2.2}$	$6.2^{+4.0}_{-3.9}$	$6.5^{+5.8}_{-4.6}$	$0.2^{+10.0}_{-0.2}$	$1.7^{+0.4}_{-0.4}$	$0.1^{+0.9}_{-0.1}$	...	$1.6^{+0.9}_{-0.8}$	$3.9^{+3.2}_{-2.3}$	$74.9^{+4.7}_{-7.0}$	$2.7^{+0.5}_{-0.4}$	$0.1^{+1.0}_{-0.1}$	...
11	4.4	$0.3^{+1.0}_{-0.2}$	$26.2^{+5.7}_{-3.8}$	$7.2^{+12.3}_{-6.9}$	...	$6.7^{+2.5}_{-2.4}$	$25.0^{+10.3}_{-12.6}$	$2.4^{+0.4}_{-0.3}$	$0.1^{+0.1}_{-0.1}$	...	$0.2^{+0.3}_{-0.1}$	$0.7^{+1.0}_{-0.6}$	$25.2^{+3.3}_{-3.2}$	...	...	$6.2^{+2.8}_{-2.0}$
Long wavelength																
5	58.4	...	$17.2^{+1.6}_{-1.6}$	$1.1^{+2.1}_{-0.9}$	...	$68.5^{+1.6}_{-1.7}$	...	$4.8^{+0.1}_{-0.1}$	$0.1^{+0.1}_{-0.1}$	...	$2.0^{+0.1}_{-0.1}$	...	...	...	...	$6.4^{+0.3}_{-0.3}$
10	4.0	$1.6^{+14.2}_{-1.6}$	$80.6^{+5.2}_{-5.2}$	$1.1^{+9.2}_{-1.0}$	...	$6.6^{+4.9}_{-4.9}$	$0.1^{+0.1}_{-0.1}$	$0.7^{+0.4}_{-0.4}$	...	...	$1.2^{+0.5}_{-0.8}$	$0.7^{+1.5}_{-0.7}$	...	...	...	$7.6^{+1.2}_{-1.2}$
11	6.3	...	$70.0^{+3.0}_{-3.0}$	...	$8.7^{+8.4}_{-6.9}$	$8.6^{+5.3}_{-7.3}$	$0.1^{+2.9}_{-0.1}$	$2.6^{+0.3}_{-0.3}$	$0.1^{+0.2}_{-0.1}$	$0.8^{+1.7}_{-0.8}$	$0.4^{+0.4}_{-0.3}$	$0.1^{+0.4}_{-0.1}$	$8.4^{+1.5}_{-1.6}$	$0.1^{+0.2}_{-0.1}$	...	$0.2^{+0.6}_{-0.2}$

Table 2.5: Summary of the results of the spectral decomposition for the ϵ Cha members: mass averaged grain sizes and mass fractions of crystalline silicates.

(1)	(2)	(3)	(4)	(5)	(6)	(7)
	$\langle a \rangle^{\rm S}_{\rm am.sil.}$	$\langle a \rangle^{\rm S}_{\rm cryst.sil.}$	$f^{\rm S}_{\rm cryst}$	$\langle a \rangle^{\rm L}_{\rm am.sil.}$	$\langle a \rangle^{\rm L}_{\rm cryst.sil.}$	$f^{\rm L}_{\rm cryst}$
ID	(μm)	(μm)	(%)	(μm)	(μm)	(%)
5	$5.1^{+0.1}_{-0.1}$	$1.6^{+0.4}_{-0.3}$	$10.6^{+1.4}_{-1.2}$	$1.6^{+0.1}_{-0.1}$	$0.1^{+0.1}_{-0.1}$	$6.8^{+0.2}_{-0.2}$
7	$2.0^{+0.9}_{-1.0}$	$2.0^{+2.2}_{-1.4}$	$11.0^{+7.0}_{-5.1}$	...	...	...
10	$1.3^{+1.3}_{-0.7}$	$5.5^{+0.1}_{-0.2}$	$82.1^{+4.3}_{-5.1}$	$1.5^{+0.5}_{-0.1}$	$0.4^{+0.6}_{-0.3}$	$2.5^{+1.3}_{-0.9}$
11	$3.6^{+0.5}_{-0.8}$	$5.4^{+0.1}_{-0.2}$	$28.4^{+3.8}_{-2.8}$	$1.4^{+0.1}_{-0.1}$	$4.5^{+0.3}_{-0.5}$	$12.3^{+2.2}_{-1.5}$

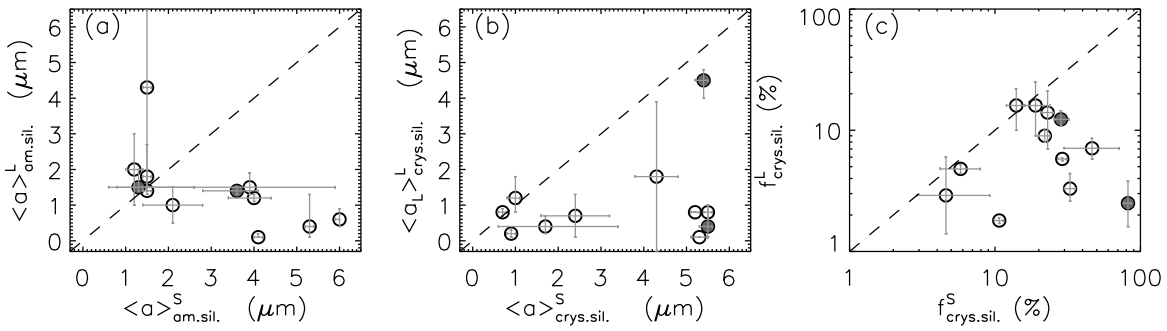

Figure 2.12: (a) Comparison of the mass-averaged sizes of amorphous dust grains as derived from the shorter and longer wavelength part of the IRS spectra (indicated with "S" and "L" superscripts) of sources in ϵ Cha, MBM 12, η Cha, and the Coronet cluster. The filled circles indicate the two M-type object ID#10 and 11 in ϵ Cha. (b) Similar to (a), but for the average sizes of crystalline dust grains. (c) Comparison of the mass fraction of crystalline dust grains as derived from the shorter and longer wavelength part of the IRS spectra.

(b) Dust properties of disks around cool T Tauri stars

We will now join the dust properties derived for the ϵ Cha members with those derived for several other regions, and do a statistical analysis of the combined data set. We collected the available literature data for protoplanetary disks surrounding young stars of spectral type M0 or later in the MBM 12 (Meeus et al. 2009) and η Cha (Sicilia-Aguilar et al. 2009) associations and the Coronet cluster (Sicilia-Aguilar et al. 2008). The dust properties for these targets are all derived from Spitzer IRS spectra using the same TLTD spectral decomposition routines that we used for the ϵ Cha data. As described in Section 2.2.2(5a), the IRS spectra are divided into two regions, a short (7-17 μm) wavelength part tracing the warm inner disk regions and a long (17-37 μm) wavelength part that is more sensitive to cooler regions further from the central star. In Fig. 2.12 we compare the dust properties in the warmer and cooler regions. We compare the average size of dust grains for both the amorphous and crystalline grain population, and the mass fractions of crystalline silicates. As shown in Fig. 2.12(a)(b), the average sizes of the amorphous and crystalline silicates in the warmer regions of protoplanetary disks are substantially larger than the those in the cooler disk. This may indicate that dust growth has been more efficient closer to the central star than in regions at larger distance, but it may also mean that the disks are more turbulent in the warm inner regions than further out, allowing larger grains to remain visible in the disk surface instead of settling to the midplane. A combination of both effects is also plausible. Fig. 2.12(c) shows that the dust in the warm inner regions of protoplanetary disks contains a higher fraction of crystalline material than the dust in cooler regions. This is consistent with earlier findings (e.g. van Boekel et al. 2004; Meeus et al. 2009).

We estimated the accretion rates for all stars from their Hα line luminosity using the method described in Section 2.2.2(1) and list these in Table 2.7. In Fig. 2.13, we plot the average grain sizes of amorphous and crystalline silicates as against accretion rate. The data suggest a positive correlation between the average grain size of the amorphous grains and the accretion rate if the latter is above $\sim 10^{-9}\, M_{\odot}\, \mathrm{yr}^{-1}$(see panel a of Fig. 2.13). Below this value, the grains in the majority of disks are small, independently of the accretion rate. A possible explanation for this relation is that both accretion and the presence of large grains in the disk surface require some level of turbulence in the disk. Thus, both a large average grain size and a high accretion rate are tell tale signs of a turbulent disk, though there need not be a direct causal connection between both observables. There are two outliers in this diagram, MBM 12-10 and G-14, which both are are classified as WTTSs due to their small Hα equivalent widths. Yet, both show show large average grain sizes in their IRS spectra. A possible explanation for this deviant behavior lies in the time-variability of the accretion: objects that appear as WTTSs may turn into CTTSs when observed at a different time. The variations in the accretion rate are likely caused by dynamical processes occurring near the very inner disk edge, i.e. at much smaller scales than the region responsible for the emission seen in the IRS spectra. It is unlikely that the turbulence in the

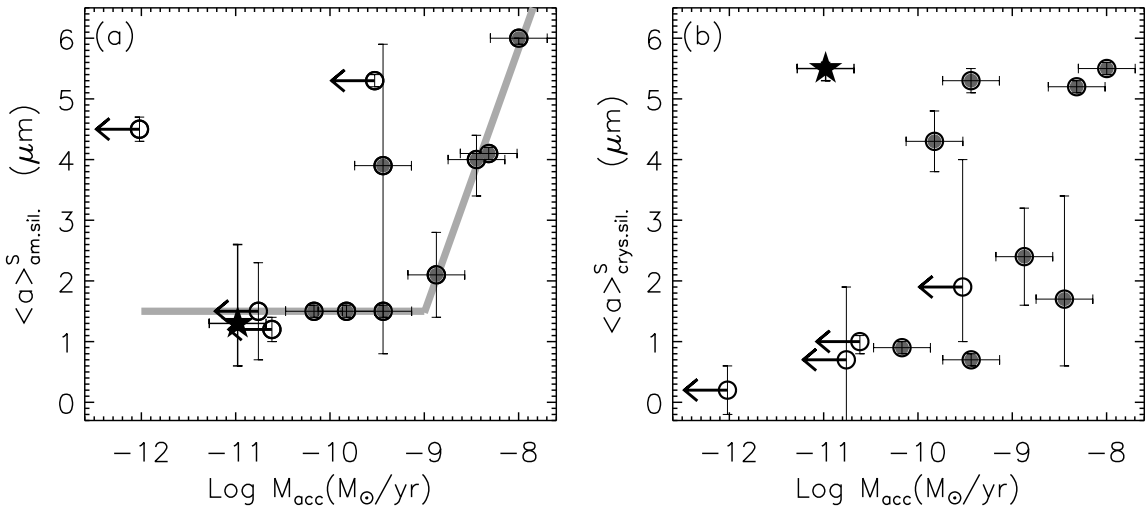

Figure 2.13: (a) The average sizes of amorphous grains plotted versus the accretion rate of the central stars. The grain sizes are derived in 7-17 μm region of the IRS spectra. The thick solid lines are the fits to the relation between the accretion rates and the grain sizes. (b) The average sizes of crystalline grains vs accretion rates. In each panel, the filled circles show the CTTSs, and the open circles represent the WTTSs. The accretion rates are estimated from the Hα line luminosity, for the WTTSs only upper limits can be derived. The pentagram represents object ID#10 in ϵ Cha.

latter region varies on the same timescale as the accretion, thereby destroying the one-to-one correlation. If this proposed explanation is correct, Hα monitoring of MBM 12-10 and G-14 should reveal a variable accretion rate.

Fig. 2.13(b) shows the average grain sizes of crystalline silicates as plotted against accretion rates. In order to see whether there is any correlation between both observables we apply a Kendall τ test. If two datasets are fully correlated this test returns a value of $\tau = 1$, if they are anti-correlated we get $\tau =$ -1, and if they are independent independent τ has a value of 0. The Kendall τ test also returns a probability p which is smaller when the correlation is more significant. We find a very weak correlation (τ=0.36, p=0.22) between the average grain sizes of crystalline silicates and the accretion rates.

Sicilia-Aguilar et al. (2007) have discovered a similar correlation between the average grain sizes of silicates and accretion rates as we find for accretion rates above $10^{-9}\,M_\odot\,\mathrm{yr}^{-1}$. They also argue that turbulence in disks prevents large grains from settling into the disk interior where they are invisible to Spitzer, and also promotes a accretion, thereby leading to a correlation between both observables. What is new in the current study is that the correlation between the accretion rates and grain sizes is breaks down for $\dot{M}_{acc}$ $<10^{-9}$ $M_\odot\,\mathrm{yr}^{-1}$, suggesting that the turbulence for required to sustain such accretion rates is insufficient to support large grains against settling. We

fit the relation between the average grain size of the amorphous dust and the accretion rate with the following curve:

$$\langle a \rangle^{\rm S}_{\rm am.sil.} = \begin{cases} 36.95 + 3.95 \times Log\dot{M}_{acc} & \text{if } \dot{M}_{acc} > 10^{-9}\ M_{\odot}\,{\rm yr}^{-1} \\ \sim 1.5 & \text{if } \dot{M}_{acc} \leq 10^{-9}\ M_{\odot}\,{\rm yr}^{-1} \end{cases}$$

Here, $\langle a \rangle^{\rm S}_{\rm am.sil.}$, in unite of μm, is the average sizes of amorphous silicates in the "warmer" disk regions, and $\dot{M}_{\rm acc}$ is the accretion rates in unit of $M_{\odot}\,{\rm yr}^{-1}$.

Fig. 2.14 shows the mass fraction of crystalline material in the "warmer" and "colder" disk regions versus the effective temperatures of the central stars for our sample of cool T-Tauri stars. Again we use the Kendall τ test to evaluate any possible correlation between both quantities, which yields τ=0.01 and p=0.95 for the warm disk part (panel a in Fig. 2.14), and τ=−0.25 and p=0.31 for the cooler disk part (panel b). Thus there is no significant correlation between the mass fraction of crystalline silicates in the disk and the stellar effective temperature for cool T Tauri stars.

In Fig. 2.15 we plot the crystallinity of the disk material against the mass accretion rates. Once again we run the Kendall τ test, and find essentially no correlation in the warm disk regions (τ=−0.14, p=0.62) and possibly a slight anti-correlation (τ=−0.57, p=0.05) between both observables in the colder parts of the disks.

2.3 Summary

We have studied the members of the ϵ Cha association focusing on the properties of the central stars and their circumstellar disks, using a combination of available archive data and our own Spitzer spectroscopy and VLT/VISIR imaging data.

Using proper motions we confirm the membership of most studied stars but question the membership of stars CXOU J120152.8 (ID#9) and 2MASS J12074597(ID#12). We estimated the masses and ages of the ϵ Cha members and find HD 104237C to be a sub-stellar object with a very low mass of 13-15 $M_{\rm Jup}$, putting it at the boundary between brown dwarfs and "free floating planets"

The object 2MASS J12014343-7835472 (ID#11) is unusually faint at optical wavelengths while also showing exceptionally large equivalent widths of some optical emission lines and an exceptionally strong infrared excess. Similar objects have been discovered in other star-forming regions and we tentatively explain this behavior with a flared disk seen at moderately high inclination in which the cold outer disk regions cause sufficient extinction to effectively screen

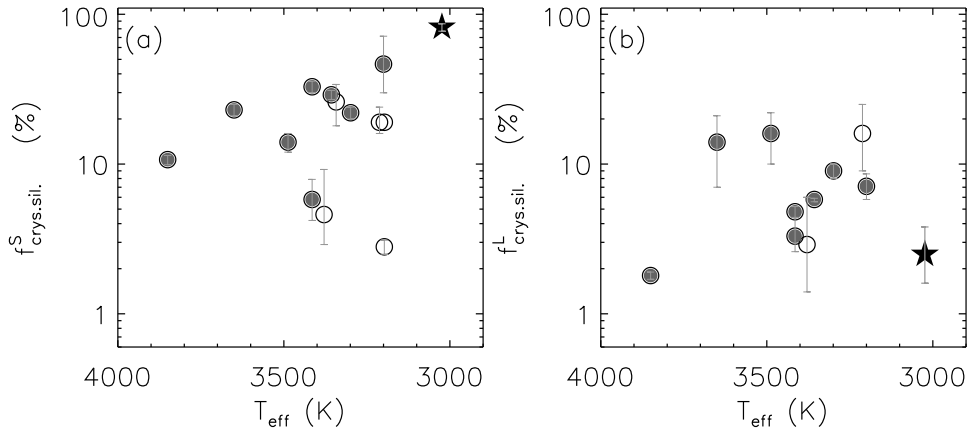

Figure 2.14: (a)The mass fractions of crystalline material compared to the effective temperature of the central stars (which correlates closely with the bolometric luminosity, see Fig. 4.8. The crystallinities are derived from the 7-17 μm part of the IRS spectra. (b) similar to (a), except that the crystallinities are derived from in 17-37 μm part of the IRS spectra. The filled circles show the CTTSs, and the open circles represent the WTTSs. The pentagram marks object ID#10 in ϵ Cha.

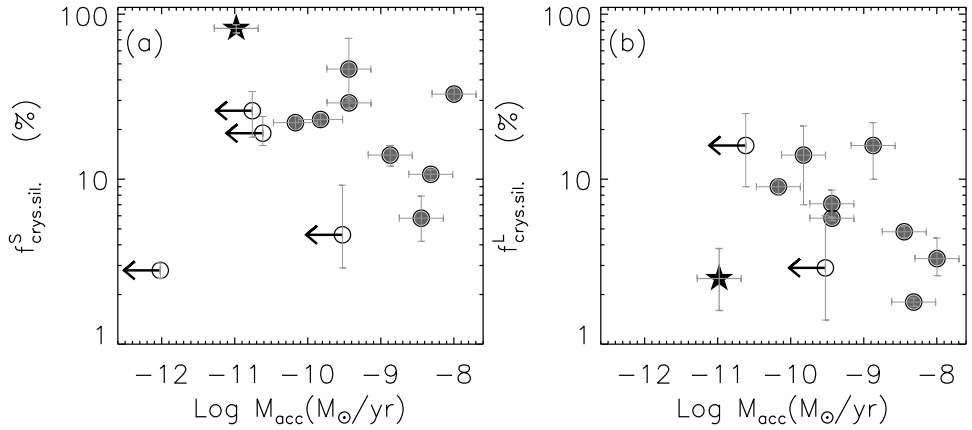

Figure 2.15: (a)The mass fractions of crystalline silicates plotted versus the accretion rates of the central objects. Panel (a) shows the crystallinities as derived from the 7-17 μm part of the IRS spectra, panel (b) shows the same quantity derived in the 17-37 μm spectral region. The symbols are identical to those in Fig. 2.14.

the central star which is then seen mostly in scattered light, but allow most of the infrared light from the warm disk regions to pass. The protoplanetary disks surrounding the cool stars USNO-B120144.7 and 2MASS J12005517 show evidence for a reduced height of the optically thick disk due to dust settling. The disk around HD 104237E shows evidence for partial dissipation in its inner part while its outer disk remains essentially intact.

We found that both the disk frequency and the accretor frequency in the ϵ Cha association are higher than those in relatively dense clusters of similar age. Three other sparse stellar associations for which data are available in the literature also show comparatively high disk frequencies. Disk evolutions appears to proceed substantially slower in sparse associations compared to denser environments.

We derive the mineralogical composition and grain size distribution of the (sub-) micron sized dust in the disk atmosphere using the Two Layer Temperature Distribution (TLTD) method. We find that the average grain sizes and fraction of crystalline material are higher in the warm inner disk regions that dominate the short wavelength part of the IRS spectra compared to cooler regions at larger distance from the central star that contribute mostly to the longer wavelength range covered by the IRS. We also find that the average sizes of amorphous grains in the warm inner disk regions show a positive correlation with the accretion rates if the latter is higher than $\sim 10^{-9}\, M_{\odot}\, \mathrm{yr}^{-1}$.

appendix

(1) The disk frequencies in star-formation regions

In Table 2.6, we list each SFR used in Fig. 2.8. In total 16 SFRs are included with median ages ranging from ~0.9 to ~11 Myr. It can be noted that the disk frequencies in the sparse stellar association, MBM 12, ϵ Cha, η Cha, and TW hya tend to be systematically above those of the other SFRs with similar ages.

MBM 12 In this association, there are 12 known members with K to M spectral types. Among these, 8 objects have been detected by the Spitzer IRS, and 7 objects show evidence for a circumstellar disk (MBM 12-2,3,4,5,6,10,12) (Meeus et al. 2009). If we only use the Spitzer IRS spectra to judge the presence of disks in MBM 12, its disk frequency can be underestimated compared to other SFRs toward which the Spitzer IRAC photometric data are used to characterize the disks. To remedy it, we use all the available information related to the disks, e.g. Hα emission line that can be used as a tracer of accretion activity, therefore an indication of the presence of disks. Among the 4 objects without Spitzer IRS spectra, MBM 12-8 shows signs of active

accretion in the form of a strong Hα emission line ($EW_{H\alpha}$=-120Å), suggesting that also around MBM 12-8 a disk is present. Thus, the disk frequency for all known members is ~67±24% (8/12), and the one for the members with masses of 0.1-0.6 $M_{\odot}$ is ~67±27% (6/9).

η Cha In the η Cha association 18 members have been observed with Spitzer. The disk frequency is estimated to be ~44±16% (8/18) (Megeath et al. 2005b; Sicilia-Aguilar et al. 2009). For the members with masses of 0.1-0.6 $M_{\odot}$, the disk frequency is ~58±22% (7/12).

TW hya To estimate the disk frequency of this association we first constructed a catalog of members of this group. Our catalog is based on the TW Hya membership criteria as refined by Mamajek (2005), and includes TWA-1, 2A, 2B, 3A, 3B, 4, 5A, 5B, 6, 7, 8A, 8B, 9A, 9B, 10, 11A, 11B, 13A, 13B, 14, 15A, 15B, 16, 20, 21, 23, 25, 26, 27, 28, plus new identified members TWA-29 30A, 30B (Looper et al. 2007, 2010a,b). Among these members, TWA-1, 3A, 4, 7, 11A, 27, 28, 30A, and 30B show evidence for a disk (Jayawardhana et al. 1999; Riaz & Gizis 2008; Looper et al. 2010a,b). Thus, the disk frequency for all known members is estimated to be ~27±9%(8/33), and the disk frequency for members with masses of 0.1-0.6 $M_{\odot}$ is ~24±12% (4/17).

The dust properties around M-type pre-main-sequence stars in MBM 12, η Cha, and Coronet cluster

In Table 2.7, we list the targets used in Figs. 2.12, 2.13, 2.14, and 2.15. The total luminosity, extinction, and accretion rates listed here for each object are derived using the procedure described in Section 2.1.1 and in Chapter 3. The stellar masses and ages are estimated by comparison to theoretical pre-main sequence (PMS) evolutionary tracks from Dotter et al. (2008). We collected the dust properties for each disk from the literature (Sicilia-Aguilar et al. 2008; Meeus et al. 2009; Sicilia-Aguilar et al. 2009). These include the average size of amorphous and crystalline silicate grains, and the mass fractions of crystalline silicate grains, and were derived using the same TLTD method as we used for the analysis of the spectra of the ϵ Cha members, as described in Section 2.1.3.

Table 2.6: the fractions of YSO with disks in different SFRs. Column 2: the median age of each SFR. Column 3: the references for the median age of SFR. Column 4: the disk frequencies for all known members. Column 5: the references for disk frequencies of all known members. Column 6: the disk frequencies for the members with masses of 0.1-0.6 $M_{\odot}$. Column 7: the references for disk frequencies listed in Column 6.

(1)	(2)	(3)	(4)	(5)	(6)	(7)
	Age		DF_{All}		$DF_{0.1-0.6M_{\odot}}$	
SFR	(Myr)	Ref	(%)	Ref	(%)	Ref
L988	0.6	(1)	83±8	(2)	···	···
NGC 2068/71	0.9	(3)	79±9	(3,4)	68±13	(3,4)
Taurus	1.5	(5)	64±4	(6)	71±11	(7)
Cha I	2.0	(8)	53±5	(9)	51±9	(7)
IC 348	2.5	(10)	50±6	(10)	41±5	(7)
NGC 2264	2.5	(11)	38±3	(12)	···	···
σ Ori	3.0	(13)	36±4	(13)	···	···
Tr 37	4.0	(14)	48±6	(15)	70±15	(7)
λ Ori	5.0	(16)	28±4	(16)	···	···
NGC 2362	5.0	(17)	19±2	(18)	9±4	(7)
Ori OB1 b	5.0	(19,20)	13±4	(21)	14±7	(7)
25 Ori	8.0	(19,20)	6±3	(21)	3±3	(7)
NGC 7160	11.0	(14)	4±3	(15)	13±13	(7)
Upper Sco	5.	(7)	9±2	(7)	15±4	(7)
MBM 12	2.	(22)	67±24	(23)	67±27	(24)
ϵ Cha	4.	(24)	50±20	(25)	67±33	(24)
η Cha	6.	(22)	44±16	(25,26)	58±22	(24)
TW hya	10.	(27)	27±9	(24)	24±12	(24)

(1) Herbig & Dahm (2006); (2) Luhman et al. (2010); (3) Chapter 3; (4) Flaherty & Muzerolle (2008); (5) Briceño et al. (2002); (6) Luhman et al. (2010); (7) Kennedy & Kenyon (2009);(8) Luhman (2007); (9) Luhman et al. (2008a); (10) Lada et al. (2006); (11) Dahm et al. (2007); (12) Sung et al. (2009); (13) Luhman et al. (2008b); (14) Sicilia-Aguilar et al. (2005); (15) Sicilia-Aguilar et al. (2006a); (16) Barrado y Navascués et al. (2007); (17) Moitinho et al. (2001); (18) Currie et al. (2009); (19) Briceño et al. (2005); (20) Briceño et al. (2007); (21) Hernández et al. (2007a); (22) Luhman & Steeghs (2004); (23) Meeus et al. (2009); (24) this paper; (25) Megeath et al. (2005b); (26) Sicilia-Aguilar et al. (2009); (27) Webb et al. (1999).

Table 2.7: Stellar and disk properties for young stellar objects. Column 13, 14, 15: the average size of amorphous ($\langle a \rangle^{\rm S}_{\rm am.sil.}$) and crystalline grains ($\langle a \rangle^{\rm S}_{\rm cryst.sil.}$) and the mass fractions of crystalline grains ($f^{\rm S}_{\rm cryst}$) are derived from 7-17 μm, besides the objects CRA-466, CRA-4107, G-14, G-85, and G-87, of which IRS spectra between 7-14 μm are used for fitting. Column 16, 17, 18: the average size of amorphous ($\langle a \rangle^{\rm L}_{\rm am.sil.}$) and crystalline grains ($\langle a \rangle^{\rm L}_{\rm cryst.sil.}$) and the mass fractions of crystalline grains ($f^{L}_{\rm cryst}$) are derived from 17-35 μm.

(1)	(2)	(3)	(4)	(5)	(6)	(7)	(8)	(9)	(10)	(11)	(12)	(13)	(14)	(15)	(16)	(17)	(18)	(19)
	RA	DEC		$T_{\rm eff}$	$L_{\rm bol}$	$A_{\rm v}$	EW(Hα)		Log $\dot{M}_{\rm acc}$	Mass	Age	$\langle a \rangle^{\rm S}_{\rm am.sil.}$	$\langle a \rangle^{\rm S}_{\rm cryst.sil.}$	$f^{\rm S}_{\rm cryst}$	$\langle a \rangle^{\rm L}_{\rm am.sil.}$	$\langle a \rangle^{\rm L}_{\rm cryst.sil.}$	$f^{\rm L}_{\rm cryst}$	
Object	(J2000)	(J2000)	Spt	(K)	($L_\odot$)	(mag)	(Å)	class	($M_\odot$ yr^{-1})	($M_\odot$)	(Myr)	(μm)	(μm)	(%)	(μm)	(μm)	(%)	Ref
MBM 12-2	02:56:07.99	+20:03:24.3	M0	3850	0.476	0.5	-40.0	C	-8.32	0.57	1.8	$4.1^{+0.1}_{-0.1}$	$5.2^{+0.1}_{-0.1}$	$10.7^{+0.7}_{-0.8}$	$0.1^{+0.1}_{-0.0}$	$0.8^{+0.0}_{-0.0}$	$1.8^{+0.1}_{-0.1}$	(1)
MBM 12-3	02:56:08.42	+20:03:38.6	M3	3415	0.636	0.0	-25.0	C	-8.45	0.27	0.2	$4.0^{+0.4}_{-0.6}$	$1.7^{+1.7}_{-1.1}$	$5.8^{+2.1}_{-1.6}$	$1.2^{+0.1}_{-0.1}$	$0.4^{+0.3}_{-0.2}$	$4.8^{+0.4}_{-0.4}$	(1)
MBM 12-6	02:58:16.09	+19:47:19.6	M5	3200	0.204	0.0	-29.0	C	-9.44	0.21	0.6	$3.9^{+2.0}_{-3.1}$	$5.3^{+0.2}_{-0.2}$	$46.5^{+24.9}_{-16.6}$	$1.5^{+0.4}_{-0.2}$	$0.1^{+0.0}_{-0.0}$	$7.1^{+1.5}_{-1.3}$	(1)
MBM 12-10	02:58:21.10	+20:32:52.7	M3.25	3379	0.280	0.0	-12.0	W	···	0.28	0.8	$5.3^{+0.1}_{-0.1}$	$1.9^{+2.1}_{-0.9}$	$4.6^{+4.6}_{-1.7}$	$0.4^{+0.9}_{-0.3}$	···	$2.9^{+3.1}_{-1.5}$	(1)
MBM 12-12	03:02:21.05	+17:10:34.2	M3	3415	0.563	0.0	-69.0	C	-8.00	0.27	0.3	$6.0^{+0.0}_{-0.1}$	$5.5^{+0.1}_{-0.1}$	$32.8^{+2.9}_{-2.8}$	$0.6^{+0.3}_{-0.2}$	$0.8^{+0.2}_{-0.2}$	$3.3^{+1.1}_{-0.7}$	(1)
CRA-466	19:01:18.93	−36:58:28.2	M2	3650	0.154	6.4	-14.5	C	-9.82	0.54	7.8	$1.5^{+0.1}_{-0.1}$	$4.3^{+0.5}_{-0.5}$	$23.0^{+2.0}_{-2.0}$	$4.3^{+2.9}_{-2.9}$	$1.8^{+2.1}_{-2.1}$	$14.0^{+7.0}_{-7.0}$	(2)
CRA-4107	19:02:54.65	−36:46:19.1	M4.5	3198	0.029	0.0	···	...	···	0.19	10.9	$5.7^{+2.6}_{-2.6}$	$4.1^{+3.3}_{-3.3}$	$19.0^{+11.0}_{-11.0}$	···	···	···	(2)
G-14	19:02:12.02	−37:03:09.3	M4.5	3198	0.016	1.1	-7.4	W	···	0.18	22.9	$4.5^{+0.2}_{-0.2}$	$0.2^{+0.4}_{-0.4}$	$2.8^{+0.3}_{-0.3}$	···	···	···	(2)
G-85	19:01:33.86	−36:57:44.8	M2.5	3488	0.348	15.5	-27.0	C	-8.87	0.33	0.8	$2.1^{+0.7}_{-0.7}$	$2.4^{+0.8}_{-0.8}$	$14.0^{+2.0}_{-2.0}$	$1.0^{+0.5}_{-0.5}$	$0.7^{+0.6}_{-0.6}$	$16.0^{+6.0}_{-6.0}$	(2)
G-87	19:01:32.33	−36:58:03.0	M3.5	3343	0.127	13.6	-4.0	W	···	0.29	2.7	$1.5^{+0.8}_{-0.8}$	$0.7^{+1.2}_{-1.2}$	$26.0^{+8.0}_{-8.0}$	···	···	···	(2)
J0843	08:43:18.58	−79:05:18.2	M3.4	3357	0.080	0.0	-90.0	C	-9.44	0.30	6.2	$1.5^{+0.1}_{-0.1}$	$0.7^{+0.1}_{-0.1}$	$29.0^{+2.0}_{-2.0}$	$1.4^{+0.1}_{-0.1}$	$0.8^{+0.1}_{-0.1}$	$5.8^{+0.1}_{-0.2}$	(3)
RECX-5	08:42:27.11	−78:57:47.9	M3.8	3299	0.061	0.0	-35.0	C	-10.17	0.26	6.8	$1.5^{+0.1}_{-0.1}$	$0.9^{+0.1}_{-0.1}$	$22.0^{+2.0}_{-2.0}$	$1.8^{+0.9}_{-0.3}$	$0.2^{+0.1}_{-0.1}$	$9.0^{+1.0}_{-1.0}$	(3)
RECX-9	08:44:16.38	−78:59:08.1	M4.4	3212	0.092	0.0	-10.0	W	···	0.21	2.4	$1.2^{+0.2}_{-0.2}$	$1.0^{+0.1}_{-0.2}$	$19.0^{+5.0}_{-3.0}$	$2.0^{+1.0}_{-1.0}$	$1.2^{+0.6}_{-0.4}$	$16.0^{+9.0}_{-7.0}$	(3)

(1) Meeus et al. (2009); (2) Sicilia-Aguilar et al. (2008); (3) Sicilia-Aguilar et al. (2009)

Chapter 3

Star and protoplanetary disk properties in Orion's suburbs

M. Fang, R. van Boekel, W. Wang, A. Carmona, A. Sicilia-Aguilar, and Th. Henning
A&A 2009, 504, 461–489

Circumstellar disks play a key role in the formation of new stars and planetary systems, and form as a result of angular momentum conservation during the protostellar core collapse (Shu 1977; Hartmann 2005a). Through the disks, a significant fraction of the stellar mass is accreted, while the excess angular momentum is transported outward.

After the main accretion phase has ended, gas-rich circumstellar disks can survive at low accretion rates until they are eroded by stellar winds, photo-evaporation, or interaction with giant gas planets or stellar companions (Artymowicz & Lubow 1994; Clarke et al. 2001; Alexander et al. 2006; Rice et al. 2003; Quillen et al. 2004; Hillenbrand 2008). It is during this phase that planets are believed to form inside the disks. A direct observational link between planet formation and disk evolution was recently proposed by Setiawan et al. (2008), who found evidence for a massive planet in close orbit around TW Hya, whose disk is currently being dissipated and is thought to be in a transition state between a gas-rich disk typical of classical T-Tauri stars and a gas-poor debris disk. This finding was, however, questioned by Huélamo et al. (2008), who instead attribute the observed radial velocities to a large stellar spot that rotationally modulates the signal. However, the brightness variations that are inherent to the spot model were not detected in 2008 by Rucinski et al. (2008) while the radial velocity variations first seen by Setiawan et al. (2008) remain present (Setiawan et al. in prep), seriously challenging the spot model of Huélamo et al. (2008). At any rate, knowledge of disk evolution is clearly pivotal to understanding planet formation (Henning 2008).

The disk dissipation process has been constrained observationally by investigating the fraction of young stars that have strong excess emission from disk material at near-infrared wavelengths, in clusters exhibiting a range of ages. Near-infrared imaging surveys have suggested that the inner disk frequency is >50% at ages of 1-2 Myr, and dramatically decreases to ~10% at ages of 5-10 Myr, indicating that the lifetime of inner disks is a few Myr (Strom et al. 1989; Haisch et al. 2001; Hillenbrand 2002). Observations at longer mid-infrared to millimeter wavelengths, tracing

cooler dust at larger radii within the disks, have suggested that the outer parts of the disks survive somewhat longer than the regions close to the central star (Osterloh & Beckwith 1995; Meyer & Beckwith 2000; Mamajek et al. 2004; Andrews & Williams 2005; Carpenter et al. 2005).

The rate at which disk material accretes onto the central star can be estimated from the infrared excess, veiling in optical spectra, and emission lines that are thought to be due to magnetospheric accretion (Hillenbrand et al. 1992; Hartigan et al. 1995; Gullbring et al. 1998; Muzerolle et al. 1998b; Calvet et al. 2000; Muzerolle et al. 2001). The accretion rate has been found to scale approximately with the square of the stellar mass from the brown dwarf to the HAeBe star regime (Muzerolle et al. 2003; Natta et al. 2006; Calvet et al. 2004; Muzerolle et al. 2005; Herczeg & Hillenbrand 2008). Additionally, a clear trend of decreasing accretion rate with increasing age has been identified (Hartmann et al. 1998; Calvet et al. 2000; Sicilia-Aguilar et al. 2004; Hartmann 2005b).

With the advent of the Spitzer Space Telescope our ability to study disk evolution has dramatically increased, both by largely increasing of the number of stars and clusters studied, as well as extending the wavelength range at which large samples of objects can be accurately measured further into the infrared. Many young stars in clusters with ages from 1 Myr to tens of Myrs have been studied (e.g. Gutermuth et al. 2004; Young et al. 2004; Hartmann et al. 2005; Megeath et al. 2005b; Lada et al. 2006; Sicilia-Aguilar et al. 2006a, 2008; Hernández et al. 2006; Dahm & Hillenbrand 2007; Hernández et al. 2007b; Flaherty & Muzerolle 2008). The inner disk fraction changes from >54±15% in the core of the 1-Myr-old cluster NGC 7129 (Gutermuth et al. 2004), to ∼44±7% in the cluster IC 348 with an age of 2-3 Myr (Lada et al. 2006), ∼33.9±3.1% in the 3-Myr-old cluster σ Orionis (Hernández et al. 2007b), ∼20% in the 5-Myr-old cluster NGC 2362(Dahm & Hillenbrand 2007), to 4% in the cluster NGC 7160 with an age of ∼10 Myr (Sicilia-Aguilar et al. 2006a). Generally, the disk fraction decreases with increasing cluster age, confirming previous results on the dissipation timescale based mainly on ground-based near-infrared data.

Some studies show that the disk fraction peaks for stars in the T Tauri mass range (Hernández et al. 2007b), especially for those of K6-M2 types with masses around one solar mass, suggesting that planet formation is favored around solar-mass young stars (Lada et al. 2006; Hernández et al. 2007a). Research on weak-line T Tauri stars (WTTS) with ages of 1-2 Myr shows that up to 50% of WTTSs no longer possess inner disks, indicating that some young stars can dissipate their disks at very early ages (Cieza et al. 2007). Observations at mid-infrared or longer wavelengths identify many stars with prominent excesses at these wavelengths, in some cases also in objects showing no near-infrared excess, whose inner disk regions appear to already have dissipated (Muzerolle et al. 2004; Young et al. 2004; D'Alessio et al. 2005; Calvet et al. 2005; Gautier et al. 2008).

In this chapter, we combine optical spectroscopy with optical, near-, and mid-infrared photometry to characterize the stellar- and disk properties of a large set of young stars located in the Lynds 1630 and Lynds 1641 clouds, located in the Orion molecular cloud complex. The distance to this complex is estimated to be between 400 and 500 pc (e.g. Anthony-Twarog 1982; Hirota et al. 2007), and the region probably has a "depth" of at least several tens of parcecs. Throughout this work we will assume a distance of 450 pc for both the L1630 and L1641 clouds. L1630 lies in the northern part of the Orion complex (Orion B), and L1641 is located in the southern part (Orion A). Toward L1630, near-infrared surveys show that most young stars are found in four clusters (NGC 2023, NGC 2024, NGC 2068, and NGC 2071) rather than being uniformly distributed (Lada et al. 1991; Li et al. 1997). In NGC 2068/2071, which are located in the northern part of L1630 and named L1630N hereafter, a previous study shows that 53 out of the 67 identified members have infrared excesses, and all stars with infrared excess also display active accretion (Flaherty & Muzerolle 2008). Here, we extend the number of identified and characterized young stars in this region. In contrast to the L1630 region, the L1641 cloud harbors a large population of young stars existing in relative isolation, in addition to a population of stars in a number of clusters or aggregates (Strom et al. 1993; Allen 1995). Thus, a comparative study of disks around young stars in L1630 and L1641 offers the opportunity to study the effect of a clustered or isolated environment on the disk evolution.

We arrange the chapter as follows: in § 3.1 we describe the observations and data reduction, in § 3.2 we delineate our data analysis, we present our result in § 3.3, followed by a discussion in § 3.4, and we summarize the results of this study in § 3.5.

3.1 Observations and data reduction

The data employed in this work consist of photometry in the 0.4 to 24 μm range, and optical spectroscopy from ~4000 to ~9000 Å. The optical photometry of the south-east half of L1641 is new, and the rest of the photometry are publicly available archive data. We performed optical spectroscopy with the multi-object spectrograph VIMOS at the ESO-VLT.

3.1.1 Optical photometry

Optical photometry was taken from the Sloan Digital Sky Survey (SDSS, York et al. 2000) in the $u'g'r'i'z'$ bands centered on 0.35, 0.48, 0.62, 0.76 and 0.91 μm, respectively. The L1630N cloud was covered entirely and scanned multiple times (~3.3 times on average), resulting in average 10σ limiting magnitudes of 21.9, 23.0, 22.4, 21.8, and 20.2, respectively. The L1630N data are

publicly available in the SDSS "Low Galactic Latitude Fields" data release (Finkbeiner et al. 2004). Only about half of the L1641 cloud was covered by SDSS and the covered parts were scanned an average of ∼1.3 times, with resulting 10σ limiting magnitudes of about 20.5, 21.7, 21.4, 21.1 and 19.7, respectively. The south-east half of the L1641 cloud has not been observed by SDSS.

Table 3.1: Observing log for the LAICA imaging observations of L1641.

	Pointing center	Observation date	Airmass	Exposure times	
Fields	(J2000)	(UT)	(g'/r'/i'/z')	(second)	Calibartion fields
L1641-1	05 39 17.29 −07 12 41.7	2007-12-15 21:52:15–22:37:36	1.6/1.6/1.6/1.7	1, 45, 300	SA98
L1641-2	05 40 18.76 −07 28 03.5	2007-12-15 22:40:01–23:24:01	1.4/1.5/1.5/1.5	1, 45, 300	SA98
L1641-3	05 41 20.10 −07 43 26.3	2007-12-15 23:27:25–00:12:01	1.4/1.4/1.4/1.4	1, 45, 300	SA98
L1641-4	05 42 21.46 −07 58 48.9	2007-12-16 00:13:57–00:57:30	1.4/1.4/1.4/1.4	1, 45, 300	SA98
L1641-5	05 43 22.91 −08 14 10.5	2007-12-16 00:59:17–01:43:11	1.5/1.5/1.5/1.5	1, 45, 300	SA98
L1641-6	05 44 24.25 −08 29 33.3	2007-12-16 01:45:51–02:29:56	1.7/1.7/1.6/1.6	1, 45, 300	SA98
L1641-7	05 40 18.20 −07 43 35.7	2008-03-11 20:07:04–20:54:23	1.6/1.7/1.7/1.8	1, 45, 300	SA98
L1641-8	05 41 19.55 −07 58 58.6	2008-03-11 20:58:16–21:41:39	2.0/2.0/2.2/1.8	1, 45, 300	SA98
L1641-9	05 42 20.89 −08 14 20.5	2008-03-12 20:19:18–20:34:37	1.6/1.6/1.6/1.7	1, 45, 300	SA95,SA98
L1641-10	05 43 22.35 −08 29 43.5	2008-03-12 20:47:01–21:26:38	1.8/1.9/2.0/2.1	1, 45, 300	SA95,SA98

We complemented the SDSS photometry of L1641 with CCD imaging in the SDSS $g'r'i'z'$ bands performed at the Calar Alto 3.5m telescope, using the Large Area Imager for Calar Alto (LAICA). LAICA is a wide field optical imager employing four 4k×4k CCDs. Part of the south-east half of L1641 was observed on December 15, 2007. Conditions were photometric, but the seeing was poor (2-3″), somewhat limiting the sensitivity for faint point sources (∼19.6, 19.6, 19.9, and 18.9 mag at $g'r'i'z'$ band, respectively). In order to increase the dynamic range, three exposures were taken at each position and in each filter, with integration times of 1/45/300 seconds (see table 3.1). Standard data reduction for optical CCD imaging consisted of bias subtraction, flat-fielding using sky flats, and removal of fringing due to night sky airglow in the i' and z' bands.

The astrometric solution was determined for each individual CCD frame by correlating stellar positions with the USNO A-2 catalog, typically using a few dozen stars but never fewer than 5. The resulting positional uncertainties of detected stars are less than 0.″5 over the whole field, sufficient for unambiguous cross-identification with sources detected in the infrared data. Photometric calibration was performed by observing Landolt standard field SA98, and SA95. These fields have been observed by SDSS. We used the SDSS photometry of all the isolated stars to calibrate our LAICA observation. The photometry for each star was chosen from the longest unsaturated exposure. In total, almost the entire L1630N and L1641 Spitzer fields are covered by our optical imaging.

3.1.2 Infrared photometry

Near-infrared photometry in the J, H, and K_S bands was taken from the Two-Micron All Sky Survey (2MASS, Skrutskie et al. 2006), with 10σ limiting magnitudes of 16.2, 15.3, and 14.6 magnitudes, respectively. The L1630N and L1641 clouds were imaged using the Spitzer Space Telescope IRAC (Fazio et al. 2004) and MIPS (Rieke et al. 2004) cameras.

(1) IRAC photometry

IRAC images at 3.6, 4.5, 5.8, and 8.0 μm were made in High-Dynamic Range mode with integration times of 0.4 and 10.4 seconds (Spitzer program ID 43). Four mosaics were made of each cloud, with a fair amount of overlap between the individual exposures in each mosaic. The IRAC data of the L1630 and L1641 clouds were published previously by Megeath et al. (2005a).

The Spitzer archive provides pipeline reduced (version S14.0.0) image mosaics as well as the corresponding pixel to pixel flux uncertainty maps. For each field the individual mosaics were combined into a final image by making a weighted average (after cosmic ray rejection by a sigma-clipping procedure, and using the uncertainty maps as weights). Separate images were created from the 0.4 and 10.4 second exposures.

A custom made IDL program was used to search for point sources in the IRAC images. At its heart is the `find.pro` procedure from the `astrolib` library. However, rather than searching for point sources in the images themselves, we let `find` search in an image *minus* a smoothed version of that image, thus effectively removing the sometimes bright and inhomogenous nebular background. Moreover, we used a variable detection threshold that is low in "clean" regions, but higher in regions with a high background. After determining proper extraction parameters and extensive testing of the procedure, checking the results by eye, we found that our procedure is very robust and effectively finds all but the very faintest sources in the whole image, without yielding false detections in regions with high and variable background.

The source finder was run in each of the 4 IRAC bands, on the short and long exposures separately. Source detections in the various bands were correlated by spatial coincidence within 1 pixel (1.″2). Only sources that were seen in both the 3.6 and 4.5 micron bands were kept in the analysis (source counts amount to ~25000 and ~40000 in the L1630N and L1641 fields, respectively).

PSF photometry was performed on the detected sources. For each band, the point spread function was determined from bright, isolated, non-saturated stars. The psf-fitting program is based on the StarFinder code (Diolaiti et al. 2000). The psf-fitting extraction box is 15.6″×15.6″for each

IRAC band. The zero-point magnitudes are 17.30, 16.82, 16.33, and 15.69 in the 3.6, 4.5, 5.8, and 8.0 μm bands, respectively. We compared the photometry at short and long exposures to determine the saturation level for the longer exposures. If the stars are not saturated on the long-exposure images, we select their photometry from these long-exposure images. Otherwise, we select them from the short-exposure images. Flaherty & Muzerolle (2008) present photometry of 69 stars in L1630N. A comparison between their photometric magnitudes and ours shows rms differences of ~0.06-0.1 mag for the four IRAC bands. Adopting these values as typical uncertainties in our photometry, we conclude that the photometric accuracy of the pipeline processed data as we have used them, without any custom post-processing, is perfectly adequate for our purposes[1].

(2) MIPS photometry

The L1630N and L1641 clouds were mapped with the MIPS instrument (Spitzer program ID 47). The effective integration time was 80, 40, and 8 seconds at 24, 70, and 160 μm, respectively. Following Flaherty & Muzerolle (2008), who previously presented the L1630N data, we included only the 24 μm data due to lack of detected Class II sources at the longer wavelengths[2]. The same searching and psf-fitting programs as used for the IRAC data were used on the 24 μm image, with a psf-fitting extraction box of 56.35″×56.35″and a zero-point magnitude of 11.76.

3.1.3 Optical spectroscopy

The main new data set presented in this chapter is VLT/VIMOS optical spectroscopy of over 700 targets in the direction of the L1630 N and L1641 star-forming clouds. Accurate stellar parameters and extinction estimates for individual objects cannot be derived from photometry alone, but instead require the combination of spectroscopy and photometry.

(1) Target Selection

The L1630 and L1641 clouds subtend large solid angles on the sky, and to cover them completely with VIMOS observations would require very large amounts of telescope time. Instead, we concentrated on a number of subfields, 3 VIMOS pointings in L1630 N and 5 in L1641. The

[1]The [5.8] magnitude for YSO #105 in L1630N, as well as the [8.0] magnitudes for the YSOs #24, 54, 76, 84,105, 116, 125, 128 in L1630N, were adopted from Flaherty & Muzerolle (2008).

[2]The MIPS [24] magnitudes for YSOs #24, 81, 125, 126 in L1630N were adopted from Flaherty & Muzerolle (2008).

pointings were chosen on the basis of the Spitzer IRAC data and we selected those fields with many potential YSO candidates, i.e. IR excess sources, for optical follow-up. In the [5.8]-[8.0] vs. [3.6]-[4.5] color-color diagrams, we selected YSO candidates using the following criteria (see Fig. 3.1): (1) 0.4≤[5.8]-[8.0] ≤1.1 and 0.1≤[3.6]-[4.5] ≤0.8 (classical T Tauri candidates), (2) 0.2≤[5.8]-[8.0] ≤1.0 and -0.1≤[3.6]-[4.5] ≤0.2 (transition disk candidates), or (3) 0.4≤[5.8]-[8.0] ≤1.4 and 0.8≤[3.6]-[4.5] ≤2.0 (class 0/I candidates), see also Allen et al. (2004).

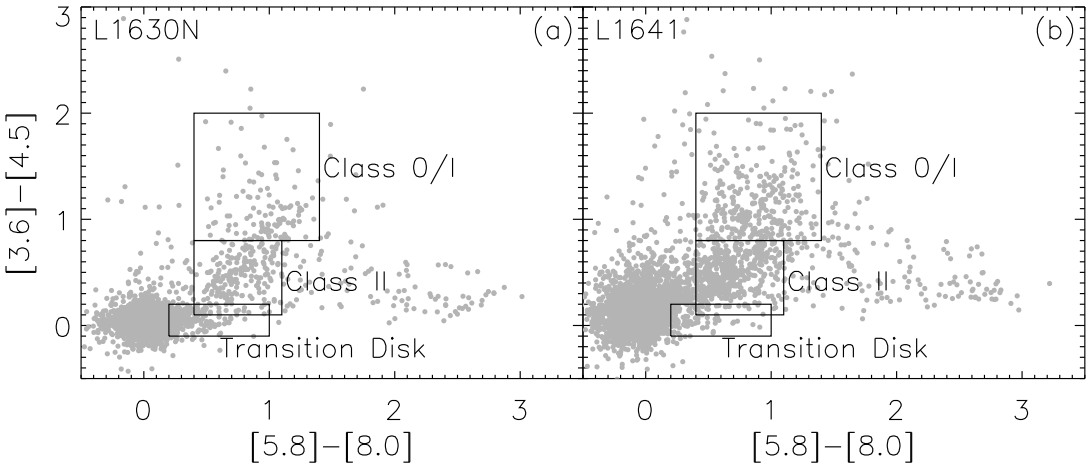

Figure 3.1: Spitzer [5.8]-[8.0] vs. [3.6]-[4.5] color-color diagrams for all objects detected at all four IRAC bands in L1630N and L1641. Three boxes enclose the boundaries of candidate selection regions for three types of YSOs, i.e. class 0/I YSOs, class II YSOs, and YSOs with transition disks.

Pre-imaging in R-band of the selected fields was performed with VIMOS. Based on these data, targets that are sufficiently bright were selected for spectroscopic follow-up. Here, preference was given to sources with IRAC colors that suggest they are young stars possessing disks, but many sources that do not posses colors within the boxes outlined above were selected as well, mostly sources without obvious IR excess emission. This approach has the advantage that a large fraction of available resources are spent on young stars instead of unrelated background objects, but it also introduces a bias toward IR excess sources in the sample of cluster members (see Sect. 3.1.3(3)).

(2) VLT/VIMOS observations

We used *VIMOS*, the Visible Multi-Object Spectrograph (LeFevre et al. 2003) mounted on the ESO Very Large Telescope to obtain optical spectra. The observations were performed during the period from December 2006 to March 2007 with two intermediate resolution grisms, the HR blue ($\lambda/\Delta\lambda$=2050 for a slit width of 1″) and HR red ($\lambda/\Delta\lambda$=2500 for a slit width of 1″)

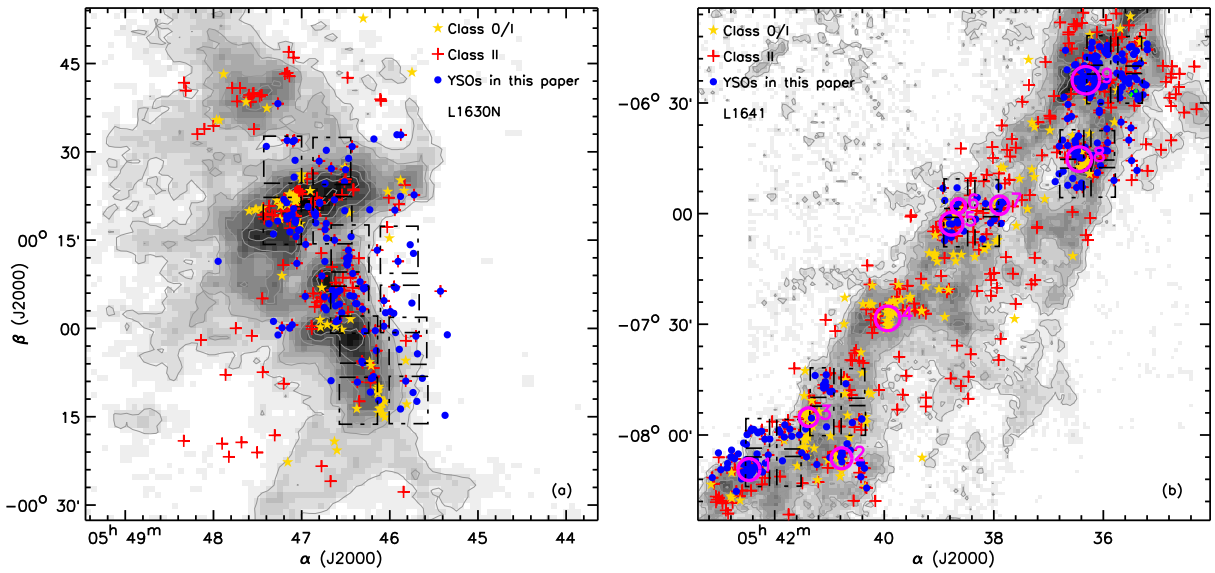

Figure 3.2: The distribution of YSOs in L1630N and L1641 overplotted on a ^{13}CO integrated intensity image (Bally et al. 1987; Miesch & Bally 1994). The filled circles mark the YSOs discussed in this chapter, which have confirmed spectral types. The asterisks and pluses represent the class 0/I and class II YSOs, respectively. The boxes show our fields of view of our VIMOS observations, each set of four quadrants representing one VIMOS pointing.

grisms, covering the wavelength range from 4100Å to 8750Å (see table 3.2). We observed 322 targets in L1630N and 393 in L1641, distributed over 3 and 5 VIMOS pointings, respectively (see Fig. 3.2). For each pointing we performed three 25-minute exposures. The VIMOS spectra were reduced using the VIMOS pipeline provided by ESO (Carlo Izzo, private communication). Two methods can be applied to subtract telluric and nebular emission lines from the stellar spectra: the "skylocal" and "skymedian" options. In the "skylocal" method, the sky spectrum is subtracted from CCD science data before the data are corrected for optical distortions. In the "skymedian" method, the sky subtraction is performed on the distortion-corrected science data, which have been resampled. We prefered the skylocal method, and only very occasionally used spectra from the skymedian method, in cases where the the reductions using the skylocal method contain artifacts.

(3) Biases introduced in target selection

We observed a large number of cloud members with and without infrared excess emission, as well as unrelated field objects, mostly background stars. However, since sources with IR excess emission were more likely (see Sect. 3.1.3(1)) to be included in the optical spectrocopic obser-

Table 3.2: Observing log for the VIMOS optical spectroscopy.

	Pointing center	Data/time of observations	Integration time	
Fields	(J2000)	(UT)	(second)	Airmass
L1630-1 BLUE	05 46 57.08 +00 23 34.4	2007-02-11 01:14:15/01:40:37/02:07:10	3×1526	1.1/1.1/1.1
RED	05 46 57.08 +00 23 34.2	2007-02-09 02:13:46/02:40:08/03:06:40	3×1526	1.1/1.2/1.3
L1630-2 BLUE	05 46 11.01 +00 08 33.3	2007-02-19 01:07:22/01:33:44/02:00:16	3×1526	1.1/1.1/1.2
RED	05 46 11.00 +00 08 33.0	2007-02-18 01:19:07/01:45:29/02:12:00	3×1526	1.1/1.2/1.2
L1630-3 BLUE	05 46 04.81 −00 06 54.8	2007-02-20 00:54:26/01:20:48/01:47:19	3×1526	1.1/1.1/1.2
RED	05 46 04.80 −00 06 54.8	2007-02-21 00:52:21/01:18:42/01:45:13	3×1526	1.1/1.1/1.2
L1641-1 BLUE	05 35 50.41 −06 20 43.3	2007-01-28 01:35:00/02:01:22/02:27:54	3×1526	1.0/1.1/1.1
RED	05 35 50.41 −06 20 43.3	2007-01-28 03:08:50/03:35:12/04:01:46	3×1526	1.1/1.2/1.2
L1641-2 BLUE	05 36 19.38 −06 46 15.1	2006-12-22 04:53:29/05:16:31/05:39:44	3×1326	1.1/1.1/1.1
RED	05 36 19.38 −06 46 15.2	2006-12-21 04:33:45/04:56:47/05:20:01	3×1327	1.1/1.1/1.1
L1641-3 BLUE	05 38 25.92 −06 59 43.2	2007-02-17 00:58:59/01:25:21/01:51:51	3×1526	1.1/1.1/1.1
RED	05 38 25.92 −06 59 43.2	2007-02-15 01:11:09/01:37:31/02:04:01	3×1526	1.1/1.1/1.1
L1641-4 BLUE	05 42 01.92 −08 04 49.0	2007-02-22 01:30:08/01:56:30/02:23:01	3×1526	1.1/1.1/1.2
RED	05 42 01.94 −08 04 49.4	2007-03-12 00:56:23/01:22:45/01:49:16	3×1526	1.2/1.2/1.3
L1641-5 BLUE	05 40 51.60 −07 51 01.4	2007-01-25 01:54:00/02:20:21/02:46:55	3×1526	1.0/1.0/1.1
RED	05 40 51.60 −07 51 02.0	2007-01-27 01:16:57/01:43:19/02:09:49	3×1526	1.1/1.0/1.0

vations, our sample will be biased towards these. Therefore, quantities like the *absolute* disk fraction will be affected, and in general will be over-estimated. However, *relative* trends, such as the disk fraction as a function of stellar mass, are in principle unaffected by our target selection.

3.1.4 Matching of optical and IR data.

We matched the different photometric data sets and spectra based on spatial coincidence using a 2″ tolerance. Since the investigated fields are not very crowded this approach is adequate.

3.2 Analysis

In this section we will describe the methods that we applied to extract the physically interesting information from our data. The main goals are the identification of young stars, the determination of their stellar parameters, characterization of their disk geometry and estimation of the rate at which disk material is accreted onto the central star.

3.2.1 YSO selection criteria

A star in our sample observed with VIMOS is classified as a young star if it obeys any of the following criteria:

1. IR excess
2. Li I absorption
3. Hα emission

We find that sources with IR excess emission always show Hα emission, though the opposite is not necessarily true, i.e. some sources show Hα emission but no IR excess. A large fraction of the sources with Hα emission show Li I absorption in their spectra, and all sources showing Li I also show Hα emission. We note that there may be a small contamination of our sample with dMe stars, which are old, M-type stars that show Hα emission due to chromospheric activity.

3.2.2 Spectral classification

We determined the spectral types of the stars for which we have VIMOS spectroscopy using the classification scheme developed by Hernández et al. (2004). The method uses empirical relations between the equivalent widths of selected atomic and molecular absorption lines and the effective temperature. In general, each individual line or molecular band is a sensitive measure of $T_{\rm eff}$ over a limited range in spectral types only, but the combination of a number of absorption features yields a unique determination of the spectral type in the range of early B to late M. The classification scheme consists of 3 subregimes, each spanning a range in $T_{\rm eff}$: the ”HAeBe” type, ”G” type, and ”late” type scheme. For a detailed description of the method, we refer to Hernández et al. (2004).

In Fig. 3.3, we show several examples of VIMOS spectra of our target stars, covering the early K to mid M spectral type range, representative of the vast majority of the young stars in our sample. The changes in spectral shape over this range are well visible, in particular TiO absorption bands become prominent in spectral types later than M2. Since VIMOS does not use fibers but rather employs masks with multiple slits that are directly imaged onto the detectors, the spectral range covered depends on the position of a star within the field of view. This is illustrated by, e.g. spectra (b) and (d) in Fig. 3.3.

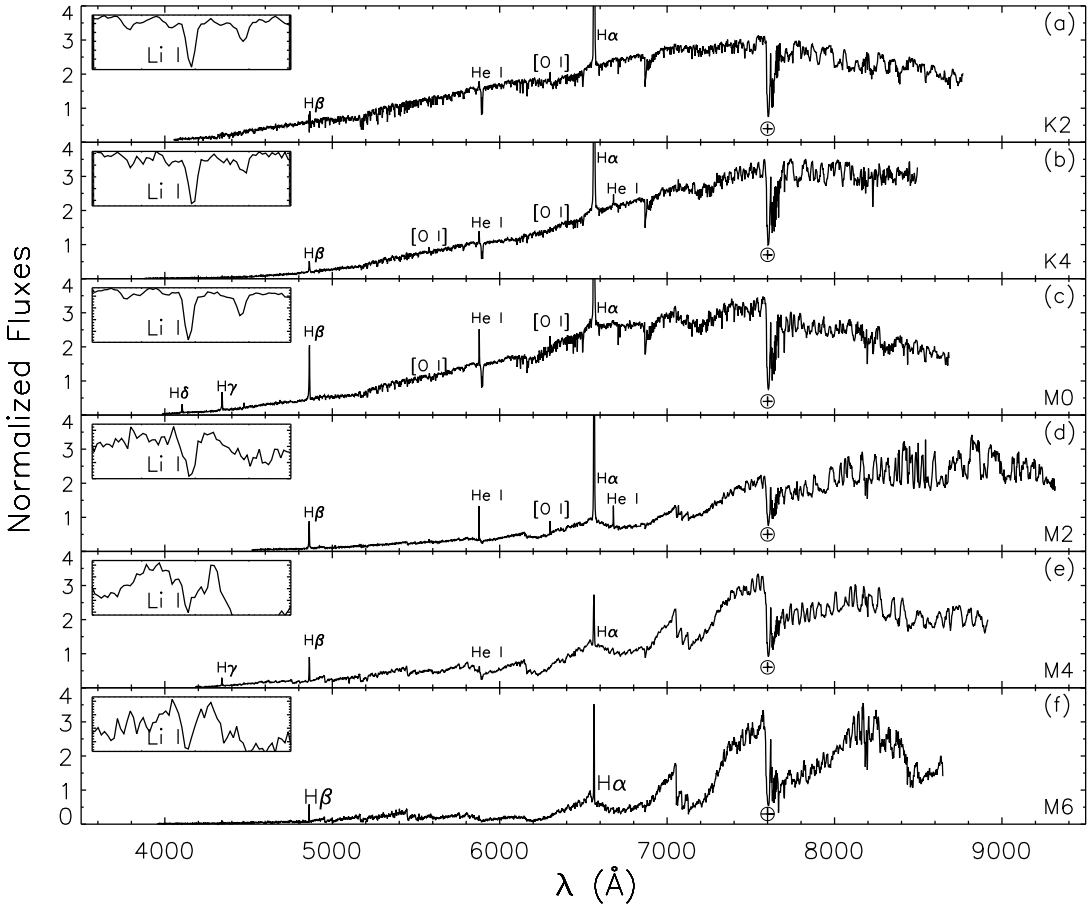

Figure 3.3: Example spectra of our VIMOS observations covering the range of spectral types of the young stars discussed in this work. The main emission lines have been marked, and the insets show the Li I λ6707 absorption line.

(1) Reliability and accuracy of the classification code

In order to test the accuracy and reliability of our spectral classification code, we ran it on 1273 spectral templates from the Indo-US library (Valdes et al. 2004) and compared the spectral types derived using our code to those listed in the spectral library. We found that we accurately recovered the spectral types of the templates over the whole spectral region from early B to late M, with a standard deviation of ~1 sub type. Since the spectral templates in the library have their own intrinsic uncertainty that is not much better than 1 sub type, we may safely assume 1 sub type as the intrinsic accuracy of our method.

In order to assess the effect of limited SNR in our spectra, we ran the classification code again after adding normally distributed noise to the template spectra, such that their SNR was reduced to 30 and 10, respectively. From this exercise, we found that for a SNR of 30, we recovered the

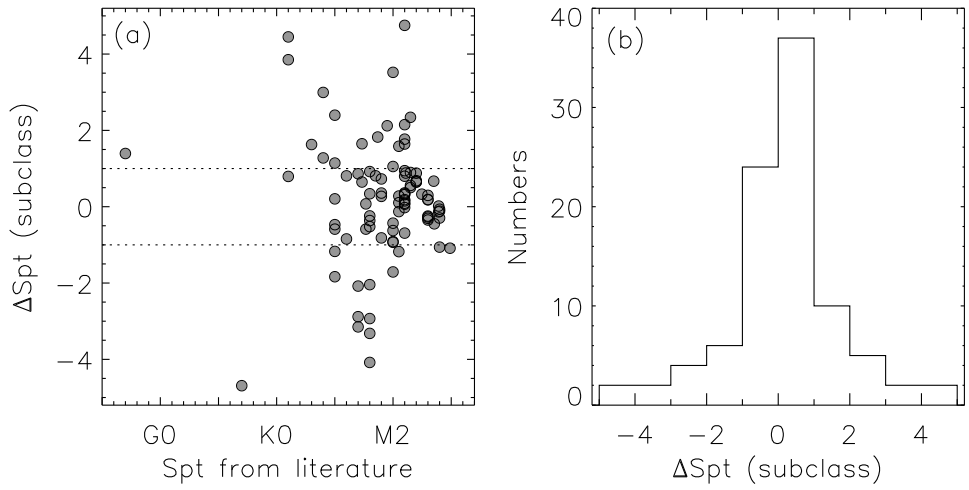

Figure 3.4: Left panel: the differences between the spectral types in this chapter and in the literature vs their spectral types in literature. Right panel: the distribution of spectral-type differences in left panel. Among the total of 95 stars, there are 65% with differences less than one subclass, and ~ 82% with less than two subclasses.

spectral types nearly as well as for the original templates. For a SNR of 10, we reliably recovered spectral types later than ~F5, with a accuracy of ~1 sub type. For spectral types earlier than F5, the method can yield results that are off by as much as 10 sub types for spectra with a SNR of 10, and no robust estimates can be made.

Of the 540 stars for which we could reliably determine the spectral types from our VIMOS data, 94 have been classified previously by other authors (Allen 1995; Flaherty & Muzerolle 2008; Gâlfalk & Olofsson 2008), allowing an independent check on our classification. Fig. 3.4 shows the direct comparison between the spectral types we derived and those quoted in the literature. 65% of this sample agrees within 1 subclass, 82% within 2 subclasses.

(2) Complementary literature spectroscopy

A substantial number of young stellar objects with confirmed spectral types can be found in the literature, which we used to complement our sample. Allen (1995) presents a list of 337 YSO candidates. Among these, there are 78 stars that we did not observe with VIMOS, and which have published equivalent widths of the Hα emission line or exhibit IR excess emission in our Spitzer data. In Gâlfalk & Olofsson (2008) we found 39 YSOs with Hα emission and confirmed spectral types, of which 10 were not covered by our VIMOS observations and were added to our YSO sample in L1641. Flaherty & Muzerolle (2008) identify 67 YSOs in L1630N, of which we observed 23 with VIMOS. In total, the literature data add 44 and 88 YSOs to our sample in

the L1630N and L1641, respectively. We used only the spectral types and Hα equivalent widths given in the quoted papers, and complemented these data with our own optical and infrared photometry. Subsequently, we derived stellar and disk properties in the same way as for the VIMOS sample.

3.2.3 Determining the stellar properties

Our optical spectroscopy and photometry provide the observational basis for determining the stellar parameters of our targets. First, the effective temperatures of the target stars are inferred from their measured spectral types. Reddened model atmospheres are then fitted to the optical photometry to determine the angular diameter and the extinction towards each star. Together with the assumed distance, the angular diameter and effective temperature yield the bolometric luminosity. Subsequent placement in the HR diagram finally yields estimates of the stellar mass and age by comparison to theoretical pre-main sequence evolutionary tracks.

(1) Effective temperatures, model atmospheres, and extinction

We transformed the spectral types to effective temperatures using the relation given by Kenyon & Hartmann (1995) for stars with spectral types earlier than M0, and those by Luhman et al. (2003) for stars of type later than M0. We used model atmospheres to represent the optical SED of our target stars. At temperatures above 4500 K we used the models by Kurucz (1979, 1994), at lower temperatures we adopted MARCS models (Gustafsson et al. 2008). The surface gravity was assumed to be those of ZAMS stars and we adopted solar metallicity.

The optical spectra of our stars may suffer from strong extinction by intervening dust. We used the extinction law of Cardelli et al. (1989) to model this, and adopted a total to selective extinction value typical of ISM dust ($R_{\rm V}$=3.1).

(2) Optical SED fitting

We fitted the optical photometry of each star with a (reddened) model atmosphere, keeping the effective temperature fixed at the spectroscopically determined value. Our SED fit thus has only 2 free parameters: the angular diameter θ and the extinction in the V band $A_{\rm V}$. In general we used the photometric g', r', i', z', and J bands in our SED fit, but for stars without near-infrared excess emission we also included the H and K_s bands. We calculated model fluxes by integrating the intensity of the (reddened) model atmospheres over the spectral response curve of the system for

each filter. The synthetic photometry thus obtained was compared to the observations and the resulting χ^2 was minimized in an automated iterative procedure, in which the optimum values for θ and A_V are found.

(3) HR diagrams

The bolometric luminosity of our stars L_{bol} is easily calculated from the effective temperatures and angular diameters, if the distance is known:

$$L_{bol} = \pi\theta^2 d^2 \sigma T_{eff}^4 \tag{3.1}$$

where θ is the angular diameter, d is the distance, σ is the Stefan-Boltzmann constant, and T_{eff} is the effective temperature. We adopt a distance of 450 pc for both L1630N and L1641 (Genzel et al. 1981; Anthony-Twarog 1982; Maddalena et al. 1986; Wilson et al. 2005). Note that we have implicitly corrected for extinction by calculating the bolometric luminosities in this way.

The thus determined effective temperatures and bolometric luminosities allow placement of our stars in the HR diagram. Stellar masses and ages can then be estimated by comparison to theoretical pre-main sequence (PMS) evolutionary tracks. However, several sets of such tracks exist, by various authors, which yield significantly different results, in particular for the age (see e.g. Hillenbrand et al. 2008for a discussion). We estimated masses and ages using four different sets of publicly available PMS evolutionary tracks: those by D'Antona & Mazzitelli (1997) (DM97), Baraffe et al. (1998) (B98), Siess et al. (2000) (S00), and Dotter et al. (2008) (D08). In the remainder of the discussion, we will adopt the values obtained by employing the PMS evolution tracks from Dotter et al. (2008), as these have the best resolution in both mass and age. We stress, however, that there are substantial systematic differences between the different sets of tracks (e.g. Hillenbrand et al. 2008), and our motives for choosing those by Dotter et al. (2008) are merely pragmatic.

The uncertainties in mass and age of the individual stars were estimated using a simple Monte-Carlo method, in which we created a large number of synthetic [T_{eff},L_*] points for each star, assuming the errors in both quantities to be normally distributed. These points were then interpolated in the HR diagram, and the standard deviations in the resulting mass and age distribution were adopted as the uncertainties in these quantities. This procedure accounts well for the observational errors, but we stress that systematic uncertainties remain. As noted above, the choice of theoretical PMS tracks can influence the resulting mass and age strongly, by factors upto ~2–3. Also, for highly extincted sources, the shape of the adopted extinction law matters, with higher values for the total to selective extinction R leading to higher stellar luminosities and correspond-

ingly younger ages and, for the earlier spectral types, higher masses.

3.2.4 Determining the disk properties

The disk properties that we can determine from our data are twofold: the spatial structure of the disk as inferred by the infrared SED, and the accretion rate as deduced from optical emission lines. Optical emission lines also trace outflow activity, a process intimately related to accretion.

(1) Disk structure from the infrared SED

Excess emission above the stellar photospheric level is the most employed indicator for dusty circumstellar material. The infrared emission from the disks around T Tauri stars is essentially fully comprised of reprocessed stellar radiation, with generally minor contributions from the release of gravitational energy close to the central star. Therefore, they are usually referred to as "passive" disks[3]. The infrared SED is directly related to the spatial structure of the circumstellar material, even though models fitted solely to SED data may suffer from degeneracies in the derived material distribution. In general, models of circumstellar disks adequately reproduce the SEDs of young stars, and observations that spatially resolve these objects confirm that interpretation (e.g. Eisner et al. 2003; Leinert et al. 2004; Monnier et al. 2005; Akeson et al. 2005a,b; Isella et al. 2006; Monnier et al. 2006; Eisner et al. 2007; Acke et al. 2008; Kraus et al. 2008), though there is continued discussion on the relative imporance of an *additional* "spherical halo" component (e.g. Vinković et al. 2003, 2006).

The near-infrared excess ($\sim 1.5\,\mu\mathrm{m} \lesssim \lambda \lesssim 5\,\mu\mathrm{m}$) traces hot dust in the inner disk ($\lesssim 1$ AU), with a possible contribution from small amounts of material in an optically thin envelope. In the longer part of the observed wavelength range ($\sim 6\,\mu\mathrm{m} \lesssim \lambda \lesssim 24\,\mu\mathrm{m}$) the slope of the SED is related to the shape of the disk on scales[4] of $\sim 1-10$ AU: "red" slopes indicate disks with "flared" geometries, whereas "blue" slopes in this wavelength range point at "flat" disks (see e.g. Meeus et al. 2001; Dullemond & Dominik 2004; Leinert et al. 2004). It has been suggested that disks with flared geometries evolve into disks with flat geometries, and that dust settling and grain growth have proceeded in the latter (e.g. Acke et al. 2004). We use $\alpha_{5.8-24}$, the slope between the Spitzer IRAC 5.8 μm and MIPS 24 μm bands as a measure for the disk flaring.

[3]Even in objects where accretion is the dominant source of luminosity (e.g. FUOR and EXOR systems), irradiation by the hot, innermost disk regions is the dominant energy source in most of the disk, except close to the central star. Such disks thus have an "active" character within a certain radius and are "passive" further out.

[4]This is approximately the spatial range probed in this wavelength regime for YSOs of $\sim 1\,L_\odot$, characteristic for our sample. The range scales with $\sqrt{L_*}$, and is correspondingly larger for e.g. HAe stars and smaller for young brown dwarfs.

A distinct population of young stars shows essentially photospheric emission or a small and very blue excess at short wavelengths ($\lambda \lesssim 6\,\mu$m), while simultaneously exhibiting moderate to strong excess emission at longer wavelengths. In these objects, the inner disks appears to have largely or completely dissipated, whereas the disk at larger radii is still relatively intact. They are thought to be in a transition stage between optically thick disks and debris disks. Recently, Muzerolle (2008) discussed these so-called "Transition Disks", and distinguished three types: (1) objects with weak or zero IRAC excess and strong MIPS-24 excess ("canonical transition disks"); (2) objects with moderate IRAC excess and strong MIPS-24 excess ("pre-transition disks"); and (3) objects with weak or zero IRAC excess and weak MIPS-24 excess (weak or evolved disks). We have visually inspected the SEDs of all stars in our sample and selected all objects that match one of the aforementioned descriptions. These objects all occupy the lower right part of a 2MASS/Spitzer Ks-[5.8] vs. [8.0]-[24] color-color diagram (see Sect. 3.3.3).

(2) Accretion rates

Several diagnostics can be used to estimate $\dot{M}_{\rm acc}$, the rate at which disk material is accreted onto the central star. UV excess emission above the photospheric level is generally attributed to hot spots on the star, shock-heated by accreting material hitting the stellar surface at high velocities. If the amount of excess emission can be well determined, it provides a robust estimate of the accretion rate (e.g. Gullbring et al. 1998). Similarly, veiling of optical stellar spectra in which an additional, featureless continuum from accreting material reduces the contrast of photospheric absorption features can be used (e.g. Hartigan et al. 1991). Optical and near-infrared emission lines, in particular of hydrogen, are widely used as accretion measures. Their fluxes are relatively easy to measure and they are sensitive to accretion even at very low levels. However, geometrical and optical depth effects can strongly influence the appearance of the emission lines, and while the average line strength correlates strongly with the mass accretion rate, individual objects can scatter up to two orders of magnitude around the average relation (e.g. Natta et al. 2006). More detailed studies of emission line profiles, in particular measuring the full width of the line close to the base, provide more robust $\dot{M}_{\rm acc}$ estimates for individual objects, but are feasible for very broad profiles only in medium resolution spectra like ours.

While many of our target stars are detected in SDSS u' band, these measurements cannot be used to estimate the mass accretion rate, for the following reason. In objects with very red optical SEDs, the observed U-band flux can be severely contaminated by photons that "leak in" from longer wavelengths, since here the throughput of the u' filter is close to, but not perfectly, zero. The typical YSO in our sample has K or M spectral type and an optical extinction of several magnitudes, leading to very red optical SEDs and a strong "red leak". We note that the U-band filters in other photometric systems suffer from the same effect. We do *not* employ the u'-band

photometry to determine accretion rates, neither do we use it in the fits to the optical SEDs (Sect. 3.2.3(2)).

Rather, we used the Hα, Hβ, and He I $\lambda = 5876$ emission lines, whose luminosity ($L_{\mathrm{H}\alpha}$, $L_{\mathrm{H}\beta}$, and L_{HeI}) correlates with the accretion luminosity (L_{acc}) for YSOs with masses ranging from vastly subsolar to several solar masses (Dahm 2008; Herczeg & Hillenbrand 2008). In Appendix (2) we derive the proportionalities between the line strengths and accretion luminosities. We applied these relations to derive the accretion luminosities for our target stars in L1630N and L1641. These were converted into mass accretion rates via the following relation:

$$\dot{M}_{\mathrm{acc}} = \frac{L_{\mathrm{acc}} R_\star}{GM_\star(1 - \frac{R_\star}{R_{\mathrm{in}}})}, \tag{3.2}$$

where R_{in} denotes the truncation radius of the disk, and is taken to be 5 $\mathrm{R}_\star$ (Gullbring et al. 1998). The stellar radii ($R_\star$) were obtained using the SED fitting procedure described in Sect. 3.2.3(2), and the stellar masses were derived from the location of our YSOs in the HR diagram.

3.2.5 Spatial distribution of YSOs

The young stars in L1630N are mostly confined to two clusters (NGC 2068 and NGC 2071, see e.g. Lada et al. 1991). In L1641, there are a large number of clusters or aggregates, as well as a more distributed population (Strom et al. 1993). Following Román-Zúñiga et al. (2008), we applied the nearest neighbor method (NNM) towards the YSO population in L1641 to determine which YSOs are in isolation and which are in aggregates or clusters, and to outline the extension of the clusters. For each star we located the 10^{th} nearest neighbor and calculated the surface density of YSOs within the corresponding radius. If this density is higher than the average surface density over the whole cloud, the star is taken to be a member of a cluster/aggregate.

3.3 Results

From our multi-wavelength data of the L1630N and L1641 clouds, we derived the stellar properties of the observed objects as well as properties of their disks. To some extent, we also gained information about the molecular clouds in the form of accurate "pencil-beam" extinction measurements towards our targets. In L1641, we frequently discriminate between the "clustered" (L1641C) and "distributed" (L1641D) populations.

3.3.1 Survey products

The main product of our survey is a list of identified YSOs. For each object we give the spectral type, bolometric luminosity, Hα and Li I equivalent widths, CTTS/WTTS classification, line of sight extinction, the precence in a clustered or distributed environment, IRAC infrared spectral indice, mass and age estimates using the PMS evolutionary tracks of Dotter et al. (2008), an SED-based classification of the disk, and estimates of the mass accretion rate using Hα, Hβ and He I in Tables 3.3 and 3.4, for stars in L1630N and L1641, respectively. We list the photometric magnitudes in a number of optical and infrared filters in Tables 3.5 and 3.6. Mass and age estimates using the PMS evolutionary tracks of D'Antona & Mazzitelli (1997), Baraffe et al. (1998), Siess et al. (2000), and Dotter et al. (2008) are listed in Tables 3.7 and 3.8. The equivalent widths of a number of optical emission lines are listed in Tables 3.9 and 3.10.

We further supply an ensemble of stars that were identified as foreground or background objects by the presence of an Hα absorption line and the absence of Li I λ6707 absorption, and list their photometric magnitudes, spectral types and optical extinction estimates in Tables 3.11 and 3.12 for the fields of L1630N and L1641, respectively.

Additionally, we provide optical and infrared magnitudes of a total of 21694 sources detected in our optical imaging data with matching sources in the 2MASS catalog. These consist of public SDSS data for L1630N (Finkbeiner et al. 2004), previously unpublished SDSS data and new LAICA data for L1641, publicly available NIR photometry from 2MASS (Skrutskie et al. 2006), as well as publicly accessible and previously published (Megeath et al. 2005a) Spitzer data. Without measured spectral types, reliable estimation of the luminosity and effective temperature is hampered by a degeneracy between the stellar temperature and reddening. Therefore, these object are not included in our analysis, and we instead provide these data as a photometric catalog only. This list contains many young stars as well as numerous background objects. We list the optical and infrared magnitudes of these sources in Tables 3.13 and 3.14.

Table 3.3: Parameters for YSOs in L1630N. Column 4: [a] the values estimated from our VIMOS spectra; [b] the values from Flaherty & Muzerolle (2008). Column 6: stellar bolometric luminosity derived from optical SED fitting (see Sect. 3.2.3). Column 9: classification based on the criteria in Appendix (1). Column 11: aggregate/cluster population or distributed population. Column 13-14: stellar masses and ages estimated using PMS evolutionary tracks from Dotter et al. (2008). Column 16-18: accretion rates estimated with Hα, Hβ, and He I 5876Å emission line luminosities, respectively.

(1)	(2)	(3)	(4)	(5)	(6)	(7)	(8)	(9)	(10)	(11)	(12)	(13)	(14)	(15)	(16)	(17)	(18)
	RA	DEC		adopted	Lum	EW(Hα)	EW(Li)	TTS	A_V			Mass	Age	Disk	Log $\dot{M}_{acc}$	Log $\dot{M}_{acc}$	Log $\dot{M}_{acc}$
ID	(J2000)	(J2000)	Spectral type	Spectral type	($L_\odot$)	(Å)	(Å)	type	(mag)	clu	$\alpha(3.6-8.0\mu m)$	($M_\odot$)	(Myr)	property	($M_\odot$ yr^{-1})	($M_\odot$ yr^{-1})	($M_\odot$ yr^{-1})
1	05 45 21.38	−00 00 45.9	M3[b]	M3	0.298	−4.4[b]	0.2[b]	WTTS	0.9	yes	−2.69	$0.30^{+0.10}_{-0.06}$	$0.84^{+1.11}_{-0.39}$	No disk	...	...	...
2	05 45 22.68	−00 14 27.5	M6[b]	M6	0.128	−12.2[b]	0.6[b]	WTTS	0.0	yes	−2.58	$0.13^{+0.06}_{-0.01}$	$0.38^{+0.70}_{-0.12}$	No disk	...	...	...
3	05 45 26.16	+00 06 37.9	M3[b]	M3	0.393	−20.8[b]	0.3[b]	CTTS	0.4	yes	−1.39	$0.29^{+0.09}_{-0.06}$	$0.51^{+0.51}_{-0.22}$	Thick	−8.94	...	...
4	05 45 38.26	−00 08 11.0	M0[b]	M0	0.552	−4.1[b]	0.4[b]	WTTS	2.1	yes	−2.60	$0.55^{+0.21}_{-0.11}$	$1.36^{+3.15}_{-0.61}$	No disk	...	...	...
5	05 45 41.68	−00 04 02.4	M4[a],M3[b]	M4	0.273	−10.0[a],−5.4[b]	0.4[b]	WTTS	0.2	yes	−2.77	$0.24^{+0.03}_{-0.03}$	$0.56^{+0.20}_{-0.15}$	No disk	...	...	...
6	05 45 41.94	−00 12 05.3	K5.5[a],K4[b]	K5.5	0.994	−2.5[a],−1.2[b]	0.5[a],0.5[b]	WTTS	1.3	yes	−2.57	$0.92^{+0.23}_{-0.23}$	$2.00^{+4.04}_{-0.93}$	Transition disk	...	...	...
7	05 45 42.80	−00 01 01.8	M5.5[a]	M5.5	0.093	−14.8[a]	0.4[a]	WTTS	0.3	yes	−1.24	$0.15^{+0.04}_{-0.03}$	$1.07^{+0.89}_{-0.40}$	Thick	...	...	...
8	05 45 44.37	+00 22 58.2	M1[b]	M1	0.608	−29.4[b]	0.6[b]	CTTS	0.8	yes	−1.37	$0.43^{+0.12}_{-0.08}$	$0.68^{+0.82}_{-0.28}$	Thick	−8.26	...	...
9	05 45 44.56	−00 10 35.6	M4.5[a]	M4.5	0.075	−7.0[a]	0.8[a]	WTTS	1.0	yes	−2.55	$0.20^{+0.03}_{-0.02}$	$2.68^{+1.10}_{-0.68}$	Thin	...	...	...
10	05 45 44.64	+00 13 00.6	M0.5[a]	M0.5	0.434	−1.8[a]	...	WTTS	0.2	yes	−2.84	$0.53^{+0.08}_{-0.07}$	$1.72^{+0.74}_{-0.45}$	No disk	...	...	...
11	05 45 45.58	+00 04 35.6	M5[a]	M5	0.245	−6.2[a]	0.5[a]	WTTS	0.1	yes	−2.68	$0.19^{+0.02}_{-0.01}$	$0.37^{+0.09}_{-0.07}$	No disk	...	...	...
12	05 45 46.91	+00 14 29.4	M4.5[a],M4[b]	M4.5	0.089	−7.0[a],−6.8[b]	0.6[a],0.7[b]	WTTS	0.0	yes	−2.71	$0.19^{+0.03}_{-0.03}$	$2.00^{+0.88}_{-0.56}$	No disk	...	...	...
13	05 45 49.56	−00 08 38.8	M5[a]	M5	0.048	−19.3[a]	...	CTTS	1.1	yes	−1.06	$0.16^{+0.06}_{-0.03}$	$3.38^{+4.85}_{-1.24}$	Thick	−10.74	...	...
14	05 45 53.11	−00 13 24.9	M1.5[a],M1[b]	M1.5	0.308	−11.1[a],−18.1[b]	0.5[a],0.6[b]	CTTS	0.7	yes	−2.43	$0.46^{+0.09}_{-0.07}$	$2.10^{+1.44}_{-0.68}$	Transition disk	−9.38	−9.42	−8.50
15	05 45 53.54	+00 33 08.8	M2[b]	M2	0.468	−150.0[b]	0.2[b]	CTTS	1.6	yes	−1.15	$0.36^{+0.10}_{-0.07}$	$0.65^{+0.70}_{-0.28}$	Thick	−7.64	...	...
16	05 45 53.60	+00 22 42.1	K7[b]	K7	0.300	−2.4[b]	0.3[b]	WTTS	0.6	yes	−2.73	$0.88^{+0.02}_{-0.18}$	$10.53^{+7.60}_{-4.92}$	No disk	...	...	...
17	05 45 54.09	−00 03 16.7	M5.5[a]	M5.5	0.053	−9.4[a]	...	WTTS	1.8	yes	...	$0.14^{+0.04}_{-0.02}$	$2.18^{+2.21}_{-0.70}$	...	...	...	...
18	05 45 55.13	+00 11 39.4	M5.5[a]	M5.5	0.039	−34.7[a]	...	CTTS	0.9	yes	−1.42	$0.13^{+0.06}_{-0.02}$	$3.12^{+6.05}_{-1.07}$	Thick	−10.59	...	...
19	05 45 56.20	+00 33 10.3	M5.5[b]	M5.5	0.252	−8.3[b]	0.4[b]	WTTS	0.2	yes	−2.65	$0.16^{+0.05}_{-0.03}$	$0.21^{+0.28}_{-0.12}$	No disk	...	...	...
20	05 45 56.31	+00 07 08.6	K7.5[a],K9[b]	K7.5	0.769	−6.5[a],−6.2[b]	0.6[a],0.7[b]	WTTS	1.4	yes	−1.59	$0.55^{+0.16}_{-0.10}$	$0.86^{+0.92}_{-0.32}$	Thick	...	...	...
21	05 45 56.73	−00 00 25.4	M3[a]	M3	0.249	−3.4[a]	0.6[a]	WTTS	6.0	yes	−1.20	$0.31^{+0.03}_{-0.03}$	$1.17^{+0.31}_{-0.23}$	Transition disk	...	...	...
22	05 45 57.38	+00 20 22.2	K7[b]	K7	0.997	−35.3[b]	0.5[b]	CTTS	1.6	yes	−1.65	$0.65^{+0.17}_{-0.16}$	$0.89^{+10.44}_{-0.39}$	Thick	−7.80	...	...
23	05 45 57.62	+00 07 21.1	M5.5[a]	M5.5	0.078	−26.4[a]	...	CTTS	0.3	yes	−1.18	$0.13^{+0.03}_{-0.02}$	$1.00^{+0.61}_{-0.28}$	Thick	−10.25	−10.59	−10.32
24	05 45 57.93	+00 02 48.6	M4.5[a],M4[b]	M4.5	0.121	−81.3[a],−75.0[b]	0.4[a],0.4[b]	CTTS	0.2	yes	−1.84	$0.20^{+0.02}_{-0.02}$	$1.32^{+0.51}_{-0.28}$	Thin	−9.28	−9.64	−9.14
25	05 46 00.18	+00 03 07.0	M4.5[a],M4[b]	M4.5	0.477	−37.1[a],−27.2[b]	0.5[a],0.4[b]	CTTS	0.4	yes	−1.01	$0.19^{+0.02}_{-0.02}$	$0.12^{+0.04}_{-0.03}$	Thick	−8.65	−8.99	−8.92
26	05 46 03.53	+00 02 54.7	M5.5[a]	M5.5	0.146	−12.6[a]	...	WTTS	0.7	yes	...	$0.16^{+0.02}_{-0.02}$	$0.54^{+0.20}_{-0.29}$	...	...	...	...
27	05 46 04.64	+00 04 58.1	K7[a],K9[b]	K7	0.989	−131.5[a],−126.0[b]	0.4[a],0.3[b]	CTTS	1.9	yes	−1.19	$0.64^{+0.11}_{-0.11}$	$0.85^{+0.55}_{-0.29}$	Thick	−7.09	−7.64	−7.22
28	05 46 04.58	+00 00 38.2	M2[b]	M2	0.267	−7.4[b]	0.2[b]	WTTS	2.5	yes	−1.35	$0.40^{+0.13}_{-0.09}$	$1.89^{+6.61}_{-0.93}$	Thick	...	...	...
29	05 46 07.89	−00 11 56.9	K3[b]	K3	16.767	−3.2[b]	0.6[b]	CTTS	4.5	yes	−1.90	$1.61^{+0.40}_{-0.27}$	$0.10^{+0.10}_{-0.04}$	Thin	−7.31	...	...
30	05 46 09.27	+00 13 32.6	M1[b]	M1	1.088	−10.8[b]	0.5[b]	CTTS	1.2	yes	−1.19	$0.38^{+0.10}_{-0.07}$	$0.23^{+0.25}_{-0.09}$	Thick	−8.32	...	...
31	05 46 09.61	−00 03 31.2	M1.5[a]	M1.5	0.235	−12.2[a]	...	CTTS	5.5	yes	−1.49	$0.48^{+0.20}_{-0.17}$	$3.38^{+21.68}_{-2.29}$	Thick	−9.56	...	...
32	05 46 10.31	−00 00 06.7	M2[a]	M2	0.142	−38.6[a]	0.4[a]	CTTS	2.4	yes	−0.86	$0.45^{+0.12}_{-0.11}$	$6.00^{+15.20}_{-3.03}$	Thick	−9.39	−9.01	−8.69
33	05 46 11.34	−00 07 55.1	M3.5[a]	M3.5	0.004	−211.4[a]	...	CTTS	0.7	yes	−0.26	...	...	Thick	...	...	...

Table 3.3: continued.

(1)	(2)	(3)	(4)	(5)	(6)	(7)	(8)	(9)	(10)	(11)	(12)	(13)	(14)	(15)	(16)	(17)	(18)
	RA	DEC		adopted	Lum	EW(Hα)	EW(Li)	TTS	A_V			Mass	Age	Disk	Log $\dot{M}_{acc}$	Log $\dot{M}_{acc}$	Log $\dot{M}_{acc}$
ID	(J2000)	(J2000)	Spectral type	Spectral type	($L_\odot$)	(Å)	(Å)	type	(mag)	clu	$\alpha(3.6-8.0\mu m)$	($M_\odot$)	(Myr)	property	($M_\odot$ yr^{-1})	($M_\odot$ yr^{-1})	($M_\odot$ yr^{-1})
34	05 46 11.86	+00 32 25.9	K2[b]	K2	5.010	−3.8[b]	0.7[b]	CTTS	3.5	yes	−2.37	$1.64^{+0.26}_{-0.29}$	$0.81^{+0.61}_{-0.29}$	Transition disk	−8.13	...	...
35	05 46 12.27	−00 08 07.8	M7[a]	M7	0.053	−116.5[a]	...	CTTS	1.9	yes	−0.99	...	...	Thick	...	...	...
36	05 46 12.99	−00 08 14.8	M4.5[a]	M4.5	0.008	−29.3[a]	...	CTTS	0.1	yes	0.91	$0.16^{+0.08}_{-0.04}$	$56.18^{+26.86}_{-30.77}$	Thick	−11.82	−12.13	...
37	05 46 13.58	−00 10 34.0	M5.5[a]	M5.5	0.008	−4.6[a]	...	WTTS	0.0	yes	...	$0.11^{+0.05}_{-0.01}$	$25.56^{+34.01}_{-3.97}$	...	...	...	...
38	05 46 14.48	+00 20 24.4	M4[b]	M4	0.115	−3.6[b]	0.3[b]	WTTS	0.8	yes	−1.90	$0.25^{+0.10}_{-0.06}$	$2.24^{+3.62}_{-1.09}$	Transition disk	...	...	...
39	05 46 16.75	+00 07 13.5	M5[a]	M5	0.563	−29.9[a]	...	CTTS	4.0	yes	−1.82	$0.17^{+0.03}_{-0.01}$	$0.04^{+0.10}_{-0.02}$	Thin	−8.69	...	...
40	05 46 17.71	−00 00 14.3	K3.5[a]	K3.5	3.056	−19.6[a]	0.4[a]	CTTS	8.2	yes	0.51	$1.22^{+0.29}_{-0.32}$	$0.83^{+0.94}_{-0.40}$	Thick	−7.50	...	...
41	05 46 18.30	+00 06 57.8	K5.5[a],K1[b]	K5.5	1.572	−16.6[a],−34.7[b]	0.5[a],0.4[b]	CTTS	4.3	yes	−0.90	$0.81^{+0.35}_{-0.19}$	$0.79^{+1.97}_{-0.35}$	Thick	−7.95	−8.17	...
42	05 46 18.60	+00 07 08.0	M3.5[a]	M3.5	0.236	−45.8[a]	...	CTTS	5.1	yes	−0.71	$0.26^{+0.12}_{-0.07}$	$0.83^{+5.23}_{-0.46}$	Thick	−8.97	...	...
43	05 46 18.89	−00 05 38.1	K7[a],K4[b]	K7	2.144	−9.3[a],−3.9[b]	0.7[b]	CTTS	2.4	yes	−1.32	$0.57^{+0.13}_{-0.13}$	$0.22^{+0.26}_{-0.10}$	Thick	−7.89	...	...
44	05 46 19.06	+00 03 29.6	K6[a],K5[b]	K6	20.667	−31.0[a],−44.5[b]	0.4[b]	CTTS	8.9	yes	−1.23	$0.80^{+0.91}_{-0.16}$	$0.01^{+0.16}_{-0.00}$	Thick	−5.63	−6.34	−4.54
45	05 46 19.47	−00 05 20.0	K2.5[b]	K2.5	6.154	−28.5[b]	0.5[b]	CTTS	3.7	yes	−0.76	$1.50^{+0.32}_{-0.26}$	$0.48^{+0.39}_{-0.17}$	Thick	−6.85	...	...
46	05 46 20.88	+00 08 09.4	K8[b]	K8	1.053	−8.7[b]	0.7[b]	CTTS	4.6	yes	−0.80	$0.58^{+0.17}_{-0.13}$	$0.63^{+4.18}_{-0.28}$	Thick	−8.50	...	...
47	05 46 22.43	−00 08 52.6	K2[a],K1[b]	K2	2.732	−28.9[a],−32.0[b]	0.4[a],0.6[b]	CTTS	3.5	yes	−1.70	$1.61^{+0.08}_{-0.28}$	$2.12^{+1.51}_{-0.83}$	Transition disk	−7.49	−8.26	...
48	05 46 22.99	+00 04 26.4	M2[b]	M2	0.386	−104.0[b]	0.5[b]	CTTS	2.8	yes	−1.06	$0.37^{+0.12}_{-0.08}$	$0.93^{+1.38}_{-0.39}$	Thick	−8.00	...	...
49	05 46 23.83	+00 04 27.2	M3[a]	M3	0.333	−3.3[a]	...	WTTS	4.1	yes	...	$0.30^{+0.16}_{-0.08}$	$0.72^{+9.48}_{-0.42}$	...	...	...	...
50	05 46 25.09	+00 05 41.2	K7.5[a]	K7.5	0.844	−82.7[a]	...	CTTS	8.0	yes	−1.16	$0.62^{+0.38}_{-0.26}$	$0.99^{+15.43}_{-0.67}$	Thick	−7.47	...	...
51	05 46 25.89	+00 09 32.0	M3.5[a],M2[b]	M3.5	0.201	−13.9[a],−32.4[b]	0.6[a],0.4[b]	WTTS	1.0	yes	−1.18	$0.27^{+0.07}_{-0.05}$	$1.20^{+0.95}_{-0.46}$	Thick	...	...	...
52	05 46 26.65	+00 31 07.5	K7[a],K6[b]	K7	1.231	−5.5[a],−4.9[b]	0.5[a],0.6[b]	WTTS	4.6	yes	−1.22	$0.65^{+0.20}_{-0.17}$	$0.65^{+3.75}_{-0.31}$	Thick	...	...	...
53	05 46 27.13	+00 15 49.7	M4.5[a]	M4.5	0.108	−3.1[a]	...	WTTS	0.0	yes	...	$0.20^{+0.04}_{-0.03}$	$1.65^{+0.80}_{-0.50}$	...	...	...	...
54	05 46 27.83	+00 05 48.4	M2.5[b]	M2.5	0.543	−3.0[b]	0.3[b]	WTTS	3.1	yes	−2.72	$0.31^{+0.09}_{-0.06}$	$0.37^{+0.39}_{-0.16}$	No disk	...	...	...
55	05 46 28.36	+00 12 27.0	M3.5[a]	M3.5	0.346	−29.3[a]	...	CTTS	6.0	yes	−1.17	$0.28^{+0.16}_{-0.07}$	$0.55^{+8.81}_{-0.31}$	Thick	−8.87	...	...
56	05 46 28.87	+00 13 30.7	M0.5[a]	M0.5	0.833	−214.9[a]	...	CTTS	6.1	yes	−0.89	$0.45^{+0.31}_{-0.14}$	$0.50^{+11.86}_{-0.31}$	Thick	−6.91	...	...
57	05 46 29.00	+00 29 07.2	M1.5[b]	M1.5	0.769	−4.8[b]	0.5[b]	WTTS	1.8	yes	−2.70	$0.37^{+0.10}_{-0.07}$	$0.33^{+0.42}_{-0.14}$	No disk	...	...	...
58	05 46 29.06	+00 11 45.7	M4.5[a]	M4.5	0.023	−7.2[a]	...	WTTS	0.0	yes	...	$0.17^{+0.11}_{-0.04}$	$12.20^{+26.38}_{-5.45}$	...	...	...	...
59	05 46 29.59	+00 10 57.2	M5.5[a]	M5.5	0.294	−53.5[a]	...	CTTS	3.3	yes	−1.09	$0.16^{+0.03}_{-0.03}$	$0.17^{+0.20}_{-0.08}$	Thick	−8.90	...	...
60	05 46 30.03	+00 11 11.1	M6[a]	M6	0.050	−31.3[a]	...	CTTS	2.8	yes	...	...	...	...	...	...	...
61	05 46 30.06	+00 12 09.7	M1.5[b]	M1.5	0.774	−15.4[b]	0.5[b]	CTTS	4.1	yes	−1.33	$0.36^{+0.12}_{-0.07}$	$0.33^{+5.39}_{-0.16}$	Thick	−8.42	...	...
62	05 46 31.03	+00 27 12.1	M7.5[a]	M7.5	0.018	...	...	...	0.7	yes	−1.26	...	...	Thick	...	...	...
63	05 46 31.46	+00 20 15.8	M3.5[a]	M3.5	0.036	−2.7[a]	...	WTTS	0.0	yes	...	$0.27^{+0.09}_{-0.06}$	$16.36^{+17.48}_{-6.85}$	...	...	...	...
64	05 46 31.71	+00 25 08.2	M3.5[a]	M3.5	0.199	−12.9[a]	...	WTTS	4.3	yes	−1.61	$0.28^{+0.07}_{-0.05}$	$1.34^{+2.63}_{-0.53}$	Thick	...	...	...
65	05 46 33.28	+00 02 51.9	K4[a],K7[b]	K4	1.869	−31.4[a],−24.4[b]	0.4[a],0.6[b]	CTTS	4.9	yes	−1.01	$1.12^{+0.24}_{-0.32}$	$1.36^{+1.49}_{-0.68}$	Thick	−7.60	−7.63	−6.85
66	05 46 34.54	+00 06 43.5	K4[b]	K4	4.380	−5.5[b]	0.5[b]	CTTS	7.0	yes	−1.35	$1.12^{+0.21}_{-0.27}$	$0.40^{+0.28}_{-0.17}$	Thick	−7.89	...	...
67	05 46 34.90	+00 04 20.7	M4[a],M2.5[b]	M4	0.420	−6.1[a],−5.0[b]	0.6[a],0.2[b]	WTTS	2.1	yes	−1.54	$0.22^{+0.04}_{-0.03}$	$0.24^{+0.26}_{-0.09}$	Thick	...	...	...
68	05 46 35.50	+00 01 38.9	M6[a]	M6	0.233	−28.5[a]	...	CTTS	2.4	yes	...	$0.14^{+0.08}_{-0.02}$	$0.15^{+0.67}_{-0.08}$	...	−9.44	...	...
69	05 46 36.10	+00 06 26.8	M0[a]	M0	6.114	−2.7[a]	...	WTTS	13.3	yes	−0.66	$0.44^{+0.72}_{-0.10}$	$0.02^{+3.20}_{-0.01}$	Thick	...	...	...
70	05 46 37.06	+00 01 21.8	K5.5[b]	K5.5	1.991	−61.0[b]	0.4[b]	CTTS	3.7	yes	−1.24	$0.77^{+0.22}_{-0.13}$	$0.51^{+0.57}_{-0.18}$	Thick	−7.04	...	...
71	05 46 37.57	+00 04 02.5	M5[a]	M5	0.276	−10.8[a]	...	WTTS	2.1	yes	...	$0.19^{+0.02}_{-0.02}$	$0.30^{+0.10}_{-0.08}$	...	...	...	...
72	05 46 38.33	+00 05 48.7	M6[a]	M6	0.541	−83.6[a]	...	CTTS	5.8	yes	−0.88	$0.15^{+0.05}_{-0.01}$	$0.02^{+0.13}_{-0.01}$	Thick	−8.24	...	...
73	05 46 38.40	+00 15 11.6	M5.5[a]	M5.5	0.185	−10.6[a]	0.6[a]	WTTS	1.6	yes	−1.71	$0.16^{+0.03}_{-0.03}$	$0.39^{+0.33}_{-0.16}$	Thick	...	...	...
74	05 46 38.57	+00 22 06.0	M1[a],M1[b]	M1	0.395	−7.3[a],−5.8[b]	0.6[a],0.2[b]	WTTS	3.9	yes	−1.44	$0.47^{+0.07}_{-0.06}$	$1.52^{+0.95}_{-0.47}$	Thick	...	...	...
75	05 46 39.89	+00 06 44.9	M2[a]	M2	0.880	−63.6[a]	...	CTTS	8.5	yes	−1.34	$0.31^{+0.34}_{-0.09}$	$0.19^{+10.54}_{-0.12}$	Thick	−7.58	...	...
76	05 46 40.18	+00 05 01.9	M1[b]	M1	0.584	−7.8[b]	0.8[b]	WTTS	2.9	yes	−2.42	$0.43^{+0.11}_{-0.09}$	$0.74^{+0.85}_{-0.32}$	Thin	...	...	...
77	05 46 40.44	−00 08 38.2	M2.5[a]	M2.5	0.038	−4.5[a]	...	WTTS	2.3	yes	...	$0.43^{+0.15}_{-0.19}$	$42.16^{+32.27}_{-31.12}$	...	...	...	...

Table 3.3: continued.

(1)	(2)	(3)	(4)	(5)	(6)	(7)	(8)	(9)	(10)	(11)	(12)	(13)	(14)	(15)	(16)	(17)	(18)
	RA	DEC		adopted	Lum	EW(Hα)	EW(Li)	TTS	A_V			Mass	Age	Disk	Log $\dot{M}_{acc}$	Log $\dot{M}_{acc}$	Log $\dot{M}_{acc}$
ID	(J2000)	(J2000)	Spectral type	Spectral type	($L_\odot$)	(Å)	(Å)	type	(mag)	clu	$\alpha(3.6-8.0\mu m)$	($M_\odot$)	(Myr)	property	($M_\odot$ yr^{-1})	($M_\odot$ yr^{-1})	($M_\odot$ yr^{-1})
78	05 46 40.43	+00 05 07.7	M2.5[a]	M2.5	0.702	−3.6[a]	0.6[a]	WTTS	1.9	yes	...	$0.29^{+0.03}_{-0.03}$	$0.22^{+0.09}_{-0.06}$	...	...	...	...
79	05 46 40.77	+00 27 22.5	M3[a],M3[b]	M3	0.233	−154.1[a],−166.0[b]	0.1[b]	CTTS	1.7	yes	−1.27	$0.30^{+0.07}_{-0.05}$	$1.17^{+1.57}_{-0.47}$	Thick	−8.29	−8.53	−8.50
80	05 46 43.82	+00 03 21.8	M5[a]	M5	0.040	−9.7[a]	...	WTTS	0.5	yes	...	$0.16^{+0.15}_{-0.03}$	$4.29^{+21.87}_{-1.74}$	...	...	...	...
81	05 46 43.84	+00 15 32.4	M1.5[a],M2[b]	M1.5	0.430	−11.5[a],−4.9[b]	0.6[a],0.6[b]	CTTS	2.2	yes	−1.60	$0.43^{+0.08}_{-0.06}$	$1.08^{+0.79}_{-0.35}$	Thick	−9.07	−9.11	−8.53
82	05 46 44.08	+00 18 03.2	K5[a],K6[b]	K5	2.072	−8.5[a],−7.1[b]	0.6[a],0.7[b]	CTTS	2.9	yes	−1.17	$0.82^{+0.40}_{-0.21}$	$0.56^{+1.62}_{-0.27}$	Thick	−8.13	−7.74	...
83	05 46 44.25	+00 30 29.5	M5.5[a]	M5.5	0.192	−19.4[a]	...	CTTS	2.3	yes	−2.65	$0.15^{+0.02}_{-0.02}$	$0.31^{+0.20}_{-0.12}$	No disk	−9.80	...	...
84	05 46 44.84	+00 16 59.8	M1[b]	M1	0.481	−14.0[b]	0.4[b]	CTTS	3.7	yes	−1.94	$0.46^{+0.14}_{-0.09}$	$1.08^{+3.81}_{-0.51}$	Transition disk	−8.87	...	...
85	05 46 45.00	+00 11 32.7	M4.5[a]	M4.5	0.112	−22.5[a]	...	CTTS	4.0	yes	−0.91	$0.19^{+0.02}_{-0.02}$	$1.38^{+0.43}_{-0.50}$	Thick	−10.03	−10.53	...
86	05 46 45.00	+00 24 48.7	M5.5[a]	M5.5	0.040	−9.9[a]	...	WTTS	0.0	yes	...	$0.12^{+0.03}_{-0.01}$	$2.52^{+1.95}_{-0.50}$	...	...	...	...
87	05 46 45.04	+00 05 33.9	M0.5[a]	M0.5	1.268	−26.7[a]	...	CTTS	2.8	yes	−0.89	$0.40^{+0.06}_{-0.05}$	$0.21^{+0.11}_{-0.06}$	Thick	−7.69	...	...
88	05 46 45.14	+00 03 46.4	M2.5[a]	M2.5	0.298	−33.6[a]	...	CTTS	3.9	yes	...	$0.36^{+0.08}_{-0.06}$	$1.25^{+0.77}_{-0.41}$	...	−8.86	...	...
89	05 46 46.87	+00 09 07.6	M0[b]	M0	1.105	−45.0[b]	0.4[b]	CTTS	3.8	yes	−0.76	$0.47^{+0.18}_{-0.09}$	$0.37^{+0.68}_{-0.16}$	Thick	−7.53	...	...
90	05 46 48.55	+00 21 28.2	K6.5[a]	K6.5	0.037	−275.7[a]	...	CTTS	6.8	yes	−0.21	...	...	Thick	...	...	...
91	05 46 48.73	+00 21 38.3	M4.5[a]	M4.5	0.237	−6.6[a]	...	WTTS	6.5	yes	−1.45	$0.21^{+0.09}_{-0.05}$	$0.54^{+1.90}_{-0.26}$	Thick	...	...	...
92	05 46 49.09	+00 28 38.3	M5[a]	M5	0.096	−13.7[a]	1.2[a]	WTTS	4.2	yes	−1.21	$0.17^{+0.06}_{-0.03}$	$1.22^{+2.07}_{-0.60}$	Thick	...	...	...
93	05 46 51.19	+00 18 08.2	M5.5[a]	M5.5	0.090	−20.9[a]	0.6[a]	CTTS	1.1	yes	...	$0.15^{+0.03}_{-0.02}$	$1.16^{+0.58}_{-0.38}$	...	−10.27	−10.43	−10.49
94	05 46 51.40	+00 19 47.2	M2[a]	M2	0.028	−113.3[a]	...	CTTS	4.8	yes	0.68	...	...	Thick	...	...	...
95	05 46 51.48	+00 19 21.3	M3.5[a],M1.5[b]	M3.5	0.179	−25.7[a],−25.1[b]	0.6[a],0.3[b]	CTTS	1.0	yes	−0.86	$0.27^{+0.03}_{-0.02}$	$1.40^{+0.34}_{-0.37}$	Thick	−9.49	−9.32	−9.34
96	05 46 51.85	+00 19 38.6	M4[a]	M4	0.264	−28.5[a]	0.7[a]	CTTS	3.9	yes	−0.78	$0.24^{+0.04}_{-0.03}$	$0.60^{+0.63}_{-0.24}$	Thick	−9.17	...	−9.08
97	05 46 52.41	+00 20 01.7	K9[b]	K9	0.586	−41.0[b]	0.5[b]	CTTS	3.3	yes	−1.02	$0.61^{+0.20}_{-0.13}$	$1.54^{+6.64}_{-0.72}$	Thick	−8.14	...	...
98	05 46 56.54	+00 20 52.9	K3[b]	K3	2.238	−2.3[b]	0.7[b]	WTTS	4.5	yes	−2.64	$1.34^{+0.17}_{-0.20}$	$1.65^{+1.10}_{-0.53}$	No disk	...	...	...
99	05 46 58.03	+00 14 27.8	M3[b]	M3	0.327	−19.0[b]	0.4[b]	CTTS	2.0	yes	−0.80	$0.30^{+0.10}_{-0.06}$	$0.71^{+1.50}_{-0.34}$	Thick	−9.14	...	...
100	05 46 58.13	+00 05 38.1	M0[b]	M0	2.957	−2.0[b]	0.7[b]	WTTS	3.6	yes	−1.71	$0.42^{+0.15}_{-0.07}$	$0.06^{+0.11}_{-0.03}$	Transition disk	...	...	...
101	05 47 01.95	+00 16 56.7	M6[a]	M6	0.046	−20.7[a]	...	CTTS	2.5	yes	...	$0.10^{+0.07}_{-...}$	$1.28^{+4.19}_{-0.15}$	...	−10.71	...	...
102	05 47 02.87	+00 16 51.9	M4.5[a]	M4.5	0.111	−19.6[a]	...	CTTS	3.6	yes	...	$0.21^{+0.10}_{-0.05}$	$1.65^{+4.69}_{-0.79}$	...	−10.11	...	...
103	05 47 03.97	+00 11 14.4	M2[b]	M2	0.378	−42.0[b]	0.4[b]	CTTS	0.9	yes	−1.00	$0.37^{+0.12}_{-0.08}$	$0.97^{+1.25}_{-0.43}$	Thick	−8.51	...	...
104	05 47 04.48	+00 15 47.2	K7[a]	K7	2.393	−1.5[a]	...	WTTS	11.3	yes	−1.38	$0.57^{+0.52}_{-0.20}$	$0.19^{+4.81}_{-0.12}$	Thick	...	...	...
105	05 47 04.94	+00 18 31.6	M1.5[a],M0.5[b]	M1.5	1.123	−3.5[a],−2.3[b]	0.4[b]	WTTS	3.6	yes	−2.23	$0.36^{+0.23}_{-0.09}$	$0.18^{+1.12}_{-0.11}$	Thin	...	...	...
106	05 47 04.98	+00 18 12.6	M5[a]	M5	0.100	−9.8[a]	...	WTTS	3.3	yes	...	$0.17^{+0.05}_{-0.04}$	$1.25^{+1.31}_{-0.50}$	...	...	...	...
107	05 47 05.06	+00 18 34.8	M1.5[a]	M1.5	0.640	−13.0[a]	...	CTTS	4.5	yes	−1.21	$0.36^{+0.09}_{-0.06}$	$0.43^{+3.04}_{-0.18}$	Thick	−8.68	...	...
108	05 47 05.12	+00 18 26.7	M3.5[a]	M3.5	0.249	−10.3[a]	...	WTTS	3.0	yes	...	$0.28^{+0.08}_{-0.05}$	$0.94^{+2.99}_{-0.39}$	...	...	...	...
109	05 47 05.34	+00 28 46.1	M3[a],M1.5[b]	M3	0.151	−4.3[a],−6.0[b]	0.3[b]	WTTS	1.5	yes	−2.37	$0.34^{+0.08}_{-0.06}$	$2.94^{+2.28}_{-1.07}$	Thin	...	...	...
110	05 47 06.00	+00 32 08.5	K0[b]	K0	8.749	−20.0[b]	0.7[b]	CTTS	8.5	yes	−1.26	$2.42^{+0.08}_{-0.28}$	$1.06^{+0.58}_{-0.36}$	Thick	−7.01	...	...
111	05 47 05.98	+00 25 53.1	M4.5[a]	M4.5	0.060	...	...	...	4.1	yes	−1.66	$0.21^{+0.11}_{-0.05}$	$4.15^{+13.27}_{-2.10}$	Thick	...	...	...
112	05 47 06.17	+00 20 32.5	M1[a]	M1	1.230	−14.1[a]	0.8[a]	CTTS	6.9	yes	−0.81	$0.37^{+0.08}_{-0.06}$	$0.17^{+0.79}_{-0.07}$	Thick	−8.07	...	...
113	05 47 06.96	+00 00 47.7	K4.5[b]	K4.5	1.907	−28.4[b]	0.5[b]	CTTS	2.0	yes	−0.94	$1.00^{+0.24}_{-0.21}$	$1.00^{+0.99}_{-0.42}$	Transition disk	−7.60	...	...
114	05 47 06.99	+00 31 55.9	M1[b]	M1	0.450	−63.0[b]	0.3[b]	CTTS	3.7	yes	−0.72	$0.46^{+0.14}_{-0.10}$	$1.23^{+6.78}_{-0.62}$	Thick	−8.11	...	...
115	05 47 07.26	+00 19 32.2	M0[b]	M0	6.445	−48.0[b]	0.3[b]	CTTS	3.9	yes	−1.13	$0.42^{+0.15}_{-0.05}$	$0.01^{+0.04}_{-0.01}$	Thick	−6.11	...	...
116	05 47 08.69	+00 00 14.0	M3[b]	M3	0.961	−9.4[b]	0.4[b]	WTTS	0.8	yes	−2.65	$0.25^{+0.08}_{-0.04}$	$0.09^{+1.74}_{-0.05}$	No disk	...	...	...
117	05 47 08.62	+00 19 23.9	M3[a]	M3	0.308	−39.4[a]	0.5[a]	CTTS	5.1	yes	−1.41	$0.30^{+0.04}_{-0.03}$	$0.77^{+0.47}_{-0.18}$	Thick	−8.80	...	−8.36
118	05 47 08.71	+00 16 34.7	M4.5[a]	M4.5	0.120	−78.9[a]	...	CTTS	5.1	yes	...	$0.20^{+0.09}_{-0.05}$	$1.36^{+2.30}_{-0.66}$	...	−9.30	...	...
119	05 47 10.72	+00 18 46.3	M1[a]	M1	0.684	−5.0[a]	0.6[a]	WTTS	6.1	yes	−0.85	$0.40^{+0.09}_{-0.06}$	$0.50^{+1.18}_{-0.19}$	Thick	...	...	...
120	05 47 10.89	+00 32 06.0	M1.5[b]	M1.5	0.520	−8.4[b]	0.6[b]	WTTS	1.9	yes	−1.43	$0.40^{+0.11}_{-0.08}$	$0.70^{+0.85}_{-0.31}$	Thick	...	...	...
121	05 47 10.98	+00 19 14.8	G6[b]	G6	11.106	−17.0[b]	0.6[b]	CTTS	6.1	yes	−1.27	$2.43^{+0.08}_{-0.09}$	$2.33^{+0.38}_{-0.32}$	Thick	−6.99	...	...

Table 3.3: continued.

(1)	(2)	(3)	(4)	(5)	(6)	(7)	(8)	(9)	(10)	(11)	(12)	(13)	(14)	(15)	(16)	(17)	(18)
	RA	DEC		adopted	Lum	EW(Hα)	EW(Li)	TTS	A_V			Mass	Age	Disk	Log $\dot{M}_{acc}$	Log $\dot{M}_{acc}$	Log $\dot{M}_{acc}$
ID	(J2000)	(J2000)	Spectral type	Spectral type	($L_\odot$)	(Å)	(Å)	type	(mag)	clu	$\alpha(3.6-8.0\mu m)$	($M_\odot$)	(Myr)	property	($M_\odot$ yr^{-1})	($M_\odot$ yr^{-1})	($M_\odot$ yr^{-1})
122	05 47 10.98	+00 21 32.2	M1[a]	M1	0.283	−2.5[a]	0.6[a]	WTTS	5.0	yes	−2.84	$0.50^{+0.12}_{-0.10}$	$2.78^{+8.28}_{-1.17}$	No disk	...	...	...
123	05 47 12.92	+00 22 06.5	M0[a]	M0	2.706	−154.1[a]	...	CTTS	12.7	yes	−1.27	$0.42^{+0.20}_{-0.08}$	$0.08^{+5.52}_{-0.04}$	Thick	−6.14	...	...
124	05 47 13.85	+00 00 17.1	M1[b]	M1	1.868	−30.4[b]	0.7[b]	CTTS	1.4	yes	−1.60	$0.36^{+0.09}_{-0.06}$	$0.08^{+0.10}_{-0.04}$	Thick	−7.31	...	...
125	05 47 16.58	−00 00 56.4	M4[b]	M4	0.249	−10.3[b]	0.4[b]	WTTS	1.1	yes	−1.45	$0.24^{+0.08}_{-0.05}$	$0.63^{+0.80}_{-0.31}$	Thick	...	...	...
126	05 47 17.16	+00 18 24.6	M1[b]	M1	0.234	−65.5[b]	0.3[b]	CTTS	2.3	yes	−1.55	$0.54^{+0.14}_{-0.12}$	$4.31^{+9.24}_{-2.20}$	Thick	−8.65	...	...
127	05 47 17.28	+00 38 21.4	K7[b]	K7	1.320	−8.3[b]	0.6[b]	CTTS	1.7	yes	−1.38	$0.61^{+0.17}_{-0.14}$	$0.53^{+10.55}_{-0.23}$	Thick	−8.35	...	...
128	05 47 19.72	+00 01 21.8	M5[b]	M5	0.070	−300.0[b]	0.5[b]	CTTS	0.0	yes	−1.29	$0.17^{+0.08}_{-0.04}$	$2.16^{+3.79}_{-0.95}$	Thick	−8.98	...	...
129	05 47 19.90	+00 16 13.1	M5[a]	M5	0.240	−60.9[a]	...	CTTS	4.1	yes	−1.17	$0.19^{+0.03}_{-0.03}$	$0.40^{+0.40}_{-0.14}$	Thick	−8.92	...	...
130	05 47 22.99	+00 17 56.7	M4[a]	M4	0.110	−4.5[a]	0.6[a]	WTTS	1.6	yes	...	$0.23^{+0.05}_{-0.04}$	$2.06^{+1.23}_{-0.71}$	...	...	...	...
131	05 47 25.05	+00 31 05.0	K7[b]	K7	0.250	−1.3[b]	0.2[b]	WTTS	0.3	yes	−2.72	$0.86^{+0.02}_{-0.15}$	$15.09^{+6.21}_{-7.29}$	No disk	...	...	...
132	05 47 57.53	+00 11 31.2	M4[b]	M4	0.396	−9.5[b]	0.4[b]	WTTS	1.0	yes	−2.68	$0.23^{+0.07}_{-0.04}$	$0.28^{+0.30}_{-0.14}$	No disk	...	...	...

Table 3.4: Parameters for YSOs in L1641. Column 4: [a] the values estimated from our VIMOS spectra; [b] the values from Allen (1995); [c] the values from Gâlfalk & Olofsson (2008). Column 6: stellar bolometric luminosity derived from optical SED fitting (see Sect. 3.2.3). Column 9: classification based on the criteria in Appendix (1). Column 11: aggregate/cluster population or distributed population. Column 13-14: stellar masses and ages estimated using PMS evolutionary tracks from Dotter et al. (2008). Column 16-18: accretion rates estimated with Hα, Hβ, and He I 5876Å emission line luminosities, respectively.

(1)	(2)	(3)	(4)	(5)	(6)	(7)	(8)	(9)	(10)	(11)	(12)	(13)	(14)	(15)	(16)	(17)	(18)
	RA	DEC		adopted	Lum	EW(Hα)	EW(Li)	TTS	A_V			Mass	Age	Disk	Log $\dot{M}_{acc}$	Log $\dot{M}_{acc}$	Log $\dot{M}_{acc}$
ID	(J2000)	(J2000)	Spectral type	Spectral type	($L_\odot$)	(Å)	(Å)	type	(mag)	clu	$\alpha(3.6-8.0\mu m)$	($M_\odot$)	(Myr)	property	($M_\odot$ yr^{-1})	($M_\odot$ yr^{-1})	($M_\odot$ yr^{-1})
1	05 35 14.56	-06 15 12.7	M1[a]	M1	0.569	−9.8[a]	...	CTTS	2.3	no	−1.20	$0.42^{+0.06}_{-0.05}$	$0.70^{+0.52}_{-0.22}$	Thick	−8.92	−9.11	−8.74
2	05 35 14.67	−06 15 07.3	M5[a]	M5	0.168	−23.2[a]	...	CTTS	2.6	no	−0.75	$0.19^{+0.04}_{-0.03}$	$0.69^{+0.53}_{-0.24}$	Thick	−9.71	...	...
3	05 35 14.72	−06 13 39.9	M5.5[a]	M5.5	0.292	−19.6[a]	...	CTTS	0.8	no	−2.60	$0.15^{+0.03}_{-0.02}$	$0.14^{+0.12}_{-0.06}$	No disk	−9.48	−9.86	−9.79
4	05 35 15.83	−06 24 45.7	M5[a]	M5	0.126	−10.9[a]	0.9[a]	WTTS	0.0	no	−2.56	$0.18^{+0.03}_{-0.02}$	$0.99^{+0.47}_{-0.27}$	Thin	...	...	...
5	05 35 17.80	−06 24 38.4	M1[a],M2[b]	M1	0.964	−6.3[a],−24.0[b]	0.7[a]	WTTS	0.3	no	−0.35	$0.39^{+0.03}_{-0.03}$	$0.28^{+0.07}_{-0.06}$	Thick	...	...	...
6	05 35 18.26	−06 24 30.3	M6[a],M3.5[b]	M6	0.116	−12.7[a]	...	WTTS	0.0	no	−2.48	$0.13^{+0.06}_{-0.02}$	$0.51^{+1.06}_{-0.16}$	Thin	...	...	...
7	05 35 18.95	−06 27 25.6	M4[b]	M4	0.187	−80.0[b]	...	CTTS	0.0	no	−1.16	$0.24^{+0.09}_{-0.06}$	$1.02^{+1.17}_{-0.47}$	Thick	−8.90	...	...
8	05 35 19.34	−06 24 14.5	M2.5[a],M2.5[b]	M2.5	0.262	−3.4[a]	...	WTTS	0.0	no	−2.65	$0.34^{+0.04}_{-0.03}$	$1.34^{+0.48}_{-0.26}$	No disk	...	...	...
9	05 35 21.77	−06 18 51.2	M4.5[a]	M4.5	0.116	−23.4[a]	...	CTTS	0.0	no	−1.77	$0.19^{+0.01}_{-0.01}$	$1.30^{+0.23}_{-0.20}$	Thick	−9.98	−10.31	−10.56
10	05 35 23.60	−06 28 24.4	M4[a],M3.5[b]	M4	0.633	−5.0[a]	...	WTTS	0.0	no	−2.80	$0.21^{+0.05}_{-0.03}$	$0.11^{+0.09}_{-0.05}$	No disk	...	...	...
11	05 35 24.45	−06 27 47.2	M4.5[a],M3.5[b]	M4.5	0.048	−0.2[a],−59.0[b]	...	WTTS	0.0	no	...	$0.21^{+0.06}_{-0.04}$	$5.91^{+4.99}_{-2.07}$	...	...	...	...
12	05 35 24.49	−06 28 40.5	M5[b]	M5	0.153	−13.0[b]	...	WTTS	0.0	no	−2.55	$0.18^{+0.07}_{-0.04}$	$0.70^{+1.09}_{-0.32}$	Thin	...	...	...
13	05 35 25.11	−06 47 56.6	M0[b]	M0	1.146	...	...	...	1.1	no	−0.84	$0.47^{+0.18}_{-0.09}$	$0.35^{+1.48}_{-0.16}$	Thick	...	...	...
14	05 35 25.70	−06 23 18.9	M3.5[a],M3[b]	M3.5	0.284	−3.9[a]	0.6[a]	WTTS	0.0	no	−2.62	$0.28^{+0.06}_{-0.04}$	$0.75^{+0.64}_{-0.26}$	No disk	...	...	...
15	05 35 26.59	−06 15 32.8	M3.5[a]	M3.5	0.187	−7.8[a]	...	WTTS	0.0	no	−2.79	$0.27^{+0.04}_{-0.03}$	$1.27^{+0.85}_{-0.43}$	No disk	...	...	...

Table 3.4: continued.

(1)	(2)	(3)	(4)	(5)	(6)	(7)	(8)	(9)	(10)	(11)	(12)	(13)	(14)	(15)	(16)	(17)	(18)
	RA	DEC		adopted	Lum	EW(Hα)	EW(Li)	TTS	A_V			Mass	Age	Disk	Log $\dot{M}_{acc}$	Log $\dot{M}_{acc}$	Log $\dot{M}_{acc}$
ID	(J2000)	(J2000)	Spectral type	Spectral type	($L_\odot$)	(Å)	(Å)	type	(mag)	clu	α(3.6 – 8.0μm)	($M_\odot$)	(Myr)	property	($M_\odot$ yr^{-1})	($M_\odot$ yr^{-1})	($M_\odot$ yr^{-1})
16	05 35 26.80	−06 15 34.4	M4[a]	M4	0.186	−4.9[a]	...	WTTS	0.0	no	−2.70	$0.25^{+0.03}_{-0.03}$	$1.09^{+0.61}_{-0.32}$	No disk	...	...	...
17	05 35 26.83	−06 26 47.6	M0[a],M0[b]	M0	0.567	−2.2[a]	0.5[a]	WTTS	0.0	no	−2.80	$0.59^{+0.20}_{-0.13}$	$1.54^{+1.78}_{-0.68}$	No disk	...	...	...
18	05 35 26.96	−06 27 13.0	M4.5[a]	M4.5	0.050	−6.2[a]	...	WTTS	0.0	no	...	$0.18^{+0.04}_{-0.03}$	$4.43^{+2.17}_{-1.22}$	...	...	...	...
19	05 35 27.17	−06 19 42.0	M1.5[a],M2.5[b]	M1.5	1.203	−8.5[a],−10.0[b]	...	WTTS	0.6	no	−1.62	$0.35^{+0.04}_{-0.04}$	$0.16^{+0.06}_{-0.04}$	Thick	...	...	...
20	05 35 27.35	−06 19 31.3	M1[a]	M1	0.021	−32.4[a]	...	CTTS	1.1	no	−0.52	...	...	Thick	...	...	...
21	05 35 28.28	−06 22 29.3	M6[a]	M6	0.024	−15.5[a]	...	WTTS	0.0	no	...	...	...	...	...	...	...
22	05 35 29.21	−06 16 29.7	M5[a],M5[b]	M5	0.553	−10.6[a],−14.0[b]	...	WTTS	1.0	no	−2.73	$0.19^{+0.02}_{-0.02}$	$0.08^{+0.04}_{-0.03}$	No disk	...	...	...
23	05 35 29.46	−06 16 26.6	M2.5[a]	M2.5	0.500	−3.3[a]	...	WTTS	1.1	no	−1.88	$0.30^{+0.03}_{-0.03}$	$0.39^{+0.14}_{-0.11}$	Thin	...	...	...
24	05 35 30.41	−06 27 07.2	M5.5[a]	M5.5	0.018	−11.9[a]	...	WTTS	0.0	no	...	$0.11^{+0.06}_{-0.00}$	$6.73^{+14.43}_{-0.48}$	...	...	...	...
25	05 35 31.05	−06 45 18.1	M3[b]	M3	0.627	...	...	...	0.0	no	−1.02	$0.27^{+0.08}_{-0.05}$	$0.21^{+0.20}_{-0.11}$	Thick	...	...	...
26	05 35 31.49	−06 14 18.9	M3[a]	M3	0.193	−10.8[a]	0.5[a]	WTTS	0.0	no	−2.78	$0.31^{+0.04}_{-0.03}$	$1.67^{+0.61}_{-0.37}$	No disk	...	...	...
27	05 35 31.89	−06 36 25.5	M6[b]	M6	0.070	...	...	...	0.0	no	−1.17	$0.11^{+0.06}_{-0.01}$	$0.82^{+2.05}_{-0.10}$	Thick	...	...	...
28	05 35 33.93	−06 14 32.8	M5[a]	M5	0.235	−50.4[a]	0.5[a]	CTTS	0.0	no	−1.11	$0.19^{+0.01}_{-0.01}$	$0.40^{+0.08}_{-0.07}$	Thick	−9.04	...	...
29	05 35 34.17	−06 22 57.8	M3[a]	M3	0.217	−3.2[a]	0.4[a]	WTTS	0.0	no	−2.61	$0.31^{+0.04}_{-0.03}$	$1.48^{+0.55}_{-0.34}$	No disk	...	...	...
30	05 35 34.19	−06 39 43.3	M3.5[b]	M3.5	0.274	...	...	...	0.0	no	−1.52	$0.27^{+0.09}_{-0.06}$	$0.72^{+0.82}_{-0.31}$	Thick	...	...	...
31	05 35 34.34	−06 24 22.8	M5.5[a]	M5.5	0.032	−17.3[a]	...	WTTS	0.0	no	−1.86	$0.13^{+0.04}_{-0.02}$	$3.93^{+4.41}_{-0.89}$	Thin	...	...	...
32	05 35 38.59	−06 23 43.1	M4[a],M3[b]	M4	0.145	−6.1[a],−13.0[b]	0.6[a]	WTTS	0.0	no	−2.46	$0.26^{+0.04}_{-0.03}$	$1.77^{+0.74}_{-0.46}$	Thin	...	...	...
33	05 35 40.83	−06 18 06.7	M3[a]	M3	0.202	−6.5[a]	0.5[a]	WTTS	0.0	no	−2.89	$0.33^{+0.04}_{-0.03}$	$1.79^{+0.71}_{-0.41}$	No disk	...	...	...
34	05 35 41.02	−06 22 45.4	M0[a],M1[b]	M0	1.839	−11.6[a],−14.0[b]	0.6[a]	CTTS	1.0	no	−1.74	$0.42^{+0.07}_{-0.05}$	$0.13^{+0.08}_{-0.04}$	Thick	−7.84	−8.01	...
35	05 35 41.65	−06 25 19.2	M6[a]	M6	0.024	−18.6[a]	...	CTTS	0.5	no	...	...	...	...	...	...	...
36	05 35 42.09	−06 16 20.8	M6[a]	M6	0.027	−21.0[a]	...	CTTS	0.0	no	−1.82	$0.10^{+0.05}_{-0.00}$	$3.28^{+4.83}_{-0.22}$	Thin	−11.09	...	...
37	05 35 42.84	−06 21 44.6	M2.5[a]	M2.5	0.264	−4.9[a]	...	WTTS	0.0	no	−1.42	$0.35^{+0.04}_{-0.03}$	$1.36^{+0.54}_{-0.27}$	Thick	...	...	...
38	05 35 42.76	−06 34 51.9	M0.5[b]	M0.5	0.491	...	...	...	0.0	no	−1.06	$0.51^{+0.18}_{-0.10}$	$1.35^{+2.05}_{-0.50}$	Thick	...	...	...
39	05 35 43.37	−06 22 19.6	M1.5[a]	M1.5	0.820	−103.4[a]	0.3[a]	CTTS	2.9	no	−1.55	$0.34^{+0.07}_{-0.05}$	$0.26^{+2.69}_{-0.10}$	Thick	−7.35	−7.63	−6.97
40	05 35 44.18	−06 28 16.4	M2[a]	M2	0.073	−141.6[a]	...	CTTS	1.2	no	−0.90	$0.47^{+0.09}_{-0.16}$	$18.64^{+27.19}_{-10.22}$	Thick	−9.23	−9.11	−8.82
41	05 35 44.27	−06 26 39.5	M6[a]	M6	0.035	−17.2[a]	...	WTTS	0.0	no	...	...	...	...	...	...	...
42	05 35 47.65	−06 21 36.1	M4[b]	M4	0.293	−30.0[b]	...	CTTS	0.0	no	−1.26	$0.23^{+0.07}_{-0.05}$	$0.48^{+0.49}_{-0.22}$	Thick	−9.08	...	...
43	05 35 48.28	−06 17 59.4	M2[b]	M2	0.287	−10.0[b]	...	WTTS	0.3	no	−2.73	$0.40^{+0.12}_{-0.09}$	$1.65^{+1.50}_{-0.72}$	No disk	...	...	...
44	05 35 48.39	−06 17 36.2	M4[b]	M4	0.214	−11.0[b]	...	WTTS	0.0	no	−2.65	$0.24^{+0.09}_{-0.05}$	$0.81^{+0.94}_{-0.37}$	No disk	...	...	...
45	05 35 50.19	−06 50 40.2	K7[a]	K7	0.285	−124.9[a]	...	CTTS	1.3	no	−0.67	$0.88^{+0.03}_{-0.21}$	$11.83^{+14.86}_{-6.24}$	Thick	−8.19	...	...
46	05 35 57.30	−06 40 28.1	M3.5[a],M3[b]	M3.5	0.303	−113.8[a]	0.4[a]	CTTS	0.0	no	−0.94	$0.27^{+0.01}_{-0.01}$	$0.66^{+0.10}_{-0.08}$	Thick	−8.25	−8.81	−8.95
47	05 35 57.31	−06 15 37.7	M2.5[a],M3[b]	M2.5	0.284	−34.9[a],−60.0[b]	0.4[a]	CTTS	0.0	no	−1.46	$0.36^{+0.07}_{-0.05}$	$1.39^{+0.65}_{-0.43}$	Thick	−8.88	−8.71	−8.62
48	05 35 57.45	−06 42 41.9	K4[a],M0[b]	K4	3.208	...	...	...	2.0	no	−0.62	$1.13^{+0.33}_{-0.35}$	$0.65^{+1.00}_{-0.35}$	Thick	...	...	...
49	05 35 57.45	−06 16 35.0	M3[a],M3[b]	M3	0.900	−1.7[a]	...	WTTS	0.0	no	−2.66	$0.25^{+0.03}_{-0.02}$	$0.10^{+0.05}_{-0.03}$	No disk	...	...	...
50	05 35 57.85	−06 23 44.4	M5[a]	M5	0.156	−19.3[a]	...	CTTS	0.0	no	−1.12	$0.19^{+0.04}_{-0.03}$	$0.79^{+0.48}_{-0.27}$	Thick	−9.87	−10.13	...
51	05 35 58.10	−06 14 50.9	M6[b]	M6	0.144	−13.0[b]	...	WTTS	0.0	no	−2.62	$0.13^{+0.06}_{-0.02}$	$0.32^{+0.61}_{-0.10}$	No disk	...	...	...
52	05 35 58.25	−06 36 43.1	M0[b]	M0	0.985	...	...	...	1.1	no	−1.37	$0.48^{+0.18}_{-0.09}$	$0.46^{+0.70}_{-0.19}$	Thick	...	...	...
53	05 35 58.26	−06 14 04.6	M0.5[a]	M0.5	0.105	−2.6[a]	...	WTTS	4.2	no	−1.02	$0.64^{+0.05}_{-0.16}$	$25.05^{+31.16}_{-13.54}$	Thick	...	...	...
54	05 35 59.75	−06 16 06.4	K4.5[a],M0[b]	K4.5	1.336	−4.0[a],−20.0[b]	0.4[a]	WTTS	0.0	no	−1.49	$1.00^{+0.22}_{-0.25}$	$1.64^{+10.29}_{-0.77}$	Thick	...	...	...
55	05 35 59.84	−06 42 30.5	M4.5[a]	M4.5	0.140	−132.2[a]	...	CTTS	0.0	no	−0.97	$0.22^{+0.04}_{-0.03}$	$1.36^{+0.73}_{-0.35}$	Thick	−8.91	−9.45	−9.08
56	05 36 00.18	−06 42 33.9	K5[b]	K5	3.383	...	...	...	2.2	no	−1.46	$0.82^{+0.32}_{-0.14}$	$0.27^{+0.43}_{-0.10}$	Thick	...	−7.42	...
57	05 36 01.09	−06 25 07.7	M4[a],M3.5[b]	M4	0.254	−7.9[a],−45.0[b]	0.6[a]	WTTS	0.0	no	−1.74	$0.24^{+0.03}_{-0.02}$	$0.61^{+0.31}_{-0.16}$	Thick	...	...	...
58	05 36 01.10	−06 15 31.4	M1.5[a],M1[b]	M1.5	0.458	−35.0[a],−120.0[b]	0.6[a]	CTTS	0.3	no	−1.15	$0.43^{+0.08}_{-0.07}$	$1.02^{+0.56}_{-0.34}$	Thick	−8.41	−8.41	−8.23
59	05 36 01.66	−06 42 36.2	M5.5[a],M5[b]	M5.5	0.128	−53.9[a]	0.4[a]	CTTS	0.1	no	−1.65	$0.16^{+0.04}_{-0.03}$	$0.74^{+0.57}_{-0.30}$	Thick	−9.50	−10.09	...

Table 3.4: continued.

(1)	(2)	(3)	(4)	(5)	(6)	(7)	(8)	(9)	(10)	(11)	(12)	(13)	(14)	(15)	(16)	(17)	(18)
	RA	DEC		adopted	Lum	EW(Hα)	EW(Li)	TTS	A_V			Mass	Age	Disk	Log $\dot{M}_{acc}$	Log $\dot{M}_{acc}$	Log $\dot{M}_{acc}$
ID	(J2000)	(J2000)	Spectral type	Spectral type	($L_\odot$)	(Å)	(Å)	type	(mag)	clu	$\alpha(3.6-8.0\mu m)$	($M_\odot$)	(Myr)	property	($M_\odot$ yr^{-1})	($M_\odot$ yr^{-1})	($M_\odot$ yr^{-1})
60	05 36 05.00	−06 42 44.0	M5[a],M5[b]	M5	0.361	−19.0[a]	0.3[a]	CTTS	0.0	no	−1.55	$0.17^{+0.03}_{-0.02}$	$0.14^{+0.08}_{-0.05}$	Thick	−9.27	−9.65	−9.72
61	05 36 04.98	−06 46 41.4	M0.5[b]	M0.5	1.027	...	...	...	0.0	no	−1.96	$0.43^{+0.13}_{-0.08}$	$0.33^{+0.32}_{-0.14}$	Thin	...	...	...
62	05 36 05.08	−06 29 32.2	M0[b]	M0	0.549	−14.0[b]	...	CTTS	0.0	no	−1.35	$0.55^{+0.20}_{-0.11}$	$1.37^{+1.75}_{-0.65}$	Thick	−8.76	...	...
63	05 36 05.16	−06 25 25.4	M1.5[b],M0[c]	M1.5	0.550	−4.8[c]	0.6[c]	WTTS	0.0	no	−2.75	$0.39^{+0.11}_{-0.08}$	$0.63^{+0.50}_{-0.27}$	No disk	...	...	...
64	05 36 06.59	−06 31 43.0	M3.5[b]	M3.5	0.159	...	...	...	0.0	no	−1.23	$0.28^{+0.11}_{-0.07}$	$1.84^{+2.32}_{-0.82}$	Transition disk	...	...	...
65	05 36 06.65	−06 32 17.2	K5[b]	K5	1.917	−18.0[b]	...	CTTS	4.2	no	−1.38	$0.86^{+0.30}_{-0.15}$	$0.70^{+1.08}_{-0.27}$	Thick	−7.81	...	...
66	05 36 06.66	−06 14 25.9	K6[a],M0[b]	K6	1.092	−13.1[a],−22.0[b]	0.5[a]	CTTS	1.6	no	−1.42	$0.78^{+0.18}_{-0.13}$	$1.22^{+1.06}_{-0.43}$	Thick	−8.31	−8.01	−7.51
67	05 36 06.93	−06 18 53.4	M4.5[b]	M4.5	0.878	−10.0[b]	...	WTTS	0.0	no	−2.74	$0.19^{+0.05}_{-0.01}$	$0.03^{+0.06}_{-0.01}$	No disk	...	...	...
68	05 36 08.29	−06 48 36.3	M0.5[a],M2[b]	M0.5	0.705	−67.5[a]	...	CTTS	1.7	no	−0.41	$0.49^{+0.04}_{-0.04}$	$0.75^{+0.23}_{-0.15}$	Thick	−7.69	−7.88	...
69	05 36 08.34	−06 24 37.9	M5.5[a],M6[b],M7[c]	M5.5	0.252	−14.0[a],−17.0[b],−27.4[c]	0.5[a]	WTTS	0.0	yes	−1.79	$0.15^{+0.03}_{-0.02}$	$0.18^{+0.13}_{-0.09}$	Thick	...	...	...
70	05 36 08.57	−06 40 33.6	M6[a],M5.5[b]	M6	0.046	−32.8[a]	0.5[a]	CTTS	0.0	no	...	...	...	...	...	...	...
71	05 36 09.35	−06 17 10.8	M3[a],M2.5[b]	M3	0.483	−3.2[a]	0.7[a]	WTTS	0.0	no	−2.77	$0.30^{+0.03}_{-0.02}$	$0.40^{+0.09}_{-0.08}$	No disk	...	...	...
72	05 36 09.49	−06 18 36.3	M2[b],M1[c]	M2	0.744	−6.2[c]	0.4[c]	WTTS	0.0	no	−2.63	$0.33^{+0.09}_{-0.06}$	$0.27^{+0.21}_{-0.11}$	No disk	...	...	...
73	05 36 09.52	−06 24 33.7	M4.5[b],M4.5[c]	M4.5	0.044	−188.0[b],−66.1[c]	...	CTTS	0.0	yes	−1.53	$0.20^{+0.11}_{-0.05}$	$6.17^{+13.10}_{-2.83}$	Thick	−10.13	...	...
74	05 36 10.19	−06 18 54.8	K7.5[a],K5[b]	K7.5	0.163	0.2[a],−13.0[b]	...	CTTS	3.1	no	−2.47	$0.75^{+0.05}_{-0.16}$	$23.25^{+27.23}_{-12.47}$	Thin	−9.81	...	...
75	05 36 10.44	−06 20 01.5	K3[b],K7.5[c]	K3	0.964	−2.3[c]	0.3[c]	WTTS	0.9	no	−2.76	$1.25^{+0.03}_{-0.07}$	$6.50^{+3.47}_{-1.85}$	No disk	...	...	...
76	05 36 11.12	−06 18 14.1	M6[a],M6[c]	M6	0.043	−19.7[a],−22.4[c]	0.8[a]	CTTS	0.0	no	...	$0.11^{+0.05}_{-0.01}$	$1.89^{+2.67}_{-0.34}$	...	−10.82	−11.12	...
77	05 36 11.31	−06 16 56.0	M5.5[a]	M5.5	0.077	−12.2[a]	0.5[a]	WTTS	0.0	no	−1.62	$0.13^{+0.06}_{-0.02}$	$1.03^{+2.32}_{-0.30}$	Thick	...	...	...
78	05 36 11.46	−06 22 22.1	K7[c]	K7	1.436	−21.6[c]	...	CTTS	6.3	yes	−1.14	$0.60^{+0.16}_{-0.14}$	$0.44^{+1.54}_{-0.19}$	Thick	−7.76	...	...
79	05 36 11.67	−06 24 58.4	M5[a],M6.5[c]	M5	0.045	−7.7[a],−11.3[c]	...	WTTS	0.0	yes	−1.23	$0.16^{+0.07}_{-0.03}$	$3.55^{+5.18}_{-1.33}$	Transition disk	...	...	...
80	05 36 12.61	−06 23 39.6	M5[a],M5[b],M3[c]	M5	0.232	−23.2[a],−36.0[b],−39.3[c]	...	CTTS	0.4	yes	−1.51	$0.17^{+0.02}_{-0.01}$	$0.31^{+0.10}_{-0.07}$	Thick	−9.50	−10.12	−9.87
81	05 36 12.97	−06 23 33.0	M2.5[a],M1.5[c]	M2.5	0.910	−4.1[a],−5.0[c]	0.6[a],0.2[c]	WTTS	1.9	yes	−2.67	$0.28^{+0.04}_{-0.03}$	$0.14^{+0.06}_{-0.05}$	No disk	...	...	...
82	05 36 12.97	−06 23 33.0	M1.5[c]	M1.5	1.699	−7.3[c]	...	WTTS	3.5	yes	−2.06	$0.38^{+0.11}_{-0.06}$	$0.12^{+0.46}_{-0.08}$	Transition disk	...	...	...
83	05 36 13.15	−06 25 41.1	M3[a],M3[b],M2.5[c]	M3	0.223	−2.6[a],−3.4[c]	0.6[a],0.5[c]	WTTS	0.0	yes	−2.74	$0.32^{+0.04}_{-0.03}$	$1.44^{+0.58}_{-0.36}$	No disk	...	...	...
84	05 36 13.45	−06 43 55.1	M3[a]	M3	0.005	−36.5[a]	...	CTTS	1.8	no	...	...	...	...	...	...	...
85	05 36 14.76	−06 13 16.9	M1[a]	M1	0.355	−66.7[a]	0.5[a]	CTTS	0.2	no	−1.19	$0.51^{+0.09}_{-0.08}$	$2.09^{+1.02}_{-0.70}$	Thick	−8.29	−8.21	−8.05
86	05 36 15.07	−06 17 36.9	K3[a],K5[b]	K3	2.356	−2.3[a],−11.0[b]	0.4[a]	WTTS	1.6	no	−1.19	$1.30^{+0.15}_{-0.14}$	$1.42^{+0.67}_{-0.35}$	Thick	...	...	...
87	05 36 15.60	−06 27 20.0	M3.5[a]	M3.5	0.128	−4.4[a]	0.5[a]	WTTS	0.0	no	−2.72	$0.26^{+0.05}_{-0.04}$	$2.25^{+1.47}_{-0.70}$	No disk	...	...	...
88	05 36 15.84	−06 14 50.7	M2.5[a],M2.5[b]	M2.5	0.214	−106.4[a],−63.0[b]	0.6[a]	CTTS	0.0	no	−1.50	$0.38^{+0.08}_{-0.06}$	$2.24^{+2.14}_{-0.84}$	Transition disk	−8.52	−9.38	−9.40
89	05 36 17.11	−06 28 20.2	M5[a]	M5	0.022	−78.5[a]	...	CTTS	1.0	no	−1.44	$0.14^{+0.12}_{-0.02}$	$8.57^{+31.43}_{-3.57}$	Thick	−10.52	−11.51	...
90	05 36 17.23	−06 17 24.5	M5[a]	M5	0.372	−6.4[a]	0.6[a]	WTTS	0.0	no	−1.61	$0.19^{+0.02}_{-0.02}$	$0.18^{+0.09}_{-0.06}$	Transition disk	...	...	...
91	05 36 18.48	−06 20 38.7	M0[b],M0.5[c]	M0	0.533	−75.0[b],−44.8[c]	0.5[c]	CTTS	0.6	yes	−1.52	$0.56^{+0.21}_{-0.11}$	$1.45^{+2.76}_{-0.61}$	Thick	−8.16	...	...
92	05 36 18.88	−06 22 04.2	M3[a],M3[b],M2.5[c]	M3	0.130	−7.9[a],−5.3[c]	...	WTTS	0.0	yes	...	$0.32^{+0.03}_{-0.03}$	$3.27^{+0.86}_{-0.60}$	...	...	...	...
93	05 36 19.09	−06 22 50.6	M6[a],M7[c]	M6	0.033	−11.6[a],−13.9[c]	...	WTTS	0.0	yes	...	$0.11^{+0.07}_{-0.00}$	$2.50^{+6.87}_{-0.54}$	...	...	...	...
94	05 36 19.38	−06 25 51.3	M5[a],M4.5[c]	M5	0.189	−123.7[a],−123.0[c]	0.3[a]	CTTS	0.4	yes	−1.11	$0.19^{+0.03}_{-0.03}$	$0.58^{+0.28}_{-0.20}$	Thick	−8.72	−9.05	−9.38
95	05 36 21.10	−06 17 17.3	M4.5[a],M5[b]	M4.5	0.249	−11.9[a],−14.0[b]	...	WTTS	0.0	no	−2.64	$0.20^{+0.01}_{-0.01}$	$0.40^{+0.09}_{-0.07}$	No disk	...	...	...
96	05 36 21.16	−06 26 56.9	M4.5[a]	M4.5	0.049	−22.1[a]	0.9[a]	CTTS	0.0	yes	−1.46	$0.19^{+0.03}_{-0.02}$	$4.58^{+1.85}_{-1.09}$	Thick	−10.63	−10.80	−10.41
97	05 36 21.57	−06 22 52.4	M0.5[c]	M0.5	0.636	−70.7[c]	...	CTTS	9.5	yes	−0.83	$0.50^{+0.18}_{-0.10}$	$0.89^{+1.48}_{-0.36}$	Thick	−7.75	...	...
98	05 36 21.84	−06 26 02.0	M0[a],K7[b],K7.5[c]	M0	1.166	−10.2[a],−71.0[b],−18.3[c]	0.6[a],0.7[c]	CTTS	3.8	yes	−1.01	$0.49^{+0.08}_{-0.05}$	$0.37^{+0.20}_{-0.10}$	Thick	−8.30	...	...
99	05 36 21.88	−06 23 29.9	M1[b],M4[c]	M1	2.138	−10.0[b],−12.7[c]	...	CTTS	10.2	yes	0.14	$0.35^{+0.10}_{-0.06}$	$0.06^{+3.24}_{-0.03}$	Thick	−7.68	...	...
100	05 36 21.96	−06 41 42.0	M5[b]	M5	0.231	...	...	...	0.0	no	−1.43	$0.18^{+0.06}_{-0.04}$	$0.36^{+0.46}_{-0.18}$	Thick	...	...	...
101	05 36 22.47	−06 23 44.8	M0.5[c]	M0.5	0.451	−243.3[c]	1.3[c]	CTTS	6.0	yes	−1.49	$0.54^{+0.18}_{-0.11}$	$1.70^{+7.39}_{-0.76}$	Thick	−7.38	...	...
102	05 36 23.26	−06 19 37.5	M3.5[b],M2.5[c]	M3.5	0.156	−8.1[c]	0.9[c]	WTTS	1.2	no	−2.60	$0.28^{+0.11}_{-0.07}$	$1.90^{+2.64}_{-0.84}$	No disk	...	...	...
103	05 36 24.48	−06 22 23.2	M4[a],M3[c]	M4	0.380	−8.5[a],−16.5[c]	0.6[a]	WTTS	2.5	yes	−2.06	$0.23^{+0.03}_{-0.03}$	$0.30^{+0.22}_{-0.11}$	Thin	...	...	...

Table 3.4: continued.

(1)	(2)	(3)	(4)	(5)	(6)	(7)	(8)	(9)	(10)	(11)	(12)	(13)	(14)	(15)	(16)	(17)	(18)
	RA	DEC		adopted	Lum	EW(Hα)	EW(Li)	TTS	A_V			Mass	Age	Disk	Log $\dot{M}_{acc}$	Log $\dot{M}_{acc}$	Log $\dot{M}_{acc}$
ID	(J2000)	(J2000)	Spectral type	Spectral type	($L_\odot$)	(Å)	(Å)	type	(mag)	clu	$\alpha(3.6-8.0\mu m)$	($M_\odot$)	(Myr)	property	($M_\odot$ yr^{-1})	($M_\odot$ yr^{-1})	($M_\odot$ yr^{-1})
104	05 36 24.54	−06 52 34.2	M5[a]	M5	0.132	−50.0[a]	0.5[a]	CTTS	0.0	no	−1.51	$0.19^{+0.02}_{-0.02}$	$0.99^{+0.31}_{-0.21}$	Thick	−9.48	−9.67	−9.64
105	05 36 25.13	−06 44 41.9	K4.5[a],K3[b]	K4.5	3.575	−8.7[a]	0.4[a]	CTTS	6.0	yes	−0.34	$0.92^{+0.40}_{-0.25}$	$0.34^{+0.70}_{-0.17}$	Thick	−7.73	...	...
106	05 36 25.28	−06 23 07.2	M7[c]	M7	0.041	−13.7[c]	0.9[c]	WTTS	0.0	yes	...	...	...	...	...	...	...
107	05 36 25.41	−06 24 31.2	M6[a],M6[c]	M6	0.083	−9.8[a],−17.6[c]	...	WTTS	0.0	yes	−2.70	$0.12^{+0.06}_{-0.01}$	$0.71^{+1.49}_{-0.15}$	No disk	...	...	...
108	05 36 25.55	−06 51 28.3	M5[a]	M5	0.112	−10.2[a]	0.5[a]	WTTS	0.0	no	−2.53	$0.16^{+0.04}_{-0.03}$	$0.93^{+0.80}_{-0.34}$	Thin	...	...	...
109	05 36 26.08	−06 26 15.5	M3.5[b],M8.5[c]	M3.5	0.094	−12.4[a],−10.0[b],−74.2[c]	...	WTTS	2.9	yes	−2.72	$0.29^{+0.13}_{-0.07}$	$4.34^{+6.75}_{-1.97}$	No disk	...	...	...
110	05 36 26.71	−06 26 29.0	M0.5[b],K7.5[c]	M0.5	1.866	−3.2[c]	0.4[c]	WTTS	1.1	yes	−2.66	$0.39^{+0.12}_{-0.07}$	$0.11^{+0.14}_{-0.05}$	No disk	...	...	...
111	05 36 26.83	−06 24 57.5	M5[c]	M5	0.196	−16.9[c]	0.6[c]	WTTS	0.0	yes	−2.81	$0.17^{+0.06}_{-0.04}$	$0.42^{+0.63}_{-0.19}$	No disk	...	...	...
112	05 36 27.01	−06 21 07.6	M3[b],M2.5[c]	M3	0.023	−15.0[b]	...	CTTS	0.0	yes	...	$0.36^{+0.04}_{-0.11}$	$59.50^{+24.98}_{-31.27}$	...	...	...	...
113	05 36 27.72	−06 23 12.3	M5[c]	M5	0.570	−36.5[c]	...	CTTS	0.3	yes	−1.23	$0.17^{+0.05}_{-0.01}$	$0.04^{+0.09}_{-0.02}$	Thick	−8.56	...	...
114	05 36 27.89	−06 25 36.0	M3[c]	M3	0.230	−21.9[c]	0.2[c]	CTTS	0.1	yes	−1.91	$0.30^{+0.10}_{-0.07}$	$1.26^{+1.31}_{-0.59}$	Transition disk	−9.35	...	...
115	05 36 28.10	−06 44 32.6	M2.5[b]	M2.5	0.252	...	...	...	0.4	yes	−1.87	$0.35^{+0.12}_{-0.08}$	$1.54^{+1.71}_{-0.70}$	Thin	...	...	...
116	05 36 29.06	−06 38 40.7	M8[a],M3[b]	M8	0.053	−42.0[a]	...	CTTS	0.0	no	−1.49	...	...	Thick	...	...	...
117	05 36 29.59	−06 38 50.4	M4.5[a],M5[b]	M4.5	0.109	−8.2[a]	0.3[a]	WTTS	0.0	no	...	$0.19^{+0.04}_{-0.03}$	$1.43^{+0.76}_{-0.44}$	...	...	...	...
118	05 36 30.10	−06 23 10.2	M0.5[b],K6[c]	M0.5	0.450	−13.0[b],−7.3[c]	0.5[c]	WTTS	0.9	yes	−1.16	$0.52^{+0.18}_{-0.11}$	$1.58^{+2.59}_{-0.69}$	Thick	...	...	...
119	05 36 30.23	−06 42 46.1	M1.5[a],M2[b]	M1.5	0.664	−35.8[a]	...	CTTS	6.5	yes	−1.08	$0.37^{+0.10}_{-0.06}$	$0.42^{+5.19}_{-0.16}$	Thick	−8.09	...	...
120	05 36 30.50	−06 23 56.6	M4.5[b],M6[c]	M4.5	0.028	−36.1[c]	...	CTTS	0.0	yes	−1.75	$0.19^{+0.10}_{-0.05}$	$11.35^{+20.32}_{-5.38}$	Thick	−10.78	...	...
121	05 36 30.52	−06 42 03.2	M6[a],M6[b]	M6	0.030	−21.1[a]	0.6[a]	CTTS	0.0	yes	...	$0.10^{+0.06}_{-0.00}$	$2.56^{+6.39}_{-0.01}$	...	−11.00	−11.13	−11.30
122	05 36 30.96	−06 52 41.0	M2[a]	M2	0.012	...	...	...	1.7	no	0.40	...	...	Thick	...	...	...
123	05 36 31.84	−06 23 23.1	M6.5[c]	M6.5	0.040	−37.0[c]	...	CTTS	0.0	yes	−1.27	$0.12^{+0.07}_{-0.01}$	$2.63^{+6.52}_{-0.59}$	Thick	−10.55	...	...
124	05 36 32.38	−06 19 19.9	G8[b]	G8	4.874	...	...	...	2.9	no	−2.03	$1.96^{+0.07}_{-0.10}$	$3.67^{+0.99}_{-0.73}$	Transition disk	...	...	...
125	05 36 32.42	−06 40 43.0	M5[a]	M5	0.144	−39.2[a]	0.4[a]	CTTS	0.0	no	−1.25	$0.19^{+0.02}_{-0.02}$	$0.90^{+0.29}_{-0.22}$	Thick	−9.54	−9.83	−9.88
126	05 36 32.82	−06 39 54.9	K7.5[a],M0[b]	K7.5	0.442	−0.7[a]	0.3[a]	WTTS	0.3	no	−2.99	$0.69^{+0.16}_{-0.14}$	$3.10^{+2.61}_{-1.27}$	No disk	...	...	...
127	05 36 32.89	−06 44 20.9	M1[a],M2[b]	M1	0.544	−70.7[a]	...	CTTS	4.8	yes	−1.04	$0.43^{+0.20}_{-0.12}$	$0.81^{+10.19}_{-0.47}$	Thick	−7.88	−8.13	−7.95
128	05 36 33.81	−06 19 27.0	M5[c]	M5	0.155	−9.7[c]	1.1[c]	WTTS	0.0	no	−2.72	$0.17^{+0.07}_{-0.04}$	$0.60^{+0.96}_{-0.27}$	No disk	...	...	...
129	05 36 35.23	−06 50 12.2	M6[a],M6[b]	M6	0.058	−5.1[a]	0.5[a]	WTTS	0.0	no	...	$0.11^{+0.06}_{-0.01}$	$1.11^{+2.54}_{-0.14}$	...	...	...	...
130	05 36 35.76	−06 42 49.9	M2.5[a]	M2.5	0.213	−34.1[a]	...	CTTS	2.5	yes	−1.10	$0.34^{+0.14}_{-0.09}$	$1.87^{+6.00}_{-0.99}$	Thick	−9.18	−9.40	−9.24
131	05 36 36.93	−06 33 24.2	K8[b]	K8	1.913	−110.0[b]	...	CTTS	3.9	no	−1.27	$0.53^{+0.14}_{-0.11}$	$0.22^{+0.24}_{-0.10}$	Thick	−6.63	...	...
132	05 36 40.69	−06 30 09.3	M0[b]	M0	0.570	...	...	...	0.0	no	−1.57	$0.55^{+0.20}_{-0.11}$	$1.28^{+1.70}_{-0.57}$	Thick	...	...	...
133	05 36 40.69	−06 52 04.5	M2[a]	M2	0.383	−6.2[a]	0.5[a]	WTTS	0.0	no	−2.64	$0.37^{+0.06}_{-0.05}$	$0.90^{+0.36}_{-0.26}$	No disk	...	...	...
134	05 36 40.94	−06 41 17.8	M5[a]	M5	0.204	−20.1[a]	0.5[a]	CTTS	0.5	no	−1.23	$0.19^{+0.02}_{-0.02}$	$0.54^{+0.16}_{-0.12}$	Thick	−9.64	−10.15	−10.00
135	05 36 41.35	−06 34 00.4	M0[b]	M0	4.188	−148.0[b]	...	CTTS	5.7	no	−0.30	$0.41^{+0.16}_{-0.06}$	$0.03^{+0.06}_{-0.02}$	Thick	−5.82	...	...
136	05 36 41.98	−06 20 45.4	M6[b]	M6	0.056	−17.0[b]	...	WTTS	0.0	no	−2.72	$0.11^{+0.06}_{-0.00}$	$1.08^{+2.41}_{-0.08}$	No disk	...	...	...
137	05 36 43.77	−06 15 28.6	M4[b]	M4	0.215	−10.0[b]	...	WTTS	0.0	no	−1.36	$0.24^{+0.09}_{-0.05}$	$0.81^{+0.96}_{-0.36}$	Thick	...	...	...
138	05 36 45.21	−06 28 09.6	M3.5[b]	M3.5	0.453	−12.0[b]	...	WTTS	0.0	no	−2.66	$0.25^{+0.07}_{-0.05}$	$0.29^{+0.26}_{-0.14}$	No disk	...	...	...
139	05 36 45.79	−06 48 16.0	M4.5[a]	M4.5	0.007	−4.6[a]	...	WTTS	0.0	no	...	$0.16^{+0.02}_{-0.03}$	$65.63^{+21.97}_{-24.53}$	...	...	...	...
140	05 36 46.62	−06 39 50.0	M5.5[a],M2[b]	M5.5	0.065	−15.2[a]	0.4[a]	WTTS	0.0	no	...	$0.14^{+0.03}_{-0.02}$	$1.53^{+1.13}_{-0.44}$	...	...	...	...
141	05 36 50.14	−06 41 29.2	K5[a],M0[b]	K5	1.849	−7.6[a]	0.5[a]	CTTS	3.5	no	−1.68	$0.85^{+0.31}_{-0.18}$	$0.72^{+1.22}_{-0.30}$	Thick	−8.30	−7.96	−7.34
142	05 36 50.23	−06 48 58.2	M4.5[a],M5[b]	M4.5	0.333	−5.3[a]	0.6[a]	WTTS	0.0	no	−2.57	$0.20^{+0.01}_{-0.01}$	$0.25^{+0.04}_{-0.04}$	No disk	...	...	...
143	05 36 54.41	−06 51 05.5	M5.5[a]	M5.5	0.019	−1.8[a]	...	WTTS	0.0	no	...	$0.11^{+0.10}_{-0.01}$	$6.56^{+24.94}_{-0.88}$	...	...	...	...
144	05 37 49.54	−06 56 27.4	M3.5[a]	M3.5	0.586	−20.0[a]	0.6[a]	CTTS	0.6	yes	−1.98	$0.26^{+0.03}_{-0.03}$	$0.20^{+0.08}_{-0.06}$	Transition disk	−8.65	−8.88	−8.75
145	05 37 51.72	−06 56 51.9	M1.5[a]	M1.5	1.324	−39.0[a]	0.5[a]	CTTS	1.4	yes	−1.43	$0.34^{+0.08}_{-0.05}$	$0.12^{+0.15}_{-0.05}$	Thick	−7.47	−7.38	−7.02
146	05 37 53.28	−07 02 27.2	M4.5[a]	M4.5	0.059	−3.7[a]	...	WTTS	0.0	no	...	$0.20^{+0.05}_{-0.04}$	$4.13^{+3.06}_{-1.44}$	...	...	...	...
147	05 37 54.48	−06 57 31.1	K6.5[a]	K6.5	0.939	−2.6[a]	0.4[a]	WTTS	0.9	yes	−1.11	$0.72^{+0.28}_{-0.24}$	$1.21^{+4.48}_{-0.70}$	Thick	...	...	...

Table 3.4: continued.

(1)	(2)	(3)	(4)	(5)	(6)	(7)	(8)	(9)	(10)	(11)	(12)	(13)	(14)	(15)	(16)	(17)	(18)
	RA	DEC		adopted	Lum	EW(Hα)	EW(Li)	TTS	A_V			Mass	Age	Disk	Log $\dot{M}_{acc}$	Log $\dot{M}_{acc}$	Log $\dot{M}_{acc}$
ID	(J2000)	(J2000)	Spectral type	Spectral type	($L_\odot$)	(Å)	(Å)	type	(mag)	clu	$\alpha(3.6-8.0\mu m)$	($M_\odot$)	(Myr)	property	($M_\odot$ yr^{-1})	($M_\odot$ yr^{-1})	($M_\odot$ yr^{-1})
148	05 37 54.51	−06 56 45.5	K7[a]	K7	2.799	−0.5[a]	0.5[a]	WTTS	1.9	yes	−2.65	$0.57^{+0.10}_{-0.10}$	$0.15^{+0.10}_{-0.05}$	No disk	...	...	...
149	05 37 55.15	−06 57 40.7	M5.5[a]	M5.5	0.135	−14.5[a]	0.6[a]	WTTS	0.2	yes	...	$0.16^{+0.05}_{-0.03}$	$0.62^{+0.70}_{-0.26}$	...	...	...	...
150	05 37 55.22	−06 57 35.8	M4.5[a]	M4.5	0.273	−6.3[a]	0.6[a]	WTTS	0.2	yes	−1.80	$0.20^{+0.03}_{-0.02}$	$0.35^{+0.15}_{-0.11}$	Thin	...	...	...
151	05 37 55.65	−06 57 18.1	M0[a]	M0	1.554	−1.2[a]	...	WTTS	2.1	yes	−2.58	$0.44^{+0.23}_{-0.10}$	$0.19^{+0.49}_{-0.10}$	No disk	...	...	...
152	05 37 55.74	−06 58 37.9	M3[a]	M3	0.243	−3.7[a]	...	WTTS	1.3	yes	−1.00	$0.30^{+0.06}_{-0.04}$	$1.10^{+0.78}_{-0.35}$	Thick	...	...	...
153	05 37 55.99	−06 52 33.7	M5.5[a]	M5.5	0.161	−11.8[a]	...	WTTS	0.0	no	−2.66	$0.15^{+0.02}_{-0.02}$	$0.42^{+0.23}_{-0.14}$	No disk	...	...	...
154	05 38 00.67	−07 01 14.3	M4[a]	M4	0.021	−5.6[a]	...	WTTS	0.0	no	...	$0.25^{+0.09}_{-0.07}$	$29.50^{+33.28}_{-14.72}$	...	...	...	...
155	05 38 04.84	−07 02 21.6	M5.5[a]	M5.5	0.136	−12.8[a]	...	WTTS	2.7	no	−1.12	$0.15^{+0.03}_{-0.03}$	$0.55^{+0.57}_{-0.20}$	Thick	...	...	...
156	05 38 10.50	−06 57 07.1	M3[a]	M3	0.194	−9.7[a]	0.6[a]	WTTS	1.5	no	−1.71	$0.34^{+0.05}_{-0.04}$	$2.10^{+1.08}_{-0.67}$	Transition disk	...	...	...
157	05 38 13.45	−07 06 43.3	K4.5[a]	K4.5	2.519	−5.4[a]	...	WTTS	10.3	no	−0.99	$0.92^{+0.45}_{-0.34}$	$0.56^{+7.23}_{-0.35}$	Thick	...	...	...
158	05 38 19.52	−06 55 29.7	M3[a]	M3	0.382	−2.7[a]	...	WTTS	7.1	no	−2.73	$0.30^{+0.11}_{-0.07}$	$0.60^{+0.75}_{-0.27}$	No disk	...	...	...
159	05 38 21.22	−07 01 20.3	M5[a]	M5	0.102	−47.5[a]	...	CTTS	1.4	no	−1.27	$0.17^{+0.03}_{-0.03}$	$1.25^{+0.75}_{-0.38}$	Thick	−9.70	−10.04	−9.59
160	05 38 34.06	−07 04 36.8	M4[a]	M4	0.007	−1.3[a]	...	WTTS	0.0	no	...	$0.20^{+0.02}_{-0.06}$	$101.66^{+4.08}_{-51.84}$	...	...	...	...
161	05 38 40.22	−06 56 53.3	M2[a]	M2	0.208	−3.1[a]	...	WTTS	2.4	yes	−2.63	$0.39^{+0.13}_{-0.09}$	$2.61^{+9.58}_{-1.34}$	No disk	...	...	...
162	05 38 40.59	−07 02 23.8	M3[a]	M3	0.155	−107.1[a]	...	CTTS	3.5	yes	−1.11	$0.32^{+0.23}_{-0.12}$	$2.59^{+19.02}_{-1.68}$	Thick	−8.81	−9.65	−9.33
163	05 38 41.48	−07 01 52.6	M4.5[a]	M4.5	0.183	−9.6[a]	0.5[a]	WTTS	2.6	yes	−1.15	$0.21^{+0.05}_{-0.04}$	$0.78^{+0.65}_{-0.36}$	Thick	...	...	...
164	05 38 41.56	−06 52 51.0	M5[a]	M5	0.140	−9.4[a]	0.6[a]	WTTS	0.2	no	−2.68	$0.19^{+0.06}_{-0.04}$	$0.91^{+0.77}_{-0.38}$	No disk	...	...	...
165	05 38 43.22	−06 58 08.9	K7.5[a]	K7.5	14.069	−98.7[a]	...	CTTS	12.6	yes	−1.27	...	...	Thick	...	...	...
166	05 38 43.84	−06 58 22.3	M2.5[a]	M2.5	0.359	−66.9[a]	...	CTTS	4.5	yes	−0.52	$0.33^{+0.15}_{-0.08}$	$0.80^{+6.68}_{-0.48}$	Thick	−8.36	−9.13	−9.00
167	05 38 44.95	−06 58 14.7	M1[a]	M1	0.598	−37.3[a]	...	CTTS	6.0	yes	−0.97	$0.45^{+0.03}_{-0.03}$	$0.77^{+0.17}_{-0.14}$	Thick	−8.15	−7.22	−7.56
168	05 38 46.84	−07 05 08.9	M2.5[a]	M2.5	0.243	−99.3[a]	...	CTTS	4.3	yes	−1.64	$0.34^{+0.07}_{-0.06}$	$1.52^{+1.38}_{-0.62}$	Thick	−8.49	−9.19	−9.14
169	05 38 47.17	−07 02 40.4	K7[a]	K7	6.562	−2.3[a]	...	WTTS	13.0	yes	−2.69	$0.53^{+0.76}_{-0.14}$	$0.03^{+2.60}_{-0.02}$	No disk	...	...	...
170	05 38 47.74	−07 06 14.9	M1[a]	M1	1.473	−76.8[a]	...	CTTS	10.4	no	−1.19	$0.37^{+0.31}_{-0.10}$	$0.13^{+6.60}_{-0.08}$	Thick	−7.00	...	...
171	05 38 47.93	−07 05 06.1	M5[a]	M5	0.378	−10.3[a]	0.5[a]	WTTS	4.1	yes	−2.62	$0.18^{+0.03}_{-0.02}$	$0.16^{+1.16}_{-0.06}$	No disk	...	...	...
172	05 38 49.88	−07 02 35.4	M0[a]	M0	0.087	−4.4[a]	...	WTTS	6.6	yes	...	$0.63^{+0.08}_{-0.30}$	$44.51^{+26.80}_{-33.82}$	...	...	...	...
173	05 38 50.44	−07 00 43.0	K6[a]	K6	4.113	−1.5[a]	...	WTTS	10.9	yes	−2.35	$0.65^{+0.56}_{-0.22}$	$0.12^{+3.62}_{-0.07}$	Thin	...	...	...
174	05 38 52.97	−07 05 50.6	M6[a]	M6	0.055	−32.0[a]	...	CTTS	0.0	no	−2.56	$0.10^{+0.07}_{-0.00}$	$0.97^{+2.95}_{-0.10}$	No disk	−10.35	...	...
175	05 38 53.33	−07 05 45.2	K3.5[a]	K3.5	0.016	−30.9[a]	...	CTTS	2.1	no	0.47	...	...	Thick	...	...	...
176	05 38 54.45	−07 04 46.7	M3[a]	M3	0.177	−7.7[a]	0.6[a]	WTTS	2.6	yes	−2.72	$0.33^{+0.04}_{-0.03}$	$2.18^{+1.45}_{-0.52}$	No disk	...	...	...
177	05 38 54.93	−07 07 10.9	M3.5[a]	M3.5	0.156	−12.1[a]	0.7[a]	WTTS	2.1	no	−1.30	$0.30^{+0.03}_{-0.02}$	$2.16^{+0.67}_{-0.56}$	Thick	...	...	...
178	05 38 55.02	−06 56 18.6	F5[a]	F5	0.120	−0.5[a]	...	WTTS	5.8	no	0.01	...	...	Thick	...	...	...
179	05 38 57.04	−06 52 59.3	M1.5[a]	M1.5	0.156	−184.8[a]	0.3[a]	CTTS	0.7	no	−1.33	$0.55^{+0.09}_{-0.10}$	$8.06^{+5.66}_{-2.99}$	Thick	−8.44	−8.76	−8.34
180	05 40 19.41	−08 14 16.4	K7[b]	K7	1.152	...	...	...	5.8	no	−0.67	$0.63^{+0.16}_{-0.15}$	$0.68^{+0.75}_{-0.29}$	Thick	...	...	...
181	05 40 21.84	−08 08 55.9	M3[b]	M3	0.269	−25.0[b]	...	CTTS	2.4	no	−1.24	$0.31^{+0.11}_{-0.07}$	$1.01^{+2.93}_{-0.53}$	Thick	−9.15	...	...
182	05 40 24.97	−07 55 35.3	M2[a]	M2	1.723	−77.5[a]	...	CTTS	8.2	no	−0.91	$0.28^{+0.10}_{-0.04}$	$0.05^{+0.08}_{-0.03}$	Thick	−6.94	−7.63	−6.88
183	05 40 24.97	−08 07 33.2	K0[b]	K0	8.857	−47.0[b]	...	CTTS	4.4	no	−0.53	$2.43^{+0.09}_{-0.27}$	$1.05^{+0.64}_{-0.35}$	Thick	−6.54	...	...
184	05 40 24.97	−07 55 35.3	M3[b]	M3	1.557	...	...	...	8.0	no	−0.91	$0.24^{+0.06}_{-0.02}$	$0.03^{+0.05}_{-0.02}$	Thick	...	...	...
185	05 40 25.75	−08 11 16.8	M3[b]	M3	0.385	−38.0[b]	...	CTTS	4.2	no	−1.16	$0.29^{+0.09}_{-0.06}$	$0.53^{+0.63}_{-0.23}$	Thick	−8.63	...	...
186	05 40 27.14	−08 07 36.5	M3[b]	M3	0.184	−230.0[b]	...	CTTS	1.5	no	−0.80	$0.32^{+0.12}_{-0.08}$	$1.98^{+6.20}_{-1.02}$	Thick	−8.26	...	...
187	05 40 35.44	−07 56 36.5	M0.5[a]	M0.5	0.596	−2.3[a]	...	WTTS	8.5	no	−2.76	$0.51^{+0.38}_{-0.21}$	$1.04^{+11.36}_{-0.71}$	No disk	...	...	...
188	05 40 37.36	−08 04 03.0	F[b]	F	60.687	...	...	...	6.7	no	−0.82	$3.01^{+0.18}_{-0.06}$	$1.94^{+0.16}_{-0.30}$	Thick	...	...	...
189	05 40 41.01	−08 02 18.6	M0[b]	M0	1.126	...	...	...	7.9	no	−1.16	$0.47^{+0.17}_{-0.09}$	$0.36^{+0.51}_{-0.14}$	Thick	...	...	...
190	05 40 42.66	−07 46 03.0	M5.5[a]	M5.5	0.024	−7.9[a]	...	WTTS	0.0	no	...	$0.12^{+0.05}_{-0.01}$	$4.97^{+6.84}_{-0.75}$	...	...	...	...
191	05 40 46.22	−08 05 24.3	K1[b]	K1	13.154	−16.0[b]	...	CTTS	4.8	yes	−1.79	$2.34^{+0.31}_{-0.43}$	$0.42^{+0.32}_{-0.16}$	Thick	−6.79	...	...

Table 3.4: continued.

(1)	(2)	(3)	(4)	(5)	(6)	(7)	(8)	(9)	(10)	(11)	(12)	(13)	(14)	(15)	(16)	(17)	(18)
	RA	DEC		adopted	Lum	EW(Hα)	EW(Li)	TTS	A_V			Mass	Age	Disk	Log $\dot{M}_{acc}$	Log $\dot{M}_{acc}$	Log $\dot{M}_{acc}$
ID	(J2000)	(J2000)	Spectral type	Spectral type	($L_\odot$)	(Å)	(Å)	type	(mag)	clu	$\alpha(3.6-8.0\mu m)$	($M_\odot$)	(Myr)	property	($M_\odot$ yr^{-1})	($M_\odot$ yr^{-1})	($M_\odot$ yr^{-1})
192	05 40 46.40	−08 04 36.1	K7[b]	K7	4.795	...	...	...	2.0	yes	−2.48	$0.55^{+0.15}_{-0.11}$	$0.06^{+4.66}_{-0.03}$	Debris disk	...	...	...
193	05 40 46.62	−08 07 12.8	K7[b]	K7	8.229	...	...	...	10.0	yes	−2.61	$0.57^{+0.13}_{-0.10}$	$0.02^{+0.03}_{-0.01}$	Transition disk	...	...	...
194	05 40 46.84	−08 04 54.6	M2.5[b]	M2.5	1.231	−13.0[b]	...	CTTS	5.2	yes	0.08	$0.27^{+0.07}_{-0.04}$	$0.08^{+0.09}_{-0.04}$	Thick	...	...	...
195	05 40 48.07	−08 05 58.7	K7[b]	K7	5.832	...	...	...	1.9	yes	−1.26	$0.55^{+0.13}_{-0.11}$	$0.04^{+0.05}_{-0.02}$	Thick	...	...	...
196	05 40 57.49	−07 48 08.8	M2.5[a]	M2.5	0.566	−37.3[a]	...	CTTS	4.6	no	−1.04	$0.32^{+0.20}_{-0.09}$	$0.38^{+6.95}_{-0.24}$	Thick	−8.26	...	...
197	05 40 59.75	−08 06 03.2	M6[b]	M6	0.097	−42.0[b]	...	CTTS	0.0	no	−0.35	$0.12^{+0.06}_{-0.01}$	$0.55^{+1.13}_{-0.11}$	Thick	−9.83	...	...
198	05 40 59.92	−07 48 16.1	M2.5[a]	M2.5	0.187	−65.0[a]	...	CTTS	4.2	no	−1.41	$0.40^{+0.28}_{-0.17}$	$3.10^{+24.67}_{-2.28}$	Thick	−8.89	...	−8.94
199	05 41 03.55	−07 57 46.3	M6[a]	M6	0.027	−17.5[a]	...	WTTS	0.0	no	−2.77	...	...	No disk	...	...	...
200	05 41 04.09	−07 43 38.6	M3[a]	M3	0.138	−7.0[a]	0.5[a]	WTTS	1.5	no	−1.31	$0.32^{+0.07}_{-0.06}$	$2.99^{+5.19}_{-1.92}$	Thick	...	...	...
201	05 41 04.36	−07 46 40.6	M5[a]	M5	0.045	−5.7[a]	...	WTTS	0.0	no	...	$0.16^{+0.06}_{-0.03}$	$3.93^{+4.75}_{-1.40}$	...	...	...	...
202	05 41 05.03	−07 45 34.2	M4.5[a]	M4.5	0.179	−7.7[a]	...	WTTS	2.4	no	−2.67	$0.20^{+0.09}_{-0.05}$	$0.71^{+1.09}_{-0.34}$	No disk	...	...	...
203	05 41 05.49	−07 47 07.5	G1[a]	G1	8.105	−53.8[a]	...	CTTS	10.6	no	−1.59	$1.95^{+0.16}_{-0.16}$	$4.82^{+2.01}_{-1.09}$	Thick	−6.56	−6.51	...
204	05 41 07.00	−07 47 15.9	M3.5[a]	M3.5	0.108	−136.6[a]	...	CTTS	0.0	no	−2.07	$0.30^{+0.09}_{-0.06}$	$3.78^{+2.87}_{-1.73}$	Transition disk	−8.97	−9.20	...
205	05 41 07.08	−07 46 22.5	M3.5[a]	M3.5	0.155	−18.0[a]	...	CTTS	1.3	no	−1.32	$0.30^{+0.12}_{-0.07}$	$2.23^{+6.13}_{-1.16}$	Thick	−9.79	−9.83	...
206	05 41 14.03	−08 07 57.4	M2[b]	M2	0.953	−10.0[b]	...	WTTS	1.2	no	−1.25	$0.32^{+0.09}_{-0.06}$	$0.17^{+1.03}_{-0.09}$	Thick	...	...	...
207	05 41 16.25	−07 43 51.4	M5.5[a]	M5.5	0.024	−8.0[a]	...	WTTS	0.9	no	−2.69	$0.13^{+0.04}_{-0.02}$	$6.51^{+6.82}_{-1.92}$	No disk	...	...	...
208	05 41 20.12	−07 55 24.0	M4[a]	M4	0.581	−48.9[a]	...	CTTS	10.2	yes	−1.41	$0.23^{+0.10}_{-0.04}$	$0.15^{+0.28}_{-0.08}$	Thick	−8.23	...	...
209	05 41 25.35	−08 05 54.7	K1[b]	K1	4.941	−110.0[b]	...	CTTS	2.6	no	0.18	$1.94^{+0.10}_{-0.29}$	$1.36^{+0.76}_{-0.49}$	Thick	−6.40	...	...
210	05 41 26.37	−07 58 17.8	M5[a],M6[b]	M5	0.030	−7.0[a]	0.6[a]	WTTS	0.0	no	...	$0.16^{+0.07}_{-0.03}$	$7.09^{+9.96}_{-2.77}$	...	...	...	...
211	05 41 30.59	−08 04 48.2	K7[b]	K7	3.357	−40.0[b]	...	CTTS	10.0	no	−0.80	$0.55^{+0.13}_{-0.12}$	$0.11^{+0.12}_{-0.05}$	Thick	−6.74	...	...
212	05 41 33.38	−07 59 56.3	M1.5[a]	M1.5	1.097	−69.8[a]	...	CTTS	9.7	no	−1.38	$0.34^{+0.12}_{-0.07}$	$0.17^{+0.23}_{-0.08}$	Thick	−7.31	...	...
213	05 41 41.66	−08 00 18.5	K7.5[a]	K7.5	0.047	−28.4[a]	...	CTTS	4.5	no	−1.02	...	...	Thick	...	...	...
214	05 41 43.74	−07 58 22.3	M5.5[a]	M5.5	0.468	−405.3[a]	0.4[a]	CTTS	2.4	no	−1.01	$0.16^{+0.03}_{-0.01}$	$0.04^{+0.09}_{-0.02}$	Thick	−7.49	−8.40	−8.68
215	05 41 49.23	−07 57 12.3	M3.5[a]	M3.5	0.150	−18.5[a]	...	CTTS	3.1	no	−1.53	$0.28^{+0.09}_{-0.06}$	$2.09^{+4.47}_{-0.91}$	Thick	−9.80	...	...
216	05 41 49.74	−08 00 32.3	K5[b]	K5	8.432	−18.0[b]	...	CTTS	0.4	no	−0.94	$0.86^{+0.36}_{-0.16}$	$0.07^{+0.14}_{-0.03}$	Thick	−6.69	...	...
217	05 41 51.84	−08 06 56.6	M4.5[a]	M4.5	0.129	−5.5[a]	0.7[a]	WTTS	2.7	no	−2.70	$0.20^{+0.02}_{-0.02}$	$1.23^{+0.25}_{-0.22}$	No disk	...	...	...
218	05 41 54.66	−07 59 12.4	K3.5[a],K8[b]	K3.5	2.039	−6.6[a]	0.6[a]	CTTS	5.9	no	−1.73	$1.20^{+0.24}_{-0.37}$	$1.42^{+1.63}_{-0.75}$	Thick	−8.40	...	...
219	05 41 55.96	−07 58 36.6	M4[a]	M4	0.063	−4.1[a]	...	WTTS	3.8	no	−2.04	$0.23^{+0.12}_{-0.06}$	$4.83^{+9.01}_{-2.24}$	Thin	...	...	...
220	05 42 05.59	−08 01 05.6	M2[b]	M2	0.192	...	...	...	0.9	no	−1.76	$0.43^{+0.13}_{-0.10}$	$3.51^{+11.00}_{-1.73}$	Transition disk	...	...	...
221	05 42 07.25	−08 05 24.4	M6[b]	M6	0.049	...	...	...	1.6	no	−1.18	$0.10^{+0.06}_{-0.00}$	$1.27^{+3.53}_{-0.46}$	Thick	...	...	...
222	05 42 10.51	−08 07 35.1	M5[a],M4[b]	M5	0.084	−7.8[a]	...	WTTS	0.0	no	...	$0.18^{+0.04}_{-0.03}$	$1.84^{+1.07}_{-0.62}$	...	...	...	...
223	05 42 11.04	−08 01 05.4	M4.5[a],M3[b]	M4.5	0.056	...	0.5[a]	...	0.0	no	−1.16	$0.19^{+0.05}_{-0.03}$	$3.87^{+3.06}_{-1.34}$	Thick	...	...	−10.98
224	05 42 13.51	−08 10 01.5	M3[b]	M3	0.080	−50.0[b]	...	CTTS	1.6	no	−1.09	$0.35^{+0.12}_{-0.10}$	$8.43^{+22.49}_{-4.73}$	Thick	−9.76	...	...
225	05 42 14.60	−07 58 57.9	M3.5[a]	M3.5	0.200	−13.2[a]	0.6[a]	WTTS	1.1	no	−1.09	$0.29^{+0.05}_{-0.04}$	$1.36^{+1.08}_{-0.42}$	Thick	...	...	...
226	05 42 15.93	−08 09 37.8	M5[a]	M5	0.134	−6.3[a]	...	WTTS	3.3	no	−2.31	$0.18^{+0.06}_{-0.04}$	$0.85^{+0.96}_{-0.36}$	Thin	...	...	...
227	05 42 18.11	−08 08 10.9	K4.5[a],K5[b]	K4.5	0.924	−1.0[a]	0.5[a]	WTTS	1.5	yes	−2.96	$1.13^{+0.09}_{-0.28}$	$3.89^{+4.95}_{-1.95}$	No disk	...	...	...
228	05 42 18.56	−07 59 23.0	M4.5[a]	M4.5	0.069	−6.9[a]	0.6[a]	WTTS	0.0	no	−2.74	$0.19^{+0.02}_{-0.01}$	$2.68^{+0.56}_{-0.43}$	No disk	...	...	...
229	05 42 19.05	−07 59 12.2	M5.5[a]	M5.5	0.041	−18.9[a]	0.8[a]	CTTS	0.0	no	...	$0.11^{+0.04}_{-0.01}$	$2.09^{+2.29}_{-0.46}$	...	−10.87	...	...
230	05 42 19.56	−08 05 07.6	M2.5[b]	M2.5	0.134	...	...	...	2.0	no	−1.31	$0.39^{+0.13}_{-0.10}$	$4.88^{+13.33}_{-2.62}$	Thick	...	...	...
231	05 42 21.36	−08 06 47.9	M3.5[a]	M3.5	0.237	−12.9[a]	...	WTTS	4.8	no	−2.57	$0.26^{+0.04}_{-0.03}$	$0.88^{+0.41}_{-0.24}$	No disk	...	...	...
232	05 42 21.56	−08 08 29.8	M0[a],K8[b]	M0	0.464	−39.3[a],−10.0[b]	0.5[a]	CTTS	0.5	yes	−2.12	$0.58^{+0.12}_{-0.08}$	$1.95^{+2.21}_{-0.89}$	Transition disk	−8.35	−8.42	−7.98
233	05 42 23.24	−07 58 28.9	M5[a]	M5	0.034	−5.9[a]	0.7[a]	WTTS	0.1	no	...	$0.17^{+0.05}_{-0.03}$	$6.87^{+5.77}_{-2.54}$	...	...	...	...
234	05 42 23.61	−08 09 10.3	M3[a],M2[b]	M3	0.248	−44.5[a],−65.0[b]	0.9[a]	CTTS	1.1	yes	−1.49	$0.30^{+0.05}_{-0.04}$	$1.14^{+0.63}_{-0.32}$	Thick	−8.91	−9.07	−8.75
235	05 42 23.94	−08 09 45.9	K4[a],K5[b]	K4	1.197	−0.9[a]	0.4[a]	WTTS	3.1	yes	−2.88	$1.23^{+0.10}_{-0.32}$	$3.42^{+4.88}_{-1.81}$	No disk	...	...	...

Table 3.4: continued.

(1)	(2)	(3)	(4)	(5)	(6)	(7)	(8)	(9)	(10)	(11)	(12)	(13)	(14)	(15)	(16)	(17)	(18)
	RA	DEC		adopted	Lum	EW(Hα)	EW(Li)	TTS	A_V			Mass	Age	Disk	Log $\dot{M}_{acc}$	Log $\dot{M}_{acc}$	Log $\dot{M}_{acc}$
ID	(J2000)	(J2000)	Spectral type	Spectral type	($L_\odot$)	(Å)	(Å)	type	(mag)	clu	$\alpha(3.6-8.0\mu m)$	($M_\odot$)	(Myr)	property	($M_\odot$ yr^{-1})	($M_\odot$ yr^{-1})	($M_\odot$ yr^{-1})
236	05 42 25.32	−08 10 18.0	M1[a],M0[b]	M1	0.420	−3.3[a]	0.7[a]	WTTS	0.7	yes	−2.82	$0.48^{+0.33}_{-0.18}$	$1.47^{+9.16}_{-0.96}$	No disk	...	...	...
237	05 42 25.44	−08 09 55.4	M1[a],K8[b]	M1	0.216	−21.2[a],−27.0[b]	...	CTTS	1.8	yes	−1.66	$0.55^{+0.11}_{-0.09}$	$5.10^{+7.10}_{-2.07}$	Thick	−9.34	−9.38	−9.40
238	05 42 25.68	−07 58 22.0	M3[a]	M3	0.135	−3.3[a]	0.2[a]	WTTS	0.5	no	−2.60	$0.34^{+0.05}_{-0.04}$	$3.66^{+1.69}_{-0.99}$	No disk	...	...	...
239	05 42 25.79	−08 08 50.1	M2.5[a]	M2.5	0.210	−61.8[a]	0.5[a]	CTTS	1.2	yes	−1.30	$0.34^{+0.04}_{-0.04}$	$1.89^{+0.77}_{-0.44}$	Thick	−8.87	−9.33	−9.32
240	05 42 26.50	−07 58 50.9	K6[a]	K6	1.542	−91.6[a]	0.4[a]	CTTS	4.4	no	−0.64	$0.69^{+0.49}_{-0.30}$	$0.57^{+11.54}_{-0.40}$	Thick	−6.95	...	...
241	05 42 26.96	−08 09 17.3	M3.5[a]	M3.5	0.109	−3.4[a]	...	WTTS	0.0	yes	...	$0.31^{+0.03}_{-0.02}$	$4.08^{+0.91}_{-0.64}$	...	...	...	...
242	05 42 27.50	−08 11 03.8	M5[a],M3[b]	M5	0.034	−9.4[a]	...	WTTS	0.0	yes	−2.09	$0.15^{+0.04}_{-0.02}$	$4.92^{+3.31}_{-1.71}$	Transition disk	...	...	...
243	05 42 27.59	−08 09 52.6	M1[b]	M1	0.294	−13.0[b]	...	CTTS	1.1	yes	−1.20	$0.51^{+0.15}_{-0.11}$	$2.82^{+9.09}_{-1.30}$	Thick	−9.33	...	...
244	05 42 29.78	−08 07 26.4	M1[a]	M1	0.372	−3.4[a]	0.6[a]	WTTS	2.8	yes	...	$0.50^{+0.44}_{-0.23}$	$1.92^{+22.80}_{-1.49}$	...	...	...	...
245	05 42 30.62	−07 59 54.0	M2[a]	M2	0.108	−2.2[a]	0.5[a]	WTTS	0.1	no	−2.87	$0.47^{+0.10}_{-0.11}$	$10.32^{+20.81}_{-4.36}$	No disk	...	...	...
246	05 42 30.87	−08 10 45.7	M5[a]	M5	0.090	−5.0[a]	0.6[a]	WTTS	0.9	yes	−1.64	$0.18^{+0.03}_{-0.02}$	$1.71^{+0.65}_{-0.44}$	Transition disk	...	...	...
247	05 42 31.00	−08 06 38.1	M3.5[b]	M3.5	0.166	−30.0[b]	...	CTTS	0.0	yes	−1.72	$0.28^{+0.10}_{-0.07}$	$1.71^{+2.01}_{-0.91}$	Thick	−9.46	...	...
248	05 42 31.33	−08 02 35.3	M4.5[a]	M4.5	0.086	−8.3[a]	0.7[a]	WTTS	0.0	no	−2.79	$0.19^{+0.03}_{-0.02}$	$2.12^{+0.72}_{-0.50}$	No disk	...	...	...
249	05 42 31.55	−08 08 22.8	M4[a],M2[b]	M4	0.270	−12.4[a],−15.0[b]	...	WTTS	2.8	yes	−0.60	$0.22^{+0.04}_{-0.04}$	$0.47^{+0.38}_{-0.20}$	Thick	...	...	...
250	05 42 32.66	−08 10 07.9	M4.5[a]	M4.5	0.119	−6.7[a]	...	WTTS	1.5	yes	...	$0.20^{+0.02}_{-0.02}$	$1.41^{+0.48}_{-0.32}$	...	...	...	...
251	05 42 32.77	−08 07 04.8	M5[a]	M5	0.132	−11.0[a]	...	WTTS	0.3	yes	...	$0.19^{+0.02}_{-0.01}$	$1.02^{+0.32}_{-0.20}$	...	...	...	...
252	05 42 34.02	−08 09 59.7	K4[a],K7[b]	K4	2.186	−1.9[a]	0.5[a]	WTTS	5.0	yes	−2.33	$1.17^{+0.26}_{-0.38}$	$1.22^{+1.36}_{-0.67}$	Transition disk	...	...	...
253	05 42 34.31	−08 02 12.1	M5[a],M4[b]	M5	0.068	−86.0[a],−48.0[b]	0.4[a]	CTTS	0.0	no	−1.28	$0.16^{+0.24}_{-0.04}$	$1.99^{+29.05}_{-0.78}$	Thick	−9.68	...	−9.98
254	05 42 34.92	−08 07 50.5	M5[a]	M5	0.126	−6.0[a]	...	WTTS	1.9	yes	...	$0.19^{+0.05}_{-0.04}$	$1.08^{+1.19}_{-0.43}$	...	...	...	...
255	05 42 36.41	−08 10 17.8	M3[b]	M3	0.063	−36.0[b]	...	CTTS	2.8	yes	...	$0.36^{+0.12}_{-0.10}$	$12.49^{+16.77}_{-6.16}$	...	−10.12	...	...
256	05 42 36.51	−08 11 51.5	K5[a]	K5	0.687	−1.7[a]	0.5[a]	WTTS	3.0	no	...	$1.06^{+0.06}_{-0.20}$	$5.06^{+7.10}_{-2.17}$	...	...	...	...
257	05 42 40.06	−08 05 07.7	M2[b]	M2	0.086	−12.0[b]	...	CTTS	0.4	no	−1.85	$0.49^{+0.09}_{-0.13}$	$15.81^{+16.78}_{-7.46}$	Transition disk	−10.43	...	...
258	05 42 42.10	−08 15 15.3	M1[b]	M1	0.356	...	...	...	3.5	no	−1.18	$0.49^{+0.14}_{-0.11}$	$1.95^{+4.72}_{-0.75}$	Thick	...	...	...
259	05 42 44.12	−08 06 26.4	M3[b]	M3	0.251	−22.0[b]	...	CTTS	0.2	no	−1.22	$0.31^{+0.10}_{-0.07}$	$1.15^{+1.16}_{-0.49}$	Thick	−9.28	...	...
260	05 42 47.18	−08 05 57.0	M2[b]	M2	0.110	...	...	...	0.2	no	−1.99	$0.47^{+0.12}_{-0.13}$	$9.97^{+9.87}_{-4.64}$	Transition disk	...	...	...
261	05 42 47.44	−08 04 05.4	M2.5[b]	M2.5	0.115	−76.0[b]	...	CTTS	0.8	no	−0.87	$0.40^{+0.13}_{-0.10}$	$6.39^{+13.83}_{-3.36}$	Thick	−9.23	...	...
262	05 42 48.24	−08 05 57.1	M1[b]	M1	0.088	−24.0[b]	...	CTTS	0.8	no	...	$0.61^{+0.03}_{-0.12}$	$28.01^{+22.19}_{-12.32}$	...	−9.99	...	...
263	05 42 51.65	−08 07 41.2	M1[b]	M1	0.093	−34.0[b]	...	CTTS	2.0	no	−1.56	$0.61^{+0.03}_{-0.12}$	$25.51^{+20.61}_{-10.84}$	Thick	−9.76	...	...
264	05 42 52.30	−08 08 54.9	M5[b]	M5	0.065	...	...	...	0.6	no	−1.38	$0.17^{+0.09}_{-0.04}$	$2.37^{+5.70}_{-0.94}$	Thick	...	...	...
265	05 42 59.13	−08 09 23.6	M1[b]	M1	0.389	−67.0[b]	...	CTTS	2.0	no	−0.88	$0.48^{+0.14}_{-0.10}$	$1.63^{+5.27}_{-0.62}$	Thick	−8.20	...	...
266	05 43 01.78	−08 04 50.6	K5[b]	K5	1.869	−32.0[b]	...	CTTS	2.7	no	−2.12	$0.86^{+0.29}_{-0.15}$	$0.73^{+0.99}_{-0.24}$	Transition disk	−7.52	...	...
267	05 43 08.49	−08 11 32.3	M2[b]	M2	0.053	...	...	...	0.1	no	−1.59	$0.50^{+0.06}_{-0.13}$	$36.34^{+24.57}_{-19.52}$	Thick	...	...	...

Table 3.5: Photometric magnitudes of YSOs in L1630N.

ID	RA (J2000)	DEC (J2000)	u′ (mag)	g′ (mag)	r′ (mag)	i′ (mag)	z′ (mag)	J (mag)	H (mag)	K_s (mag)	[3.6] (mag)	[4.5] (mag)	[5.8] (mag)	[8.0] (mag)	[24]
1	05 45 21.38	−00 00 45.9	21.51± 0.06	18.71± 0.01	17.09± 0.01	15.46± 0.01	14.55± 0.01	12.96± 0.02	12.22± 0.02	11.93± 0.02	11.62± 0.06	11.64± 0.06	11.44± 0.06	11.52± 0.06	...
2	05 45 22.68	−00 14 27.5	22.36± 0.11	19.91± 0.01	18.35± 0.01	16.39± 0.01	15.25± 0.01	13.50± 0.02	12.87± 0.03	12.54± 0.03	12.21± 0.06	12.05± 0.06	12.03± 0.06	11.96± 0.07	...
3	05 45 26.16	+00 06 37.9	19.24± 0.01	17.62± 0.01	16.18± 0.01	14.87± 0.01	13.93± 0.01	12.37± 0.02	11.61± 0.02	11.21± 0.02	10.50± 0.06	10.30± 0.06	9.91± 0.06	9.25± 0.06	...
4	05 45 38.26	−00 08 11.0	21.16± 0.05	18.10± 0.01	16.30± 0.01	15.13± 0.01	14.37± 0.01	12.65± 0.02	11.82± 0.02	11.53± 0.02	11.38± 0.06	11.38± 0.06	11.20± 0.06	11.17± 0.06	...
5	05 45 41.68	−00 04 02.4	21.03± 0.05	18.37± 0.01	16.79± 0.01	15.26± 0.01	14.41± 0.01	12.86± 0.03	12.09± 0.03	11.85± 0.03	11.50± 0.06	11.46± 0.06	11.36± 0.06	11.45± 0.06	...
6	05 45 41.94	−00 12 05.3	18.55± 0.01	15.85± 0.01	14.44± 0.01	14.05± 0.01	13.32± 0.01	11.93± 0.02	11.18± 0.02	10.99± 0.02	10.84± 0.06	10.93± 0.06	10.86± 0.06	10.61± 0.06	6.45± 0.06
7	05 45 42.80	−00 01 01.8	22.97± 0.22	20.59± 0.01	18.98± 0.01	16.89± 0.01	15.67± 0.01	13.85± 0.02	13.18± 0.03	12.75± 0.03	11.93± 0.06	11.68± 0.06	11.25± 0.19	10.55± 0.06	...
8	05 45 44.37	+00 22 58.2	18.53± 0.01	16.88± 0.01	15.31± 0.01	14.87± 0.01	13.70± 0.01	12.02± 0.02	11.05± 0.02	10.38± 0.02	9.35± 0.06	8.99± 0.06	8.62± 0.06	8.05± 0.06	5.18± 0.06
9	05 45 44.56	−00 10 35.6	...	21.51± 0.03	19.43± 0.01	17.40± 0.01	16.20± 0.01	14.23± 0.03	13.27± 0.02	12.88± 0.03	12.52± 0.06	12.46± 0.06	12.30± 0.06	12.27± 0.08	...
10	05 45 44.64	+00 13 00.6	18.90± 0.01	16.39± 0.01	14.98± 0.01	14.50± 0.01	13.76± 0.01	12.52± 0.03	11.78± 0.02	11.59± 0.02	11.44± 0.06	11.47± 0.06	11.53± 0.06	11.42± 0.22	...
11	05 45 45.58	+00 04 35.6	21.35± 0.06	18.83± 0.01	17.31± 0.01	15.53± 0.01	14.54± 0.01	12.90± 0.02	12.21± 0.02	11.91± 0.02	11.53± 0.06	11.56± 0.06	11.45± 0.06	11.42± 0.06	...
12	05 45 46.91	+00 14 29.4	22.02± 0.11	19.76± 0.01	18.27± 0.01	16.58± 0.01	15.61± 0.01	14.01± 0.03	13.35± 0.03	13.04± 0.03	12.70± 0.06	12.62± 0.06	12.65± 0.06	12.56± 0.09	...
13	05 45 49.56	−00 08 38.8	23.57± 0.61	22.08± 0.06	20.20± 0.02	18.05± 0.01	16.73± 0.01	14.76± 0.03	13.85± 0.03	13.30± 0.03	12.80± 0.06	12.16± 0.06	11.91± 0.06	11.16± 0.06	8.58± 0.06
14	05 45 53.11	−00 13 24.9	19.65± 0.02	17.60± 0.01	16.08± 0.01	15.04± 0.01	14.35± 0.01	12.78± 0.02	11.96± 0.02	11.69± 0.02	11.38± 0.06	11.27± 0.06	11.17± 0.06	11.01± 0.06	6.37± 0.06
15	05 45 53.54	+00 33 08.8	20.26± 0.02	18.58± 0.01	16.60± 0.01	15.33± 0.01	14.36± 0.01	12.45± 0.02	11.40± 0.02	10.87± 0.02	10.14± 0.06	9.90± 0.06	9.38± 0.06	8.68± 0.06	5.93± 0.06
16	05 45 53.60	+00 22 42.1	19.17± 0.01	16.66± 0.01	15.32± 0.01	14.96± 0.01	14.28± 0.01	13.04± 0.03	12.34± 0.02	12.15± 0.02	12.04± 0.06	12.04± 0.06	11.90± 0.06	11.96± 0.09	...
17	05 45 54.09	−00 03 16.7	...	23.34± 0.15	21.02± 0.03	18.50± 0.01	17.02± 0.01	14.83± 0.03	13.85± 0.04	13.44± 0.04	12.84± 0.07	12.45± 0.07	...	...	...
18	05 45 55.13	+00 11 39.4	...	22.21± 0.05	20.39± 0.01	18.25± 0.01	16.90± 0.01	14.74± 0.03	13.92± 0.03	13.30± 0.03	12.49± 0.06	12.12± 0.06	11.80± 0.08	11.23± 0.19	...
19	05 45 56.20	+00 33 10.3	21.42± 0.05	19.29± 0.01	17.85± 0.01	15.77± 0.01	14.61± 0.01	12.82± 0.02	12.25± 0.02	11.92± 0.02	11.48± 0.06	11.49± 0.06	11.29± 0.06	11.35± 0.06	...
20	05 45 56.31	+00 07 08.6	19.54± 0.01	16.81± 0.01	15.21± 0.01	15.41± 0.01	13.64± 0.01	12.13± 0.02	11.33± 0.02	11.03± 0.02	10.19± 0.06	9.85± 0.06	9.42± 0.06	9.11± 0.07	5.34± 0.06
21	05 45 56.73	−00 00 25.4	...	22.59± 0.06	20.01± 0.01	18.47± 0.01	17.18± 0.01	13.99± 0.03	12.85± 0.03	12.38± 0.02	11.80± 0.06	11.39± 0.06	10.85± 0.14	...	6.06± 0.06
22	05 45 57.38	+00 20 22.2	18.05± 0.01	16.40± 0.01	14.89± 0.01	14.40± 0.01	13.42± 0.01	11.75± 0.02	10.82± 0.02	10.22± 0.02	9.16± 0.06	8.92± 0.06	8.74± 0.06	8.07± 0.06	4.94± 0.06
23	05 45 57.62	+00 07 21.1	23.15± 0.26	21.09± 0.02	19.36± 0.01	17.19± 0.01	15.90± 0.01	14.01± 0.02	13.31± 0.02	12.99± 0.03	12.33± 0.07	12.16± 0.06	11.82± 0.08	10.88± 0.15	...
24	05 45 57.93	+00 02 48.6	20.40± 0.03	19.50± 0.01	17.98± 0.01	16.37± 0.01	15.27± 0.01	13.52± 0.03	12.68± 0.03	12.15± 0.02	11.33± 0.06	10.98± 0.06	10.87± 0.14	10.41± 0.06	7.83± 0.07
25	05 46 00.18	+00 03 07.0	20.25± 0.02	18.24± 0.01	16.58± 0.01	15.16± 0.01	13.79± 0.01	12.05± 0.02	11.22± 0.02	10.90± 0.02	10.46± 0.06	10.18± 0.06	9.67± 0.08	8.89± 0.15	5.62± 0.06
26	05 46 03.53	+00 02 54.7	22.62± 0.17	20.79± 0.01	18.88± 0.01	17.50± 0.01	15.43± 0.01	13.41± 0.02	12.52± 0.02	12.20± 0.03	11.77± 0.06	11.76± 0.06	11.25± 0.19	...	...
27	05 46 04.64	+00 04 58.1	18.29± 0.01	16.78± 0.01	15.28± 0.01	15.20± 0.01	13.55± 0.01	11.34± 0.03	10.13± 0.03	9.45± 0.02	8.28± 0.06	7.96± 0.06	7.51± 0.06	6.83± 0.06	3.74± 0.06
28	05 46 04.58	+00 00 38.2	22.32± 0.11	20.22± 0.01	18.11± 0.01	16.48± 0.01	15.38± 0.01	13.36± 0.02	12.28± 0.02	11.74± 0.03	11.03± 0.06	10.79± 0.06	10.40± 0.11	9.72± 0.33	6.68± 0.06
29	05 46 07.89	−00 11 56.9	...	...	...	...	...	9.80± 0.04	8.65± 0.05	8.40± 0.03	8.14± 0.06	7.96± 0.06	7.64± 0.06	7.28± 0.06	5.06± 0.06
30	05 46 09.27	+00 13 32.6	19.07± 0.01	16.71± 0.01	15.03± 0.01	14.48± 0.01	13.25± 0.01	11.69± 0.03	10.70± 0.03	10.05± 0.02	8.91± 0.06	8.56± 0.06	8.07± 0.06	7.48± 0.06	4.30± 0.06
31	05 46 09.61	−00 03 31.2	...	23.63± 0.19	20.44± 0.02	18.44± 0.01	16.95± 0.01	14.01± 0.03	12.45± 0.02	11.72± 0.02	10.84± 0.06	10.57± 0.06	10.24± 0.10	9.59± 0.26	6.32± 0.06
32	05 46 10.31	−00 00 06.7	21.82± 0.09	20.71± 0.01	18.74± 0.01	17.16± 0.01	15.98± 0.01	14.23± 0.03	12.91± 0.03	12.02± 0.02	10.59± 0.06	10.04± 0.06	9.65± 0.07	8.79± 0.14	5.71± 0.06
33	05 46 11.34	−00 07 55.1	24.47± 0.94	23.29± 0.12	21.33± 0.04	20.38± 0.02	19.42± 0.04	17.61± 0.28	15.86± 0.14	15.15± 0.15	13.75± 0.06	13.14± 0.06	12.72± 0.07	11.44± 0.07	7.99± 0.06
34	05 46 11.86	+00 32 25.9	17.02± 0.01	15.88± 0.01	13.27± 0.01	12.92± 0.01	13.65± 0.01	10.94± 0.02	10.05± 0.02	9.45± 0.02	8.52± 0.06	8.52± 0.06	8.36± 0.06	8.09± 0.06	4.33± 0.06
35	05 46 12.27	−00 08 07.8	...	23.43± 0.14	21.19± 0.03	18.67± 0.01	16.90± 0.01	14.63± 0.03	13.94± 0.02	13.51± 0.04	12.71± 0.06	12.29± 0.06	11.91± 0.06	11.05± 0.06	8.33± 0.06
36	05 46 12.99	−00 08 14.8	...	22.87± 0.09	20.99± 0.03	19.29± 0.01	18.21± 0.02	16.55± 0.10	15.63± 0.11	14.98± 0.12	14.11± 0.06	13.60± 0.06	12.67± 0.07	10.88± 0.06	6.26± 0.06
37	05 46 13.58	−00 10 34.0	...	22.95± 0.09	21.32± 0.04	19.33± 0.01	18.23± 0.02	16.66± 0.13	16.08± 0.20	15.69± 0.23	15.27± 0.06	15.21± 0.07	15.24± 0.26	...	...
38	05 46 14.48	+00 20 24.4	22.61± 0.19	20.31± 0.01	18.47± 0.01	16.64± 0.01	15.61± 0.01	13.82± 0.03	12.89± 0.03	12.52± 0.02	12.17± 0.06	12.05± 0.06	11.66± 0.06	11.38± 0.22	7.94± 0.06
39	05 46 16.75	+00 07 13.5	...	23.26± 0.10	19.95± 0.01	17.27± 0.01	15.45± 0.01	12.88± 0.02	11.62± 0.02	11.05± 0.02	10.56± 0.06	10.30± 0.06	9.92± 0.06	9.64± 0.08	...
40	05 46 17.71	−00 00 14.3	...	21.76± 0.04	18.57± 0.01	16.92± 0.01	15.54± 0.01	12.84± 0.03	11.28± 0.03	10.40± 0.03	9.96± 0.06	9.76± 0.06	8.62± 0.06	7.06± 0.07	...
41	05 46 18.30	+00 06 57.8	21.23± 0.05	18.82± 0.01	16.49± 0.01	15.25± 0.01	14.29± 0.01	12.21± 0.02	11.07± 0.02	10.47± 0.02	9.36± 0.06	9.08± 0.06	8.50± 0.06	7.65± 0.06	4.85± 0.06
42	05 46 18.60	+00 07 08.0	24.49± 0.93	23.97± 0.20	21.06± 0.03	18.59± 0.01	16.82± 0.01	13.99± 0.03	12.51± 0.02	11.78± 0.02	10.24± 0.06	9.81± 0.06	9.09± 0.06	8.37± 0.06	5.46± 0.06
43	05 46 18.89	−00 05 38.1	19.43± 0.01	16.55± 0.01	14.79± 0.01	15.51± 0.01	13.01± 0.01	11.20± 0.02	10.16± 0.02	9.72± 0.02	8.87± 0.06	8.76± 0.06	8.12± 0.06	7.60± 0.07	5.69± 0.06
44	05 46 19.06	+00 03 29.6	20.61± 0.03	18.59± 0.01	16.28± 0.01	14.83± 0.01	13.61± 0.01	10.63± 0.03	9.03± 0.03	7.87± 0.01	6.50± 0.06	6.10± 0.06	5.56± 0.06	5.00± 0.06	2.18± 0.06
45	05 46 19.47	−00 05 20.0	17.99± 0.01	15.70± 0.01	14.08± 0.01	13.96± 0.01	12.67± 0.01	10.69± 0.02	9.65± 0.02	9.00± 0.02	7.98± 0.06	7.49± 0.06	7.07± 0.06	6.09± 0.06	2.95± 0.06

Table 3.5: continued.

ID	RA (J2000)	DEC (J2000)	u′ (mag)	g′ (mag)	r′ (mag)	i′ (mag)	z′ (mag)	J (mag)	H (mag)	K_s (mag)	[3.6] (mag)	[4.5] (mag)	[5.8] (mag)	[8.0] (mag)	[24]
46	05 46 20.88	+00 08 09.4	22.14± 0.10	19.94± 0.01	17.44± 0.01	15.99± 0.01	14.85± 0.01	12.53± 0.03	11.32± 0.03	10.69± 0.02	9.94± 0.06	9.41± 0.06	9.04± 0.06	8.06± 0.06	4.91± 0.06
47	05 46 22.43	−00 08 52.6	18.41± 0.01	15.96± 0.01	14.44± 0.01	13.87± 0.01	13.15± 0.01	11.51± 0.02	10.65± 0.02	10.21± 0.02	9.59± 0.06	9.28± 0.06	9.21± 0.06	8.49± 0.06	4.74± 0.06
48	05 46 22.99	+00 04 26.4	...	20.05± 0.05	17.96± 0.05	16.35± 0.05	15.22± 0.05	13.06± 0.03	11.97± 0.03	11.43± 0.02	10.76± 0.06	10.34± 0.06	9.87± 0.08	9.17± 0.19	6.28± 0.06
49	05 46 23.83	+00 04 27.2	23.00± 0.34	22.09± 0.06	19.70± 0.01	17.46± 0.01	15.96± 0.01	13.47± 0.03	12.19± 0.02	11.63± 0.02	11.17± 0.06	11.11± 0.06	10.98± 0.16	...	...
50	05 46 25.09	+00 05 41.2	...	25.36± 0.90	20.54± 0.02	18.44± 0.01	16.74± 0.01	13.60± 0.03	11.74± 0.02	10.74± 0.02	9.89± 0.06	9.46± 0.06	9.03± 0.07	8.31± 0.10	5.31± 0.06
51	05 46 25.89	+00 09 32.0	21.12± 0.06	19.65± 0.01	17.73± 0.01	16.13± 0.01	15.08± 0.01	13.19± 0.02	12.19± 0.02	11.64± 0.02	10.74± 0.06	10.28± 0.06	10.08± 0.06	9.22± 0.07	6.78± 0.06
52	05 46 26.65	+00 31 07.5	21.97± 0.09	19.60± 0.01	17.18± 0.01	15.75± 0.01	14.69± 0.01	12.69± 0.02	11.33± 0.02	10.52± 0.02	9.59± 0.06	9.16± 0.06	8.82± 0.06	8.09± 0.06	5.84± 0.06
53	05 46 27.13	+00 15 49.7	21.75± 0.09	19.35± 0.01	17.84± 0.01	16.24± 0.01	15.38± 0.01	13.91± 0.02	13.35± 0.02	13.02± 0.03	12.67± 0.06	12.66± 0.06	12.50± 0.11	...	...
54	05 46 27.83	+00 05 48.4	...	20.37± 0.05	18.19± 0.05	16.27± 0.05	15.02± 0.05	12.71± 0.02	11.58± 0.02	11.11± 0.02	10.77± 0.06	10.62± 0.06	10.55± 0.12	10.61± 0.08	...
55	05 46 28.36	+00 12 27.0	24.00± 0.68	24.05± 0.26	21.05± 0.03	18.65± 0.01	16.90± 0.01	13.95± 0.02	12.45± 0.02	11.75± 0.02	10.22± 0.06	9.71± 0.06	9.34± 0.06	8.65± 0.06	5.57± 0.06
56	05 46 28.87	+00 13 30.7	23.15± 0.35	22.07± 0.05	19.30± 0.01	17.40± 0.01	15.84± 0.01	12.66± 0.04	11.11± 0.05	9.99± 0.03	9.15± 0.06	8.63± 0.06	8.17± 0.06	7.36± 0.06	4.29± 0.06
57	05 46 29.00	+00 29 07.2	20.70± 0.03	18.03± 0.01	16.11± 0.01	14.80± 0.01	13.92± 0.01	12.17± 0.02	11.30± 0.02	10.99± 0.02	10.63± 0.06	10.59± 0.06	10.54± 0.06	10.48± 0.06	...
58	05 46 29.06	+00 11 45.7	22.71± 0.27	21.14± 0.03	19.71± 0.01	18.04± 0.01	17.00± 0.01	15.45± 0.05	14.83± 0.05	14.50± 0.08	14.30± 0.07	14.18± 0.06	...	...	...
59	05 46 29.59	+00 10 57.2	23.02± 0.63	22.41± 0.13	20.05± 0.03	17.60± 0.01	15.83± 0.01	13.38± 0.02	12.25± 0.02	11.67± 0.02	10.81± 0.06	10.35± 0.06	9.91± 0.06	9.23± 0.07	6.60± 0.06
60	05 46 30.03	+00 11 11.1	...	24.28± 0.70	21.64± 0.10	19.35± 0.02	17.33± 0.02	14.95± 0.04	14.16± 0.04	13.66± 0.04	12.96± 0.06	12.96± 0.06	12.82± 0.13	...	...
61	05 46 30.06	+00 12 09.7	22.11± 0.16	20.46± 0.02	18.12± 0.01	16.35± 0.01	14.98± 0.01	12.64± 0.02	11.38± 0.02	10.72± 0.02	9.79± 0.06	9.51± 0.06	9.19± 0.06	8.41± 0.06	5.41± 0.06
62	05 46 31.03	+00 27 12.1	23.60± 0.37	23.05± 0.09	21.14± 0.03	18.97± 0.01	17.49± 0.01	15.44± 0.05	14.82± 0.06	14.25± 0.06	13.45± 0.06	13.18± 0.06	12.70± 0.06	12.09± 0.09	...
63	05 46 31.46	+00 20 15.8	23.02± 0.27	20.22± 0.01	18.73± 0.01	17.33± 0.01	16.54± 0.01	15.14± 0.04	14.53± 0.05	14.24± 0.06	13.95± 0.06	13.93± 0.06	13.86± 0.09	...	...
64	05 46 31.71	+00 25 08.2	24.83± 0.88	23.42± 0.10	20.58± 0.01	18.23± 0.01	16.63± 0.01	13.79± 0.02	12.34± 0.02	11.57± 0.02	10.61± 0.06	10.48± 0.06	10.05± 0.06	9.52± 0.06	6.52± 0.06
65	05 46 33.28	+00 02 51.9	20.97± 0.06	18.99± 0.01	16.70± 0.01	15.42± 0.01	14.27± 0.01	12.72± 0.02	11.17± 0.02	10.21± 0.02	8.82± 0.06	8.35± 0.06	7.92± 0.06	7.15± 0.07	4.75± 0.06
66	05 46 34.54	+00 06 43.5	24.11± 0.87	20.22± 0.01	17.53± 0.01	15.94± 0.01	14.65± 0.01	11.96± 0.03	10.57± 0.03	9.73± 0.03	8.73± 0.06	8.29± 0.06	7.94± 0.06	7.31± 0.07	5.02± 0.06
67	05 46 34.90	+00 04 20.7	...	20.16± 0.05	18.11± 0.05	16.15± 0.05	14.96± 0.05	12.71± 0.02	11.56± 0.03	11.10± 0.02	10.66± 0.06	10.56± 0.06	10.06± 0.09	9.56± 0.26	...
68	05 46 35.50	+00 01 38.9	...	...	...	...	...	13.27± 0.03	12.24± 0.02	11.61± 0.02	10.73± 0.06	10.51± 0.06	10.29± 0.10	...	...
69	05 46 36.10	+00 06 26.8	...	...	22.99± 0.26	19.73± 0.02	17.56± 0.02	13.19± 0.02	10.97± 0.02	9.67± 0.02	8.27± 0.06	7.84± 0.06	7.41± 0.06	6.16± 0.06	2.38± 0.06
70	05 46 37.06	+00 01 21.8	19.23± 0.03	17.83± 0.01	15.75± 0.01	14.67± 0.01	13.69± 0.01	11.67± 0.02	10.42± 0.02	9.52± 0.02	8.19± 0.06	7.74± 0.06	7.40± 0.06	6.71± 0.07	3.09± 0.06
71	05 46 37.57	+00 04 02.5	...	...	19.40± 0.02	16.77± 0.01	15.29± 0.01	13.08± 0.02	12.18± 0.03	11.71± 0.03	11.25± 0.06	11.04± 0.06	11.26± 0.20	...	...
72	05 46 38.33	+00 05 48.7	...	...	...	...	...	13.37± 0.04	11.96± 0.04	11.08± 0.03	9.86± 0.06	9.30± 0.06	8.85± 0.06	8.05± 0.09	5.17± 0.06
73	05 46 38.40	+00 15 11.6	22.87± 0.23	21.46± 0.03	19.35± 0.01	17.03± 0.01	15.55± 0.01	13.40± 0.03	12.48± 0.02	11.99± 0.02	11.33± 0.06	11.04± 0.06	10.84± 0.06	10.30± 0.10	...
74	05 46 38.57	+00 22 06.0	23.37± 0.67	20.98± 0.03	18.53± 0.01	16.80± 0.01	15.60± 0.01	13.41± 0.02	12.19± 0.02	11.70± 0.02	11.01± 0.06	10.87± 0.06	10.51± 0.06	9.76± 0.07	7.68± 0.06
75	05 46 39.89	+00 06 44.9	...	...	21.47± 0.07	18.93± 0.01	17.03± 0.01	13.84± 0.03	12.07± 0.02	11.12± 0.02	9.58± 0.06	9.08± 0.06	8.67± 0.07	8.14± 0.06	5.26± 0.06
76	05 46 40.18	+00 05 01.9	...	19.64± 0.02	17.05± 0.01	15.70± 0.01	14.70± 0.01	12.78± 0.03	11.77± 0.03	11.40± 0.03	10.93± 0.06	10.80± 0.06	10.71± 0.13	10.52± 0.11	...
77	05 46 40.44	−00 08 38.2	...	23.19± 0.12	20.47± 0.02	18.55± 0.01	17.50± 0.01	0.01± 0.01	0.01± 0.01	0.01± 0.01	13.56± 0.06	13.60± 0.06	13.54± 0.07	...	...
78	05 46 40.43	+00 05 07.7	20.69± 0.09	18.93± 0.01	16.55± 0.01	15.10± 0.01	14.13± 0.01	12.23± 0.04	11.24± 0.04	10.88± 0.03	10.61± 0.06	10.47± 0.06	10.44± 0.11	...	...
79	05 46 40.77	+00 27 22.5	20.63± 0.03	19.83± 0.01	18.07± 0.01	16.39± 0.01	15.09± 0.01	12.90± 0.02	12.04± 0.03	11.39± 0.03	10.20± 0.06	9.90± 0.06	9.46± 0.06	8.83± 0.06	6.30± 0.06
80	05 46 43.82	+00 03 21.8	...	...	...	...	...	14.73± 0.03	13.81± 0.03	13.24± 0.02	12.50± 0.07	12.04± 0.07	...	...	...
81	05 46 43.84	+00 15 32.4	21.37± 0.12	19.07± 0.01	17.00± 0.01	15.62± 0.01	14.70± 0.01	12.93± 0.02	11.93± 0.02	11.39± 0.02	10.32± 0.06	10.19± 0.06	9.67± 0.09	9.27± 0.07	6.91± 0.07
82	05 46 44.08	+00 18 03.2	19.20± 0.02	16.88± 0.01	15.02± 0.01	14.33± 0.01	13.25± 0.01	11.56± 0.02	10.61± 0.02	10.22± 0.02	9.42± 0.06	9.12± 0.06	8.68± 0.06	7.94± 0.06	5.93± 0.06
83	05 46 44.25	+00 30 29.5	23.36± 0.28	22.32± 0.05	20.08± 0.01	17.46± 0.01	15.84± 0.01	13.48± 0.02	12.59± 0.02	12.13± 0.02	11.55± 0.06	11.55± 0.06	11.38± 0.07	11.39± 0.19	...
84	05 46 44.84	+00 16 59.8	22.12± 0.17	20.54± 0.02	18.12± 0.01	16.47± 0.01	15.28± 0.01	13.19± 0.02	12.06± 0.02	11.57± 0.02	10.95± 0.06	10.73± 0.06	10.58± 0.17	10.09± 0.06	5.84± 0.06
85	05 46 45.00	+00 11 32.7	...	22.29± 0.12	20.48± 0.04	18.96± 0.02	17.17± 0.02	14.54± 0.03	13.18± 0.03	12.44± 0.02	11.29± 0.06	10.83± 0.06	10.22± 0.13	...	5.86± 0.06
86	05 46 45.00	+00 24 48.7	23.10± 0.28	21.20± 0.02	19.68± 0.01	17.66± 0.01	16.55± 0.01	14.84± 0.04	14.20± 0.05	14.03± 0.05	13.52± 0.06	13.47± 0.06	13.29± 0.16	...	...
87	05 46 45.04	+00 05 33.9	...	...	...	...	...	11.89± 0.04	10.67± 0.03	10.04± 0.02	9.41± 0.06	8.94± 0.06	8.47± 0.06	7.66± 0.09	4.78± 0.06
88	05 46 45.14	+00 03 46.4	...	...	...	...	...	13.68± 0.02	12.30± 0.02	11.53± 0.02	10.68± 0.06	10.14± 0.06	10.10± 0.11	...	...
89	05 46 46.87	+00 09 07.6	20.27± 0.06	18.92± 0.01	16.96± 0.01	15.90± 0.01	14.70± 0.01	12.29± 0.02	11.13± 0.02	10.40± 0.02	9.48± 0.06	9.04± 0.06	8.60± 0.07	7.60± 0.09	4.37± 0.06
90	05 46 48.55	+00 21 28.2	23.19± 0.81	...	21.46± 0.10	20.28± 0.05	19.07± 0.08	16.96± 0.20	15.47± 0.10	14.15± 0.06	11.77± 0.06	11.11± 0.06	10.42± 0.06	9.39± 0.07	5.49± 0.06

Table 3.5: continued.

ID	RA (J2000)	DEC (J2000)	u′ (mag)	g′ (mag)	r′ (mag)	i′ (mag)	z′ (mag)	J (mag)	H (mag)	K_s (mag)	[3.6] (mag)	[4.5] (mag)	[5.8] (mag)	[8.0] (mag)	[24]
91	05 46 48.73	+00 21 38.3	...	...	23.16± 0.31	19.54± 0.02	17.53± 0.02	14.51± 0.03	13.00± 0.02	12.24± 0.02	11.35± 0.06	11.12± 0.06	10.74± 0.06	10.06± 0.08	7.24± 0.06
92	05 46 49.09	+00 28 38.3	...	25.60± 0.95	22.00± 0.06	19.30± 0.01	17.51± 0.01	14.72± 0.03	13.21± 0.03	12.50± 0.03	11.64± 0.06	11.22± 0.06	10.83± 0.06	10.14± 0.09	7.68± 0.06
93	05 46 51.19	+00 18 08.2	22.21± 0.19	21.58± 0.04	19.72± 0.01	17.48± 0.01	16.06± 0.01	14.08± 0.03	13.24± 0.02	12.84± 0.03	12.19± 0.07	12.04± 0.07	...	...	...
94	05 46 51.40	+00 19 47.2	...	24.59± 0.73	22.17± 0.14	20.41± 0.04	19.04± 0.06	16.30± 0.09	14.89± 0.06	14.10± 0.05	12.27± 0.07	11.29± 0.06	10.36± 0.06	9.13± 0.06	5.74± 0.06
95	05 46 51.48	+00 19 21.3	21.91± 0.14	19.85± 0.01	17.75± 0.01	16.28± 0.01	15.13± 0.01	13.29± 0.02	12.30± 0.03	11.84± 0.02	11.14± 0.06	11.00± 0.06	10.55± 0.06	9.42± 0.07	6.68± 0.06
96	05 46 51.85	+00 19 38.6	23.95± 0.90	23.18± 0.16	20.02± 0.02	17.79± 0.01	16.16± 0.01	13.55± 0.02	12.28± 0.03	11.56± 0.02	10.97± 0.06	10.75± 0.06	10.24± 0.13	9.15± 0.07	5.77± 0.06
97	05 46 52.41	+00 20 01.7	20.73± 0.07	19.09± 0.01	17.16± 0.01	15.87± 0.01	14.86± 0.01	12.66± 0.02	11.48± 0.02	10.80± 0.02	9.70± 0.06	9.21± 0.06	8.82± 0.07	8.04± 0.06	4.83± 0.06
98	05 46 56.54	+00 20 52.9	20.70± 0.07	18.09± 0.01	15.94± 0.01	14.74± 0.01	13.88± 0.01	11.94± 0.02	10.92± 0.02	10.56± 0.02	10.31± 0.06	10.32± 0.06	10.16± 0.13	10.10± 0.08	...
99	05 46 58.03	+00 14 27.8	21.19± 0.15	19.89± 0.02	18.03± 0.01	16.12± 0.01	14.88± 0.01	13.01± 0.02	12.10± 0.02	11.64± 0.02	10.65± 0.06	10.20± 0.06	9.75± 0.10	8.83± 0.21	5.97± 0.06
100	05 46 58.13	+00 05 38.1	20.58± 0.06	18.04± 0.01	15.71± 0.01	14.27± 0.01	13.27± 0.01	11.23± 0.02	10.13± 0.02	9.69± 0.02	9.32± 0.06	9.16± 0.06	8.90± 0.07	8.30± 0.13	5.24± 0.06
101	05 47 01.95	+00 16 56.7	...	23.33± 0.23	22.16± 0.14	19.23± 0.02	17.42± 0.01	15.02± 0.04	14.19± 0.04	13.68± 0.04	13.10± 0.09	12.95± 0.09	...	...	...
102	05 47 02.87	+00 16 51.9	...	...	21.50± 0.06	18.63± 0.01	17.01± 0.01	14.45± 0.03	13.33± 0.03	12.76± 0.03	11.83± 0.06	11.57± 0.06	...	...	...
103	05 47 03.97	+00 11 14.4	19.05± 0.01	17.90± 0.01	16.32± 0.01	15.14± 0.01	14.20± 0.01	12.46± 0.02	11.40± 0.02	10.80± 0.02	9.89± 0.06	9.63± 0.06	9.15± 0.07	8.29± 0.14	5.30± 0.06
104	05 47 04.48	+00 15 47.2	...	...	23.03± 0.22	19.35± 0.01	17.13± 0.01	13.69± 0.02	11.72± 0.02	10.63± 0.02	9.62± 0.06	9.03± 0.06	8.75± 0.07	8.14± 0.12	...
105	05 47 04.94	+00 18 31.6	21.77± 0.14	19.71± 0.01	17.16± 0.01	15.55± 0.01	14.32± 0.01	11.84± 0.01	10.88± 0.07	10.45± 0.05	10.06± 0.06	9.99± 0.06	9.81± 0.07	9.50± 0.09	...
106	05 47 04.98	+00 18 12.6	22.93± 0.69	23.05± 0.29	...	18.64± 0.01	16.99± 0.01	14.45± 0.02	13.37± 0.02	12.92± 0.02	12.41± 0.07	12.34± 0.07	...	...	...
107	05 47 05.06	+00 18 34.8	23.64± 0.74	21.84± 0.07	18.71± 0.01	16.75± 0.01	15.38± 0.01	12.09± 0.01	11.67± 0.05	11.09± 0.03	10.48± 0.06	10.16± 0.06	9.63± 0.09	9.04± 0.24	...
108	05 47 05.12	+00 18 26.7	23.88± 0.93	21.28± 0.04	19.35± 0.01	17.10± 0.01	15.74± 0.01	13.40± 0.04	12.34± 0.03	11.94± 0.03	11.65± 0.06	11.48± 0.06	...	...	...
109	05 47 05.34	+00 28 46.1	23.11± 0.23	20.39± 0.01	18.26± 0.01	16.61± 0.01	15.59± 0.01	13.72± 0.03	12.73± 0.02	12.41± 0.03	11.97± 0.06	12.01± 0.06	11.97± 0.08	11.53± 0.24	...
110	05 47 06.00	+00 32 08.5	22.33± 0.12	20.10± 0.01	17.73± 0.01	16.38± 0.01	15.11± 0.01	11.74± 0.03	10.40± 0.03	9.37± 0.02	8.10± 0.06	7.58± 0.06	7.28± 0.06	6.56± 0.06	3.05± 0.06
111	05 47 05.98	+00 25 53.1	...	...	22.34± 0.07	19.57± 0.01	17.95± 0.01	14.55± 0.04	13.32± 0.03	12.72± 0.03	12.86± 0.06	12.32± 0.06	12.08± 0.08	11.72± 0.25	...
112	05 47 06.17	+00 20 32.5	...	22.66± 0.11	19.72± 0.01	17.53± 0.01	15.82± 0.01	12.96± 0.02	11.37± 0.02	10.64± 0.02	9.67± 0.06	9.32± 0.06	8.75± 0.07	7.83± 0.06	4.52± 0.06
113	05 47 06.96	+00 00 47.7	17.56± 0.01	15.72± 0.01	14.20± 0.01	13.73± 0.01	12.94± 0.01	11.35± 0.02	10.57± 0.02	10.22± 0.02	9.83± 0.06	9.61± 0.06	9.24± 0.07	8.15± 0.11	4.83± 0.06
114	05 47 06.99	+00 31 55.9	21.88± 0.08	20.41± 0.01	18.21± 0.01	16.58± 0.01	15.36± 0.01	12.86± 0.02	11.69± 0.02	10.89± 0.02	10.00± 0.06	9.58± 0.06	9.11± 0.06	8.09± 0.06	4.65± 0.06
115	05 47 07.26	+00 19 32.2	19.77± 0.03	17.60± 0.01	15.11± 0.01	15.15± 0.01	12.61± 0.01	10.23± 0.02	9.02± 0.02	8.32± 0.02	7.26± 0.06	6.77± 0.06	6.39± 0.06	5.70± 0.06	3.38± 0.06
116	05 47 08.69	+00 00 14.0	19.93± 0.02	17.31± 0.01	15.64± 0.01	14.59± 0.01	13.29± 0.01	11.56± 0.02	10.80± 0.02	10.52± 0.03	10.20± 0.06	10.25± 0.06	10.03± 0.11	10.07± 0.06	...
117	05 47 08.62	+00 19 23.9	...	...	20.59± 0.03	18.18± 0.01	16.52± 0.01	13.83± 0.03	12.51± 0.02	11.86± 0.02	10.80± 0.06	10.52± 0.06	10.09± 0.12	9.51± 0.07	...
118	05 47 08.71	+00 16 34.7	...	...	...	...	...	14.86± 0.04	13.41± 0.02	12.76± 0.03	11.90± 0.06	11.51± 0.06	11.30± 0.29	...	...
119	05 47 10.72	+00 18 46.3	...	...	19.82± 0.01	17.62± 0.01	16.07± 0.01	13.43± 0.03	11.93± 0.03	11.26± 0.02	10.41± 0.06	9.81± 0.06	9.25± 0.08	8.58± 0.17	...
120	05 47 10.89	+00 32 06.0	21.23± 0.05	18.55± 0.01	16.55± 0.01	15.24± 0.01	14.39± 0.01	12.56± 0.02	11.64± 0.03	11.19± 0.02	10.32± 0.06	9.90± 0.06	9.61± 0.06	9.04± 0.06	6.62± 0.06
121	05 47 10.98	+00 19 14.8	19.98± 0.03	17.49± 0.01	15.33± 0.01	14.29± 0.01	13.16± 0.01	11.00± 0.02	9.84± 0.02	9.08± 0.02	8.24± 0.06	7.84± 0.06	7.69± 0.06	6.72± 0.07	3.35± 0.06
122	05 47 10.98	+00 21 32.2	...	22.87± 0.15	19.87± 0.02	17.88± 0.01	16.51± 0.01	14.04± 0.03	12.71± 0.04	12.14± 0.03	11.60± 0.06	11.61± 0.06	11.58± 0.07	11.53± 0.22	...
123	05 47 12.92	+00 22 06.5	...	...	22.69± 0.19	19.87± 0.02	17.79± 0.02	14.03± 0.03	11.84± 0.02	10.54± 0.02	9.36± 0.06	8.77± 0.06	8.55± 0.06	7.75± 0.06	4.76± 0.06
124	05 47 13.85	+00 00 17.1	18.53± 0.01	16.41± 0.01	14.67± 0.01	14.90± 0.01	12.78± 0.01	10.75± 0.06	9.80± 0.05	9.23± 0.05	8.25± 0.06	7.88± 0.06	7.64± 0.06	7.13± 0.07	4.40± 0.06
125	05 47 16.58	−00 00 56.4	22.22± 0.15	19.73± 0.01	18.09± 0.01	16.03± 0.01	14.89± 0.01	13.06± 0.02	12.32± 0.02	11.89± 0.02	11.06± 0.06	10.77± 0.06	10.44± 0.14	9.83± 0.06	7.52± 0.07
126	05 47 17.16	+00 18 24.6	21.13± 0.06	19.58± 0.01	17.69± 0.01	16.43± 0.01	15.33± 0.01	13.03± 0.02	11.86± 0.02	11.18± 0.02	9.96± 0.06	9.48± 0.06	9.19± 0.08	8.77± 0.19	5.80± 0.08
127	05 47 17.28	+00 38 21.4	18.05± 0.01	16.24± 0.01	14.74± 0.01	14.40± 0.01	13.17± 0.01	11.52± 0.02	10.54± 0.02	9.91± 0.02	8.74± 0.06	8.43± 0.06	8.04± 0.06	7.45± 0.06	4.68± 0.06
128	05 47 19.72	+00 01 21.8	19.80± 0.02	19.58± 0.01	17.95± 0.01	17.00± 0.01	15.72± 0.01	13.76± 0.02	13.09± 0.02	12.67± 0.02	11.57± 0.06	11.02± 0.06	10.75± 0.18	10.17± 0.06	7.07± 0.06
129	05 47 19.90	+00 16 13.1	23.66± 0.50	24.32± 0.34	20.70± 0.02	18.16± 0.01	16.41± 0.01	13.82± 0.02	12.54± 0.02	11.95± 0.02	11.10± 0.06	10.67± 0.06	10.16± 0.13	...	6.77± 0.06
130	05 47 22.99	+00 17 56.7	21.75± 0.44	21.20± 0.10	19.35± 0.03	17.34± 0.01	15.93± 0.01	14.04± 0.03	12.91± 0.02	11.97± 0.01	11.99± 0.07	11.96± 0.07	...	...	...
131	05 47 25.05	+00 31 05.0	19.04± 0.01	16.53± 0.01	15.18± 0.01	16.05± 0.01	14.38± 0.01	12.64± 0.03	12.10± 0.04	11.83± 0.03	11.63± 0.06	11.74± 0.06	11.56± 0.07	11.57± 0.22	...
132	05 47 57.53	+00 11 31.2	21.40± 0.06	19.11± 0.01	17.34± 0.01	15.47± 0.01	14.37± 0.01	12.56± 0.02	11.75± 0.03	11.41± 0.02	11.12± 0.06	10.96± 0.06	10.85± 0.06	10.97± 0.06	...

Table 3.6: Photometric magnitudes of YSOs in L1641.

ID	RA (J2000)	DEC (J2000)	u′ (mag)	g′ (mag)	r′ (mag)	i′ (mag)	z′ (mag)	J (mag)	H (mag)	K_s (mag)	[3.6] (mag)	[4.5] (mag)	[5.8] (mag)	[8.0] (mag)	[24]
1	05 35 14.56	−06 15 12.7	21.82± 0.22	18.89± 0.01	16.78± 0.01	15.42± 0.01	14.48± 0.01	12.49± 0.04	11.38± 0.04	10.86± 0.03	10.02± 0.06	9.35± 0.06	9.32± 0.06	8.43± 0.06	4.80± 0.06
2	05 35 14.67	−06 15 07.3	...	22.04± 0.09	19.86± 0.02	17.65± 0.01	16.08± 0.01	13.58± 0.04	12.43± 0.04	11.79± 0.02	10.93± 0.06	10.36± 0.06	9.96± 0.06	9.03± 0.06	...
3	05 35 14.72	−06 13 39.9	21.89± 0.24	20.14± 0.02	18.29± 0.01	16.03± 0.01	14.70± 0.01	12.67± 0.03	11.85± 0.03	11.49± 0.02	11.03± 0.06	10.92± 0.06	10.87± 0.06	10.80± 0.08	...
4	05 35 15.83	−06 24 45.7	21.43± 0.14	19.19± 0.01	17.76± 0.01	15.99± 0.01	15.02± 0.01	13.42± 0.02	12.84± 0.03	12.55± 0.02	12.20± 0.06	12.07± 0.06	12.05± 0.07	11.93± 0.17	...
5	05 35 17.80	−06 24 38.4	17.85± 0.01	15.78± 0.01	14.38± 0.01	15.25± 0.01	12.94± 0.01	11.31± 0.02	10.52± 0.03	10.22± 0.02	9.21± 0.06	8.53± 0.06	7.95± 0.06	7.01± 0.06	4.94± 0.06
6	05 35 18.26	−06 24 30.3	22.61± 0.72	19.95± 0.02	18.51± 0.01	16.51± 0.01	15.37± 0.01	13.69± 0.03	13.11± 0.03	12.80± 0.03	12.36± 0.06	12.21± 0.06	12.17± 0.07	12.02± 0.22	...
7	05 35 18.95	−06 27 25.6	20.04± 0.06	18.59± 0.01	17.20± 0.01	15.64± 0.01	14.73± 0.01	13.14± 0.03	12.39± 0.03	11.89± 0.02	11.19± 0.06	10.89± 0.06	10.46± 0.06	9.73± 0.06	6.59± 0.06
8	05 35 19.34	−06 24 14.5	19.02± 0.03	17.18± 0.01	15.79± 0.01	15.05± 0.01	14.17± 0.01	12.82± 0.02	12.11± 0.03	11.91± 0.02	11.73± 0.06	11.65± 0.06	11.63± 0.06	11.55± 0.13	...
9	05 35 21.77	−06 18 51.2	21.12± 0.19	19.05± 0.01	17.67± 0.01	15.99± 0.01	15.08± 0.01	13.52± 0.03	12.87± 0.03	12.53± 0.02	12.02± 0.06	11.76± 0.06	11.59± 0.06	11.06± 0.11	...
10	05 35 23.60	−06 28 24.4	19.18± 0.04	16.66± 0.01	15.29± 0.01	17.49± 0.01	13.00± 0.01	11.49± 0.03	10.76± 0.03	10.56± 0.02	10.33± 0.06	10.07± 0.06	10.25± 0.06	10.22± 0.07	...
11	05 35 24.45	−06 27 47.2	22.27± 0.45	19.80± 0.02	18.28± 0.01	16.78± 0.01	15.98± 0.01	14.52± 0.03	13.97± 0.05	13.73± 0.04	13.31± 0.06	13.30± 0.06	13.30± 0.12	...	...
12	05 35 24.49	−06 28 40.5	21.21± 0.22	19.01± 0.01	17.60± 0.01	15.79± 0.01	14.80± 0.01	13.23± 0.03	12.52± 0.03	12.28± 0.02	12.05± 0.06	11.90± 0.06	11.81± 0.07	11.80± 0.16	...
13	05 35 25.11	−06 47 56.6	15.14± 0.01	14.65± 0.01	14.11± 0.01	13.71± 0.01	12.97± 0.01	11.37± 0.03	10.47± 0.03	9.97± 0.02	9.51± 0.06	8.91± 0.06	8.56± 0.06	7.70± 0.06	5.06± 0.06
14	05 35 25.70	−06 23 18.9	20.10± 0.08	17.59± 0.01	16.16± 0.01	14.93± 0.01	14.18± 0.01	12.73± 0.03	12.01± 0.03	11.82± 0.02	11.65± 0.06	11.62± 0.06	11.46± 0.06	11.49± 0.13	...
15	05 35 26.59	−06 15 32.8	20.80± 0.14	18.25± 0.01	16.80± 0.01	15.43± 0.01	14.66± 0.01	13.17± 0.03	12.44± 0.08	12.22± 0.06	11.83± 0.06	11.90± 0.06	11.85± 0.07	11.80± 0.17	...
16	05 35 26.80	−06 15 34.4	20.69± 0.13	18.30± 0.01	16.87± 0.01	15.47± 0.01	14.69± 0.01	13.19± 0.07	12.51± 0.04	12.29± 0.03	12.07± 0.06	12.05± 0.06	11.97± 0.07	11.95± 0.17	...
17	05 35 26.83	−06 26 47.6	18.10± 0.01	15.58± 0.01	14.29± 0.01	13.74± 0.01	13.29± 0.01	12.07± 0.02	11.36± 0.03	11.18± 0.02	11.00± 0.06	10.95± 0.06	10.97± 0.06	10.95± 0.09	...
18	05 35 26.96	−06 27 13.0	22.48± 0.55	19.86± 0.02	18.46± 0.01	16.78± 0.01	15.86± 0.01	14.33± 0.03	13.77± 0.03	13.50± 0.03	13.03± 0.06	13.03± 0.06	12.90± 0.09	...	...
19	05 35 27.17	−06 19 42.0	18.16± 0.02	16.03± 0.01	14.57± 0.01	13.98± 0.01	12.86± 0.01	11.29± 0.02	10.49± 0.03	10.14± 0.02	9.65± 0.06	9.35± 0.06	9.08± 0.06	8.56± 0.06	5.96± 0.06
20	05 35 27.35	−06 19 31.3	21.81± 0.37	20.87± 0.04	19.13± 0.01	18.14± 0.01	17.37± 0.01	15.91± 0.08	14.70± 0.07	13.94± 0.04	12.67± 0.06	11.97± 0.06	11.36± 0.06	10.62± 0.08	7.82± 0.06
21	05 35 28.28	−06 22 29.3	...	21.82± 0.08	20.33± 0.03	18.23± 0.01	17.02± 0.01	15.30± 0.05	14.73± 0.06	14.47± 0.06	14.02± 0.06	13.85± 0.06	13.90± 0.18	...	...
22	05 35 29.21	−06 16 29.7	22.66± 0.74	19.27± 0.01	17.37± 0.01	15.28± 0.01	14.05± 0.01	12.09± 0.06	11.28± 0.07	10.86± 0.05	10.52± 0.06	10.36± 0.06	10.32± 0.06	10.39± 0.07	...
23	05 35 29.46	−06 16 26.6	21.67± 0.30	18.50± 0.01	16.49± 0.01	15.04± 0.01	14.13± 0.01	12.38± 0.02	11.42± 0.03	10.95± 0.02	10.35± 0.06	9.96± 0.06	9.66± 0.06	9.49± 0.06	6.81± 0.06
24	05 35 30.41	−06 27 07.2	...	...	...	...	...	15.32± 0.04	14.84± 0.08	14.58± 0.08	13.95± 0.06	13.78± 0.06	...	...	...
25	05 35 31.05	−06 45 18.1	16.36± 0.01	15.61± 0.01	14.60± 0.01	14.14± 0.01	13.04± 0.01	11.55± 0.02	10.85± 0.03	10.52± 0.02	9.94± 0.06	9.61± 0.06	9.24± 0.06	8.34± 0.06	5.21± 0.06
26	05 35 31.49	−06 14 18.9	20.16± 0.13	17.81± 0.01	16.35± 0.01	15.17± 0.01	14.49± 0.01	13.04± 0.02	12.39± 0.03	12.21± 0.02	11.93± 0.06	11.75± 0.06	11.86± 0.07	11.82± 0.15	...
27	05 35 31.89	−06 36 25.5	21.71± 0.34	20.36± 0.03	18.78± 0.01	17.10± 0.01	15.90± 0.01	14.11± 0.02	13.19± 0.03	12.48± 0.02	11.54± 0.06	10.99± 0.06	10.66± 0.06	10.04± 0.08	7.13± 0.06
28	05 35 33.93	−06 14 32.8	20.05± 0.13	18.53± 0.01	17.03± 0.01	15.42± 0.01	14.42± 0.01	12.75± 0.02	12.11± 0.03	11.81± 0.02	11.25± 0.06	10.91± 0.06	10.40± 0.06	9.77± 0.06	7.01± 0.06
29	05 35 34.17	−06 22 57.8	20.19± 0.09	17.67± 0.01	16.24± 0.01	15.12± 0.01	14.51± 0.01	13.17± 0.02	12.47± 0.03	12.23± 0.02	12.10± 0.06	12.06± 0.06	11.90± 0.07	11.93± 0.17	...
30	05 35 34.19	−06 39 43.3	19.90± 0.11	17.53± 0.01	16.04± 0.01	15.16± 0.01	14.23± 0.01	12.80± 0.02	12.08± 0.04	11.73± 0.02	11.08± 0.06	10.80± 0.06	10.44± 0.06	9.94± 0.08	7.47± 0.06
31	05 35 34.34	−06 24 22.8	...	20.79± 0.04	19.33± 0.01	17.51± 0.01	16.42± 0.01	14.82± 0.04	14.24± 0.05	13.90± 0.05	13.47± 0.06	13.28± 0.06	13.30± 0.12	12.55± 0.28	...
32	05 35 38.59	−06 23 43.1	20.61± 0.13	18.42± 0.01	17.01± 0.01	15.62± 0.01	14.85± 0.01	13.41± 0.03	12.75± 0.03	12.47± 0.02	12.12± 0.06	12.17± 0.06	11.94± 0.06	11.84± 0.16	...
33	05 35 40.83	−06 18 06.7	20.26± 0.09	17.77± 0.01	16.32± 0.01	15.18± 0.01	14.55± 0.01	13.16± 0.02	12.46± 0.03	12.21± 0.02	11.98± 0.06	11.90± 0.06	11.86± 0.06	12.03± 0.15	...
34	05 35 41.02	−06 22 45.4	17.24± 0.01	15.54± 0.01	14.08± 0.01	16.80± 0.01	12.52± 0.01	10.91± 0.02	10.07± 0.03	9.70± 0.02	9.05± 0.06	8.67± 0.06	8.41± 0.06	8.06± 0.06	4.74± 0.06
35	05 35 41.65	−06 25 19.2	22.66± 0.72	22.59± 0.17	21.14± 0.06	18.61± 0.01	17.18± 0.01	15.33± 0.01	14.85± 0.09	14.60± 0.10	13.98± 0.06	13.94± 0.06	...	...	...
36	05 35 42.09	−06 16 20.8	22.42± 0.59	21.64± 0.07	20.11± 0.02	18.10± 0.01	16.91± 0.01	15.12± 0.05	14.52± 0.08	14.15± 0.05	13.48± 0.06	13.24± 0.06	13.02± 0.10	12.59± 0.27	...
37	05 35 42.84	−06 21 44.6	19.81± 0.07	17.32± 0.01	15.88± 0.01	14.86± 0.01	14.24± 0.01	12.98± 0.02	12.25± 0.03	11.96± 0.02	11.49± 0.06	11.15± 0.06	11.06± 0.06	10.18± 0.06	7.74± 0.06
38	05 35 42.76	−06 34 51.9	16.35± 0.01	15.66± 0.01	14.67± 0.01	14.32± 0.01	13.69± 0.01	12.37± 0.02	11.58± 0.03	11.16± 0.02	10.46± 0.06	9.98± 0.06	9.55± 0.06	8.90± 0.06	6.43± 0.06
39	05 35 43.37	−06 22 19.6	20.86± 0.16	18.87± 0.01	17.18± 0.01	15.47± 0.01	14.31± 0.01	12.10± 0.02	11.21± 0.03	10.67± 0.02	10.00± 0.06	9.53± 0.06	9.28± 0.06	8.80± 0.06	6.06± 0.06
40	05 35 44.18	−06 28 16.4	20.51± 0.12	20.12± 0.03	18.74± 0.01	17.04± 0.01	15.87± 0.01	14.12± 0.03	13.61± 0.04	13.15± 0.03	12.57± 0.06	12.04± 0.06	11.60± 0.07	10.84± 0.08	8.13± 0.06
41	05 35 44.27	−06 26 39.5	...	21.62± 0.06	20.13± 0.02	17.87± 0.01	16.57± 0.01	14.76± 0.04	14.23± 0.05	13.83± 0.04	13.36± 0.06	13.25± 0.06	13.24± 0.11	...	...
42	05 35 47.65	−06 21 36.1	17.43± 0.01	17.34± 0.01	16.34± 0.01	15.35± 0.01	14.26± 0.01	12.58± 0.02	11.91± 0.03	11.39± 0.02	10.57± 0.06	10.14± 0.06	9.78± 0.06	9.18± 0.06	6.29± 0.06
43	05 35 48.28	−06 17 59.4	20.08± 0.04	17.50± 0.01	16.09± 0.01	14.94± 0.01	14.24± 0.01	12.80± 0.02	12.10± 0.03	11.90± 0.02	11.70± 0.06	11.60± 0.06	11.47± 0.06	11.62± 0.11	...
44	05 35 48.39	−06 17 36.2	20.78± 0.08	18.22± 0.01	16.80± 0.01	15.32± 0.01	14.50± 0.01	13.01± 0.02	12.35± 0.03	12.11± 0.02	11.86± 0.06	11.71± 0.06	11.67± 0.06	11.68± 0.11	...
45	05 35 50.19	−06 50 40.2	18.82± 0.03	17.40± 0.01	15.89± 0.01	15.25± 0.01	14.59± 0.01	13.01± 0.02	11.82± 0.03	10.86± 0.02	9.57± 0.06	9.04± 0.06	8.31± 0.06	7.70± 0.06	4.83± 0.06

Table 3.6: continued.

ID	RA (J2000)	DEC (J2000)	u′ (mag)	g′ (mag)	r′ (mag)	i′ (mag)	z′ (mag)	J (mag)	H (mag)	K_s (mag)	[3.6] (mag)	[4.5] (mag)	[5.8] (mag)	[8.0] (mag)	[24]
46	05 35 57.30	−06 40 28.1	18.30± 0.02	17.47± 0.01	16.05± 0.01	15.02± 0.01	14.27± 0.01	12.86± 0.02	12.14± 0.03	11.81± 0.02	11.33± 0.06	10.88± 0.06	10.45± 0.06	9.66± 0.07	7.26± 0.06
47	05 35 57.31	−06 15 37.7	17.46± 0.01	16.74± 0.01	15.71± 0.01	14.81± 0.01	14.13± 0.01	12.62± 0.02	11.90± 0.03	11.45± 0.02	10.67± 0.06	10.32± 0.06	10.01± 0.06	9.45± 0.06	6.95± 0.06
48	05 35 57.45	−06 42 41.9	16.52± 0.01	14.99± 0.01	14.94± 0.01	12.24± 0.01	12.61± 0.01	10.96± 0.03	10.14± 0.03	9.65± 0.02	8.38± 0.06	7.70± 0.06	7.21± 0.06	6.38± 0.06	4.08± 0.06
49	05 35 57.45	−06 16 35.0	19.23± 0.03	16.26± 0.01	14.80± 0.01	13.62± 0.01	12.95± 0.01	11.62± 0.02	11.00± 0.03	10.82± 0.02	10.53± 0.06	10.42± 0.06	10.38± 0.06	10.36± 0.07	...
50	05 35 57.85	−06 23 44.4	19.30± 0.03	18.67± 0.01	17.44± 0.01	15.89± 0.01	15.09± 0.01	12.84± 0.03	12.30± 0.04	12.01± 0.03	11.40± 0.06	11.05± 0.06	10.66± 0.06	9.90± 0.06	7.45± 0.06
51	05 35 58.10	−06 14 50.9	21.58± 0.19	18.95± 0.01	17.53± 0.01	15.77± 0.01	14.79± 0.01	13.29± 0.02	12.69± 0.03	12.42± 0.02	12.03± 0.06	11.93± 0.06	11.90± 0.06	11.83± 0.15	...
52	05 35 58.25	−06 36 43.1	18.04± 0.02	16.33± 0.01	14.87± 0.01	14.33± 0.01	13.57± 0.01	11.71± 0.03	10.85± 0.03	10.38± 0.02	9.75± 0.06	9.37± 0.06	8.99± 0.06	8.45± 0.06	5.24± 0.06
53	05 35 58.26	−06 14 04.6	22.61± 0.41	20.78± 0.04	19.72± 0.02	18.42± 0.01	17.45± 0.01	14.98± 0.04	13.68± 0.05	12.91± 0.02	11.34± 0.06	10.75± 0.06	10.34± 0.06	9.66± 0.06	5.80± 0.06
54	05 35 59.75	−06 16 06.4	15.99± 0.01	14.74± 0.01	14.86± 0.01	15.51± 0.01	12.36± 0.01	0.01± 0.01	0.01± 0.01	0.01± 0.01	8.60± 0.06	8.28± 0.06	7.95± 0.06	7.42± 0.06	5.32± 0.06
55	05 35 59.84	−06 42 30.5	18.21± 0.02	18.69± 0.01	17.44± 0.01	16.03± 0.01	15.16± 0.01	13.44± 0.05	12.74± 0.06	12.24± 0.05	11.29± 0.06	10.55± 0.06	10.29± 0.06	9.58± 0.07	...
56	05 36 00.18	−06 42 33.9	17.54± 0.01	15.57± 0.01	13.77± 0.01	15.18± 0.01	13.04± 0.01	10.94± 0.03	10.05± 0.03	9.48± 0.02	8.53± 0.06	8.26± 0.06	7.78± 0.06	7.33± 0.06	4.81± 0.06
57	05 36 01.09	−06 25 07.7	20.10± 0.04	18.01± 0.01	16.62± 0.01	15.25± 0.01	14.48± 0.01	12.98± 0.02	12.27± 0.03	12.10± 0.02	11.74± 0.06	11.42± 0.06	11.28± 0.06	10.75± 0.07	8.46± 0.06
58	05 36 01.10	−06 15 31.4	16.65± 0.01	15.97± 0.01	14.89± 0.01	14.29± 0.01	13.60± 0.01	12.18± 0.02	11.44± 0.03	11.05± 0.02	10.36± 0.06	10.05± 0.06	9.63± 0.06	8.89± 0.06	6.33± 0.06
59	05 36 01.66	−06 42 36.2	21.40± 0.23	19.98± 0.02	18.43± 0.01	16.44± 0.01	15.22± 0.01	13.35± 0.03	12.73± 0.03	12.33± 0.02	11.60± 0.06	11.42± 0.06	11.04± 0.06	10.59± 0.10	...
60	05 36 05.00	−06 42 44.0	20.53± 0.11	18.56± 0.01	17.09± 0.01	15.23± 0.01	14.08± 0.01	12.31± 0.02	11.65± 0.03	11.30± 0.02	10.65± 0.06	10.29± 0.06	10.06± 0.06	9.50± 0.07	6.88± 0.06
61	05 36 04.98	−06 46 41.4	17.50± 0.01	15.13± 0.01	13.73± 0.01	13.14± 0.01	12.48± 0.01	11.03± 0.02	10.34± 0.03	10.12± 0.02	9.78± 0.06	9.71± 0.06	9.51± 0.06	9.02± 0.06	6.77± 0.06
62	05 36 05.08	−06 29 32.2	17.36± 0.01	15.67± 0.01	14.41± 0.01	13.44± 0.01	13.41± 0.01	12.37± 0.02	11.27± 0.03	10.49± 0.02	9.03± 0.06	8.58± 0.06	8.12± 0.06	7.74± 0.06	5.34± 0.06
63	05 36 05.16	−06 25 25.4	18.68± 0.01	16.21± 0.01	14.86± 0.01	13.98± 0.01	13.31± 0.01	11.82± 0.02	11.09± 0.03	10.91± 0.02	10.51± 0.06	10.57± 0.06	10.35± 0.06	10.49± 0.07	...
64	05 36 06.59	−06 31 43.0	20.70± 0.08	18.30± 0.01	16.92± 0.01	15.57± 0.01	14.78± 0.01	13.32± 0.03	12.69± 0.03	12.47± 0.02	12.14± 0.06	11.93± 0.06	11.61± 0.07	10.74± 0.09	7.57± 0.06
65	05 36 06.65	−06 32 17.2	19.88± 0.04	17.78± 0.01	16.16± 0.01	15.20± 0.01	14.04± 0.01	12.13± 0.02	10.66± 0.03	9.68± 0.01	8.40± 0.06	7.98± 0.06	7.62± 0.06	7.05± 0.06	4.73± 0.06
66	05 36 06.66	−06 14 25.9	18.02± 0.01	16.06± 0.01	14.65± 0.01	15.88± 0.01	13.29± 0.01	11.53± 0.04	10.72± 0.05	10.10± 0.03	8.75± 0.06	8.27± 0.06	7.99± 0.06	7.45± 0.06	4.71± 0.06
67	05 36 06.93	−06 18 53.4	19.44± 0.02	16.99± 0.01	15.58± 0.01	16.27± 0.01	13.02± 0.01	11.50± 0.02	10.81± 0.03	10.53± 0.02	10.23± 0.06	10.14± 0.06	10.11± 0.06	10.14± 0.06	...
68	05 36 08.29	−06 48 36.3	19.19± 0.02	17.28± 0.01	15.77± 0.01	14.65± 0.01	13.71± 0.01	12.08± 0.02	11.13± 0.03	10.63± 0.02	9.29± 0.06	8.64± 0.06	7.95± 0.06	7.17± 0.06	4.09± 0.06
69	05 36 08.34	−06 24 37.9	21.23± 0.10	19.33± 0.01	17.83± 0.01	15.75± 0.01	14.50± 0.01	12.70± 0.02	12.08± 0.03	11.74± 0.02	11.14± 0.06	10.90± 0.06	10.67± 0.06	10.22± 0.07	8.08± 0.06
70	05 36 08.57	−06 40 33.6	22.10± 0.37	21.34± 0.06	19.90± 0.02	17.61± 0.01	16.18± 0.01	14.43± 0.03	13.84± 0.04	13.53± 0.03	13.03± 0.06	12.86± 0.06	12.86± 0.13	...	...
71	05 36 09.35	−06 17 10.8	19.50± 0.02	16.85± 0.01	15.34± 0.01	14.35± 0.01	13.58± 0.01	12.03± 0.02	11.31± 0.03	11.12± 0.02	10.91± 0.06	10.67± 0.06	10.79± 0.06	10.79± 0.07	...
72	05 36 09.49	−06 18 36.3	18.47± 0.01	15.93± 0.01	14.51± 0.01	13.75± 0.01	13.11± 0.01	11.75± 0.02	11.04± 0.03	10.91± 0.02	10.74± 0.06	10.61± 0.06	10.57± 0.06	10.54± 0.07	...
73	05 36 09.52	−06 24 33.7	21.12± 0.09	20.39± 0.02	18.99± 0.01	17.33± 0.01	16.27± 0.01	14.64± 0.03	14.08± 0.05	13.74± 0.03	13.16± 0.06	12.84± 0.06	12.59± 0.08	12.00± 0.14	...
74	05 36 10.19	−06 18 54.8	23.42± 0.67	20.52± 0.02	18.26± 0.01	17.05± 0.01	16.18± 0.01	14.30± 0.03	13.29± 0.03	12.96± 0.02	12.61± 0.06	12.69± 0.06	12.48± 0.07	12.29± 0.18	...
75	05 36 10.44	−06 20 01.5	17.01± 0.01	14.82± 0.01	13.97± 0.01	13.35± 0.01	13.00± 0.01	11.66± 0.02	11.07± 0.03	10.91± 0.02	10.77± 0.06	10.73± 0.06	10.62± 0.06	10.70± 0.07	...
76	05 36 11.12	−06 18 14.1	22.74± 0.36	21.29± 0.04	19.74± 0.01	17.63± 0.01	16.40± 0.01	14.64± 0.04	14.06± 0.05	13.79± 0.04	13.23± 0.06	13.21± 0.06	13.08± 0.09	...	...
77	05 36 11.31	−06 16 56.0	21.69± 0.14	20.38± 0.02	18.94± 0.01	16.95± 0.01	15.75± 0.01	13.99± 0.02	13.41± 0.03	13.11± 0.03	12.46± 0.06	12.17± 0.06	11.90± 0.06	11.38± 0.10	8.42± 0.06
78	05 36 11.46	−06 22 22.1	...	21.25± 0.04	18.49± 0.01	16.73± 0.01	15.34± 0.01	12.69± 0.04	11.24± 0.04	10.43± 0.03	9.76± 0.06	9.19± 0.06	8.80± 0.06	8.16± 0.06	5.74± 0.06
79	05 36 11.67	−06 24 58.4	...	20.76± 0.02	19.33± 0.01	17.41± 0.01	16.31± 0.01	14.75± 0.03	14.04± 0.04	13.83± 0.04	13.26± 0.06	13.01± 0.06	12.83± 0.08	11.81± 0.12	7.39± 0.06
80	05 36 12.61	−06 23 39.6	21.15± 0.10	19.33± 0.01	17.59± 0.01	15.87± 0.01	14.74± 0.01	12.74± 0.03	11.80± 0.04	11.36± 0.03	10.70± 0.06	10.29± 0.06	10.09± 0.06	9.50± 0.06	6.72± 0.06
81	05 36 12.97	−06 23 33.0	21.79± 0.20	18.74± 0.01	16.45± 0.01	14.92± 0.01	13.83± 0.01	11.48± 0.03	10.47± 0.05	10.04± 0.04	9.69± 0.06	9.61± 0.06	9.40± 0.06	9.54± 0.10	...
82	05 36 12.97	−06 23 33.0	21.79± 0.20	18.74± 0.01	16.45± 0.01	14.92± 0.01	13.83± 0.01	11.48± 0.03	10.47± 0.05	10.04± 0.04	9.63± 0.06	9.53± 0.06	9.35± 0.06	8.91± 0.06	5.19± 0.06
83	05 36 13.15	−06 25 41.1	20.28± 0.04	17.74± 0.01	16.34± 0.01	15.18± 0.01	14.52± 0.01	13.11± 0.02	12.47± 0.03	12.23± 0.02	12.05± 0.06	11.94± 0.06	11.94± 0.06	11.95± 0.14	...
84	05 36 13.45	−06 43 55.1	21.69± 0.42	22.43± 0.38	21.57± 0.16	20.39± 0.07	19.68± 0.11	17.20± 0.22	16.25± 0.22	15.87± 0.23	15.47± 0.09	15.07± 0.07	...	...	...
85	05 36 14.76	−06 13 16.9	17.84± 0.01	16.71± 0.01	15.44± 0.01	14.53± 0.01	13.91± 0.01	12.47± 0.02	11.74± 0.03	11.50± 0.02	10.99± 0.06	10.71± 0.06	10.27± 0.06	9.56± 0.06	7.33± 0.06
86	05 36 15.07	−06 17 36.9	16.45± 0.01	14.80± 0.01	14.09± 0.01	14.89± 0.01	12.66± 0.01	11.19± 0.02	10.42± 0.03	9.99± 0.02	9.33± 0.06	9.06± 0.06	8.82± 0.06	7.84± 0.06	5.03± 0.06
87	05 36 15.60	−06 27 20.0	21.06± 0.08	18.62± 0.01	17.23± 0.01	15.86± 0.01	15.08± 0.01	13.65± 0.02	13.00± 0.03	12.80± 0.04	12.49± 0.06	12.46± 0.06	12.35± 0.07	12.40± 0.19	...
88	05 36 15.84	−06 14 50.7	19.23± 0.02	17.55± 0.01	16.09± 0.01	15.04± 0.01	14.38± 0.01	13.01± 0.02	12.29± 0.03	12.08± 0.02	11.83± 0.06	11.82± 0.06	11.54± 0.06	10.68± 0.07	6.72± 0.06
89	05 36 17.11	−06 28 20.2	...	23.08± 0.17	20.94± 0.04	18.86± 0.01	17.55± 0.01	15.51± 0.05	14.69± 0.06	14.29± 0.05	13.58± 0.06	13.28± 0.06	12.91± 0.09	12.35± 0.18	...
90	05 36 17.23	−06 17 24.5	20.44± 0.05	18.10± 0.01	16.63± 0.01	14.89± 0.01	13.89± 0.01	12.22± 0.02	11.60± 0.03	11.32± 0.02	10.85± 0.06	10.66± 0.06	10.37± 0.06	9.79± 0.06	6.46± 0.06

Table 3.6: continued.

ID	RA (J2000)	DEC (J2000)	u′ (mag)	g′ (mag)	r′ (mag)	i′ (mag)	z′ (mag)	J (mag)	H (mag)	K_s (mag)	[3.6] (mag)	[4.5] (mag)	[5.8] (mag)	[8.0] (mag)	[24]
91	05 36 18.48	−06 20 38.7	17.95± 0.01	16.36± 0.01	15.03± 0.01	14.21± 0.01	13.64± 0.01	12.20± 0.02	11.43± 0.03	11.10± 0.02	10.25± 0.06	9.90± 0.06	9.66± 0.06	9.07± 0.06	6.51± 0.06
92	05 36 18.88	−06 22 04.2	20.71± 0.07	18.43± 0.01	16.96± 0.01	15.77± 0.01	15.08± 0.01	0.01± 0.01	0.01± 0.01	0.01± 0.01	...	...	...	...	...
93	05 36 19.09	−06 22 50.6	23.46± 0.76	21.59± 0.05	20.15± 0.02	17.92± 0.01	16.65± 0.01	14.90± 0.03	14.28± 0.05	13.95± 0.04	13.53± 0.06	13.24± 0.06	12.97± 0.08	...	...
94	05 36 19.38	−06 25 51.3	20.29± 0.04	19.51± 0.01	17.99± 0.01	16.17± 0.01	14.86± 0.01	13.16± 0.02	12.36± 0.03	11.80± 0.01	10.80± 0.06	10.43± 0.06	10.01± 0.06	9.29± 0.06	6.36± 0.06
95	05 36 21.10	−06 17 17.3	20.77± 0.06	18.44± 0.01	17.00± 0.01	15.30± 0.01	14.34± 0.01	12.77± 0.02	12.18± 0.03	11.94± 0.02	11.53± 0.06	11.36± 0.06	11.47± 0.06	11.30± 0.09	...
96	05 36 21.16	−06 26 56.9	21.86± 0.17	20.02± 0.01	18.66± 0.01	16.93± 0.01	15.97± 0.01	14.61± 0.04	13.97± 0.05	13.52± 0.04	12.91± 0.06	12.55± 0.06	12.05± 0.07	11.73± 0.22	...
97	05 36 21.57	−06 22 52.4	...	24.57± 0.82	22.00± 0.12	19.76± 0.02	17.85± 0.02	14.45± 0.03	12.29± 0.03	10.97± 0.02	9.22± 0.06	8.56± 0.06	7.98± 0.06	7.33± 0.06	4.13± 0.06
98	05 36 21.84	−06 26 02.0	19.43± 0.03	18.04± 0.01	16.88± 0.01	15.97± 0.01	15.06± 0.01	12.27± 0.02	11.13± 0.04	10.26± 0.03	9.00± 0.06	8.51± 0.06	7.89± 0.06	7.39± 0.06	5.32± 0.06
99	05 36 21.88	−06 23 29.9	...	...	22.30± 0.14	18.99± 0.01	16.79± 0.01	13.44± 0.03	11.58± 0.03	10.45± 0.02	9.02± 0.06	8.11± 0.06	7.25± 0.06	6.29± 0.06	3.18± 0.06
100	05 36 21.96	−06 41 42.0	20.64± 0.08	18.68± 0.01	17.27± 0.01	15.50± 0.01	14.51± 0.01	12.87± 0.03	12.22± 0.03	11.90± 0.02	11.46± 0.06	11.11± 0.06	10.79± 0.06	10.22± 0.08	...
101	05 36 22.47	−06 23 44.8	23.28± 0.87	22.61± 0.19	19.59± 0.02	17.96± 0.01	16.47± 0.01	13.91± 0.02	12.46± 0.03	11.58± 0.02	10.57± 0.06	10.05± 0.06	9.75± 0.06	9.28± 0.06	...
102	05 36 23.26	−06 19 37.5	21.23± 0.10	19.80± 0.01	18.63± 0.01	17.84± 0.01	16.27± 0.01	13.21± 0.02	12.57± 0.03	12.36± 0.02	12.23± 0.06	12.08± 0.06	12.04± 0.06	11.99± 0.14	...
103	05 36 24.48	−06 22 23.2	21.96± 0.20	20.94± 0.03	18.68± 0.01	16.53± 0.01	15.08± 0.01	12.75± 0.02	11.52± 0.03	11.07± 0.02	10.54± 0.06	10.30± 0.06	10.13± 0.06	9.81± 0.06	...
104	05 36 24.54	−06 52 34.2	20.79± 0.09	19.35± 0.01	17.90± 0.01	16.19± 0.01	15.17± 0.01	13.50± 0.02	12.85± 0.03	12.53± 0.02	12.00± 0.06	11.67± 0.06	11.38± 0.06	10.83± 0.09	8.15± 0.06
105	05 36 25.13	−06 44 41.9	23.33± 0.88	19.58± 0.01	16.97± 0.01	15.44± 0.01	14.17± 0.01	11.30± 0.03	9.47± 0.03	8.21± 0.02	6.55± 0.06	5.84± 0.06	5.16± 0.06	4.28± 0.06	0.55± 0.06
106	05 36 25.28	−06 23 07.2	23.54± 0.82	21.20± 0.03	19.67± 0.01	17.60± 0.01	16.46± 0.01	14.73± 0.03	14.15± 0.05	13.95± 0.05	13.54± 0.06	13.32± 0.06	...	...	...
107	05 36 25.41	−06 24 31.2	22.49± 0.30	20.48± 0.02	18.98± 0.01	16.90± 0.01	15.70± 0.01	13.98± 0.03	13.32± 0.03	13.02± 0.02	12.62± 0.06	12.49± 0.06	12.42± 0.08	12.50± 0.21	...
108	05 36 25.55	−06 51 28.3	21.85± 0.29	19.38± 0.01	17.84± 0.01	16.13± 0.01	15.14± 0.01	13.54± 0.03	12.99± 0.04	12.69± 0.03	12.35± 0.06	12.19± 0.06	12.17± 0.07	12.06± 0.19	...
109	05 36 26.08	−06 26 15.5	23.47± 0.96	22.45± 0.14	20.65± 0.04	18.09± 0.01	16.36± 0.01	14.22± 0.02	13.49± 0.03	13.00± 0.03	12.45± 0.06	12.23± 0.06	12.22± 0.07	12.28± 0.18	...
110	05 36 26.71	−06 26 29.0	18.67± 0.01	15.80± 0.01	14.12± 0.01	15.04± 0.01	12.59± 0.01	11.04± 0.03	10.21± 0.03	10.00± 0.02	9.87± 0.06	9.66± 0.06	9.66± 0.06	9.66± 0.06	...
111	05 36 26.83	−06 24 57.5	21.23± 0.10	18.98± 0.01	17.53± 0.01	15.78± 0.01	14.77± 0.01	13.16± 0.03	12.59± 0.03	12.28± 0.02	11.90± 0.06	11.93± 0.06	11.76± 0.06	11.92± 0.26	...
112	05 36 27.01	−06 21 07.6	22.76± 0.37	20.16± 0.02	18.68± 0.01	17.52± 0.01	16.87± 0.01	15.55± 0.06	15.02± 0.09	14.56± 0.07	14.42± 0.06	14.32± 0.06	14.13± 0.15	...	...
113	05 36 27.72	−06 23 12.3	20.21± 0.04	18.26± 0.01	16.72± 0.01	14.86± 0.01	13.73± 0.01	11.90± 0.03	11.21± 0.03	10.77± 0.02	10.25± 0.06	9.98± 0.06	9.55± 0.06	8.86± 0.06	6.30± 0.06
114	05 36 27.89	−06 25 36.0	19.84± 0.03	18.07± 0.01	16.70± 0.01	15.26± 0.01	14.43± 0.01	12.93± 0.03	12.31± 0.03	12.04± 0.02	11.77± 0.06	11.67± 0.06	11.51± 0.06	10.95± 0.13	6.73± 0.06
115	05 36 28.10	−06 44 32.6	20.05± 0.05	18.14± 0.01	16.48± 0.01	15.29± 0.01	14.49± 0.01	12.83± 0.03	11.97± 0.03	11.68± 0.02	10.87± 0.06	10.59± 0.06	10.43± 0.06	9.99± 0.07	...
116	05 36 29.06	−06 38 40.7	20.13± 0.07	19.47± 0.01	18.35± 0.01	16.90± 0.01	15.83± 0.01	14.27± 0.03	13.48± 0.03	12.96± 0.03	11.93± 0.06	11.46± 0.06	11.16± 0.06	10.73± 0.11	...
117	05 36 29.59	−06 38 50.4	21.39± 0.19	19.27± 0.01	17.86± 0.01	16.21± 0.01	15.24± 0.01	13.79± 0.03	13.07± 0.03	12.86± 0.03	12.53± 0.06	12.43± 0.06	12.37± 0.10	...	...
118	05 36 30.10	−06 23 10.2	18.72± 0.01	17.15± 0.01	15.55± 0.01	14.68± 0.01	14.02± 0.01	12.17± 0.03	11.04± 0.03	10.32± 0.02	9.30± 0.06	8.84± 0.06	8.49± 0.06	7.80± 0.06	4.20± 0.06
119	05 36 30.23	−06 42 46.1	...	...	20.17± 0.02	17.94± 0.01	16.32± 0.01	13.42± 0.03	11.94± 0.03	11.26± 0.02	10.21± 0.06	9.90± 0.06	9.36± 0.06	8.63± 0.06	5.49± 0.06
120	05 36 30.50	−06 23 56.6	21.35± 0.12	20.81± 0.02	19.56± 0.01	17.84± 0.01	16.72± 0.01	15.07± 0.04	14.49± 0.05	14.18± 0.05	13.56± 0.06	13.49± 0.06	13.20± 0.09	12.63± 0.23	...
121	05 36 30.52	−06 42 03.2	...	21.45± 0.05	20.06± 0.02	17.97± 0.01	16.82± 0.01	15.15± 0.04	14.49± 0.05	14.20± 0.05	13.89± 0.06	13.68± 0.06	...	...	...
122	05 36 30.96	−06 52 41.0	...	...	...	...	...	16.45± 0.11	15.50± 0.10	15.00± 0.10	14.10± 0.06	13.34± 0.06	12.44± 0.08	11.28± 0.11	7.35± 0.06
123	05 36 31.84	−06 23 23.1	22.87± 0.45	21.05± 0.03	19.59± 0.01	17.66± 0.01	16.52± 0.01	14.94± 0.04	14.30± 0.04	13.85± 0.05	13.38± 0.06	13.11± 0.06	12.72± 0.09	12.02± 0.14	...
124	05 36 32.38	−06 19 19.9	16.79± 0.01	14.87± 0.01	13.16± 0.01	14.54± 0.01	12.87± 0.01	10.89± 0.03	10.20± 0.03	9.94± 0.02	9.22± 0.06	9.12± 0.06	8.90± 0.06	8.48± 0.06	5.75± 0.06
125	05 36 32.42	−06 40 43.0	20.66± 0.08	19.01± 0.01	17.60± 0.01	15.94± 0.01	15.00± 0.01	13.37± 0.03	12.67± 0.03	12.40± 0.02	11.62± 0.06	11.34± 0.06	10.97± 0.06	10.24± 0.07	7.63± 0.06
126	05 36 32.82	−06 39 54.9	18.83± 0.02	16.09± 0.01	14.72± 0.01	14.84± 0.01	13.73± 0.01	12.51± 0.03	11.81± 0.03	11.60± 0.02	11.57± 0.06	11.60± 0.06	11.53± 0.06	11.72± 0.23	...
127	05 36 32.89	−06 44 20.9	22.94± 0.63	21.63± 0.06	18.87± 0.01	17.11± 0.01	15.70± 0.01	13.02± 0.03	11.52± 0.03	10.68± 0.02	9.66± 0.06	9.12± 0.06	8.83± 0.06	7.96± 0.06	4.60± 0.06
128	05 36 33.81	−06 19 27.0	21.78± 0.15	19.30± 0.01	17.88± 0.01	16.07± 0.01	15.06± 0.01	13.44± 0.02	12.84± 0.03	12.57± 0.02	12.21± 0.06	12.18± 0.06	12.07± 0.07	12.12± 0.16	...
129	05 36 35.23	−06 50 12.2	...	20.90± 0.03	19.44± 0.01	17.28± 0.01	16.07± 0.01	14.30± 0.03	13.72± 0.03	13.41± 0.03	12.88± 0.06	12.81± 0.06	12.78± 0.14	...	...
130	05 36 35.76	−06 42 49.9	...	21.03± 0.04	18.66± 0.01	16.86± 0.01	15.65± 0.01	13.58± 0.03	12.44± 0.03	11.94± 0.02	11.31± 0.06	11.01± 0.06	10.46± 0.06	9.80± 0.06	7.10± 0.06
131	05 36 36.93	−06 33 24.2	17.57± 0.01	16.64± 0.01	15.33± 0.01	14.73± 0.01	13.88± 0.01	11.77± 0.03	10.62± 0.03	9.66± 0.02	8.25± 0.06	7.77± 0.06	7.30± 0.06	6.83± 0.06	4.83± 0.06
132	05 36 40.69	−06 30 09.3	17.87± 0.01	15.58± 0.01	14.31± 0.01	13.78± 0.01	13.12± 0.01	11.98± 0.03	11.28± 0.03	10.94± 0.02	10.51± 0.06	10.17± 0.06	9.91± 0.06	9.38± 0.07	6.82± 0.06
133	05 36 40.69	−06 52 04.5	19.30± 0.03	16.91± 0.01	15.50± 0.01	14.49± 0.01	13.83± 0.01	12.34± 0.03	11.61± 0.03	11.40± 0.02	11.31± 0.06	11.21± 0.06	11.08± 0.06	11.14± 0.10	...
134	05 36 40.94	−06 41 17.8	22.66± 0.49	19.77± 0.01	17.98± 0.01	16.02± 0.01	14.89± 0.01	13.03± 0.02	12.17± 0.03	11.81± 0.02	11.35± 0.06	11.01± 0.06	10.59± 0.06	9.94± 0.07	6.16± 0.06
135	05 36 41.35	−06 34 00.4	19.83± 0.09	17.45± 0.01	15.73± 0.01	14.57± 0.01	13.90± 0.01	11.08± 0.03	10.15± 0.04	9.52± 0.03	8.48± 0.06	7.85± 0.06	7.04± 0.06	6.23± 0.06	2.29± 0.06

Table 3.6: continued.

ID	RA (J2000)	DEC (J2000)	u′ (mag)	g′ (mag)	r′ (mag)	i′ (mag)	z′ (mag)	J (mag)	H (mag)	K_s (mag)	[3.6] (mag)	[4.5] (mag)	[5.8] (mag)	[8.0] (mag)	[24]
136	05 36 41.98	−06 20 45.4	...	20.91± 0.03	19.27± 0.01	17.28± 0.01	16.22± 0.01	14.09± 0.04	13.53± 0.04	13.28± 0.04	12.83± 0.06	12.77± 0.06	12.59± 0.07	12.76± 0.25	...
137	05 36 43.77	−06 15 28.6	20.29± 0.13	18.16± 0.01	16.77± 0.01	15.31± 0.01	14.48± 0.01	13.03± 0.03	12.37± 0.03	12.10± 0.02	11.58± 0.06	11.26± 0.06	10.93± 0.06	10.28± 0.07	8.22± 0.06
138	05 36 45.21	−06 28 09.6	19.53± 0.04	17.26± 0.01	15.85± 0.01	14.48± 0.01	13.68± 0.01	12.15± 0.02	11.50± 0.03	11.23± 0.02	10.96± 0.06	10.81± 0.06	10.67± 0.06	10.81± 0.12	...
139	05 36 45.79	−06 48 16.0	...	22.12± 0.09	20.42± 0.03	18.77± 0.01	17.85± 0.02	16.56± 0.11	15.73± 0.14	15.31± 0.13	15.29± 0.07	15.10± 0.06	...	...	...
140	05 36 46.62	−06 39 50.0	23.01± 0.68	20.48± 0.02	19.03± 0.01	17.03± 0.01	15.94± 0.01	14.25± 0.03	13.66± 0.04	13.40± 0.03	12.94± 0.06	12.76± 0.06	12.91± 0.11	...	...
141	05 36 50.14	−06 41 29.2	20.54± 0.08	17.75± 0.01	15.64± 0.01	14.54± 0.01	13.75± 0.01	12.01± 0.02	10.99± 0.03	10.49± 0.02	9.88± 0.06	9.64± 0.06	9.28± 0.06	8.84± 0.06	5.81± 0.06
142	05 36 50.23	−06 48 58.2	20.41± 0.07	17.92± 0.01	16.50± 0.01	15.00± 0.01	14.16± 0.01	12.64± 0.03	12.02± 0.03	11.74± 0.02	11.49± 0.06	11.44± 0.06	11.18± 0.06	11.30± 0.11	...
143	05 36 54.41	−06 51 05.5	...	22.24± 0.10	20.53± 0.03	18.42± 0.01	17.34± 0.01	15.61± 0.05	14.93± 0.07	14.70± 0.08	14.35± 0.06	14.32± 0.06	...	...	...
144	05 37 49.54	−06 56 27.4	20.01± 0.04	17.75± 0.01	16.08± 0.01	14.60± 0.01	13.74± 0.01	12.00± 0.02	11.10± 0.02	10.66± 0.02	10.26± 0.06	9.98± 0.06	9.83± 0.06	9.48± 0.06	6.81± 0.07
145	05 37 51.72	−06 56 51.9	18.44± 0.02	16.88± 0.01	15.27± 0.01	13.93± 0.01	13.12± 0.01	11.45± 0.02	10.50± 0.02	10.05± 0.02	8.90± 0.06	8.53± 0.06	8.12± 0.06	7.66± 0.06	5.06± 0.07
146	05 37 53.28	−07 02 27.2	22.22± 0.32	19.66± 0.01	18.22± 0.01	16.73± 0.01	15.91± 0.01	14.39± 0.03	13.83± 0.04	13.45± 0.05	13.35± 0.06	13.24± 0.06	13.16± 0.09	...	...
147	05 37 54.48	−06 57 31.1	17.67± 0.01	15.57± 0.01	14.08± 0.01	13.64± 0.01	13.12± 0.01	11.37± 0.02	10.51± 0.02	9.99± 0.02	9.11± 0.06	8.58± 0.06	8.34± 0.06	7.52± 0.06	4.72± 0.06
148	05 37 54.51	−06 56 45.5	17.22± 0.02	15.71± 0.01	13.08± 0.01	13.88± 0.01	13.45± 0.01	10.70± 0.02	9.92± 0.02	9.70± 0.02	9.62± 0.06	9.58± 0.06	9.38± 0.06	9.46± 0.06	...
149	05 37 55.15	−06 57 40.7	22.41± 0.37	20.27± 0.02	18.62± 0.01	16.46± 0.01	15.27± 0.01	13.38± 0.03	12.73± 0.03	12.45± 0.03	12.09± 0.06	11.90± 0.06	11.81± 0.06	...	...
150	05 37 55.22	−06 57 35.8	21.36± 0.15	18.93± 0.01	17.27± 0.01	15.44± 0.01	14.47± 0.01	12.67± 0.04	11.96± 0.04	11.67± 0.05	11.34± 0.06	11.03± 0.06	10.88± 0.06	10.39± 0.07	...
151	05 37 55.65	−06 57 18.1	17.76± 0.02	15.87± 0.01	15.34± 0.01	14.02± 0.01	13.28± 0.01	11.19± 0.02	10.42± 0.02	10.19± 0.02	10.16± 0.06	9.85± 0.06	10.02± 0.06	9.82± 0.06	...
152	05 37 55.74	−06 58 37.9	22.57± 0.44	19.74± 0.02	17.70± 0.01	16.01± 0.01	15.03± 0.01	13.07± 0.03	12.08± 0.02	11.69± 0.03	11.31± 0.06	11.00± 0.06	10.59± 0.06	9.69± 0.06	6.50± 0.06
153	05 37 55.99	−06 52 33.7	21.82± 0.19	19.55± 0.01	18.12± 0.01	16.14± 0.01	15.04± 0.01	13.36± 0.03	12.74± 0.02	12.48± 0.03	12.00± 0.06	12.14± 0.06	11.94± 0.06	11.90± 0.13	...
154	05 38 00.67	−07 01 14.3	...	20.73± 0.03	19.19± 0.01	17.76± 0.01	16.97± 0.01	15.55± 0.07	14.90± 0.09	14.76± 0.12	14.40± 0.06	14.34± 0.06	14.36± 0.16	...	...
155	05 38 04.84	−07 02 21.6	...	23.15± 0.23	20.67± 0.04	18.06± 0.01	16.44± 0.01	14.07± 0.03	12.96± 0.03	12.32± 0.03	11.34± 0.06	10.83± 0.06	10.41± 0.06	9.79± 0.06	7.53± 0.06
156	05 38 10.50	−06 57 07.1	22.56± 0.41	20.05± 0.02	17.86± 0.01	16.32± 0.01	15.32± 0.01	13.17± 0.02	12.15± 0.02	11.80± 0.02	11.50± 0.06	11.16± 0.06	10.98± 0.06	10.46± 0.06	7.18± 0.07
157	05 38 13.45	−07 06 43.3	23.02± 0.65	...	21.04± 0.06	18.51± 0.01	16.70± 0.01	13.49± 0.03	11.61± 0.02	10.77± 0.02	10.05± 0.06	9.55± 0.06	9.09± 0.06	8.28± 0.06	5.11± 0.07
158	05 38 19.52	−06 55 29.7	23.46± 0.95	...	21.52± 0.11	18.91± 0.02	17.21± 0.01	14.32± 0.03	12.62± 0.03	11.91± 0.03	11.32± 0.06	11.20± 0.06	11.10± 0.06	11.13± 0.07	...
159	05 38 21.22	−07 01 20.3	...	21.65± 0.06	19.52± 0.02	17.44± 0.01	16.07± 0.01	13.88± 0.03	12.92± 0.03	12.41± 0.03	11.62± 0.06	11.18± 0.06	10.84± 0.06	10.21± 0.06	7.15± 0.06
160	05 38 34.06	−07 04 36.8	...	22.60± 0.15	20.91± 0.05	19.19± 0.02	18.18± 0.02	16.79± 0.19	15.66± 0.16	15.58± 0.01	15.29± 0.06	15.29± 0.07	...	...	...
161	05 38 40.22	−06 56 53.3	23.12± 0.64	20.72± 0.02	18.37± 0.01	16.75± 0.01	15.63± 0.01	13.41± 0.03	12.27± 0.03	11.77± 0.03	11.23± 0.06	11.11± 0.06	10.96± 0.06	11.03± 0.08	...
162	05 38 40.59	−07 02 23.8	...	22.73± 0.13	20.08± 0.02	17.89± 0.01	16.43± 0.01	14.12± 0.03	13.09± 0.03	12.57± 0.03	11.83± 0.06	11.27± 0.06	10.89± 0.06	10.24± 0.06	7.26± 0.06
163	05 38 41.48	−07 01 52.6	...	22.39± 0.15	19.80± 0.02	17.47± 0.01	16.00± 0.01	13.52± 0.03	12.23± 0.02	11.73± 0.02	10.89± 0.06	10.63± 0.06	10.16± 0.06	9.41± 0.06	6.34± 0.06
164	05 38 41.56	−06 52 51.0	21.62± 0.44	19.82± 0.02	18.19± 0.01	16.24± 0.01	15.13± 0.01	13.29± 0.02	12.61± 0.03	12.29± 0.03	11.97± 0.06	11.65± 0.06	11.64± 0.06	11.79± 0.11	...
165	05 38 43.22	−06 58 08.9	...	22.65± 0.21	19.69± 0.02	17.61± 0.01	15.82± 0.01	12.05± 0.03	9.98± 0.03	8.62± 0.02	7.29± 0.06	6.63± 0.06	6.28± 0.06	5.70± 0.06	2.82± 0.06
166	05 38 43.84	−06 58 22.3	...	22.84± 0.24	19.67± 0.02	17.58± 0.01	16.04± 0.01	13.53± 0.03	12.02± 0.03	11.10± 0.03	10.01± 0.06	9.29± 0.06	8.81± 0.06	7.88± 0.06	4.56± 0.06
167	05 38 44.95	−06 58 14.7	...	22.57± 0.18	19.63± 0.02	17.72± 0.01	16.22± 0.01	13.32± 0.02	11.61± 0.02	10.65± 0.02	9.69± 0.06	9.11± 0.06	8.58± 0.06	7.97± 0.06	5.33± 0.06
168	05 38 46.84	−07 05 08.9	...	22.45± 0.17	19.86± 0.02	17.86± 0.01	16.38± 0.01	13.73± 0.02	12.28± 0.02	11.34± 0.02	10.22± 0.06	9.75± 0.06	9.56± 0.06	9.06± 0.06	5.96± 0.06
169	05 38 47.17	−07 02 40.4	...	...	21.16± 0.07	18.82± 0.02	16.82± 0.01	13.12± 0.03	10.94± 0.03	9.91± 0.02	9.26± 0.06	9.17± 0.06	8.90± 0.06	8.99± 0.06	...
170	05 38 47.74	−07 06 14.9	...	...	21.60± 0.09	19.35± 0.02	17.44± 0.02	13.89± 0.03	12.04± 0.02	10.95± 0.02	10.38± 0.06	9.90± 0.06	9.45± 0.06	8.79± 0.06	6.04± 0.06
171	05 38 47.93	−07 05 06.1	...	23.09± 0.31	20.30± 0.04	17.63± 0.01	15.96± 0.01	13.26± 0.02	12.01± 0.03	11.45± 0.02	11.03± 0.06	10.69± 0.06	10.66± 0.06	10.74± 0.07	...
172	05 38 49.88	−07 02 35.4	...	...	22.09± 0.14	20.05± 0.04	18.55± 0.04	15.83± 0.08	14.21± 0.05	13.82± 0.06	13.20± 0.06	13.19± 0.06	13.08± 0.08	...	...
173	05 38 50.44	−07 00 43.0	...	22.97± 0.25	20.02± 0.03	17.95± 0.01	16.30± 0.01	13.04± 0.02	11.15± 0.02	10.27± 0.02	9.76± 0.06	9.54± 0.06	9.34± 0.06	9.19± 0.06	...
174	05 38 52.97	−07 05 50.6	16.67± 0.23	17.82± 0.14	17.09± 0.11	...	15.72± 0.19	14.16± 0.03	13.21± 0.03	12.68± 0.04	12.24± 0.06	11.90± 0.06	11.86± 0.06	11.96± 0.11	...
175	05 38 53.33	−07 05 45.2	...	...	...	...	...	16.49± 0.14	16.02± 0.22	15.33± 0.01	13.98± 0.06	12.87± 0.06	12.14± 0.06	11.01± 0.07	7.86± 0.06
176	05 38 54.45	−07 04 46.7	...	21.61± 0.08	19.00± 0.01	17.16± 0.01	15.91± 0.01	13.75± 0.03	12.64± 0.03	12.14± 0.02	11.80± 0.06	11.61± 0.06	11.61± 0.06	11.63± 0.09	...
177	05 38 54.93	−07 07 10.9	...	21.32± 0.07	18.90± 0.01	17.07± 0.01	15.84± 0.01	13.61± 0.03	12.53± 0.03	12.04± 0.02	11.30± 0.06	10.85± 0.06	10.47± 0.06	9.91± 0.06	7.70± 0.06
178	05 38 55.02	−06 56 18.6	...	21.66± 0.08	19.84± 0.02	18.98± 0.02	17.62± 0.02	16.08± 0.09	14.69± 0.06	13.43± 0.04	11.43± 0.06	10.43± 0.06	9.63± 0.06	8.84± 0.06	5.42± 0.06
179	05 38 57.04	−06 52 59.3	18.86± 0.05	18.22± 0.01	16.89± 0.01	15.78± 0.01	15.00± 0.01	13.49± 0.02	12.75± 0.03	12.33± 0.02	11.51± 0.06	11.03± 0.06	11.03± 0.06	10.08± 0.06	7.67± 0.06
180	05 40 19.41	−08 14 16.4	...	18.53± 0.01	16.92± 0.01	16.04± 0.01	15.32± 0.01	13.09± 0.03	11.39± 0.02	10.22± 0.02	8.49± 0.06	7.90± 0.06	7.29± 0.06	6.53± 0.06	2.91± 0.06

Table 3.6: continued.

ID	RA (J2000)	DEC (J2000)	u′ (mag)	g′ (mag)	r′ (mag)	i′ (mag)	z′ (mag)	J (mag)	H (mag)	K_s (mag)	[3.6] (mag)	[4.5] (mag)	[5.8] (mag)	[8.0] (mag)	[24]
181	05 40 21.84	−08 08 55.9	...	20.86± 0.03	18.40± 0.01	16.57± 0.01	15.36± 0.01	13.07± 0.02	11.90± 0.03	11.39± 0.02	10.75± 0.06	10.23± 0.06	9.96± 0.06	9.27± 0.06	6.82± 0.06
182	05 40 24.97	−07 55 35.3	...	...	18.59± 0.01	17.34± 0.01	16.08± 0.01	12.45± 0.02	11.37± 0.02	10.66± 0.02	9.84± 0.06	8.79± 0.06	8.68± 0.06	7.89± 0.06	5.75± 0.06
183	05 40 24.97	−08 07 33.2	...	14.60± 0.01	13.11± 0.01	12.70± 0.01	12.29± 0.01	10.57± 0.02	9.63± 0.02	8.92± 0.02	7.91± 0.06	7.56± 0.06	6.79± 0.06	5.90± 0.06	3.11± 0.06
184	05 40 24.97	−07 55 35.3	...	...	18.59± 0.01	17.34± 0.01	16.08± 0.01	12.45± 0.02	11.37± 0.02	10.66± 0.02	9.84± 0.06	8.79± 0.06	8.68± 0.06	7.89± 0.06	5.75± 0.06
185	05 40 25.75	−08 11 16.8	...	...	18.64± 0.01	16.88± 0.01	15.81± 0.01	13.31± 0.02	12.11± 0.03	11.52± 0.03	10.51± 0.06	10.08± 0.06	9.66± 0.06	8.98± 0.06	6.36± 0.06
186	05 40 27.14	−08 07 36.5	...	...	18.20± 0.01	16.39± 0.01	15.34± 0.01	12.94± 0.02	12.02± 0.02	11.33± 0.02	10.58± 0.06	9.99± 0.06	9.35± 0.06	8.80± 0.06	5.96± 0.06
187	05 40 35.44	−07 56 36.5	...	...	...	18.97± 0.01	17.35± 0.01	14.25± 0.02	12.61± 0.03	11.89± 0.03	11.47± 0.06	11.28± 0.06	10.97± 0.06	11.34± 0.07	...
188	05 40 37.36	−08 04 03.0	...	15.55± 0.01	13.46± 0.01	12.38± 0.01	11.77± 0.01	9.74± 0.02	8.73± 0.02	7.93± 0.05	6.72± 0.06	6.22± 0.06	5.77± 0.06	4.85± 0.06	0.88± 0.06
189	05 40 41.01	−08 02 18.6	...	...	19.82± 0.01	17.73± 0.01	16.35± 0.01	13.50± 0.02	11.79± 0.02	10.85± 0.02	...	9.47± 0.06	9.15± 0.06	8.43± 0.06	4.92± 0.06
190	05 40 42.66	−07 46 03.0	...	...	...	...	17.03± 0.01	15.30± 0.05	14.78± 0.08	14.30± 0.09	14.17± 0.06	14.02± 0.06	13.92± 0.08	...	...
191	05 40 46.22	−08 05 24.3	...	14.70± 0.01	13.02± 0.01	12.41± 0.01	12.02± 0.01	10.16± 0.02	9.22± 0.02	8.59± 0.02	...	...	6.57± 0.06	6.21± 0.06	3.31± 0.06
192	05 40 46.40	−08 04 36.1	...	15.26± 0.01	13.45± 0.01	12.59± 0.01	12.14± 0.01	10.36± 0.02	9.39± 0.02	9.10± 0.02	9.21± 0.06	8.87± 0.06	9.01± 0.06	8.78± 0.06	7.93± 0.06
193	05 40 46.62	−08 07 12.8	...	20.40± 0.01	18.07± 0.01	16.42± 0.01	15.13± 0.01	11.93± 0.03	10.20± 0.03	9.33± 0.02	8.81± 0.06	8.77± 0.06	8.51± 0.06	8.51± 0.06	5.33± 0.06
194	05 40 46.84	−08 04 54.6	...	19.29± 0.01	16.95± 0.01	15.90± 0.01	15.01± 0.01	12.34± 0.02	11.10± 0.02	10.45± 0.02	9.76± 0.06	8.99± 0.06	8.18± 0.06	7.15± 0.06	4.44± 0.06
195	05 40 48.07	−08 05 58.7	...	13.72± 0.01	12.52± 0.01	12.01± 0.01	11.70± 0.01	9.91± 0.02	9.14± 0.03	8.75± 0.02	8.48± 0.06	7.90± 0.06	7.55± 0.06	7.04± 0.06	3.78± 0.06
196	05 40 57.49	−07 48 08.8	...	...	19.23± 0.01	17.08± 0.01	15.59± 0.01	12.90± 0.02	11.16± 0.02	10.19± 0.02	9.07± 0.06	8.81± 0.06	8.14± 0.06	7.51± 0.06	3.95± 0.06
197	05 40 59.75	−08 06 03.2	...	21.40± 0.01	18.97± 0.01	16.73± 0.01	15.61± 0.01	13.21± 0.02	12.38± 0.03	11.98± 0.02	11.33± 0.06	10.79± 0.06	10.25± 0.06	9.14± 0.06	6.21± 0.06
198	05 40 59.92	−07 48 16.1	...	...	20.02± 0.01	17.99± 0.01	16.58± 0.01	13.97± 0.02	12.62± 0.03	11.89± 0.03	10.76± 0.06	10.32± 0.06	9.85± 0.06	9.47± 0.06	6.90± 0.06
199	05 41 03.55	−07 57 46.3	...	...	20.08± 0.01	18.02± 0.01	16.97± 0.01	15.14± 0.05	14.61± 0.06	14.12± 0.09	13.81± 0.06	13.61± 0.06	13.74± 0.08	13.69± 0.22	...
200	05 41 04.09	−07 43 38.6	...	...	18.81± 0.01	16.72± 0.01	15.68± 0.01	13.31± 0.03	12.14± 0.03	11.59± 0.02	10.91± 0.06	10.49± 0.06	10.16± 0.06	9.54± 0.06	6.87± 0.06
201	05 41 04.36	−07 46 40.6	...	20.18± 0.01	18.79± 0.01	17.16± 0.01	16.28± 0.01	14.63± 0.04	14.12± 0.04	13.78± 0.06	13.74± 0.06	13.36± 0.06	13.51± 0.07	...	...
202	05 41 05.03	−07 45 34.2	...	...	19.07± 0.01	...	15.92± 0.01	13.51± 0.03	12.62± 0.03	12.19± 0.03	11.82± 0.06	11.79± 0.06	11.65± 0.06	11.65± 0.07	...
203	05 41 05.49	−07 47 07.5	...	...	17.81± 0.01	...	15.44± 0.01	12.65± 0.02	11.23± 0.03	10.26± 0.02	9.17± 0.06	8.70± 0.06	8.38± 0.06	7.91± 0.06	4.97± 0.06
204	05 41 07.00	−07 47 15.9	...	18.54± 0.01	17.74± 0.01	16.06± 0.01	15.27± 0.01	13.55± 0.02	13.01± 0.03	12.64± 0.03	12.36± 0.06	12.18± 0.06	12.09± 0.06	11.66± 0.07	7.03± 0.06
205	05 41 07.08	−07 46 22.5	...	20.35± 0.01	18.32± 0.01	16.50± 0.01	15.42± 0.01	13.46± 0.02	12.54± 0.03	12.08± 0.03	11.55± 0.06	11.25± 0.06	10.90± 0.06	10.20± 0.06	7.45± 0.06
206	05 41 14.03	−08 07 57.4	...	17.42± 0.01	15.52± 0.01	14.19± 0.01	13.35± 0.01	11.68± 0.02	10.69± 0.02	10.31± 0.02	10.04± 0.06	9.63± 0.06	9.16± 0.06	8.65± 0.06	5.53± 0.06
207	05 41 16.25	−07 43 51.4	...	...	...	18.71± 0.01	17.43± 0.01	15.25± 0.05	14.54± 0.07	14.07± 0.08	13.55± 0.06	13.70± 0.06	13.65± 0.08	13.43± 0.16	...
208	05 41 20.12	−07 55 24.0	...	...	...	19.93± 0.01	18.19± 0.01	14.48± 0.03	12.68± 0.03	11.73± 0.02	10.72± 0.06	10.10± 0.06	9.75± 0.06	9.30± 0.06	5.97± 0.06
209	05 41 25.35	−08 05 54.7	...	...	13.27± 0.01	14.48± 0.01	...	10.60± 0.03	9.82± 0.02	9.29± 0.02	7.91± 0.06	7.10± 0.06	6.33± 0.06	5.23± 0.06	1.41± 0.06
210	05 41 26.37	−07 58 17.8	...	...	19.87± 0.01	17.81± 0.01	16.77± 0.01	14.93± 0.04	14.13± 0.04	13.87± 0.05	13.64± 0.06	13.62± 0.06	13.22± 0.07	...	...
211	05 41 30.59	−08 04 48.2	...	...	19.45± 0.01	17.66± 0.01	16.12± 0.01	12.79± 0.03	11.16± 0.02	10.10± 0.02	8.38± 0.06	7.66± 0.06	7.27± 0.06	6.40± 0.06	2.93± 0.06
212	05 41 33.38	−07 59 56.3	...	...	20.71± 0.01	18.69± 0.01	17.21± 0.01	13.73± 0.03	12.04± 0.02	11.22± 0.02	10.18± 0.06	9.76± 0.06	9.30± 0.06	8.78± 0.06	4.49± 0.06
213	05 41 41.66	−08 00 18.5	...	...	19.89± 0.01	18.98± 0.01	18.21± 0.01	16.15± 0.09	14.79± 0.06	14.11± 0.07	13.61± 0.06	13.57± 0.06	12.49± 0.06	12.15± 0.12	7.08± 0.06
214	05 41 43.74	−07 58 22.3	...	20.98± 0.01	18.73± 0.01	16.53± 0.01	14.94± 0.01	12.34± 0.03	11.44± 0.03	10.86± 0.02	10.17± 0.06	9.52± 0.06	9.27± 0.06	8.46± 0.06	5.39± 0.06
215	05 41 49.23	−07 57 12.3	...	...	19.91± 0.01	17.72± 0.01	16.34± 0.01	13.72± 0.03	12.44± 0.02	12.00± 0.02	11.69± 0.06	11.08± 0.06	11.08± 0.06	10.39± 0.06	8.58± 0.06
216	05 41 49.74	−08 00 32.3	...	...	11.31± 0.01	10.90± 0.01	11.38± 0.01	9.41± 0.03	8.54± 0.03	7.81± 0.01	6.70± 0.06	6.31± 0.06	5.71± 0.06	5.07± 0.06	2.16± 0.06
217	05 41 51.84	−08 06 56.6	...	...	18.94± 0.01	16.85± 0.01	16.41± 0.01	13.83± 0.03	13.01± 0.03	12.62± 0.03	12.34± 0.06	12.32± 0.06	12.05± 0.06	12.24± 0.09	...
218	05 41 54.66	−07 59 12.4	...	19.83± 0.01	17.32± 0.01	15.87± 0.01	14.78± 0.01	12.36± 0.02	11.06± 0.02	10.35± 0.02	9.56± 0.06	9.06± 0.06	9.05± 0.06	8.42± 0.06	5.47± 0.06
219	05 41 55.96	−07 58 36.6	...	...	...	19.04± 0.01	17.68± 0.01	15.17± 0.04	13.94± 0.03	13.42± 0.03	13.16± 0.06	12.90± 0.06	12.76± 0.07	12.38± 0.14	...
220	05 42 05.59	−08 01 05.6	...	18.80± 0.01	17.07± 0.01	15.77± 0.01	14.97± 0.01	13.27± 0.02	12.41± 0.03	12.04± 0.02	11.69± 0.06	11.45± 0.06	11.02± 0.06	10.77± 0.07	7.18± 0.06
221	05 42 07.25	−08 05 24.4	...	...	20.83± 0.01	18.48± 0.01	16.98± 0.01	14.39± 0.03	13.43± 0.03	12.84± 0.03	12.08± 0.06	11.63± 0.06	11.20± 0.06	10.61± 0.07	8.64± 0.06
222	05 42 10.51	−08 07 35.1	...	20.59± 0.01	18.75± 0.01	16.67± 0.01	16.29± 0.01	13.95± 0.02	13.19± 0.03	12.81± 0.03	12.55± 0.06	12.56± 0.06	12.41± 0.10	...	...
223	05 42 11.04	−08 01 05.4	...	20.29± 0.01	18.66± 0.01	16.96± 0.01	16.01± 0.01	14.27± 0.03	13.51± 0.04	13.24± 0.03	12.76± 0.06	12.60± 0.06	11.89± 0.06	11.40± 0.08	9.55± 0.06
224	05 42 13.51	−08 10 01.5	...	...	19.38± 0.01	17.37± 0.01	16.32± 0.01	14.04± 0.02	13.03± 0.03	12.38± 0.03	11.27± 0.06	10.70± 0.06	10.31± 0.06	9.69± 0.06	6.68± 0.06
225	05 42 14.60	−07 58 57.9	...	19.70± 0.01	17.74± 0.01	16.07± 0.01	15.05± 0.01	12.76± 0.02	11.85± 0.02	11.40± 0.02	10.85± 0.06	10.43± 0.06	10.18± 0.06	9.26± 0.06	5.94± 0.06

Table 3.6: continued.

ID	RA (J2000)	DEC (J2000)	u′ (mag)	g′ (mag)	r′ (mag)	i′ (mag)	z′ (mag)	J (mag)	H (mag)	K_s (mag)	[3.6] (mag)	[4.5] (mag)	[5.8] (mag)	[8.0] (mag)	[24]
226	05 42 15.93	−08 09 37.8	...	...	20.68± 0.01	17.98± 0.01	16.69± 0.01	14.14± 0.02	13.08± 0.02	12.61± 0.02	12.17± 0.06	12.01± 0.06	11.88± 0.08	11.66± 0.15	...
227	05 42 18.11	−08 08 10.9	...	16.06± 0.01	14.47± 0.01	13.69± 0.01	13.93± 0.01	12.05± 0.03	11.23± 0.02	11.03± 0.02	10.78± 0.06	10.87± 0.06	10.79± 0.06	10.90± 0.10	...
228	05 42 18.56	−07 59 23.0	...	20.19± 0.01	18.58± 0.01	16.86± 0.01	15.90± 0.01	14.14± 0.03	13.41± 0.03	13.10± 0.04	13.02± 0.06	12.59± 0.06	12.79± 0.07	12.83± 0.20	...
229	05 42 19.05	−07 59 12.2	...	...	19.77± 0.01	17.65± 0.01	16.46± 0.01	14.51± 0.03	13.84± 0.03	13.52± 0.05	13.13± 0.06	12.86± 0.06	12.91± 0.07	...	...
230	05 42 19.56	−08 05 07.6	...	...	18.77± 0.01	17.01± 0.01	15.93± 0.01	13.84± 0.03	12.82± 0.02	12.36± 0.03	11.72± 0.06	11.47± 0.06	10.79± 0.07	10.45± 0.06	8.51± 0.06
231	05 42 21.36	−08 06 47.9	...	...	19.35± 0.01	17.20± 0.01	16.66± 0.01	13.84± 0.03	12.68± 0.03	12.26± 0.03	11.95± 0.06	11.68± 0.06	11.77± 0.07	11.59± 0.09	...
232	05 42 21.56	−08 08 29.8	...	...	15.00± 0.01	14.22± 0.01	13.76± 0.01	12.05± 0.02	11.28± 0.02	10.94± 0.02	10.61± 0.06	10.66± 0.06	10.52± 0.06	9.98± 0.10	4.93± 0.06
233	05 42 23.24	−07 58 28.9	...	...	19.65± 0.01	17.71± 0.01	16.62± 0.01	14.68± 0.03	13.91± 0.03	13.57± 0.04	13.28± 0.06	13.37± 0.06	13.17± 0.07	...	...
234	05 42 23.61	−08 09 10.3	...	19.97± 0.01	17.67± 0.01	16.20± 0.01	15.36± 0.01	13.03± 0.02	11.95± 0.02	11.39± 0.02	10.76± 0.06	10.32± 0.06	10.02± 0.06	9.55± 0.08	6.81± 0.06
235	05 42 23.94	−08 09 45.9	...	17.44± 0.01	15.30± 0.01	14.39± 0.01	13.88± 0.01	12.16± 0.02	11.31± 0.02	11.02± 0.02	10.75± 0.06	10.86± 0.06	10.65± 0.06	10.81± 0.18	...
236	05 42 25.32	−08 10 18.0	...	17.31± 0.01	15.38± 0.01	14.48± 0.01	13.99± 0.01	12.37± 0.03	11.53± 0.03	11.25± 0.03	11.09± 0.06	10.89± 0.06	10.94± 0.06	11.03± 0.21	...
237	05 42 25.44	−08 09 55.4	...	21.35± 0.02	17.36± 0.01	16.04± 0.01	15.24± 0.01	13.07± 0.03	11.91± 0.02	11.30± 0.02	10.67± 0.06	10.40± 0.06	10.02± 0.06	9.64± 0.09	7.31± 0.06
238	05 42 25.68	−07 58 22.0	...	19.36± 0.01	17.46± 0.01	16.05± 0.01	15.18± 0.01	13.41± 0.02	12.62± 0.02	12.29± 0.03	12.17± 0.06	12.13± 0.06	11.90± 0.06	11.99± 0.11	...
239	05 42 25.79	−08 08 50.1	...	19.79± 0.01	17.56± 0.01	15.98± 0.01	15.02± 0.01	12.78± 0.02	11.66± 0.02	11.06± 0.02	10.31± 0.06	9.91± 0.06	9.60± 0.06	8.93± 0.07	5.85± 0.06
240	05 42 26.50	−07 58 50.9	...	18.46± 0.01	16.40± 0.01	15.31± 0.01	14.28± 0.01	11.96± 0.04	10.73± 0.04	9.96± 0.04	8.72± 0.06	8.21± 0.06	7.56± 0.06	6.77± 0.06	3.02± 0.06
241	05 42 26.96	−08 09 17.3	...	17.95± 0.01	16.33± 0.01	15.19± 0.01	14.71± 0.01	13.34± 0.02	12.76± 0.03	12.53± 0.02	12.38± 0.06	12.16± 0.06	12.05± 0.08	...	...
242	05 42 27.50	−08 11 03.8	...	...	19.95± 0.01	17.63± 0.01	16.66± 0.01	14.68± 0.03	13.95± 0.03	13.48± 0.04	13.12± 0.06	12.81± 0.06	12.71± 0.17	...	9.00± 0.06
243	05 42 27.59	−08 09 52.6	...	17.91± 0.01	16.17± 0.01	15.26± 0.01	14.57± 0.01	12.83± 0.02	11.87± 0.02	11.27± 0.02	10.26± 0.06	9.89± 0.06	9.40± 0.06	8.83± 0.07	5.53± 0.06
244	05 42 29.78	−08 07 26.4	...	20.02± 0.01	17.61± 0.01	16.28± 0.01	15.15± 0.01	13.22± 0.02	12.16± 0.02	11.77± 0.03	11.48± 0.06	11.20± 0.06	11.35± 0.08	...	...
245	05 42 30.62	−07 59 54.0	...	18.70± 0.01	17.11± 0.01	15.69± 0.01	15.63± 0.01	13.57± 0.02	12.83± 0.02	12.52± 0.03	12.46± 0.06	12.42± 0.06	12.26± 0.12	12.53± 0.15	...
246	05 42 30.87	−08 10 45.7	...	20.93± 0.02	19.15± 0.01	17.21± 0.01	15.96± 0.01	14.19± 0.03	13.35± 0.02	13.03± 0.04	12.75± 0.07	12.22± 0.06	12.09± 0.08	...	8.77± 0.06
247	05 42 31.00	−08 06 38.1	...	19.19± 0.01	17.37± 0.01	15.91± 0.01	14.77± 0.01	12.99± 0.02	12.03± 0.02	11.49± 0.02	10.76± 0.06	10.14± 0.06	10.07± 0.06	9.69± 0.09	6.87± 0.06
248	05 42 31.33	−08 02 35.3	...	19.80± 0.01	18.17± 0.01	16.25± 0.01	15.97± 0.01	13.70± 0.02	13.00± 0.03	12.68± 0.03	12.55± 0.06	12.20± 0.06	12.25± 0.12	12.45± 0.15	...
249	05 42 31.55	−08 08 22.8	...	...	19.21± 0.01	17.09± 0.01	15.61± 0.01	13.11± 0.03	12.04± 0.03	11.48± 0.03	10.83± 0.06	10.29± 0.06	9.87± 0.06	8.81± 0.07	5.10± 0.06
250	05 42 32.66	−08 10 07.9	...	21.32± 0.02	19.23± 0.01	17.22± 0.01	15.91± 0.01	13.93± 0.02	13.00± 0.02	12.61± 0.02	12.77± 0.06	12.20± 0.06	12.19± 0.09	...	...
251	05 42 32.77	−08 07 04.8	...	20.72± 0.01	18.62± 0.01	16.34± 0.01	15.82± 0.01	13.24± 0.02	12.38± 0.02	11.97± 0.02	11.52± 0.06	11.68± 0.06	11.46± 0.08	...	...
252	05 42 34.02	−08 09 59.7	...	18.75± 0.01	16.44± 0.01	15.21± 0.01	14.14± 0.01	12.03± 0.02	10.97± 0.03	10.58± 0.02	10.52± 0.06	10.23± 0.06	10.18± 0.07	9.97± 0.10	5.68± 0.06
253	05 42 34.31	−08 02 12.1	...	20.53± 0.01	18.90± 0.01	16.97± 0.01	16.55± 0.01	14.17± 0.03	13.53± 0.03	13.14± 0.04	12.42± 0.06	12.44± 0.06	11.68± 0.09	11.19± 0.07	8.57± 0.06
254	05 42 34.92	−08 07 50.5	...	...	19.61± 0.01	17.48± 0.01	16.07± 0.01	13.92± 0.02	12.98± 0.02	12.58± 0.02	12.10± 0.06	12.04± 0.06	11.90± 0.10	...	...
255	05 42 36.41	−08 10 17.8	...	...	...	18.71± 0.01	17.11± 0.01	14.73± 0.04	13.86± 0.03	13.38± 0.04	13.32± 0.06	12.53± 0.06	...	...	...
256	05 42 36.51	−08 11 51.5	...	18.14± 0.01	16.26± 0.01	15.33± 0.01	14.50± 0.01	12.89± 0.02	12.00± 0.02	11.72± 0.03	11.58± 0.06	11.32± 0.06	11.39± 0.07	...	...
257	05 42 40.06	−08 05 07.7	...	20.32± 0.01	18.33± 0.01	16.51± 0.01	15.59± 0.01	13.87± 0.05	13.12± 0.05	12.85± 0.04	12.61± 0.06	12.45± 0.07	12.08± 0.11	...	9.32± 0.06
258	05 42 42.10	−08 15 15.3	...	19.74± 0.01	17.89± 0.01	16.64± 0.01	15.52± 0.01	13.49± 0.03	12.31± 0.02	11.54± 0.02	10.98± 0.06	10.28± 0.06	10.24± 0.06	9.36± 0.08	5.93± 0.06
259	05 42 44.12	−08 06 26.4	...	17.72± 0.01	16.04± 0.01	15.21± 0.01	14.14± 0.01	12.71± 0.02	11.81± 0.02	11.17± 0.02	9.95± 0.06	9.45± 0.06	9.00± 0.06	8.54± 0.06	5.11± 0.06
260	05 42 47.18	−08 05 57.0	...	19.48± 0.01	17.43± 0.01	16.12± 0.01	15.23± 0.01	13.72± 0.03	12.87± 0.03	12.42± 0.03	12.09± 0.06	11.85± 0.06	11.73± 0.09	11.31± 0.27	8.40± 0.06
261	05 42 47.44	−08 04 05.4	...	19.97± 0.01	17.93± 0.01	16.36± 0.01	15.49± 0.01	13.72± 0.02	12.91± 0.02	12.55± 0.03	12.28± 0.06	11.55± 0.06	11.66± 0.09	10.37± 0.13	7.23± 0.06
262	05 42 48.24	−08 05 57.1	...	20.32± 0.01	18.30± 0.01	16.58± 0.01	15.73± 0.01	14.02± 0.02	13.34± 0.03	13.01± 0.04	12.68± 0.06	12.64± 0.06	12.43± 0.14	...	...
263	05 42 51.65	−08 07 41.2	...	19.72± 0.01	18.17± 0.01	17.32± 0.01	16.27± 0.01	14.26± 0.02	13.41± 0.02	12.87± 0.03	...	11.43± 0.06	11.39± 0.08	10.67± 0.17	7.14± 0.06
264	05 42 52.30	−08 08 54.9	...	...	19.18± 0.01	17.36± 0.01	16.17± 0.01	14.33± 0.02	13.57± 0.02	13.17± 0.03	12.55± 0.06	12.30± 0.06	11.90± 0.10	11.29± 0.26	8.48± 0.06
265	05 42 59.13	−08 09 23.6	...	18.03± 0.01	16.48± 0.01	15.57± 0.01	14.71± 0.01	13.02± 0.02	12.05± 0.02	11.51± 0.02	10.87± 0.06	10.43± 0.06	9.95± 0.06	9.14± 0.07	6.12± 0.06
266	05 43 01.78	−08 04 50.6	...	16.15± 0.01	14.53± 0.01	14.05± 0.01	13.34± 0.01	11.97± 0.02	10.96± 0.03	10.43± 0.02	9.75± 0.06	9.60± 0.06	9.42± 0.06	9.08± 0.07	5.25± 0.06
267	05 43 08.49	−08 11 32.3	...	19.68± 0.01	17.90± 0.01	16.39± 0.01	15.40± 0.01	14.64± 0.03	13.41± 0.02	12.63± 0.02	11.46± 0.06	11.27± 0.06	10.85± 0.06	10.41± 0.06	6.56± 0.06

Table 3.7: Mass and age estimate for YSOs in L1630N with different PMS evolutionary tracks.

ID	RA (J2000)	DEC (J2000)	mass ($M_\odot$, DM97)	age (Myr, DM97)	mass ($M_\odot$, D08)	age (Myr, D08)	mass ($M_\odot$, S00)	age (Myr, S00)	mass ($M_\odot$, B98)	age (Myr, B98)
1	05 45 21.38	-00 00 45.9	$0.24^{+0.10}_{-0.05}$	$0.92^{+0.65}_{-0.47}$	$0.30^{+0.10}_{-0.06}$	$0.84^{+1.11}_{-0.39}$	$0.28^{+0.09}_{-0.03}$	$1.92^{+0.75}_{-0.53}$	$0.41^{+0.15}_{-0.06}$	$1.76^{+2.08}_{-0.41}$
2	05 45 22.68	-00 14 27.5	$0.13^{+0.03}_{-0.02}$	$0.82^{+0.55}_{-0.45}$	$0.13^{+0.06}_{-0.01}$	$0.38^{+0.70}_{-0.12}$	$0.13^{+0.04}_{-0.02}$	$0.61^{+2.06}_{-0.16}$	...	...
3	05 45 26.16	+00 06 37.9	$0.23^{+0.08}_{-0.05}$	$0.68^{+0.22}_{-0.42}$	$0.29^{+0.09}_{-0.06}$	$0.51^{+0.51}_{-0.22}$	$0.32^{+0.07}_{-0.05}$	$1.54^{+0.41}_{-0.51}$	$0.45^{+0.14}_{-0.03}$	$1.33^{+1.23}_{-0.19}$
4	05 45 38.26	-00 08 11.0	$0.43^{+0.14}_{-0.08}$	$0.90^{+1.56}_{-0.31}$	$0.55^{+0.21}_{-0.11}$	$1.36^{+3.15}_{-0.61}$	$0.57^{+0.22}_{-0.10}$	$2.14^{+3.60}_{-0.68}$	$0.96^{+0.12}_{-0.17}$	$4.41^{+4.86}_{-1.82}$
5	05 45 41.68	-00 04 02.4	$0.18^{+0.03}_{-0.02}$	$0.72^{+0.18}_{-0.36}$	$0.24^{+0.03}_{-0.03}$	$0.56^{+0.20}_{-0.15}$	$0.25^{+0.02}_{-0.02}$	$2.04^{+0.06}_{-0.13}$	$0.31^{+0.05}_{-0.02}$	$1.15^{+0.37}_{-0.08}$
6	05 45 41.94	-00 12 05.3	$0.61^{+0.27}_{-0.13}$	$0.93^{+2.30}_{-0.33}$	$0.92^{+0.23}_{-0.23}$	$2.00^{+4.04}_{-0.93}$	$1.07^{+0.15}_{-0.26}$	$3.52^{+5.77}_{-1.42}$	$1.35^{+0.03}_{-0.16}$	$6.09^{+8.46}_{-2.48}$
7	05 45 42.80	-00 01 01.8	$0.15^{+0.02}_{-0.02}$	$1.74^{+0.35}_{-0.34}$	$0.15^{+0.04}_{-0.03}$	$1.07^{+0.89}_{-0.40}$	$0.15^{+0.04}_{-0.02}$	$3.77^{+0.45}_{-2.02}$	$0.15^{+0.06}_{-0.02}$	$1.53^{+4.80}_{-0.19}$
8	05 45 44.37	+00 22 58.2	$0.34^{+0.08}_{-0.07}$	$0.60^{+0.38}_{-0.23}$	$0.43^{+0.12}_{-0.08}$	$0.68^{+0.82}_{-0.28}$	$0.46^{+0.11}_{-0.08}$	$1.40^{+0.94}_{-0.25}$	$0.78^{+0.16}_{-0.13}$	$2.33^{+2.08}_{-0.76}$
9	05 45 44.56	-00 10 35.6	$0.18^{+0.02}_{-0.02}$	$2.71^{+0.59}_{-0.32}$	$0.20^{+0.03}_{-0.02}$	$2.68^{+1.10}_{-0.68}$	$0.18^{+0.02}_{-0.02}$	$4.74^{+0.60}_{-0.26}$	$0.20^{+0.03}_{-0.03}$	$3.18^{+1.00}_{-0.67}$
10	05 45 44.64	+00 13 00.6	$0.43^{+0.06}_{-0.05}$	$1.16^{+0.38}_{-0.23}$	$0.53^{+0.08}_{-0.07}$	$1.72^{+0.74}_{-0.45}$	$0.51^{+0.08}_{-0.05}$	$2.44^{+0.97}_{-0.44}$	$0.85^{+0.08}_{-0.11}$	$4.94^{+1.65}_{-1.39}$
11	05 45 45.58	+00 04 35.6	$0.15^{+0.01}_{-0.01}$	$0.26^{+0.15}_{-0.04}$	$0.19^{+0.02}_{-0.01}$	$0.37^{+0.09}_{-0.07}$	$0.22^{+0.01}_{-0.01}$	$2.08^{+0.06}_{-0.43}$	...	...
12	05 45 46.91	+00 14 29.4	$0.18^{+0.02}_{-0.02}$	$2.13^{+0.44}_{-0.21}$	$0.19^{+0.03}_{-0.03}$	$2.00^{+0.88}_{-0.56}$	$0.18^{+0.02}_{-0.02}$	$4.13^{+0.50}_{-0.39}$	$0.20^{+0.03}_{-0.03}$	$2.50^{+0.99}_{-0.52}$
13	05 45 49.56	-00 08 38.8	$0.17^{+0.04}_{-0.03}$	$4.22^{+3.32}_{-0.97}$	$0.16^{+0.06}_{-0.03}$	$3.38^{+4.85}_{-1.24}$	$0.13^{+0.04}_{-0.02}$	$5.87^{+2.66}_{-0.80}$	$0.15^{+0.06}_{-0.03}$	$3.52^{+3.85}_{-1.02}$
14	05 45 53.11	-00 13 24.9	$0.40^{+0.07}_{-0.07}$	$1.56^{+0.87}_{-0.41}$	$0.46^{+0.09}_{-0.07}$	$2.10^{+1.44}_{-0.68}$	$0.43^{+0.07}_{-0.05}$	$2.74^{+1.25}_{-0.52}$	$0.66^{+0.11}_{-0.11}$	$4.72^{+2.53}_{-1.53}$
15	05 45 53.54	+00 33 08.8	$0.30^{+0.08}_{-0.07}$	$0.68^{+0.36}_{-0.33}$	$0.36^{+0.10}_{-0.07}$	$0.65^{+0.70}_{-0.28}$	$0.39^{+0.09}_{-0.06}$	$1.49^{+0.70}_{-0.34}$	$0.59^{+0.17}_{-0.09}$	$1.85^{+1.83}_{-0.50}$
16	05 45 53.60	+00 22 42.1	$0.72^{+0.08}_{-0.17}$	$5.58^{+5.43}_{-2.24}$	$0.88^{+0.02}_{-0.18}$	$10.53^{+7.60}_{-4.92}$	$0.81^{+0.05}_{-0.20}$	$11.54^{+8.82}_{-5.32}$	$0.94^{+0.00}_{-0.10}$	$17.38^{+10.01}_{-6.92}$
17	05 45 54.09	-00 03 16.7	$0.16^{+0.03}_{-0.02}$	$3.22^{+1.62}_{-0.56}$	$0.14^{+0.04}_{-0.02}$	$2.18^{+2.21}_{-0.70}$	$0.12^{+0.03}_{-0.01}$	$5.01^{+1.50}_{-0.47}$	$0.13^{+0.04}_{-0.03}$	$2.61^{+2.06}_{-0.58}$
18	05 45 55.13	+00 11 39.4	$0.16^{+0.04}_{-0.03}$	$4.84^{+4.63}_{-1.41}$	$0.13^{+0.06}_{-0.02}$	$3.12^{+6.05}_{-1.07}$	$0.11^{+0.04}_{-0.01}$	$5.76^{+3.72}_{-0.73}$	$0.12^{+0.06}_{-0.03}$	$3.38^{+4.17}_{-0.92}$
19	05 45 56.20	+00 33 10.3	$0.14^{+0.03}_{-0.02}$	$0.17^{+0.37}_{-0.06}$	$0.16^{+0.05}_{-0.03}$	$0.21^{+0.28}_{-0.12}$	$0.18^{+0.04}_{-0.03}$	$0.61^{+1.36}_{-0.31}$	...	...
20	05 45 56.31	+00 07 08.6	$0.41^{+0.10}_{-0.07}$	$0.60^{+0.37}_{-0.15}$	$0.55^{+0.16}_{-0.10}$	$0.86^{+0.92}_{-0.32}$	$0.61^{+0.18}_{-0.10}$	$1.61^{+1.35}_{-0.39}$	$1.05^{+0.10}_{-0.15}$	$3.33^{+2.03}_{-1.16}$
21	05 45 56.73	-00 00 25.4	$0.24^{+0.03}_{-0.02}$	$1.10^{+0.16}_{-0.10}$	$0.31^{+0.03}_{-0.03}$	$1.17^{+0.31}_{-0.23}$	$0.32^{+0.02}_{-0.04}$	$2.28^{+0.20}_{-0.11}$	$0.40^{+0.05}_{-0.04}$	$2.15^{+0.63}_{-0.39}$
22	05 45 57.38	+00 20 22.2	$0.46^{+0.15}_{-0.10}$	$0.55^{+5.17}_{-0.19}$	$0.65^{+0.17}_{-0.16}$	$0.89^{+10.44}_{-0.39}$	$0.75^{+0.18}_{-0.18}$	$1.80^{+6.14}_{-0.60}$	$1.18^{+0.10}_{-0.20}$	$3.17^{+8.37}_{-1.00}$
23	05 45 57.62	+00 07 21.1	$0.14^{+0.02}_{-0.01}$	$1.96^{+0.26}_{-0.18}$	$0.13^{+0.03}_{-0.02}$	$1.00^{+0.61}_{-0.28}$	$0.13^{+0.02}_{-0.01}$	$4.10^{+0.26}_{-1.27}$	$0.13^{+0.05}_{-0.01}$	$1.59^{+4.55}_{-0.21}$
24	05 45 57.93	+00 02 48.6	$0.17^{+0.02}_{-0.01}$	$1.54^{+0.25}_{-0.07}$	$0.20^{+0.02}_{-0.02}$	$1.32^{+0.51}_{-0.28}$	$0.18^{+0.03}_{-0.01}$	$3.23^{+0.34}_{-1.07}$	$0.21^{+0.03}_{-0.03}$	$1.80^{+0.58}_{-0.29}$
25	05 46 00.18	+00 03 07.0	$0.15^{+0.01}_{-0.01}$	$0.08^{+0.02}_{-0.01}$	$0.19^{+0.02}_{-0.02}$	$0.12^{+0.04}_{-0.03}$	$0.24^{+0.02}_{-0.01}$	$0.26^{+0.31}_{-0.04}$	...	...
26	05 46 03.53	+00 02 54.7	$0.14^{+0.01}_{-0.01}$	$1.02^{+0.17}_{-0.72}$	$0.16^{+0.02}_{-0.02}$	$0.54^{+0.20}_{-0.29}$	$0.16^{+0.03}_{-0.02}$	$1.82^{+0.69}_{-1.26}$	...	...
27	05 46 04.64	+00 04 58.1	$0.45^{+0.06}_{-0.07}$	$0.54^{+0.22}_{-0.11}$	$0.64^{+0.11}_{-0.11}$	$0.85^{+0.55}_{-0.29}$	$0.73^{+0.12}_{-0.12}$	$1.78^{+0.75}_{-0.46}$	$1.16^{+0.09}_{-0.10}$	$3.07^{+1.33}_{-0.82}$
28	05 46 04.58	+00 00 38.2	$0.34^{+0.13}_{-0.08}$	$1.46^{+3.89}_{-0.58}$	$0.40^{+0.13}_{-0.09}$	$1.89^{+6.61}_{-0.93}$	$0.38^{+0.09}_{-0.07}$	$2.67^{+4.04}_{-0.77}$	$0.54^{+0.16}_{-0.12}$	$3.74^{+6.93}_{-1.56}$
29	05 46 07.89	-00 11 56.9	$1.33^{+0.47}_{-0.23}$	$0.13^{+0.09}_{-0.06}$	$1.61^{+0.40}_{-0.27}$	$0.10^{+0.10}_{-0.04}$	$2.62^{+0.33}_{-0.46}$	$0.46^{+0.29}_{-0.12}$	...	...
30	05 46 09.27	+00 13 32.6	$0.28^{+0.07}_{-0.05}$	$0.12^{+0.25}_{-0.05}$	$0.38^{+0.10}_{-0.07}$	$0.23^{+0.25}_{-0.09}$	$0.46^{+0.11}_{-0.08}$	$0.85^{+0.38}_{-0.27}$	$0.85^{+0.17}_{-0.08}$	$1.01^{+0.88}_{-0.01}$
31	05 46 09.61	-00 03 31.2	$0.41^{+0.20}_{-0.15}$	$2.41^{+11.81}_{-1.49}$	$0.48^{+0.20}_{-0.17}$	$3.38^{+21.68}_{-2.29}$	$0.42^{+0.22}_{-0.11}$	$3.73^{+11.67}_{-1.88}$	$0.62^{+0.23}_{-0.20}$	$6.39^{+14.89}_{-3.55}$
32	05 46 10.31	-00 00 06.7	$0.35^{+0.14}_{-0.09}$	$3.84^{+8.80}_{-1.77}$	$0.45^{+0.12}_{-0.11}$	$6.00^{+15.20}_{-3.03}$	$0.36^{+0.09}_{-0.06}$	$5.59^{+7.22}_{-1.92}$	$0.50^{+0.13}_{-0.12}$	$8.32^{+11.60}_{-3.89}$
33	05 46 11.34	-00 07 55.1	...	...	$...^{+0.00}_{-0.00}$	...	...	...	...	...
34	05 46 11.86	+00 32 25.9	$1.41^{+0.32}_{-0.37}$	$0.63^{+0.53}_{-0.25}$	$1.64^{+0.26}_{-0.29}$	$0.81^{+0.61}_{-0.29}$	$2.11^{+0.07}_{-0.21}$	$2.12^{+1.17}_{-0.70}$	...	...
35	05 46 12.27	-00 08 07.8	$0.11^{+0.05}_{-0.04}$	$2.36^{+4.34}_{-1.53}$	$...^{+0.00}_{-0.00}$	...	...	...	...	...
36	05 46 12.99	-00 08 14.8	...	...	$0.16^{+0.08}_{-0.04}$	$56.18^{+26.86}_{-30.77}$	...	...	$0.14^{+0.05}_{-0.06}$	$39.41^{+6.20}_{-26.51}$
37	05 46 13.58	-00 10 34.0	$0.13^{+0.02}_{-0.04}$	$34.36^{+8.76}_{-16.89}$	$0.11^{+0.05}_{-0.01}$	$25.56^{+34.01}_{-3.97}$	$0.10^{+0.02}_{-0.00}$	$28.20^{+10.62}_{-2.49}$	$0.10^{+0.03}_{-0.03}$	$19.70^{+13.99}_{-8.45}$
38	05 46 14.48	+00 20 24.4	$0.20^{+0.08}_{-0.04}$	$1.93^{+2.15}_{-0.58}$	$0.25^{+0.10}_{-0.06}$	$2.24^{+3.62}_{-1.09}$	$0.23^{+0.06}_{-0.06}$	$3.90^{+1.99}_{-1.28}$	$0.26^{+0.12}_{-0.06}$	$2.83^{+5.38}_{-0.95}$
39	05 46 16.75	+00 07 13.5	$0.13^{+0.02}_{-0.01}$	$0.04^{+0.12}_{-0.02}$	$0.17^{+0.03}_{-0.01}$	$0.04^{+0.10}_{-0.02}$	$0.22^{+0.03}_{-0.03}$	$0.15^{+0.50}_{-0.05}$	...	...
40	05 46 17.71	-00 00 14.3	$0.80^{+0.45}_{-0.23}$	$0.43^{+0.80}_{-0.19}$	$1.22^{+0.29}_{-0.32}$	$0.83^{+0.94}_{-0.40}$	$1.67^{+0.13}_{-0.42}$	$2.03^{+1.81}_{-0.90}$	...	...
41	05 46 18.30	+00 06 57.8	$0.53^{+0.30}_{-0.11}$	$0.44^{+1.19}_{-0.15}$	$0.81^{+0.35}_{-0.19}$	$0.79^{+1.97}_{-0.35}$	$1.02^{+0.31}_{-0.24}$	$1.68^{+3.34}_{-0.57}$	...	...
42	05 46 18.60	+00 07 08.0	$0.20^{+0.11}_{-0.05}$	$0.98^{+3.75}_{-0.64}$	$0.26^{+0.12}_{-0.07}$	$0.83^{+5.23}_{-0.46}$	$0.28^{+0.09}_{-0.07}$	$2.25^{+3.14}_{-1.12}$	$0.32^{+0.18}_{-0.07}$	$1.51^{+6.41}_{-0.28}$
43	05 46 18.89	-00 05 38.1	$0.39^{+0.08}_{-0.08}$	$0.12^{+0.22}_{-0.06}$	$0.57^{+0.13}_{-0.13}$	$0.22^{+0.26}_{-0.10}$	$0.79^{+0.14}_{-0.20}$	$0.82^{+0.40}_{-0.23}$	$1.27^{+0.08}_{-0.08}$	$1.01^{+0.75}_{-0.00}$
44	05 46 19.06	+00 03 29.6	...	...	$0.80^{+0.91}_{-0.16}$	$0.01^{+0.16}_{-0.00}$	...	...	...	...
45	05 46 19.47	-00 05 20.0	$1.27^{+0.35}_{-0.36}$	$0.39^{+0.31}_{-0.16}$	$1.50^{+0.32}_{-0.26}$	$0.48^{+0.39}_{-0.17}$	$2.17^{+0.10}_{-0.30}$	$1.40^{+0.81}_{-0.44}$	...	...

Table 3.7: continued.

ID	RA (J2000)	DEC (J2000)	mass ($M_\odot$, DM97)	age (Myr, DM97)	mass ($M_\odot$, D08)	age (Myr, D08)	mass ($M_\odot$, S00)	age (Myr, S00)	mass ($M_\odot$, B98)	age (Myr, B98)
46	05 46 20.88	+00 08 09.4	$0.41^{+0.12}_{-0.08}$	$0.46^{+1.52}_{-0.20}$	$0.58^{+0.17}_{-0.13}$	$0.63^{+4.18}_{-0.28}$	$0.68^{+0.19}_{-0.14}$	$1.49^{+2.79}_{-0.48}$	$1.13^{+0.12}_{-0.16}$	$2.53^{+3.72}_{-0.86}$
47	05 46 22.43	-00 08 52.6	$1.40^{+0.21}_{-0.42}$	$1.50^{+1.53}_{-0.72}$	$1.61^{+0.08}_{-0.28}$	$2.12^{+1.51}_{-0.83}$	$1.74^{+0.04}_{-0.15}$	$4.42^{+2.64}_{-1.53}$	...	...
48	05 46 22.99	+00 04 26.4	$0.31^{+0.10}_{-0.07}$	$0.85^{+0.91}_{-0.31}$	$0.37^{+0.12}_{-0.08}$	$0.93^{+1.38}_{-0.39}$	$0.38^{+0.09}_{-0.07}$	$1.79^{+1.18}_{-0.36}$	$0.57^{+0.17}_{-0.10}$	$2.33^{+3.01}_{-0.72}$
49	05 46 23.83	+00 04 27.2	$0.24^{+0.15}_{-0.07}$	$0.83^{+5.75}_{-0.55}$	$0.30^{+0.16}_{-0.08}$	$0.72^{+9.48}_{-0.42}$	$0.28^{+0.13}_{-0.06}$	$1.76^{+4.94}_{-0.85}$	$0.43^{+0.23}_{-0.11}$	$1.62^{+7.13}_{-0.36}$
50	05 46 25.09	+00 05 41.2	$0.45^{+0.38}_{-0.18}$	$0.62^{+9.62}_{-0.40}$	$0.62^{+0.38}_{-0.26}$	$0.99^{+15.43}_{-0.67}$	$0.69^{+0.37}_{-0.28}$	$2.00^{+12.43}_{-1.13}$	$1.10^{+0.16}_{-0.29}$	$3.45^{+15.73}_{-1.54}$
51	05 46 25.89	+00 09 32.0	$0.21^{+0.06}_{-0.04}$	$1.18^{+0.49}_{-0.36}$	$0.27^{+0.07}_{-0.05}$	$1.20^{+0.95}_{-0.46}$	$0.28^{+0.05}_{-0.04}$	$2.60^{+0.56}_{-0.36}$	$0.32^{+0.09}_{-0.05}$	$1.94^{+1.63}_{-0.48}$
52	05 46 26.65	+00 31 07.5	$0.45^{+0.13}_{-0.11}$	$0.44^{+2.14}_{-0.20}$	$0.65^{+0.20}_{-0.17}$	$0.65^{+3.75}_{-0.31}$	$0.77^{+0.23}_{-0.20}$	$1.43^{+3.63}_{-0.48}$	$1.23^{+0.09}_{-0.17}$	$2.49^{+4.11}_{-0.81}$
53	05 46 27.13	+00 15 49.7	$0.18^{+0.02}_{-0.02}$	$1.75^{+0.34}_{-0.19}$	$0.20^{+0.04}_{-0.03}$	$1.65^{+0.80}_{-0.50}$	$0.18^{+0.04}_{-0.02}$	$3.55^{+0.43}_{-0.68}$	$0.21^{+0.04}_{-0.03}$	$2.14^{+2.11}_{-0.46}$
54	05 46 27.83	+00 05 48.4	$0.25^{+0.07}_{-0.06}$	$0.50^{+0.19}_{-0.33}$	$0.31^{+0.09}_{-0.06}$	$0.37^{+0.39}_{-0.16}$	$0.35^{+0.07}_{-0.06}$	$1.28^{+0.31}_{-0.46}$	$0.55^{+0.15}_{-0.05}$	$1.20^{+1.16}_{-0.12}$
55	05 46 28.36	+00 12 27.0	$0.22^{+0.15}_{-0.06}$	$0.72^{+5.38}_{-0.50}$	$0.28^{+0.16}_{-0.07}$	$0.55^{+8.81}_{-0.31}$	$0.27^{+0.13}_{-0.06}$	$1.63^{+5.19}_{-0.90}$	$0.40^{+0.22}_{-0.11}$	$1.29^{+7.67}_{-0.16}$
56	05 46 28.87	+00 13 30.7	$0.34^{+0.24}_{-0.10}$	$0.47^{+6.34}_{-0.33}$	$0.45^{+0.31}_{-0.14}$	$0.50^{+11.86}_{-0.31}$	$0.51^{+0.33}_{-0.14}$	$1.13^{+7.51}_{-0.54}$	$0.91^{+0.25}_{-0.25}$	$1.87^{+9.79}_{-0.54}$
57	05 46 29.00	+00 29 07.2	$0.28^{+0.08}_{-0.05}$	$0.38^{+0.24}_{-0.24}$	$0.37^{+0.10}_{-0.07}$	$0.33^{+0.42}_{-0.14}$	$0.42^{+0.09}_{-0.06}$	$1.04^{+0.51}_{-0.28}$	$0.72^{+0.17}_{-0.09}$	$1.28^{+1.26}_{-0.16}$
58	05 46 29.06	+00 11 45.7	$0.19^{+0.07}_{-0.05}$	$14.12^{+12.77}_{-6.31}$	$0.17^{+0.11}_{-0.04}$	$12.20^{+26.38}_{-5.45}$	$0.14^{+0.07}_{-0.02}$	$12.15^{+12.81}_{-3.09}$	$0.14^{+0.08}_{-0.04}$	$9.04^{+14.31}_{-4.22}$
59	05 46 29.59	+00 10 57.2	$0.14^{+0.02}_{-0.01}$	$0.13^{+0.28}_{-0.04}$	$0.16^{+0.03}_{-0.03}$	$0.17^{+0.20}_{-0.08}$	$0.20^{+0.03}_{-0.03}$	$0.94^{+0.96}_{-0.59}$	...	...
60	05 46 30.03	+00 11 11.1	$0.13^{+0.10}_{-0.05}$	$2.78^{+8.97}_{-1.69}$	$...^{+0.00}_{-0.00}$	...	...	...	$0.09^{+0.14}_{-0.02}$	$1.74^{+10.64}_{-0.34}$
61	05 46 30.06	+00 12 09.7	$0.28^{+0.10}_{-0.05}$	$0.37^{+3.46}_{-0.25}$	$0.36^{+0.12}_{-0.07}$	$0.33^{+5.39}_{-0.16}$	$0.42^{+0.10}_{-0.07}$	$1.04^{+3.25}_{-0.34}$	$0.72^{+0.18}_{-0.14}$	$1.27^{+3.78}_{-0.16}$
62	05 46 31.03	+00 27 12.1	$0.07^{+0.06}_{-0.03}$	$4.01^{+8.79}_{-2.84}$	$...^{+0.00}_{-0.00}$	...	...	...	...	...
63	05 46 31.46	+00 20 15.8	$0.25^{+0.06}_{-0.04}$	$13.05^{+8.76}_{-4.20}$	$0.27^{+0.09}_{-0.06}$	$16.36^{+17.48}_{-6.85}$	$0.20^{+0.04}_{-0.04}$	$13.45^{+6.97}_{-3.83}$	$0.25^{+0.08}_{-0.06}$	$14.32^{+11.72}_{-6.27}$
64	05 46 31.71	+00 25 08.2	$0.22^{+0.06}_{-0.04}$	$1.25^{+1.76}_{-0.40}$	$0.28^{+0.07}_{-0.05}$	$1.34^{+2.63}_{-0.53}$	$0.29^{+0.05}_{-0.04}$	$2.65^{+2.30}_{-0.45}$	$0.33^{+0.09}_{-0.06}$	$2.14^{+2.87}_{-0.57}$
65	05 46 33.28	+00 02 51.9	$0.70^{+0.35}_{-0.18}$	$0.60^{+1.12}_{-0.24}$	$1.12^{+0.24}_{-0.32}$	$1.36^{+1.49}_{-0.68}$	$1.44^{+0.10}_{-0.40}$	$2.94^{+2.28}_{-1.38}$	...	...
66	05 46 34.54	+00 06 43.5	$0.70^{+0.31}_{-0.18}$	$0.23^{+0.22}_{-0.12}$	$1.12^{+0.21}_{-0.27}$	$0.40^{+0.28}_{-0.17}$	$1.61^{+0.22}_{-0.43}$	$1.09^{+0.63}_{-0.41}$	...	...
67	05 46 34.90	+00 04 20.7	$0.17^{+0.03}_{-0.02}$	$0.14^{+0.31}_{-0.05}$	$0.22^{+0.04}_{-0.03}$	$0.24^{+0.26}_{-0.09}$	$0.26^{+0.03}_{-0.03}$	$1.29^{+0.38}_{-0.80}$	...	...
68	05 46 35.50	+00 01 38.9	$0.13^{+0.05}_{-0.02}$	$0.15^{+0.65}_{-0.07}$	$0.14^{+0.08}_{-0.02}$	$0.15^{+0.67}_{-0.08}$	$0.16^{+0.07}_{-0.03}$	$0.35^{+1.64}_{-0.14}$	...	...
69	05 46 36.10	+00 06 26.8	...	...	$0.44^{+0.72}_{-0.10}$	$0.02^{+3.20}_{-0.01}$	$0.63^{+0.91}_{-0.17}$	$0.05^{+2.38}_{-0.00}$	...	...
70	05 46 37.06	+00 01 21.8	$0.50^{+0.15}_{-0.08}$	$0.32^{+0.23}_{-0.10}$	$0.77^{+0.22}_{-0.13}$	$0.51^{+0.57}_{-0.18}$	$0.99^{+0.29}_{-0.16}$	$1.20^{+1.14}_{-0.28}$	...	...
71	05 46 37.57	+00 04 02.5	$0.15^{+0.01}_{-0.01}$	$0.20^{+0.13}_{-0.04}$	$0.19^{+0.02}_{-0.02}$	$0.30^{+0.10}_{-0.08}$	$0.22^{+0.02}_{-0.02}$	$1.90^{+0.09}_{-0.60}$	...	...
72	05 46 38.33	+00 05 48.7	$0.12^{+0.04}_{-0.01}$	$0.02^{+0.12}_{-0.01}$	$0.15^{+0.05}_{-0.01}$	$0.02^{+0.13}_{-0.01}$	$0.19^{+0.06}_{-0.03}$	$0.12^{+0.53}_{-0.04}$	...	...
73	05 46 38.40	+00 15 11.6	$0.14^{+0.02}_{-0.01}$	$0.34^{+0.60}_{-0.11}$	$0.16^{+0.03}_{-0.03}$	$0.39^{+0.33}_{-0.16}$	$0.17^{+0.03}_{-0.03}$	$1.60^{+0.85}_{-1.08}$	...	...
74	05 46 38.57	+00 22 06.0	$0.39^{+0.05}_{-0.05}$	$1.11^{+0.62}_{-0.26}$	$0.47^{+0.07}_{-0.06}$	$1.52^{+0.95}_{-0.47}$	$0.46^{+0.05}_{-0.04}$	$2.23^{+0.88}_{-0.43}$	$0.73^{+0.09}_{-0.09}$	$4.01^{+1.88}_{-1.11}$
75	05 46 39.89	+00 06 44.9	$0.24^{+0.25}_{-0.07}$	$0.11^{+5.11}_{-0.06}$	$0.31^{+0.34}_{-0.09}$	$0.19^{+10.54}_{-0.12}$	$0.38^{+0.36}_{-0.11}$	$0.91^{+6.00}_{-0.61}$	...	...
76	05 46 40.18	+00 05 01.9	$0.35^{+0.09}_{-0.07}$	$0.63^{+0.47}_{-0.25}$	$0.43^{+0.11}_{-0.09}$	$0.74^{+0.85}_{-0.32}$	$0.46^{+0.11}_{-0.07}$	$1.46^{+1.03}_{-0.30}$	$0.78^{+0.16}_{-0.13}$	$2.45^{+2.36}_{-0.82}$
77	05 46 40.44	-00 08 38.2	$0.35^{+0.17}_{-0.15}$	$25.82^{+12.49}_{-18.56}$	$0.43^{+0.15}_{-0.19}$	$42.16^{+32.27}_{-31.12}$	$0.28^{+0.15}_{-0.10}$	$23.58^{+12.81}_{-14.89}$	$0.39^{+0.19}_{-0.19}$	$34.94^{+7.62}_{-24.72}$
78	05 46 40.43	+00 05 07.7	$0.23^{+0.03}_{-0.02}$	$0.14^{+0.16}_{-0.04}$	$0.29^{+0.03}_{-0.03}$	$0.22^{+0.09}_{-0.06}$	$0.35^{+0.03}_{-0.03}$	$1.05^{+0.07}_{-0.21}$	...	...
79	05 46 40.77	+00 27 22.5	$0.23^{+0.07}_{-0.04}$	$1.12^{+0.84}_{-0.38}$	$0.30^{+0.07}_{-0.05}$	$1.17^{+1.57}_{-0.47}$	$0.30^{+0.05}_{-0.04}$	$2.33^{+1.02}_{-0.39}$	$0.37^{+0.10}_{-0.06}$	$2.05^{+2.11}_{-0.54}$
80	05 46 43.82	+00 03 21.8	$0.17^{+0.09}_{-0.05}$	$5.42^{+9.20}_{-2.23}$	$0.16^{+0.15}_{-0.03}$	$4.29^{+21.87}_{-1.74}$	$0.13^{+0.10}_{-0.02}$	$6.57^{+9.47}_{-1.06}$	$0.14^{+0.12}_{-0.03}$	$4.09^{+12.26}_{-1.43}$
81	05 46 43.84	+00 15 32.4	$0.36^{+0.06}_{-0.05}$	$0.87^{+0.39}_{-0.18}$	$0.43^{+0.08}_{-0.06}$	$1.08^{+0.79}_{-0.35}$	$0.43^{+0.06}_{-0.05}$	$1.85^{+0.68}_{-0.30}$	$0.68^{+0.11}_{-0.10}$	$2.94^{+1.76}_{-0.85}$
82	05 46 44.08	+00 18 03.2	$0.53^{+0.38}_{-0.12}$	$0.33^{+1.08}_{-0.15}$	$0.82^{+0.40}_{-0.21}$	$0.56^{+1.62}_{-0.27}$	$1.08^{+0.36}_{-0.29}$	$1.31^{+2.98}_{-0.47}$	...	...
83	05 46 44.25	+00 30 29.5	$0.14^{+0.02}_{-0.01}$	$0.27^{+0.38}_{-0.07}$	$0.15^{+0.02}_{-0.02}$	$0.31^{+0.20}_{-0.12}$	$0.17^{+0.03}_{-0.02}$	$0.58^{+1.34}_{-0.19}$	...	...
84	05 46 44.84	+00 16 59.8	$0.37^{+0.11}_{-0.08}$	$0.83^{+2.71}_{-0.31}$	$0.46^{+0.14}_{-0.09}$	$1.08^{+3.81}_{-0.51}$	$0.46^{+0.11}_{-0.08}$	$1.81^{+3.08}_{-0.49}$	$0.76^{+0.15}_{-0.15}$	$3.16^{+4.78}_{-1.22}$
85	05 46 45.00	+00 11 32.7	$0.17^{+0.01}_{-0.01}$	$1.64^{+0.21}_{-0.50}$	$0.19^{+0.02}_{-0.02}$	$1.38^{+0.43}_{-0.50}$	$0.17^{+0.03}_{-0.01}$	$3.47^{+0.23}_{-0.79}$	$0.20^{+0.03}_{-0.02}$	$1.86^{+0.47}_{-0.42}$
86	05 46 45.00	+00 24 48.7	$0.15^{+0.02}_{-0.02}$	$4.36^{+1.27}_{-0.63}$	$0.12^{+0.03}_{-0.01}$	$2.52^{+1.95}_{-0.50}$	$0.11^{+0.02}_{-0.00}$	$5.30^{+1.61}_{-0.21}$	$0.11^{+0.02}_{-0.02}$	$2.98^{+1.20}_{-0.57}$
87	05 46 45.04	+00 05 33.9	$0.29^{+0.04}_{-0.03}$	$0.10^{+0.15}_{-0.03}$	$0.40^{+0.06}_{-0.05}$	$0.21^{+0.11}_{-0.06}$	$0.49^{+0.07}_{-0.05}$	$0.78^{+0.12}_{-0.09}$	...	...
88	05 46 45.14	+00 03 46.4	$0.30^{+0.07}_{-0.06}$	$1.08^{+0.41}_{-0.22}$	$0.36^{+0.08}_{-0.06}$	$1.25^{+0.77}_{-0.41}$	$0.36^{+0.05}_{-0.06}$	$2.19^{+0.57}_{-0.26}$	$0.49^{+0.12}_{-0.07}$	$2.61^{+1.68}_{-0.77}$
89	05 46 46.87	+00 09 07.6	$0.34^{+0.12}_{-0.06}$	$0.37^{+0.29}_{-0.23}$	$0.47^{+0.18}_{-0.09}$	$0.37^{+0.68}_{-0.16}$	$0.56^{+0.20}_{-0.09}$	$0.96^{+0.95}_{-0.22}$	$1.03^{+0.16}_{-0.13}$	$1.65^{+1.75}_{-0.39}$
90	05 46 48.55	+00 21 28.2	...	...	$...^{+0.00}_{-0.00}$	...	...	...	...	...

Table 3.7: continued.

ID	RA (J2000)	DEC (J2000)	mass ($M_\odot$, DM97)	age (Myr, DM97)	mass ($M_\odot$, D08)	age (Myr, D08)	mass ($M_\odot$, S00)	age (Myr, S00)	mass ($M_\odot$, B98)	age (Myr, B98)
91	05 46 48.73	+00 21 38.3	$0.17^{+0.06}_{-0.03}$	$0.64^{+1.11}_{-0.41}$	$0.21^{+0.09}_{-0.05}$	$0.54^{+1.90}_{-0.26}$	$0.24^{+0.06}_{-0.05}$	$2.20^{+1.73}_{-0.98}$	...	...
92	05 46 49.09	+00 28 38.3	$0.16^{+0.04}_{-0.02}$	$1.74^{+1.32}_{-0.78}$	$0.17^{+0.06}_{-0.03}$	$1.22^{+2.07}_{-0.60}$	$0.16^{+0.05}_{-0.03}$	$3.80^{+1.38}_{-1.99}$	$0.16^{+0.08}_{-0.03}$	$1.68^{+5.39}_{-0.29}$
93	05 46 51.19	+00 18 08.2	$0.15^{+0.02}_{-0.01}$	$1.80^{+0.25}_{-0.17}$	$0.15^{+0.03}_{-0.02}$	$1.16^{+0.58}_{-0.38}$	$0.15^{+0.02}_{-0.02}$	$3.89^{+0.25}_{-1.63}$	$0.15^{+0.05}_{-0.02}$	$1.62^{+4.30}_{-0.21}$
94	05 46 51.40	+00 19 47.2	...	...	$...^{+0.00}_{-0.00}$	...	...	...	...	...
95	05 46 51.48	+00 19 21.3	$0.21^{+0.02}_{-0.02}$	$1.31^{+0.14}_{-0.20}$	$0.27^{+0.03}_{-0.02}$	$1.40^{+0.34}_{-0.37}$	$0.27^{+0.02}_{-0.02}$	$2.87^{+0.14}_{-0.36}$	$0.31^{+0.04}_{-0.03}$	$2.11^{+0.49}_{-0.44}$
96	05 46 51.85	+00 19 38.6	$0.19^{+0.04}_{-0.02}$	$0.80^{+0.34}_{-0.48}$	$0.24^{+0.04}_{-0.03}$	$0.60^{+0.63}_{-0.24}$	$0.26^{+0.03}_{-0.03}$	$2.08^{+0.46}_{-0.55}$	$0.31^{+0.07}_{-0.04}$	$1.21^{+0.82}_{-0.10}$
97	05 46 52.41	+00 20 01.7	$0.46^{+0.14}_{-0.09}$	$0.95^{+3.21}_{-0.34}$	$0.61^{+0.20}_{-0.13}$	$1.54^{+6.64}_{-0.72}$	$0.63^{+0.20}_{-0.13}$	$2.47^{+5.35}_{-0.92}$	$1.02^{+0.10}_{-0.17}$	$4.95^{+6.60}_{-1.99}$
98	05 46 56.54	+00 20 52.9	$0.93^{+0.35}_{-0.19}$	$0.84^{+1.00}_{-0.30}$	$1.34^{+0.17}_{-0.20}$	$1.65^{+1.10}_{-0.53}$	$1.63^{+0.05}_{-0.14}$	$3.56^{+1.82}_{-1.04}$	...	...
99	05 46 58.03	+00 14 27.8	$0.24^{+0.09}_{-0.05}$	$0.84^{+0.71}_{-0.48}$	$0.30^{+0.10}_{-0.06}$	$0.71^{+1.50}_{-0.34}$	$0.28^{+0.09}_{-0.03}$	$1.78^{+0.80}_{-0.59}$	$0.42^{+0.16}_{-0.07}$	$1.60^{+2.55}_{-0.34}$
100	05 46 58.13	+00 05 38.1	$0.28^{+0.10}_{-0.02}$	$0.01^{+0.09}_{-0.00}$	$0.42^{+0.15}_{-0.07}$	$0.06^{+0.11}_{-0.03}$	$0.56^{+0.24}_{-0.08}$	$0.45^{+0.22}_{-0.28}$	...	...
101	05 47 01.95	+00 16 56.7	$0.13^{+0.05}_{-0.03}$	$3.09^{+2.31}_{-1.02}$	$0.10^{+0.07}_{-...}$	$1.28^{+4.19}_{-0.15}$	...	...	$0.09^{+0.07}_{-0.01}$	$2.08^{+2.92}_{-0.45}$
102	05 47 02.87	+00 16 51.9	$0.18^{+0.07}_{-0.03}$	$1.73^{+2.52}_{-0.59}$	$0.21^{+0.10}_{-0.05}$	$1.65^{+4.69}_{-0.79}$	$0.18^{+0.08}_{-0.04}$	$3.50^{+2.47}_{-1.57}$	$0.22^{+0.11}_{-0.05}$	$2.16^{+5.83}_{-0.53}$
103	05 47 03.97	+00 11 14.4	$0.32^{+0.09}_{-0.08}$	$0.88^{+0.66}_{-0.34}$	$0.37^{+0.12}_{-0.08}$	$0.97^{+1.25}_{-0.43}$	$0.38^{+0.09}_{-0.07}$	$1.83^{+1.19}_{-0.38}$	$0.56^{+0.18}_{-0.09}$	$2.40^{+2.70}_{-0.79}$
104	05 47 04.48	+00 15 47.2	$0.38^{+0.44}_{-0.10}$	$0.08^{+4.02}_{-0.05}$	$0.57^{+0.52}_{-0.20}$	$0.19^{+4.81}_{-0.12}$	$0.80^{+0.52}_{-0.29}$	$0.74^{+4.44}_{-0.38}$	...	...
105	05 47 04.94	+00 18 31.6	$0.27^{+0.14}_{-0.06}$	$0.10^{+0.50}_{-0.06}$	$0.36^{+0.23}_{-0.09}$	$0.18^{+1.12}_{-0.11}$	$0.44^{+0.26}_{-0.10}$	$0.83^{+1.52}_{-0.51}$	...	...
106	05 47 04.98	+00 18 12.6	$0.16^{+0.03}_{-0.02}$	$1.71^{+0.64}_{-0.34}$	$0.17^{+0.05}_{-0.04}$	$1.25^{+1.31}_{-0.50}$	$0.16^{+0.04}_{-0.03}$	$3.74^{+0.68}_{-1.77}$	$0.17^{+0.07}_{-0.02}$	$1.71^{+4.96}_{-0.24}$
107	05 47 05.06	+00 18 34.8	$0.29^{+0.08}_{-0.05}$	$0.52^{+2.50}_{-0.31}$	$0.36^{+0.09}_{-0.06}$	$0.43^{+3.04}_{-0.18}$	$0.41^{+0.08}_{-0.05}$	$1.18^{+1.82}_{-0.27}$	$0.67^{+0.14}_{-0.12}$	$1.49^{+3.80}_{-0.29}$
108	05 47 05.12	+00 18 26.7	$0.22^{+0.07}_{-0.04}$	$1.01^{+1.67}_{-0.45}$	$0.28^{+0.08}_{-0.05}$	$0.94^{+2.99}_{-0.39}$	$0.27^{+0.07}_{-0.03}$	$2.14^{+2.06}_{-0.42}$	$0.36^{+0.11}_{-0.07}$	$1.77^{+3.27}_{-0.41}$
109	05 47 05.34	+00 28 46.1	$0.26^{+0.07}_{-0.04}$	$2.10^{+1.32}_{-0.55}$	$0.34^{+0.08}_{-0.06}$	$2.94^{+2.28}_{-1.07}$	$0.31^{+0.04}_{-0.04}$	$3.89^{+1.43}_{-0.74}$	$0.37^{+0.09}_{-0.06}$	$4.07^{+2.90}_{-1.38}$
110	05 47 06.00	+00 32 08.5	$2.33^{+0.12}_{-0.35}$	$0.96^{+0.67}_{-0.34}$	$2.42^{+0.08}_{-0.28}$	$1.06^{+0.58}_{-0.36}$	$2.33^{+0.17}_{-0.14}$	$2.71^{+0.93}_{-0.79}$	...	...
111	05 47 05.98	+00 25 53.1	$0.20^{+0.07}_{-0.04}$	$3.95^{+6.98}_{-1.51}$	$0.21^{+0.11}_{-0.05}$	$4.15^{+13.27}_{-2.10}$	$0.18^{+0.06}_{-0.04}$	$5.86^{+6.02}_{-1.66}$	$0.20^{+0.11}_{-0.05}$	$4.33^{+8.88}_{-1.68}$
112	05 47 06.17	+00 20 32.5	$0.27^{+0.06}_{-0.04}$	$0.09^{+0.72}_{-0.03}$	$0.37^{+0.08}_{-0.06}$	$0.17^{+0.79}_{-0.07}$	$0.45^{+0.08}_{-0.06}$	$0.78^{+0.70}_{-0.26}$	...	...
113	05 47 06.96	+00 00 47.7	$0.63^{+0.23}_{-0.12}$	$0.48^{+0.57}_{-0.14}$	$1.00^{+0.24}_{-0.21}$	$1.00^{+0.99}_{-0.42}$	$1.32^{+0.17}_{-0.29}$	$2.24^{+1.75}_{-0.84}$	...	...
114	05 47 06.99	+00 31 55.9	$0.38^{+0.12}_{-0.08}$	$0.91^{+3.57}_{-0.38}$	$0.46^{+0.14}_{-0.10}$	$1.23^{+6.78}_{-0.62}$	$0.46^{+0.12}_{-0.07}$	$1.96^{+3.68}_{-0.58}$	$0.76^{+0.15}_{-0.16}$	$3.48^{+6.61}_{-1.46}$
115	05 47 07.26	+00 19 32.2	...	...	$0.42^{+0.15}_{-0.05}$	$0.01^{+0.04}_{-0.01}$	...	...	...	...
116	05 47 08.69	+00 00 14.0	$0.20^{+0.06}_{-0.03}$	$0.06^{+2.65}_{-0.03}$	$0.25^{+0.08}_{-0.04}$	$0.09^{+1.74}_{-0.05}$	$0.32^{+0.07}_{-0.05}$	$0.47^{+2.20}_{-0.34}$	...	...
117	05 47 08.62	+00 19 23.9	$0.23^{+0.04}_{-0.03}$	$0.88^{+0.25}_{-0.21}$	$0.30^{+0.04}_{-0.03}$	$0.77^{+0.47}_{-0.18}$	$0.28^{+0.05}_{-0.01}$	$1.85^{+0.39}_{-0.12}$	$0.41^{+0.05}_{-0.05}$	$1.66^{+0.74}_{-0.30}$
118	05 47 08.71	+00 16 34.7	$0.17^{+0.06}_{-0.03}$	$1.56^{+1.04}_{-0.58}$	$0.20^{+0.09}_{-0.05}$	$1.36^{+2.30}_{-0.66}$	$0.18^{+0.08}_{-0.03}$	$3.26^{+1.12}_{-1.70}$	$0.21^{+0.11}_{-0.04}$	$1.84^{+5.42}_{-0.41}$
119	05 47 10.72	+00 18 46.3	$0.32^{+0.07}_{-0.05}$	$0.52^{+0.82}_{-0.24}$	$0.40^{+0.09}_{-0.06}$	$0.50^{+1.18}_{-0.19}$	$0.45^{+0.07}_{-0.06}$	$1.21^{+1.08}_{-0.19}$	$0.76^{+0.13}_{-0.11}$	$1.80^{+2.64}_{-0.46}$
120	05 47 10.89	+00 32 06.0	$0.32^{+0.08}_{-0.07}$	$0.66^{+0.50}_{-0.28}$	$0.40^{+0.11}_{-0.08}$	$0.70^{+0.85}_{-0.31}$	$0.42^{+0.10}_{-0.07}$	$1.47^{+0.81}_{-0.30}$	$0.67^{+0.17}_{-0.11}$	$2.16^{+2.14}_{-0.69}$
121	05 47 10.98	+00 19 14.8	$2.22^{+0.15}_{-0.03}$	$2.68^{+0.13}_{-0.44}$	$2.43^{+0.08}_{-0.09}$	$2.33^{+0.38}_{-0.32}$	$2.12^{+0.12}_{-0.04}$	$4.43^{+0.27}_{-0.76}$	...	...
122	05 47 10.98	+00 21 32.2	$0.42^{+0.12}_{-0.09}$	$1.96^{+4.61}_{-0.67}$	$0.50^{+0.12}_{-0.10}$	$2.78^{+8.28}_{-1.17}$	$0.45^{+0.10}_{-0.07}$	$3.29^{+4.20}_{-0.88}$	$0.69^{+0.11}_{-0.13}$	$5.89^{+7.20}_{-2.22}$
123	05 47 12.92	+00 22 06.5	$0.28^{+0.15}_{-0.04}$	$0.02^{+2.75}_{-0.01}$	$0.42^{+0.20}_{-0.08}$	$0.08^{+5.52}_{-0.04}$	$0.56^{+0.25}_{-0.09}$	$0.49^{+3.46}_{-0.29}$	...	...
124	05 47 13.85	+00 00 17.1	$0.25^{+0.06}_{-0.03}$	$0.04^{+0.07}_{-0.02}$	$0.36^{+0.09}_{-0.06}$	$0.08^{+0.10}_{-0.04}$	$0.46^{+0.11}_{-0.07}$	$0.56^{+0.17}_{-0.35}$	...	...
125	05 47 16.58	-00 00 56.4	$0.18^{+0.07}_{-0.03}$	$0.85^{+0.47}_{-0.55}$	$0.24^{+0.08}_{-0.05}$	$0.63^{+0.80}_{-0.31}$	$0.25^{+0.06}_{-0.05}$	$2.17^{+0.56}_{-0.87}$	$0.30^{+0.12}_{-0.04}$	$1.23^{+3.50}_{-0.12}$
126	05 47 17.16	+00 18 24.6	$0.47^{+0.13}_{-0.12}$	$3.10^{+6.47}_{-1.48}$	$0.54^{+0.14}_{-0.12}$	$4.31^{+9.24}_{-2.20}$	$0.46^{+0.13}_{-0.08}$	$4.50^{+7.26}_{-1.61}$	$0.70^{+0.12}_{-0.15}$	$8.21^{+10.18}_{-3.62}$
127	05 47 17.28	+00 38 21.4	$0.43^{+0.14}_{-0.09}$	$0.39^{+5.66}_{-0.18}$	$0.61^{+0.17}_{-0.14}$	$0.53^{+10.55}_{-0.23}$	$0.74^{+0.18}_{-0.17}$	$1.30^{+6.38}_{-0.40}$	$1.21^{+0.09}_{-0.20}$	$2.08^{+8.23}_{-0.55}$
128	05 47 19.72	+00 01 21.8	$0.17^{+0.05}_{-0.03}$	$2.60^{+2.06}_{-0.63}$	$0.17^{+0.08}_{-0.04}$	$2.16^{+3.79}_{-0.95}$	$0.15^{+0.06}_{-0.03}$	$4.69^{+1.88}_{-0.88}$	$0.17^{+0.09}_{-0.04}$	$2.64^{+4.58}_{-0.70}$
129	05 47 19.90	+00 16 13.1	$0.16^{+0.02}_{-0.02}$	$0.28^{+0.58}_{-0.09}$	$0.19^{+0.03}_{-0.03}$	$0.40^{+0.40}_{-0.14}$	$0.22^{+0.03}_{-0.03}$	$2.11^{+0.44}_{-0.88}$	...	...
130	05 47 22.99	+00 17 56.7	$0.19^{+0.03}_{-0.02}$	$1.91^{+0.66}_{-0.34}$	$0.23^{+0.05}_{-0.04}$	$2.06^{+1.23}_{-0.71}$	$0.22^{+0.04}_{-0.04}$	$3.81^{+0.83}_{-0.64}$	$0.24^{+0.06}_{-0.04}$	$2.64^{+1.89}_{-0.75}$
131	05 47 25.05	+00 31 05.0	$0.76^{+0.05}_{-0.17}$	$8.48^{+4.22}_{-3.61}$	$0.86^{+0.02}_{-0.15}$	$15.09^{+6.21}_{-7.29}$	$0.80^{+0.04}_{-0.20}$	$15.62^{+7.89}_{-7.38}$	$0.89^{+0.03}_{-0.09}$	$22.23^{+8.58}_{-8.94}$
132	05 47 57.53	+00 11 31.2	$0.17^{+0.06}_{-0.03}$	$0.17^{+0.39}_{-0.08}$	$0.23^{+0.07}_{-0.04}$	$0.28^{+0.30}_{-0.14}$	$0.27^{+0.06}_{-0.04}$	$1.43^{+0.19}_{-0.90}$	...	...

Table 3.8: Mass and age estimate for YSOs in L1641 with different PMS evolutionary tracks. A complete version of this table, containing 267 stars, is available at the CDS. Here we only show the first 10 entries.

	RA	DEC	Mass	Age	Mass	Age	Mass	Age	Mass	Age
ID	(J2000)	(J2000)	($M_\odot$, DM97)	(Myr, DM97)	($M_\odot$, D08)	(Myr, D08)	($M_\odot$, S00)	(Myr, S00)	($M_\odot$, B98)	(Myr, B98)
1	05 35 14.56	−06 15 12.7	$0.34^{+0.05}_{-0.04}$	$0.63^{+0.26}_{-0.15}$	$0.42^{+0.06}_{-0.05}$	$0.70^{+0.52}_{-0.22}$	$0.45^{+0.05}_{-0.04}$	$1.44^{+0.47}_{-0.22}$	$0.74^{+0.10}_{-0.08}$	$2.29^{+1.18}_{-0.63}$
2	05 35 14.67	−06 15 07.3	$0.16^{+0.02}_{-0.02}$	$1.11^{+0.28}_{-0.51}$	$0.19^{+0.04}_{-0.03}$	$0.69^{+0.53}_{-0.24}$	$0.20^{+0.03}_{-0.03}$	$2.55^{+0.46}_{-0.94}$	...	...
3	05 35 14.72	−06 13 39.9	$0.13^{+0.01}_{-0.01}$	$0.12^{+0.09}_{-0.03}$	$0.15^{+0.03}_{-0.02}$	$0.14^{+0.12}_{-0.06}$	$0.19^{+0.03}_{-0.02}$	$0.37^{+1.03}_{-0.11}$	...	...
4	05 35 15.83	−06 24 45.7	$0.16^{+0.02}_{-0.01}$	$1.42^{+0.19}_{-0.21}$	$0.18^{+0.03}_{-0.02}$	$0.99^{+0.47}_{-0.27}$	$0.17^{+0.03}_{-0.01}$	$3.17^{+0.28}_{-1.00}$	$0.19^{+0.04}_{-0.02}$	$1.45^{+2.29}_{-0.19}$
5	05 35 17.80	−06 24 38.4	$0.29^{+0.02}_{-0.02}$	$0.19^{+0.15}_{-0.06}$	$0.39^{+0.03}_{-0.03}$	$0.28^{+0.07}_{-0.06}$	$0.46^{+0.03}_{-0.03}$	$0.93^{+0.06}_{-0.04}$	$0.82^{+0.06}_{-0.04}$	$1.17^{+0.27}_{-0.10}$
6	05 35 18.26	−06 24 30.3	$0.14^{+0.04}_{-0.02}$	$1.32^{+0.42}_{-0.70}$	$0.13^{+0.06}_{-0.02}$	$0.51^{+1.06}_{-0.16}$	$0.14^{+0.05}_{-0.02}$	$0.74^{+2.46}_{-0.18}$	...	...
7	05 35 18.95	−06 27 25.6	$0.19^{+0.07}_{-0.04}$	$1.15^{+0.53}_{-0.51}$	$0.24^{+0.09}_{-0.06}$	$1.02^{+1.17}_{-0.47}$	$0.25^{+0.06}_{-0.05}$	$2.68^{+0.69}_{-0.83}$	$0.28^{+0.11}_{-0.04}$	$1.64^{+3.22}_{-0.33}$
8	05 35 19.34	−06 24 14.5	$0.27^{+0.04}_{-0.03}$	$1.16^{+0.27}_{-0.12}$	$0.34^{+0.04}_{-0.03}$	$1.34^{+0.48}_{-0.26}$	$0.34^{+0.02}_{-0.03}$	$2.35^{+0.33}_{-0.18}$	$0.44^{+0.06}_{-0.04}$	$2.57^{+0.92}_{-0.48}$
9	05 35 21.77	−06 18 51.2	$0.17^{+0.01}_{-0.01}$	$1.57^{+0.08}_{-0.06}$	$0.19^{+0.01}_{-0.01}$	$1.30^{+0.23}_{-0.20}$	$0.17^{+0.02}_{-0.01}$	$3.36^{+0.09}_{-0.06}$	$0.20^{+0.02}_{-0.02}$	$1.78^{+0.25}_{-0.21}$
10	05 35 23.60	−06 28 24.4	$0.16^{+0.04}_{-0.02}$	$0.07^{+0.10}_{-0.03}$	$0.21^{+0.05}_{-0.03}$	$0.11^{+0.09}_{-0.05}$	$0.26^{+0.05}_{-0.04}$	$0.24^{+0.68}_{-0.09}$	...	...
11	05 35 24.45	-06 27 47.2	$0.20^{+0.03}_{-0.03}$	$5.67^{+2.61}_{-1.20}$	$0.21^{+0.06}_{-0.04}$	$5.91^{+4.99}_{-2.07}$	$0.17^{+0.03}_{-0.03}$	$7.23^{+2.61}_{-1.16}$	$0.18^{+0.06}_{-0.03}$	$5.29^{+4.82}_{-1.44}$
12	05 35 24.49	-06 28 40.5	$0.16^{+0.05}_{-0.02}$	$1.18^{+0.51}_{-0.63}$	$0.18^{+0.07}_{-0.04}$	$0.70^{+1.09}_{-0.32}$	$0.19^{+0.06}_{-0.04}$	$2.64^{+0.78}_{-1.69}$	...	...
13	05 35 25.11	-06 47 56.6	$0.34^{+0.12}_{-0.06}$	$0.35^{+0.48}_{-0.22}$	$0.47^{+0.18}_{-0.09}$	$0.35^{+1.48}_{-0.16}$	$0.56^{+0.21}_{-0.09}$	$0.92^{+1.52}_{-0.24}$	$1.03^{+0.16}_{-0.15}$	$1.56^{+2.47}_{-0.33}$
14	05 35 25.70	-06 23 18.9	$0.22^{+0.05}_{-0.03}$	$0.90^{+0.31}_{-0.41}$	$0.28^{+0.06}_{-0.04}$	$0.75^{+0.64}_{-0.26}$	$0.26^{+0.06}_{-0.01}$	$1.91^{+0.43}_{-0.28}$	$0.37^{+0.08}_{-0.05}$	$1.54^{+0.99}_{-0.27}$
15	05 35 26.59	-06 15 32.8	$0.21^{+0.03}_{-0.02}$	$1.24^{+0.47}_{-0.32}$	$0.27^{+0.04}_{-0.03}$	$1.27^{+0.85}_{-0.43}$	$0.27^{+0.03}_{-0.03}$	$2.75^{+0.69}_{-0.43}$	$0.31^{+0.05}_{-0.04}$	$1.97^{+1.03}_{-0.46}$
16	05 35 26.80	-06 15 34.4	$0.19^{+0.03}_{-0.02}$	$1.17^{+0.33}_{-0.26}$	$0.25^{+0.03}_{-0.03}$	$1.09^{+0.61}_{-0.32}$	$0.26^{+0.03}_{-0.03}$	$2.70^{+0.54}_{-0.30}$	$0.29^{+0.04}_{-0.04}$	$1.74^{+0.79}_{-0.36}$
17	05 35 26.83	-06 26 47.6	$0.45^{+0.13}_{-0.09}$	$0.96^{+0.79}_{-0.30}$	$0.59^{+0.20}_{-0.13}$	$1.54^{+1.78}_{-0.68}$	$0.61^{+0.21}_{-0.12}$	$2.40^{+2.42}_{-0.79}$	$1.01^{+0.10}_{-0.18}$	$4.97^{+3.28}_{-2.02}$
18	05 35 26.96	-06 27 13.0	$0.19^{+0.02}_{-0.02}$	$4.72^{+1.22}_{-0.74}$	$0.18^{+0.04}_{-0.03}$	$4.43^{+2.17}_{-1.22}$	$0.16^{+0.02}_{-0.02}$	$6.38^{+1.19}_{-0.67}$	$0.17^{+0.03}_{-0.02}$	$4.42^{+1.85}_{-0.95}$
19	05 35 27.17	-06 19 42.0	$0.26^{+0.03}_{-0.02}$	$0.08^{+0.06}_{-0.02}$	$0.35^{+0.04}_{-0.04}$	$0.16^{+0.06}_{-0.04}$	$0.43^{+0.04}_{-0.04}$	$0.79^{+0.05}_{-0.11}$	...	...
20	05 35 27.35	-06 19 31.3	...	...	$\cdots^{+0.00}_{-0.00}$	...	...	...	...	...
21	05 35 28.28	-06 22 29.3	$0.13^{+0.08}_{-0.06}$	$7.01^{+13.30}_{-4.01}$	$\cdots^{+0.00}_{-0.00}$	...	...	...	$0.09^{+0.09}_{-0.02}$	$3.85^{+12.61}_{-1.02}$
22	05 35 29.21	-06 16 29.7	$0.14^{+0.01}_{-0.01}$	$0.06^{+0.02}_{-0.02}$	$0.19^{+0.02}_{-0.02}$	$0.08^{+0.04}_{-0.03}$	$0.23^{+0.02}_{-0.02}$	$0.19^{+0.20}_{-0.04}$	...	...
23	05 35 29.46	-06 16 26.6	$0.24^{+0.03}_{-0.03}$	$0.53^{+0.11}_{-0.29}$	$0.30^{+0.03}_{-0.03}$	$0.39^{+0.14}_{-0.11}$	$0.34^{+0.03}_{-0.03}$	$1.34^{+0.09}_{-0.13}$	$0.51^{+0.06}_{-0.03}$	$1.20^{+0.37}_{-0.11}$
24	05 35 30.41	-06 27 07.2	$0.14^{+0.04}_{-0.03}$	$11.66^{+9.84}_{-4.12}$	$0.11^{+0.06}_{-0.00}$	$6.73^{+14.43}_{-0.48}$	...	...	$0.09^{+0.05}_{-0.02}$	$5.75^{+9.06}_{-1.42}$
25	05 35 31.05	-06 45 18.1	$0.21^{+0.06}_{-0.04}$	$0.13^{+0.25}_{-0.06}$	$0.27^{+0.08}_{-0.05}$	$0.21^{+0.20}_{-0.11}$	$0.32^{+0.07}_{-0.05}$	$1.14^{+0.10}_{-0.63}$	...	...
26	05 35 31.49	-06 14 18.9	$0.24^{+0.04}_{-0.03}$	$1.40^{+0.33}_{-0.16}$	$0.31^{+0.04}_{-0.03}$	$1.67^{+0.61}_{-0.37}$	$0.30^{+0.03}_{-0.02}$	$2.82^{+0.37}_{-0.16}$	$0.36^{+0.06}_{-0.04}$	$2.59^{+0.98}_{-0.55}$
27	05 35 31.89	-06 36 25.5	$0.14^{+0.04}_{-0.02}$	$2.07^{+0.96}_{-0.57}$	$0.11^{+0.06}_{-0.01}$	$0.82^{+2.05}_{-0.10}$	$0.11^{+0.05}_{-0.01}$	$3.87^{+1.20}_{-0.20}$	...	...
28	05 35 33.93	-06 14 32.8	$0.15^{+0.01}_{-0.01}$	$0.29^{+0.19}_{-0.05}$	$0.19^{+0.01}_{-0.01}$	$0.40^{+0.08}_{-0.07}$	$0.21^{+0.01}_{-0.01}$	$2.13^{+0.08}_{-0.25}$	...	...
29	05 35 34.17	-06 22 57.8	$0.25^{+0.04}_{-0.03}$	$1.27^{+0.30}_{-0.15}$	$0.31^{+0.04}_{-0.03}$	$1.48^{+0.55}_{-0.34}$	$0.31^{+0.02}_{-0.03}$	$2.58^{+0.37}_{-0.20}$	$0.38^{+0.06}_{-0.04}$	$2.48^{+0.97}_{-0.51}$
30	05 35 34.19	-06 39 43.3	$0.21^{+0.09}_{-0.04}$	$0.89^{+0.45}_{-0.48}$	$0.27^{+0.09}_{-0.06}$	$0.72^{+0.82}_{-0.31}$	$0.26^{+0.08}_{-0.03}$	$1.99^{+0.56}_{-0.51}$	$0.35^{+0.12}_{-0.03}$	$1.46^{+2.58}_{-0.22}$
31	05 35 34.34	-06 24 22.8	$0.16^{+0.03}_{-0.03}$	$6.31^{+3.16}_{-1.39}$	$0.13^{+0.04}_{-0.02}$	$3.93^{+4.41}_{-0.89}$	$0.11^{+0.03}_{-0.00}$	$6.37^{+3.13}_{-0.28}$	$0.11^{+0.04}_{-0.02}$	$3.97^{+2.91}_{-0.94}$
32	05 35 38.59	-06 23 43.1	$0.21^{+0.03}_{-0.02}$	$1.57^{+0.37}_{-0.20}$	$0.26^{+0.04}_{-0.03}$	$1.77^{+0.74}_{-0.46}$	$0.25^{+0.02}_{-0.03}$	$3.40^{+0.47}_{-0.35}$	$0.28^{+0.04}_{-0.04}$	$2.44^{+0.91}_{-0.54}$
33	05 35 40.83	-06 18 06.7	$0.25^{+0.04}_{-0.03}$	$1.44^{+0.42}_{-0.19}$	$0.33^{+0.04}_{-0.03}$	$1.79^{+0.71}_{-0.41}$	$0.32^{+0.03}_{-0.02}$	$2.86^{+0.53}_{-0.26}$	$0.39^{+0.06}_{-0.04}$	$2.88^{+1.13}_{-0.63}$
34	05 35 41.02	-06 22 45.4	$0.29^{+0.05}_{-0.03}$	$0.06^{+0.08}_{-0.02}$	$0.42^{+0.07}_{-0.05}$	$0.13^{+0.08}_{-0.04}$	$0.53^{+0.10}_{-0.06}$	$0.63^{+0.14}_{-0.11}$	...	...
35	05 35 41.65	-06 25 19.2	$0.12^{+0.08}_{-0.05}$	$5.89^{+13.29}_{-3.64}$	$\cdots^{+0.00}_{-0.00}$	...	...	...	$0.08^{+0.09}_{-0.01}$	$3.38^{+12.03}_{-0.89}$
36	05 35 42.09	-06 16 20.8	$0.14^{+0.04}_{-0.03}$	$6.47^{+3.62}_{-1.64}$	$0.10^{+0.05}_{-0.00}$	$3.28^{+4.83}_{-0.22}$	...	...	$0.09^{+0.04}_{-0.02}$	$3.65^{+3.19}_{-0.75}$
37	05 35 42.84	-06 21 44.6	$0.28^{+0.04}_{-0.03}$	$1.17^{+0.30}_{-0.12}$	$0.35^{+0.04}_{-0.03}$	$1.36^{+0.54}_{-0.27}$	$0.34^{+0.02}_{-0.03}$	$2.35^{+0.40}_{-0.21}$	$0.45^{+0.05}_{-0.04}$	$2.63^{+0.93}_{-0.48}$
38	05 35 42.76	-06 34 51.9	$0.41^{+0.13}_{-0.07}$	$0.93^{+1.09}_{-0.20}$	$0.51^{+0.18}_{-0.10}$	$1.35^{+2.05}_{-0.50}$	$0.51^{+0.18}_{-0.08}$	$2.06^{+2.48}_{-0.40}$	$0.86^{+0.13}_{-0.17}$	$4.07^{+4.17}_{-1.47}$
39	05 35 43.37	-06 22 19.6	$0.27^{+0.06}_{-0.04}$	$0.18^{+1.47}_{-0.08}$	$0.34^{+0.07}_{-0.05}$	$0.26^{+2.69}_{-0.10}$	$0.40^{+0.06}_{-0.04}$	$0.98^{+0.93}_{-0.22}$	$0.71^{+0.13}_{-0.10}$	$1.05^{+1.43}_{-0.03}$
40	05 35 44.18	-06 28 16.4	$0.36^{+0.14}_{-0.11}$	$10.89^{+15.39}_{-5.39}$	$0.47^{+0.09}_{-0.16}$	$18.64^{+27.19}_{-10.22}$	$0.33^{+0.10}_{-0.08}$	$12.27^{+13.13}_{-4.75}$	$0.48^{+0.10}_{-0.16}$	$20.04^{+14.99}_{-10.62}$
41	05 35 44.27	-06 26 39.5	$0.13^{+0.04}_{-0.02}$	$4.28^{+2.31}_{-1.01}$	$\cdots^{+0.00}_{-0.00}$	...	...	...	$0.09^{+0.04}_{-0.01}$	$2.63^{+2.49}_{-0.59}$
42	05 35 47.65	-06 21 36.1	$0.18^{+0.07}_{-0.03}$	$0.43^{+0.49}_{-0.25}$	$0.23^{+0.07}_{-0.05}$	$0.48^{+0.49}_{-0.22}$	$0.25^{+0.06}_{-0.04}$	$1.95^{+0.24}_{-0.71}$	...	...

Table 3.8: continued.

ID	RA (J2000)	DEC (J2000)	Mass ($M_\odot$, DM97)	Age (Myr, DM97)	Mass ($M_\odot$, D08)	Age (Myr, D08)	Mass ($M_\odot$, S00)	Age (Myr, S00)	Mass ($M_\odot$, B98)	Age (Myr, B98)
43	05 35 48.28	-06 17 59.4	$0.33^{+0.11}_{-0.08}$	$1.31^{+0.91}_{-0.43}$	$0.40^{+0.12}_{-0.09}$	$1.65^{+1.50}_{-0.72}$	$0.38^{+0.09}_{-0.07}$	$2.46^{+1.34}_{-0.51}$	$0.54^{+0.17}_{-0.11}$	$3.40^{+3.27}_{-1.34}$
44	05 35 48.39	-06 17 36.2	$0.19^{+0.07}_{-0.03}$	$1.02^{+0.49}_{-0.53}$	$0.24^{+0.09}_{-0.05}$	$0.81^{+0.94}_{-0.37}$	$0.26^{+0.06}_{-0.05}$	$2.41^{+0.47}_{-0.74}$	$0.29^{+0.12}_{-0.03}$	$1.41^{+2.90}_{-0.20}$
45	05 35 50.19	-06 50 40.2	$0.74^{+0.07}_{-0.20}$	$6.38^{+10.20}_{-3.10}$	$0.88^{+0.03}_{-0.21}$	$11.83^{+14.86}_{-6.24}$	$0.81^{+0.06}_{-0.21}$	$12.78^{+12.15}_{-6.46}$	$0.92^{+0.04}_{-0.13}$	$18.99^{+12.18}_{-8.30}$
46	05 35 57.30	-06 40 28.1	$0.21^{+0.01}_{-0.01}$	$0.83^{+0.05}_{-0.10}$	$0.27^{+0.01}_{-0.01}$	$0.66^{+0.10}_{-0.08}$	$0.26^{+0.01}_{-0.00}$	$1.81^{+0.08}_{-0.05}$	$0.38^{+0.02}_{-0.02}$	$1.42^{+0.17}_{-0.14}$
47	05 35 57.31	-06 15 37.7	$0.30^{+0.07}_{-0.05}$	$1.16^{+0.38}_{-0.23}$	$0.36^{+0.07}_{-0.05}$	$1.39^{+0.65}_{-0.43}$	$0.36^{+0.04}_{-0.05}$	$2.31^{+0.48}_{-0.30}$	$0.49^{+0.11}_{-0.07}$	$2.83^{+1.53}_{-0.85}$
48	05 35 57.45	-06 42 41.9	$0.71^{+0.47}_{-0.21}$	$0.33^{+0.83}_{-0.17}$	$1.13^{+0.33}_{-0.35}$	$0.65^{+1.00}_{-0.35}$	$1.58^{+0.21}_{-0.49}$	$1.62^{+1.92}_{-0.75}$	...	...
49	05 35 57.45	-06 16 35.0	$0.20^{+0.02}_{-0.02}$	$0.06^{+0.03}_{-0.02}$	$0.25^{+0.03}_{-0.02}$	$0.10^{+0.05}_{-0.03}$	$0.31^{+0.03}_{-0.02}$	$0.57^{+0.26}_{-0.36}$	...	...
50	05 35 57.85	-06 23 44.4	$0.16^{+0.02}_{-0.02}$	$1.20^{+0.16}_{-0.40}$	$0.19^{+0.04}_{-0.03}$	$0.79^{+0.48}_{-0.27}$	$0.20^{+0.03}_{-0.03}$	$2.67^{+0.30}_{-0.96}$	$0.19^{+0.06}_{-0.02}$	$1.17^{+2.78}_{-0.09}$
51	05 35 58.10	-06 14 50.9	$0.13^{+0.03}_{-0.02}$	$0.42^{+0.76}_{-0.15}$	$0.13^{+0.06}_{-0.02}$	$0.32^{+0.61}_{-0.10}$	$0.14^{+0.05}_{-0.02}$	$0.55^{+1.85}_{-0.15}$	...	...
52	05 35 58.25	-06 36 43.1	$0.35^{+0.11}_{-0.06}$	$0.43^{+0.25}_{-0.21}$	$0.48^{+0.18}_{-0.09}$	$0.46^{+0.70}_{-0.19}$	$0.56^{+0.21}_{-0.09}$	$1.07^{+1.09}_{-0.22}$	$1.02^{+0.15}_{-0.14}$	$1.93^{+1.78}_{-0.55}$
53	05 35 58.26	-06 14 04.6	$0.59^{+0.08}_{-0.20}$	$17.99^{+15.69}_{-10.52}$	$0.64^{+0.05}_{-0.16}$	$25.05^{+31.16}_{-13.54}$	$0.49^{+0.12}_{-0.13}$	$17.11^{+15.27}_{-8.44}$	$0.67^{+0.06}_{-0.18}$	$31.07^{+10.12}_{-16.59}$
54	05 35 59.75	-06 16 06.4	$0.65^{+0.29}_{-0.15}$	$0.74^{+4.61}_{-0.26}$	$1.00^{+0.22}_{-0.25}$	$1.64^{+10.29}_{-0.77}$	$1.24^{+0.11}_{-0.32}$	$3.24^{+8.21}_{-1.41}$	...	...
55	05 35 59.84	-06 42 30.5	$0.19^{+0.03}_{-0.02}$	$1.43^{+0.34}_{-0.11}$	$0.22^{+0.04}_{-0.03}$	$1.36^{+0.73}_{-0.35}$	$0.23^{+0.03}_{-0.03}$	$3.13^{+0.49}_{-0.39}$	$0.24^{+0.04}_{-0.03}$	$1.92^{+0.87}_{-0.37}$
56	05 36 00.18	-06 42 33.9	$0.51^{+0.28}_{-0.08}$	$0.20^{+0.28}_{-0.11}$	$0.82^{+0.32}_{-0.14}$	$0.27^{+0.43}_{-0.10}$	$1.13^{+0.39}_{-0.19}$	$0.79^{+0.87}_{-0.18}$	...	...
57	05 36 01.09	-06 25 07.7	$0.18^{+0.02}_{-0.02}$	$0.82^{+0.22}_{-0.40}$	$0.24^{+0.03}_{-0.02}$	$0.61^{+0.31}_{-0.16}$	$0.25^{+0.02}_{-0.02}$	$2.14^{+0.31}_{-0.18}$	$0.30^{+0.04}_{-0.03}$	$1.20^{+0.43}_{-0.09}$
58	05 36 01.10	-06 15 31.4	$0.36^{+0.06}_{-0.06}$	$0.82^{+0.29}_{-0.16}$	$0.43^{+0.08}_{-0.07}$	$1.02^{+0.56}_{-0.34}$	$0.44^{+0.07}_{-0.05}$	$1.78^{+0.65}_{-0.27}$	$0.70^{+0.13}_{-0.11}$	$2.86^{+1.60}_{-0.88}$
59	05 36 01.66	-06 42 36.2	$0.15^{+0.02}_{-0.02}$	$1.33^{+0.18}_{-0.51}$	$0.16^{+0.04}_{-0.03}$	$0.74^{+0.57}_{-0.30}$	$0.16^{+0.04}_{-0.02}$	$3.21^{+0.35}_{-1.68}$	...	...
60	05 36 05.00	-06 42 44.0	$0.14^{+0.02}_{-0.01}$	$0.10^{+0.04}_{-0.02}$	$0.17^{+0.03}_{-0.02}$	$0.14^{+0.08}_{-0.05}$	$0.21^{+0.02}_{-0.02}$	$0.35^{+0.74}_{-0.10}$	...	...
61	05 36 04.98	-06 46 41.4	$0.32^{+0.08}_{-0.06}$	$0.34^{+0.12}_{-0.21}$	$0.43^{+0.13}_{-0.08}$	$0.33^{+0.32}_{-0.14}$	$0.51^{+0.15}_{-0.08}$	$0.93^{+0.49}_{-0.16}$	$0.93^{+0.18}_{-0.06}$	$1.38^{+1.01}_{-0.25}$
62	05 36 05.08	-06 29 32.2	$0.43^{+0.13}_{-0.09}$	$0.91^{+0.70}_{-0.36}$	$0.55^{+0.20}_{-0.11}$	$1.37^{+1.75}_{-0.65}$	$0.57^{+0.21}_{-0.10}$	$2.16^{+2.55}_{-0.77}$	$0.96^{+0.14}_{-0.16}$	$4.44^{+3.29}_{-1.95}$
63	05 36 05.16	-06 25 25.4	$0.32^{+0.07}_{-0.07}$	$0.62^{+0.22}_{-0.26}$	$0.39^{+0.11}_{-0.08}$	$0.63^{+0.50}_{-0.27}$	$0.42^{+0.10}_{-0.07}$	$1.39^{+0.59}_{-0.24}$	$0.68^{+0.18}_{-0.09}$	$2.01^{+1.58}_{-0.61}$
64	05 36 06.59	-06 31 43.0	$0.22^{+0.08}_{-0.05}$	$1.56^{+1.16}_{-0.43}$	$0.28^{+0.11}_{-0.07}$	$1.84^{+2.32}_{-0.82}$	$0.27^{+0.07}_{-0.06}$	$3.26^{+1.48}_{-0.75}$	$0.31^{+0.13}_{-0.06}$	$2.61^{+3.57}_{-0.83}$
65	05 36 06.65	-06 32 17.2	$0.55^{+0.26}_{-0.09}$	$0.38^{+0.63}_{-0.11}$	$0.86^{+0.30}_{-0.15}$	$0.70^{+1.08}_{-0.27}$	$1.12^{+0.30}_{-0.20}$	$1.56^{+1.78}_{-0.50}$	...	...
66	05 36 06.66	-06 14 25.9	$0.53^{+0.11}_{-0.09}$	$0.64^{+0.43}_{-0.16}$	$0.78^{+0.18}_{-0.13}$	$1.22^{+1.06}_{-0.43}$	$0.92^{+0.20}_{-0.17}$	$2.24^{+1.78}_{-0.65}$	$1.33^{+0.04}_{-0.13}$	$4.09^{+2.80}_{-1.30}$
67	05 36 06.93	-06 18 53.4	$0.14^{+0.04}_{-0.01}$	$0.01^{+0.04}_{-0.01}$	$0.19^{+0.05}_{-0.01}$	$0.03^{+0.06}_{-0.01}$	$0.24^{+0.05}_{-0.03}$	$0.10^{+0.31}_{-0.03}$	...	...
68	05 36 08.29	-06 48 36.3	$0.37^{+0.03}_{-0.03}$	$0.58^{+0.12}_{-0.06}$	$0.49^{+0.04}_{-0.04}$	$0.75^{+0.23}_{-0.15}$	$0.53^{+0.04}_{-0.03}$	$1.43^{+0.29}_{-0.17}$	$0.93^{+0.06}_{-0.06}$	$2.68^{+0.74}_{-0.50}$
69	05 36 08.34	-06 24 37.9	$0.13^{+0.02}_{-0.01}$	$0.15^{+0.11}_{-0.04}$	$0.15^{+0.03}_{-0.02}$	$0.18^{+0.13}_{-0.09}$	$0.18^{+0.03}_{-0.02}$	$0.42^{+1.17}_{-0.14}$	...	...
70	05 36 08.57	-06 40 33.6	$0.13^{+0.03}_{-0.02}$	$3.02^{+1.16}_{-0.55}$	$...^{+0.00}_{-0.00}$	...	...	...	$0.09^{+0.04}_{-0.01}$	$1.99^{+1.39}_{-0.46}$
71	05 36 09.35	-06 17 10.8	$0.24^{+0.03}_{-0.02}$	$0.52^{+0.09}_{-0.25}$	$0.30^{+0.03}_{-0.02}$	$0.40^{+0.09}_{-0.08}$	$0.34^{+0.02}_{-0.02}$	$1.36^{+0.04}_{-0.04}$	$0.50^{+0.04}_{-0.02}$	$1.19^{+0.24}_{-0.11}$
72	05 36 09.49	-06 18 36.3	$0.26^{+0.06}_{-0.05}$	$0.19^{+0.25}_{-0.09}$	$0.33^{+0.09}_{-0.06}$	$0.27^{+0.21}_{-0.11}$	$0.39^{+0.09}_{-0.06}$	$1.03^{+0.21}_{-0.32}$	$0.66^{+0.16}_{-0.01}$	$1.05^{+0.76}_{-0.03}$
73	05 36 09.52	-06 24 33.7	$0.20^{+0.07}_{-0.04}$	$6.21^{+6.79}_{-1.97}$	$0.20^{+0.11}_{-0.05}$	$6.17^{+13.10}_{-2.83}$	$0.16^{+0.06}_{-0.03}$	$7.57^{+5.47}_{-1.62}$	$0.17^{+0.11}_{-0.04}$	$5.29^{+10.28}_{-1.93}$
74	05 36 10.19	-06 18 54.8	$0.73^{+0.04}_{-0.19}$	$17.03^{+15.78}_{-9.48}$	$0.75^{+0.05}_{-0.16}$	$23.25^{+27.23}_{-12.47}$	$0.70^{+0.06}_{-0.21}$	$23.43^{+13.11}_{-13.19}$	$0.78^{+0.06}_{-0.15}$	$32.93^{+9.22}_{-16.05}$
75	05 36 10.44	-06 20 01.5	$1.00^{+0.15}_{-0.15}$	$3.16^{+2.84}_{-1.12}$	$1.25^{+0.03}_{-0.07}$	$6.50^{+3.47}_{-1.85}$	$1.24^{+0.05}_{-0.07}$	$10.72^{+4.52}_{-2.99}$	$1.21^{+0.08}_{-0.09}$	$15.70^{+6.18}_{-3.84}$
76	05 36 11.12	-06 18 14.1	$0.14^{+0.04}_{-0.02}$	$3.72^{+1.77}_{-0.72}$	$0.11^{+0.05}_{-0.01}$	$1.89^{+2.67}_{-0.34}$	$0.10^{+0.04}_{-0.00}$	$4.80^{+2.24}_{-0.19}$	$0.10^{+0.05}_{-0.02}$	$2.52^{+2.31}_{-0.55}$
77	05 36 11.31	-06 16 56.0	$0.15^{+0.04}_{-0.02}$	$1.99^{+1.03}_{-0.46}$	$0.13^{+0.06}_{-0.02}$	$1.03^{+2.32}_{-0.30}$	$0.13^{+0.05}_{-0.01}$	$4.16^{+1.17}_{-0.83}$	$0.13^{+0.06}_{-0.02}$	$1.63^{+3.64}_{-0.22}$
78	05 36 11.46	-06 22 22.1	$0.41^{+0.10}_{-0.09}$	$0.36^{+0.84}_{-0.18}$	$0.60^{+0.16}_{-0.14}$	$0.44^{+1.54}_{-0.19}$	$0.73^{+0.19}_{-0.17}$	$1.18^{+2.33}_{-0.34}$	$1.21^{+0.10}_{-0.13}$	$1.79^{+2.69}_{-0.44}$
79	05 36 11.67	-06 24 58.4	$0.17^{+0.04}_{-0.03}$	$4.49^{+3.06}_{-1.17}$	$0.16^{+0.07}_{-0.03}$	$3.55^{+5.18}_{-1.33}$	$0.13^{+0.05}_{-0.02}$	$6.03^{+2.88}_{-0.87}$	$0.14^{+0.07}_{-0.03}$	$3.62^{+4.93}_{-1.09}$
80	05 36 12.61	-06 23 39.6	$0.14^{+0.01}_{-0.01}$	$0.23^{+0.14}_{-0.04}$	$0.17^{+0.02}_{-0.01}$	$0.31^{+0.10}_{-0.07}$	$0.20^{+0.02}_{-0.02}$	$2.03^{+0.13}_{-1.01}$	...	...
81	05 36 12.97	-06 23 33.0	$0.22^{+0.03}_{-0.02}$	$0.08^{+0.04}_{-0.03}$	$0.28^{+0.04}_{-0.03}$	$0.14^{+0.06}_{-0.05}$	$0.35^{+0.04}_{-0.03}$	$0.83^{+0.06}_{-0.41}$	...	...
82	05 36 12.97	-06 23 33.0	$0.27^{+0.08}_{-0.04}$	$0.06^{+0.40}_{-0.03}$	$0.38^{+0.11}_{-0.06}$	$0.12^{+0.46}_{-0.08}$	$0.48^{+0.15}_{-0.07}$	$0.64^{+0.57}_{-0.38}$	...	...
83	05 36 13.15	-06 25 41.1	$0.25^{+0.04}_{-0.03}$	$1.25^{+0.33}_{-0.17}$	$0.32^{+0.04}_{-0.03}$	$1.44^{+0.58}_{-0.36}$	$0.31^{+0.02}_{-0.03}$	$2.54^{+0.45}_{-0.25}$	$0.39^{+0.05}_{-0.04}$	$2.45^{+0.92}_{-0.52}$
84	05 36 13.45	-06 43 55.1	...	...	$...^{+0.00}_{-0.00}$	...	...	...	...	...
85	05 36 14.76	-06 13 16.9	$0.42^{+0.07}_{-0.06}$	$1.45^{+0.56}_{-0.37}$	$0.51^{+0.09}_{-0.08}$	$2.09^{+1.02}_{-0.70}$	$0.47^{+0.08}_{-0.06}$	$2.74^{+1.14}_{-0.59}$	$0.76^{+0.10}_{-0.13}$	$5.21^{+2.18}_{-1.77}$
86	05 36 15.07	-06 17 36.9	$0.88^{+0.27}_{-0.13}$	$0.70^{+0.57}_{-0.19}$	$1.30^{+0.15}_{-0.14}$	$1.42^{+0.67}_{-0.35}$	$1.63^{+0.05}_{-0.11}$	$3.16^{+1.09}_{-0.75}$	...	...
87	05 36 15.60	-06 27 20.0	$0.21^{+0.03}_{-0.02}$	$1.87^{+0.80}_{-0.37}$	$0.26^{+0.05}_{-0.04}$	$2.25^{+1.47}_{-0.70}$	$0.25^{+0.03}_{-0.03}$	$3.84^{+0.88}_{-0.60}$	$0.28^{+0.05}_{-0.04}$	$2.90^{+1.65}_{-0.78}$

Table 3.8: continued.

ID	RA (J2000)	DEC (J2000)	Mass ($M_\odot$, DM97)	Age (Myr, DM97)	Mass ($M_\odot$, D08)	Age (Myr, D08)	Mass ($M_\odot$, S00)	Age (Myr, S00)	Mass ($M_\odot$, B98)	Age (Myr, B98)
88	05 36 15.84	-06 14 50.7	$0.30^{+0.07}_{-0.05}$	$1.67^{+1.26}_{-0.43}$	$0.38^{+0.08}_{-0.06}$	$2.24^{+2.14}_{-0.84}$	$0.35^{+0.04}_{-0.04}$	$3.09^{+1.37}_{-0.62}$	$0.47^{+0.10}_{-0.08}$	$3.88^{+2.73}_{-1.28}$
89	05 36 17.11	-06 28 20.2	$0.16^{+0.07}_{-0.06}$	$11.74^{+14.87}_{-5.92}$	$0.14^{+0.12}_{-0.02}$	$8.57^{+31.43}_{-3.57}$	$0.11^{+0.07}_{-0.01}$	$9.73^{+14.56}_{-2.18}$	$0.11^{+0.09}_{-0.03}$	$6.40^{+15.90}_{-2.45}$
90	05 36 17.23	-06 17 24.5	$0.15^{+0.01}_{-0.01}$	$0.12^{+0.06}_{-0.03}$	$0.19^{+0.02}_{-0.02}$	$0.18^{+0.09}_{-0.06}$	$0.23^{+0.02}_{-0.02}$	$0.47^{+0.99}_{-0.16}$	...	...
91	05 36 18.48	-06 20 38.7	$0.43^{+0.14}_{-0.08}$	$0.95^{+1.16}_{-0.31}$	$0.56^{+0.21}_{-0.11}$	$1.45^{+2.76}_{-0.61}$	$0.57^{+0.21}_{-0.10}$	$2.24^{+3.20}_{-0.67}$	$0.95^{+0.11}_{-0.17}$	$4.61^{+4.45}_{-1.82}$
92	05 36 18.88	-06 22 04.2	$0.25^{+0.02}_{-0.02}$	$2.33^{+0.44}_{-0.29}$	$0.32^{+0.03}_{-0.03}$	$3.27^{+0.86}_{-0.60}$	$0.29^{+0.02}_{-0.02}$	$4.32^{+0.46}_{-0.32}$	$0.34^{+0.04}_{-0.03}$	$4.22^{+1.18}_{-0.77}$
93	05 36 19.09	-06 22 50.6	$0.14^{+0.05}_{-0.03}$	$5.07^{+4.00}_{-1.55}$	$0.11^{+0.07}_{-0.00}$	$2.50^{+6.87}_{-0.54}$	...	...	$0.10^{+0.07}_{-0.01}$	$3.06^{+5.15}_{-0.74}$
94	05 36 19.38	-06 25 51.3	$0.16^{+0.02}_{-0.02}$	$0.88^{+0.19}_{-0.48}$	$0.19^{+0.03}_{-0.03}$	$0.58^{+0.28}_{-0.20}$	$0.21^{+0.03}_{-0.03}$	$2.39^{+0.16}_{-0.88}$	...	...
95	05 36 21.10	-06 17 17.3	$0.16^{+0.01}_{-0.01}$	$0.28^{+0.21}_{-0.05}$	$0.20^{+0.01}_{-0.01}$	$0.40^{+0.09}_{-0.07}$	$0.22^{+0.01}_{-0.01}$	$2.08^{+0.09}_{-0.17}$	...	...
96	05 36 21.16	-06 26 56.9	$0.19^{+0.02}_{-0.01}$	$4.84^{+1.04}_{-0.71}$	$0.19^{+0.03}_{-0.02}$	$4.58^{+1.85}_{-1.09}$	$0.16^{+0.02}_{-0.02}$	$6.48^{+1.02}_{-0.64}$	$0.17^{+0.03}_{-0.02}$	$4.52^{+1.50}_{-0.87}$
97	05 36 21.57	-06 22 52.4	$0.38^{+0.11}_{-0.07}$	$0.65^{+0.58}_{-0.19}$	$0.50^{+0.18}_{-0.10}$	$0.89^{+1.48}_{-0.36}$	$0.53^{+0.18}_{-0.09}$	$1.59^{+1.73}_{-0.37}$	$0.91^{+0.15}_{-0.16}$	$2.98^{+2.92}_{-1.07}$
98	05 36 21.84	-06 26 02.0	$0.35^{+0.05}_{-0.03}$	$0.37^{+0.07}_{-0.16}$	$0.49^{+0.08}_{-0.05}$	$0.37^{+0.20}_{-0.10}$	$0.58^{+0.09}_{-0.05}$	$0.95^{+0.33}_{-0.11}$	$1.07^{+0.07}_{-0.09}$	$1.70^{+0.59}_{-0.38}$
99	05 36 21.88	-06 23 29.9	$0.24^{+0.07}_{-0.02}$	$0.02^{+1.04}_{-0.01}$	$0.35^{+0.10}_{-0.06}$	$0.06^{+3.24}_{-0.03}$	$0.46^{+0.11}_{-0.06}$	$0.44^{+0.63}_{-0.31}$	...	...
100	05 36 21.96	-06 41 42.0	$0.15^{+0.04}_{-0.02}$	$0.27^{+0.58}_{-0.10}$	$0.18^{+0.06}_{-0.04}$	$0.36^{+0.46}_{-0.18}$	$0.21^{+0.05}_{-0.04}$	$2.13^{+0.23}_{-1.42}$	...	...
101	05 36 22.47	-06 23 44.8	$0.43^{+0.16}_{-0.09}$	$1.14^{+5.05}_{-0.40}$	$0.54^{+0.18}_{-0.11}$	$1.70^{+7.39}_{-0.76}$	$0.53^{+0.19}_{-0.09}$	$2.46^{+6.72}_{-0.75}$	$0.88^{+0.12}_{-0.17}$	$4.94^{+7.81}_{-2.04}$
102	05 36 23.26	-06 19 37.5	$0.22^{+0.09}_{-0.04}$	$1.59^{+1.55}_{-0.44}$	$0.28^{+0.11}_{-0.07}$	$1.90^{+2.64}_{-0.84}$	$0.27^{+0.06}_{-0.06}$	$3.32^{+1.49}_{-0.80}$	$0.31^{+0.13}_{-0.06}$	$2.66^{+4.25}_{-0.87}$
103	05 36 24.48	-06 22 23.2	$0.18^{+0.03}_{-0.02}$	$0.19^{+0.36}_{-0.07}$	$0.23^{+0.03}_{-0.03}$	$0.30^{+0.22}_{-0.11}$	$0.27^{+0.03}_{-0.02}$	$1.52^{+0.35}_{-0.77}$	...	...
104	05 36 24.54	-06 52 34.2	$0.16^{+0.01}_{-0.01}$	$1.37^{+0.11}_{-0.11}$	$0.19^{+0.02}_{-0.02}$	$0.99^{+0.31}_{-0.21}$	$0.17^{+0.03}_{-0.01}$	$3.02^{+0.18}_{-0.50}$	$0.19^{+0.03}_{-0.02}$	$1.44^{+1.40}_{-0.19}$
105	05 36 25.13	-06 44 41.9	$0.56^{+0.45}_{-0.13}$	$0.22^{+0.49}_{-0.13}$	$0.92^{+0.40}_{-0.25}$	$0.34^{+0.70}_{-0.17}$	$1.28^{+0.40}_{-0.35}$	$0.92^{+1.48}_{-0.32}$	...	...
106	05 36 25.28	-06 23 07.2	$0.11^{+0.03}_{-0.04}$	$2.92^{+1.79}_{-1.65}$	$\cdots^{+0.00}_{-0.00}$	...	...	...	...	...
107	05 36 25.41	-06 24 31.2	$0.14^{+0.04}_{-0.02}$	$1.80^{+0.59}_{-0.61}$	$0.12^{+0.06}_{-0.01}$	$0.71^{+1.49}_{-0.15}$	$0.12^{+0.05}_{-0.01}$	$3.13^{+1.26}_{-1.35}$	...	...
108	05 36 25.55	-06 51 28.3	$0.15^{+0.02}_{-0.02}$	$1.51^{+0.34}_{-0.34}$	$0.16^{+0.04}_{-0.03}$	$0.93^{+0.80}_{-0.34}$	$0.16^{+0.03}_{-0.03}$	$3.50^{+0.42}_{-1.77}$	$0.16^{+0.07}_{-0.01}$	$1.35^{+5.86}_{-0.14}$
109	05 36 26.08	-06 26 15.5	$0.24^{+0.10}_{-0.05}$	$3.18^{+4.00}_{-0.96}$	$0.29^{+0.13}_{-0.07}$	$4.34^{+6.75}_{-1.97}$	$0.25^{+0.07}_{-0.06}$	$5.49^{+3.27}_{-1.38}$	$0.30^{+0.14}_{-0.07}$	$5.04^{+7.69}_{-2.06}$
110	05 36 26.71	-06 26 29.0	$0.28^{+0.07}_{-0.04}$	$0.05^{+0.12}_{-0.02}$	$0.39^{+0.12}_{-0.07}$	$0.11^{+0.14}_{-0.05}$	$0.50^{+0.16}_{-0.08}$	$0.61^{+0.23}_{-0.30}$	...	...
111	05 36 26.83	-06 24 57.5	$0.15^{+0.04}_{-0.02}$	$0.36^{+0.70}_{-0.14}$	$0.17^{+0.06}_{-0.04}$	$0.42^{+0.63}_{-0.19}$	$0.19^{+0.05}_{-0.04}$	$2.18^{+0.43}_{-1.56}$	...	...
112	05 36 27.01	-06 21 07.6	$0.30^{+0.03}_{-0.07}$	$39.72^{+5.67}_{-16.84}$	$0.36^{+0.04}_{-0.11}$	$59.50^{+24.98}_{-31.27}$	$0.24^{+0.03}_{-0.06}$	$34.14^{+8.34}_{-13.54}$	$0.30^{+0.03}_{-0.09}$	$42.36^{+4.58}_{-21.97}$
113	05 36 27.72	-06 23 12.3	$0.13^{+0.03}_{-0.01}$	$0.04^{+0.06}_{-0.02}$	$0.17^{+0.05}_{-0.01}$	$0.04^{+0.09}_{-0.02}$	$0.22^{+0.04}_{-0.03}$	$0.15^{+0.41}_{-0.05}$	...	...
114	05 36 27.89	-06 25 36.0	$0.24^{+0.10}_{-0.05}$	$1.16^{+0.76}_{-0.47}$	$0.30^{+0.10}_{-0.07}$	$1.26^{+1.31}_{-0.59}$	$0.31^{+0.07}_{-0.05}$	$2.39^{+0.94}_{-0.45}$	$0.38^{+0.15}_{-0.06}$	$2.21^{+2.56}_{-0.69}$
115	05 36 28.10	-06 44 32.6	$0.29^{+0.12}_{-0.07}$	$1.27^{+1.09}_{-0.45}$	$0.35^{+0.12}_{-0.08}$	$1.54^{+1.71}_{-0.70}$	$0.35^{+0.08}_{-0.07}$	$2.50^{+1.33}_{-0.53}$	$0.46^{+0.16}_{-0.09}$	$2.90^{+3.07}_{-1.09}$
116	05 36 29.06	-06 38 40.7	$0.08^{+0.12}_{-0.03}$	$0.64^{+9.31}_{-0.38}$	$\cdots^{+0.00}_{-0.00}$	...	...	...	...	...
117	05 36 29.59	-06 38 50.4	$0.17^{+0.02}_{-0.02}$	$1.68^{+0.33}_{-0.15}$	$0.19^{+0.04}_{-0.03}$	$1.43^{+0.76}_{-0.44}$	$0.17^{+0.04}_{-0.02}$	$3.54^{+0.38}_{-0.93}$	$0.20^{+0.04}_{-0.03}$	$1.91^{+1.95}_{-0.36}$
118	05 36 30.10	-06 23 10.2	$0.42^{+0.12}_{-0.08}$	$1.08^{+1.18}_{-0.34}$	$0.52^{+0.18}_{-0.11}$	$1.58^{+2.59}_{-0.69}$	$0.51^{+0.18}_{-0.09}$	$2.31^{+2.83}_{-0.64}$	$0.85^{+0.13}_{-0.17}$	$4.62^{+4.55}_{-1.91}$
119	05 36 30.23	-06 42 46.1	$0.29^{+0.08}_{-0.05}$	$0.51^{+2.61}_{-0.27}$	$0.37^{+0.10}_{-0.06}$	$0.42^{+5.19}_{-0.16}$	$0.42^{+0.07}_{-0.06}$	$1.16^{+2.60}_{-0.20}$	$0.69^{+0.13}_{-0.11}$	$1.51^{+3.75}_{-0.30}$
120	05 36 30.50	-06 23 56.6	$0.20^{+0.06}_{-0.05}$	$12.11^{+10.53}_{-4.75}$	$0.19^{+0.10}_{-0.05}$	$11.35^{+20.32}_{-5.38}$	$0.15^{+0.06}_{-0.03}$	$11.31^{+9.13}_{-3.07}$	$0.16^{+0.09}_{-0.05}$	$8.65^{+12.86}_{-3.97}$
121	05 36 30.52	-06 42 03.2	$0.14^{+0.04}_{-0.03}$	$5.42^{+4.17}_{-1.37}$	$0.10^{+0.06}_{-0.00}$	$2.56^{+6.39}_{-0.01}$	...	...	$0.09^{+0.05}_{-0.01}$	$3.18^{+4.08}_{-0.66}$
122	05 36 30.96	-06 52 41.0	...	...	$\cdots^{+0.00}_{-0.00}$	...	...	...	...	...
123	05 36 31.84	-06 23 23.1	$0.15^{+0.05}_{-0.03}$	$4.42^{+4.17}_{-1.11}$	$0.12^{+0.07}_{-0.01}$	$2.63^{+6.52}_{-0.59}$	$0.11^{+0.05}_{-0.00}$	$5.39^{+3.95}_{-0.27}$	$0.12^{+0.07}_{-0.02}$	$3.05^{+5.11}_{-0.76}$
124	05 36 32.38	-06 19 19.9	$1.89^{+0.11}_{-0.11}$	$3.83^{+1.10}_{-0.96}$	$1.96^{+0.07}_{-0.10}$	$3.67^{+0.99}_{-0.73}$	$1.72^{+0.10}_{-0.08}$	$7.30^{+1.42}_{-1.23}$	...	...
125	05 36 32.42	-06 40 43.0	$0.17^{+0.01}_{-0.01}$	$1.29^{+0.09}_{-0.14}$	$0.19^{+0.02}_{-0.02}$	$0.90^{+0.29}_{-0.22}$	$0.20^{+0.02}_{-0.02}$	$2.81^{+0.19}_{-0.59}$	$0.20^{+0.03}_{-0.02}$	$1.34^{+0.39}_{-0.16}$
126	05 36 32.82	-06 39 54.9	$0.54^{+0.11}_{-0.10}$	$1.79^{+1.17}_{-0.61}$	$0.69^{+0.16}_{-0.14}$	$3.10^{+2.61}_{-1.27}$	$0.68^{+0.16}_{-0.13}$	$4.41^{+3.17}_{-1.64}$	$0.99^{+0.06}_{-0.13}$	$7.86^{+4.21}_{-2.64}$
127	05 36 32.89	-06 44 20.9	$0.35^{+0.16}_{-0.10}$	$0.68^{+5.85}_{-0.40}$	$0.43^{+0.20}_{-0.12}$	$0.81^{+10.19}_{-0.47}$	$0.46^{+0.20}_{-0.10}$	$1.55^{+7.47}_{-0.61}$	$0.76^{+0.22}_{-0.18}$	$2.53^{+8.16}_{-0.94}$
128	05 36 33.81	-06 19 27.0	$0.15^{+0.04}_{-0.02}$	$1.08^{+0.47}_{-0.63}$	$0.17^{+0.07}_{-0.04}$	$0.60^{+0.96}_{-0.27}$	$0.18^{+0.06}_{-0.04}$	$2.49^{+0.75}_{-1.76}$	...	...
129	05 36 35.23	-06 50 12.2	$0.14^{+0.04}_{-0.02}$	$2.51^{+1.22}_{-0.52}$	$0.11^{+0.06}_{-0.01}$	$1.11^{+2.54}_{-0.14}$	$0.11^{+0.04}_{-0.00}$	$4.24^{+1.49}_{-0.09}$	$0.10^{+0.06}_{-0.01}$	$1.80^{+2.92}_{-0.32}$
130	05 36 35.76	-06 42 49.9	$0.27^{+0.14}_{-0.07}$	$1.47^{+5.22}_{-0.66}$	$0.34^{+0.14}_{-0.09}$	$1.87^{+6.00}_{-0.99}$	$0.33^{+0.10}_{-0.07}$	$2.86^{+4.40}_{-0.90}$	$0.42^{+0.18}_{-0.10}$	$3.11^{+6.94}_{-1.25}$
131	05 36 36.93	-06 33 24.2	$0.36^{+0.08}_{-0.07}$	$0.11^{+0.19}_{-0.05}$	$0.53^{+0.14}_{-0.11}$	$0.22^{+0.24}_{-0.10}$	$0.67^{+0.21}_{-0.14}$	$0.82^{+0.42}_{-0.26}$	$1.21^{+0.10}_{-0.08}$	$1.03^{+0.56}_{-0.02}$
132	05 36 40.69	-06 30 09.3	$0.42^{+0.13}_{-0.08}$	$0.85^{+0.69}_{-0.29}$	$0.55^{+0.20}_{-0.11}$	$1.28^{+1.70}_{-0.57}$	$0.57^{+0.21}_{-0.10}$	$2.05^{+2.18}_{-0.65}$	$0.96^{+0.13}_{-0.17}$	$4.25^{+3.24}_{-1.76}$

Table 3.8: continued.

ID	RA (J2000)	DEC (J2000)	Mass ($M_\odot$, DM97)	Age (Myr, DM97)	Mass ($M_\odot$, D08)	Age (Myr, D08)	Mass ($M_\odot$, S00)	Age (Myr, S00)	Mass ($M_\odot$, B98)	Age (Myr, B98)
133	05 36 40.69	-06 52 04.5	$0.31^{+0.05}_{-0.05}$	$0.85^{+0.17}_{-0.16}$	$0.37^{+0.06}_{-0.05}$	$0.90^{+0.36}_{-0.26}$	$0.38^{+0.04}_{-0.03}$	$1.78^{+0.28}_{-0.18}$	$0.55^{+0.09}_{-0.06}$	$2.25^{+0.98}_{-0.58}$
134	05 36 40.94	-06 41 17.8	$0.16^{+0.01}_{-0.01}$	$0.69^{+0.25}_{-0.29}$	$0.19^{+0.02}_{-0.02}$	$0.54^{+0.16}_{-0.12}$	$0.21^{+0.02}_{-0.02}$	$2.32^{+0.11}_{-0.47}$	...	...
135	05 36 41.35	-06 34 00.4	...	...	$0.41^{+0.16}_{-0.06}$	$0.03^{+0.06}_{-0.02}$	$0.57^{+0.24}_{-0.05}$	$0.10^{+0.34}_{-0.03}$	...	...
136	05 36 41.98	-06 20 45.4	$0.14^{+0.04}_{-0.02}$	$2.56^{+1.38}_{-0.54}$	$0.11^{+0.06}_{-0.00}$	$1.08^{+2.41}_{-0.08}$	$0.10^{+0.04}_{-0.00}$	$4.20^{+1.82}_{-0.03}$	$0.10^{+0.06}_{-0.01}$	$1.75^{+2.38}_{-0.29}$
137	05 36 43.77	-06 15 28.6	$0.19^{+0.07}_{-0.03}$	$1.02^{+0.50}_{-0.54}$	$0.24^{+0.09}_{-0.05}$	$0.81^{+0.96}_{-0.36}$	$0.26^{+0.06}_{-0.05}$	$2.40^{+0.48}_{-0.76}$	$0.29^{+0.11}_{-0.03}$	$1.41^{+3.97}_{-0.20}$
138	05 36 45.21	-06 28 09.6	$0.20^{+0.07}_{-0.04}$	$0.18^{+0.37}_{-0.08}$	$0.25^{+0.07}_{-0.05}$	$0.29^{+0.26}_{-0.14}$	$0.29^{+0.06}_{-0.05}$	$1.35^{+0.16}_{-0.72}$	...	...
139	05 36 45.79	-06 48 16.0	...	...	$0.16^{+0.02}_{-0.03}$	$65.63^{+21.97}_{-24.53}$	...	...	$0.14^{+0.01}_{-0.04}$	$47.06^{+1.76}_{-20.07}$
140	05 36 46.62	-06 39 50.0	$0.15^{+0.02}_{-0.02}$	$2.46^{+0.56}_{-0.24}$	$0.14^{+0.03}_{-0.02}$	$1.53^{+1.13}_{-0.44}$	$0.12^{+0.03}_{-0.01}$	$4.54^{+0.61}_{-0.36}$	$0.13^{+0.04}_{-0.02}$	$2.06^{+2.27}_{-0.29}$
141	05 36 50.14	-06 41 29.2	$0.55^{+0.29}_{-0.10}$	$0.39^{+0.78}_{-0.11}$	$0.85^{+0.31}_{-0.18}$	$0.72^{+1.22}_{-0.30}$	$1.10^{+0.30}_{-0.23}$	$1.59^{+2.21}_{-0.52}$	...	...
142	05 36 50.23	-06 48 58.2	$0.15^{+0.01}_{-0.01}$	$0.16^{+0.02}_{-0.02}$	$0.20^{+0.01}_{-0.01}$	$0.25^{+0.04}_{-0.04}$	$0.23^{+0.01}_{-0.01}$	$1.64^{+0.12}_{-0.37}$	...	...
143	05 36 54.41	-06 51 05.5	$0.14^{+0.06}_{-0.05}$	$11.13^{+13.19}_{-4.97}$	$0.11^{+0.10}_{-0.01}$	$6.56^{+24.94}_{-0.88}$	$0.13^{+0.05}_{-0.02}$	$21.79^{+11.15}_{-8.11}$	$0.09^{+0.07}_{-0.02}$	$5.57^{+12.64}_{-1.67}$
144	05 37 49.54	-06 56 27.4	$0.20^{+0.03}_{-0.03}$	$0.13^{+0.14}_{-0.03}$	$0.26^{+0.03}_{-0.03}$	$0.20^{+0.08}_{-0.06}$	$0.30^{+0.03}_{-0.03}$	$1.18^{+0.05}_{-0.48}$	...	...
145	05 37 51.72	-06 56 51.9	$0.25^{+0.06}_{-0.03}$	$0.06^{+0.16}_{-0.03}$	$0.34^{+0.08}_{-0.05}$	$0.12^{+0.15}_{-0.05}$	$0.42^{+0.09}_{-0.07}$	$0.73^{+0.20}_{-0.38}$	...	...
146	05 37 53.28	-07 02 27.2	$0.19^{+0.03}_{-0.02}$	$4.00^{+1.56}_{-0.77}$	$0.20^{+0.05}_{-0.04}$	$4.13^{+3.06}_{-1.44}$	$0.17^{+0.04}_{-0.03}$	$5.89^{+1.73}_{-0.71}$	$0.20^{+0.05}_{-0.04}$	$4.29^{+3.13}_{-1.23}$
147	05 37 54.48	-06 57 31.1	$0.50^{+0.22}_{-0.15}$	$0.67^{+2.61}_{-0.32}$	$0.72^{+0.28}_{-0.24}$	$1.21^{+4.48}_{-0.70}$	$0.82^{+0.28}_{-0.27}$	$2.16^{+5.56}_{-0.98}$	$1.22^{+0.09}_{-0.22}$	$4.05^{+7.16}_{-1.77}$
148	05 37 54.51	-06 56 45.5	$0.38^{+0.05}_{-0.05}$	$0.06^{+0.09}_{-0.03}$	$0.57^{+0.10}_{-0.10}$	$0.15^{+0.10}_{-0.05}$	$0.81^{+0.10}_{-0.15}$	$0.65^{+0.13}_{-0.14}$	...	...
149	05 37 55.15	-06 57 40.7	$0.15^{+0.03}_{-0.02}$	$1.22^{+0.28}_{-0.63}$	$0.16^{+0.05}_{-0.03}$	$0.62^{+0.70}_{-0.26}$	$0.16^{+0.05}_{-0.03}$	$2.96^{+0.40}_{-1.93}$	...	...
150	05 37 55.22	-06 57 35.8	$0.16^{+0.02}_{-0.01}$	$0.23^{+0.28}_{-0.06}$	$0.20^{+0.03}_{-0.02}$	$0.35^{+0.15}_{-0.11}$	$0.23^{+0.02}_{-0.02}$	$1.97^{+0.05}_{-0.61}$	...	...
151	05 37 55.65	-06 57 18.1	$0.31^{+0.13}_{-0.06}$	$0.09^{+0.28}_{-0.04}$	$0.44^{+0.23}_{-0.10}$	$0.19^{+0.49}_{-0.10}$	$0.55^{+0.28}_{-0.11}$	$0.71^{+0.84}_{-0.31}$	...	...
152	05 37 55.74	-06 58 37.9	$0.23^{+0.05}_{-0.03}$	$1.08^{+0.38}_{-0.26}$	$0.30^{+0.06}_{-0.04}$	$1.10^{+0.78}_{-0.35}$	$0.31^{+0.04}_{-0.04}$	$2.24^{+0.54}_{-0.21}$	$0.37^{+0.08}_{-0.05}$	$1.98^{+1.35}_{-0.47}$
153	05 37 55.99	-06 52 33.7	$0.14^{+0.01}_{-0.01}$	$0.48^{+0.52}_{-0.15}$	$0.15^{+0.02}_{-0.02}$	$0.42^{+0.23}_{-0.14}$	$0.16^{+0.02}_{-0.02}$	$0.67^{+1.56}_{-0.17}$	...	...
154	05 38 00.67	-07 01 14.3	$0.23^{+0.04}_{-0.05}$	$25.85^{+11.93}_{-10.34}$	$0.25^{+0.09}_{-0.07}$	$29.50^{+33.28}_{-14.72}$	$0.18^{+0.04}_{-0.04}$	$22.50^{+12.37}_{-8.21}$	$0.21^{+0.05}_{-0.07}$	$21.43^{+13.05}_{-10.91}$
155	05 38 04.84	-07 02 21.6	$0.14^{+0.02}_{-0.01}$	$1.14^{+0.54}_{-0.56}$	$0.15^{+0.03}_{-0.03}$	$0.55^{+0.57}_{-0.20}$	$0.15^{+0.03}_{-0.02}$	$0.77^{+2.24}_{-0.22}$	...	...
156	05 38 10.50	-06 57 07.1	$0.27^{+0.05}_{-0.03}$	$1.61^{+0.64}_{-0.35}$	$0.34^{+0.05}_{-0.04}$	$2.10^{+1.08}_{-0.67}$	$0.32^{+0.03}_{-0.03}$	$3.10^{+0.69}_{-0.54}$	$0.40^{+0.07}_{-0.05}$	$3.29^{+1.60}_{-0.91}$
157	05 38 13.45	-07 06 43.3	$0.57^{+0.57}_{-0.17}$	$0.31^{+4.42}_{-0.18}$	$0.92^{+0.45}_{-0.34}$	$0.56^{+7.23}_{-0.35}$	$1.24^{+0.36}_{-0.44}$	$1.35^{+7.06}_{-0.65}$	...	...
158	05 38 19.52	-06 55 29.7	$0.25^{+0.10}_{-0.06}$	$0.75^{+0.39}_{-0.43}$	$0.30^{+0.11}_{-0.07}$	$0.60^{+0.75}_{-0.27}$	$0.33^{+0.08}_{-0.06}$	$1.60^{+0.53}_{-0.48}$	$0.46^{+0.16}_{-0.05}$	$1.49^{+2.05}_{-0.28}$
159	05 38 21.22	-07 01 20.3	$0.16^{+0.02}_{-0.01}$	$1.69^{+0.43}_{-0.21}$	$0.17^{+0.03}_{-0.03}$	$1.25^{+0.75}_{-0.38}$	$0.17^{+0.03}_{-0.02}$	$3.70^{+0.47}_{-1.14}$	$0.18^{+0.04}_{-0.02}$	$1.70^{+1.82}_{-0.26}$
160	05 38 34.06	-07 04 36.8	...	...	$0.20^{+0.02}_{-0.06}$	$101.66^{+4.08}_{-51.84}$	...	...	...	...
161	05 38 40.22	-06 56 53.3	$0.32^{+0.14}_{-0.08}$	$1.89^{+5.18}_{-0.80}$	$0.39^{+0.13}_{-0.09}$	$2.61^{+9.58}_{-1.34}$	$0.36^{+0.09}_{-0.07}$	$3.34^{+4.40}_{-1.09}$	$0.49^{+0.16}_{-0.11}$	$4.45^{+8.67}_{-2.00}$
162	05 38 40.59	-07 02 23.8	$0.25^{+0.22}_{-0.09}$	$1.91^{+10.93}_{-1.12}$	$0.32^{+0.23}_{-0.12}$	$2.59^{+19.02}_{-1.68}$	$0.30^{+0.18}_{-0.10}$	$3.64^{+10.95}_{-1.77}$	$0.36^{+0.26}_{-0.12}$	$3.63^{+14.46}_{-1.60}$
163	05 38 41.48	-07 01 52.6	$0.17^{+0.03}_{-0.02}$	$1.09^{+0.32}_{-0.64}$	$0.21^{+0.05}_{-0.04}$	$0.78^{+0.65}_{-0.36}$	$0.23^{+0.03}_{-0.03}$	$2.54^{+0.50}_{-0.92}$	$0.24^{+0.07}_{-0.03}$	$1.26^{+2.80}_{-0.14}$
164	05 38 41.56	-06 52 51.0	$0.16^{+0.03}_{-0.02}$	$1.31^{+0.29}_{-0.47}$	$0.19^{+0.06}_{-0.04}$	$0.91^{+0.77}_{-0.38}$	$0.20^{+0.04}_{-0.04}$	$2.87^{+0.47}_{-1.33}$	$0.19^{+0.08}_{-0.02}$	$1.35^{+5.16}_{-0.16}$
165	05 38 43.22	-06 58 08.9	...	...	$\cdots^{+0.00}_{-0.00}$	...	...	...	...	...
166	05 38 43.84	-06 58 22.3	$0.27^{+0.14}_{-0.08}$	$0.84^{+3.69}_{-0.54}$	$0.33^{+0.15}_{-0.08}$	$0.80^{+6.68}_{-0.48}$	$0.35^{+0.11}_{-0.08}$	$1.76^{+3.87}_{-0.81}$	$0.49^{+0.21}_{-0.11}$	$1.90^{+5.70}_{-0.55}$
167	05 38 44.95	-06 58 14.7	$0.35^{+0.02}_{-0.02}$	$0.63^{+0.09}_{-0.06}$	$0.45^{+0.03}_{-0.03}$	$0.77^{+0.17}_{-0.14}$	$0.48^{+0.02}_{-0.02}$	$1.48^{+0.18}_{-0.13}$	$0.81^{+0.05}_{-0.05}$	$2.59^{+0.46}_{-0.39}$
168	05 38 46.84	-07 05 08.9	$0.27^{+0.07}_{-0.05}$	$1.27^{+0.89}_{-0.36}$	$0.34^{+0.07}_{-0.06}$	$1.52^{+1.38}_{-0.62}$	$0.34^{+0.05}_{-0.05}$	$2.52^{+1.03}_{-0.52}$	$0.44^{+0.10}_{-0.07}$	$2.79^{+2.29}_{-0.93}$
169	05 38 47.17	-07 02 40.4	...	...	$0.53^{+0.76}_{-0.14}$	$0.03^{+2.60}_{-0.02}$	$0.76^{+0.91}_{-0.20}$	$0.25^{+3.24}_{-0.14}$	...	...
170	05 38 47.74	-07 06 14.9	$0.26^{+0.24}_{-0.06}$	$0.06^{+5.28}_{-0.03}$	$0.37^{+0.31}_{-0.10}$	$0.13^{+6.60}_{-0.08}$	$0.46^{+0.37}_{-0.11}$	$0.69^{+5.37}_{-0.42}$	...	...
171	05 38 47.93	-07 05 06.1	$0.14^{+0.02}_{-0.01}$	$0.11^{+0.46}_{-0.03}$	$0.18^{+0.03}_{-0.02}$	$0.16^{+1.16}_{-0.06}$	$0.22^{+0.02}_{-0.03}$	$0.36^{+1.32}_{-0.09}$	...	...
172	05 38 49.88	-07 02 35.4	$0.61^{+0.09}_{-0.34}$	$34.20^{+8.93}_{-26.11}$	$0.63^{+0.08}_{-0.30}$	$44.51^{+26.80}_{-33.82}$	$0.55^{+0.12}_{-0.27}$	$32.79^{+9.55}_{-23.50}$	...	...
173	05 38 50.44	-07 00 43.0	$0.42^{+0.58}_{-0.08}$	$0.04^{+0.88}_{-0.02}$	$0.65^{+0.56}_{-0.22}$	$0.12^{+3.62}_{-0.07}$	$0.91^{+0.68}_{-0.24}$	$0.48^{+2.43}_{-0.22}$	...	...
174	05 38 52.97	-07 05 50.6	$0.13^{+0.04}_{-0.03}$	$2.54^{+1.51}_{-0.86}$	$0.10^{+0.07}_{-0.00}$	$0.97^{+2.95}_{-0.10}$	...	...	$0.09^{+0.07}_{-0.01}$	$1.46^{+2.65}_{-0.18}$
175	05 38 53.33	-07 05 45.2	...	...	$\cdots^{+0.00}_{-0.00}$	...	...	...	...	...
176	05 38 54.45	-07 04 46.7	$0.25^{+0.04}_{-0.03}$	$1.67^{+0.74}_{-0.25}$	$0.33^{+0.04}_{-0.03}$	$2.18^{+1.45}_{-0.52}$	$0.31^{+0.02}_{-0.02}$	$3.25^{+0.95}_{-0.34}$	$0.37^{+0.06}_{-0.04}$	$3.22^{+1.70}_{-0.72}$
177	05 38 54.93	-07 07 10.9	$0.23^{+0.02}_{-0.02}$	$1.71^{+0.36}_{-0.29}$	$0.30^{+0.03}_{-0.02}$	$2.16^{+0.67}_{-0.56}$	$0.29^{+0.02}_{-0.02}$	$3.43^{+0.45}_{-0.47}$	$0.33^{+0.04}_{-0.03}$	$2.99^{+0.83}_{-0.62}$

Table 3.8: continued.

ID	RA (J2000)	DEC (J2000)	Mass ($M_\odot$, DM97)	Age (Myr, DM97)	Mass ($M_\odot$, D08)	Age (Myr, D08)	Mass ($M_\odot$, S00)	Age (Myr, S00)	Mass ($M_\odot$, B98)	Age (Myr, B98)
178	05 38 55.02	-06 56 18.6	...	...	$\cdots^{+0.00}_{-0.00}$	...	...	...	...	...
179	05 38 57.04	-06 52 59.3	$0.46^{+0.12}_{-0.10}$	$5.58^{+4.96}_{-2.07}$	$0.55^{+0.09}_{-0.10}$	$8.06^{+5.66}_{-2.99}$	$0.42^{+0.08}_{-0.05}$	$6.83^{+4.53}_{-1.80}$	$0.62^{+0.09}_{-0.11}$	$11.90^{+8.32}_{-4.21}$
180	05 40 19.41	-08 14 16.4	$0.44^{+0.09}_{-0.09}$	$0.46^{+0.27}_{-0.17}$	$0.63^{+0.16}_{-0.15}$	$0.68^{+0.75}_{-0.29}$	$0.75^{+0.18}_{-0.17}$	$1.51^{+1.10}_{-0.48}$	$1.19^{+0.10}_{-0.14}$	$2.59^{+1.70}_{-0.83}$
181	05 40 21.84	-08 08 55.9	$0.24^{+0.10}_{-0.05}$	$1.01^{+1.99}_{-0.53}$	$0.31^{+0.11}_{-0.07}$	$1.01^{+2.93}_{-0.53}$	$0.32^{+0.07}_{-0.06}$	$2.11^{+1.88}_{-0.71}$	$0.40^{+0.15}_{-0.08}$	$1.96^{+3.24}_{-0.55}$
182	05 40 24.97	-07 55 35.3	$0.20^{+0.07}_{-0.01}$	$0.01^{+0.07}_{-0.01}$	$0.28^{+0.10}_{-0.04}$	$0.05^{+0.08}_{-0.03}$	$0.37^{+0.11}_{-0.04}$	$0.11^{+0.44}_{-0.04}$	...	...
183	05 40 24.97	-08 07 33.2	$2.34^{+0.13}_{-0.36}$	$0.94^{+0.70}_{-0.33}$	$2.43^{+0.09}_{-0.27}$	$1.05^{+0.64}_{-0.35}$	$2.34^{+0.17}_{-0.15}$	$2.68^{+0.99}_{-0.78}$	...	...
184	05 40 24.97	-07 55 35.3	...	...	$0.24^{+0.06}_{-0.02}$	$0.03^{+0.05}_{-0.02}$	$0.32^{+0.07}_{-0.03}$	$0.07^{+0.29}_{-0.01}$	...	...
185	05 40 25.75	-08 11 16.8	$0.23^{+0.08}_{-0.05}$	$0.70^{+0.30}_{-0.42}$	$0.29^{+0.09}_{-0.06}$	$0.53^{+0.63}_{-0.23}$	$0.32^{+0.07}_{-0.06}$	$1.56^{+0.43}_{-0.50}$	$0.44^{+0.14}_{-0.05}$	$1.35^{+1.40}_{-0.19}$
186	05 40 27.14	-08 07 36.5	$0.25^{+0.11}_{-0.05}$	$1.55^{+3.37}_{-0.63}$	$0.32^{+0.12}_{-0.08}$	$1.98^{+6.20}_{-1.02}$	$0.31^{+0.07}_{-0.06}$	$3.07^{+3.66}_{-0.87}$	$0.37^{+0.14}_{-0.08}$	$3.01^{+6.07}_{-1.15}$
187	05 40 35.44	-07 56 36.5	$0.39^{+0.34}_{-0.16}$	$0.73^{+7.01}_{-0.48}$	$0.51^{+0.38}_{-0.21}$	$1.04^{+11.36}_{-0.71}$	$0.54^{+0.41}_{-0.20}$	$1.76^{+11.05}_{-1.00}$	$0.91^{+0.22}_{-0.26}$	$3.42^{+13.49}_{-1.56}$
188	05 40 37.36	-08 04 03.0	...	...	$3.01^{+0.18}_{-0.06}$	$1.94^{+0.16}_{-0.30}$	$3.12^{+0.12}_{-0.13}$	$1.79^{+0.38}_{-0.16}$	...	...
189	05 40 41.01	-08 02 18.6	$0.34^{+0.11}_{-0.06}$	$0.36^{+0.20}_{-0.21}$	$0.47^{+0.17}_{-0.09}$	$0.36^{+0.51}_{-0.14}$	$0.56^{+0.20}_{-0.09}$	$0.94^{+0.79}_{-0.19}$	$1.03^{+0.16}_{-0.11}$	$1.60^{+1.49}_{-0.36}$
190	05 40 42.66	-07 46 03.0	$0.15^{+0.03}_{-0.03}$	$8.54^{+4.90}_{-2.22}$	$0.12^{+0.05}_{-0.01}$	$4.97^{+6.84}_{-0.75}$	$0.12^{+0.02}_{-0.01}$	$12.38^{+3.51}_{-3.02}$	$0.10^{+0.04}_{-0.02}$	$4.67^{+4.07}_{-1.04}$
191	05 40 46.22	-08 05 24.3	$2.17^{+0.38}_{-0.47}$	$0.40^{+0.32}_{-0.14}$	$2.34^{+0.31}_{-0.43}$	$0.42^{+0.32}_{-0.16}$	$2.84^{+0.11}_{-0.22}$	$1.32^{+0.63}_{-0.43}$	...	...
192	05 40 46.40	-08 04 36.1	...	...	$0.55^{+0.15}_{-0.11}$	$0.06^{+4.66}_{-0.03}$	$0.80^{+0.17}_{-0.17}$	$0.40^{+2.59}_{-0.18}$	...	...
193	05 40 46.62	-08 07 12.8	...	...	$0.57^{+0.13}_{-0.10}$	$0.02^{+0.03}_{-0.01}$	$0.83^{+0.22}_{-0.09}$	$0.17^{+0.15}_{-0.09}$	...	...
194	05 40 46.84	-08 04 54.6	$0.21^{+0.05}_{-0.02}$	$0.04^{+0.07}_{-0.02}$	$0.27^{+0.07}_{-0.04}$	$0.08^{+0.09}_{-0.04}$	$0.35^{+0.08}_{-0.05}$	$0.32^{+0.41}_{-0.21}$	...	...
195	05 40 48.07	-08 05 58.7	...	...	$0.55^{+0.13}_{-0.11}$	$0.04^{+0.05}_{-0.02}$	$0.79^{+0.18}_{-0.12}$	$0.34^{+0.10}_{-0.17}$	...	...
196	05 40 57.49	-07 48 08.8	$0.26^{+0.16}_{-0.07}$	$0.51^{+4.48}_{-0.38}$	$0.32^{+0.20}_{-0.09}$	$0.38^{+6.95}_{-0.24}$	$0.37^{+0.18}_{-0.10}$	$1.25^{+4.65}_{-0.73}$	$0.58^{+0.30}_{-0.17}$	$1.25^{+7.44}_{-0.15}$
197	05 40 59.75	-08 06 03.2	$0.13^{+0.03}_{-0.02}$	$1.55^{+0.40}_{-0.69}$	$0.12^{+0.06}_{-0.01}$	$0.55^{+1.13}_{-0.11}$	$0.12^{+0.05}_{-0.01}$	$0.85^{+2.56}_{-0.13}$	...	...
198	05 40 59.92	-07 48 16.1	$0.32^{+0.27}_{-0.14}$	$2.17^{+14.55}_{-1.50}$	$0.40^{+0.28}_{-0.17}$	$3.10^{+24.67}_{-2.28}$	$0.35^{+0.28}_{-0.12}$	$3.74^{+14.45}_{-2.29}$	$0.48^{+0.33}_{-0.19}$	$5.00^{+17.50}_{-2.62}$
199	05 41 03.55	-07 57 46.3	$0.14^{+0.03}_{-0.03}$	$6.36^{+3.42}_{-1.51}$	$\cdots^{+0.00}_{-0.00}$	...	...	...	$0.09^{+0.03}_{-0.01}$	$3.59^{+2.63}_{-0.68}$
200	05 41 04.09	-07 43 38.6	$0.25^{+0.06}_{-0.04}$	$2.16^{+2.76}_{-1.21}$	$0.32^{+0.07}_{-0.06}$	$2.99^{+5.19}_{-1.92}$	$0.29^{+0.05}_{-0.04}$	$4.06^{+2.71}_{-1.88}$	$0.35^{+0.11}_{-0.06}$	$3.95^{+5.01}_{-1.86}$
201	05 41 04.36	-07 46 40.6	$0.18^{+0.04}_{-0.03}$	$4.72^{+2.71}_{-1.09}$	$0.16^{+0.06}_{-0.03}$	$3.93^{+4.75}_{-1.40}$	$0.14^{+0.04}_{-0.02}$	$6.23^{+2.54}_{-0.91}$	$0.15^{+0.06}_{-0.03}$	$3.96^{+4.53}_{-1.21}$
202	05 41 05.03	-07 45 34.2	$0.16^{+0.06}_{-0.03}$	$1.06^{+0.48}_{-0.63}$	$0.20^{+0.09}_{-0.05}$	$0.71^{+1.09}_{-0.34}$	$0.21^{+0.06}_{-0.05}$	$2.51^{+0.54}_{-1.37}$	$0.19^{+0.15}_{-0.00}$	$1.04^{+6.67}_{-0.02}$
203	05 41 05.49	-07 47 07.5	$2.06^{+0.05}_{-0.22}$	$3.29^{+2.01}_{-0.27}$	$1.95^{+0.16}_{-0.16}$	$4.82^{+2.01}_{-1.09}$	$1.76^{+0.12}_{-0.08}$	$7.76^{+1.49}_{-1.25}$	...	...
204	05 41 07.00	-07 47 15.9	$0.24^{+0.07}_{-0.04}$	$2.73^{+1.81}_{-0.89}$	$0.30^{+0.09}_{-0.06}$	$3.78^{+2.87}_{-1.73}$	$0.27^{+0.05}_{-0.05}$	$4.92^{+1.56}_{-1.28}$	$0.31^{+0.10}_{-0.06}$	$4.51^{+3.79}_{-1.76}$
205	05 41 07.08	-07 46 22.5	$0.24^{+0.11}_{-0.05}$	$1.74^{+4.34}_{-0.73}$	$0.30^{+0.12}_{-0.07}$	$2.23^{+6.13}_{-1.16}$	$0.29^{+0.07}_{-0.06}$	$3.48^{+3.45}_{-1.10}$	$0.33^{+0.14}_{-0.07}$	$3.07^{+6.62}_{-1.21}$
206	05 41 14.03	-08 07 57.4	$0.24^{+0.07}_{-0.04}$	$0.10^{+0.59}_{-0.05}$	$0.32^{+0.09}_{-0.06}$	$0.17^{+1.03}_{-0.09}$	$0.38^{+0.08}_{-0.06}$	$0.87^{+1.06}_{-0.45}$	...	...
207	05 41 16.25	-07 43 51.4	$0.16^{+0.03}_{-0.03}$	$9.78^{+5.73}_{-2.73}$	$0.13^{+0.04}_{-0.02}$	$6.51^{+6.82}_{-1.92}$	$0.11^{+0.03}_{-0.00}$	$8.29^{+5.32}_{-1.02}$	$0.11^{+0.04}_{-0.02}$	$5.25^{+4.55}_{-1.29}$
208	05 41 20.12	-07 55 24.0	$0.18^{+0.07}_{-0.03}$	$0.09^{+0.27}_{-0.05}$	$0.23^{+0.10}_{-0.04}$	$0.15^{+0.28}_{-0.08}$	$0.28^{+0.09}_{-0.05}$	$0.75^{+0.50}_{-0.55}$	...	...
209	05 41 25.35	-08 05 54.7	$1.77^{+0.19}_{-0.36}$	$1.09^{+0.88}_{-0.40}$	$1.94^{+0.10}_{-0.29}$	$1.36^{+0.76}_{-0.49}$	$2.07^{+0.07}_{-0.14}$	$3.22^{+1.50}_{-0.99}$	...	...
210	05 41 26.37	-07 58 17.8	$0.18^{+0.04}_{-0.03}$	$8.81^{+5.71}_{-2.65}$	$0.16^{+0.07}_{-0.03}$	$7.09^{+9.96}_{-2.77}$	$0.13^{+0.05}_{-0.02}$	$8.58^{+5.20}_{-1.51}$	$0.13^{+0.07}_{-0.03}$	$5.46^{+7.45}_{-1.69}$
211	05 41 30.59	-08 04 48.2	$0.36^{+0.07}_{-0.05}$	$0.04^{+0.08}_{-0.02}$	$0.55^{+0.13}_{-0.12}$	$0.11^{+0.12}_{-0.05}$	$0.82^{+0.15}_{-0.18}$	$0.57^{+0.20}_{-0.21}$	...	...
212	05 41 33.38	-07 59 56.3	$0.26^{+0.08}_{-0.05}$	$0.09^{+0.23}_{-0.04}$	$0.34^{+0.12}_{-0.07}$	$0.17^{+0.23}_{-0.08}$	$0.42^{+0.13}_{-0.08}$	$0.83^{+0.35}_{-0.42}$	...	...
213	05 41 41.66	-08 00 18.5	...	...	$\cdots^{+0.00}_{-0.00}$	...	...	...	...	...
214	05 41 43.74	-07 58 22.3	$0.12^{+0.02}_{-0.01}$	$0.05^{+0.06}_{-0.02}$	$0.16^{+0.03}_{-0.01}$	$0.04^{+0.09}_{-0.02}$	$0.20^{+0.03}_{-0.02}$	$0.17^{+0.42}_{-0.06}$	...	...
215	05 41 49.23	-07 57 12.3	$0.23^{+0.07}_{-0.04}$	$1.70^{+3.12}_{-0.48}$	$0.28^{+0.09}_{-0.06}$	$2.09^{+4.47}_{-0.91}$	$0.27^{+0.05}_{-0.05}$	$3.49^{+3.04}_{-0.77}$	$0.31^{+0.10}_{-0.06}$	$2.84^{+5.76}_{-0.93}$
216	05 41 49.74	-08 00 32.3	...	...	$0.86^{+0.36}_{-0.16}$	$0.07^{+0.14}_{-0.03}$	$1.28^{+0.51}_{-0.23}$	$0.36^{+0.31}_{-0.07}$	...	...
217	05 41 51.84	-08 06 56.6	$0.17^{+0.01}_{-0.01}$	$1.46^{+0.09}_{-0.06}$	$0.20^{+0.02}_{-0.02}$	$1.23^{+0.25}_{-0.22}$	$0.18^{+0.03}_{-0.01}$	$3.09^{+0.16}_{-0.02}$	$0.21^{+0.02}_{-0.02}$	$1.72^{+0.31}_{-0.24}$
218	05 41 54.66	-07 59 12.4	$0.77^{+0.42}_{-0.22}$	$0.65^{+1.39}_{-0.29}$	$1.20^{+0.24}_{-0.37}$	$1.42^{+1.63}_{-0.75}$	$1.53^{+0.07}_{-0.40}$	$3.11^{+2.64}_{-1.50}$	...	...
219	05 41 55.96	-07 58 36.6	$0.21^{+0.07}_{-0.04}$	$4.23^{+4.51}_{-1.33}$	$0.23^{+0.12}_{-0.06}$	$4.83^{+9.01}_{-2.24}$	$0.20^{+0.07}_{-0.05}$	$6.16^{+4.05}_{-1.20}$	$0.22^{+0.12}_{-0.05}$	$4.90^{+8.63}_{-1.90}$
220	05 42 05.59	-08 01 05.6	$0.35^{+0.14}_{-0.09}$	$2.44^{+6.92}_{-1.03}$	$0.43^{+0.13}_{-0.10}$	$3.51^{+11.00}_{-1.73}$	$0.37^{+0.10}_{-0.07}$	$3.95^{+6.65}_{-1.26}$	$0.52^{+0.15}_{-0.13}$	$5.77^{+9.38}_{-2.66}$
221	05 42 07.25	-08 05 24.4	$0.14^{+0.04}_{-0.03}$	$2.94^{+2.28}_{-0.88}$	$0.10^{+0.06}_{-0.00}$	$1.27^{+3.53}_{-0.46}$	...	...	$0.10^{+0.07}_{-0.01}$	$2.04^{+3.31}_{-0.40}$
222	05 42 10.51	-08 07 35.1	$0.17^{+0.02}_{-0.02}$	$2.15^{+0.60}_{-0.32}$	$0.18^{+0.04}_{-0.03}$	$1.84^{+1.07}_{-0.62}$	$0.17^{+0.03}_{-0.02}$	$4.21^{+0.58}_{-0.84}$	$0.19^{+0.04}_{-0.03}$	$2.32^{+2.98}_{-0.51}$

Table 3.8: continued.

ID	RA (J2000)	DEC (J2000)	Mass ($M_\odot$, DM97)	Age (Myr, DM97)	Mass ($M_\odot$, D08)	Age (Myr, D08)	Mass ($M_\odot$, S00)	Age (Myr, S00)	Mass ($M_\odot$, B98)	Age (Myr, B98)
223	05 42 11.04	-08 01 05.4	$0.19^{+0.03}_{-0.02}$	$4.00^{+1.77}_{-0.79}$	$0.19^{+0.05}_{-0.03}$	$3.87^{+3.06}_{-1.34}$	$0.16^{+0.04}_{-0.03}$	$5.86^{+1.68}_{-0.75}$	$0.18^{+0.05}_{-0.04}$	$4.08^{+2.98}_{-1.17}$
224	05 42 13.51	-08 10 01.5	$0.28^{+0.10}_{-0.06}$	$5.41^{+12.08}_{-2.57}$	$0.35^{+0.12}_{-0.10}$	$8.43^{+22.49}_{-4.73}$	$0.28^{+0.08}_{-0.06}$	$7.75^{+9.98}_{-2.93}$	$0.37^{+0.13}_{-0.11}$	$9.72^{+14.30}_{-5.06}$
225	05 42 14.60	-07 58 57.9	$0.22^{+0.04}_{-0.03}$	$1.25^{+0.60}_{-0.23}$	$0.29^{+0.05}_{-0.04}$	$1.36^{+1.08}_{-0.42}$	$0.29^{+0.03}_{-0.03}$	$2.65^{+0.75}_{-0.30}$	$0.34^{+0.07}_{-0.04}$	$2.20^{+1.34}_{-0.53}$
226	05 42 15.93	-08 09 37.8	$0.16^{+0.04}_{-0.02}$	$1.33^{+0.39}_{-0.53}$	$0.18^{+0.06}_{-0.04}$	$0.85^{+0.96}_{-0.36}$	$0.17^{+0.06}_{-0.03}$	$2.99^{+0.51}_{-1.85}$	$0.17^{+0.10}_{-0.01}$	$1.23^{+5.98}_{-0.11}$
227	05 42 18.11	-08 08 10.9	$0.76^{+0.24}_{-0.19}$	$1.68^{+3.62}_{-0.75}$	$1.13^{+0.09}_{-0.28}$	$3.89^{+4.95}_{-1.95}$	$1.23^{+0.06}_{-0.25}$	$6.62^{+7.09}_{-3.21}$	$1.30^{+0.05}_{-0.15}$	$10.17^{+8.99}_{-4.49}$
228	05 42 18.56	-07 59 23.0	$0.18^{+0.01}_{-0.01}$	$2.86^{+0.31}_{-0.24}$	$0.19^{+0.02}_{-0.01}$	$2.68^{+0.56}_{-0.43}$	$0.17^{+0.01}_{-0.01}$	$4.90^{+0.27}_{-0.20}$	$0.19^{+0.01}_{-0.02}$	$3.18^{+0.47}_{-0.45}$
229	05 42 19.05	-07 59 12.2	$0.14^{+0.03}_{-0.02}$	$3.98^{+1.65}_{-0.85}$	$0.11^{+0.04}_{-0.01}$	$2.09^{+2.29}_{-0.46}$	$0.10^{+0.03}_{-0.00}$	$4.90^{+1.97}_{-0.29}$	$0.11^{+0.04}_{-0.02}$	$2.67^{+1.59}_{-0.60}$
230	05 42 19.56	-08 05 07.6	$0.30^{+0.13}_{-0.07}$	$3.15^{+8.17}_{-1.39}$	$0.39^{+0.13}_{-0.10}$	$4.88^{+13.33}_{-2.62}$	$0.33^{+0.08}_{-0.06}$	$5.11^{+6.90}_{-1.84}$	$0.43^{+0.14}_{-0.11}$	$6.66^{+11.02}_{-3.22}$
231	05 42 21.36	-08 06 47.9	$0.20^{+0.04}_{-0.02}$	$1.00^{+0.18}_{-0.25}$	$0.26^{+0.04}_{-0.03}$	$0.88^{+0.41}_{-0.24}$	$0.28^{+0.03}_{-0.03}$	$2.25^{+0.19}_{-0.08}$	$0.33^{+0.06}_{-0.03}$	$1.61^{+0.70}_{-0.28}$
232	05 42 21.56	-08 08 29.8	$0.46^{+0.08}_{-0.07}$	$1.24^{+0.96}_{-0.49}$	$0.58^{+0.12}_{-0.08}$	$1.95^{+2.21}_{-0.89}$	$0.57^{+0.11}_{-0.06}$	$2.77^{+2.18}_{-0.96}$	$0.94^{+0.08}_{-0.09}$	$5.69^{+3.33}_{-2.10}$
233	05 42 23.24	-07 58 28.9	$0.19^{+0.03}_{-0.03}$	$7.92^{+3.47}_{-2.20}$	$0.17^{+0.05}_{-0.03}$	$6.87^{+5.77}_{-2.54}$	$0.14^{+0.04}_{-0.02}$	$8.33^{+3.36}_{-1.66}$	$0.14^{+0.06}_{-0.03}$	$5.42^{+5.33}_{-1.54}$
234	05 42 23.61	-08 09 10.3	$0.24^{+0.04}_{-0.03}$	$1.09^{+0.30}_{-0.20}$	$0.30^{+0.05}_{-0.04}$	$1.14^{+0.63}_{-0.32}$	$0.31^{+0.03}_{-0.04}$	$2.25^{+0.44}_{-0.21}$	$0.39^{+0.06}_{-0.05}$	$2.07^{+0.99}_{-0.46}$
235	05 42 23.94	-08 09 45.9	$0.82^{+0.29}_{-0.23}$	$1.46^{+3.66}_{-0.70}$	$1.23^{+0.10}_{-0.32}$	$3.42^{+4.88}_{-1.81}$	$1.35^{+0.07}_{-0.28}$	$6.19^{+6.64}_{-3.05}$	$1.38^{+0.01}_{-0.18}$	$9.48^{+8.61}_{-5.36}$
236	05 42 25.32	-08 10 18.0	$0.40^{+0.28}_{-0.16}$	$1.05^{+5.74}_{-0.63}$	$0.48^{+0.33}_{-0.18}$	$1.47^{+9.16}_{-0.96}$	$0.47^{+0.33}_{-0.16}$	$2.18^{+9.52}_{-1.03}$	$0.77^{+0.23}_{-0.21}$	$4.02^{+12.04}_{-1.97}$
237	05 42 25.44	-08 09 55.4	$0.49^{+0.10}_{-0.10}$	$3.74^{+5.05}_{-1.52}$	$0.55^{+0.11}_{-0.09}$	$5.10^{+7.10}_{-2.07}$	$0.46^{+0.09}_{-0.06}$	$5.07^{+5.91}_{-1.48}$	$0.69^{+0.09}_{-0.11}$	$9.20^{+7.86}_{-3.30}$
238	05 42 25.68	-07 58 22.0	$0.27^{+0.04}_{-0.03}$	$2.52^{+1.00}_{-0.53}$	$0.34^{+0.05}_{-0.04}$	$3.66^{+1.69}_{-0.99}$	$0.31^{+0.02}_{-0.02}$	$4.44^{+1.01}_{-0.64}$	$0.38^{+0.06}_{-0.05}$	$4.84^{+2.12}_{-1.20}$
239	05 42 25.79	-08 08 50.1	$0.27^{+0.04}_{-0.03}$	$1.48^{+0.48}_{-0.21}$	$0.34^{+0.04}_{-0.04}$	$1.89^{+0.77}_{-0.44}$	$0.33^{+0.03}_{-0.02}$	$2.89^{+0.55}_{-0.30}$	$0.42^{+0.06}_{-0.05}$	$3.11^{+1.29}_{-0.64}$
240	05 42 26.50	-07 58 50.9	$0.47^{+0.54}_{-0.18}$	$0.38^{+8.09}_{-0.26}$	$0.69^{+0.49}_{-0.30}$	$0.57^{+11.54}_{-0.40}$	$0.86^{+0.44}_{-0.37}$	$1.25^{+10.89}_{-0.70}$	$1.34^{+0.04}_{-0.30}$	$2.15^{+17.15}_{-0.79}$
241	05 42 26.96	-08 09 17.3	$0.25^{+0.02}_{-0.01}$	$2.86^{+0.45}_{-0.29}$	$0.31^{+0.03}_{-0.02}$	$4.08^{+0.91}_{-0.64}$	$0.27^{+0.02}_{-0.01}$	$5.06^{+0.42}_{-0.33}$	$0.33^{+0.03}_{-0.03}$	$4.93^{+1.19}_{-0.75}$
242	05 42 27.50	-08 11 03.8	$0.17^{+0.02}_{-0.02}$	$6.64^{+2.38}_{-1.72}$	$0.15^{+0.04}_{-0.02}$	$4.92^{+3.31}_{-1.71}$	$0.12^{+0.03}_{-0.01}$	$7.01^{+2.16}_{-1.06}$	$0.13^{+0.03}_{-0.02}$	$4.40^{+2.44}_{-1.08}$
243	05 42 27.59	-08 09 52.6	$0.44^{+0.13}_{-0.10}$	$1.96^{+5.88}_{-0.76}$	$0.51^{+0.15}_{-0.11}$	$2.82^{+9.09}_{-1.30}$	$0.46^{+0.13}_{-0.08}$	$3.35^{+5.52}_{-1.04}$	$0.72^{+0.13}_{-0.16}$	$6.17^{+7.63}_{-2.70}$
244	05 42 29.78	-08 07 26.4	$0.42^{+0.42}_{-0.22}$	$1.33^{+15.09}_{-0.99}$	$0.50^{+0.44}_{-0.23}$	$1.92^{+22.80}_{-1.49}$	$0.48^{+0.48}_{-0.21}$	$2.58^{+17.84}_{-1.76}$	$0.77^{+0.31}_{-0.32}$	$4.94^{+19.60}_{-2.74}$
245	05 42 30.62	-07 59 54.0	$0.37^{+0.12}_{-0.08}$	$6.24^{+11.87}_{-2.41}$	$0.47^{+0.10}_{-0.11}$	$10.32^{+20.81}_{-4.36}$	$0.35^{+0.08}_{-0.06}$	$8.05^{+10.29}_{-2.17}$	$0.50^{+0.10}_{-0.12}$	$12.71^{+13.01}_{-5.30}$
246	05 42 30.87	-08 10 45.7	$0.17^{+0.02}_{-0.01}$	$2.01^{+0.31}_{-0.20}$	$0.18^{+0.03}_{-0.02}$	$1.71^{+0.65}_{-0.44}$	$0.17^{+0.02}_{-0.02}$	$4.04^{+0.29}_{-0.46}$	$0.19^{+0.03}_{-0.03}$	$2.19^{+1.66}_{-0.42}$
247	05 42 31.00	-08 06 38.1	$0.22^{+0.09}_{-0.05}$	$1.48^{+1.21}_{-0.64}$	$0.28^{+0.10}_{-0.07}$	$1.71^{+2.01}_{-0.91}$	$0.28^{+0.07}_{-0.05}$	$3.12^{+1.25}_{-0.98}$	$0.31^{+0.14}_{-0.06}$	$2.48^{+3.46}_{-0.83}$
248	05 42 31.33	-08 02 35.3	$0.18^{+0.02}_{-0.01}$	$2.23^{+0.38}_{-0.20}$	$0.19^{+0.03}_{-0.02}$	$2.12^{+0.72}_{-0.50}$	$0.18^{+0.02}_{-0.02}$	$4.25^{+0.39}_{-0.14}$	$0.20^{+0.03}_{-0.03}$	$2.62^{+0.80}_{-0.50}$
249	05 42 31.55	-08 08 22.8	$0.17^{+0.04}_{-0.02}$	$0.41^{+0.51}_{-0.22}$	$0.22^{+0.04}_{-0.04}$	$0.47^{+0.38}_{-0.20}$	$0.25^{+0.03}_{-0.03}$	$2.07^{+0.27}_{-0.82}$	...	...
250	05 42 32.66	-08 10 07.9	$0.18^{+0.02}_{-0.01}$	$1.58^{+0.23}_{-0.13}$	$0.20^{+0.02}_{-0.02}$	$1.41^{+0.48}_{-0.32}$	$0.18^{+0.04}_{-0.01}$	$3.29^{+0.34}_{-0.25}$	$0.21^{+0.03}_{-0.03}$	$1.90^{+0.53}_{-0.33}$
251	05 42 32.77	-08 07 04.8	$0.17^{+0.01}_{-0.01}$	$1.39^{+0.18}_{-0.12}$	$0.19^{+0.02}_{-0.01}$	$1.02^{+0.32}_{-0.20}$	$0.18^{+0.02}_{-0.01}$	$3.03^{+0.32}_{-0.29}$	$0.20^{+0.02}_{-0.02}$	$1.48^{+0.34}_{-0.20}$
252	05 42 34.02	-08 09 59.7	$0.74^{+0.42}_{-0.23}$	$0.56^{+1.17}_{-0.26}$	$1.17^{+0.26}_{-0.38}$	$1.22^{+1.36}_{-0.67}$	$1.53^{+0.09}_{-0.44}$	$2.74^{+2.48}_{-1.35}$	...	...
253	05 42 34.31	-08 02 12.1	$0.16^{+0.17}_{-0.07}$	$2.55^{+12.99}_{-1.51}$	$0.16^{+0.24}_{-0.04}$	$1.99^{+29.05}_{-0.78}$	$0.14^{+0.16}_{-0.03}$	$4.67^{+12.22}_{-0.48}$	$0.16^{+0.21}_{-0.04}$	$2.43^{+16.09}_{-0.56}$
254	05 42 34.92	-08 07 50.5	$0.17^{+0.03}_{-0.02}$	$1.44^{+0.66}_{-0.43}$	$0.19^{+0.05}_{-0.04}$	$1.08^{+1.19}_{-0.43}$	$0.17^{+0.05}_{-0.03}$	$3.14^{+0.98}_{-1.40}$	$0.20^{+0.07}_{-0.03}$	$1.54^{+3.58}_{-0.24}$
255	05 42 36.41	-08 10 17.8	$0.28^{+0.11}_{-0.06}$	$8.00^{+10.41}_{-3.09}$	$0.36^{+0.12}_{-0.10}$	$12.49^{+16.77}_{-6.16}$	$0.27^{+0.08}_{-0.06}$	$10.10^{+8.01}_{-3.12}$	$0.36^{+0.11}_{-0.11}$	$13.59^{+13.82}_{-6.71}$
256	05 42 36.51	-08 11 51.5	$0.75^{+0.20}_{-0.15}$	$2.27^{+4.34}_{-0.87}$	$1.06^{+0.06}_{-0.20}$	$5.06^{+7.10}_{-2.17}$	$1.12^{+0.03}_{-0.19}$	$7.79^{+8.97}_{-3.24}$	$1.20^{+0.02}_{-0.12}$	$11.80^{+11.19}_{-4.26}$
257	05 42 40.06	-08 05 07.7	$0.38^{+0.13}_{-0.09}$	$9.28^{+12.36}_{-3.96}$	$0.49^{+0.09}_{-0.13}$	$15.81^{+16.78}_{-7.46}$	$0.35^{+0.09}_{-0.07}$	$10.76^{+9.89}_{-3.45}$	$0.51^{+0.09}_{-0.13}$	$17.67^{+14.40}_{-7.80}$
258	05 42 42.10	-08 15 15.3	$0.41^{+0.12}_{-0.09}$	$1.38^{+3.13}_{-0.36}$	$0.49^{+0.14}_{-0.11}$	$1.95^{+4.72}_{-0.75}$	$0.46^{+0.13}_{-0.08}$	$2.61^{+3.66}_{-0.53}$	$0.74^{+0.12}_{-0.17}$	$4.89^{+5.67}_{-1.89}$
259	05 42 44.12	-08 06 26.4	$0.24^{+0.11}_{-0.05}$	$1.09^{+0.73}_{-0.38}$	$0.31^{+0.10}_{-0.07}$	$1.15^{+1.16}_{-0.49}$	$0.32^{+0.07}_{-0.06}$	$2.25^{+0.83}_{-0.29}$	$0.39^{+0.15}_{-0.06}$	$2.12^{+2.38}_{-0.58}$
260	05 42 47.18	-08 05 57.0	$0.37^{+0.15}_{-0.09}$	$6.05^{+8.00}_{-2.56}$	$0.47^{+0.12}_{-0.13}$	$9.97^{+9.87}_{-4.64}$	$0.36^{+0.10}_{-0.07}$	$7.85^{+6.64}_{-2.36}$	$0.51^{+0.12}_{-0.13}$	$12.36^{+12.15}_{-5.64}$
261	05 42 47.44	-08 04 05.4	$0.31^{+0.13}_{-0.07}$	$4.01^{+8.03}_{-1.78}$	$0.40^{+0.13}_{-0.10}$	$6.39^{+13.83}_{-3.36}$	$0.32^{+0.08}_{-0.06}$	$6.10^{+6.48}_{-2.12}$	$0.43^{+0.14}_{-0.11}$	$8.19^{+12.11}_{-4.03}$
262	05 42 48.24	-08 05 57.1	$0.53^{+0.07}_{-0.15}$	$18.82^{+13.70}_{-8.95}$	$0.61^{+0.03}_{-0.12}$	$28.01^{+22.19}_{-12.32}$	$0.44^{+0.09}_{-0.09}$	$17.69^{+13.53}_{-6.62}$	$0.63^{+0.03}_{-0.12}$	$33.60^{+8.87}_{-14.84}$
263	05 42 51.65	-08 07 41.2	$0.53^{+0.08}_{-0.14}$	$17.18^{+13.78}_{-8.02}$	$0.61^{+0.03}_{-0.12}$	$25.51^{+20.61}_{-10.84}$	$0.44^{+0.09}_{-0.09}$	$16.41^{+13.79}_{-6.24}$	$0.64^{+0.03}_{-0.12}$	$30.77^{+10.46}_{-12.85}$
264	05 42 52.30	-08 08 54.9	$0.17^{+0.05}_{-0.03}$	$2.84^{+2.95}_{-0.63}$	$0.17^{+0.09}_{-0.04}$	$2.37^{+5.70}_{-0.94}$	$0.15^{+0.06}_{-0.03}$	$4.90^{+3.04}_{-0.49}$	$0.17^{+0.09}_{-0.04}$	$2.82^{+5.54}_{-0.73}$
265	05 42 59.13	-08 09 23.6	$0.40^{+0.11}_{-0.09}$	$1.17^{+2.80}_{-0.29}$	$0.48^{+0.14}_{-0.10}$	$1.63^{+5.27}_{-0.62}$	$0.46^{+0.13}_{-0.08}$	$2.33^{+3.77}_{-0.45}$	$0.75^{+0.12}_{-0.17}$	$4.31^{+5.33}_{-1.64}$
266	05 43 01.78	-08 04 50.6	$0.55^{+0.25}_{-0.08}$	$0.39^{+0.58}_{-0.07}$	$0.86^{+0.29}_{-0.15}$	$0.73^{+0.99}_{-0.24}$	$1.12^{+0.28}_{-0.20}$	$1.61^{+2.01}_{-0.45}$	...	...
267	05 43 08.49	-08 11 32.3	$0.40^{+0.09}_{-0.10}$	$21.23^{+13.49}_{-11.02}$	$0.50^{+0.06}_{-0.13}$	$36.34^{+24.57}_{-19.52}$	$0.33^{+0.09}_{-0.07}$	$20.13^{+12.24}_{-8.79}$	$0.49^{+0.08}_{-0.13}$	$36.35^{+7.44}_{-19.23}$

Table 3.9: The equivalent widths of emission lines on the optical spectra for YSOs in L1630N.

ID	RA (J2000)	DEC (J2000)	[O I] (5577 Å)	[O I] (6300 Å)	[O I] (6363 Å)	[N II] (6548 Å)	[N II] (6583 Å)	He I (6678 Å)	[S II] (6716 Å)	[S II] (6731 Å)	Ca II (8498 Å)	Ca II (8542 Å)	Ca II (8662 Å)
14	05 45 53.11	−00 13 24.9	...	−0.6± 0.01	...	...	...	−0.5± 0.01	...	...	...	...	...
20	05 45 56.31	+00 07 08.6	...	−1.3± 0.01	...	...	...	...	...	...	...	...	...
23	05 45 57.62	+00 07 21.1	−1.0± 0.02	−5.1± 0.15	...	...	...	−1.3± 0.02	...	...	...	...	...
24	05 45 57.93	+00 02 48.6	−0.8± 0.01	−3.2± 0.04	...	...	...	−2.0± 0.02	...	...	−3.6± 0.03	−4.6± 0.04	−4.6± 0.04
25	05 46 00.18	+00 03 07.0	...	−0.4± 0.01	...	...	...	−0.8± 0.01	...	...	...	...	...
27	05 46 04.64	+00 04 58.1	−0.6± 0.01	−1.5± 0.01	−0.6± 0.01	...	...	−0.7± 0.01	...	...	...	...	...
32	05 46 10.31	−00 00 06.7	−0.9± 0.01	−1.9± 0.02	−0.8± 0.01	...	...	−2.7± 0.02	...	...	−2.0± 0.02	−2.2± 0.02	−1.6± 0.01
33	05 46 11.34	−00 07 55.1	−42.0± 2.26	−85.9± 6.18	−27.7± 1.32	−2.1± 0.10	−7.8± 0.38	...	−1.9± 0.08	−4.2± 0.17	...	...	...
36	05 46 12.99	−00 08 14.8	−2.8± 0.08	−15.8± 0.41	−4.3± 0.10	...	−1.9± 0.04	...	...	−1.5± 0.03	...	...	...
42	05 46 18.60	+00 07 08.0	...	...	...	...	...	...	...	...	−2.0± 0.05	−2.5± 0.04	−1.7± 0.02
44	05 46 19.06	+00 03 29.6	...	−1.5± 0.01	...	...	...	−0.8± 0.01	...	...	−3.6± 0.03	−4.5± 0.04	−4.0± 0.03
47	05 46 22.43	−00 08 52.6	...	−0.6± 0.01	...	...	...	...	...	...	...	...	...
51	05 46 25.89	+00 09 32.0	−205.4± 10.03	−241.7± 20.40	−148.6± 22.99	...	...	−1.4± 0.03	...	...	...	...	...
52	05 46 26.65	+00 31 07.5	...	...	...	...	...	...	...	...	−0.7± 0.01	−0.7± 0.01	−0.5± 0.01
55	05 46 28.36	+00 12 27.0	...	−10.8± 0.91	...	...	...	...	...	...	...	−1.7± 0.03	−1.7± 0.03
56	05 46 28.87	+00 13 30.7	...	...	...	...	...	...	...	...	−14.4± 0.29	−20.8± 0.39	−13.8± 0.21
58	05 46 29.06	+00 11 45.7	−21.9± 1.74	...	...	...	...	...	...	...	...	...	...
59	05 46 29.59	+00 10 57.2	...	...	...	...	...	...	...	...	−0.7± 0.01	−1.4± 0.01	−1.4± 0.01
65	05 46 33.28	+00 02 51.9	...	...	...	...	...	−0.6± 0.01	...	...	−5.6± 0.04	−3.7± 0.03	−3.7± 0.03
69	05 46 36.10	+00 06 26.8	...	−17.0± 1.34	...	...	...	...	...	...	...	...	...
73	05 46 38.40	+00 15 11.6	−6.3± 0.22	−19.5± 1.22	...	...	...	...	...	...	...	...	...
74	05 46 38.57	+00 22 06.0	...	...	...	...	...	...	...	...	−0.7± 0.01	−0.7± 0.01	−0.7± 0.01
79	05 46 40.77	+00 27 22.5	...	−2.4± 0.02	...	...	...	−2.0± 0.03	...	...	−11.6± 0.11	−9.6± 0.08	−9.6± 0.10
85	05 46 45.00	+00 11 32.7	−1.7± 0.03	−5.6± 0.13	−1.4± 0.03	...	...	...	...	...	...	...	...
87	05 46 45.04	+00 05 33.9	...	...	...	−0.7± 0.01	−1.0± 0.01	...	...	...	...	...	...
90	05 46 48.55	+00 21 28.2	...	−124.5± 7.12	−36.0± 1.55	−4.9± 0.24	−11.9± 0.55	...	−11.1± 0.52	−23.0± 1.04	...	...	...
93	05 46 51.19	+00 18 08.2	...	−11.8± 0.22	−2.7± 0.04	...	...	...	...	...	...	...	...
94	05 46 51.40	+00 19 47.2	...	−18.5± 2.17	...	...	−9.3± 0.90	...	...	...	...	...	...
95	05 46 51.48	+00 19 21.3	...	−0.7± 0.01	...	...	...	−1.1± 0.01	...	...	...	...	...
96	05 46 51.85	+00 19 38.6	...	...	...	...	...	−0.8± 0.01	...	...	...	...	...
104	05 47 04.48	+00 15 47.2	−16.2± 2.31	...	...	...	...	...	...	...	...	...	...
107	05 47 05.06	+00 18 34.8	...	...	...	...	...	...	...	...	−0.7± 0.01	−0.7± 0.01	−0.7± 0.01
108	05 47 05.12	+00 18 26.7	...	...	...	...	...	...	...	...	−0.7± 0.01	−0.7± 0.01	−0.7± 0.01
112	05 47 06.17	+00 20 32.5	...	−2.5± 0.08	...	...	...	...	...	...	...	...	...
117	05 47 08.62	+00 19 23.9	−5.6± 0.47	...	...	...	...	...	...	...	−0.5± 0.01	−0.7± 0.01	−0.7± 0.01
118	05 47 08.71	+00 16 34.7	...	...	...	...	...	...	...	...	−2.5± 0.03	−3.4± 0.05	−3.4± 0.05
123	05 47 12.92	+00 22 06.5	...	...	...	...	...	...	...	...	−8.8± 0.11	−10.1± 0.15	−6.6± 0.08
129	05 47 19.90	+00 16 13.1	...	−2.9± 0.09	...	...	...	...	...	...	...	...	...

Table 3.10: The equivalent widths of emission lines on the optical spectra for YSOs in L1641.

ID	RA (J2000)	DEC (J2000)	[O I] (5577 Å)	[O I] (6300 Å)	[O I] (6363 Å)	[N II] (6548 Å)	[N II] (6583 Å)	He I (6678 Å)	[S II] (6716 Å)	[S II] (6731 Å)	Ca II (8498 Å)	Ca II (8542 Å)	Ca II (8662 Å)
5	05 35 17.80	−06 24 38.4	...	...	...	...	...	...	...	...	−0.6± 0.01	−0.6± 0.01	−0.6± ...
20	05 35 27.35	−06 19 31.3	...	−3.5± 0.12	...	...	...	...	...	...	...	...	...
28	05 35 33.93	−06 14 32.8	...	−1.2± 0.01	...	...	...	−0.9± 0.01	...	...	...	...	...
34	05 35 41.02	−06 22 45.4	−0.7± 0.01	−1.6± 0.02	...	...	...	...	...	...	...	...	...
39	05 35 43.37	−06 22 19.6	...	−4.6± 0.05	−1.6± 0.01	...	...	−2.4± 0.02	...	...	...	...	...
40	05 35 44.18	−06 28 16.4	...	...	...	...	...	−4.3± 0.06	...	...	...	...	...
45	05 35 50.19	−06 50 40.2	−283.0± 28.22	−56.5± 6.12	...	...	−12.2± 1.46	...	...	...	...	...	...
46	05 35 57.30	−06 40 28.1	...	...	...	...	...	−1.0± 0.01	...	...	...	...	...
47	05 35 57.31	−06 15 37.7	...	...	...	...	...	−1.2± 0.01	...	...	−1.6± 0.01	−0.8± 0.01	−0.7± 0.01
55	05 35 59.84	−06 42 30.5	−1.1± 0.01	−11.4± 0.16	−3.4± 0.04	...	...	−4.2± 0.05	...	−2.2± 0.01	−3.2± 0.03	−4.6± 0.03	−3.2± 0.03
56	05 36 00.18	−06 42 33.9	...	...	...	...	...	...	...	...	−2.0± 0.01	−3.1± 0.01	−3.1± 0.01
57	05 36 01.09	−06 25 07.7	−0.8± 0.01	−1.5± 0.01	...	...	...	...	...	...	...	...	...
58	05 36 01.10	−06 15 31.4	−0.4± 0.01	−0.7± 0.01	...	...	...	−0.7± 0.01	...	...	−1.0± 0.01	−1.0± 0.01	−0.5± 0.01
66	05 36 06.66	−06 14 25.9	...	−1.0± 0.01	...	...	...	...	...	...	−1.9± 0.02	−0.8± 0.01	−2.9± 0.05
68	05 36 08.29	−06 48 36.3	−190.5± 13.46	−12.4± 0.08	−4.0± 0.02	−0.6± 0.01	−1.3± 0.01	−1.6± 0.01	−5.1± 0.03	−9.3± 0.04	...	...	...
80	05 36 12.61	−06 23 39.6	...	−1.1± 0.01	...	...	...	−1.2± 0.01	...	...	...	...	...
84	05 36 13.45	−06 43 55.1	...	−7.5± 0.40	...	−1.8± 0.08	−5.1± 0.21	...	−4.4± 0.23	−5.4± 0.26	...	...	...

Table 3.10: continued.

ID	RA (J2000)	DEC (J2000)	[O I] (5577 Å)	[O I] (6300 Å)	[O I] (6363 Å)	[N II] (6548 Å)	[N II] (6583 Å)	He I (6678 Å)	[S II] (6716 Å)	[S II] (6731 Å)	Ca II (8498 Å)	Ca II (8542 Å)	Ca II (8662 Å)
85	05 36 14.76	−06 13 16.9	...	−1.3± 0.01	−0.5± 0.01	...	...	−1.1± 0.01	...	...	...	...	...
88	05 36 15.84	−06 14 50.7	...	−0.8± 0.01	...	...	...	−0.6± 0.01	...	...	...	...	...
94	05 36 19.38	−06 25 51.3	−1.2± 0.03	−10.3± 0.26	−2.4± 0.04	...	−1.0± 0.01	−1.4± 0.02	−1.1± 0.02	−2.1± 0.04	...	...	...
96	05 36 21.16	−06 26 56.9	...	−2.2± 0.05	...	...	...	−1.1± 0.03	...	...	...	...	...
104	05 36 24.54	−06 52 34.2	−0.9± 0.01	−1.2± 0.01	...	...	...	−1.5± 0.01	...	...	...	...	...
105	05 36 25.13	−06 44 41.9	...	−6.6± 0.06	−1.9± 0.01	...	...	...	−1.1± 0.01	−3.1± 0.02	−12.5± 0.07	−9.5± 0.04	−7.6± 0.04
122	05 36 30.96	−06 52 41.0	−3.8± 0.08	−40.9± 0.72	−13.7± 0.25	−1.8± 0.04	−9.5± 0.37	−2.6± 0.07	−16.9± 0.55	−34.1± 1.22	−11.1± 0.28	−5.3± 0.12	−3.7± 0.09
125	05 36 32.42	−06 40 43.0	...	−1.1± 0.01	...	...	...	−0.9± 0.01	...	...	...	...	...
127	05 36 32.89	−06 44 20.9	−1.3± 0.03	...	...	...	...	...	...	...	−3.7± 0.09	−3.2± 0.07	−2.7± 0.04
130	05 36 35.76	−06 42 49.9	−1.2± 0.04	−1.6± 0.03	...	...	...	...	...	...	...	...	...
134	05 36 40.94	−06 41 17.8	...	−0.7± 0.01	...	...	...	...	...	...	...	...	...
140	05 36 46.62	−06 39 50.0	...	...	...	...	...	−1.4± 0.02	...	...	...	...	...
143	05 36 54.41	−06 51 05.5	...	−3.4± 0.17	...	...	...	...	...	...	...	...	...
144	05 37 49.54	−06 56 27.4	−0.6± 0.01	−0.9± 0.01	...	...	...	...	...	...	...	...	...
145	05 37 51.72	−06 56 51.9	−0.5± 0.01	−1.2± 0.01	−0.5± 0.01	...	...	−1.1± 0.01	...	...	...	...	...
147	05 37 54.48	−06 57 31.1	...	−0.8± 0.01	...	...	...	...	...	...	...	...	...
152	05 37 55.74	−06 58 37.9	...	−1.2± 0.01	...	...	...	...	...	...	...	...	...
156	05 38 10.50	−06 57 07.1	...	−1.3± 0.01	...	...	...	...	...	...	...	...	...
159	05 38 21.22	−07 01 20.3	...	...	...	...	...	−1.5± 0.04	...	...	...	...	...
160	05 38 34.06	−07 04 36.8	−3.9± 0.20	...	...	...	...	...	...	...	...	...	...
162	05 38 40.59	−07 02 23.8	−0.7± 0.01	−2.6± 0.02	−0.8± 0.01	...	...	−2.3± 0.05	...	...	−0.8± 0.01	−0.8± 0.01	−0.8± 0.01
163	05 38 41.48	−07 01 52.6	...	...	...	...	...	...	...	...	...	−0.5± 0.01	−0.5± 0.01
165	05 38 43.22	−06 58 08.9	...	...	...	...	...	...	...	...	−4.3± 0.10	−4.2± 0.05	−3.3± 0.06
166	05 38 43.84	−06 58 22.3	...	...	...	...	...	...	...	...	−0.9± 0.01	−0.7± 0.01	−0.6± 0.01
167	05 38 44.95	−06 58 14.7	...	−9.5± 0.57	...	...	...	...	...	...	−0.8± 0.01	−1.3± 0.01	−1.3± 0.02
168	05 38 46.84	−07 05 08.9	...	...	...	...	...	−1.8± 0.07	...	...	−11.6± 0.30	−15.0± 0.37	−15.0± 0.40
170	05 38 47.74	−07 06 14.9	−21.8± 1.94	...	...	...	...	...	...	...	...	...	...
173	05 38 50.44	−07 00 43.0	−5.6± 0.26	...	...	...	...	...	...	...	...	...	...
175	05 38 53.33	−07 05 45.2	−1.8± 0.05	−6.0± 0.14	−2.4± 0.05	...	...	...	...	...	...	...	...
177	05 38 54.93	−07 07 10.9	−15.4± 0.30	...	...	...	...	...	...	...	...	...	...
179	05 38 57.04	−06 52 59.3	−0.8± 0.01	−1.6± 0.01	−0.7± 0.01	...	...	−2.4± 0.01	...	...	...	...	...
182	05 40 24.97	−07 55 35.3	−0.6± 0.01	−1.9± 0.01	−0.9± 0.01	...	...	...	...	−1.0± 0.01	−25.5± 0.23	−44.6± 0.43	−26.5± 0.17
196	05 40 57.49	−07 48 08.8	...	−7.3± 0.33	...	...	...	...	...	...	...	−3.0± 0.03	−3.0± 0.03
200	05 41 04.09	−07 43 38.6	−1.6± 0.04	−2.0± 0.03	...	...	...	...	...	...	−0.6± 0.01	−0.5± 0.01	−0.5± 0.01
203	05 41 05.49	−07 47 07.5	...	...	...	...	...	...	...	...	−6.8± 0.08	−4.0± 0.04	−3.3± 0.04
204	05 41 07.00	−07 47 15.9	−0.9± 0.01	−2.5± 0.02	−0.6± 0.01	...	...	−3.5± 0.05	...	...	−0.9± 0.01	−1.9± 0.02	−0.5± 0.01
205	05 41 07.08	−07 46 22.5	−0.5± 0.01	...	...	...	...	...	...	...	...	...	...
210	05 41 26.37	−07 58 17.8	−123.8± 12.69	...	...	...	...	...	...	...	...	...	...
212	05 41 33.38	−07 59 56.3	...	−2.7± 0.10	...	...	...	...	...	...	...	...	...
213	05 41 41.66	−08 00 18.5	−8.6± 0.94	...	−4.3± 0.13	...	−1.9± 0.04	...	...	...	...	...	...
214	05 41 43.74	−07 58 22.3	−4.5± 0.13	−24.5± 0.69	−6.8± 0.13	...	...	−3.0± 0.04	−3.4± 0.05	−4.2± 0.06	−6.3± 0.08	−7.1± 0.07	−5.8± 0.04
215	05 41 49.23	−07 57 12.3	−3.2± 0.23	−7.5± 0.61	...	...	...	...	...	...	...	...	...
219	05 41 55.96	−07 58 36.6	...	−21.5± 1.60	...	...	...	...	...	...	...	...	...
225	05 42 14.60	−07 58 57.9	...	−5.9± 0.09	−2.6± 0.03	...	...	−0.6± 0.01	...	−0.6± 0.01	...	...	...
231	05 42 21.36	−08 06 47.9	...	...	...	...	...	...	...	...	−0.6± 0.01	−0.8± 0.01	−0.8± 0.01
232	05 42 21.56	−08 08 29.8	...	−0.8± 0.01	...	...	...	...	...	...	...	...	...
233	05 42 23.24	−07 58 28.9	...	−31.9± 1.93	...	...	...	...	...	...	...	...	...
234	05 42 23.61	−08 09 10.3	...	−1.8± 0.02	...	...	...	−1.0± 0.01	...	...	...	...	...
239	05 42 25.79	−08 08 50.1	−1.2± 0.02	−1.6± 0.02	...	...	...	−0.7± 0.01	...	...	...	...	...
240	05 42 26.50	−07 58 50.9	...	...	...	...	...	−0.6± 0.01	...	...	...	...	...
245	05 42 30.62	−07 59 54.0	−7.4± 0.07	−1.6± 0.04	...	...	...	...	...	...	...	...	...
248	05 42 31.33	−08 02 35.3	...	−2.8± 0.05	...	...	...	...	...	...	...	...	...
253	05 42 34.31	−08 02 12.1	...	−10.2± 0.33	−2.5± 0.06	...	...	−1.5± 0.02	...	...	...	...	...

Table 3.11: Unrelated field stars with photometric magnitudes in L1630N. A complete version of this table, containing 108 stars, is available at the CDS. Here we only show the first 10 entries.

	RA	DEC	u′	g′	r′	i′	z′	J	H	K_s	[3.6]	[4.5]	[5.8]	[8.0]	[24]		A_V
ID	(J2000)	(J2000)	(mag)	(mag)	(mag)	(mag)	(mag)	(mag)	(mag)	(mag)	(mag)	(mag)	(mag)	(mag)	(mag)	Spt	(mag)
1	05 45 29.13	−00 13 49.4	24.24± 0.68	20.82± 0.02	18.82± 0.01	17.88± 0.01	17.21± 0.01	15.43± 0.05	14.73± 0.05	14.29± 0.09	14.21± 0.06	14.24± 0.06	14.19± 0.10	14.23± 0.26	...	K6	2.7
2	05 45 29.45	−00 12 12.9	...	21.09± 0.02	19.27± 0.01	18.02± 0.01	17.35± 0.01	15.87± 0.08	15.48± 0.14	15.18± 0.17	14.87± 0.06	14.84± 0.06	...	...	...	M3.5	0.1
3	05 45 30.81	−00 09 43.1	23.43± 0.36	20.69± 0.01	19.22± 0.01	18.41± 0.01	17.83± 0.01	16.20± 0.11	15.87± 0.17	15.36± 0.20	15.29± 0.06	15.40± 0.06	...	...	...	F8	3.8
4	05 45 31.70	−00 08 33.5	21.99± 0.10	19.37± 0.01	17.71± 0.01	16.83± 0.01	16.21± 0.01	14.60± 0.03	13.86± 0.03	13.67± 0.05	13.40± 0.06	13.40± 0.06	13.45± 0.07	13.25± 0.13	...	G1.5	4.0
5	05 45 33.01	−00 04 55.0	23.72± 0.46	21.73± 0.03	20.11± 0.01	19.21± 0.01	18.60± 0.02	....	...	...	15.96± 0.06	15.91± 0.07	...	...	...	G0	4.1
6	05 45 33.72	−00 04 49.0	21.28± 0.06	18.28± 0.01	16.68± 0.01	15.90± 0.01	15.37± 0.01	13.91± 0.02	13.11± 0.02	12.93± 0.03	12.75± 0.06	12.78± 0.06	12.77± 0.06	12.83± 0.10	...	K4	2.3
7	05 45 34.32	−00 04 27.5	23.46± 0.42	21.19± 0.02	18.91± 0.01	17.39± 0.01	16.45± 0.01	14.69± 0.03	13.63± 0.04	13.36± 0.03	13.20± 0.06	13.07± 0.06	12.98± 0.06	12.91± 0.10	...	M2.5	1.6
8	05 45 36.34	−00 13 33.9	24.52± 0.88	21.86± 0.04	19.49± 0.01	18.03± 0.01	17.09± 0.01	15.39± 0.06	14.44± 0.06	14.09± 0.07	13.60± 0.06	13.65± 0.06	13.55± 0.07	13.83± 0.19	...	M1.5	2.3
9	05 45 38.07	−00 10 08.9	23.42± 0.35	20.05± 0.01	18.28± 0.01	17.34± 0.01	16.70± 0.01	15.10± 0.06	14.25± 0.04	14.19± 0.07	13.98± 0.06	13.98± 0.06	13.85± 0.08	13.68± 0.17	...	K1.5	3.7
10	05 45 39.17	+00 09 36.3	22.60± 0.15	20.09± 0.01	18.76± 0.01	18.13± 0.01	17.68± 0.01	16.36± 0.12	15.73± 0.13	15.60± 0.21	15.47± 0.06	15.48± 0.06	...	...	...	K3.5	1.9

Table 3.12: Unrelated field stars with photometric magnitudes in L1641. A complete version of this table, containing 71 stars, is available at the CDS. Here we only show the first 10 entries.

	RA	DEC	u′	g′	r′	i′	z′	J	H	K_s	[3.6]	[4.5]	[5.8]	[8.0]	[24]		A_V
ID	(J2000)	(J2000)	(mag)	(mag)	(mag)	(mag)	(mag)	(mag)	(mag)	(mag)	(mag)	(mag)	(mag)	(mag)	(mag)	Spt	(mag)
1	05 35 18.65	−06 25 09.7	21.12± 0.16	18.42± 0.01	17.01± 0.01	15.76± 0.01	15.10± 0.01	13.72± 0.02	13.01± 0.03	12.82± 0.02	12.51± 0.06	12.47± 0.06	12.33± 0.07	12.02± 0.18	...	M3.5	0.1
2	05 35 28.58	−06 17 00.0	22.40± 0.59	22.67± 0.17	19.77± 0.02	18.06± 0.01	16.83± 0.01	14.48± 0.03	13.42± 0.03	12.86± 0.02	12.52± 0.06	12.38± 0.06	12.39± 0.07	12.48± 0.25	...	K5	5.7
3	05 35 32.41	−06 16 48.0	21.02± 0.18	20.81± 0.04	16.86± 0.01	13.63± 0.01	11.75± 0.01	7.93± 0.03	6.24± 0.06	5.43± 0.01	5.59± 0.06	4.94± 0.06	4.79± 0.06	4.64± 0.06	4.05± 0.06	M6	7.3
4	05 35 34.81	−06 21 51.3	13.71± 0.01	10.91± 0.01	10.44± 0.01	10.35± 0.01	12.83± 0.01	9.50± 0.02	9.25± 0.03	9.17± 0.01	9.11± 0.06	9.12± 0.06	8.99± 0.06	9.17± 0.06	...	B8.5	2.1
5	05 35 39.41	−06 16 02.7	19.87± 0.07	17.15± 0.01	15.71± 0.01	15.14± 0.01	14.54± 0.01	13.27± 0.03	12.61± 0.03	12.39± 0.02	12.09± 0.06	12.27± 0.06	12.23± 0.07	12.23± 0.20	...	M1.5	0.1
6	05 35 40.03	−06 23 54.3	...	21.44± 0.06	18.99± 0.01	17.58± 0.01	16.54± 0.01	14.48± 0.03	13.51± 0.03	13.10± 0.02	12.78± 0.06	12.65± 0.06	12.71± 0.07	12.67± 0.23	...	K5	4.5
7	05 35 46.67	−06 39 55.1	22.35± 0.75	20.62± 0.04	19.03± 0.01	18.22± 0.01	17.59± 0.01	16.03± 0.09	15.46± 0.12	15.36± 0.16	15.12± 0.08	15.06± 0.07	...	...	...	F6.5	4.0
8	05 35 48.24	−06 41 35.2	...	...	...	...	...	17.23± 0.21	16.10± 0.21	15.56± 0.17	15.19± 0.08	15.03± 0.07	...	...	...	K5.5	4.7
9	05 35 56.56	−06 52 45.7	...	21.95± 0.09	19.94± 0.02	18.97± 0.01	18.28± 0.03	16.85± 0.15	15.61± 0.13	15.58± 0.19	15.29± 0.07	15.17± 0.06	...	...	...	K6.5	2.5
10	05 35 56.58	−06 50 35.2	21.61± 0.27	18.48± 0.01	16.83± 0.01	15.94± 0.01	15.34± 0.01	13.85± 0.02	13.14± 0.04	12.91± 0.03	12.76± 0.06	12.64± 0.06	12.62± 0.07	12.53± 0.14	...	K4	2.6

Table 3.13: Photometric magnitudes for stars in L1630N. A complete version of this table, containing 12199 stars, is available at the CDS. Here we only show the first 10 entries.

	RA	DEC	u′	g′	r′	i′	z′	J	H	K_s	[3.6]	[4.5]	[5.8]	[8.0]	[24]
ID	(J2000)	(J2000)	(mag)	(mag)	(mag)	(mag)	(mag)	(mag)	(mag)	(mag)	(mag)	(mag)	(mag)	(mag)	(mag)
1	05 45 21.05	+00 00 52.7	...	...	23.79± 0.30	22.20± 0.11	21.18± 0.21	...	...	...	17.08± 0.08	17.03± 0.10	...	...	...
2	05 45 21.07	+00 49 19.8	21.10± 0.06	19.60± 0.01	18.79± 0.01	18.43± 0.01	18.25± 0.02	...	...	...	16.51± 0.07	16.21± 0.07	...	...	...
3	05 45 21.11	+00 38 36.9	...	...	23.15± 0.39	21.93± 0.21	21.21± 0.38	...	...	...	16.63± 0.08	16.66± 0.08	...	...	...
4	05 45 21.14	+00 37 48.4	23.91± 0.44	21.20± 0.02	19.82± 0.01	19.20± 0.01	18.77± 0.02	...	...	...	16.30± 0.07	16.46± 0.07	...	...	...
5	05 45 21.15	−00 11 05.2	19.82± 0.02	17.44± 0.01	16.03± 0.01	15.31± 0.01	14.80± 0.01	13.38± 0.02	12.82± 0.04	12.57± 0.02	12.45± 0.06	12.46± 0.06	12.39± 0.06	12.04± 0.07	...
6	05 45 21.15	+00 18 48.0	...	24.52± 0.38	22.44± 0.10	20.86± 0.04	20.00± 0.08	...	...	...	...	16.97± 0.10	...	...	...
7	05 45 21.16	+00 47 15.0	...	...	22.93± 0.35	21.50± 0.16	20.06± 0.14	...	...	...	16.96± 0.09	...	...	...	...
8	05 45 21.17	+00 00 06.5	19.05± 0.01	17.01± 0.01	15.82± 0.01	15.21± 0.01	14.79± 0.01	13.51± 0.02	13.05± 0.02	12.86± 0.03	12.71± 0.06	12.72± 0.06	12.55± 0.06	12.62± 0.09	...
9	05 45 21.19	+00 45 35.9	...	21.40± 0.03	19.67± 0.01	18.61± 0.01	18.02± 0.02	16.74± 0.17	15.89± 0.15	15.82± 0.25	15.75± 0.06	15.78± 0.06	15.64± 0.28	...	...
10	05 45 21.19	+00 26 07.1	17.04± 0.01	15.71± 0.01	14.30± 0.01	12.81± 0.01	13.32± 0.01	11.34± 0.02	10.76± 0.02	10.58± 0.02	10.32± 0.06	10.40± 0.06	10.41± 0.06	10.38± 0.06	...

Table 3.14: Photometric magnitudes for stars in L1641. A complete version of this table, containing 9495 stars, is available at the CDS. Here we only show the first 10 entries.

	RA	DEC	u′	g′	r′	i′	z′	J	H	K_s	[3.6]	[4.5]	[5.8]	[8.0]	[24]
ID	(J2000)	(J2000)	(mag)	(mag)	(mag)	(mag)	(mag)	(mag)	(mag)	(mag)	(mag)	(mag)	(mag)	(mag)	(mag)
1	05 34 04.47	−06 31 37.9	22.43± 0.56	19.53± 0.02	18.10± 0.01	16.47± 0.01	15.52± 0.01	13.90± 0.03	13.13± 0.04	12.68± 0.02	...	...	...	11.40± 0.08	...
2	05 34 05.73	−06 28 51.7	21.67± 0.18	17.90± 0.01	15.61± 0.01	14.46± 0.01	13.63± 0.01	11.77± 0.02	10.84± 0.03	10.47± 0.02	...	...	...	10.03± 0.06	...
3	05 34 06.23	−06 30 45.1	19.71± 0.06	16.74± 0.01	15.24± 0.01	16.37± 0.01	13.14± 0.01	11.59± 0.02	10.84± 0.03	10.59± 0.02	...	...	...	10.18± 0.06	5.70± 0.06
4	05 34 06.28	−06 28 39.8	23.47± 0.91	19.76± 0.01	17.69± 0.01	16.57± 0.01	15.79± 0.01	14.04± 0.03	13.10± 0.03	12.73± 0.02	...	...	...	12.26± 0.13	...
5	05 34 06.96	−06 32 07.9	20.87± 0.15	18.22± 0.01	16.80± 0.01	15.45± 0.01	14.71± 0.01	13.29± 0.02	12.59± 0.03	12.26± 0.02	...	...	...	9.34± 0.06	5.67± 0.06
6	05 34 09.07	−06 33 56.7	21.05± 0.18	19.26± 0.01	17.91± 0.01	16.30± 0.01	15.38± 0.01	13.84± 0.02	13.20± 0.03	12.99± 0.02	...	...	...	12.43± 0.15	...
7	05 34 09.57	−06 25 41.4	...	22.92± 0.16	21.33± 0.05	20.54± 0.04	19.99± 0.07	...	...	...	17.40± 0.16	17.12± 0.13	...	...	...
8	05 34 10.01	−06 26 22.5	...	22.42± 0.10	20.28± 0.02	19.21± 0.01	18.50± 0.02	16.87± 0.16	15.96± 0.16	15.51± 0.17	15.31± 0.06	15.34± 0.06	...	...	...
9	05 34 10.36	−06 24 37.9	21.52± 0.16	18.40± 0.01	16.83± 0.01	16.09± 0.01	15.61± 0.01	14.16± 0.03	13.44± 0.04	13.24± 0.03	12.95± 0.06	13.06± 0.06	12.88± 0.09	13.05± 0.24	...
10	05 34 10.51	−06 30 40.0	...	...	21.13± 0.06	19.09± 0.02	17.68± 0.02	15.18± 0.04	13.81± 0.04	13.24± 0.03	...	...	...	12.58± 0.17	...

3.3.2 Stellar properties

We determined the spectral type for each star in our sample as described Sect. 3.2.2, and estimated masses and ages using the methods described in Sect. 3.2.3. We could obtain reliable spectral types for 71% of the observed sample in L1630N and 78% in L1641, the remainder of the sample usually having too low SNR for a robust analysis.

(1) Spectral types

In Fig. 3.5 we show a histogram of spectral types within our sample. The distribution is bimodal, with peaks around spectral type G0 and mid M. In this figure, we distinguish between YSO candidates, selected according to the criteria outlined in Sect. 3.2.1 and shaded gray in the histogram, and probable "field" objects. The young stars in our sample are all of K or M type, with the exception of one F and one G star in L1641. The field stars comprise essentially the entire peak around spectral type G0 and placement of these objects in the HR diagram shows that 11% (7/61) in L1630 and 25% (5/20) are foreground dwarfs, the majority of the rest are main sequence stars behind the clouds. The second peak in the field objects distribution, around K and M spectral types, consists mostly of foreground dwarfs and background giants.

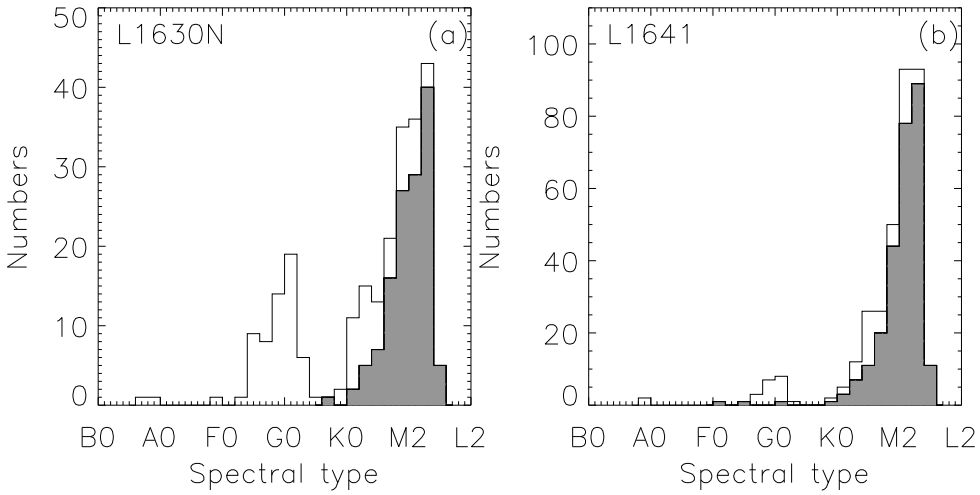

Figure 3.5: The spectral-type distributions of our sample observed with VIMOS in L1630N and L1641. The open histograms show the distribution of all the stars with reliable spectral types. The filled histograms display the YSO distribution

.

(2) Stellar masses and ages

In Fig. 3.6 we show the HR diagrams of the L1630N and L1641 clouds, from which we derive mass and age estimates as outlined in Sect. 3.2.3(3). We show separate diagrams for the "distributed" and "clustered" population in L1641, as defined using the NNM (Sect. 3.2.5). The vast majority of objects lie between the 0.1 and 3 Myr isochrones. We use distinct symbols (filled asterisks) for objects with SEDs typical for transition disks (see also Sect. 3.3.3), as well as four "exotic" objects that are apparently under-luminous and have very high emission line equivalent widths (blue-boxed points, see Sect.3.3.4(1)).

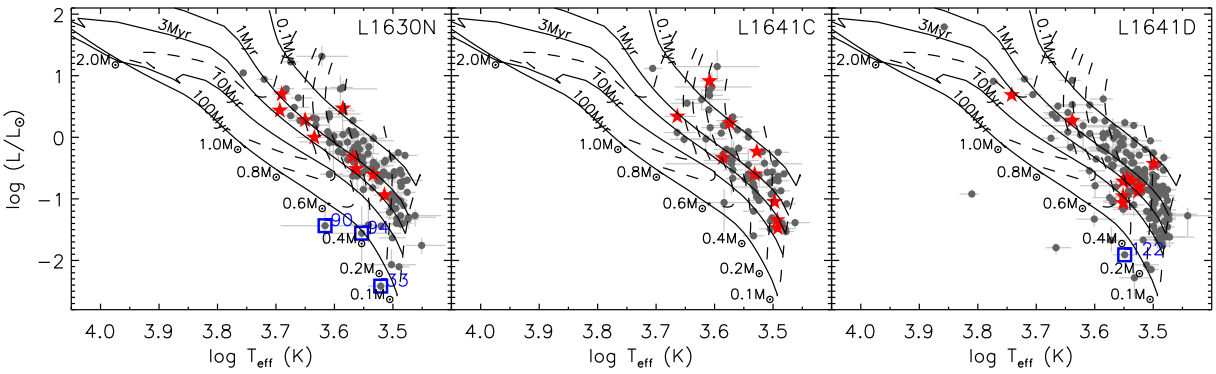

Figure 3.6: HR diagrams of YSOs in L1630N (left panel), L1641C (middle panel) and L1641D (right panel). Gray circles: YSOs. The error bars for the effective temperatures reflect the uncertainties of the deduced spectral types provided by the classification code. The errors bars for the lumonisity come from the optical SED fitting and include the uncertainties in the photometry as well as the effective temperatures. Asterisks: YSOs with transition disks. Open squares: the exotic objects, see Sect. 3.3.4(1).

In Fig. 3.7, we show the age distribution of L1630N, L1641C, and L1641D. The median ages are 0.9 Myr in L1630N, 1.1 Myr in L1641C, and 1.3 Myr in L1641D, if a distance of 450 pc is assumed for both clouds. In this case, a Kolmogorov-Smirnov (KS) test yields a very low probability ($P \sim 0.03$) that the YSOs in L1641 and L1630N are drawn randomly from the same age distribution. However, if one assumes a distance of 400 pc for L1630N, which is within current uncertainties (Flaherty & Muzerolle 2008; Anthony-Twarog 1982), the discrepancy between the age distributions of both clouds disappears completely.

In Fig. 3.8, we show the mass distributions (filled histograms) derived for our sample. The median masses are $\sim$0.34 $M_\odot$ in L1630N, 0.33 $M_\odot$ in L1641C, and 0.28 $M_\odot$ in L1641D, respectively. A KS test toward the mass distributions in L1630N and L1641D reveals a relatively low probability ($P \sim 0.08$) for stars in both clouds to be drawn randomly from the same distribution. In Fig. 3.8 we see that there are fewer objects in the lowest mass bins in L1641C compared to

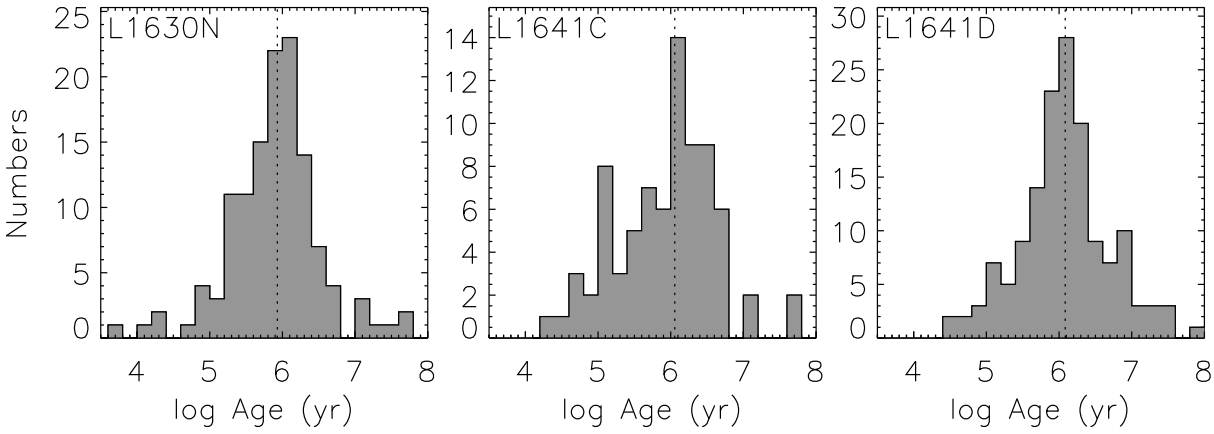

Figure 3.7: The age distribution of YSOs in L1630N, L1641C, and L1641D. The dotted lines show the median masses of YSOs, i.e. ~0.9 Myr in L1630N, 1.1 Myr in L1641C ,and 1.3 Myr in L1641D.

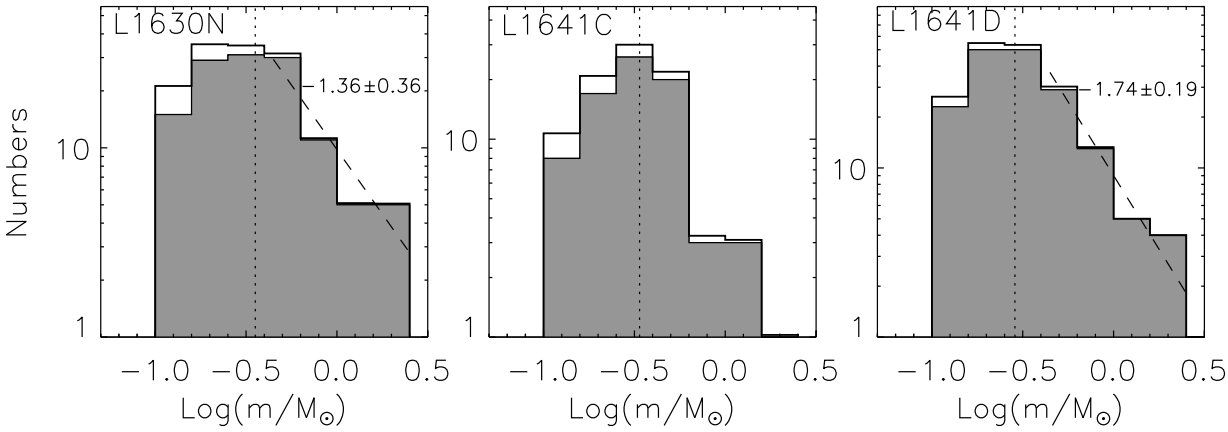

Figure 3.8: The mass distribution of YSOs in L1630N and L1641. The dotted lines show the median masses of YSOs, i.e. ~0.34 $M_{\odot}$ in L1630N, 0.33 $M_{\odot}$ in L1641C, and 0.28 $M_{\odot}$ in L1641D. The shaded histograms are the mass distributions without incompleteness correction, while the open histograms are the mass distribution corrected for incompleteness (see Sect.3.3.2(2)). A linear regression toward the latter mass spectra in the range of -0.4 $\leq \log(M_{\star}/M_{\odot}) \leq$ 0.4 gives slopes of -1.36±0.36 and -1.74±0.19 for the population in L1630N and L1641D (dashed lines), respectively.

L1641D and L1630N. This may, however, be caused by higher extinction in the former population, causing the lowest mass members to be excluded from our sample as they are too faint for optical spectroscopy. The mass distributions for stars above 0.5 $M_{\odot}$ in L1630N and L1641D are indistinguishable, with a probability of $P \sim 0.9$ for both samples being drawn at random from the same parent distribution, in a KS test.

We used a Monte-Carlo method to estimate the incompleteness of our sample. According to an assumed mass function, we constructed 1000 synthetic stellar populations, each containing 2×10^5 stars. Assuming ages of 0.9 Myr for L1630N, 1.1 Myr for L1641C and 1.3 Myr for L1641D, we obtained synthetic photometry for each star using the PMS evolutionary tracks from Dotter et al. (2008). We reddened the photometry using $A_{\rm v}$ values randomly sampled from the observed extinction distributions in both regions, respectively. We used r'=21.5 mag as a flux limit, and assumed that stars brighter than this limit have spectra of sufficient signal-to-noise for reliable spectral classification. Examination of the VIMOS spectra of our sample shows that this limit is realistic. The incompleteness correction factors for each mass bin can be obtained by comparing the input mass function and the "observed" mass function, including all stars brighter than 21.5 mag at r'. The open histograms in Fig. 3.8 show the mass distribution corrected for incompleteness. A linear regression toward this mass function within the mass range $-0.4 \leq \log(M_{\star}/M_{\odot}) \leq 0.4$ yields slopes of -1.36±0.36 and -1.74±0.19 for the population in L1630N and L1641D, respectively.

3.3.3 Disk properties

From our infrared SED data we derived approximate disk geometries for the observed objects whereas optical emission lines yield accretion and outflow signatures. See Sect. 3.2.4 for a description of the diagnostics used.

(1) Disk geometry

(a) Qualitative description of SEDs & physical interpretation

In Fig. 3.9 we show a set of representative SEDs of YSOs displaying a range of spectral shapes that are thought to indicate different stages of disk evolution. In Table 3.15 we list the infrared excess from 3.6 μm to 24 μm of these same stars in magnitudes.

The object displayed in Fig. 3.9(a) shows a strong IR excess with an approximately flat spectrum (in λF_{λ}). The SED of the system in Fig. 3.9(b) shows excesses that are reduced by a similar factor across the whole wavelength range compared to the object in Fig. 3.9(a). The excess fluxes of the

object shown Fig. 3.9(c) are substantially smaller still, in particular at 24 μm. The SEDs shown in Figs. 3.9(a) to (c) can be understood in terms of dust growth and settling, which decrease the vertical scale height of the disk and thus the amount of stellar radiation that is absorbed by the disk and re-emitted in the infrared. The corresponding disk geometries could be referred to as "strongly flaring" (a), "mildly flaring" (b), and "flat" (c). Note that the designation "flat" does not imply a geometrically thin disk, but rather indicates that the ratio of the disk vertical scale height and the distance (H/R) doesn't increase significantly with radius. For flared disks, this ratio does increase with radius, the classical solution for an optically thick disk being $H/R \propto R^{2/7}$ (Kenyon & Hartmann 1987).

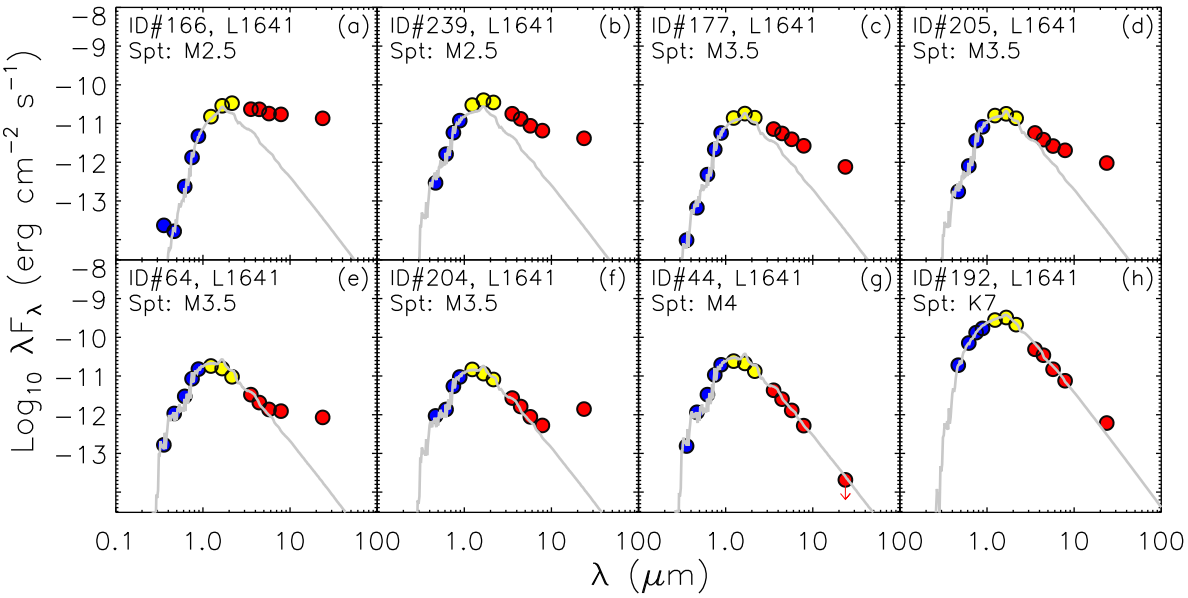

Figure 3.9: Example SEDs of YSOs whose disks are in different evolutionary stages. The photospheric emission level is indiacted with a grey curve in each panel. From (a) to (e-f), the disks evolve from a "strongly flared" optially thick disk to a "transition disk". (g): a star showing no excess emission in any of the Spitzer bands. (h): a debris-disk candidate with a weak excess at 24 μm only.

From Fig. 3.9(c) to Fig. 3.9(e) the excess emission from 3.6 μm to 8.0 μm decreases steadily while the flux at 24 μm remains roughly constant. This indicates that the very inner parts of the disk are dissipated while the outer disk remains essentially intact, i.e. an inner hole may form. Going from Fig. 3.9(e) to Fig. 3.9(f) we see that the excess emission at 8.0 μm is significantly reduced, while the excess at 24 μm has more than doubled. This may be understood in terms of an inner disk that has essentially dissipated, i.e. an inner gap of order 1 AU in radius, combined with a dusty outer disk whose inner edge is no longer partially shielded by the inner disk but rather is fully exposed to the stellar radiation field, and has a temperature of $\lesssim$200 K making it very bright at 24 μm but very faint at $\lesssim$8 μm.

The star shown in Fig. 3.9(g) displays no excess emission at any of the Spitzer bands, indicating it has essentially no circumstellar material within ~20 AU. In Fig. 3.9(h) we show a star that has essentially photospheric emission levels at $\lambda \leq 8\,\mu$m but shows a weak excess at $24\,\mu$m. Such an SED is typical of "debris disks", which possess relatively small amounts of circumstellar material originating in the collisional grind-down of larger bodies ("planetesimals"). While the source shown in Fig. 3.9(g) does show a debris disk-like SED, it is unclear whether it is of the same physical nature, given its young age of $\lesssim$4 Myrs.

Table 3.15: Excess emission fluxes for YSOs in Fig. 3.9

sub-panel	ID (L1641)	[3.6] (mag)	[4.5] (mag)	[5.8] (mag)	[8.0] (mag)	[24] (mag)
(a)	166	1.39	2.07	2.46	3.34	6.45
(b)	239	1.49	1.89	2.15	2.81	5.71
(c)	177	0.84	1.24	1.57	2.12	4.12
(d)	205	0.56	0.82	1.13	1.83	4.38
(e)	64	...	0.05	0.34	1.22	4.20
(f)	204	0.06	0.23	0.29	0.72	5.17
(g)	44	...	...	...	...	...
(h)	192	...	...	...	...	0.75

(b) Disk frequency

In Fig. 3.10(a) we show the "classical Spitzer IRAC color-color" diagram of all YSOs in our sample, i.e. the [3.6]-[4.5] vs. [5.8]-[8.0] colors. A number of stars cluster around the origin, indicating approximately photospheric near-infrared colors and the absence of an optically thick inner disk. Most stars are located towards the top-right of the origin due to infrared excess emission indicative of hot dust in the inner disk. Note that in Fig. 3.10, the Hα equivalent width of each star is indicated using a color coding, this will be further discussed in Sect. 3.3.3(2).

The average slope $\alpha_{\rm IRAC}$ of the SED in the IRAC spectral range is often used as a proxy for the nature of the inner disk. Fig. 3.11 shows this slope as a function of stellar effective tempareture, again with symbols color-coded according to Hα equivalent width. Diskless M-type stars show a spectral slope of $\alpha_{\rm IRAC} \lesssim -2.56$, while objects with an optically thick inner disk have $\alpha_{\rm IRAC} \geq$ -1.8. An intermediate spectral slope of $-2.56 \leq \alpha_{\rm IRAC} < -1.8$ points at a partially dissipated "evolved" inner disks. Using these criteria, we find the following disk statistics in our sample of YSOs *with detections in all four IRAC bands*. In L1630N, the YSOs with optically thick disks and evolved

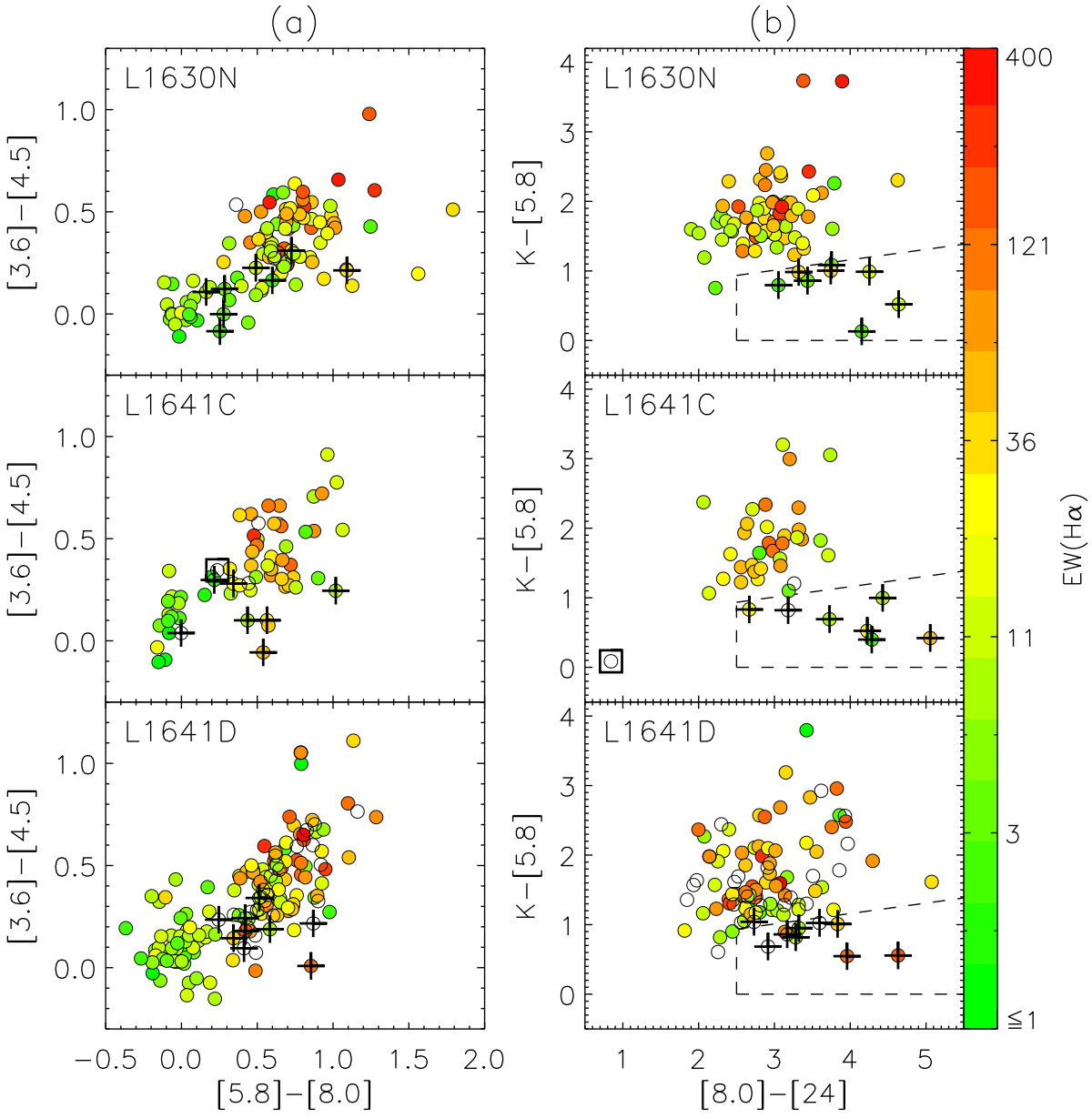

Figure 3.10: Spitzer [3.6]-[4.5] vs. [5.8]-[8.0] (left) and K_s-[5.8] vs. [8.0]-[24] (right) color-color diagrams for our YSO sample in L1630N, L1641C, and L1641. The pluses mark YSOs with transition disks. The debris disk candidate is marked with a square box. All points are color-coded according to the Hα equivalent width (blank circles represent sources where our VIMOS spectra did not cover the Hα spectral region)

.

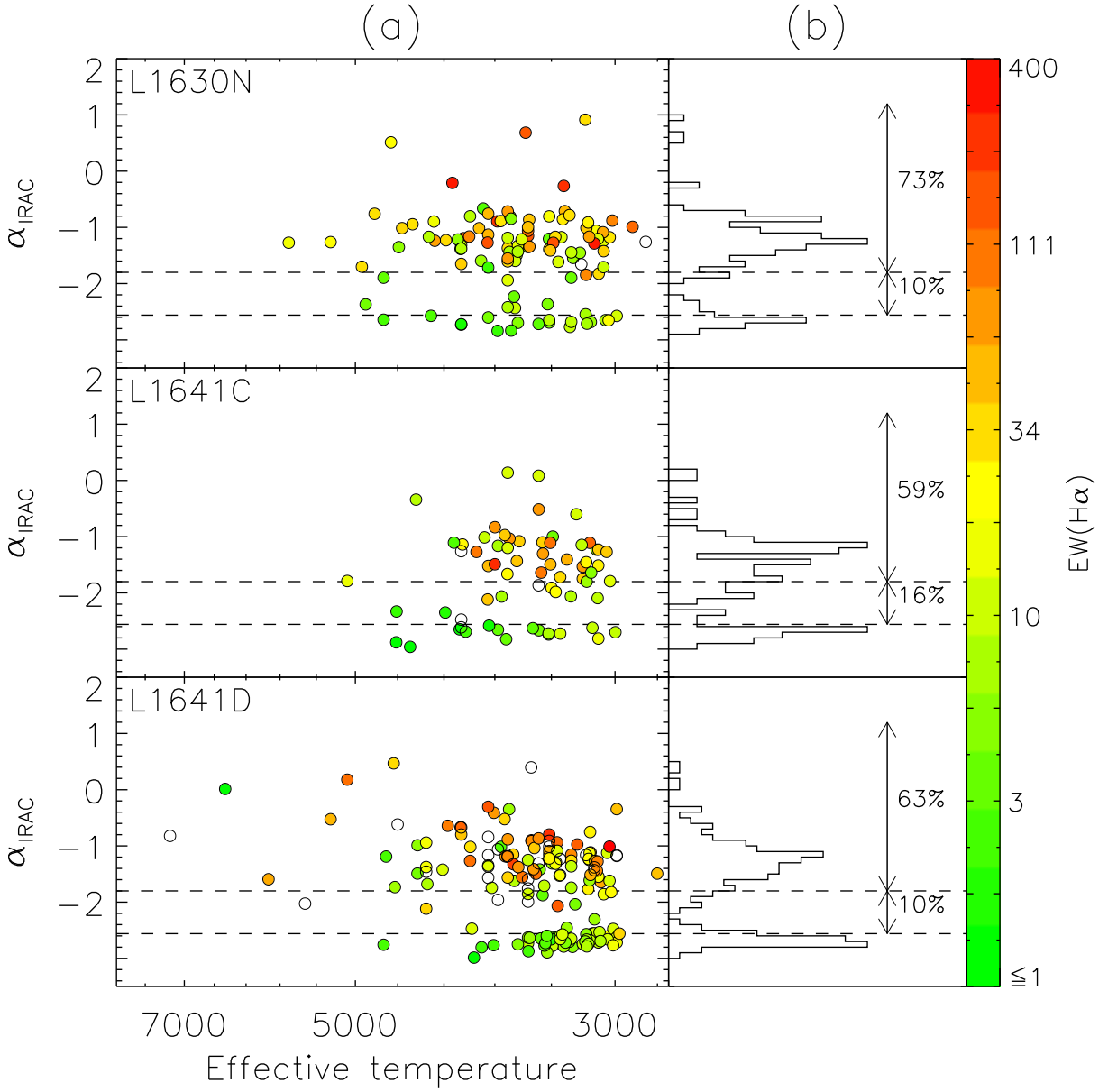

Figure 3.11: (a): The dereddened power-law slope of the IRAC SEDs ($\alpha_{\rm IRAC}$) for YSOs in L1630N, L1641C, and L1641D, plotted as a function of effective temperature. (b): Distributions of $\alpha_{\rm IRAC}$for YSOs in L1630N, L1641C, and L1641D.

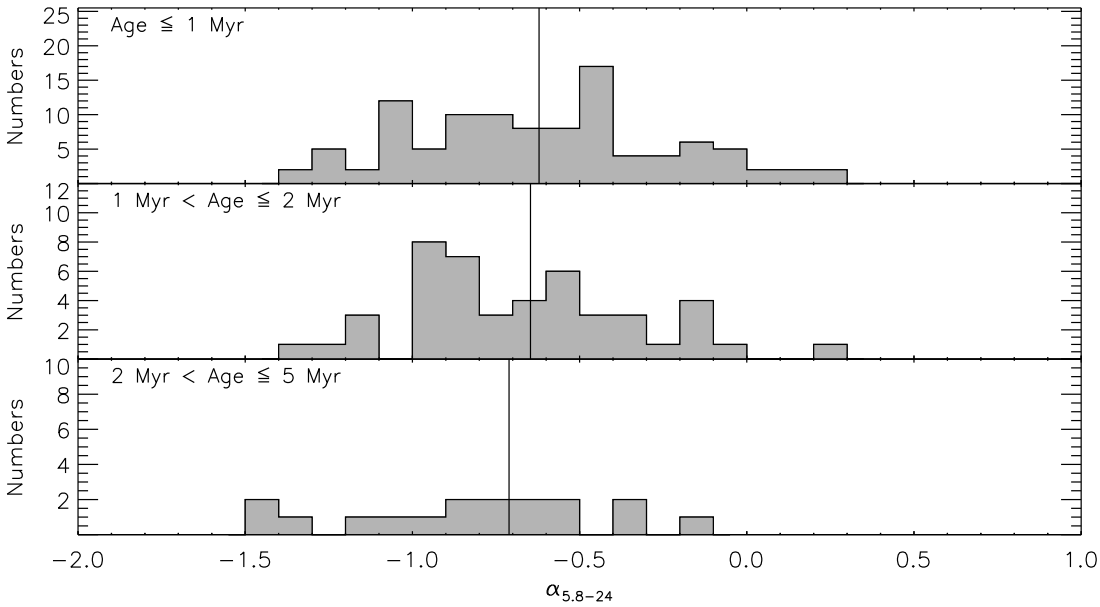

Figure 3.12: The spectral slope $\alpha_{5.8-24}$ between the IRAC 5.8 and MIPS 24 bands in different age bins. This slope is a measure for the disk geometry on scales of a few AU, see Sect. 3.3.3(1c). The solid lines show the median value of this slope for each age bin.

disks account for 73±9% and 10±3% of all sources, respectively. In L1641C, 59±11% of sources have an optically thick disk and 16±6% have an evolved disk. In L1641D, these fractions are 63±7% and 10±3%, respectively.

Some YSOs, preferentially those without strong excess emission, did not have solid detections in all four IRAC bands. For these sources, we visually inspected the SEDs for signs of infrared excess emission, by comparing the observed IRAC fluxes with the reddened model atmospheres fitted to the optical and near-infrared data. Including these stars leads to somewhat lower total disk frequencies (optically thick + evolved) compared to the numbers quoted above: 70% in L1630N, 67% in L1641C (aggregate/clutser population in L1641), and 59% in L1641D (distributed population in L1641). We remind the reader that these values likely still slightly overestimate the true disk frequencies in an abolute sense, due to the bias introduced by our target selection (see Sect. 3.1.3(3)).

(c) Disk flaring & dust settling

In Fig. 3.12 we show histograms of the spectral slope between the IRAC 5.8 and MIPS 24 bands. As discussed in Sect. 3.2.4(1), this slope is a measure of the disk geometry on scales of a few AU. We have split our sample into three age bins, and have excluded sources with an SED indicative

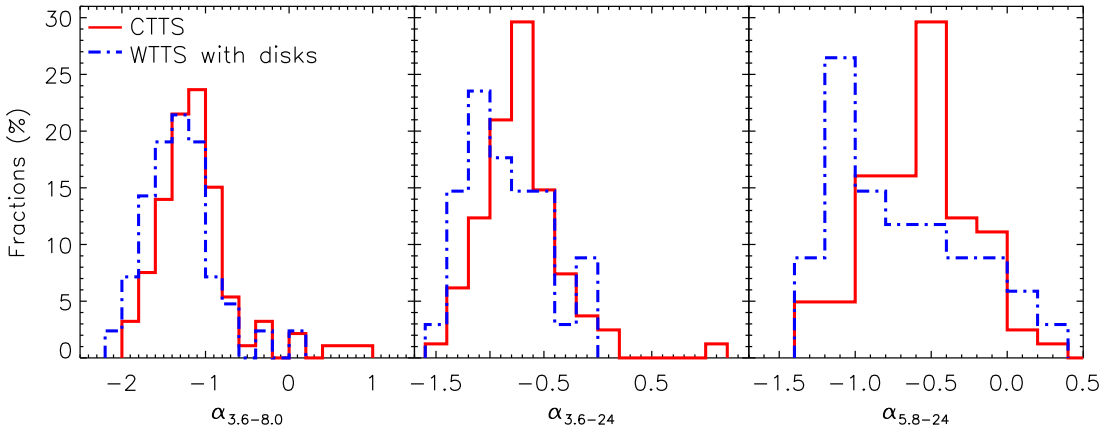

Figure 3.13: The distributions of the spectral slopes between the IRAC 3.6 and 8.0 bands, the IRAC 3.6 and MIPS 24 bands, and the IRAC 5.8 and MIPS 24 bands for CTTSs and WTTSs with disks.

of a transition disk. Since the special geometry of transition systems causes the 5.8 μm radiation to mostly not arise in the disk whereas the stellar photons are converted into 24 μm radiation with above average efficiency, their $\alpha_{5.8-24}$ as a proxy for the disk geometry cannot be compared directly with that of normal disks.

From Fig. 3.12 it becomes immediately apparent that there is a large range of observed spectral slopes $\alpha_{5.8-24}$ in each of the age bins. The median slope decreases slightly when going to larger ages, but this effect is much smaller than the scatter within the individual age bins. Thus, while our data do suggest the occurence of "flat" disks to increase with progressing age, they also imply that age is not the main factor determining whether a disk has a flared or a flat geometry. Assuming that all disks start out with a flared geometry, the rate at which dust settling turns them into flat disks varies strongly from source to source. The uncertainties in the ages of the individual objects are too small to explain the observed spread in the rates at which the disks evolve, and the spread must instead be intrinsic. A prime candidate mechanism for influencing this process is binarity (e.g. Bouwman et al. 2006), a property which we do not assess in this work.

In Fig. 3.13 we show distributions of the spectral slopes between the IRAC 3.6 and 8.0 bands ($\alpha_{3.6-8}$), the IRAC 3.6 and MIPS 24 bands ($\alpha_{3.6-24}$), and the IRAC 5.8 and MIPS 24 bands($\alpha_{5.8-24}$), for CTTSs and WTTSs with disks. For the same reason as discussed above, we have excluded transition disk objects. Though a large dispersion in the spectral slopes is present for both populations, the CTTSs show on average "redder" slopes than the WTTSs with disks in all the spectral indices considered, especially for $\alpha_{3.6-24}$, and $\alpha_{5.8-24}$. A KS test toward the distributions of the specral slopes hints that $\alpha_{3.6-8}$ is different for both populations, with a probability of $P \sim 0.14$ for

CTTSs and WTTSs with disks to be drawn randomly from the same parent distribution. The difference in the other two indices $\alpha_{3.6-24}$ and $\alpha_{5.8-24}$ is more evident, with probabilities of $P \sim 0.02$ and $P \sim 0.03$ for both sets to be drawn randomly from the same population, respetively. Since the infrared spectral slopes trace the disk geometry, our observations provide evidence for a correlation between disk geometry evolution and accretion evolution (see also e.g. Sicilia-Aguilar et al. 2006b). This does, however, not necessarily imply a causal connection between the two.

(d) Transition disks

The SEDs of all sample stars were visually inspected to select those that comply with the description of a transition disk given by Muzerolle (2008). We include all 3 flavors of transition disks discussed by Muzerolle (2008), see also Sect. 3.2.4(1). The SEDs are shown in Fig. 3.14, in which we also show the best fit (reddened) model atmospheres. In Fig. 3.10(b) we show a Ks-[5.8] vs. [8.0]-[24] color-color diagram incorporating 2MASS and Spitzer data. In this diagram, the transition disks have been marked with + symbols. They occupy a well defined area in the lower right part of the diagram, outlined by the folowing borders:

$$[8.0] - [24] \geq 2.5 \tag{3.3}$$

$$K_s - [5.8] \leq 0.56 + ([8.0] - [24]) \times 0.15 \tag{3.4}$$

Note that the transition objects are much more clearly separated from the rest of the population in this diagram than in the "classical" IRAC [3.6]-[4.5] vs. [5.8]-[8.0] color-color diagram shown in Fig. 3.10(a). In the latter diagram, the transition objects cover on average intermediate positions between "diskless" stars and normal disks, but show a signifiant overlap with both distributions. Stars with little or no excess emission at $\lambda \leq 8\,\mu$m but strong excess at $24\,\mu$m are naturally properly identified only in the Ks-[5.8] vs. [8.0]-[24] diagram (Fig. 3.10(b)). Among the 256 stars we identify to possess a circumstellar disk there are 28 transition disk objects, i.e. the transition disks constitute ~11% of the disk population. Note that, Using the criteria described above, we indentify 47 additional transition disk candidates based on their photometry. Their photometric magnitudes at optical and infrared wavelengths are listed in Table 3.16.

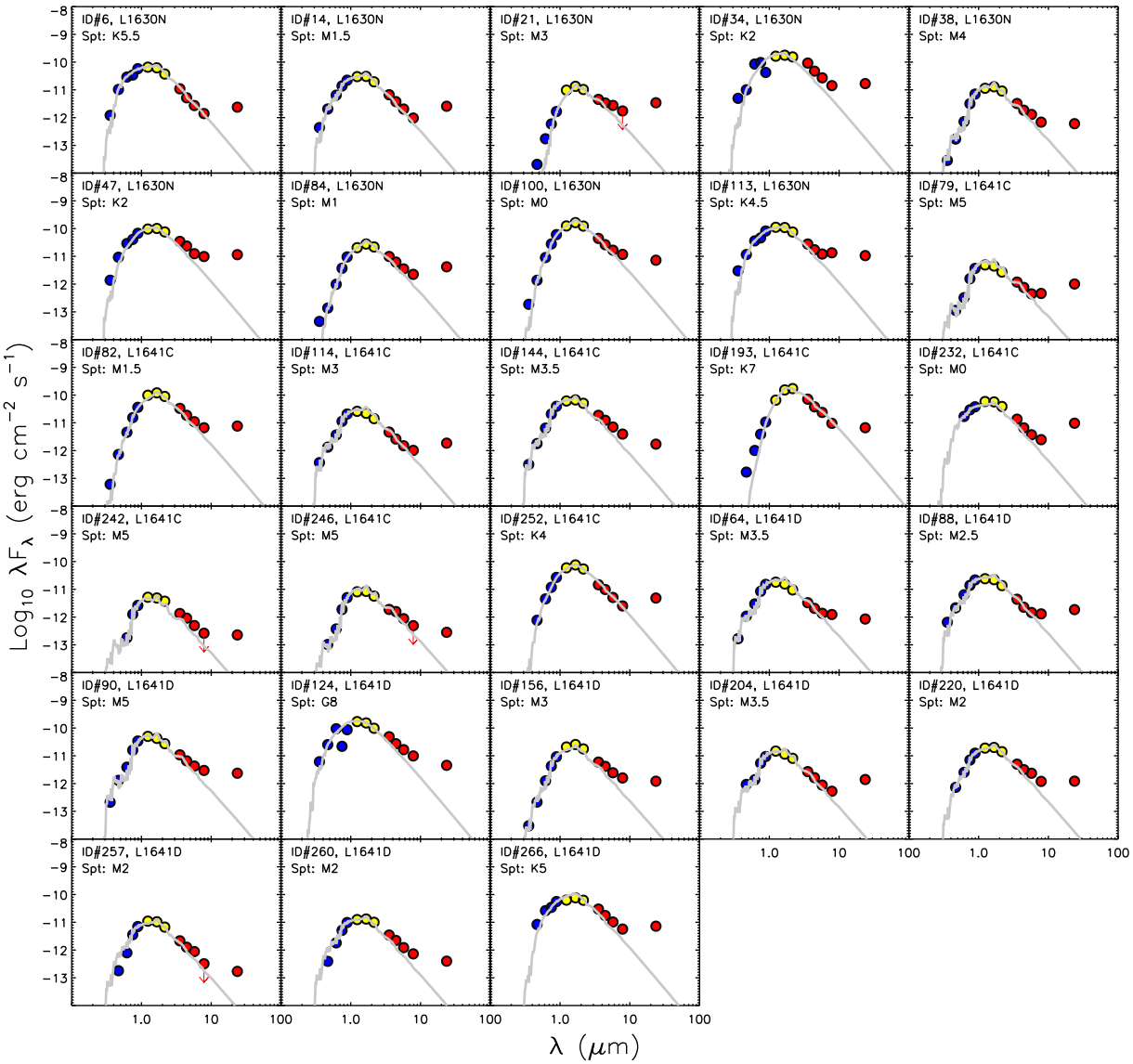

Figure 3.14: The SEDs of YSOs with transition disks in L1630N and L1641. The photospheric emission level is indiacted with a grey curve in each panel.

Table 3.16: Photometric magnitudes for transition disk object candidates.

ID	RA (J2000)	DEC (J2000)	u′ (mag)	g′ (mag)	r′ (mag)	i′ (mag)	z′ (mag)	J (mag)	H (mag)	K_s (mag)	[3.6] (mag)	[4.5] (mag)	[5.8] (mag)	[8.0] (mag)	[24] (mag)
1	05 42 56.39	−08 37 45.9	...	...	17.76± 0.01	16.26 0.01	...	13.74± 0.02	12.87± 0.02	12.57± 0.02	12.41± 0.06	12.17± 0.06	12.27± 0.06	12.36± 0.09	8.85± 0.06
2	05 42 45.03	−08 33 36.2	...	...	20.31± 0.01	18.06 0.01	16.79± 0.01	13.26± 0.03	12.02± 0.04	11.40± 0.02	10.90± 0.06	10.96± 0.06	10.46± 0.06	10.23± 0.06	6.40± 0.06
3	05 42 30.62	−08 32 55.2	...	13.97± 0.01	12.92± 0.01	12.48 0.01	12.52± 0.01	10.82± 0.02	10.13± 0.02	9.76± 0.02	9.20± 0.06	8.92± 0.06	8.70± 0.06	8.47± 0.06	3.89± 0.06
4	05 43 13.53	−08 31 00.5	...	...	20.88± 0.01	18.70 0.01	17.25± 0.01	14.22± 0.03	12.54± 0.03	11.77± 0.02	11.21± 0.06	10.87± 0.06	10.78± 0.06	10.82± 0.06	5.90± 0.06
5	05 42 39.33	−08 26 28.2	...	17.48± 0.01	15.59± 0.01	14.57 0.01	14.05± 0.01	12.59± 0.02	11.73± 0.02	11.53± 0.02	11.39± 0.06	11.20± 0.06	10.78± 0.06	9.89± 0.06	6.38± 0.06
6	05 42 53.59	−08 20 22.7	...	19.02± 0.01	16.89± 0.01	15.72 0.01	14.72± 0.01	12.80± 0.02	11.77± 0.02	11.35± 0.02	10.88± 0.06	10.39± 0.06	10.34± 0.06	9.52± 0.06	5.68± 0.06
7	05 43 04.56	−08 16 39.1	...	...	18.92± 0.01	17.12 0.01	15.88± 0.01	13.63± 0.02	12.49± 0.03	11.94± 0.02	11.69± 0.06	11.04± 0.06	10.96± 0.06	10.07± 0.06	6.87± 0.06
8	05 42 35.59	−08 15 01.9	...	18.79± 0.01	16.98± 0.01	15.72 0.01	14.69± 0.01	13.01± 0.02	12.07± 0.02	11.69± 0.02	11.34± 0.06	11.31± 0.06	11.07± 0.06	10.66± 0.08	5.77± 0.06
9	05 42 49.78	−08 12 10.2	...	20.26± 0.01	17.80± 0.01	16.44 0.01	15.29± 0.01	13.06± 0.02	11.93± 0.02	11.56± 0.02	11.02± 0.06	11.00± 0.06	10.81± 0.06	10.42± 0.14	5.19± 0.06
10	05 42 27.56	−08 05 26.0	...	...	...	17.82 0.01	17.29± 0.01	14.62± 0.03	13.61± 0.03	13.14± 0.04	12.88± 0.06	12.59± 0.06	12.26± 0.12	11.90± 0.10	8.38± 0.06
11	05 42 47.40	−08 04 05.3	...	19.90± 0.01	17.97± 0.01	16.38 0.01	15.51± 0.01	13.72± 0.02	12.91± 0.02	12.55± 0.03	12.28± 0.06	11.55± 0.06	11.66± 0.09	10.37± 0.13	7.23± 0.06
12	05 40 13.75	−08 02 59.4	...	22.46± 0.12	20.65± 0.04	19.12 0.02	18.17± 0.03	16.15± 0.12	15.96± 0.22	15.27± 0.22	15.19± 0.06	15.04± 0.06	14.54± 0.11	13.43± 0.12	8.22± 0.06
13	05 42 29.13	−07 58 29.5	...	19.55± 0.01	17.75± 0.01	15.77 0.01	15.43± 0.01	12.95± 0.02	12.14± 0.02	11.78± 0.02	11.23± 0.06	11.31± 0.06	11.23± 0.06	11.06± 0.07	8.49± 0.06
14	05 39 46.05	−07 53 00.6	22.10± 0.34	20.15± 0.02	18.41± 0.01	16.56 0.01	15.54± 0.01	13.80± 0.03	13.10± 0.03	12.83± 0.04	12.46± 0.06	12.44± 0.06	11.94± 0.06	11.45± 0.06	8.83± 0.06
15	05 42 04.41	−07 51 49.8	...	...	20.48± 0.01	18.26 0.01	17.01± 0.01	14.69± 0.03	13.88± 0.03	13.46± 0.04	12.98± 0.06	12.95± 0.06	12.82± 0.06	12.66± 0.10	8.58± 0.06
16	05 41 52.59	−07 50 25.0	...	...	...	17.38 0.01	16.73± 0.01	14.75± 0.04	14.12± 0.04	13.77± 0.05	13.23± 0.06	12.80± 0.06	12.74± 0.06	12.64± 0.09	9.21± 0.06
17	05 38 35.19	−07 50 19.5	16.12± 0.01	15.48± 0.01	12.85± 0.01	12.40 0.01	13.27± 0.01	10.69± 0.02	9.97± 0.02	9.71± 0.02	9.58± 0.06	9.13± 0.06	9.09± 0.06	7.84± 0.06	4.05± 0.06
18	05 41 54.06	−07 49 53.2	...	17.64± 0.01	16.10± 0.01	14.55 0.01	14.11± 0.01	12.23± 0.03	11.45± 0.03	11.08± 0.02	10.89± 0.06	10.50± 0.06	10.52± 0.06	10.57± 0.06	6.50± 0.06
19	05 40 06.25	−07 47 44.3	19.21± 0.04	17.76± 0.01	16.20± 0.01	15.15 0.01	14.45± 0.01	12.98± 0.02	12.23± 0.03	11.98± 0.02	11.74± 0.06	11.56± 0.06	11.48± 0.06	10.84± 0.06	5.96± 0.06
20	05 40 49.33	−07 46 32.7	...	...	...	... ...	17.07± 0.01	14.00± 0.02	12.40± 0.02	11.72± 0.02	11.34± 0.06	11.13± 0.06	11.03± 0.06	10.78± 0.06	5.25± 0.06
21	05 41 04.62	−07 45 40.3	...	17.44± 0.01	15.60± 0.01	14.39 0.01	13.53± 0.01	11.63± 0.02	10.67± 0.03	10.30± 0.02	10.07± 0.06	10.09± 0.06	9.87± 0.06	9.86± 0.06	6.18± 0.06
22	05 40 59.83	−07 43 14.3	...	...	...	18.10 0.01	16.78± 0.01	14.76± 0.04	14.14± 0.04	13.61± 0.06	13.16± 0.06	12.85± 0.06	12.71± 0.06	11.92± 0.08	9.12± 0.06
23	05 37 53.26	−07 33 44.7	21.69± 0.18	20.20± 0.02	18.81± 0.01	17.03 0.01	15.99± 0.01	14.35± 0.04	13.80± 0.04	13.41± 0.05	12.99± 0.06	12.65± 0.06	12.50± 0.06	12.09± 0.07	9.18± 0.06
24	05 40 20.39	−07 25 53.6	19.97± 0.06	17.82± 0.01	16.04± 0.01	14.91 0.01	14.22± 0.01	12.67± 0.02	11.85± 0.03	11.59± 0.03	11.59± 0.06	11.31± 0.06	11.35± 0.06	10.93± 0.07	5.96± 0.06
25	05 39 18.39	−07 20 23.4	...	24.04± 0.74	21.12± 0.07	19.41 0.03	18.23± 0.04	16.20± 0.12	15.13± 0.11	14.73± 0.12	14.33± 0.06	14.01± 0.06	13.62± 0.09	13.46± 0.29	6.91± 0.06
26	05 39 20.54	−07 17 31.1	...	...	...	20.29 0.01	...	15.65± 0.08	14.21± 0.04	13.49± 0.05	12.92± 0.06	12.65± 0.06	12.40± 0.06	11.98± 0.10	8.00± 0.06
27	05 38 33.84	−07 17 02.8	17.75± 0.01	15.79± 0.01	14.33± 0.01	13.51 0.01	12.75± 0.01	11.09± 0.02	10.36± 0.02	10.14± 0.02	9.94± 0.06	9.95± 0.06	9.79± 0.06	10.00± 0.06	7.40± 0.06
28	05 37 16.41	−07 11 46.3	18.33± 0.04	17.79± 0.02	17.08± 0.01	16.79 0.01	16.04± 0.02	14.65± 0.03	13.98± 0.04	13.63± 0.05	13.00± 0.06	12.59± 0.06	12.86± 0.06	12.18± 0.10	7.78± 0.09
29	05 38 17.44	−07 09 39.4	22.79± 0.54	20.25± 0.02	17.71± 0.01	15.77 0.01	14.60± 0.01	12.44± 0.02	11.26± 0.02	10.83± 0.03	10.43± 0.06	10.38± 0.06	10.05± 0.06	9.46± 0.06	4.35± 0.06
30	05 36 20.55	−07 05 31.6	18.99± 0.03	16.74± 0.01	15.35± 0.01	14.39 0.01	13.72± 0.01	12.16± 0.02	11.40± 0.03	11.16± 0.02	10.78± 0.06	10.44± 0.06	10.20± 0.06	9.36± 0.06	6.50± 0.06
31	05 37 56.03	−07 01 49.9	...	...	...	21.15 0.10	18.79± 0.04	15.42± 0.07	13.76± 0.04	13.03± 0.04	12.47± 0.06	12.19± 0.06	12.05± 0.06	11.57± 0.09	8.02± 0.12
32	05 37 49.34	−06 51 37.1	21.12± 0.10	18.79± 0.01	17.09± 0.01	15.52 0.01	14.58± 0.01	12.86± 0.02	12.05± 0.03	11.77± 0.03	11.45± 0.06	11.43± 0.06	11.31± 0.06	10.75± 0.07	6.62± 0.07
33	05 34 59.02	−06 42 17.6	19.07± 0.02	17.34± 0.01	15.96± 0.01	14.94 0.01	14.30± 0.01	12.73± 0.02	11.94± 0.03	11.68± 0.02	11.38± 0.06	11.19± 0.06	11.13± 0.06	10.32± 0.06	7.31± 0.06
34	05 37 32.44	−06 39 04.9	19.69± 0.08	17.71± 0.01	16.32± 0.01	15.09 0.01	14.41± 0.01	12.97± 0.02	12.28± 0.02	12.07± 0.03	11.99± 0.06	11.68± 0.06	11.77± 0.06	11.59± 0.13	6.88± 0.07
35	05 37 47.46	−06 36 29.7	22.64± 0.37	19.68± 0.01	17.32± 0.01	15.95 0.01	14.95± 0.01	12.91± 0.02	11.84± 0.03	11.38± 0.03	10.98± 0.06	10.91± 0.06	10.70± 0.06	10.54± 0.07	6.29± 0.06
36	05 36 39.32	−06 30 10.9	20.68± 0.06	18.68± 0.01	17.31± 0.01	15.74 0.01	14.85± 0.01	13.34± 0.03	12.67± 0.03	12.46± 0.03	12.14± 0.06	11.84± 0.06	11.99± 0.07	11.33± 0.17	6.70± 0.06
37	05 36 58.98	−06 29 04.7	20.05± 0.05	17.76± 0.01	16.33± 0.01	14.92 0.01	14.14± 0.01	12.62± 0.02	11.88± 0.03	11.65± 0.03	11.32± 0.06	11.28± 0.06	11.13± 0.06	10.87± 0.12	6.89± 0.06
38	05 34 49.97	−06 28 12.0	17.96± 0.01	15.80± 0.01	14.49± 0.01	13.82 0.01	13.36± 0.01	12.08± 0.03	11.32± 0.03	11.14± 0.02	10.98± 0.06	10.82± 0.06	10.54± 0.06	9.52± 0.06	6.49± 0.06
39	05 35 37.32	−06 23 26.3	18.88± 0.03	17.13± 0.01	15.74± 0.01	14.91 0.01	13.98± 0.01	12.52± 0.02	11.88± 0.03	11.61± 0.02	11.33± 0.06	11.31± 0.06	11.23± 0.06	11.17± 0.09	5.89± 0.06
40	05 36 55.22	−06 20 25.7	19.41± 0.03	17.58± 0.01	16.20± 0.01	15.04 0.01	14.38± 0.01	13.00± 0.03	12.30± 0.03	12.08± 0.03	11.88± 0.06	11.67± 0.06	11.64± 0.06	10.61± 0.07	6.64± 0.06
41	05 34 57.45	−06 19 33.1	20.29± 0.04	18.03± 0.01	16.64± 0.01	15.27 0.01	14.55± 0.01	13.16± 0.03	12.40± 0.03	12.23± 0.02	11.89± 0.06	11.85± 0.06	11.75± 0.06	11.02± 0.11	6.94± 0.06
42	05 36 40.40	−06 13 33.3	17.77± 0.01	16.11± 0.01	14.74± 0.01	14.52 0.01	13.48± 0.01	12.20± 0.02	11.51± 0.03	11.28± 0.02	10.97± 0.06	10.94± 0.06	10.91± 0.06	10.49± 0.07	6.13± 0.06
43	05 36 47.51	−06 08 20.2	19.93± 0.05	17.69± 0.01	16.30± 0.01	15.12 0.01	14.40± 0.01	13.05± 0.03	12.36± 0.03	12.12± 0.02	11.74± 0.06	11.39± 0.06	11.50± 0.06	11.58± 0.11	6.99± 0.06
44	05 48 06.03	−00 15 16.8	...	...	...	... ...	...	17.18± 0.21	16.43± 0.24	15.43± 0.18	15.36± 0.06	15.05± 0.06	14.62± 0.09	13.29± 0.09	9.21± 0.06
45	05 47 21.50	−00 08 59.6	22.74± 0.21	20.73± 0.02	19.23± 0.01	17.62 0.01	16.66± 0.01	15.18± 0.04	14.54± 0.04	14.33± 0.08	13.84± 0.06	13.74± 0.06	13.85± 0.08	13.10± 0.11	9.39± 0.06
46	05 46 40.58	−00 08 10.4	...	...	...	... ...	...	16.88± 0.01	16.19± 0.22	14.95± 0.15	14.67± 0.06	14.48± 0.06	14.09± 0.08	11.69± 0.07	9.08± 0.06
47	05 46 42.48	+00 23 01.3	...	...	...	... ...	...	16.47± 0.01	15.19± 0.09	14.36± 0.07	13.56± 0.06	13.20± 0.06	13.11± 0.07	12.73± 0.14	5.92± 0.06

(2) Accretion signatures

Accretion characteristics are obtained from observations of optical emission lines, in particular the hydrogen Balmer series and the He I 5876Å line.

(a) Hα emission profiles

We observed Hα emission in 86 young stars in L1630N, and 178 objects in L1641. The vast majority of these stars, 78% in L1630N and 88% in L1641, show symmetrical profiles with a single peak in our observations. These have a median full width at 10% of the peak intensity of $FW_{10\%}$~270 km s^{-1}. If we divide the sample into CTTSs and WTTSs according to their Hα EWs (see Appendix (1)), we find that the former have broader lines with a median $FW_{10\%}$~320 km s^{-1} and the latter are narrower with a median $FW_{10\%}$~230 km s^{-1}. The limited spectral resolution of our observations would yield a $FW_{10\%}$~180 km s^{-1} for a line with zero intrinsic width. Therefore, the majority of the observed Hα lines are spectrally resolved, even if in some cases only marginally so.

About 22% and 12% of YSOs in L1630N and L1641, respectively, show broad asymmetrical Hα lines that are easily resolved in our observations. We show normalized Hα profiles for most of these in Fig. 3.15. The median $FW_{10\%}$ of these stars is approximately 500 km s^{-1}, i.e. their Hα lines are much broader than those of the CTTSs with symmetrical line profiles. We generally see clear substructure in the line, mostly in the form of double-peaked emission. For comparison, we have overplotted their Hβ profiles, which are usually similar but on occasions strikingly different from the Hα lines. They illustrate a complex accretion geometry in which the line emission is at least partially optically thick.

(b) Hα equivalent widths

The equivalent widths of the Hα lines we observed in our sample range from less than 1 Å to over 300 Å. Equivalent widths of more than 3 to 20 Å (depending on spectral type) point at active accretion and our measurements reveal a range of accretion rates spanning several orders of magnitude (see Appendix (1) for an exact description of the Hα equivalent width threshold used to distinguish between CTTSs and WTTSs, as a function of spectral type). Hα emission with an equivalent width below the CTTS/WTTS threshold cannot be unambiguously attributed to accretion activity, as it may also be caused by stellar coronal activity. While Hα emission below the threshold may in some cases be caused by weak accretion (Sicilia-Aguilar et al. 2006b), our purpose here is to define the EW limit above which we can be sure that the Hα emission is dominantly accretion induced.

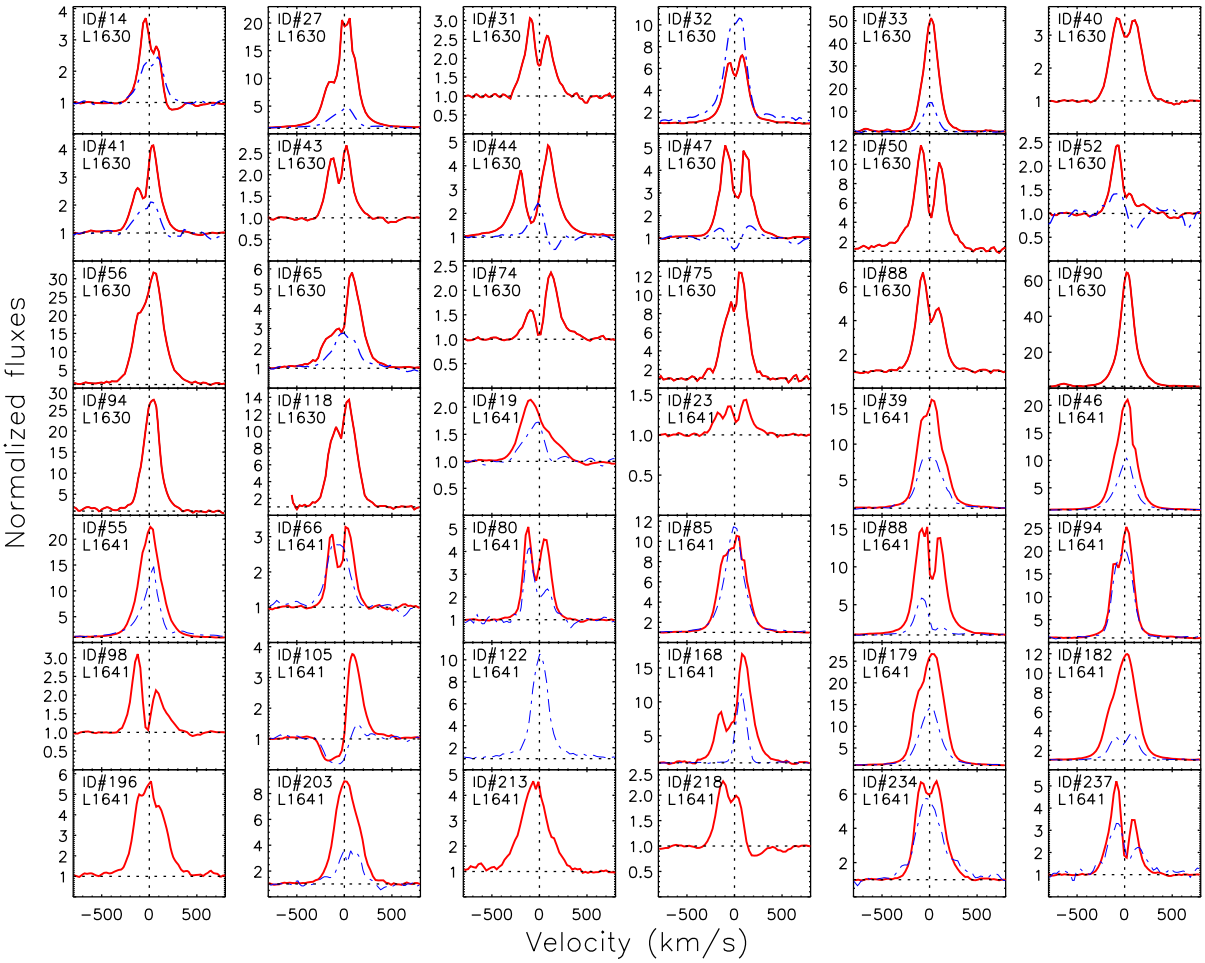

Figure 3.15: Normalized Hα (solid lines) and Hβ (dashed lines) emission lines of sources that show particularly broad and complex line profiles. Note that the majority of sources show single-peaked, much more symmetric profiles.

(c) Accretion rates derived from Hα, Hβ, and He I

In Fig. 3.16(a-c) we show the accretion rates as derived from the Hα, Hβ, and He I equivalent widths using the methods described in Sect. 3.2.4(2) and Appendix (2), as a function of stellar mass. The uncertainties in the accretion rates were calculated from the uncertainties in the equivalent width measurements, and assuming a 10% error in the continuum flux when converting equivalent widths to line luminosities. For the Hα EWs from the literature that did not have published uncertainties, we assigned an error of 10% of emission-line flux. Since these diagrams are mostly populated with the same stars, we can use them to investigate whether the derived mass accretion rate of an ensemble of stars depends on which line is used as a diagnostic. We have excluded stars with extinctions above A_V=5 mag.

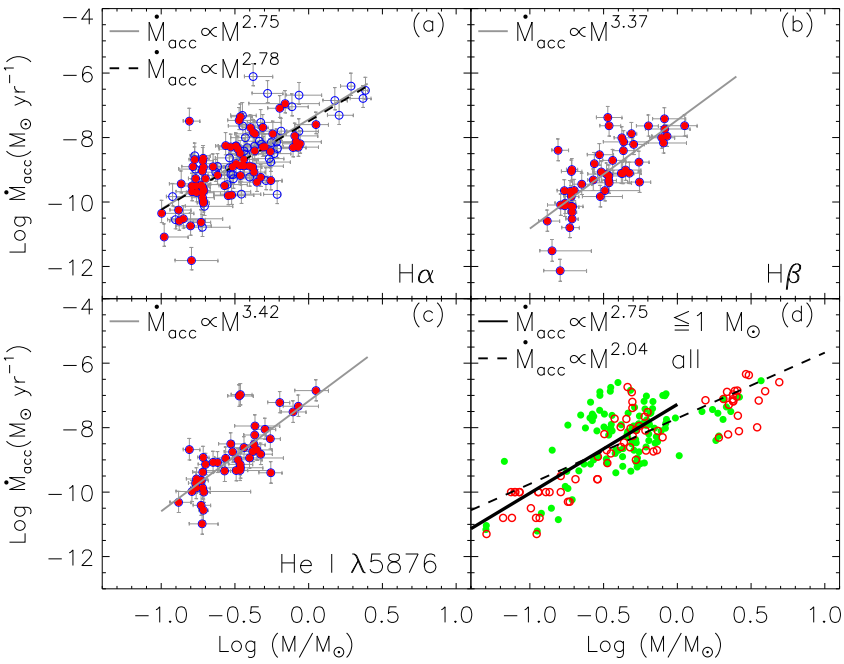

Figure 3.16: (a)(b)(c): The relation between accretion rates deduced from the Hα(a), Hβ (b), or He I $\lambda = 5876$ (c) emission line luminosity and stellar mass for the YSOs in our spectroscopic sample in L1630N and L1641. In panel (a), the filled circles represent the YSOs observed with VIMOS, and the open circles show the YSOs from literature. The solid line in each figure represents the best fit power law to the observed distribution for all sources in the VIMOS sample. In panel (a), the dashed line shows the best fit if also literature values are included. (d): the relation between accretion rates and stellar masses for YSOs in the literature, i.e. explicitly excluding our results (see Sect. 3.4.2). The filled circles represent YSOs with accretion rates estimated from U-band excess emission or veiling in UV/optical spectra, the open circles represent stars for which accretion rates were estimated from emission lines (Hα, Ca IIλ8662, Brγ, Paβ, and Paγ).

The relation between the mass accretion rate as derived from the Hα emission line and the stellar mass is shown in Fig. 3.16(a). A linear regression in log-log space of the entire sample investigated (including spectral types and Hα EWs from the literature), taking into account the uncertainty in the mass accretion rate of individual objects, yields the following best fit:

$$Log\dot{M}_{\rm acc} = -7.44(\pm0.11) + 2.78(\pm0.22) \times logM_{*} \quad (3.5)$$

where $\dot{M}_{\rm acc}$ is the mass accretion rate in $M_{\odot}$ yr^{-1}, and M_{*} is the stellar mass in $M_{\odot}$. If we include only those stars that we observed with VIMOS, the best fit remains essentially unchanged:

$$log\dot{M}_{\rm acc} = -7.50(\pm0.17) + 2.7(\pm0.30) \times logM_{*} \quad (3.6)$$

If we use the Hβ emission line to estimate the accretion rate, a linear regression gives a best fit

of:

$$log\dot{M}_{\rm acc} = -7.46(\pm0.18) + 3.36(\pm0.38) \times logM_{*} \quad (3.7)$$

and in case of the He I λ 5876 Å emission line, we get:

$$log\dot{M}_{\rm acc} = -7.18(\pm0.21) + 3.42(\pm0.38) \times logM_{*} \quad (3.8)$$

Thus, within uncertainties, we find the same behavior of the accretion rate with stellar mass from each of the three emission lines investigated. Taking simply a weighted average of the exponents in the above relations, we find: $\dot{M}_{\rm acc} \propto M_{*}^{3.13\pm0.34}$, where the standard deviation in the distribution was adopted as the uncertainty in the exponent.

(d) Accretion rates as a function of stellar mass and age

As outlined above, we find that the mass accretion rate in our sample shows an approximate power law relation with the stellar mass, with an exponent of 2.8−3.4. This is only an average relation, and individual objects scatter around this relation by at least an order of magnitude. Interestingly, the relation that we find is steeper than those found in previous work, where exponents in the range of 1.0−2.1 were found (White & Basri 2003; Muzerolle et al. 2003; Calvet et al. 2004; Muzerolle et al. 2005; Mohanty et al. 2005; Natta et al. 2006; Garcia Lopez et al. 2006; Herczeg & Hillenbrand 2008; Gatti et al. 2008). We will discuss this further in Sect. 3.4.2.

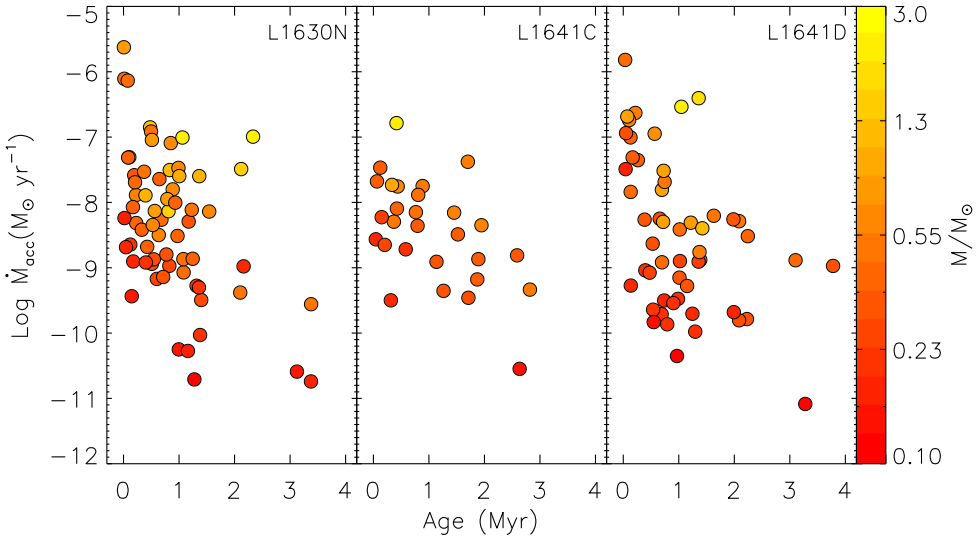

Figure 3.17: The relations between accretion rates from Hα emission luminosity and stellar ages for YSOs in L1630N, L1641C, and L1641D. The symbol colors correspond to different stellar masses.

In Fig. 3.17 we show the accretion rates as a function of stellar age. In this figure, each star is color-coded according to its mass. On the whole, we observe a clear trend of decreasing accretion rate with increasing age. This trend is more obvious for stars below $0.5\,M_{\odot}$ than for the more massive members, though. For very low mass stars (M_{*}<$0.3\,M_{\odot}$), the accretion rate evolves from $\sim 10^{-8} - 10^{-9}\,M_{\odot}\,\mathrm{yr}^{-1}$ at ages below 1 Myr to $\sim 10^{-9} - 10^{-11}\,M_{\odot}\,\mathrm{yr}^{-1}$ at ages above 3 Myr. Our ensemble of stars with measured accretion rates contains only 11 stars with a mass above $1.0\,M_{\odot}$. These all are younger than 3 Myr and have accretion rates of order $10^{-9} - 10^{-11}\,M_{\odot}\,\mathrm{yr}^{-1}$. Within this sample there is no clear evidence for an evolution of accretion rate with age.

(3) Other emission lines

In addition to the hydrogen and helium emission lines, which were discussed in the previous section, a number of other emission lines are frequently seen in the optical spectra of our sample stars. These may trace accreting material, the disk surface, jets, or stellar/disk winds. In the following paragraph we briefly recall existing knowledge concerning these lines.

Forbidden line emission in the [O I] 6300 Å line often shows a low- and a high-velocity component. The low-velocity component may trace the disk surface (e.g. Acke & van den Ancker 2006) or in a poorly collimated disk wind (e.g. Kwan & Tademaru 1995), whereas the high-velocity component arises in a jet close to the star (Hartigan et al. 1995). Forbidden line emission in the [O I] 5577Å line appears primarily as a low-velocity component (Hamann 1994; Hartigan et al. 1995). Note that this line may suffer from terrestrial atmospheric contamination in some cases. Forbidden line emission in the [N II] 6583 Å and 6678 Å lines usually shows up only in the high-velocity component, tracing the unresolved stellar jet (Hartigan et al. 1995). The Ca II near-infrared triplet (8498, 8542, and 8662 Å) often shows anomalous intensity ratios in T Tauri stars, strongly deviating from the nominal 1:9:5 line ratio for optically thin media, with the 8498Å line being stronger than the 8542Å line in some sources (Hamann 1994). The Ca II triplet often shows a broad emission profile, and the line fluxes correlate strongly with the accretion rate, suggesting these lines are formed in the magnetospheric infall flow (Muzerolle et al. 1998a). Forbidden emission in the [S II] line is rarely observed towards T Tauri stars due to the low abundance of sulfur in the interstellar medium (Hartigan et al. 1995).

We examined all young stars observed with VIMOS for the abovementioned emission lines. In Tables 3.9 and 3.10 we give an inventory of the lines detected in the individual stars, listing their equivalent widths. In Fig. 3.18, we compare the observed luminosities in six emission lines with the accretion luminosities (L_{acc}) as derived from Hα. All lines are strongly correlated with the accretion luminosity, but some lines show a larger dispersion around the average correlation than others. In particular, the [O I] 5577 and 6300 Å lines show a rather large scatter. This agrees with the notion that these lines are not directly related to the accretion process but instead arise

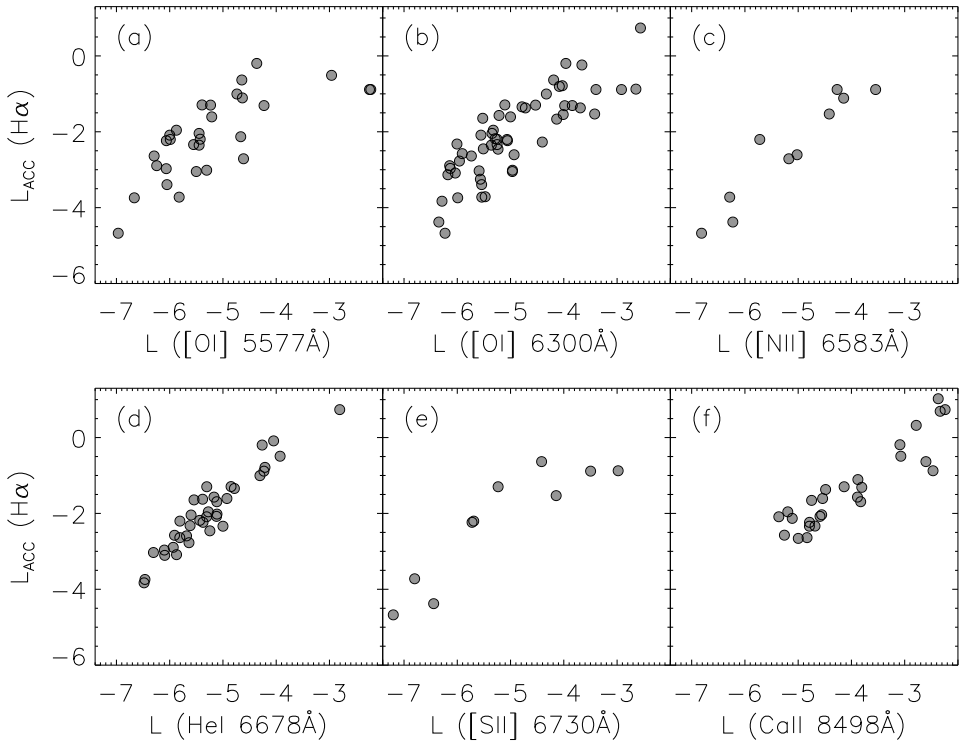

Figure 3.18: The correlation between accretion luminosities and the emission luminosities of different emission lines: (a) [O I] 5577 Å, (b) [O I]6300 Å, (c) [N II] 6583 Å, (d) He I 6678 Å, (e) [S II] 6730 Å, and (f) Ca II 8498 Å. The accretion luminosities are calculated from Hα emission luminosity using the formulae in Appendix (2).

in, e.g., the disk surface (see e.g. Acke & van den Ancker 2006; Fedele et al. 2008; van der Plas et al. 2008). For these lines, the correlation between line luminosity and accretion luminosity may simply be explained by the scaling of $L_{\rm acc}$ with stellar mass, and the fact that more massive, more luminous stars will induce more [O I] emission in their vicinity. The He I 6678 Å line is very strongly correlated with $L_{\rm acc}$, showing only a very small dispersion. This confirms that it is a good tracer for accretion. The Ca II 8498 Å line only appears in objects with $L_{\rm acc}$>3×10^{-4} $L_{\odot}$ and also shows a relatively small dispersion around the average relation. The [N II] 6583 Å and [S II] 6730 Å lines are detected in too few sources (~10) to properly assess how tightly they correlate with $L_{\rm acc}$. These lines are thought to arise in jets emerging from accreting systems and therefore their luminosities are expected to roughly scale with $L_{\rm acc}$. Based on our data we cannot distinguish between such an accretion-jet relation and a simple scaling of the line luminosities with the stellar luminosity. Note also that line emission in jets depends on shocks being present, i.e. the jet impinging on an ambient medium or having varying outflow rates and velocities, causing jet-internal shocks. Thus, a relation between the luminosity of line emission from jets and the accretion rate may be dilluted by temporal variations in both quantities, as well as by

source to source differences in the ambient medium.

Eight of the young stars we observed show both the [S II] 6716 and 6731 Å lines. The flux ratio of these lines provides a direct measure of the electron density. The relative intensities (6716/6731) are identical within uncertainties, with a median ratio of 0.53, suggesting that both [S II] lines are saturated with electron density $>7\times10^3$ cm^{-3} (Hamann 1994).

3.3.4 Exotic objects

A natural consequence of conducting a survey in which large numbers of sources are studied, is the discovery of objects with extreme properties. We will briefly discuss several objects we considered worth special attention.

(1) Subluminous objects with high emission line equivalent widths

Three stars in L1630 (#33, #90, and #94) and one star in L1641 (#122) show exceptionally rich emission line spectra, with the emission lines exhibiting very high equivalent widths. In addition to the hydrogen balmer series, emission lines of He I, N II, S II, O I, O II, Ca II, Fe I, Fe II, and Na I are identified. All these stars have strong infrared excesses in the IRAC and MIPS bands, but generally show little or no excess in the near-infrared 2MASS bands. Their optical spectra and SEDs are shown in Fig. 3.19.

The high equivalent widths of e.g. Hα are not due to abnormally high line luminosities, but instead seem to be caused by reduced photospheric continuum levels, making the lines appear bright in contrast. We have marked these sources in the HR diagram (Fig. 3.6), and they appear subluminous by a factor ~10 with respect to the bulk of objects of similar spectral type.

Comerón et al. (2003) have previously identified sources with similar properties in the Lupus 3 dark cloud. They investigated 3 possible explanations: (1) the sources are embedded, strongly accreting Class I sources seen in scattered light; (2) they are sources with edge-on disks of which we see the photosphere only in scattered light but the emission lines (more) directly, making the latter appear bright in contrast; (3) they are sources in which strong sustained accretion alters the pre-main sequence evolution making objects appear subluminous for their spectral type (Hartmann et al. 1997; Siess et al. 1997).

Option (1) is excluded by Comerón et al. (2003) since Class I sources seen in scattered light would have easily been spatially resolved in their observations, which instead revealed point sources. In our VIMOS pre-imaging observations, stars #33 and #90 in L1630N appear as single

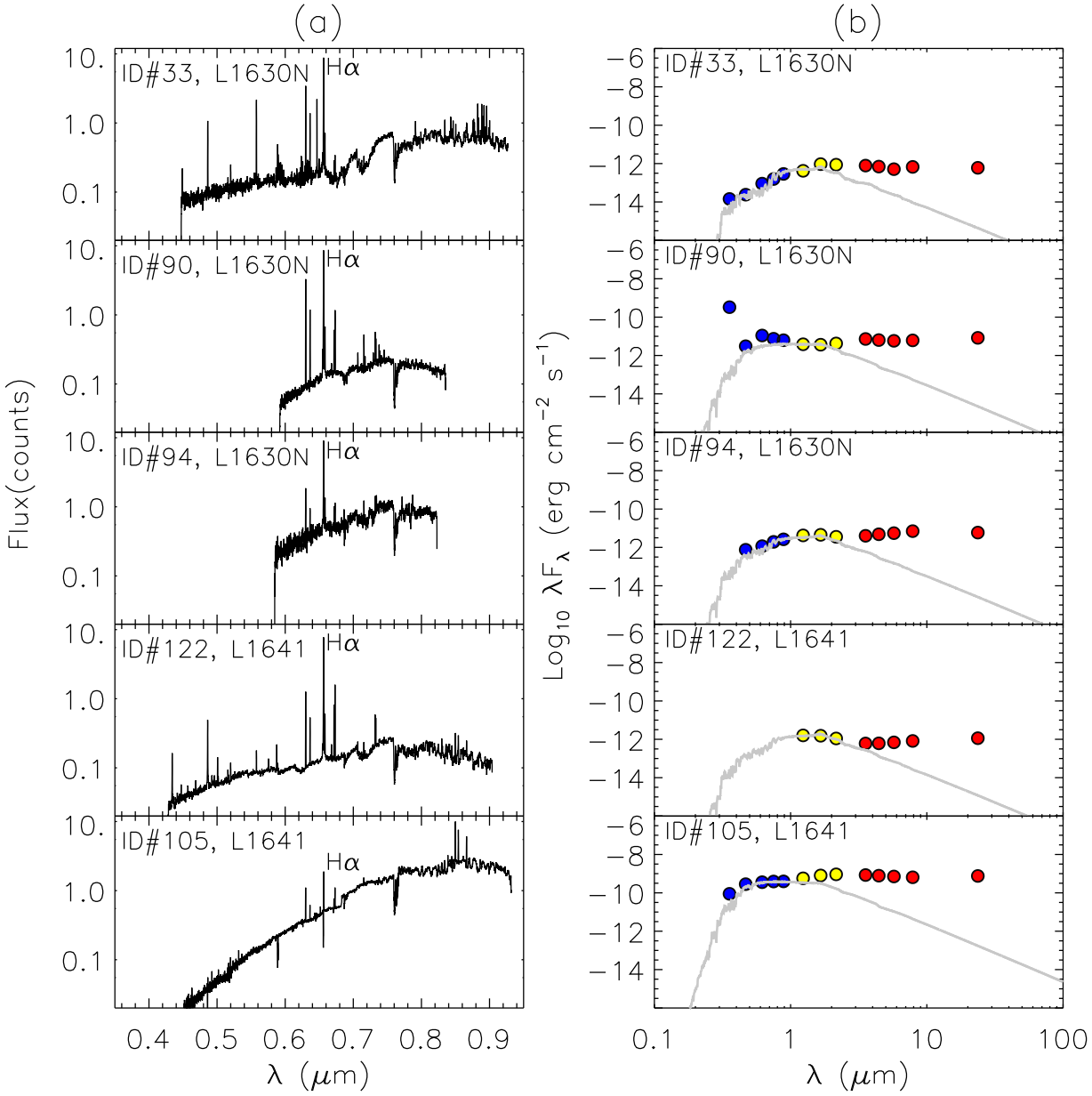

Figure 3.19: The optical spectra (left panels) and dereddened SEDs (right panels) for the four exotic stars in L1630 and L1641 (see Sect. 3.3.4(1)), and a new the FU Orionis object (ID#105 in L1641, see Sect. 3.3.4). The photospheric emission level is indiacted with a grey curve in each panel. The blue points represent the optical photometry from SDSS or LAICA, the yellow points indicate 2MASS photometry, and the red points indicate Spitzer photometry.

point sources at the resolution limit of our observations of $fwhm \sim 0\farcs7$ (315 AU). Our image of star #94 in L1630N is well reproduced by the sum of two point sources, suggesting that this star is a binary at a separation of $0\farcs66$ (~300 AU). The fainter component (in the R-band) is located south-east of the brighter component at a position angle of ~109° E of N. We do not think that this object is an edge-on disk seen in scattered light, since in that case the individual "blobs" of scattered light would be expected to be spatially resolved, given their large separation. Star #122 in L1641 appears as a point source, but has a faint, spatially extended "blob" of emission about $0\farcs8$ north of the star. This may be shock-induced Hα emission from a jet emerging from this object. We conclude that we do not find spatially extended emission from the central sources, in agreement with Comerón et al. (2003).

Option (2) was considered to be unlikely by Comerón et al. (2003) since there is strong evidence from the Hα line strengths and line widths that they are formed in magnetospheric accretion columns very close to the star. Thus, an hypothetical edge-on disk would obscure the emission lines as much as the photospheric continuum and the equivalent widths would remain unaltered, though the apparent under-luminosity can be explained in such a scenario. Also in our observations the balmer lines are clearly spectrally resolved and likely arise close to the central star. Thus, we agree with Comerón et al. (2003) that edge-on disks do not provide a satisfactory explanation of the nature of these objects.

Comerón et al. (2003) consider option (3) the most likely scenario for their exotic objects. Even though the magnitude of the "under-luminosity" in their objects is clearly larger than predicted by theory, the models do provide a good qualitative match to the observations. Comerón et al. (2003) argue, though, that the effect will be stronger for their sources because of the lower mass compared to the range studied by Hartmann et al. (1997).

(2) A new FU Orionis object

Star #105 in L1641 shows a clear P-cygni profile in both the Hα and Hβ lines. Blue-shifted absorption is observed at a range of velocities up to approximately -300 km s^{-1}, the peak of the Hα emission is redshifted to ~100 km s^{-1} (see Fig. 3.15), a typical profile of Hα emission line from FU Orionis type stars (Reipurth et al. 1996; Fedele et al. 2007). In Fig. 3.19, its optical spectrum and SED are shown. The IR excess of this source is extraordinarily strong and the IR luminosity exceeds the estimated stellar luminosity by a factor of $\gtrsim$5. Emission in forbidden transitions of [O I], [S II], and [N II], as well as permitted transitions of Fe I and Fe II are detected. We derived a spectral type of K5.5 for this star, which compares reasonably well with an earlier determination of K3 by Allen (1995).

The observed properties of this object provide a perfect match to those of FUOR stars, a rel-

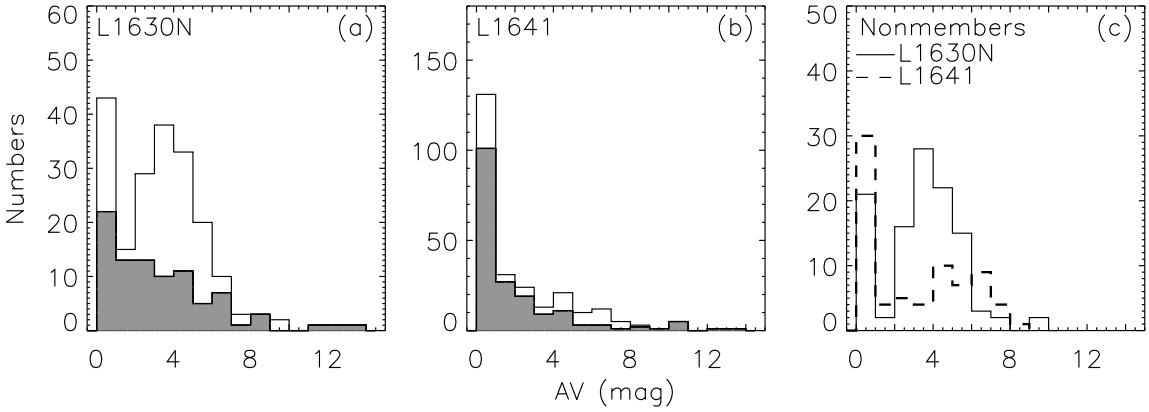

Figure 3.20: (a)(b): The visual extinction distribution of our sample observed with VIMOS in L1630N and L1641. The open histograms show the distribution of all the stars with reliable spectral types. The filled histograms display the YSO distribution among them. (c): The visual extinction distribution for non-members in L1630N (solid-line histogram) and L1641 (dashed-line histogram).

atively rare class of young stars thought to undergo an accretion outburst, and whose system luminosity is dominated by the release of gravitational energy of accreting material rather than stellar photospheric emission. The IR excess emission constitutes an estimated luminosity of $20\,L_{\odot}$. Given the estimated stellar mass and radius, an accretion rate of a few times $10^{-6}\,M_{\odot}\,\mathrm{yr}^{-1}$ is implied. The forbidden emission points at strong outflow activity.

3.3.5 Extinction

Robust extinction estimates were made for each individual object using the method outlined in Sect. 3.2.3(2). In Fig. 3.20(a,b) we show the resulting A_V distributions, distinguishing between cloud members (shaded grey) and field stars. In Fig. 3.20(c) we zoom in on the field population.

The YSOs show a similar distribution of extinction values in both clouds: a peak in the distribution at very low extinction (A_{V}<1 mag) and a gradual decrease in number counts towards higher A_{V}. The fraction of sources with very high optical extinctions (A_{V}>5 mag) is somewhat higher in L1630 than in L1641, the opposite is true for sources with A_{V}<1. The distribution of extinction values may reflect the distribution of the young stars within the molecular cloud: stars located "on the near side" of the cloud will on average have low extinction, whereas objects located "on the far side" have higher extinctions. However, "local" density variations within the cloud may affect the distribution equally well: some sources will be located behind very dense clumps whereas others are not. Additionally, some objects may have a disk inclination such that our sight line goes through the outer part of their flared disks, causing additional local

"circumstellar" extinction. Remnant envelopes may have the same effect.

The field population shows a different distribution of extinctions, best seen in Fig. 3.20(c). Also here there is a peak at A_V<1 mag, consisting of foreground objects and background objects at relatively "clean" sight lines. In addition, there is a distribution between 1 and ~8 magnitudes of A_V. This distribution is relatively well defined in L1630N with a clear peak around A_V=3−4 mag, but is somewhat broader in L1641. It reflects the total column density of dust in the entire cloud in the sight lines towards the respective stars. Note that in both the YSO and field population there is a bias *against* objects with very high extinctions, since such objects are too faint for optical spectroscopy.

3.3.6 Spatial distribution of YSOs in L1630N and L1641

The spatial distributions of young stars in the L1630N and L1641 clouds are shown in Fig. 3.2, overplotted on ^{13}CO maps by Bally et al. (1987) and Miesch & Bally (1994). The positions of (Lada) Class 0/I and Class II sources, identified on the basis of their infrared colors using the criteria in Gutermuth et al. (2008), have been indicated with yellow asterisks and red + signs, respectively. The young stars included in our spectroscopic (VIMOS) sample have been marked with blue dots. Note that these include both Class II and Class III sources.

As noted before by numerous authors (e.g. Hartmann 2002; Megeath et al. 2005a; Evans et al. 2009), the distribution of Class 0/I sources closely follows the densest parts of the molecular cloud as traced by the ^{13}CO data, and shows a filamentary structure. The Class II sources are distributed more evenly, though they also show concentrations in the densest cloud parts. The YSOs in L1630N are mainly distributed in two clusters, which are associated with two dense regions of ^{13}CO molecular clouds. In L1641 the young stars are more dispersed across the whole region, with several local concentrations. Based on their near-infrared image survey, Strom et al. (1993) have identified 8 aggregates in this region. Since their observations do not cover the entire L1641 region, we applied the nearest neighbor method to the spitzer data to find the new aggregates/clusters. With the NNM, we find 9 aggregates in L1641, named groups 1-9. Among these, group 3 and 4 are newly identified. Groups 1, 2, 5, 6, 7, 8 and 9 correspond to the L1641 south cluster, the CK group, L1641 C, KMS 36, KMS 35, the V380 Ori group, and L1641N, respectively, as identified by Strom et al. (1993). We do not recover the aggregate HH 34/KMS 12 due to the small number of stars (~5) it possesses.

3.4 Discussion

A general goal of surveys like ours is to gain insight in the physics of disk evolution by finding empirical relations between observable properties. In particular, we may seek for correlations of disk geometry and accretion rate with stellar mass, age, and formation environment. An evolution of the disk geometry and the accretion rate with age is certainly expected, as well as a dependence of the accretion rate on stellar mass. Disk evolution is a function of stellar mass as well, in the sense that disks around high-mass stars (approximately B type and earlier on the main sequence) evolve faster than those around low-mass stars (e.g. Natta et al. 2000a; Alonso-Albi et al. 2009). Whether the evolution of the disk depends on stellar mass within the low-mass regime probed here, is not clear. The influence of the formation environmment, i.e. whether a star formed in a clustered environment or in isolation, is a matter of debate. One may consider how the disk evolution is affected by gravitational interactions with other cluster members and by the strongly enhanced (far-) UV radiation field compared to interstellar space, causing photo-evaporation of the outer disk regions. When making quantitave theoretical assessments of these effects, one finds that the disk regions we see at $\lambda \lesssim 24\,\mu$m are not noticably affected, even in clusters of 100-1000 members (Adams 2008). The number of members in the aggregates or clusters that we identify is usually considerably smaller (N<100), and thus, from a theoretical vantage point, we do not expect to see a significant effect of the formation environment on the disk properties.

3.4.1 Disk frequency: trends with stellar mass and age

In Fig. 3.21 we display the fraction of YSOs which show clear indications of circumstellar material in the form of infrared excess emission, as a function of stellar mass[5]. For reasons outlined in Sect. 3.1.3(3), these numbers may somewhat over-estimate the true disk frequency, but trends with stellar mass and age remain unaffected. In Fig. 3.21 we also show the disk frequencies for IC 348 as found by Lada et al. (2006) and Chamaeleon I as found by Luhman et al. (2008a). For L1630N and L1641D, we find some evidence for a disk frequency that *increases* with stellar mass: the increase between ~0.2 $M_\odot$ and ~1.5 $M_\odot$ is ~2σ and ~3σ for these populations, respectively. For the clustered population in L1641, our data are consistent with a disk fraction that is constant with stellar mass (the highest mass bin contains just 3 stars, of which 1 has a disk, and the apparent decrease is not significant). The trend of increasing disk frequency with increasing stellar mass that we tentatively identify in L1630N and L1641D is remarkably similar to that seen by Luhman et al. (2008a) in the ~2 Myr old Chamaeleon I cloud. In the somewhat older IC 348 (Lada et al. 2006) and σ Orionis (Hernández et al. 2007b) regions, the disk frequency

[5]The mass bins used are, in $\log(M_*/M_\odot)$, -1 to -0.5, -0.5 to 0, and 0 to 0.5.

is lower for the stars in the highest mass bin (see Fig. 3.21). If the behavior of increasing disk frequency with increasing stellar mass at young ages, and a reduced disk frequency for the higher mass stars at later times is universal, it may be naturally explained if the higher mass stars form somewhat later than the low mass stars but subsequently dissipate their disks faster.

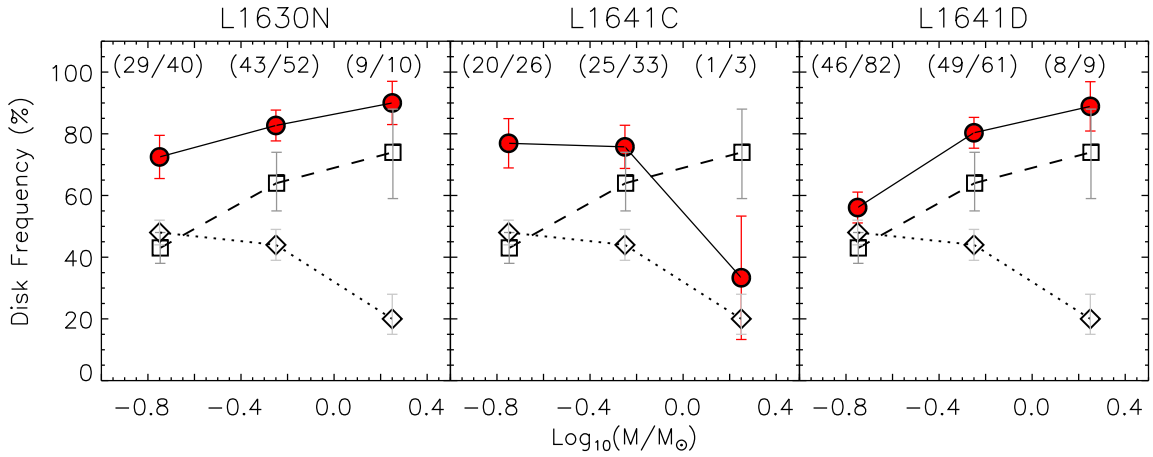

Figure 3.21: The disk frequency as a function of stellar mass for YSOs in L1630N (filled circles) and L1641C (filled circles, cluster/aggregate population), and L1641D (filled circles, distributed population), IC 348 (open diamonds, Lada et al. 2006), Chamaeleon I (open squares, Luhman et al. 2008a). Absolute number counts are given at the top of each panel, for each mass bin.

The disk frequency as a function of stellar age is shown in Fig. 3.22 (top panel). For the distributed population in L1641 we see a constant disk frequency for the first 3–4 Myr, after which we see a $\sim 2\sigma$ decrease in the last age bin. In the clustered populations L1630N and L1641C we observe a quantitatively different behavior: in the first 1–2 Myr, the disk frequency is approximately constant and consistent with that observed in L1641D, within uncertainties. In the age bin 2–3 Myr the disk frequency is reduced by $\sim 2\sigma$ in both the L1630N and L1641C populations. Both the magnitude and the timing of the decrease in disk frequency are strikingly similar in L1630N and L1641C, underlining the significance of the result. The age bins above 3 Myrs contain insufficient stars in the clustered populations to give meaningful disk frequencies. Our results strongly support the notion that disk dissipation proceeds faster in objects that form in a clustered environments than in objects that form in isolation. Qualitatively, this behavior is expected from theory. However, given the relatively low stellar densities in the clustered environments that we consider here, compared to dense clusters such as the Orion nebula cluster, the magnitude of the observed effect is higher than expected (Adams 2008).

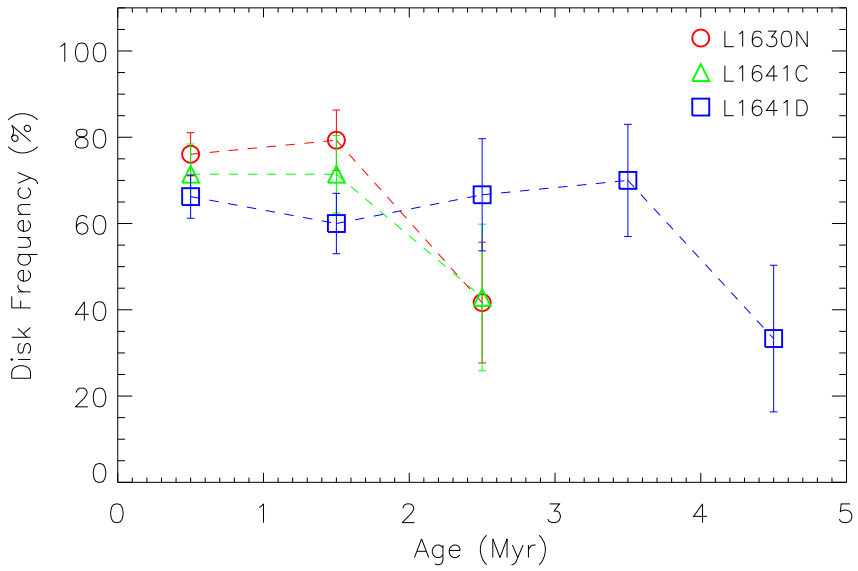

Figure 3.22: The disk frequency as a function of age for YSOs in L1630N (open circles) and L1641 (open triangles for cluster/aggregate population, and open squares for distributed population).

3.4.2 Accretion rate as a function of stellar mass

How the rate at which material accretes depends on the mass of the central star has been a topic of considerable attention. Power law fits of the form $\dot{M}_{\rm acc} \propto M_*^{\alpha}$ have yielded values in the range 1.0−2.1 for the exponent α (White & Basri 2003; Muzerolle et al. 2003; Calvet et al. 2004; Muzerolle et al. 2005; Mohanty et al. 2005; Natta et al. 2006; Garcia Lopez et al. 2006; Herczeg & Hillenbrand 2008; Gatti et al. 2008). As shown in Sect. 3.3.3(2) and Fig. 3.16(a-c), we consistently find a steeper exponent of $\alpha = 2.8-3.4$ from each of the three emission lines we use as a tracer of $\dot{M}_{\rm acc}$ (Hα, Hβ, He I). The sample we investigated contains numerous stars in the mass range of 0.1−1.0 $M_{\odot}$ but only very few stars more massive than the sun.

To investigate this further we gathered a large set of accretion rate estimates from the literature (Gullbring et al. 1998; White & Basri 2003; Muzerolle et al. 2003; Hartigan & Kenyon 2003; Calvet et al. 2004; Muzerolle et al. 2005; Natta et al. 2006; Mohanty et al. 2005; Garcia Lopez et al. 2006; Herczeg & Hillenbrand 2008; Dahm 2008), of stars in a range of star forming regions including Taurus-Aurigae, IC 348, ρ Oph, λ Ori, Orion OB and upper Scorpius. We estimate their masses using their luminosities and effective temperatures, which were taken directly from the literature, with the PMS evolutionary tracks from Dotter et al. (2008) (for M_* $\geq$0.1 $M_{\odot}$), and Baraffe et al. (1998) (for M_* <0.1 $M_{\odot}$). From the stars discussed in Natta et al. (2006) we included only those with confirmed spectral types and adopted their spectral types and luminosities from Luhman & Rieke (1999).

The result is shown in Fig. 3.16(d). The red open circles in this figure represent measurements of the mass accretion rate derived from emission line strengths, the filled green circles represent those derived from UV excess emission and veiling of optical spectra. The usual picture emerges: a clear trend of increasing accretion rate with increasing stellar mass, and a large scatter of individual sources around the average relation. If we make a power law fit of the form $\dot{M}_{\rm acc} \propto M_*^{\alpha}$, and we restrict the fit to the mass range $M_* \leq 1.0\,M_\odot$, we find a value of $\alpha \sim 2.8$ for the exponent. This is very similar to the result we have obtained from the sample studied in this work, which covers the same mass range. If we perform the same fit over the whole mass range plotted in Fig. 3.16(d), which includes a number of HAeBe stars, we find an exponent of $\alpha \sim 2.0$. The latter value agrees with that found by previous authors. Our results indicate that the dependence of accretion rate on stellar mass is not uniform over the entire mass regime, but instead is considerably steeper below $\sim 1\ M_\odot$ than at higher masses (see also Hartmann et al. 2006).

Due to the dependence of the mass accretion rate on the system age, it is important to consider this aspect. If the stars with a mass above $1\ M_\odot$ would be significantly older than those of lower mass, the the difference between the $\dot{M}_{\rm acc}(R_*)$ in the subsolar and super-solar mass regime as seen in Fig. 3.16(d) could be an artifact. We therefore checked what would happen if we include only stars from Taurus-Aurigae, IC 348, ρ Oph, and λ Ori, i.e. from regions that all have an age of $\lesssim$3 Myr. This yielded results that are consistent with those described above[6], and thus the mass dependence of the accretion rate that we derived is robust.

3.4.3 Ages of the different populations

In the traditional view of low-mass star formation, CTTSs evolve into WTTSs when their circumstellar disks dissipate, and WTTSs should therefore on average be older than CTTSs. Observations of various star-forming regions, however, did usually *not* yield evidence for an age difference between the CTTS and WTTS population (e.g. Herbig 1998; Hartmann 2001; Herbig & Dahm 2002; Dahm & Simon 2005), though in some cases the WTTS are indeed found to be older than the CTTSs (Hartigan et al. 1995; Bertout et al. 2007).

The age distribution of both classes of objects is shown in Fig. 3.23(a). This figure encompasses our entire sample of YSOs, i.e. the sources in L1630N and L1641 have been put together. The median ages of the CTTSs and WTTSs are $\sim$0.8 Myr and $\sim$1.2 Myr, respectively. A KS test reveals a relatively low probability ($P \sim 0.03$) for the WTTSs and CTTSs to be drawn randomly from the same age distribution. The WTTSs are further divided into disk harboring objects with

[6] In a fit over the whole mass regime in which only stars from the four mentioned star forming regions were included, we find $\alpha = 2.27$, i.e. only slightly larger than in the fit including all objects in Fig. 3.16(d). This small difference is due to the fact that the abovementioned star forming regions contain relatively few $M_* > 1.0\,M_\odot$ stars, thus biasing the fit towards the slope of the low-mass regime.

clear IR excess emission, and those who appear diskless. The probability that the WTTSs with and without disks are drawn randomly from the same population is low (P ~0.05), whereas the age distributions of WTTSs with disks and CTTSs are indistinguishable (P ~0.94).

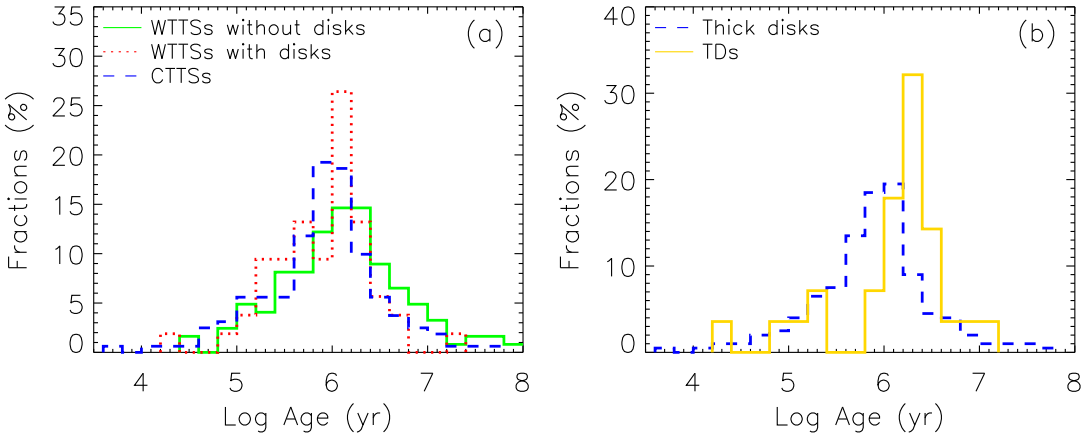

Figure 3.23: Left panel: The histograms showing the distribution of ages for the WTTSs without disks, WTTSs with disks, and CTTSs. Right panel: The distributions of ages for YSOs with "normal" optically thick disks and transition disks.

In Fig. 3.23(b) we show the age distributions for YSOs with optically thick disks and those with transition disks. The median ages for both populations are 0.8 Myr and 1.9 Myr, respectively, and the transition disks thus are on average clearly older. A KS test yields a very low probability (P ~0.003) for the stars with normal optically thick disks and the transition objects to be randomly drawn from the same population. In contrast, the age distributions of the WTTSs without disks and the transition objects are indistinguishable (P ~0.53 in a KS test).

Transition disk objects are on average older than the normal disk population. This suggests that disk-binary interaction and gravitational instabilities in the disk are not the dominant mechanisms causing a transition disk appearance, as these mechanisms would take effect from the earliest stages and would not lead to an "old" transition disk population.

3.4.4 Median SEDs

In Fig. 3.24 we show the median SEDs of the YSOs in our sample that are surrounded by "normal" optically thick disks, defined as those having $\alpha_{\rm IRAC} \geq$-1.8 (Lada et al. 2006). We also show the SEDs of sources classified as having transition disks. Following Lada et al. (2006), we divide the sample in six spectral type bins. We also show the median SEDs of the ~2-3 Myr old cluster IC 348 from Lada et al. (2006) with dotted curves, of the ~1-2 Myr old distributed population in

Taurus (Furlan et al. 2006) with solid curves, and the ~5 Myr old population in upper Scorpius (Dahm & Carpenter 2009b) with dashed curves. For the cluster IC 348, Lada et al. (2006) only presents 'observed' SEDs. We determine reddening by fitting model atmospheres of corresponding spectral types to the observations in optical bands. The derived visual extinctions are around 1-3 mag for different spectral types. Note that the Taurus median SED covers spectraly types K4-M2 without distinguishing between various sub types, the upper Scorpius SEDs distinguish only between spectral types earlier and later than M2.

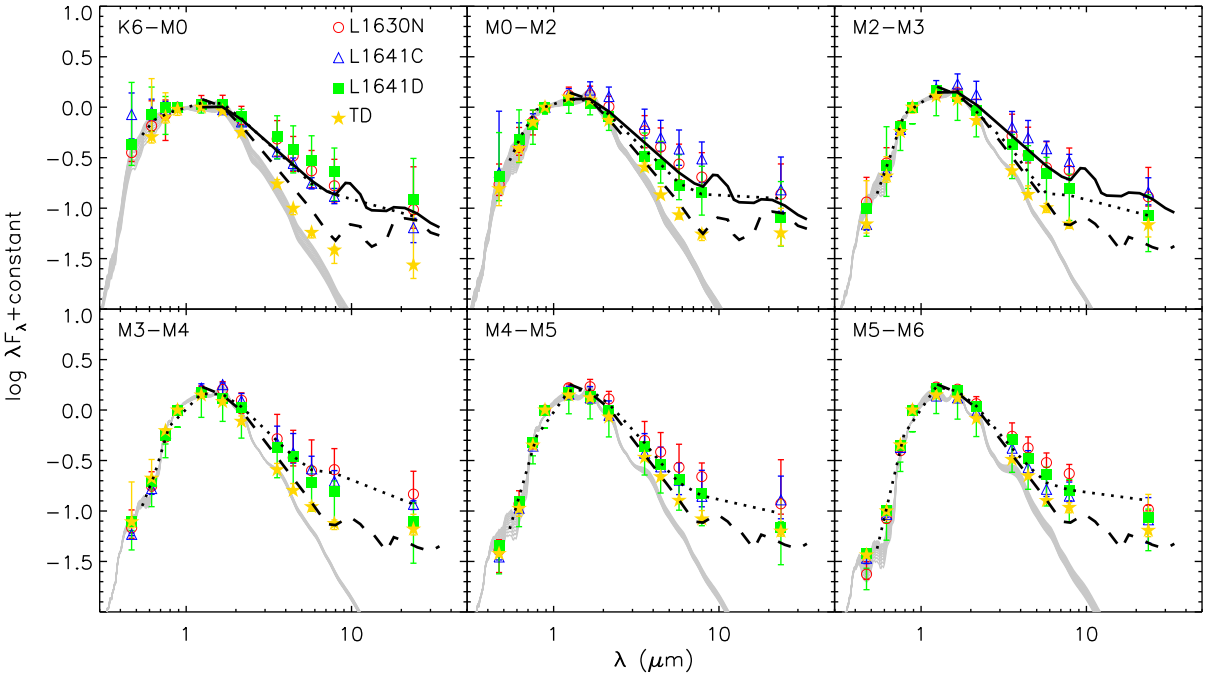

Figure 3.24: Median SEDs of the stars with optically thick disks in L1630N, L1641C and L1641D. We also plot the median SED of the transition disks, as well as those of the IC 348 (dotted line, 2-3 Myr, Lada et al. 2006), Taurus (solid line, 1-2 Myr, Furlan et al. 2006), and upper Scorpius (dashed line, ~5 Myr, Dahm & Carpenter 2009b) regions. The photospheric emission level is indicated with a grey curve in each panel.

The median SEDs of the "normal" optically thick disks in L1630N, L1641C and L1641D are identical within errors at all wavelengths and for all spectral types, except for a marginal (~2 σ) difference at 24 μm for the K6-M0 spectral bin. These SEDs are also indistinguishable from the population in IC 348 and Taurus. The transition disk SEDs are clearly different, and closely resemble the median SED of upper Scorpius.

The excess emission of the optically thick disks in the IRAC bands is a function of spectral type, with the excess being strongest for the K-type stars and becoming progressively weaker towards later spectral types. This trend is fully consistent with that found by Lada et al. (2006) in IC 348.

The transition disk sources show an opposite trend: the IRAC excess is lowest at the early spectral types but becomes noticably stronger at spectral types later than M4. The combined effect is that for spectral types later than M4, the discrimination between stars classified as having optically thick disks and those having transition disks is no longer obvious. The MIPS 24 μm excess of the transition disks is only slightly smaller than that of the optically thick disks for the early spectral types and equal within uncertainties for the later spectral types.

3.4.5 Star formation modes in L1641

With the Spitzer data, we have found 9 aggregates/clusters in L1641, which include 31±3% of YSOs identified by four IRAC bands. We have classified the YSOs identified by Spitzer into class 0/I or class II types. Among them, 58±5% of class 0/I sources and 79±6% of class II sources are formed in isolation. The high fraction of class 0/I sources in the distributed population suggests that most stars in L1641 are formed in isolation, since these class 0/I sources are very young (less than 0.5 Myr, Evans et al. 2009), and cannot leave their parental molecular cloud given the typical stellar velocity dispersion of in the Orion molecular cloud complex of ∼1 km s^{-1} (Strom et al. 1993).

In our sample, YSOs formed in aggregates/clusters account for 31±3% of all YSOs in L1641, consistent with previous estimates of, e.g., ∼30% (Strom et al. 1993), or 25-50% (Allen 1995). The median age for YSOs in aggregates/clusters is 1.1 Myr, which is similar to the median age (∼ 1.2 Myr) for the distributed populations. A Kolmogorov-Smirnov (KS) test yields no statistically significant difference betweeen the age distributions of both populations (P ∼0.3) and we thus find no evidence for a different star formation history between the clustered and distributed populations.

We divide the ages τ of our sample into three bins, i.e., $\tau \leq 1$ Myr, 1 Myr$\leq \tau <$3 Myr, and 3 Myr$\leq \tau <$10 Myr. For each age bin, we compute the fraction of stars that resides in the distributed population, and plot these in Fig. 3.25. We obtain an additional point in this diagram at the youngest ages by including the class 0/I sources identified from the Spitzer data and assigning an age of less than 0.5 Myr to these (Evans et al. 2009). The resulting fractions of YSOs in the distributed population are 58±6% for objects younger than ∼0.5 Myr (the class 0/I sources), 65±8% for stars younger than 1 Myr (class II sources), 69±9% in the interval 1−3 Myr, and 77±13% in the interval 3−10 Myr. These fractions are equal within the uncertainties of the individual points. However, a slight trend of an increasing fraction in the distributed population with increasing age is seen. This suggests that the older, unbound aggregate/cluster population is slowly spreading into the distributed population. We note, however, that this effect is too small to produce significant differences in the average age of the aggregate/cluser and distributed

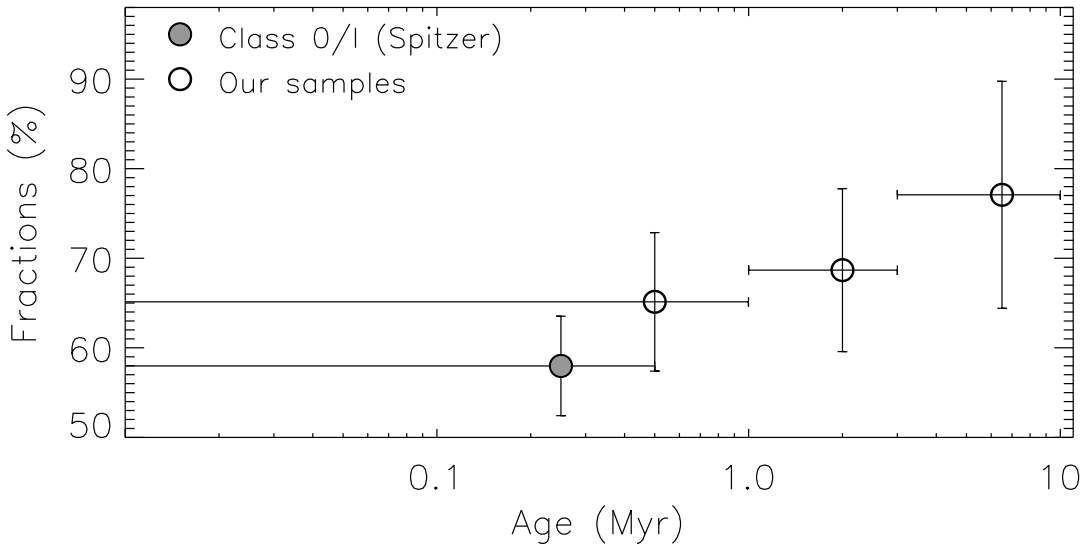

Figure 3.25: The fractions of distributed population in L1641 at different age bins.

populations, and that most of the stars that we see in isolation were formed in isolation.

3.4.6 Accretion in transition disks

Najita et al. (2007) have compiled the properties of a dozen transition disks in the Taurus-Aurigae star foming region from the literature, studying in particular the accretion rate and the disk mass. They find that, in comparison to other stars of similar age, objects harboring transition disks have a ∼10 times *lower* median accretion rate and a ∼4 times *higher* median disk mass. These results suggest an important role for forming jovian planets in the evolution from optically thick disks to transition objects: if a planet is massive enough it will open a gap in the disk, after which the disk region interior to the planet is quickly drained by viscous evolution and the accretion rate onto the central star drops. Since massive giant planets may form more easily within massive disks, this scenario would explain both the lower median accretion rates and the higher median disk masses of transition objects. Note, though, that based on SMA observations of a sample of transition disks, Cieza et al. (2008) find that the inner disks only start to be cleared out after the outer disk has been significantly dissipated. These observations therefore argue for photo-evaporation to be the dominant processes driving disk evolution.

In our spectroscopic sample there are 28 transition disks distributed over the L1630N and L1641 clouds, of which 23 have estimated Hα equivalent widths. We compare their Hα EWs with those of the other YSOs in Fig. 3.26. Among the transition disks, 26±11% (6 out of 23) show "strong" accretion activity, here defined as having an Hα equivalent width of more than 2 times

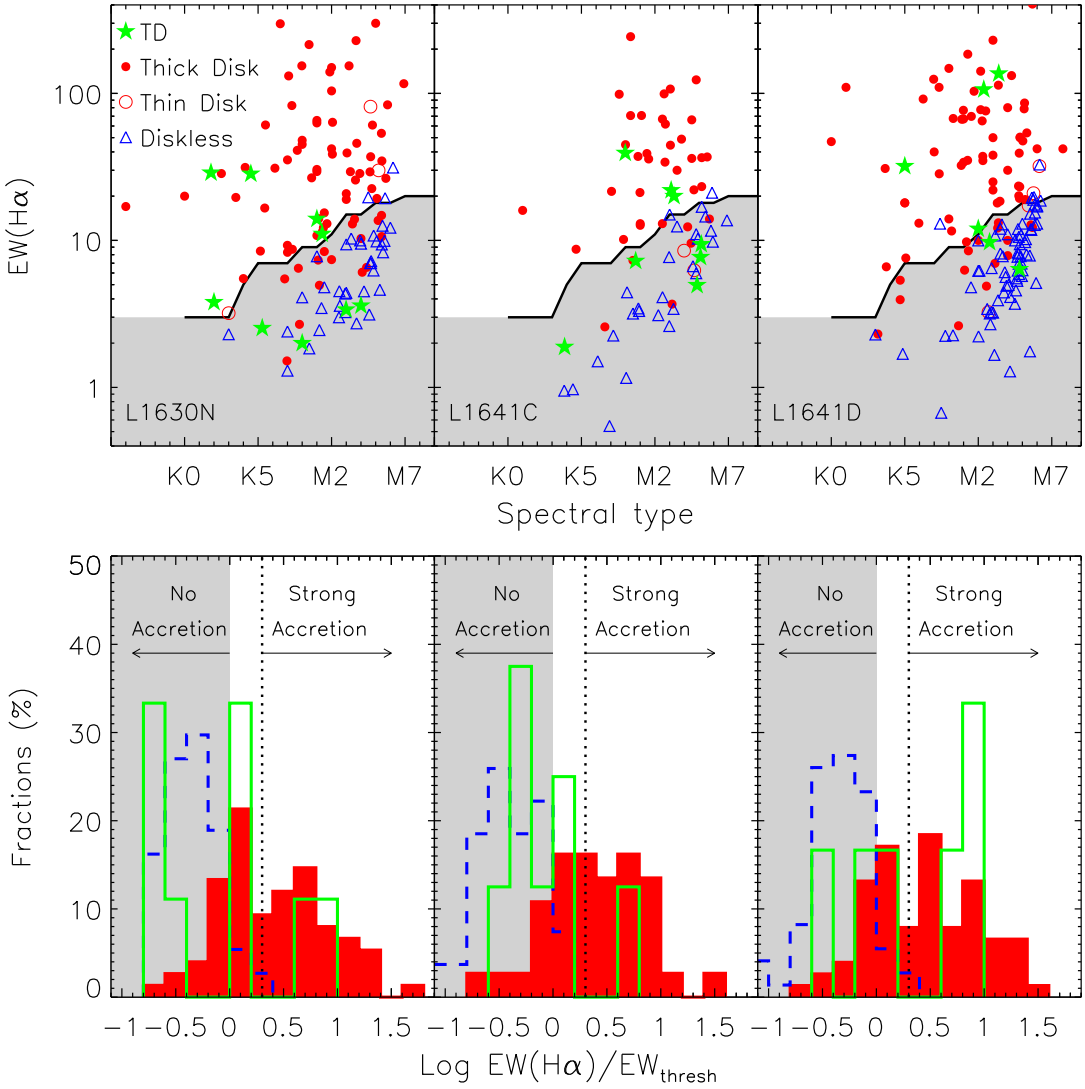

Figure 3.26: The top panels: The Hα EWs vs. spectral type for YSOs in the three populations discussed in this work. The filled circles are for YSOs with optically thick disks, open circles for YSOs with optically thin disks, asterisks for YSOs with transition disks, and triangles for YSOs without disks. The solid line is the boundary between WTTSs and CTTSs (see Appendix (1)). The bottom panels: the distribution of logarithmic ratio between the observed Hα EW and the EW threshold, which used to classify the YSOs into CTTSs or WTTSs for the corresponding spectral type, for three population: YSOs with optically thick disks (filled histogram), YSOs with transition disks (solid-line histogram), and YSOs without disks (dashed-line histogram).

the EW threshold used to distinguish between CTTSs and WTTSs (see Appendix (1)). In the stars surrounded by optically thick disks this fraction is 57±6%, and thus there are significantly fewer strong accretors among the transition disks. However, among the transition disks that do show active accretion (Hα EW above the WTTS/CTTS threshold[7]), the median accretion rate is $3.0\times10^{-9}\,M_{\odot}\,\mathrm{yr}^{-1}$, which is very similar to the median accretion rate of the CTTSs with optically thick disks in our sample: $\sim4.0\times10^{-9}\,M_{\odot}\,\mathrm{yr}^{-1}$. Note that Najita et al. (2007) find a median accretion rate of $3.2\times10^{-9}\,M_{\odot}\,\mathrm{yr}^{-1}$ for their transition disks, which is consistent with the value we find. However, Najita et al. (2007) find a much higher median accretion rate of $\sim2.5\times10^{-8}\,M_{\odot}\,\mathrm{yr}^{-1}$ for the optically thick disk-harboring CTTSs in the Taurus-Aurigae region than we find for our Orion sample ($\sim4.0\times10^{-9}\,M_{\odot}\,\mathrm{yr}^{-1}$). The latter value is consistent with the "typical" accretion rate of young T Tauri stars of $\sim3\times10^{-9}\,M_{\odot}\,\mathrm{yr}^{-1}$ (Gullbring et al. 1998; White & Basri 2003; Muzerolle et al. 2003), and is also in perfect agreement with the findings of Sicilia-Aguilar et al. (2009, in prep.) who find a median accretion rate of 2-3$\times10^{-9}\,M_{\odot}\,\mathrm{yr}^{-1}$ for both the young stars with optically thick disks and those with transition disks in Trumpler 37.

In summary, we find that the fequency of accreting stars is lower among transition disk objects than among stars with optically thick accretion disks, but the median accretion rate among the actively accreting stars is similar in both populations.

3.4.7 Clumpiness of the molecular clouds

Our observations of numerous background objects yield accurate "pencil-beam" estimates of the integrated extinction through the whole cloud. The extinction can be converted into estimates of the dust column density along each sight line. The angular scale probed by each measurement is simply the angular diameter of the respective background star, and will typically be of order 10^{-2} milli-arcseconds. The millimeter ^{13}CO data yield estimates of the gas surface density at a spatial resolution of 1.′7 (Miesch & Bally 1994). Thus, we get two measures of the surface density of the molecular cloud Σ_{cloud}, at vastly different spatial resolutions. The comparison of both yields information on the clumpiness of the regions probed: both column density measures will correlate well in the case of a homogeneous medium, whereas they will correlate poorly if the medium shows strong substructure on scales below the resolution of the millimeter data. A number of authors have studied similar correlations between pencil beam extinction estimates, usually based on near-infrared photometry, and tracers of the gas density (C^{18}O, ^{13}CO, CS, e.g. Lada et al. 1994; Kramer et al. 1999; Alves et al. 1999), and found evidence for a clumpy cloud structure.

[7]We remind the reader that Hα emission with an EW below the CTTS/WTTS threshold cannot be unambiguously attributed to accretion, and we therefore exclude the WTTSs from the current comparison.

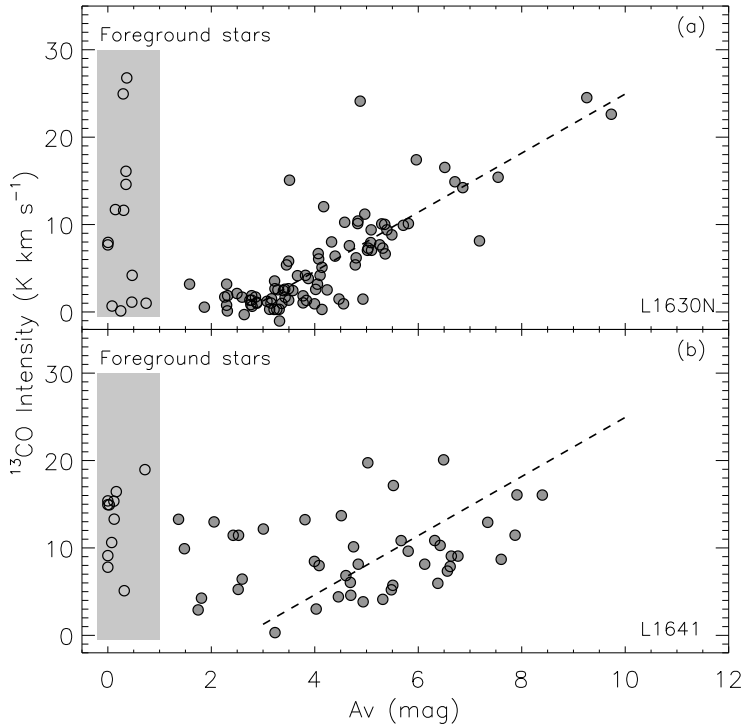

Figure 3.27: The correlation between ^{13}CO intensity and extinction estimated from the non-members in L1630N and L1641. The dashed line shows the best linear fit in L1630N, in the regime A_V>2 mag where CO is detectable. In L1641 the scatter in the distribution is much larger, and we only overplot the relation found in L1630N for reference.

The direct comparison of both measures of $\Sigma_{\rm cloud}$ depends on a number of assumptions: (1) the dust properties are homogeneous across the molecular cloud; (2) the gas to dust ratio is uniform; (3) CO freeze-out is not important in the regions probed; (4) the molecular tracer is optically thin in the regions probed. Since our sample contains only sight lines with relatively low extinction ($A_V \lesssim$10 mag, with only a handful of objects with A_V>7 mag), the ^{13}CO line remains optically thin, and we do not cover dense cores in which CO freeze-out occurs. Rather than the dense regions, which are known to show strong density enhancements on small scales (e.g. Lombardi et al. 2006), we trace the low density regions that surround the cores.

In Fig. 3.27 we show the relation between our pencil beam A_V measurements and the ^{13}CO intensities from Bally et al. (1987); Miesch & Bally (1994) interpolated at the same positions for L1630N and L1641. Apart from a few obvious outliers, we find a fairly tight correlation between both quantities in L1630N. In L1641, the correlation is much worse. A linear fit to the ^{13}CO intensity as a function of A_V, within the range 3 mag $\leq A_V \leq$ 10 mag, yields the following relation in L1630N:

$$I_{^{13}CO} = (-8.88 \pm 1.50) + (3.38 \pm 0.31) \times A_V \quad (3.9)$$

This fit yields zero ^{13}CO intensity for $A_V \approx 2$ mag, which is expected since at extinctions below this value CO is dissociated by the interstellar UV radiation field.

Since the L1630N and L1641 are at approximately the same distance, the millimeter data have the same physical resolution of ~0.2 pc. Our observations therefore suggest that the low density medium in L1630 shows relatively little substructure at these scales, whereas the L1641 medium has a substantial amount of such inhomogeneities.

3.5 Summary

We have performed a large optical spectroscopic and imaging survey of the L1630N and L1641 star-forming clouds in Orion. We combined our data with optical and infrared imaging data from the literature. The optical spectroscopy and photometry allow accurate determination of the stellar effective temperature, luminosity, and line of sight extinction through model atmosphere fitting. Mass and age estimates of individual objects were obtained by placement in the Hertzsprung-Russell diagram. Accretion rates were estimated from optical emission lines (Hα, Hβ, He I). The infrared photometry provides good measures of the IR excess emission, from which the evolutionary state of the disk can be deduced. In total we investigated 132 YSOs in L1630N and 267 in L1641, of which 65 and 117 were newly identified in the respective clouds.

Our survey products are threefold: (1) a list of identified YSOs with spectral types, optical and infrared magnitudes, equivalent widths of a number of emission lines, estimates of the stellar mass/age, an SED based disk classification, estimates of the accretion rate, and line of sight extinction (399 sources); (2) a list of unrelated field objects, mostly background stars, with photometric magnitudes, spectral types, and line of sight extinction (179 sources); (3) a photometric catalog with optical and infrared magnitudes of all sources detected in both wavelength regimes (21694 sources).

The young stars in L1630N predominantly formed in 2 clusters, whereas in L1641 some stars live in clusters (or rather "aggregates") and some in a distributed population. We distinguished between these populations using the nearest neighbor method, and identify two previously unknown aggregates in L1641.

Based on the infrared SEDs we divided the young stars into objects with still full blown optically thick disks, optically thin disks, transition objects, and diskless stars. We find that the disk frequency does not strongly depend on the mass of the star, with some evidence for an increasing disk frequency with increasing stellar mass. The disk frequency decreases with age, and does so earlier in clustered environments than in the distributed population. The latter is not expected from a theoretical vantage point, given the low densities and small sizes of the clusters/aggregates

under consideration. Our data yield no evidence for a substantial age difference between the aggregate and distributed populations, and the possible difference in disk dissipation time scales between both populations requires further investigation. In our spectroscopic sample we identified 28 transition disks, of which 20 were previously unknown. Moreover, we identified 47 additional transition disk candidates based on photometric measurements only.

We estimated accretion rates from the equivalent widths of the Hα, Hβ, and He I 5876Å lines. The mass accretion rate show a clear dependence on stellar mass, with individual objects showing a large scatter around the average relation. When making power law fits of the form $\dot{M}_{\rm acc} \propto M_*^{\alpha}$ we find values in the range of 2.8−3.4 for the exponent α, which is steeper than the range 1.0−2.1 found by previous authors. We compiled an independent set of mass and accretion rate estimates from the literature. We find that over the whole mass range of ∼0.05−5.0 $M_{\odot}$ we obtain α∼2.0, consistent with previous work. If we limit the fit to the mass range $M_* \lesssim 1.0\,M_{\odot}$, i.e. the range occupied by our sample, the literature data yield α∼2.8, which is consistent with our results. Thus, we show that the dependence of the accretion rate on stellar mass is not uniform, but instead is steeper at subsolar masses than above ∼1 $M_{\odot}$. We find a general decrease of accretion rate with age, which is less evident for the stars in our highest mass bin (M_*>1.0 $M_{\odot}$), possibly due to low number statistics.

The WTTSs are on average older than the CTTSs in our sample, but both populations show a large intrinsic scatter in their age distributions. The WTTSs with IR excess, emission indicative of a circumstelar disk, have the same average age as the CTTSs whereas apparently diskless WTTSs are on average older. The age distributions of transition disk objects and WTTSs without disks are indistinguishable, and they are on average older by a factor of $\gtrsim$2 than the CTTSs.

For L1641 we investigated what fraction of stars exist in the distributed and clustered populations. Our data suggest that the fraction of stars in the distributed population increases with age, from ∼60% at ≤0.5 Myr to ∼80% at >3 Myr, though at our current statistics this effect is $\lesssim 2\sigma$ and should be further investigated.

We find that among the stars with transition disks there are significantly fewer strong accretors (26±9%) than among stars with optically thick disks (57±6%). We find that the median accretion rate of those transitional objects that are actively accreting is similar to that of accreting stars with normal optically thick disks. This agrees with recent results in Trumpler 37 (Sicilia-Aguilar et al. 2009, in prep.), but is in contrast to earlier results for the Taurus-Aurigae region, in which transition disks were found to have a ∼10 times lower accretion rate than objects with normal optically thick disks (Najita et al. 2007). Note that the median accretion rate we derived for the Orion TDs is consistent with that found in the Taurus TDs, but that the median accretion rate derived for stars with normal optically thick disks is much higher in Taurus, and that this causes the aformentioned discrepancy.

We find one previously unknown object whose characteristics stongly suggests it is an FU Orionis star. Its bolometric (infrared) luminosity exceeds the estimated stellar luminosity by a factor $\gtrsim$5, and it shows P-Cygni profiles in both Hα and Hβ. Furthermore we identified four objects with apparently under-luminous photospheres for their spectral types which show very rich emission line spectra with very high equivalent widths. Such objects were found before (Comerón et al. 2003), who suggested that these objects are pre-main sequence stars whose evolution has been altered by strong accretion. Such stars would be less massive and less luminous than other stars of similar age and spectral type. The strong accretion and associated outflow activity yields the rich emission line spectrum.

By comparing molecular cloud column density estimates from A_V measurements of background stars (spatial resolution ~0.005 AU) and ^{13}CO intensity maps (spatial resolution ~45000 AU or 0.22 pc) we find that the low density medium in which the star forming cores are embedded shows significant substructure on scales of ~0.2 pc in L1641, but little substructure in L1630.

Appendix

(1) Classifying CTTS and WTTS

In this appendix we present the criteria we apply to separate Classical T-Tauri Stars (CTTS) from Weak-Line T-Tauri Stars (WTTS). Our classification scheme is a refined version of that of White & Basri (2003). Our basic method is very simple: we select a large number of young stars from the literature that show no evidence for a significant near-infrared excess, i.e. their (inner) disks have already dissipated. The vast majority of these will *not* be actively accreting, though the sample will contain some objects that do still accrete. We then inspect the Hα equivalent widths of all objects and, as a function of spectral type, define the region that contains the bulk of objects as the WTTS domain.

CTTSs are distinguished from WTTSs based on the equivalent width of the Hα emission line. CTTSs show relatively strong, often broad Hα emission lines that are attributed to active accretion. WTTSs exhibit weaker and narrower Hα lines which do not point at active accretion, but instead appear to have their origin in chromospheric activity. White & Basri (2003) use accretion-induced veiling of optical spectra to distinguish CTTSs and WTTSs, and classify a T Tauri star as a CTTS if EW(Hα)$\geq$ 3Å for K0-K5 stars, EW(Hα)$\geq$ 10Å for K7-M2.5 stars, EW(Hα)$\geq$ 20Å for M3-M5.5 stars, and EW(Hα)$\geq$ 40Å for M6-M7.5 stars. The EW(Hα) threshold significantly increases with spectral type due to the substantial decrease of the photospheric continuum level near the Hα line in cool stars.

We collected PMS stars from the literature and distributed in different star-formation regions, i.e. Ophiuchus, Lupus (Cieza et al. 2007), Taurus (Luhman et al. 2006,Gudel et al. 2007),Tr37, NGC7160 (Sicilia-Aguilar et al. 2005, 2006a), L1630N, L1641 (this chapter), NGC2264 (Dahm & Simon 2005; Cieza & Baliber 2007), NGC2362 (Dahm 2005; Dahm & Hillenbrand 2007), λ Orionis cluster (Barrado y Navascués et al. 2007), Orion OB1 association (Briceño et al. 2005, 2007; Hernández et al. 2007a), Chamaeleon II (Alcalá et al. 2008; Spezzi et al. 2008), σ Ori cluster (Béjar et al. 1999; Barrado y Navascués et al. 2003; Sacco et al. 2008; Hernández et al. 2007b), Coronet cluster (Sicilia-Aguilar et al. 2008), IC 348 (Luhman et al. 2003; Lada et al. 2006), Serpens cloud core, and NGC 1333 (Winston et al. 2007, 2009). In Taurus, some PMS stars have multiple measurements of the Hα EW, in which case we used the average value.

In total, we obtained a sample of 536 stars with no or weak infrared excess by constraining |[3.6]-[4.5]|$\leq$0.2,and |[5.8]-[8.0]|$\leq$0.2. The inner disks around these stars have been mostly cleared and the bulk of these objects will no longer be actively accreting. In Fig. 3.28, we show their [5.8]-[8.0] vs. [3.6]-[4.5] color-color diagram (left panel) and the distribution of Hα equivalent widths as a function of spectral type. We find that there is a quite clearly defined border between the

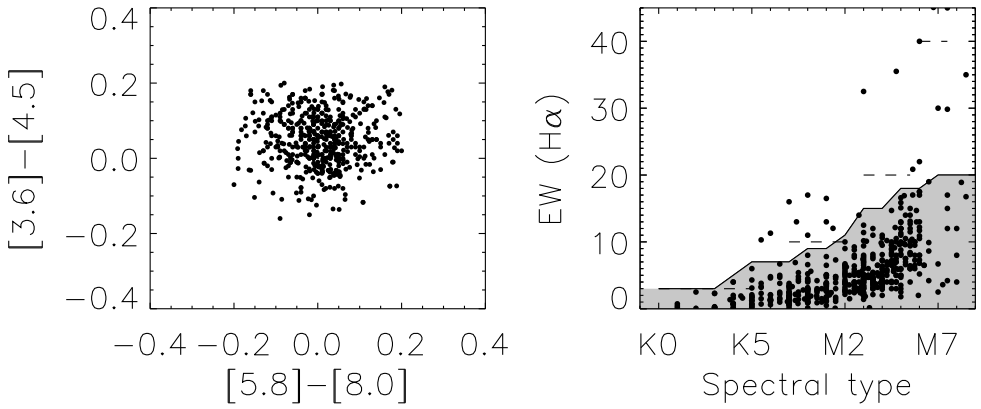

Figure 3.28: *Left panel:* Spitzer [5.8]-[8.0] vs. [3.6]-[4.5] color-color diagrams for YSOs with no or little infrared excess in different regions, i.e. Ophiuchus, Lupus, Perseus (Cieza et al. 2007), Tr37, NGC7160 (Sicilia-Aguilar et al. 2005, 2006a), L1630N, L1641 (this chapter), NGC2264 (Dahm & Simon 2005; Cieza & Baliber 2007), NGC2362 (Dahm 2005; Dahm & Hillenbrand 2007), λ Orionis cluster (Barrado y Navascués et al. 2007), Orion OB1 association (Briceño et al. 2005, 2007; Hernández et al. 2007a), Chamaeleon II (Alcalá et al. 2008; Spezzi et al. 2008), σ Ori cluster (Béjar et al. 1999; Barrado y Navascués et al. 2003; Sacco et al. 2008; Hernández et al. 2007b), Coronet cluster (Sicilia-Aguilar et al. 2008), IC 348 (Luhman et al. 2003; Lada et al. 2006), Serpens cloud core, and NGC 1333 (Winston et al. 2007, 2009).. *Right panel:* the relation between spectral types and EW(Hα) for stars in the left panel. The dashed lines show the criteria that White & Basri (2003) used to distinguish CTTSs and WTTSs. The grey-shaded area outlined by the solid line represents our refined criteria to classify CTTSs and WTTSs.

"bulk" of sources and the "outliers" with high EW. We interpret the former sources to be WTTS where the Hα emission arises in an active chromosphere, whereas the latter sources are still actively accreting, despite there weak or absent near-IR excess. These sources are rare, and most or all of them will be transition disk objects.

In the right panel we also plot the commonly used criteria for distinguishing between CTTSs and WTTSs by White & Basri (2003), with dashed horizontal lines. We can see that these criteria are not stringent enough to describe the boundary between the "bulk" and "outlier" objects, in particular many of the "outlier" objects of late-M spectral type would be classified as WTTSs according to these criteria. We propose more stringent limits to separate WTTSs from CTTSs: we consider a star to be a CTTS if EW(Hα)≥ 3Å for K0-K3 stars, EW(Hα)≥ 5Å for K4 stars, EW(Hα)≥ 7Å for K5-K7 stars, EW(Hα)≥ 9Å for M0-M1 stars, EW(Hα)≥ 11Å for M2 stars, EW(Hα)≥ 15Å for M3-M4 stars, EW(Hα)≥ 18Å for M5-M6 stars, and EW(Hα)≥ 20Å for M7-M8 stars. Our newly defined boundary is illustrated in the right panel of Fig. 3.28 by the solid line and grey-shaded area.

(2) Relations between emission line luminosity and accretion luminosity

In this appendix we derive the relations between the luminosity in several optical emission lines and the total accretion luminosity as measured using diagnostics that are independent of those lines. Both the line luminosities and the total accretion luminosities are adopted from the quoted papers.

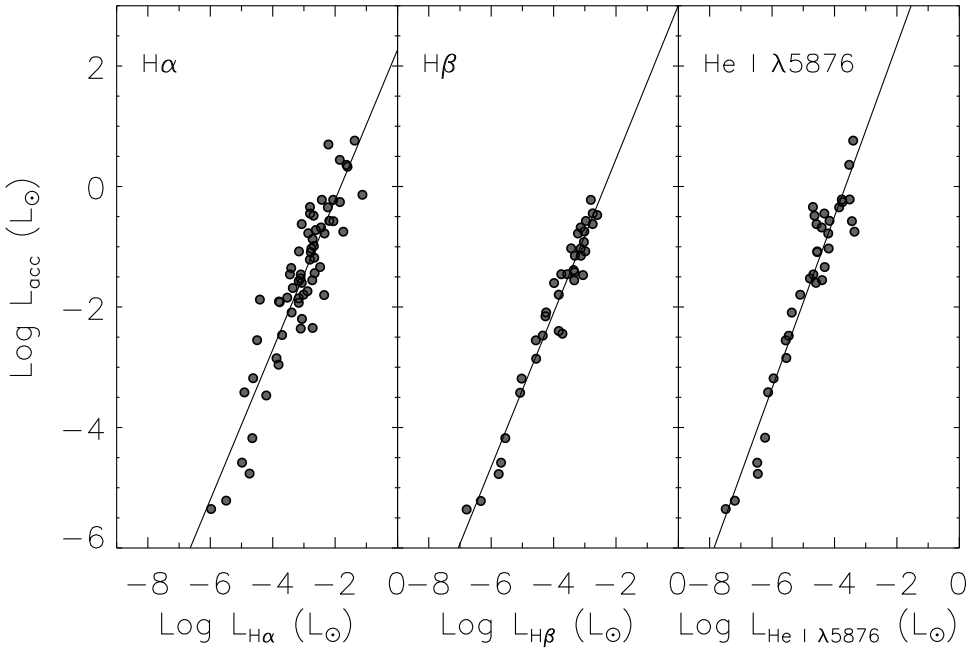

Figure 3.29: The relations between accretion luminosity and emission line luminosity. The solid lines show the best power law fits to the respective distributions.

(a) Hydrogen emission lines

We collected YSOs with measured Hα emission line luminosities and accretion luminosities from the literature (Gullbring et al. 1998; Dahm 2008; Herczeg & Hillenbrand 2008) and plotted these in Fig. 3.29. A resulting least squares fit to this distribution yields the following relation:

$$log(L_{\rm acc}/L_\odot) = (2.27 \pm 0.23) + (1.25 \pm 0.07) \times log(L_{\rm H\alpha}/L_\odot) \quad (3.10)$$

Similarly, we collected YSOs with measured Hβ emission line luminosities and accretion luminosities from the literature (Gullbring et al. 1998; Herczeg & Hillenbrand 2008). The best fit relation in this case becomes:

$$log(L_{\rm acc}/L_\odot) = (3.01 \pm 0.19) + (1.28 \pm 0.05) \times log(L_{\rm H\beta}/L_\odot) \quad (3.11)$$

(b) Helium emission line

We collected YSOs with measured He I emission line luminosities and accretion luminosities from the literature (Dahm 2008; Herczeg & Hillenbrand 2008). In this case, the best fit reads:

$$log(L_{\rm acc}/L_{\odot}) = (5.20 \pm 0.38) + (1.42 \pm 0.08) \times log(L_{\rm He\,I\,\lambda5876}/L_{\odot}) \quad (3.12)$$

Chapter 4

Star Formation and disk properties in Pismis 24

M. Fang, R. van Boekel, R. R. King, Th. Henning, J. Bouwman, Y. Doi, Y. K. Okamoto, V. Roccatagliata, and A. Sicilia-Aguilar
submitted to A&A

The influence of nearby massive young stars on the evolution of circumstellar disks is still not well understood. Spitzer observations have revealed a clear anti-correlation between the frequencies of circumstellar disks and the presence of massive stars in these clusters (e.g., NGC 2244, NGC 6611 Balog et al. 2007; Guarcello et al. 2009). UV irradiation by hot, massive stars causing photoevaporation of disks around neighboring lower mass young stars is a favored mechanism to explain the observed low disk frequencies near massive stars. In addition, massive stars preferentially reside in the centers of clusters (Zinnecker & Yorke 2007) where stellar densities are extremely high. In such environments stellar encounters, causing gravitational interaction between the circumstellar disks and nearby cluster members, are proposed to play a role in disk dissipation (Pfalzner et al. 2006; Olczak et al. 2010). The relative importance of both mechanisms for the dissipation of circumstellar disks is not well constrained. Young clusters harboring very massive stars need to be studied to shed light on this issue, Pismis 24 constitutes a well suited example of such clusters.

Pismis 24 is located in the Sagittarius spiral arm and contains dozens of massive OB-type stars, with two extremely luminous members: Pis 24-1 (O3 I) and Pis 24-17 (O3.5 III) (Massey et al. 2001). High-resolution observations have resolved Pis 24-1 into a compact hierarchical triple system consisting of Pis 24-1 NE (unresolved spectroscopic binary) and Pis 24-1 SW (Maíz Apellániz et al. 2007). Pis 24-1 NE and Pis 24-1 SW have an estimated mass of around 100 $M_{\odot}$ each. The distance to Pismis 24 has been estimated in different ways. Wilson et al. (1970) derive a kinematic distance to Pismis 24 of 1.0±2.3 kpc. Neckel (1978) obtain a distance of 1.74±0.31 kpc to Pismis 24 using a color-magnitude diagram. Employing the spectroscopic parallax method, Massey et al. (2001) derive a distance of 2.56±0.10 kpc for Pismis 24. In the current work we re-address the distance to Pismis 24 based on the positions of the most massive members in the Hertzsprung-Russell diagram (see Sect. 4.2.2(1)) and find that the most likely distance is 1.7 kpc. We adopt this value throughout the current chapter.

Our inventory of the stellar content of Pismis 24 has long been limited to the massive members (Wilson et al. 1970; Massey et al. 2001). Observations with the Chandra X-ray telescope have dramatically improved this situation and allowed hundreds of lower mass members to be identified (Wang et al. 2007). A total of 779 X-ray sources have been found in the Pismis 24 region, of which 616 sources have associated optical or infrared counterparts. With an estimated age of ~1 Myr (Massey et al. 2001) Pismis 24 is an extremely interesting laboratory for investigating the circumstellar disk evolution, with the similarly old Orion Nebula Cluster as a local reference.

The Pismis 24 cluster resides within NGC 6357, a large complex of extended nebulosity. Within NGC 6357 there are three known HII regions at different evolutionary stages: G353.2+0.9, G353.2+0.7, and G353.1+0.6 (Felli et al. 1990). G353.2+0.9, located near the Pismis 24 cluster, is the youngest and brightest region and was further resolved into three compact H II regions using the high-resolution VLA observations (Felli et al. 1990). Between G353.2+0.9 and the Pismis 24 cluster there is an ionization front shielding the cloud material from most of the UV photons emitted from massive stars in the cluster. It is therefore possible that G353.2+0.9 is ionized by its own, internal sources (Felli et al. 1990). Indeed, infrared observations have revealed several embedded objects in G353.2+0.9 (Persi et al. 1986; Felli et al. 1990; Wang et al. 2007). G353.1+0.6 is a more evolved H II region which is expanding and interacting with molecular cloud material on its northern side (Felli et al. 1990; Massi et al. 1997). G353.2+0.7 is the most evolved and diffuse H II region and shows no compact components (Haynes et al. 1979; Felli et al. 1990).

A dust continuum emission survey at 1.2 mm has revealed 163 dense cores in the NGC 6357 region, of which 16 have masses above 200 $M_{\odot}$ (Muñoz et al. 2007; Russeil et al. 2010). Follow-up observations searching for molecular line emission in 42 high-mass dense cores ($\geq$100 $M_{\odot}$) show that all of them belong to the NGC 6357 complex. Among these, 15 dense cores were identified as starless cores (Russeil et al. 2010).

In this chapter we will first investigate the star formation activity in the NGC 6357 complex as a whole, and then focus on the stellar and disk properties of the members of the central cluster Pismis 24. We arrange this chapter as follows. In section 4.1 we describe the observations and data reduction. In section 4.2 we present our results which are then discussed in section 4.3. We summarize our effort in section 4.4.

4.1 Observations and data reduction

This study is based on a large collection of observational data. We use photometric data at optical, infrared and X-ray wavelengths, as well as spectroscopy in the 4800 to 10000 Å range.

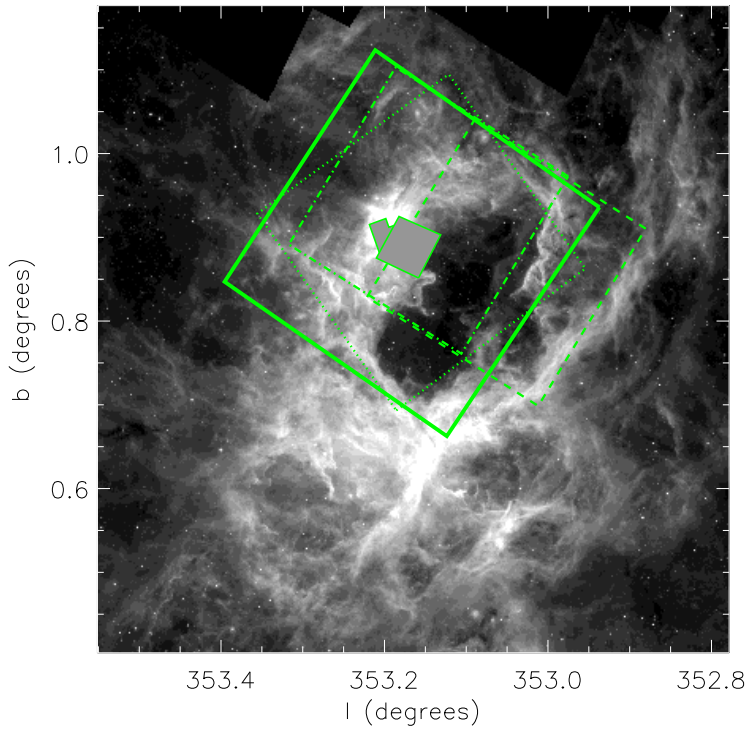

Figure 4.1: The FOVs of different observations used in this chapter. The background: 8.0 μm(GLIMPSE). The FOVs of our deep IRAC imaging are shown with the dash lines ([3.6] and [5.8] bands) and dash-dotted lines ([4.5] and [8.0] bands). The dotted lines present the FOV of the Chandra X-ray observation. The solid lines show the FOVs for VIMOS imaging and spectroscopy. The central grey filled regions show the were covered with HST observations.

The field of view (FOV) for each of the individual datasets is shown in Fig 4.1.

4.1.1 Infrared photometry

Near-infrared photometry in the J, H, and K_s bands was taken from the Two-Micron All Sky Survey (2MASS Skrutskie et al. 2006). Mid-infrared photometry at 3.6, 4.5, 5.8, and 8.0 μm obtained with the Spitzer Space Telescope IRAC camera (Fazio et al. 2004) was taken from the the Galactic Legacy Infrared Mid-Plane Survey Extraordinaire (GLIMPSE I Benjamin et al. 2003) survey, and supplemented with our own deep observations (Program ID 30726) in the central cluster regions.

(1) GLIMPSE survey

The GLIMPSE I survey covers the galactic plane ($10° < |l| < 65°$, $|b| < 1°$) with imaging in the four IRAC bands (3.6, 4.5, 5.8, and 8.0 μm). We adopted the photometry of all the point sources in NGC 6357 complex as given in the GLIMPSE catalog, with photometric uncertainties below 0.2 mag in all four IRAC bands.

(2) Deep IRAC imaging of the central Pismis 24 region

We have performed deep observations towards the Pismis 24 cluster with the Spitzer IRAC camera. The observations have been done on September 29, 2006, with exposure times of 0.4 s and 10.4 s. We performed PSF photometry using the IDL codes described in Chapter 3. We compared our photometry with the values given in the GLIMPSE catalogue for common sources and found small systematic differences between both data sets of -0.04, -0.007,-0.04,-0.1 magnitudes in the [3.6], [4.5], [5.8], and [8.0] bands, respectively. These difference may be due to the slightly different psf-fitting models. We applied the corresponding scaling factors to our deep imaging such that it has the same absolute flux levels as the GLIMPSE data.

4.1.2 Optical photometry

We have imaged the cluster Pismis 24 in the R and I-band filters using the Visible Multi-Object Spectrograph (VIMOS, LeFevre et al. 2003) at the ESO VLT. The R-band observations were performed on 2008 April 1 and 6, and the I-band observations were done on 2008 May 1. In order to increase dynamic range we took the images with five exposures (1, 14, 45, 150, and 300 seconds) for every pointing. We performed standard data reduction for optical imaging consisting of bias subtraction and flat-fielding. We then performed PSF photometry on the reduced images, taking into account that the PSF shows substantial variations in shape over the VIMOS FOV. Instead of using a single PSF for a given observation, we divided each image into 16 sub-regions. In each sub-region we extracted a PSF model from the isolated stars, and used it to do PSF fitting for each star in the sub-region. For every star that was detected in multiple exposures of different integration time, we adopt the photometry from the longest exposure in which the peak level of the star remains in the linear regime of the CCD. We calibrated the R-band photometry using observations of the standard fields SA 110 (for data taken on 2008 April 1) and Rubin 149 (for data taken on 2008 April 6). The I-band photometry was calibrated using standard stars observed in the PG 0918 field (Stetson 2000).

4.1.3 X-ray source catalogue

Pismis 24 cluster has been observed with the Imaging Array of the Advanced CCD Imaging Spectrometer (ACIS-I) mounted on the Chandra space telescope. In this region, 779 X-ray sources are detected (Wang et al. 2007). In this chapter, we match X-ray sources to the sources detected in VIMOS R and I bands based on positional coincidence, using a 1.″5 tolerance. The photometry in 9 bands between 0.55 and 9 μm for counterparts of X-ray sources are listed in Table 4.1. Since Pismis 24 is located in the direction of the galactic center the density of unrelated background sources is high, which complicates establishing cluster membership. In this work, we will use X-ray emission as the identification of the membership of the cluster. With this selection criterion, some intermediate-mass members with spectral types mid-B to A could be missing in our sample due the absence of X-ray emission from them (Wang et al. 2008).

Since the central regions of the Pismis 24 cluster have a high space density of sources and the accuracy of the optical and X-ray positions is limited to typically 0.″6 and 1.″0, respectively, matching the optical and X-ray positions requires care. Choosing a large matching radius ensures that all real optical and X-ray pairs are matched but may also result in substantial numbers of "false positives", i.e. a match between physically unrelated optical and X-ray sources. Choosing a small matching radius would cause many physically associated pairs to be lost from the analysis. We chose 1.″5 as a compromise. To test for the number of potential false positives, we applied a positional shift of 25.″to the optical positions and then matched those to the X-ray catalog. This indeed yields a fair number of false matches: roughly 1/6 of the number of matches in the original catalog. Thus, strictly speaking, statistically about 1/6 of our sources could be false positives. This, however, is a very pessimistic estimate: for individual sources it would mean that there is an optical source near the X-ray position that is unrelated to X-ray source and that the true X-ray source counterpart is much fainter in the optical than the "false match". This situation will not occur often, though for individual cases it cannot, of course, be excluded with certainty.

Table 4.1: Photometric magnitudes for stars with X-ray emission in PISMIS 24. Column 2: the identification numbers in Wang et al. (2007). Column 3: the distances between xray sources and optical/infrared counterparts.

(1)	(2)	(3)	(4)	(5)	(6)	(7)	(8)	(9)	(10)	(11)	(12)	(13)	(14)
		dis	RA	DEC	R	I	J	H	K_s	[3.6]	[4.5]	[5.8]	[8.0]
ID	W07	(arcsec)	(J2000)	(J2000)	(mag)	(mag)	(mag)	(mag)	(mag)	(mag)	(mag)	(mag)	(mag)
1	1	0.81	17 23 53.93	-34 08 50.5	22.793±0.080	21.572±0.029	...	...	...	...	...	...	...
2	2	0.48	17 23 58.39	-34 08 02.4	21.952±0.082	19.076±0.022	15.18±0.05	13.18±0.04	11.93±0.03	10.69±0.04	10.49±0.06	10.13±0.13	...
3	3	0.87	17 23 59.16	-34 12 16.9	15.595±0.001	14.080±0.001	11.93±0.02	11.18±0.03	10.69±0.03	...	...	...	...
4	6	0.32	17 24 03.22	-34 14 02.2	16.767±0.001	14.949±0.001	12.67±0.02	11.68±0.02	11.31±0.02	11.01±0.05	10.96±0.07	11.23±0.23	...
5	8	0.45	17 24 05.46	-34 12 57.5	...	...	...	...	...	12.61±0.08	11.70±0.08	11.23±0.18	...
6	9	0.53	17 24 05.61	-34 07 09.7	...	...	9.03±0.02	8.63±0.05	8.46±0.02	8.35±0.06	8.33±0.12	8.27±0.14	...
7	10	0.50	17 24 06.66	-34 13 05.1	...	...	...	14.52±0.07	13.32±0.05	12.66±0.12	12.31±0.21	...	...
8	11	0.65	17 24 06.81	-34 11 49.2	...	22.390±0.128	16.53±0.12	13.83±0.03	12.38±0.03	11.05±0.04	10.61±0.05	10.22±0.06	9.92±0.09
9	12	0.46	17 24 07.66	-34 17 52.4	19.842±0.021	17.528±0.006	14.43±0.04	13.04±0.04	12.46±0.03	12.10±0.05	12.04±0.08	11.78±0.25	...

Table 4.1: continued.

(1)	(2)	(3)	(4)	(5)	(6)	(7)	(8)	(9)	(10)	(11)	(12)	(13)	(14)
			RA	DEC	R	I	J	H	K_s	[3.6]	[4.5]	[5.8]	[8.0]
ID	W07	(arcsec)	(J2000)	(J2000)	(mag)	(mag)	(mag)	(mag)	(mag)	(mag)	(mag)	(mag)	(mag)
10	13	1.29	17 24 08.91	-34 12 11.0	18.285±0.006	16.971±0.004	15.33±0.05	14.54±0.02	14.23±0.06	...	...	...	...
11	14	1.19	17 24 09.25	-34 08 59.4	...	22.990±0.104	...	...	...	13.55±0.08	13.48±0.17	...	...
12	15	0.77	17 24 09.22	-34 12 24.1	...	22.362±0.172	15.78±0.06	12.94±0.04	11.55±0.04	10.68±0.21	9.90±0.08	9.42±0.11	...
13	16	0.86	17 24 12.35	-34 14 59.8	20.160±0.027	18.545±0.017	16.66±0.13	...	...	...	...	...	...
14	17	0.91	17 24 13.14	-34 11 46.8	19.402±0.016	17.057±0.004	13.82±0.02	11.66±0.02	10.32±0.02	9.17±0.05	9.09±0.05	8.63±0.08	8.29±0.18
15	18	0.57	17 24 13.60	-34 09 21.3	16.979±0.001	15.528±0.001	13.58±0.02	12.67±0.02	12.34±0.03	...	...	...	...
16	19	0.29	17 24 13.60	-34 16 56.7	18.590±0.006	14.260±0.001	8.33±0.03	6.32±0.05	5.33±0.02	4.50±0.15	4.96±0.11	4.25±0.02	4.19±0.02
17	20	0.80	17 24 13.62	-34 14 51.8	17.366±0.002	15.639±0.001	13.19±0.02	12.15±0.05	11.77±0.05	11.56±0.09	11.52±0.08	...	...
18	21	1.23	17 24 13.74	-34 06 57.1	...	20.140±0.058	13.76±0.05	11.39±0.04	10.24±0.02	9.53±0.03	9.54±0.05	9.19±0.05	9.21±0.04
19	22	0.57	17 24 14.72	-34 10 43.7	14.886±0.001	14.106±0.001	12.82±0.04	...	...	9.16±0.07	9.10±0.05	8.89±0.07	9.27±0.55
20	24	0.70	17 24 15.39	-34 09 58.7	...	...	...	14.77±0.10	13.53±0.07	...	...	...	...
21	26	0.92	17 24 15.78	-34 14 59.3	...	22.674±0.148	15.66±0.07	14.41±0.11	13.74±0.10	13.12±0.10	13.06±0.16	...	...
22	27	0.33	17 24 15.94	-34 14 41.1	...	...	...	14.68±0.04	13.47±0.04	12.46±0.07	12.29±0.11	...	...
23	28	0.47	17 24 16.08	-34 12 48.6	...	...	...	...	14.13±0.06	12.19±0.05	11.63±0.07	10.99±0.12	...
24	29	0.51	17 24 16.13	-34 15 26.8	21.151±0.068	18.057±0.011	14.03±0.02	12.30±0.02	11.45±0.02	10.91±0.08	10.81±0.10	...	...
25	30	0.07	17 24 16.18	-34 13 11.4	16.946±0.001	15.769±0.001	14.14±0.03	13.28±0.02	12.99±0.02	...	...	...	...
26	31	1.22	17 24 17.45	-34 06 07.3	24.419±0.137	22.188±0.058	...	...	...	...	...	...	...
27	33	1.38	17 24 18.16	-34 16 51.2	...	23.069±0.135	...	...	...	...	...	...	...
28	34	0.74	17 24 18.75	-34 06 36.6	...	21.040±0.036	14.05±0.04	12.31±0.06	11.55±0.04	10.77±0.10	10.80±0.08	11.44±0.28	...
29	35	0.35	17 24 18.79	-34 12 04.8	19.937±0.026	17.882±0.009	14.91±0.03	13.65±0.02	13.04±0.03	12.66±0.12	12.55±0.12	...	...
30	36	0.21	17 24 19.60	-34 15 44.4	18.758±0.007	16.720±0.003	...	...	11.21±0.04	10.75±0.05	10.71±0.06	10.64±0.10	...
31	38	0.21	17 24 20.25	-34 13 10.6	19.737±0.019	17.328±0.006	14.02±0.03	12.55±0.04	11.88±0.04	11.11±0.05	10.84±0.08	10.30±0.20	...
32	40	0.49	17 24 20.82	-34 10 27.8	22.060±0.067	19.588±0.042	...	...	...	14.10±0.14	14.11±0.32	...	...
33	41	0.65	17 24 21.30	-34 14 35.7	17.871±0.003	16.400±0.003	...	...	...	...	...	...	...
34	43	1.20	17 24 21.79	-34 08 43.1	13.706±0.001	12.143±0.001	10.31±0.02	9.41±0.02	9.07±0.02	...	...	...	...
35	44	0.30	17 24 21.72	-34 13 25.4	22.180±0.070	19.661±0.052	...	...	...	12.11±0.08	11.96±0.09	...	...
36	46	0.24	17 24 21.82	-34 12 59.2	20.617±0.043	18.110±0.012	15.18±0.04	13.81±0.03	13.18±0.05	12.43±0.08	12.12±0.11	...	...
37	47	0.74	17 24 22.05	-34 14 29.7	16.233±0.001	14.651±0.001	12.41±0.03	11.37±0.02	10.67±0.03	9.03±0.03	8.51±0.04	8.10±0.03	7.37±0.03
38	48	0.11	17 24 22.95	-34 12 22.0	18.740±0.007	16.906±0.003	14.38±0.03	13.26±0.03	12.82±0.03	12.66±0.08	12.62±0.10	...	...
39	50	0.10	17 24 23.47	-34 09 42.3	18.199±0.005	16.079±0.002	13.93±0.03	13.07±0.04	12.78±0.04	12.29±0.08	12.29±0.08	...	...
40	51	0.46	17 24 23.95	-34 08 15.8	18.034±0.004	15.829±0.001	13.10±0.02	11.82±0.03	11.31±0.03	10.95±0.06	10.88±0.08	10.48±0.10	...
41	52	0.78	17 24 23.95	-34 10 11.8	...	22.597±0.169	16.23±0.13	14.06±0.06	13.02±0.05	12.34±0.07	12.11±0.10	...	...
42	53	0.08	17 24 24.24	-34 15 09.9	20.190±0.028	17.830±0.011	15.00±0.04	13.65±0.03	13.15±0.04	12.35±0.04	12.13±0.08	11.93±0.10	11.47±0.12
43	55	0.76	17 24 25.40	-34 19 15.8	19.265±0.014	17.006±0.005	14.40±0.04	13.14±0.05	12.55±0.06	12.15±0.11	...	...	...
44	57	0.28	17 24 25.89	-34 11 43.1	21.655±0.092	18.864±0.017	...	13.28±0.07	12.49±0.07	11.02±0.07	10.27±0.06	9.49±0.11	8.69±0.55
45	59	0.47	17 24 26.18	-34 13 41.2	23.720±0.315	19.645±0.058	...	...	...	13.76±0.13	...	...	...
46	60	0.96	17 24 26.20	-34 15 39.8	19.925±0.021	16.861±0.003	13.12±0.03	11.59±0.05	10.87±0.03	10.46±0.07	10.45±0.05	10.29±0.08	10.20±0.12
47	62	0.81	17 24 26.72	-34 11 50.4	...	21.381±0.051	...	...	...	14.23±0.17	13.90±0.31	...	...
48	63	0.56	17 24 27.29	-34 09 03.2	16.054±0.001	15.126±0.001	13.88±0.04	12.96±0.06	12.51±0.06	11.52±0.07	11.01±0.07	10.93±0.12	...
49	64	0.29	17 24 27.30	-34 08 01.0	18.648±0.006	16.585±0.002	...	12.87±0.05	12.41±0.05	12.01±0.04	11.90±0.07	12.08±0.21	...
50	65	0.37	17 24 27.43	-34 15 54.5	21.818±0.085	18.915±0.022	...	...	...	12.75±0.09	12.48±0.12	11.88±0.18	11.66±0.90
51	66	0.42	17 24 27.39	-34 16 49.1	20.536±0.032	18.093±0.009	15.51±0.07	...	...	13.57±0.09	13.56±0.13	...	...
52	67	0.24	17 24 27.43	-34 13 56.2	21.890±0.068	18.875±0.019	15.70±0.08	14.07±0.07	13.20±0.07	12.29±0.07	11.99±0.10	...	...
53	68	0.14	17 24 27.53	-34 16 59.7	19.791±0.016	17.758±0.006	...	...	13.35±0.06	12.70±0.09	12.42±0.11	...	...
54	69	1.01	17 24 27.81	-34 12 15.8	20.822±0.042	19.115±0.022	...	14.96±0.12	13.79±0.09	13.18±0.18	12.89±0.16	...	...
55	70	0.24	17 24 28.09	-34 11 07.5	14.352±0.001	13.701±0.001	12.72±0.03	12.13±0.02	11.91±0.02	11.42±0.07	11.13±0.07	10.51±0.31	...
56	71	0.16	17 24 28.50	-34 10 40.3	22.101±0.129	19.259±0.028	16.42±0.10	...	...	12.48±0.14	11.99±0.13	...	...
57	72	0.41	17 24 28.52	-34 17 54.7	19.847±0.019	17.687±0.006	15.07±0.04	13.69±0.04	13.02±0.04	11.95±0.06	11.65±0.07	11.06±0.08	10.65±0.05
58	73	0.42	17 24 28.59	-34 11 44.3	22.150±0.101	19.124±0.022	16.14±0.07	...	...	13.91±0.10	13.94±0.22	...	...
59	74	0.16	17 24 28.70	-34 12 11.5	20.848±0.042	18.594±0.014	15.76±0.06	14.24±0.05	13.52±0.08	12.57±0.07	12.27±0.10	...	...
60	75	0.24	17 24 28.74	-34 12 41.5	23.051±0.163	20.485±0.078	...	...	...	13.12±0.07	13.00±0.20	11.64±0.20	...
61	77	0.74	17 24 28.94	-34 14 50.0	...	15.840±0.001	9.03±0.03	8.58±0.04	8.35±0.03	8.19±0.03	8.23±0.04	8.10±0.03	8.21±0.03
62	78	0.43	17 24 29.03	-34 18 13.9	17.044±0.001	15.273±0.001	12.08±0.03	11.10±0.03	10.76±0.02	...	...	...	...
63	79	0.22	17 24 29.14	-34 12 14.9	20.307±0.026	17.982±0.008	15.47±0.05	13.99±0.03	13.55±0.04	13.16±0.07	13.15±0.16	...	...
64	80	0.34	17 24 29.37	-34 10 55.5	22.740±0.108	20.532±0.091	...	...	...	12.66±0.06	12.43±0.12	...	...
65	81	0.08	17 24 29.56	-34 11 54.0	20.073±0.025	17.998±0.008	15.24±0.06	13.99±0.06	13.50±0.07	13.02±0.07	12.87±0.11	...	...
66	82	0.44	17 24 29.72	-34 13 36.9	...	22.068±0.093	...	...	...	13.27±0.10	12.97±0.12	...	...
67	83	0.48	17 24 29.80	-34 13 15.8	21.401±0.070	18.972±0.020	...	...	...	12.90±0.09	12.27±0.12	11.33±0.12	...
68	85	0.38	17 24 30.32	-34 14 29.5	14.059±0.001	13.355±0.001	12.67±0.02	12.25±0.02	12.23±0.02	12.08±0.05	12.15±0.07	12.09±0.16	...
69	88	1.44	17 24 30.65	-34 18 02.0	19.734±0.017	17.436±0.005	...	...	13.23±0.05	12.88±0.09	...	...	...
70	89	0.04	17 24 30.77	-34 15 51.5	18.455±0.004	16.530±0.002	13.95±0.04	12.53±0.05	11.55±0.03	10.07±0.04	9.40±0.03	8.77±0.03	7.71±0.02

Table 4.1: continued.

(1)	(2)	(3)	(4)	(5)	(6)	(7)	(8)	(9)	(10)	(11)	(12)	(13)	(14)
			RA	DEC	R	I	J	H	K_s	[3.6]	[4.5]	[5.8]	[8.0]
ID	W07	(arcsec)	(J2000)	(J2000)	(mag)	(mag)	(mag)	(mag)	(mag)	(mag)	(mag)	(mag)	(mag)
71	90	0.22	17 24 31.01	-34 11 14.4	12.937±0.001	12.241±0.001	11.50±0.03	11.10±0.03	10.87±0.03	10.68±0.05	10.65±0.07	10.74±0.14	...
72	91	0.35	17 24 31.01	-34 15 22.3	19.663±0.011	17.422±0.005	14.59±0.04	13.22±0.03	12.68±0.04	12.10±0.05	12.05±0.09	11.54±0.11	...
73	93	0.15	17 24 31.28	-34 11 07.5	...	19.872±0.057	...	...	...	...	...	...	...
74	94	0.19	17 24 31.35	-34 11 35.2	22.717±0.136	20.139±0.057	16.37±0.11	14.23±0.05	13.27±0.05	12.29±0.07	11.99±0.08	...	...
75	95	0.03	17 24 31.38	-34 09 34.4	20.957±0.084	18.448±0.015	...	13.34±0.06	12.24±0.04	10.64±0.06	10.06±0.06	9.66±0.16	...
76	96	1.06	17 24 31.41	-34 15 18.7	...	...	...	...	...	13.77±0.34	13.71±0.42	11.78±0.69	...
77	97	1.41	17 24 31.51	-34 21 31.1	...	22.259±0.110	...	13.76±0.11	12.52±0.06	11.80±0.07	11.48±0.10	...	...
78	98	0.15	17 24 31.66	-34 10 46.7	23.116±0.068	19.690±0.048	16.33±0.11	14.83±0.08	...	13.47±0.14	13.34±0.31	...	...
79	99	0.10	17 24 31.69	-34 11 58.5	20.449±0.029	18.309±0.011	14.95±0.06	13.67±0.03	12.86±0.04	11.78±0.06	11.24±0.06	10.67±0.06	9.84±0.06
80	101	0.10	17 24 32.04	-34 13 05.2	18.852±0.007	16.947±0.003	...	...	12.60±0.12	12.18±0.06	12.10±0.08	...	...
81	103	0.19	17 24 32.33	-34 15 38.1	22.017±0.029	18.745±0.016	...	14.26±0.13	...	12.75±0.08	12.14±0.13	11.77±0.17	10.91±0.11
82	104	0.38	17 24 32.42	-34 13 21.2	19.720±0.021	17.502±0.005	14.77±0.05	13.45±0.07	12.94±0.06	12.50±0.05	12.57±0.09	11.49±0.16	...
83	105	0.22	17 24 32.41	-34 10 11.7	21.552±0.145	19.200±0.030	15.98±0.08	14.41±0.05	13.59±0.05	12.13±0.05	11.81±0.09	...	...
84	106	0.25	17 24 32.52	-34 16 11.3	19.920±0.014	17.817±0.007	14.89±0.16	13.45±0.16	12.78±0.13	12.40±0.10	12.24±0.11	...	...
85	107	0.37	17 24 32.61	-34 12 35.3	23.613±0.293	20.171±0.059	...	...	...	14.52±0.16	13.73±0.27	...	...
86	108	0.02	17 24 32.65	-34 13 45.0	19.966±0.027	17.597±0.005	14.41±0.06	12.85±0.05	12.06±0.03	11.38±0.05	11.21±0.07	10.96±0.09	10.36±0.63
87	109	0.50	17 24 32.70	-34 14 04.0	22.035±0.037	19.020±0.021	16.21±0.11	...	...	13.77±0.08	13.86±0.15	...	...
88	110	0.13	17 24 32.86	-34 09 02.5	18.693±0.010	16.766±0.003	14.25±0.02	13.14±0.05	12.67±0.02	...	...	...	...
89	112	0.30	17 24 33.03	-34 16 54.8	19.208±0.009	17.009±0.003	14.38±0.04	12.91±0.07	12.17±0.06	11.63±0.08	11.51±0.11	11.55±0.14	11.01±0.14
90	113	0.16	17 24 33.06	-34 11 27.8	16.155±0.001	14.313±0.001	11.99±0.03	10.99±0.02	10.61±0.02	10.31±0.04	10.24±0.06	10.10±0.08	...
91	114	0.22	17 24 33.08	-34 11 55.7	20.468±0.029	18.250±0.010	15.45±0.08	14.13±0.11	13.61±0.10	13.02±0.10	12.94±0.18	...	...
92	115	0.13	17 24 33.25	-34 15 15.1	20.295±0.007	17.894±0.008	15.13±0.06	13.82±0.07	13.45±0.08	12.85±0.06	12.89±0.12	...	...
93	116	0.16	17 24 33.28	-34 10 29.8	19.667±0.026	17.708±0.008	16.28±0.12	...	...	...	...	...	...
94	117	0.41	17 24 33.37	-34 12 13.0	20.138±0.026	17.744±0.007	14.35±0.04	12.95±0.05	12.44±0.04	11.95±0.08	12.01±0.12	11.61±0.21	...
95	118	0.34	17 24 33.42	-34 14 23.7	19.610±0.019	17.343±0.004	14.73±0.05	13.48±0.05	12.97±0.05	12.55±0.06	12.56±0.10	...	...
96	119	0.14	17 24 33.41	-34 14 02.4	19.969±0.027	17.750±0.006	15.57±0.08	13.99±0.09	13.21±0.06	12.22±0.05	11.86±0.06	11.76±0.13	...
97	120	0.37	17 24 33.49	-34 13 44.7	...	...	10.58±0.03	9.98±0.02	9.65±0.02	9.14±0.04	9.05±0.05	8.88±0.03	8.89±0.05
98	122	0.18	17 24 33.50	-34 13 22.1	20.016±0.028	17.601±0.006	14.75±0.04	13.49±0.08	12.98±0.06	12.64±0.05	12.69±0.09	...	...
99	123	0.67	17 24 33.57	-34 13 33.1	19.684±0.021	17.453±0.005	14.53±0.10	13.25±0.12	12.74±0.10	12.25±0.07	12.31±0.09	...	...
100	124	0.53	17 24 33.88	-34 11 55.1	23.160±0.187	19.732±0.039	15.03±0.05	12.48±0.03	11.31±0.02	10.46±0.04	10.32±0.06	10.05±0.06	9.64±0.08
101	125	0.22	17 24 33.99	-34 05 50.3	20.351±0.006	17.659±0.006	...	13.64±0.12	13.22±0.08	12.80±0.08	12.73±0.07	12.06±0.27	11.59±0.89
102	126	0.15	17 24 34.00	-34 19 09.5	20.265±0.025	17.715±0.006	...	...	...	12.16±0.07	11.74±0.08	11.57±0.09	...
103	127	0.35	17 24 34.02	-34 13 36.9	17.345±0.002	15.431±0.001	12.62±0.05	11.09±0.06	10.12±0.04	9.08±0.06	8.60±0.04	8.25±0.04	7.69±0.04
104	128	0.19	17 24 34.11	-34 13 40.2	20.280±0.036	17.957±0.008	...	...	...	12.90±0.21	12.36±0.10	...	...
105	129	0.10	17 24 34.20	-34 14 02.2	18.973±0.011	16.817±0.003	13.97±0.03	12.68±0.03	12.25±0.03	11.65±0.05	11.73±0.07	11.57±0.10	...
106	130	0.13	17 24 34.18	-34 09 54.7	18.656±0.010	16.446±0.002	13.34±0.05	11.77±0.05	10.66±0.04	9.04±0.06	8.45±0.06	7.77±0.10	6.47±0.11
107	131	0.60	17 24 34.31	-34 09 44.4	19.832±0.030	18.011±0.010	15.68±0.12	13.55±0.09	12.36±0.05	11.41±0.13	...	...	...
108	133	0.15	17 24 34.46	-34 12 46.6	20.063±0.020	17.942±0.007	15.06±0.07	13.74±0.08	13.17±0.07	12.69±0.08	12.64±0.10	...	...
109	134	0.14	17 24 34.57	-34 12 34.3	22.552±0.109	19.849±0.043	...	...	...	13.39±0.09	12.72±0.10	...	...
110	135	0.03	17 24 34.63	-34 08 44.5	18.208±0.006	16.281±0.002	13.84±0.02	12.57±0.02	11.82±0.02	10.77±0.08	10.22±0.08	9.90±0.12	...
111	136	0.29	17 24 34.68	-34 12 26.0	19.822±0.017	17.677±0.006	15.18±0.08	...	...	13.01±0.08	13.11±0.18	...	...
112	137	0.13	17 24 34.70	-34 12 15.2	20.323±0.026	17.817±0.007	14.75±0.07	13.23±0.09	12.21±0.06	10.97±0.04	10.55±0.10	10.28±0.07	9.65±0.07
113	138	0.49	17 24 34.74	-34 15 24.7	21.248±0.048	18.861±0.018	15.84±0.09	14.46±0.12	13.77±0.09	12.72±0.06	12.45±0.08	11.97±0.21	...
114	139	0.18	17 24 34.76	-34 12 17.8	21.159±0.056	18.543±0.013	...	...	...	11.84±0.07	11.79±0.16	11.07±0.12	...
115	140	0.15	17 24 34.80	-34 13 18.1	13.639±0.001	12.332±0.001	10.74±0.03	10.09±0.02	9.79±0.02	9.59±0.03	9.56±0.05	9.52±0.04	9.55±0.06
116	141	0.25	17 24 34.87	-34 15 41.6	16.968±0.001	15.172±0.001	...	...	...	...	...	...	...
117	146	0.27	17 24 35.40	-34 12 38.9	19.919±0.018	17.753±0.006	15.06±0.08	13.64±0.10	12.87±0.07	11.99±0.07	11.56±0.06	11.19±0.11	11.10±0.30
118	147	0.09	17 24 35.50	-34 12 34.7	21.869±0.058	19.134±0.023	...	...	...	11.55±0.09	11.49±0.08	11.11±0.16	...
119	148	0.09	17 24 35.54	-34 14 23.4	...	19.017±0.021	15.09±0.05	13.80±0.08	13.33±0.05	12.46±0.10	12.70±0.11	...	...
120	149	0.51	17 24 35.92	-34 13 32.7	21.173±0.019	18.927±0.019	15.99±0.09	...	...	12.72±0.07	12.48±0.09	...	...
121	150	0.26	17 24 35.93	-34 13 23.3	22.388±0.111	19.637±0.036	...	...	...	...	...	...	...
122	151	0.31	17 24 36.05	-34 14 00.6	...	...	9.51±0.03	9.02±0.02	8.75±0.02	8.61±0.04	8.59±0.04	8.57±0.03	8.60±0.03
123	152	0.39	17 24 36.08	-34 12 43.5	22.359±0.141	19.643±0.048	...	...	...	13.37±0.13	12.94±0.09	...	...
124	153	0.43	17 24 36.14	-34 15 22.2	19.090±0.007	17.095±0.004	13.87±0.05	12.42±0.05	11.63±0.04	10.70±0.06	10.38±0.06	10.19±0.05	9.73±0.03
125	154	0.61	17 24 36.24	-34 17 51.8	19.938±0.019	17.839±0.007	...	...	...	...	...	...	...
126	155	0.48	17 24 36.46	-34 13 42.7	21.182±0.030	18.681±0.016	15.68±0.08	14.24±0.09	...	13.49±0.08	13.50±0.13	...	...
127	156	0.32	17 24 36.48	-34 12 36.9	17.136±0.002	15.591±0.001	13.40±0.04	12.34±0.06	11.57±0.05	10.46±0.04	10.08±0.04	9.73±0.04	9.02±0.05
128	157	0.33	17 24 36.64	-34 11 50.9	20.818±0.098	18.140±0.014	15.33±0.06	13.80±0.09	13.15±0.07	12.15±0.07	11.74±0.12	11.52±0.17	...
129	158	0.13	17 24 36.65	-34 15 50.8	18.390±0.004	16.575±0.002	...	12.77±0.04	12.27±0.05	11.86±0.06	11.85±0.07	11.67±0.15	...
130	159	0.67	17 24 36.65	-34 19 59.2	...	21.656±0.075	...	...	...	14.67±0.16	14.02±0.19	...	...
131	160	0.11	17 24 36.71	-34 12 01.9	20.993±0.060	18.664±0.023	...	...	...	13.68±0.10	13.50±0.20	...	...

Table 4.1: continued.

(1)	(2)	(3)	(4)	(5)	(6)	(7)	(8)	(9)	(10)	(11)	(12)	(13)	(14)
			RA	DEC	R	I	J	H	K_s	[3.6]	[4.5]	[5.8]	[8.0]
ID	W07	(arcsec)	(J2000)	(J2000)	(mag)	(mag)	(mag)	(mag)	(mag)	(mag)	(mag)	(mag)	(mag)
132	161	0.07	17 24 36.73	-34 12 28.3	21.372±0.057	18.839±0.023	16.02±0.11	14.64±0.11	...	...	...	...	...
133	162	0.29	17 24 36.77	-34 13 33.7	19.374±0.017	17.262±0.004	14.58±0.05	13.19±0.09	12.62±0.07	12.33±0.09	12.30±0.09	11.83±0.22	...
134	163	0.10	17 24 36.76	-34 11 45.5	19.529±0.030	17.233±0.007	14.53±0.06	13.14±0.07	12.74±0.06	12.29±0.05	12.17±0.09	12.09±0.22	...
135	164	0.11	17 24 37.13	-34 12 25.9	19.905±0.022	17.542±0.007	14.45±0.06	13.07±0.08	12.38±0.06	12.16±0.09	11.74±0.11	...	...
136	165	0.18	17 24 37.18	-34 12 23.6	21.117±0.067	18.767±0.021	...	...	...	12.29±0.12	11.93±0.11	11.44±0.14	...
137	166	0.55	17 24 37.54	-34 10 34.1	...	21.000±0.145	15.92±0.15	14.04±0.08	13.18±0.08	...	...	...	...
138	167	0.43	17 24 37.57	-34 14 47.9	20.226±0.035	17.884±0.008	15.09±0.07	13.64±0.10	12.95±0.07	12.52±0.08	12.38±0.11	...	...
139	168	0.24	17 24 37.65	-34 11 41.5	19.524±0.030	17.101±0.005	14.40±0.04	13.16±0.04	12.65±0.04	12.27±0.04	12.13±0.09	11.92±0.21	...
140	170	0.34	17 24 37.73	-34 15 24.2	20.239±0.020	17.142±0.004	14.62±0.03	13.06±0.02	12.18±0.02	10.63±0.04	10.19±0.04	9.68±0.04	8.75±0.03
141	171	0.53	17 24 37.80	-34 08 07.8	16.121±0.001	14.392±0.001	12.28±0.03	11.57±0.04	10.97±0.04	...	...	...	...
142	172	0.27	17 24 37.76	-34 12 14.9	22.661±0.186	19.538±0.043	...	...	...	...	...	...	...
143	173	0.22	17 24 37.79	-34 12 02.0	19.393±0.014	17.105±0.005	14.40±0.03	13.00±0.02	12.42±0.02	11.87±0.07	11.85±0.09	...	...
144	174	0.38	17 24 37.83	-34 12 33.4	22.561±0.186	19.820±0.056	...	...	...	14.37±0.15	...	...	...
145	175	0.43	17 24 37.92	-34 13 21.8	19.781±0.025	17.558±0.006	14.92±0.08	13.45±0.09	12.93±0.07	11.92±0.06	11.71±0.08	11.40±0.12	10.34±0.10
146	176	0.05	17 24 37.94	-34 10 23.9	21.646±0.126	19.150±0.050	...	...	...	...	...	...	...
147	177	0.46	17 24 38.02	-34 17 52.3	19.959±0.019	17.715±0.006	...	...	...	13.61±0.12	13.65±0.25	...	...
148	178	0.55	17 24 38.14	-34 12 42.1	20.477±0.038	18.087±0.011	15.06±0.11	...	...	12.59±0.13	12.73±0.12	...	...
149	179	0.30	17 24 38.19	-34 14 20.5	16.936±0.002	15.238±0.001	13.04±0.03	11.98±0.04	11.28±0.03	...	...	...	...
150	180	0.15	17 24 38.28	-34 11 22.4	19.791±0.039	17.600±0.009	15.06±0.02	13.59±0.02	12.85±0.02	12.17±0.06	11.81±0.11	...	...
151	181	0.23	17 24 38.38	-34 11 15.4	20.349±0.163	18.155±0.014	15.25±0.06	13.95±0.05	13.43±0.04	12.80±0.09	12.88±0.17	...	...
152	182	0.51	17 24 38.57	-34 09 59.6	...	21.514±0.224	...	...	...	...	...	...	...
153	185	0.31	17 24 38.68	-34 10 43.2	17.410±0.011	15.631±0.004	13.11±0.03	11.72±0.04	10.71±0.03	9.28±0.04	8.75±0.06	8.16±0.07	...
154	186	0.21	17 24 38.72	-34 12 08.5	19.106±0.011	17.091±0.005	14.31±0.08	12.91±0.11	...	...	...	...	...
155	187	0.56	17 24 38.76	-34 12 28.9	20.125±0.027	18.003±0.023	15.29±0.08	13.86±0.07	13.28±0.07	13.22±0.17	12.70±0.12	...	...
156	188	0.09	17 24 38.74	-34 12 03.0	16.493±0.001	14.582±0.001	12.19±0.04	11.10±0.05	10.55±0.04	10.27±0.06	10.06±0.08	9.75±0.08	9.69±0.08
157	190	0.65	17 24 38.75	-34 17 09.3	20.022±0.021	17.633±0.006	14.59±0.06	13.23±0.10	...	12.20±0.09	12.28±0.10	12.50±0.31	...
158	191	0.22	17 24 38.80	-34 13 08.6	18.669±0.009	16.786±0.004	14.28±0.02	12.99±0.02	12.52±0.02	11.98±0.04	11.91±0.08	12.00±0.25	...
159	192	0.29	17 24 38.87	-34 10 41.3	...	20.715±0.112	...	...	...	...	...	...	...
160	193	0.39	17 24 38.89	-34 14 05.4	20.640±0.018	18.499±0.019	...	...	...	...	...	...	...
161	194	0.27	17 24 38.92	-34 14 58.9	...	...	...	8.73±0.06	8.52±0.04	8.36±0.05	8.31±0.05	8.29±0.04	8.30±0.03
162	195	0.21	17 24 38.93	-34 12 03.0	20.895±0.055	18.669±0.023	...	...	...	...	...	...	...
163	196	0.17	17 24 38.99	-34 12 20.8	17.600±0.003	15.671±0.001	13.20±0.04	12.01±0.10	11.50±0.04	11.16±0.05	11.14±0.07	11.18±0.08	...
164	197	0.11	17 24 39.03	-34 10 07.8	20.206±0.127	17.767±0.024	14.44±0.04	12.94±0.02	12.02±0.02	10.65±0.05	10.25±0.06	9.70±0.11	...
165	198	0.27	17 24 39.08	-34 12 09.0	20.690±0.046	18.801±0.026	...	...	...	13.64±0.12	13.88±0.30	...	...
166	199	0.41	17 24 39.29	-34 09 39.5	19.883±0.087	17.557±0.017	14.73±0.04	13.45±0.02	12.95±0.02	...	...	...	...
167	200	0.32	17 24 39.39	-34 11 29.3	21.019±0.167	18.644±0.023	15.67±0.08	14.32±0.09	13.71±0.09	13.27±0.11	...	...	...
168	201	0.29	17 24 39.44	-34 12 01.3	19.848±0.026	17.781±0.011	14.88±0.07	13.53±0.07	12.89±0.07	12.29±0.06	12.32±0.16	11.93±0.21	...
169	202	0.27	17 24 39.44	-34 14 46.7	20.703±0.044	18.291±0.015	...	14.36±0.10	13.85±0.08	13.25±0.07	13.26±0.09	...	...
170	203	0.18	17 24 39.52	-34 13 18.2	17.821±0.004	15.915±0.002	13.45±0.04	12.28±0.04	11.81±0.03	11.35±0.07	11.50±0.10	11.30±0.11	...
171	204	0.69	17 24 39.53	-34 19 40.0	17.087±0.002	15.363±0.001	12.77±0.03	11.75±0.04	11.29±0.02	11.06±0.08	10.83±0.05	10.79±0.08	10.86±0.11
172	205	0.39	17 24 39.62	-34 14 57.3	20.440±0.035	18.004±0.011	...	...	...	...	...	...	...
173	206	0.36	17 24 39.61	-34 16 33.2	19.386±0.009	17.510±0.007	...	...	...	...	...	...	...
174	207	0.30	17 24 39.71	-34 12 19.1	19.488±0.018	17.273±0.005	14.59±0.06	13.27±0.08	12.66±0.05	12.21±0.08	12.22±0.09	...	...
175	208	0.64	17 24 39.68	-34 13 47.9	22.275±0.087	19.490±0.048	15.76±0.06	14.14±0.04	13.37±0.06	12.12±0.07	11.97±0.12	11.36±0.12	...
176	209	0.22	17 24 39.83	-34 13 37.2	19.191±0.014	17.033±0.005	14.32±0.03	13.04±0.03	12.57±0.04	12.20±0.05	12.11±0.07	11.62±0.14	...
177	210	0.09	17 24 39.82	-34 09 06.6	22.693±0.038	19.333±0.087	14.75±0.04	12.66±0.02	11.26±0.02	9.43±0.07	8.96±0.08	...	...
178	211	0.41	17 24 39.87	-34 13 09.7	20.120±0.033	17.749±0.010	14.95±0.08	...	...	12.45±0.08	12.43±0.12	...	...
179	212	0.47	17 24 39.87	-34 14 11.5	21.055±0.028	18.482±0.019	15.30±0.04	13.99±0.04	13.47±0.04	12.97±0.07	12.87±0.13	...	...
180	213	0.28	17 24 40.07	-34 14 20.5	20.285±0.013	17.846±0.011	15.02±0.04	13.72±0.04	13.20±0.05	12.66±0.06	12.73±0.09	12.68±0.28	...
181	214	0.54	17 24 40.07	-34 17 12.9	20.045±0.021	17.926±0.008	14.91±0.06	13.53±0.07	12.65±0.05	11.20±0.05	10.72±0.05	10.40±0.05	9.93±0.04
182	215	0.67	17 24 40.15	-34 17 35.2	22.721±0.065	20.478±0.074	...	...	...	13.12±0.08	12.64±0.10	12.07±0.17	...
183	216	0.21	17 24 40.17	-34 14 41.1	15.503±0.001	14.684±0.001	13.61±0.04	13.07±0.08	12.83±0.09	12.31±0.06	12.48±0.08	...	...
184	217	0.11	17 24 40.16	-34 16 49.6	18.879±0.006	16.992±0.003	14.54±0.07	13.31±0.09	12.80±0.07	12.58±0.06	12.41±0.11	...	...
185	218	0.34	17 24 40.21	-34 11 02.9	19.664±0.087	17.533±0.011	14.77±0.04	13.43±0.09	12.83±0.09	12.30±0.16	...	...	...
186	219	0.18	17 24 40.26	-34 12 10.4	19.516±0.019	17.298±0.007	14.19±0.14	...	12.45±0.07	11.98±0.08	11.89±0.16	...	...
187	220	0.27	17 24 40.29	-34 11 25.9	19.995±0.119	17.580±0.012	14.48±0.04	13.03±0.09	12.45±0.05	11.71±0.05	11.34±0.09	10.87±0.16	...
188	221	0.12	17 24 40.32	-34 11 54.9	19.465±0.044	17.370±0.010	...	12.92±0.08	12.45±0.07	11.87±0.06	12.15±0.22	11.96±0.17	...
189	223	0.04	17 24 40.45	-34 15 03.3	20.904±0.053	18.701±0.022	...	...	...	...	...	...	...
190	224	0.24	17 24 40.47	-34 11 54.5	20.056±0.076	17.805±0.014	...	...	...	...	...	...	...
191	225	0.39	17 24 40.49	-34 12 06.7	12.885±0.001	11.683±0.001	10.05±0.03	9.45±0.03	9.14±0.02	9.04±0.06	8.98±0.05	8.96±0.04	8.91±0.05
192	226	0.20	17 24 40.56	-34 13 35.4	17.494±0.003	15.675±0.002	13.42±0.04	12.33±0.06	11.89±0.05	11.58±0.06	11.52±0.08	11.66±0.10	...

Table 4.1: continued.

(1)	(2)	(3)	(4)	(5)	(6)	(7)	(8)	(9)	(10)	(11)	(12)	(13)	(14)
			RA	DEC	R	I	J	H	K_s	[3.6]	[4.5]	[5.8]	[8.0]
ID	W07	(arcsec)	(J2000)	(J2000)	(mag)	(mag)	(mag)	(mag)	(mag)	(mag)	(mag)	(mag)	(mag)
193	227	0.28	17 24 40.69	-34 14 04.1	20.746±0.052	18.515±0.020	15.70±0.06	14.50±0.10	...	13.75±0.09	13.45±0.13	...	...
194	228	0.38	17 24 40.67	-34 11 57.4	22.373±0.123	19.224±0.053	...	...	...	...	...	...	...
195	229	0.11	17 24 40.69	-34 11 21.6	21.180±0.192	18.743±0.034	...	...	...	...	...	...	...
196	230	0.49	17 24 40.73	-34 05 34.7	18.757±0.005	16.860±0.003	14.37±0.05	13.12±0.07	...	12.00±0.10	11.89±0.09	...	...
197	231	0.39	17 24 40.79	-34 15 18.6	20.944±0.055	18.700±0.021	15.74±0.08	14.29±0.04	...	13.38±0.08	13.24±0.11	...	...
198	232	0.33	17 24 40.91	-34 15 00.4	17.809±0.003	16.180±0.002	13.70±0.06	12.56±0.07	...	11.70±0.05	11.59±0.09	...	...
199	233	0.05	17 24 40.94	-34 11 04.2	20.591±0.203	18.552±0.029	15.16±0.31	...	...	...	...	...	...
200	234	0.31	17 24 40.98	-34 11 26.3	22.080±0.147	19.249±0.054	...	...	...	...	...	...	...
201	235	0.43	17 24 40.99	-34 13 17.6	21.974±0.105	19.269±0.042	15.75±0.08	14.00±0.07	13.07±0.04	12.02±0.09	11.90±0.11	11.20±0.12	10.52±0.16
202	236	0.25	17 24 41.01	-34 12 21.8	18.451±0.007	16.405±0.003	13.70±0.06	12.32±0.10	11.55±0.05	10.44±0.09	9.74±0.08	9.03±0.05	7.89±0.04
203	238	0.24	17 24 41.12	-34 11 34.9	20.270±0.150	18.147±0.020	15.23±0.08	13.89±0.11	...	13.02±0.08	13.26±0.19	...	...
204	239	0.22	17 24 41.13	-34 11 17.3	21.463±0.092	18.763±0.034	...	...	...	...	...	...	...
205	240	0.26	17 24 41.13	-34 13 34.8	18.773±0.010	16.753±0.004	13.93±0.04	12.70±0.05	...	11.93±0.05	11.99±0.08	12.31±0.31	...
206	241	0.21	17 24 41.21	-34 11 11.2	19.856±0.105	17.925±0.016	14.99±0.05	13.47±0.02	12.75±0.04	...	...	...	...
207	242	0.17	17 24 41.22	-34 11 43.4	22.212±0.169	18.902±0.039	...	...	...	...	...	...	...
208	243	0.26	17 24 41.25	-34 11 38.8	16.737±0.004	14.931±0.001	12.47±0.03	11.32±0.05	10.74±0.04	10.42±0.11	10.36±0.17	10.46±0.11	...
209	244	0.47	17 24 41.29	-34 08 59.0	21.428±0.353	18.720±0.050	16.08±0.08	14.65±0.04	14.18±0.09	...	...	...	...
210	245	1.11	17 24 41.34	-34 11 32.3	...	...	...	...	...	13.21±0.13	12.98±0.21	...	...
211	246	0.95	17 24 41.33	-34 11 40.8	...	19.703±0.082	...	...	...	...	...	...	...
212	247	0.27	17 24 41.32	-34 16 11.9	18.565±0.004	16.719±0.003	...	...	...	...	...	...	...
213	248	0.26	17 24 41.34	-34 12 16.0	19.639±0.021	17.692±0.010	14.64±0.07	13.25±0.12	12.70±0.07	12.27±0.09	12.14±0.15	...	...
214	249	0.30	17 24 41.41	-34 12 19.3	19.336±0.016	17.283±0.005	...	...	...	...	...	...	...
215	250	0.15	17 24 41.46	-34 11 56.1	19.570±0.048	17.488±0.011	...	...	...	12.33±0.09	12.27±0.19	...	...
216	251	0.19	17 24 41.48	-34 13 58.2	19.626±0.019	17.240±0.006	14.18±0.04	12.72±0.04	11.81±0.03	10.58±0.03	10.09±0.05	9.66±0.04	8.85±0.03
217	252	0.29	17 24 41.51	-34 11 48.3	19.898±0.066	17.501±0.011	14.31±0.05	12.88±0.04	12.21±0.03	...	...	...	...
218	253	0.35	17 24 41.54	-34 10 33.3	21.028±0.273	18.680±0.057	16.61±0.16	14.73±0.06	14.69±0.23	13.09±0.13	...	...	...
219	254	0.21	17 24 41.53	-34 12 24.3	19.700±0.022	17.577±0.009	...	...	...	...	...	...	...
220	255	1.30	17 24 41.50	-34 11 58.8	...	20.962±0.090	...	...	...	...	...	...	...
221	256	0.11	17 24 41.61	-34 11 31.0	22.735±0.270	19.615±0.077	...	...	...	...	...	...	...
222	257	0.14	17 24 41.62	-34 11 48.2	20.037±0.075	17.713±0.013	14.31±0.06	12.88±0.04	12.21±0.03	11.20±0.05	10.76±0.10	10.43±0.06	...
223	258	0.27	17 24 41.64	-34 12 50.3	19.210±0.014	17.350±0.007	14.38±0.02	12.86±0.02	11.89±0.02	11.00±0.05	10.44±0.03	10.22±0.06	9.77±0.05
224	259	0.55	17 24 41.66	-34 14 57.5	21.269±0.074	18.880±0.025	15.82±0.11	...	...	13.37±0.11	13.27±0.12	...	...
225	260	0.34	17 24 41.73	-34 12 04.5	22.341±0.190	19.693±0.081	...	...	...	...	...	...	...
226	261	0.28	17 24 41.75	-34 11 30.0	18.154±0.022	16.297±0.004	13.88±0.03	12.71±0.04	12.26±0.04	11.71±0.09	11.52±0.16	...	...
227	262	0.35	17 24 41.74	-34 11 57.5	20.956±0.071	18.512±0.028	...	...	...	...	...	...	...
228	263	0.68	17 24 41.82	-34 11 18.8	20.405±0.173	18.337±0.023	...	...	...	11.23±0.07	10.65±0.23	...	...
229	265	0.04	17 24 41.84	-34 11 50.3	22.373±0.211	19.720±0.085	...	...	...	...	...	...	...
230	266	0.49	17 24 41.88	-34 11 41.1	19.906±0.066	17.794±0.014	14.76±0.16	13.24±0.11	12.50±0.06	11.77±0.09	11.67±0.15	...	...
231	268	1.06	17 24 41.82	-34 11 11.3	...	19.733±0.085	...	...	...	...	...	...	...
232	269	0.99	17 24 41.88	-34 19 36.6	18.442±0.005	16.523±0.002	...	12.89±0.09	12.46±0.06	12.34±0.05	12.16±0.06	12.14±0.28	...
233	270	0.62	17 24 41.95	-34 11 58.5	14.750±0.001	13.307±0.001	11.22±0.03	10.46±0.03	10.05±0.03	9.86±0.05	9.78±0.07	9.72±0.07	...
234	271	0.08	17 24 41.94	-34 15 52.0	20.132±0.019	18.438±0.013	13.22±0.04	11.24±0.04	10.44±0.03	9.80±0.03	9.78±0.05	9.61±0.04	9.51±0.04
235	272	0.24	17 24 41.95	-34 12 26.7	21.434±0.113	18.757±0.026	...	...	...	...	...	...	...
236	273	0.23	17 24 41.95	-34 11 50.2	20.973±0.178	18.734±0.033	...	...	...	13.19±0.09	13.17±0.14	...	...
237	274	1.04	17 24 41.99	-34 11 54.5	24.072±0.396	20.150±0.124	...	...	...	...	...	...	...
238	275	0.10	17 24 42.01	-34 11 05.6	...	19.788±0.181	...	...	...	...	...	...	...
239	276	0.29	17 24 42.03	-34 11 09.7	...	20.412±0.139	...	...	...	...	...	...	...
240	277	0.12	17 24 42.03	-34 11 18.6	20.953±0.284	18.706±0.033	...	...	...	...	...	...	...
241	278	0.38	17 24 42.03	-34 15 04.2	20.136±0.026	18.013±0.011	15.21±0.06	13.88±0.06	13.35±0.05	12.75±0.07	12.65±0.09	...	...
242	279	0.27	17 24 42.07	-34 11 36.9	20.386±0.105	18.145±0.020	...	13.93±0.14	...	13.09±0.12	13.09±0.29	...	...
243	280	0.27	17 24 42.12	-34 14 35.6	20.748±0.046	18.275±0.015	15.60±0.37	13.83±0.27	12.73±0.12	11.34±0.04	10.90±0.06	10.37±0.06	9.58±0.03
244	281	0.20	17 24 42.12	-34 11 46.8	22.697±0.197	19.667±0.080	...	...	...	...	...	...	...
245	282	0.94	17 24 42.07	-34 11 34.2	...	21.690±0.193	...	...	...	...	...	...	...
246	284	0.09	17 24 42.15	-34 11 55.9	19.792±0.060	17.739±0.014	...	...	...	12.66±0.17	12.15±0.22	...	...
247	285	0.21	17 24 42.17	-34 16 23.2	19.101±0.007	17.097±0.004	14.58±0.05	13.36±0.10	12.99±0.08	12.63±0.06	12.60±0.10	12.19±0.20	...
248	286	0.37	17 24 42.20	-34 12 09.7	20.474±0.045	18.105±0.015	16.01±0.19	14.16±0.09	13.87±0.17	12.73±0.08	12.74±0.17	...	...
249	287	0.82	17 24 42.24	-34 15 56.7	19.800±0.014	17.829±0.007	14.65±0.06	13.22±0.10	12.40±0.05	11.66±0.05	11.10±0.06	10.70±0.05	9.85±0.03
250	288	0.37	17 24 42.24	-34 12 30.9	20.355±0.090	17.940±0.021	14.84±0.05	13.51±0.06	12.94±0.06	12.21±0.09	12.26±0.10	...	...
251	290	0.23	17 24 42.30	-34 11 28.3	17.224±0.009	15.439±0.002	13.08±0.02	12.02±0.04	11.57±0.06	11.25±0.06	11.13±0.08	...	...
252	291	0.11	17 24 42.29	-34 13 01.9	20.227±0.037	17.838±0.011	14.59±0.03	13.22±0.05	12.57±0.04	11.97±0.05	12.00±0.10	11.69±0.15	...
253	293	0.76	17 24 42.31	-34 13 22.2	...	14.768±0.001	9.29±0.03	8.77±0.05	8.47±0.02	8.34±0.15	8.16±0.05	8.06±0.03	8.09±0.03

Table 4.1: continued.

(1)	(2)	(3)	(4)	(5)	(6)	(7)	(8)	(9)	(10)	(11)	(12)	(13)	(14)
			RA	DEC	R	I	J	H	K_s	[3.6]	[4.5]	[5.8]	[8.0]
ID	W07	(arcsec)	(J2000)	(J2000)	(mag)	(mag)	(mag)	(mag)	(mag)	(mag)	(mag)	(mag)	(mag)
254	294	0.21	17 24 42.32	-34 11 23.4	14.890±0.001	13.630±0.001	...	11.38±0.07	10.30±0.02	10.83±0.06	10.72±0.13	...	...
255	296	0.37	17 24 42.36	-34 14 49.5	21.628±0.022	19.045±0.030	14.49±0.07	12.84±0.08	12.08±0.06	11.21±0.05	10.96±0.05	10.69±0.06	10.18±0.04
256	298	0.11	17 24 42.44	-34 11 31.2	21.754±0.111	18.971±0.042	...	...	...	12.26±0.10	11.65±0.12	10.73±0.27	...
257	300	0.46	17 24 42.52	-34 17 15.0	18.345±0.004	16.650±0.003	...	...	...	...	...	...	...
258	301	0.30	17 24 42.51	-34 11 32.7	23.562±0.151	20.095±0.118	...	...	...	12.71±0.12	12.46±0.18	...	...
259	302	0.09	17 24 42.52	-34 11 35.8	22.519±0.241	19.420±0.063	...	...	...	...	...	...	...
260	303	0.35	17 24 42.55	-34 11 13.2	18.582±0.032	16.562±0.005	...	...	...	...	...	...	...
261	306	0.20	17 24 42.53	-34 14 39.2	17.827±0.003	16.130±0.002	13.85±0.07	12.79±0.12	...	...	...	...	...
262	307	0.39	17 24 42.51	-34 11 51.8	...	20.219±0.135	...	...	...	12.88±0.13	12.73±0.23	...	...
263	308	0.37	17 24 42.58	-34 12 02.8	21.184±0.087	18.508±0.027	...	...	...	12.69±0.15	12.56±0.27	...	...
264	309	0.20	17 24 42.68	-34 11 02.8	...	19.358±0.060	...	...	...	...	...	...	...
265	310	0.55	17 24 42.74	-34 12 24.7	20.999±0.072	18.255±0.016	...	13.74±0.09	...	11.75±0.08	11.49±0.12	10.80±0.10	...
266	311	0.31	17 24 42.74	-34 10 21.2	...	19.729±0.147	...	...	...	...	...	...	...
267	312	0.29	17 24 42.88	-34 09 11.9	15.382±0.001	13.273±0.001	10.66±0.02	9.73±0.03	9.23±0.02	8.91±0.05	8.86±0.09	...	...
268	313	0.44	17 24 42.93	-34 11 52.6	19.788±0.059	17.632±0.012	...	...	...	...	...	...	...
269	315	0.21	17 24 43.00	-34 11 54.2	18.930±0.027	16.749±0.005	...	...	...	...	...	...	...
270	317	0.23	17 24 43.07	-34 11 51.3	20.794±0.125	18.848±0.038	...	...	...	...	...	...	...
271	318	0.51	17 24 43.11	-34 12 30.4	20.378±0.093	19.073±0.034	15.13±0.15	13.80±0.12	13.35±0.08	12.78±0.06	12.71±0.11	...	...
272	319	0.23	17 24 43.12	-34 12 16.2	17.246±0.002	15.361±0.001	13.19±0.02	12.04±0.02	11.49±0.03	11.18±0.07	11.13±0.08	10.93±0.11	...
273	320	0.31	17 24 43.18	-34 11 53.7	19.921±0.067	17.715±0.013	...	...	...	...	...	...	...
274	321	0.63	17 24 43.19	-34 16 42.8	18.536±0.005	16.770±0.003	14.64±0.06	13.44±0.09	13.12±0.06	12.78±0.05	12.62±0.09	...	...
275	322	0.25	17 24 43.19	-34 11 11.9	18.252±0.028	16.391±0.004	13.60±0.02	12.20±0.02	11.57±0.03	...	...	...	...
276	323	0.36	17 24 43.19	-34 12 03.8	...	19.648±0.078	...	...	...	...	...	...	...
277	325	0.95	17 24 43.29	-34 12 03.2	21.294±0.074	21.567±0.081	...	...	...	...	...	...	...
278	326	0.07	17 24 43.24	-34 12 17.8	19.013±0.012	17.125±0.006	...	...	...	12.57±0.17	...	...	...
279	328	0.29	17 24 43.26	-34 12 35.9	16.768±0.003	14.891±0.001	12.40±0.07	11.33±0.02	10.85±0.02	10.54±0.05	10.45±0.05	10.38±0.05	...
280	330	0.37	17 24 43.28	-34 13 29.2	21.111±0.083	18.620±0.023	15.49±0.07	13.98±0.07	...	12.63±0.08	12.64±0.10	...	...
281	331	0.14	17 24 43.29	-34 12 44.0	...	...	8.47±0.02	8.00±0.06	7.69±0.02	7.54±0.07	7.50±0.04	7.50±0.03	7.48±0.02
282	332	0.31	17 24 43.27	-34 11 42.1	12.938±0.001	11.707±0.001	10.00±0.05	9.31±0.06	8.97±0.05	8.78±0.05	8.70±0.05	8.66±0.03	...
283	335	0.18	17 24 43.36	-34 11 37.1	18.631±0.021	16.592±0.005	...	...	...	11.81±0.08	11.90±0.09	10.93±0.23	...
284	337	0.22	17 24 43.41	-34 12 02.2	20.902±0.091	18.803±0.036	...	...	...	...	...	...	...
285	339	0.18	17 24 43.41	-34 08 45.4	22.266±0.043	17.833±0.007	12.86±0.02	10.95±0.02	9.90±0.02	9.16±0.11	8.86±0.19	...	...
286	340	1.16	17 24 43.49	-34 11 45.9	22.018±0.113	19.363±0.060	...	...	...	...	...	...	...
287	342	0.37	17 24 43.50	-34 13 28.7	21.010±0.076	18.569±0.022	15.75±0.08	14.42±0.07	...	13.03±0.08	12.97±0.15	...	...
288	343	0.63	17 24 43.51	-34 09 15.4	21.104±0.170	19.142±0.074	16.03±0.14	14.43±0.12	...	...	...	...	...
289	344	0.18	17 24 43.50	-34 11 57.1	...	...	6.73±0.03	6.18±0.04	5.89±0.02	5.61±0.05	6.07±0.06	5.53±0.02	5.47±0.02
290	345	0.25	17 24 43.51	-34 12 40.3	20.981±0.040	18.247±0.028	...	...	...	11.31±0.08	10.90±0.10	...	...
291	348	0.35	17 24 43.55	-34 12 27.8	18.646±0.018	16.603±0.006	...	...	...	11.45±0.05	11.43±0.09	11.08±0.13	...
292	349	0.64	17 24 43.49	-34 12 04.4	...	20.198±0.070	...	...	...	...	...	...	...
293	350	0.36	17 24 43.57	-34 15 40.4	19.664±0.016	17.474±0.007	15.00±0.04	13.75±0.05	13.27±0.05	12.92±0.05	12.95±0.10	...	...
294	351	0.49	17 24 43.61	-34 11 50.2	19.742±0.057	17.554±0.014	...	...	...	...	...	...	...
295	352	0.38	17 24 43.59	-34 12 38.5	21.471±0.066	19.002±0.033	...	...	...	11.47±0.09	11.11±0.08	9.79±0.07	8.60±0.05
296	353	0.25	17 24 43.61	-34 09 43.0	21.476±0.226	18.894±0.059	14.71±0.15	13.36±0.12	12.27±0.07	...	...	...	...
297	355	0.35	17 24 43.63	-34 09 02.9	24.079±0.361	20.390±0.231	...	...	...	...	...	...	...
298	357	0.05	17 24 43.68	-34 11 49.6	...	19.247±0.136	...	...	...	12.35±0.16	12.07±0.17	...	...
299	358	0.30	17 24 43.71	-34 11 12.9	20.870±0.265	19.297±0.057	...	14.32±0.12	13.53±0.12	...	...	...	...
300	359	0.40	17 24 43.73	-34 11 39.3	20.628±0.109	17.514±0.011	...	...	...	...	...	...	...
301	362	1.01	17 24 43.74	-34 18 12.5	16.650±0.001	15.083±0.001	13.04±0.03	12.21±0.03	11.84±0.02	11.65±0.04	11.56±0.06	11.45±0.08	11.59±0.11
302	363	0.76	17 24 43.81	-34 11 53.7	...	...	...	...	...	10.70±0.15	9.62±0.14	8.32±0.04	5.32±0.06
303	364	0.25	17 24 43.77	-34 11 54.1	19.470±0.044	17.633±0.012	...	...	...	...	...	...	...
304	367	0.83	17 24 43.73	-34 11 52.1	22.099±0.117	19.455±0.065	...	...	...	...	...	...	...
305	369	0.47	17 24 43.88	-34 12 16.2	...	21.803±0.117	...	...	...	...	...	...	...
306	370	0.17	17 24 43.89	-34 13 10.9	19.721±0.023	17.615±0.009	14.85±0.05	13.30±0.05	12.53±0.05	11.53±0.05	11.18±0.05	10.78±0.06	10.31±0.09
307	372	0.22	17 24 43.90	-34 11 39.4	17.627±0.008	16.496±0.004	...	...	...	...	...	...	...
308	374	0.08	17 24 43.92	-34 11 04.0	...	19.598±0.183	...	...	...	...	...	...	...
309	376	0.15	17 24 43.94	-34 12 29.4	20.659±0.053	18.526±0.036	15.69±0.08	14.11±0.07	13.48±0.10	12.29±0.06	11.90±0.09	11.20±0.27	...
310	377	0.26	17 24 43.96	-34 12 16.8	21.264±0.055	18.669±0.024	16.00±0.13	13.40±0.19	12.41±0.12	11.48±0.08	11.08±0.11	10.60±0.07	...
311	378	0.29	17 24 43.96	-34 11 32.1	20.601±0.206	18.193±0.021	...	...	...	12.77±0.11	12.64±0.17	...	...
312	379	0.23	17 24 43.97	-34 11 45.8	19.667±0.053	17.470±0.011	...	12.95±0.25	12.30±0.42	11.91±0.06	11.48±0.11	10.95±0.09	...
313	380	0.23	17 24 44.01	-34 09 51.0	20.725±0.158	18.778±0.053	15.28±0.14	...	...	...	...	...	...
314	381	0.43	17 24 44.03	-34 12 09.8	21.384±0.103	19.063±0.037	...	...	...	11.57±0.07	11.11±0.11	10.73±0.07	9.16±0.05

Table 4.1: continued.

(1)	(2)	(3)	(4)	(5)	(6)	(7)	(8)	(9)	(10)	(11)	(12)	(13)	(14)
			RA	DEC	R	I	J	H	K_s	[3.6]	[4.5]	[5.8]	[8.0]
ID	W07	(arcsec)	(J2000)	(J2000)	(mag)	(mag)	(mag)	(mag)	(mag)	(mag)	(mag)	(mag)	(mag)
315	382	0.59	17 24 44.05	-34 13 24.4	...	22.385±0.203	...	...	...	13.30±0.09	13.51±0.32	...	...
316	383	0.27	17 24 44.04	-34 12 03.2	18.747±0.009	16.599±0.005	...	...	...	11.60±0.10	11.45±0.26	...	...
317	384	1.49	17 24 44.20	-34 14 59.8	...	...	10.27±0.02	9.50±0.02	9.23±0.02	...	...	...	...
318	386	0.27	17 24 44.11	-34 10 07.6	20.723±0.207	18.557±0.051	14.26±0.24	13.28±0.26	12.00±0.16	...	...	...	...
319	387	0.22	17 24 44.15	-34 11 38.0	21.430±0.117	18.976±0.042	...	...	...	...	...	...	...
320	388	0.95	17 24 44.20	-34 11 52.3	22.296±0.250	20.156±0.299	...	...	...	...	...	...	...
321	389	0.11	17 24 44.15	-34 13 06.8	20.844±0.061	18.484±0.020	15.66±0.07	13.54±0.05	12.43±0.06	11.72±0.05	11.59±0.08	11.67±0.17	...
322	392	1.01	17 24 44.23	-34 11 55.2	...	19.846±0.094	...	...	...	...	...	...	...
323	393	0.41	17 24 44.19	-34 13 30.1	19.838±0.024	17.430±0.007	14.69±0.12	...	...	12.47±0.12	12.31±0.11	...	...
324	394	0.16	17 24 44.19	-34 11 51.0	18.677±0.021	16.433±0.006	...	12.48±0.44	...	11.28±0.13	11.19±0.33	10.73±0.13	...
325	395	0.37	17 24 44.25	-34 11 56.4	15.667±0.001	17.930±0.023	...	...	...	...	...	...	...
326	396	0.24	17 24 44.28	-34 12 03.8	18.803±0.010	16.893±0.009	...	...	...	...	...	...	...
327	397	0.14	17 24 44.37	-34 12 40.5	17.274±0.004	15.497±0.002	13.16±0.04	12.04±0.05	11.64±0.04	11.24±0.04	11.19±0.05	10.96±0.09	...
328	399	0.18	17 24 44.39	-34 10 39.9	17.973±0.017	16.006±0.005	12.99±0.14	11.93±0.13	10.97±0.09	...	...	...	...
329	400	0.26	17 24 44.40	-34 11 50.7	21.900±0.091	18.443±0.036	...	...	...	...	...	...	...
330	401	1.01	17 24 44.38	-34 11 58.5	15.000±0.001	13.048±0.001	8.45±0.08	7.86±0.07	7.37±0.03	6.96±0.07	6.34±0.06	5.91±0.03	5.39±0.02
331	402	0.30	17 24 44.43	-34 14 40.5	19.822±0.019	17.668±0.008	...	...	...	...	...	...	...
332	403	0.58	17 24 44.48	-34 12 10.3	20.163±0.037	17.809±0.015	...	...	...	12.90±0.10	12.89±0.24	...	...
333	404	0.12	17 24 44.45	-34 11 47.2	17.957±0.010	15.928±0.004	11.41±0.04	10.28±0.04	9.46±0.03	...	...	...	...
334	405	0.78	17 24 44.43	-34 12 01.8	...	...	7.94±0.33	7.35±0.16	...	...	...	...	...
335	406	0.35	17 24 44.49	-34 11 48.4	15.353±0.001	13.682±0.001	11.41±0.04	10.28±0.04	9.46±0.03	8.22±0.05	7.70±0.06	7.28±0.03	6.87±0.03
336	408	0.78	17 24 44.43	-34 12 01.8	...	...	7.94±0.33	7.35±0.16	...	...	...	...	...
337	409	0.92	17 24 44.52	-34 16 11.9	22.847±0.072	19.996±0.065	...	...	13.48±0.09	12.09±0.06	11.68±0.08	11.20±0.10	10.75±0.06
338	411	0.29	17 24 44.57	-34 12 36.4	21.309±0.105	18.808±0.040	...	...	13.57±0.10	12.04±0.08	11.69±0.11	10.86±0.14	...
339	412	0.28	17 24 44.66	-34 12 47.5	19.851±0.028	17.382±0.011	14.61±0.07	13.20±0.12	12.67±0.11	12.08±0.07	12.07±0.09	11.65±0.14	...
340	414	0.21	17 24 44.65	-34 12 05.1	18.616±0.009	16.340±0.005	...	...	...	...	...	...	...
341	415	0.10	17 24 44.64	-34 11 00.9	14.701±0.001	13.505±0.001	11.70±0.05	11.05±0.08	10.71±0.08	10.28±0.10	9.36±0.15	7.93±0.12	...
342	416	0.39	17 24 44.68	-34 11 19.5	20.479±0.168	18.049±0.026	16.30±0.23	14.29±0.27	15.41±0.76	...	...	...	...
343	417	0.55	17 24 44.75	-34 11 40.0	21.533±0.057	19.002±0.062	...	...	...	...	...	...	...
344	419	0.14	17 24 44.72	-34 08 41.6	20.052±0.052	17.594±0.006	15.06±0.02	13.90±0.02	13.34±0.02	12.83±0.13	12.27±0.18	...	...
345	420	0.20	17 24 44.74	-34 12 02.8	...	...	7.82±0.04	7.28±0.03	6.97±0.02	7.06±0.05	6.87±0.07	6.76±0.03	6.80±0.02
346	421	0.51	17 24 44.77	-34 09 42.7	...	20.074±0.153	...	...	...	...	...	...	...
347	422	0.36	17 24 44.78	-34 12 10.7	21.988±0.089	19.125±0.049	...	...	...	...	...	...	...
348	423	0.30	17 24 44.80	-34 17 32.2	20.471±0.031	18.372±0.014	...	...	...	...	...	...	...
349	425	0.26	17 24 44.80	-34 16 36.4	20.512±0.047	17.680±0.007	14.73±0.05	13.12±0.05	12.24±0.04	10.85±0.04	10.20±0.05	9.59±0.03	8.50±0.03
350	428	0.11	17 24 44.95	-34 11 23.5	17.335±0.009	15.600±0.003	11.40±0.03	10.71±0.06	10.29±0.04	...	...	...	...
351	429	0.17	17 24 44.94	-34 11 44.9	...	21.139±0.278	...	14.40±0.17	13.15±0.10	...	...	...	...
352	430	0.23	17 24 44.95	-34 13 14.0	19.760±0.022	17.413±0.007	...	12.85±0.10	...	11.16±0.05	10.60±0.05	10.18±0.06	9.33±0.05
353	432	0.20	17 24 45.02	-34 11 58.4	19.797±0.026	17.560±0.007	...	...	...	...	...	...	...
354	433	0.96	17 24 45.06	-34 11 24.3	14.390±0.001	13.161±0.001	11.40±0.03	10.71±0.06	10.29±0.04	10.02±0.18	...	...	...
355	434	0.29	17 24 45.08	-34 12 34.6	18.896±0.020	16.808±0.006	14.24±0.02	12.94±0.02	12.39±0.04	11.96±0.08	11.92±0.09	...	...
356	435	0.36	17 24 45.11	-34 11 29.3	21.564±0.132	19.186±0.073	...	...	...	...	...	...	...
357	436	0.12	17 24 45.13	-34 10 07.9	20.555±0.157	17.525±0.017	13.79±0.02	11.97±0.02	11.19±0.02	10.60±0.14	...	...	...
358	437	0.42	17 24 45.13	-34 14 01.4	20.571±0.042	18.081±0.012	...	...	...	...	...	...	...
359	439	0.23	17 24 45.20	-34 12 54.6	17.477±0.003	15.598±0.001	13.27±0.03	12.06±0.03	11.40±0.03	10.75±0.08	10.81±0.08	10.56±0.09	...
360	440	0.30	17 24 45.24	-34 10 58.2	19.874±0.098	17.790±0.020	14.54±0.21	13.07±0.16	...	11.13±0.14	10.65±0.25	...	...
361	441	0.44	17 24 45.23	-34 19 51.8	...	21.553±0.045	...	...	...	13.99±0.10	...	...	...
362	442	0.14	17 24 45.23	-34 10 50.7	19.151±0.050	17.073±0.013	13.92±0.20	...	...	...	...	...	...
363	444	0.28	17 24 45.29	-34 09 53.2	19.891±0.075	17.771±0.019	15.30±0.07	13.85±0.05	13.88±0.25	...	...	...	...
364	446	0.35	17 24 45.32	-34 12 19.2	21.712±0.068	18.986±0.043	14.93±0.06	12.89±0.06	11.53±0.04	10.49±0.05	9.88±0.05	9.37±0.04	8.73±0.06
365	447	0.70	17 24 45.35	-34 17 48.6	24.568±0.194	20.559±0.100	...	...	...	14.41±0.10	14.09±0.33	...	...
366	448	0.27	17 24 45.39	-34 12 12.6	18.831±0.011	16.841±0.006	14.13±0.06	13.16±0.05	12.62±0.05	12.19±0.06	11.99±0.16	11.51±0.27	...
367	449	0.45	17 24 45.41	-34 13 09.8	20.785±0.056	18.321±0.016	15.37±0.06	13.89±0.19	13.20±0.14	12.22±0.05	11.76±0.09	11.40±0.11	10.42±0.15
368	450	0.38	17 24 45.44	-34 11 23.3	19.792±0.090	17.761±0.020	...	...	...	...	...	...	...
369	451	0.11	17 24 45.43	-34 14 32.9	18.991±0.012	16.796±0.003	...	...	...	11.19±0.07	11.25±0.08	10.67±0.07	9.84±0.06
370	452	0.33	17 24 45.50	-34 11 47.8	20.411±0.097	17.855±0.022	14.94±0.08	13.49±0.09	12.92±0.14	12.51±0.06	12.29±0.20	...	...
371	453	0.23	17 24 45.50	-34 09 38.9	20.325±0.107	17.877±0.020	...	...	...	...	...	...	...
372	454	0.25	17 24 45.50	-34 11 29.8	20.899±0.249	18.132±0.028	15.35±0.09	...	12.95±0.04	11.27±0.07	9.69±0.11	9.72±0.14	...
373	456	0.37	17 24 45.56	-34 15 04.1	20.274±0.037	18.046±0.011	...	...	...	11.46±0.05	11.08±0.06	10.61±0.07	9.90±0.06
374	457	0.47	17 24 45.60	-34 14 00.0	21.177±0.074	17.897±0.010	14.72±0.08	13.19±0.09	12.35±0.05	11.52±0.06	11.24±0.07	10.82±0.06	...
375	458	0.10	17 24 45.63	-34 11 34.4	23.088±0.151	19.841±0.135	...	...	...	13.09±0.15	...	...	...

Table 4.1: continued.

(1)	(2)	(3)	(4)	(5)	(6)	(7)	(8)	(9)	(10)	(11)	(12)	(13)	(14)
			RA	DEC	R	I	J	H	K_s	[3.6]	[4.5]	[5.8]	[8.0]
ID	W07	(arcsec)	(J2000)	(J2000)	(mag)	(mag)	(mag)	(mag)	(mag)	(mag)	(mag)	(mag)	(mag)
376	459	0.34	17 24 45.69	-34 12 46.5	23.174±0.075	20.589±0.146	...	...	...	...	...	...	...
377	460	0.16	17 24 45.70	-34 14 10.3	21.887±0.053	18.784±0.023	15.72±0.13	...	...	13.08±0.09	12.82±0.12	...	...
378	461	0.41	17 24 45.78	-34 11 07.0	20.441±0.162	19.297±0.081	13.36±0.15	12.29±0.15	10.88±0.08	...	...	...	...
379	462	0.31	17 24 45.79	-34 11 21.7	20.020±0.111	17.866±0.022	...	...	...	12.09±0.21	...	...	...
380	463	0.38	17 24 45.79	-34 13 02.5	21.307±0.047	19.362±0.042	16.24±0.11	...	...	12.66±0.06	12.17±0.12	11.86±0.13	11.60±0.23
381	464	0.22	17 24 45.80	-34 09 39.9	...	...	8.81±0.03	8.23±0.03	7.95±0.03	7.71±0.07	7.70±0.09	...	...
382	466	0.14	17 24 45.84	-34 11 31.4	20.124±0.131	17.787±0.025	13.71±0.02	...	12.41±0.02	11.67±0.08	11.68±0.26	...	...
383	467	0.26	17 24 45.87	-34 11 24.2	18.853±0.029	16.741±0.008	13.96±0.02	12.57±0.06	11.98±0.02	11.16±0.11	...	...	...
384	468	0.34	17 24 45.85	-34 14 54.8	18.153±0.004	16.067±0.002	12.42±0.03	11.29±0.04	10.82±0.03	10.44±0.04	10.44±0.05	10.35±0.06	10.29±0.06
385	469	0.28	17 24 45.93	-34 12 41.2	22.052±0.093	19.063±0.046	...	14.35±0.12	...	13.29±0.07	13.39±0.17	...	...
386	470	0.67	17 24 46.01	-34 14 49.7	19.996±0.022	18.032±0.011	13.44±0.05	12.67±0.09	12.07±0.05	11.32±0.07	10.99±0.08	10.53±0.08	10.05±0.05
387	471	0.22	17 24 46.02	-34 14 07.6	18.180±0.005	16.030±0.002	13.11±0.04	11.48±0.04	10.67±0.04	10.19±0.09	10.34±0.10	9.96±0.06	10.13±0.05
388	472	0.26	17 24 46.04	-34 09 42.3	18.021±0.013	15.890±0.003	...	...	...	...	...	...	...
389	473	0.23	17 24 46.04	-34 10 44.8	19.848±0.061	17.899±0.027	...	...	...	...	...	...	...
390	474	0.21	17 24 46.17	-34 11 27.4	21.857±0.133	19.642±0.115	...	...	...	...	...	...	...
391	475	0.66	17 24 46.26	-34 11 43.4	21.404±0.116	18.362±0.036	15.58±0.06	...	...	11.83±0.14	11.47±0.14	11.26±0.23	...
392	476	0.24	17 24 46.24	-34 12 30.8	18.887±0.020	16.737±0.006	13.69±0.05	12.34±0.08	11.51±0.07	...	...	...	...
393	477	0.50	17 24 46.39	-34 14 16.3	22.864±0.131	19.794±0.060	16.56±0.15	14.89±0.12	...	13.24±0.09	12.73±0.10	...	...
394	479	0.23	17 24 46.43	-34 12 32.4	...	21.501±0.102	...	...	...	...	...	...	...
395	480	0.29	17 24 46.49	-34 12 56.3	19.656±0.020	17.687±0.009	14.65±0.04	13.32±0.02	12.74±0.03	12.25±0.05	12.08±0.07	11.61±0.09	...
396	481	0.45	17 24 46.48	-34 11 58.7	22.198±0.214	18.976±0.064	...	...	...	13.82±0.18	...	...	...
397	482	0.35	17 24 46.51	-34 14 42.0	21.452±0.018	20.149±0.078	16.03±0.11	14.48±0.15	13.52±0.09	12.16±0.05	11.80±0.07	11.39±0.08	10.86±0.18
398	483	0.40	17 24 46.58	-34 12 01.5	21.140±0.138	18.428±0.039	...	...	...	...	...	...	...
399	484	0.28	17 24 46.57	-34 12 40.8	17.391±0.005	15.444±0.002	12.78±0.04	11.47±0.04	10.87±0.03	...	...	...	...
400	485	0.26	17 24 46.58	-34 12 42.4	19.632±0.017	17.137±0.009	12.78±0.04	11.47±0.04	10.87±0.04	10.36±0.09	9.90±0.11	9.47±0.06	9.07±0.05
401	487	0.43	17 24 46.64	-34 13 35.1	22.339±0.122	19.485±0.048	16.27±0.10	...	...	13.78±0.08	13.44±0.15	...	...
402	488	0.41	17 24 46.61	-34 09 55.9	...	21.190±0.313	...	...	...	...	...	...	...
403	489	0.26	17 24 46.61	-34 06 45.2	12.570±0.001	12.068±0.001	11.22±0.02	10.87±0.02	10.77±0.02	10.73±0.04	10.67±0.06	10.72±0.06	...
404	490	0.31	17 24 46.63	-34 13 30.4	20.632±0.049	17.894±0.011	14.81±0.06	13.23±0.08	12.47±0.05	11.25±0.05	10.80±0.06	10.32±0.06	9.69±0.05
405	491	0.23	17 24 46.68	-34 12 00.5	19.408±0.047	17.309±0.016	...	...	12.32±0.04	11.71±0.08	11.56±0.11	...	...
406	493	0.21	17 24 46.70	-34 12 33.6	18.195±0.010	16.106±0.003	13.26±0.05	11.90±0.11	...	10.90±0.06	10.75±0.09	10.57±0.07	...
407	494	0.42	17 24 46.75	-34 12 35.5	22.431±0.133	19.074±0.051	...	...	...	...	...	...	...
408	495	0.32	17 24 46.76	-34 12 40.0	19.694±0.041	17.591±0.013	...	...	...	12.47±0.11	...	...	...
409	496	0.23	17 24 46.80	-34 15 19.4	19.538±0.015	17.496±0.007	14.86±0.14	13.61±0.11	13.18±0.05	12.77±0.05	12.84±0.10	12.32±0.22	...
410	497	0.94	17 24 46.93	-34 12 32.7	21.908±0.092	17.558±0.013	...	...	...	...	...	...	...
411	498	0.27	17 24 46.91	-34 11 06.8	19.983±0.116	17.776±0.021	...	...	...	...	...	...	...
412	499	0.37	17 24 47.02	-34 12 31.9	18.099±0.009	16.012±0.004	13.00±0.10	...	...	10.10±0.07	9.79±0.06	9.36±0.04	8.98±0.05
413	500	0.56	17 24 47.05	-34 13 04.3	21.658±0.063	19.254±0.039	...	13.74±0.07	...	11.72±0.06	11.36±0.07	10.85±0.08	10.20±0.05
414	501	0.29	17 24 47.03	-34 13 58.3	23.531±0.075	20.693±0.040	...	...	...	...	...	...	...
415	503	0.21	17 24 47.11	-34 12 23.4	21.172±0.088	18.698±0.036	15.69±0.07	14.12±0.10	13.42±0.08	12.73±0.10	12.60±0.10	...	...
416	504	1.32	17 24 47.13	-34 10 53.1	...	19.754±0.150	14.41±0.24	13.32±0.25	11.92±0.13	...	...	...	...
417	505	0.23	17 24 47.13	-34 08 25.0	20.200±0.022	17.580±0.005	14.84±0.04	13.53±0.02	12.83±0.02	11.98±0.08	11.54±0.09	...	...
418	506	0.27	17 24 47.12	-34 15 41.2	15.802±0.001	14.128±0.001	12.00±0.03	11.09±0.09	10.60±0.06	10.19±0.08	9.89±0.06	9.77±0.05	9.04±0.03
419	507	0.20	17 24 47.19	-34 11 29.9	20.975±0.078	18.787±0.053	16.09±0.13	...	...	...	...	...	...
420	508	0.21	17 24 47.24	-34 12 33.4	18.139±0.010	16.319±0.004	13.26±0.04	...	11.29±0.03	...	...	...	...
421	509	0.93	17 24 47.33	-34 11 01.4	...	19.919±0.159	...	...	...	...	...	...	...
422	511	0.21	17 24 47.33	-34 10 30.3	18.767±0.030	17.352±0.015	...	...	...	...	...	...	...
423	512	0.32	17 24 47.36	-34 15 41.8	19.856±0.019	17.629±0.007	...	...	...	11.38±0.12	11.84±0.22	11.46±0.11	...
424	513	0.04	17 24 47.39	-34 08 56.9	...	...	...	...	13.71±0.05	...	...	...	...
425	514	0.20	17 24 47.41	-34 12 41.4	16.151±0.002	14.338±0.001	12.04±0.03	10.93±0.06	10.46±0.03	10.16±0.06	10.10±0.05	9.94±0.05	10.00±0.05
426	515	0.37	17 24 47.46	-34 12 00.4	18.046±0.014	16.032±0.004	13.24±0.03	11.89±0.04	11.23±0.03	...	...	...	...
427	516	0.31	17 24 47.50	-34 13 54.9	19.436±0.015	17.135±0.005	13.88±0.04	12.56±0.05	11.99±0.04	11.45±0.06	11.20±0.08	10.99±0.08	10.57±0.14
428	517	0.18	17 24 47.55	-34 15 07.2	13.980±0.001	12.600±0.001	10.74±0.04	9.99±0.06	...	...	9.53±0.10	9.55±0.08	9.57±0.19
429	518	0.38	17 24 47.56	-34 15 16.9	21.145±0.070	18.680±0.022	...	...	...	...	...	...	...
430	519	0.13	17 24 47.58	-34 10 48.6	17.838±0.015	15.486±0.003	12.34±0.05	10.87±0.05	10.17±0.04	9.47±0.07	9.25±0.14	...	...
431	520	0.89	17 24 47.56	-34 10 20.9	22.683±0.310	19.393±0.094	...	...	...	...	...	...	...
432	522	0.48	17 24 47.74	-34 18 16.5	21.235±0.059	18.800±0.019	...	...	...	13.54±0.23	13.43±0.16	...	...
433	523	0.38	17 24 47.77	-34 15 04.1	19.596±0.015	17.268±0.005	...	...	...	...	...	...	...
434	524	0.25	17 24 47.82	-34 14 51.0	21.010±0.055	18.519±0.017	15.04±0.06	13.52±0.06	12.90±0.05	11.71±0.07	11.40±0.09	10.68±0.13	...
435	525	0.19	17 24 47.83	-34 11 01.8	19.613±0.046	17.771±0.016	...	...	...	...	...	...	...
436	527	0.44	17 24 47.91	-34 15 16.9	...	...	9.36±0.03	8.75±0.05	8.42±0.02	8.29±0.04	8.19±0.04	8.20±0.03	8.21±0.03

Table 4.1: continued.

(1)	(2)	(3)	(4)	(5)	(6)	(7)	(8)	(9)	(10)	(11)	(12)	(13)	(14)
			RA	DEC	R	I	J	H	K_s	[3.6]	[4.5]	[5.8]	[8.0]
ID	W07	(arcsec)	(J2000)	(J2000)	(mag)	(mag)	(mag)	(mag)	(mag)	(mag)	(mag)	(mag)	(mag)
437	528	0.42	17 24 47.94	-34 13 25.2	21.069±0.067	18.885±0.026	16.07±0.14	...	...	13.81±0.10	13.56±0.18	...	...
438	529	0.10	17 24 47.95	-34 10 45.7	20.051±0.104	17.685±0.019	14.61±0.10	13.23±0.09	12.60±0.07	12.29±0.20	...	...	...
439	530	0.47	17 24 47.97	-34 17 35.8	13.066±0.001	12.040±0.001	10.53±0.03	9.84±0.03	9.59±0.02	9.51±0.03	9.45±0.04	9.39±0.04	9.37±0.03
440	531	0.37	17 24 47.97	-34 11 04.3	19.740±0.051	17.595±0.013	14.01±0.16	12.89±0.15	11.82±0.11	...	...	...	...
441	532	0.24	17 24 48.01	-34 12 18.8	21.776±0.107	18.747±0.031	15.51±0.11	13.83±0.13	...	12.80±0.09	...	...	...
442	533	0.35	17 24 48.16	-34 10 53.0	21.204±0.300	18.542±0.042	15.36±0.30	14.35±0.24	...	...	...	...	...
443	534	0.23	17 24 48.13	-34 13 50.1	22.572±0.086	19.271±0.035	15.82±0.08	...	...	13.15±0.09	12.77±0.08	...	...
444	535	0.24	17 24 48.16	-34 13 00.6	21.233±0.064	18.962±0.028	...	...	...	13.42±0.09	13.52±0.15	...	...
445	536	0.50	17 24 48.16	-34 15 47.6	19.369±0.012	17.288±0.005	14.40±0.03	13.06±0.06	12.43±0.04	11.49±0.04	11.19±0.06	11.12±0.08	10.71±0.07
446	537	0.22	17 24 48.37	-34 12 16.8	22.117±0.088	18.718±0.030	15.52±0.07	...	...	12.87±0.14	12.72±0.18	...	...
447	538	1.17	17 24 48.32	-34 17 07.6	17.718±0.003	15.919±0.001	13.50±0.06	12.30±0.11	...	11.15±0.08	11.18±0.11	11.17±0.11	10.81±0.12
448	539	0.53	17 24 48.49	-34 17 43.9	...	...	8.76±0.03	8.30±0.07	8.03±0.02	7.91±0.04	7.87±0.04	7.86±0.03	7.83±0.02
449	540	1.18	17 24 48.47	-34 14 41.5	22.877±0.071	19.847±0.068	...	...	...	...	...	...	...
450	541	0.44	17 24 48.50	-34 10 53.7	...	20.048±0.167	...	...	...	...	...	...	...
451	542	0.56	17 24 48.70	-34 12 39.0	...	20.642±0.176	...	...	...	...	...	...	...
452	543	0.31	17 24 48.74	-34 18 02.3	20.676±0.036	18.687±0.017	...	13.09±0.09	12.22±0.07	11.43±0.07	11.37±0.08	11.03±0.09	10.88±0.15
453	544	0.45	17 24 48.85	-34 09 21.9	21.003±0.168	18.711±0.037	15.87±0.13	...	...	...	...	...	...
454	546	0.35	17 24 48.95	-34 15 35.9	22.628±0.053	20.297±0.072	15.51±0.05	14.01±0.06	13.29±0.06	12.21±0.08	11.73±0.09	11.31±0.10	10.66±0.17
455	547	0.35	17 24 48.96	-34 09 24.9	...	19.862±0.129	16.02±0.12	...	...	...	...	...	...
456	548	0.34	17 24 48.96	-34 14 54.1	20.822±0.046	18.318±0.014	...	...	...	...	10.90±0.18	...	...
457	549	0.27	17 24 48.96	-34 13 50.9	19.072±0.010	16.905±0.004	14.14±0.06	12.83±0.08	12.28±0.06	...	...	...	...
458	550	0.20	17 24 48.95	-34 10 59.3	...	20.370±0.203	...	...	...	...	...	...	...
459	551	0.53	17 24 49.00	-34 14 02.3	24.732±0.191	20.894±0.042	...	14.56±0.07	13.31±0.05	...	11.33±0.16	...	...
460	552	0.54	17 24 49.05	-34 15 20.6	20.542±0.036	17.945±0.010	...	...	...	10.43±0.06	10.19±0.07	9.85±0.06	9.14±0.07
461	553	0.12	17 24 49.06	-34 12 32.8	21.739±0.055	19.125±0.044	15.99±0.14	...	...	13.70±0.13	13.91±0.32	...	...
462	554	0.80	17 24 49.15	-34 14 26.4	...	...	...	13.71±0.16	12.38±0.10	11.33±0.17	11.06±0.13	...	...
463	555	0.06	17 24 49.17	-34 14 55.3	20.398±0.031	17.677±0.008	14.32±0.06	12.68±0.06	11.73±0.04	...	10.49±0.18	...	...
464	556	0.23	17 24 49.25	-34 11 25.0	18.658±0.019	16.356±0.004	13.31±0.02	11.88±0.04	11.26±0.03	10.65±0.05	10.51±0.08	10.34±0.13	...
465	557	0.38	17 24 49.26	-34 15 19.2	19.679±0.018	17.233±0.005	...	...	...	10.26±0.06	9.73±0.05	9.31±0.04	8.69±0.04
466	558	0.59	17 24 49.31	-34 13 20.2	20.695±0.048	18.195±0.013	15.23±0.08	14.00±0.06	13.47±0.08	12.86±0.06	12.90±0.11	...	...
467	559	0.62	17 24 49.27	-34 16 48.8	20.057±0.022	17.664±0.007	14.82±0.09	13.30±0.11	12.76±0.09	12.04±0.05	11.98±0.08	11.90±0.16	...
468	560	0.30	17 24 49.46	-34 13 53.0	21.709±0.112	19.162±0.032	15.46±0.11	13.64±0.09	12.57±0.05	11.37±0.11	10.85±0.10	...	...
469	561	0.35	17 24 49.46	-34 12 29.1	19.306±0.024	17.254±0.008	14.37±0.07	13.04±0.09	12.47±0.06	11.97±0.06	11.97±0.10	11.76±0.16	...
470	562	0.12	17 24 49.49	-34 15 21.8	22.398±0.046	19.315±0.035	...	...	...	13.85±0.11	13.14±0.30	...	...
471	563	0.44	17 24 49.52	-34 12 01.4	21.992±0.065	18.803±0.041	...	...	...	12.81±0.11	12.89±0.18	...	...
472	564	0.37	17 24 49.59	-34 12 32.1	20.834±0.097	18.298±0.021	...	...	...	12.34±0.07	12.51±0.14	...	...
473	565	0.39	17 24 49.66	-34 15 27.9	18.776±0.008	16.515±0.003	...	...	11.64±0.06	11.21±0.04	11.16±0.07	11.09±0.08	...
474	566	0.54	17 24 49.71	-34 11 14.8	...	20.923±0.176	...	...	...	11.70±0.09	10.68±0.33	9.75±0.33	...
475	567	0.15	17 24 49.79	-34 15 58.9	19.298±0.011	17.039±0.004	14.38±0.07	12.96±0.08	12.19±0.05	10.75±0.04	10.33±0.04	10.05±0.05	9.48±0.04
476	568	0.23	17 24 49.79	-34 09 00.4	19.152±0.032	17.463±0.012	15.65±0.04	14.50±0.06	...	...	...	...	...
477	569	0.60	17 24 49.87	-34 14 55.4	...	...	...	...	...	...	10.42±0.19	8.86±0.23	...
478	570	0.22	17 24 49.85	-34 12 10.9	21.110±0.167	18.573±0.026	...	...	...	...	...	...	...
479	571	0.75	17 24 49.85	-34 11 36.3	20.610±0.130	18.151±0.023	14.84±0.02	13.43±0.02	12.88±0.02	12.27±0.06	12.38±0.14	...	...
480	572	0.20	17 24 50.00	-34 15 55.9	20.902±0.045	18.737±0.019	...	...	...	13.43±0.08	13.27±0.10	...	...
481	573	0.52	17 24 50.05	-34 12 13.5	16.306±0.002	14.818±0.001	12.86±0.05	12.07±0.04	11.73±0.04	11.45±0.07	11.30±0.06	...	...
482	574	0.84	17 24 50.07	-34 15 14.3	21.035±0.056	18.340±0.017	15.79±0.07	...	...	12.34±0.06	12.03±0.10	11.26±0.08	...
483	576	0.33	17 24 50.09	-34 10 30.0	22.008±0.245	19.056±0.059	15.90±0.11	14.49±0.12	...	...	...	...	...
484	577	0.28	17 24 50.16	-34 12 43.7	17.274±0.004	15.202±0.001	12.54±0.04	11.30±0.06	10.79±0.04	10.39±0.03	10.19±0.04	9.98±0.05	9.61±0.05
485	578	0.42	17 24 50.33	-34 12 46.9	19.335±0.025	17.102±0.007	14.17±0.04	12.70±0.05	12.07±0.04	11.15±0.05	10.64±0.07	10.10±0.05	9.52±0.05
486	579	0.25	17 24 50.41	-34 11 12.5	19.261±0.033	17.381±0.011	14.50±0.13	13.36±0.13	12.74±0.11	...	...	...	...
487	580	1.09	17 24 50.41	-34 16 54.7	22.708±0.052	19.444±0.036	16.12±0.12	14.54±0.09	...	12.70±0.05	12.62±0.15	11.74±0.23	11.73±0.13
488	581	0.15	17 24 50.48	-34 15 43.6	22.243±0.037	19.270±0.032	15.84±0.08	14.33±0.07	13.51±0.05	12.24±0.05	11.79±0.07	11.27±0.08	10.83±0.07
489	582	0.52	17 24 50.57	-34 12 55.6	19.318±0.013	16.940±0.004	13.96±0.05	12.43±0.05	11.69±0.03	10.94±0.08	10.69±0.06	10.19±0.06	9.88±0.07
490	583	0.44	17 24 50.73	-34 10 55.1	21.466±0.368	19.259±0.063	...	14.84±0.09	...	...	...	...	...
491	584	0.87	17 24 50.73	-34 15 30.1	20.812±0.045	18.079±0.011	15.14±0.07	13.68±0.09	13.26±0.09	12.73±0.06	12.72±0.11	...	...
492	585	0.17	17 24 50.74	-34 13 07.4	19.606±0.017	17.391±0.006	...	...	12.73±0.07	12.16±0.11	12.11±0.09	...	...
493	588	0.93	17 24 51.12	-34 17 25.7	20.588±0.036	18.252±0.012	...	14.00±0.05	...	12.27±0.07	11.86±0.08	11.45±0.09	10.60±0.06
494	589	0.11	17 24 51.17	-34 12 01.4	15.427±0.001	14.135±0.001	12.13±0.03	11.48±0.03	11.15±0.04	11.02±0.08	10.98±0.12	10.56±0.16	...
495	590	0.47	17 24 51.26	-34 10 59.8	...	20.423±0.243	...	14.82±0.11	13.91±0.16	...	...	...	...
496	591	0.65	17 24 51.35	-34 16 15.0	22.915±0.063	19.681±0.045	...	...	...	13.44±0.08	13.13±0.10	...	...
497	593	0.40	17 24 51.41	-34 14 55.2	20.510±0.034	18.041±0.011	15.05±0.07	13.66±0.08	13.06±0.06	...	12.66±0.15	...	...

Table 4.1: continued.

(1)	(2)	(3)	(4)	(5)	(6)	(7)	(8)	(9)	(10)	(11)	(12)	(13)	(14)
			RA	DEC	R	I	J	H	K_s	[3.6]	[4.5]	[5.8]	[8.0]
ID	W07	(arcsec)	(J2000)	(J2000)	(mag)	(mag)	(mag)	(mag)	(mag)	(mag)	(mag)	(mag)	(mag)
498	594	0.36	17 24 51.55	-34 13 24.8	...	22.536±0.184	...	...	...	...	...	...	...
499	596	0.36	17 24 51.78	-34 10 47.0	16.196±0.003	14.428±0.001	12.21±0.03	11.25±0.04	10.78±0.03	...	...	...	...
500	597	0.25	17 24 51.83	-34 11 00.1	20.075±0.070	17.754±0.016	14.81±0.03	13.25±0.02	12.62±0.02	11.28±0.05	10.66±0.08	9.92±0.09	...
501	598	0.26	17 24 51.91	-34 13 31.6	23.347±0.140	20.175±0.085	15.57±0.06	13.55±0.03	12.49±0.03	11.57±0.11	11.23±0.09	10.33±0.19	...
502	599	0.15	17 24 51.96	-34 15 13.2	20.245±0.027	17.977±0.010	15.11±0.06	13.78±0.07	13.20±0.06	12.84±0.08	12.74±0.12	...	...
503	600	0.62	17 24 51.95	-34 16 58.9	15.022±0.001	14.179±0.001	13.26±0.03	12.80±0.05	12.65±0.05	12.61±0.06	12.54±0.08	12.54±0.28	...
504	601	0.42	17 24 52.06	-34 09 20.9	21.166±0.199	18.624±0.035	15.76±0.06	14.25±0.05	13.74±0.06	...	...	...	...
505	602	0.62	17 24 52.17	-34 11 14.3	22.360±0.335	19.592±0.111	15.31±0.14	14.19±0.17	...	...	...	...	...
506	603	0.21	17 24 52.35	-34 10 23.8	22.336±0.105	19.528±0.067	...	...	...	...	...	...	...
507	604	0.41	17 24 52.44	-34 14 54.2	21.078±0.062	18.934±0.024	15.88±0.10	14.57±0.10	...	13.54±0.10	13.50±0.15	...	...
508	605	0.46	17 24 52.44	-34 15 14.0	22.802±0.111	19.540±0.043	16.28±0.11	14.73±0.13	...	12.44±0.05	12.15±0.10	11.72±0.11	10.84±0.07
509	606	0.32	17 24 52.46	-34 13 07.0	...	21.647±0.090	...	...	...	13.31±0.20	13.31±0.21	...	...
510	607	0.74	17 24 52.41	-34 17 27.6	...	21.170±0.048	13.54±0.05	12.39±0.06	11.88±0.05	11.45±0.10	11.45±0.08	11.38±0.07	11.77±0.17
511	608	0.22	17 24 52.58	-34 11 04.0	21.124±0.168	18.767±0.031	16.24±0.13	14.83±0.09	...	...	...	...	...
512	610	0.23	17 24 53.06	-34 12 23.0	22.157±0.069	19.285±0.042	...	...	...	...	...	...	...
513	611	0.40	17 24 53.05	-34 15 38.5	20.889±0.050	18.246±0.012	15.17±0.04	13.75±0.05	13.10±0.05	12.21±0.05	11.97±0.07	11.57±0.08	11.69±0.31
514	612	0.40	17 24 53.10	-34 15 26.0	16.516±0.001	14.541±0.001	11.99±0.03	10.85±0.04	10.36±0.03	9.96±0.05	9.96±0.05	9.72±0.05	9.58±0.05
515	613	0.61	17 24 53.11	-34 16 09.2	16.510±0.001	14.969±0.001	13.00±0.03	12.25±0.05	11.88±0.04	11.56±0.04	11.54±0.06	11.50±0.09	11.74±0.85
516	614	0.27	17 24 53.15	-34 14 17.3	...	...	...	...	...	11.82±0.11	11.24±0.07	11.18±0.71	...
517	615	1.11	17 24 53.27	-34 12 07.4	18.909±0.013	17.032±0.005	...	...	13.31±0.05	13.00±0.11	13.08±0.20	...	...
518	616	0.53	17 24 53.18	-34 13 36.6	...	...	...	14.03±0.13	12.97±0.05	11.98±0.07	11.62±0.07	...	...
519	617	0.39	17 24 53.25	-34 14 52.8	21.415±0.031	18.691±0.020	15.17±0.06	13.76±0.07	13.05±0.06	11.76±0.06	11.07±0.07	10.63±0.06	10.02±0.10
520	619	0.31	17 24 53.43	-34 15 51.4	22.025±0.045	18.915±0.023	15.71±0.07	14.07±0.11	13.44±0.12	12.96±0.11	12.86±0.15	11.98±0.20	...
521	620	0.14	17 24 53.49	-34 10 56.2	20.714±0.087	18.346±0.021	14.76±0.09	12.96±0.09	11.85±0.05	10.68±0.07	10.61±0.10	10.41±0.11	...
522	621	0.20	17 24 53.55	-34 12 01.6	21.672±0.044	19.092±0.041	16.20±0.12	...	...	...	...	...	...
523	622	0.43	17 24 53.65	-34 12 22.1	21.012±0.085	18.374±0.018	14.73±0.07	13.15±0.10	12.30±0.08	11.95±0.13	11.79±0.16	...	...
524	623	0.24	17 24 53.63	-34 12 15.3	19.060±0.014	16.617±0.004	13.62±0.04	12.29±0.07	11.81±0.05	11.45±0.08	11.41±0.10	...	...
525	624	1.01	17 24 53.69	-34 16 04.4	22.085±0.048	19.913±0.014	15.60±0.08	13.98±0.05	13.14±0.05	12.06±0.05	11.66±0.07	11.08±0.07	10.45±0.07
526	625	0.60	17 24 53.73	-34 16 51.5	17.934±0.003	16.007±0.002	13.68±0.04	12.63±0.05	12.23±0.04	11.90±0.05	11.90±0.06	11.75±0.09	...
527	627	0.40	17 24 53.79	-34 14 39.4	19.159±0.011	16.951±0.004	13.68±0.08	11.61±0.09	10.55±0.05	9.97±0.06	10.03±0.05	9.69±0.05	9.92±0.09
528	629	0.74	17 24 53.89	-34 13 55.0	...	...	...	...	...	11.97±0.05	11.02±0.06	10.32±0.08	9.73±0.22
529	630	0.10	17 24 54.01	-34 12 35.1	22.488±0.096	19.330±0.051	15.30±0.08	...	...	11.45±0.10	11.01±0.10	10.57±0.10	...
530	631	0.18	17 24 54.12	-34 10 36.2	19.629±0.038	17.440±0.009	14.77±0.08	13.51±0.06	12.98±0.05	12.74±0.10	12.81±0.21	...	...
531	632	0.56	17 24 54.27	-34 13 48.4	...	...	...	...	...	13.36±0.12	13.07±0.15	...	...
532	633	0.20	17 24 54.27	-34 14 57.6	20.020±0.023	17.851±0.009	15.05±0.07	13.32±0.09	12.13±0.05	...	...	...	...
533	634	0.30	17 24 54.33	-34 12 09.6	22.605±0.103	19.279±0.042	14.93±0.08	13.02±0.09	12.06±0.07	10.71±0.06	10.09±0.06	9.43±0.08	8.85±0.66
534	636	0.08	17 24 54.56	-34 09 52.2	19.735±0.034	17.427±0.008	14.78±0.02	13.41±0.02	13.02±0.02	12.00±0.20	11.64±0.34	...	...
535	637	0.39	17 24 54.64	-34 12 46.4	22.237±0.074	19.636±0.059	...	...	...	...	...	...	...
536	638	0.16	17 24 54.84	-34 12 58.9	20.277±0.031	17.787±0.009	...	13.07±0.04	12.41±0.04	11.91±0.05	11.79±0.09	...	...
537	639	0.30	17 24 54.91	-34 11 23.9	21.932±0.052	19.044±0.040	15.53±0.09	14.30±0.08	13.47±0.06	12.23±0.08	11.72±0.07	...	...
538	640	0.80	17 24 54.97	-34 19 03.8	20.980±0.047	18.324±0.011	15.22±0.04	13.61±0.04	12.98±0.04	12.53±0.04	12.43±0.08	11.50±0.15	...
539	642	0.39	17 24 55.10	-34 16 25.9	...	21.747±0.028	13.53±0.04	10.98±0.03	9.75±0.02	8.86±0.03	8.96±0.03	8.60±0.02	8.62±0.02
540	643	0.09	17 24 55.09	-34 11 11.7	14.196±0.001	12.346±0.001	10.09±0.02	9.29±0.03	8.87±0.02	8.62±0.03	8.56±0.04	8.49±0.06	...
541	644	0.20	17 24 55.13	-34 14 42.2	22.460±0.082	20.022±0.066	...	...	...	13.72±0.09	13.14±0.13	...	...
542	645	0.73	17 24 55.23	-34 15 26.1	22.385±0.076	19.713±0.014	...	...	...	13.85±0.12	...	...	...
543	646	0.11	17 24 55.24	-34 10 10.3	...	...	...	...	...	12.64±0.22	...	...	...
544	647	0.06	17 24 55.49	-34 15 21.6	20.371±0.032	17.564±0.007	14.21±0.07	12.68±0.09	11.98±0.07	11.58±0.07	11.46±0.07	11.33±0.07	...
545	648	1.13	17 24 55.51	-34 14 50.9	22.367±0.095	18.906±0.024	15.82±0.12	14.52±0.09	...	13.60±0.09	13.46±0.09	...	...
546	649	0.33	17 24 55.55	-34 16 31.7	18.504±0.005	16.525±0.002	13.86±0.04	12.57±0.04	12.06±0.04	11.70±0.05	11.65±0.07	11.36±0.09	11.96±0.18
547	650	0.17	17 24 55.61	-34 12 46.1	21.078±0.092	18.301±0.017	14.98±0.06	13.44±0.09	12.81±0.05	12.31±0.07	12.00±0.20	...	...
548	652	0.35	17 24 55.82	-34 12 39.7	22.613±0.094	19.514±0.043	14.95±0.14	13.37±0.14	12.65±0.10	11.72±0.08	11.45±0.10	...	...
549	653	0.84	17 24 55.83	-34 16 34.2	21.245±0.066	18.897±0.022	15.89±0.08	14.59±0.06	13.79±0.05	13.95±0.18	13.73±0.18	...	...
550	654	0.44	17 24 55.87	-34 12 34.4	15.358±0.001	13.272±0.001	10.64±0.03	9.34±0.02	8.39±0.03	6.78±0.04	6.01±0.05	5.21±0.02	4.60±0.02
551	655	0.12	17 24 56.12	-34 12 43.1	23.080±0.077	20.160±0.076	...	...	...	...	...	...	...
552	657	0.38	17 24 56.42	-34 12 33.2	23.592±0.184	21.172±0.061	...	...	...	12.76±0.09	12.05±0.29	...	...
553	658	0.78	17 24 56.48	-34 06 05.6	21.098±0.053	19.801±0.047	...	...	...	...	...	...	...
554	660	0.58	17 24 56.64	-34 09 59.9	23.687±0.125	20.149±0.062	...	...	...	...	...	...	...
555	661	0.99	17 24 56.74	-34 17 27.6	17.232±0.002	15.417±0.001	12.93±0.03	11.85±0.05	11.33±0.04	10.88±0.04	10.71±0.06	10.48±0.05	10.22±0.04
556	662	0.17	17 24 56.88	-34 07 23.1	...	21.734±0.055	...	...	...	14.22±0.11	13.37±0.22	...	...
557	663	0.27	17 24 56.91	-34 16 44.9	18.951±0.008	16.934±0.004	14.06±0.04	12.70±0.05	12.13±0.05	11.78±0.04	11.68±0.10	11.80±0.10	...
558	664	0.38	17 24 57.01	-34 16 52.0	21.395±0.075	18.832±0.021	...	...	...	...	...	...	...

Table 4.1: continued.

(1)	(2)	(3)	(4)	(5)	(6)	(7)	(8)	(9)	(10)	(11)	(12)	(13)	(14)
			RA	DEC	R	I	J	H	K_s	[3.6]	[4.5]	[5.8]	[8.0]
ID	W07	(arcsec)	(J2000)	(J2000)	(mag)	(mag)	(mag)	(mag)	(mag)	(mag)	(mag)	(mag)	(mag)
559	665	0.22	17 24 57.03	-34 11 44.3	23.436±0.218	20.003±0.052	16.09±0.08	14.53±0.04	13.63±0.05	12.94±0.09	12.77±0.12	...	...
560	666	0.44	17 24 57.04	-34 13 54.2	15.625±0.001	14.665±0.001	13.50±0.03	12.79±0.02	12.59±0.02	12.50±0.11	12.66±0.11	...	...
561	667	0.65	17 24 57.09	-34 09 17.5	21.552±0.082	18.678±0.016	15.67±0.06	14.24±0.03	13.89±0.04	13.22±0.10	13.34±0.31	...	...
562	668	0.44	17 24 57.37	-34 16 02.1	23.034±0.152	19.573±0.043	15.39±0.08	13.49±0.08	12.69±0.06	12.03±0.08	12.00±0.12	11.86±0.13	...
563	669	0.23	17 24 57.51	-34 10 39.8	...	21.457±0.080	...	...	...	...	...	...	...
564	670	0.44	17 24 57.81	-34 10 00.8	...	...	...	...	12.93±0.13	11.80±0.08	11.85±0.09	...	...
565	671	0.40	17 24 57.85	-34 10 32.9	24.293±0.109	21.779±0.085	...	...	...	11.97±0.06	11.49±0.10	...	...
566	672	0.26	17 24 57.89	-34 12 04.2	18.308±0.005	15.655±0.001	12.16±0.03	10.83±0.02	10.26±0.02	9.83±0.03	9.74±0.04	9.56±0.05	...
567	673	0.17	17 24 57.94	-34 10 25.6	21.505±0.082	19.314±0.029	...	...	...	...	...	...	...
568	678	0.68	17 24 58.69	-34 12 32.7	22.207±0.065	19.581±0.045	...	...	...	...	...	...	...
569	679	0.96	17 24 58.82	-34 16 46.3	23.548±0.067	19.825±0.052	...	...	...	...	...	...	...
570	680	0.28	17 24 58.84	-34 15 18.8	19.702±0.018	17.423±0.006	14.01±0.04	12.51±0.04	11.72±0.03	10.50±0.04	9.91±0.04	9.43±0.04	8.56±0.03
571	681	0.31	17 24 58.94	-34 10 25.0	...	20.822±0.117	15.87±0.07	13.74±0.06	12.74±0.05	11.91±0.07	11.56±0.06	...	...
572	682	0.20	17 24 58.94	-34 17 22.7	20.695±0.040	18.560±0.016	15.36±0.06	13.90±0.08	13.21±0.07	12.50±0.05	12.49±0.13	...	...
573	683	1.50	17 24 58.91	-34 17 04.4	...	...	16.47±0.14	...	...	13.86±0.09	14.10±0.25	...	...
574	684	1.31	17 24 58.96	-34 12 49.9	...	...	...	...	...	12.21±0.14	11.09±0.09	...	...
575	685	0.03	17 24 58.98	-34 11 58.1	18.528±0.006	16.697±0.003	14.38±0.09	13.44±0.10	12.91±0.10	12.83±0.06	12.72±0.18	...	...
576	688	1.47	17 24 58.97	-34 06 28.2	19.563±0.013	18.020±0.009	...	...	13.48±0.04	11.85±0.06	11.48±0.08	...	...
577	689	0.66	17 24 59.13	-34 16 47.5	18.681±0.006	16.916±0.004	14.04±0.03	12.35±0.04	11.21±0.03	9.95±0.07	9.57±0.07	9.28±0.05	8.96±0.04
578	690	0.35	17 24 59.41	-34 13 26.1	...	...	...	14.29±0.23	13.04±0.16	12.58±0.08	12.44±0.12	...	...
579	691	0.68	17 24 59.64	-34 17 16.1	24.744±0.187	20.537±0.023	15.16±0.08	13.19±0.21	12.31±0.14	11.70±0.04	11.70±0.06	11.81±0.17	...
580	692	0.08	17 24 59.75	-34 09 58.8	23.124±0.165	20.234±0.068	...	...	...	...	...	...	...
581	693	0.41	17 24 59.85	-34 13 03.3	...	20.200±0.056	14.88±0.04	12.65±0.03	11.62±0.03	10.89±0.06	10.71±0.14	...	...
582	694	0.08	17 24 59.86	-34 16 11.0	15.515±0.001	13.775±0.001	11.09±0.03	9.44±0.03	8.14±0.03	6.87±0.05	6.25±0.05	5.56±0.02	4.81±0.02
583	695	0.61	17 25 00.03	-34 11 32.4	...	21.158±0.067	...	...	...	...	...	...	...
584	696	1.20	17 24 59.99	-34 17 58.0	...	22.467±0.091	...	...	...	14.14±0.13	13.91±0.27	...	...
585	697	0.47	17 25 00.30	-34 17 12.7	21.422±0.078	18.859±0.019	...	14.32±0.06	...	12.81±0.07	12.45±0.09	12.44±0.30	11.83±0.24
586	698	0.30	17 25 00.48	-34 14 11.1	21.292±0.085	19.172±0.032	16.48±0.10	15.28±0.08	...	14.34±0.12	14.16±0.29	...	...
587	699	1.29	17 25 00.44	-34 10 18.4	23.074±0.153	19.971±0.054	15.63±0.08	13.89±0.05	12.97±0.04	12.03±0.06	12.18±0.12	11.28±0.20	...
588	700	0.46	17 25 00.82	-34 13 53.3	23.967±0.306	19.950±0.064	15.52±0.07	13.46±0.07	12.39±0.05	11.56±0.08	11.18±0.09	10.83±0.12	...
589	702	0.20	17 25 01.11	-34 14 04.5	...	...	...	...	...	12.73±0.09	12.30±0.12	...	...
590	703	0.51	17 25 01.19	-34 17 35.9	20.108±0.023	17.800±0.008	15.08±0.04	13.66±0.06	13.19±0.03	12.42±0.06	12.13±0.07	11.76±0.10	11.37±0.12
591	705	0.56	17 25 01.55	-34 11 19.2	22.611±0.141	19.592±0.047	...	...	...	14.22±0.16	14.28±0.31	...	...
592	707	0.34	17 25 01.69	-34 16 51.6	18.749±0.007	16.786±0.003	13.97±0.05	12.75±0.07	12.29±0.05	12.00±0.05	11.94±0.08	11.70±0.11	...
593	708	0.93	17 25 01.88	-34 13 45.5	...	21.723±0.081	...	...	...	13.38±0.11	13.48±0.17	...	...
594	709	0.59	17 25 02.14	-34 10 19.8	...	21.779±0.081	16.97±0.18	14.66±0.05	13.72±0.05	12.78±0.15	12.61±0.17	...	...
595	711	0.57	17 25 02.32	-34 06 26.5	19.050±0.009	17.532±0.006	15.42±0.06	14.43±0.07	...	13.04±0.09	12.51±0.11	...	...
596	712	0.20	17 25 02.40	-34 13 13.2	21.966±0.068	18.695±0.020	14.60±0.04	12.86±0.05	12.00±0.04	10.86±0.05	10.40±0.06	10.19±0.11	...
597	714	0.46	17 25 02.58	-34 16 28.3	21.940±0.040	18.951±0.025	...	...	...	13.00±0.12	13.01±0.15	...	...
598	715	0.59	17 25 02.64	-34 11 36.6	24.445±0.344	20.094±0.059	16.30±0.12	14.45±0.10	13.71±0.08	13.32±0.10	13.34±0.29	...	...
599	716	0.49	17 25 02.82	-34 09 27.5	22.581±0.097	19.684±0.011	16.68±0.13	...	...	...	...	...	...
600	718	0.03	17 25 03.17	-34 08 49.6	15.303±0.001	14.536±0.001	13.63±0.02	13.10±0.02	12.97±0.02	12.71±0.05	12.65±0.10	...	...
601	719	0.34	17 25 03.22	-34 16 25.1	23.512±0.185	20.626±0.029	...	...	...	13.78±0.09	13.55±0.20	...	...
602	721	0.55	17 25 03.33	-34 12 45.0	...	23.102±0.181	...	...	...	...	...	...	...
603	722	0.22	17 25 03.41	-34 15 52.0	19.565±0.016	17.486±0.007	14.16±0.04	12.30±0.03	11.58±0.02	10.93±0.07	10.94±0.07	10.81±0.07	10.99±0.06
604	723	0.58	17 25 03.57	-34 18 24.4	...	...	...	...	...	14.38±0.09	14.24±0.29	...	...
605	724	0.95	17 25 03.52	-34 09 49.4	23.231±0.180	19.145±0.025	14.91±0.04	13.32±0.05	12.56±0.04	12.06±0.10	12.02±0.12	...	...
606	725	0.76	17 25 03.87	-34 11 37.9	19.279±0.015	17.253±0.006	15.02±0.04	13.86±0.04	13.47±0.05	13.12±0.12	13.02±0.15	...	...
607	726	0.88	17 25 04.09	-34 11 47.2	20.629±0.055	18.081±0.012	14.77±0.05	13.12±0.07	12.40±0.05	11.84±0.12	11.96±0.09	...	...
608	727	0.70	17 25 04.65	-34 04 59.3	...	22.491±0.158	...	...	...	...	...	...	...
609	729	0.28	17 25 05.57	-34 15 06.5	20.891±0.057	18.389±0.016	15.46±0.08	14.09±0.09	13.35±0.07	12.15±0.07	11.66±0.07	11.05±0.07	10.97±0.10
610	730	0.21	17 25 05.56	-34 19 19.8	19.240±0.012	16.987±0.003	14.06±0.04	12.79±0.06	12.28±0.04	11.90±0.05	11.75±0.06	11.90±0.13	...
611	733	0.24	17 25 06.86	-34 11 28.3	23.553±0.109	19.778±0.044	...	...	13.62±0.10	...	...	...	...
612	735	0.59	17 25 07.48	-34 14 20.2	19.543±0.022	17.633±0.008	...	...	...	12.12±0.06	11.84±0.08	11.33±0.08	11.67±0.33
613	738	0.25	17 25 07.58	-34 06 09.1	18.263±0.005	16.476±0.003	14.46±0.03	13.47±0.04	13.04±0.06	12.74±0.07	12.61±0.10	...	...
614	739	0.27	17 25 07.63	-34 12 19.4	19.795±0.024	17.771±0.009	15.28±0.05	14.26±0.05	...	13.44±0.12	13.28±0.25	...	...
615	741	0.73	17 25 07.89	-34 13 14.0	20.371±0.039	18.195±0.013	15.40±0.08	13.97±0.07	13.16±0.07	...	...	...	...
616	742	0.55	17 25 07.92	-34 11 09.4	...	20.028±0.055	...	...	...	...	...	...	...
617	745	0.26	17 25 08.76	-34 11 24.5	13.119±0.001	11.964±0.001	10.62±0.03	10.14±0.03	9.90±0.03	9.85±0.09	9.72±0.08	...	...
618	747	0.30	17 25 08.85	-34 11 12.8	...	11.546±0.001	7.04±0.02	6.53±0.06	5.86±0.02	5.41±0.05	...	4.93±0.02	4.64±0.02
619	748	0.46	17 25 09.05	-34 11 21.3	...	...	...	...	...	11.89±0.13	...	...	...

Table 4.1: continued.

(1)	(2)	(3)	(4)	(5)	(6)	(7)	(8)	(9)	(10)	(11)	(12)	(13)	(14)
			RA	DEC	R	I	J	H	K_s	[3.6]	[4.5]	[5.8]	[8.0]
ID	W07	(arcsec)	(J2000)	(J2000)	(mag)	(mag)	(mag)	(mag)	(mag)	(mag)	(mag)	(mag)	(mag)
620	749	0.51	17 25 09.20	-34 11 09.2	20.740±0.057	18.618±0.007	...	...	...	...	...	...	...
621	750	1.20	17 25 09.84	-34 08 20.8	19.063±0.013	17.218±0.005	14.82±0.04	13.77±0.03	13.28±0.04	12.67±0.12	12.71±0.16	...	...
622	751	1.31	17 25 09.92	-34 10 51.3	21.202±0.087	18.614±0.016	15.99±0.07	14.67±0.06	14.39±0.11	13.77±0.14	...	...	...
623	752	0.41	17 25 09.91	-34 15 51.6	15.577±0.001	14.497±0.001	13.34±0.03	12.54±0.05	12.30±0.05	11.83±0.06	12.14±0.13	11.97±0.14	...
624	754	0.75	17 25 11.17	-34 11 11.2	19.922±0.027	18.044±0.009	...	...	...	...	...	...	...
625	755	0.41	17 25 11.35	-34 13 59.0	18.838±0.010	17.428±0.007	15.60±0.06	14.60±0.06	...	13.73±0.07	13.14±0.16	...	...
626	756	0.69	17 25 11.45	-34 12 13.6	20.542±0.040	17.963±0.008	14.90±0.05	13.45±0.11	12.73±0.12	12.52±0.10	12.43±0.14	...	...
627	757	1.28	17 25 11.52	-34 05 20.1	21.164±0.072	18.972±0.007	15.46±0.06	...	...	12.76±0.08	12.38±0.14	...	...
628	758	0.59	17 25 11.63	-34 09 33.4	13.041±0.001	12.123±0.001	11.05±0.03	10.39±0.02	10.20±0.02	10.13±0.05	10.17±0.06	...	...
629	759	1.07	17 25 11.65	-34 12 56.0	19.751±0.026	17.398±0.007	14.84±0.06	13.25±0.04	12.30±0.04	10.95±0.05	10.37±0.05	9.74±0.07	8.47±0.08
630	760	0.21	17 25 11.80	-34 18 36.7	15.747±0.001	14.655±0.001	13.27±0.03	12.52±0.02	12.28±0.02	12.07±0.05	12.02±0.07	11.94±0.12	...
631	763	0.65	17 25 11.97	-34 05 38.2	...	21.684±0.082	...	13.39±0.05	12.29±0.04	11.62±0.04	11.44±0.06	11.35±0.11	...
632	764	0.27	17 25 13.03	-34 15 25.0	19.007±0.011	16.916±0.004	14.48±0.07	13.20±0.07	12.69±0.06	12.14±0.05	12.11±0.07	12.00±0.26	...
633	765	0.27	17 25 13.43	-34 17 55.8	13.718±0.001	12.864±0.001	11.89±0.03	11.33±0.02	11.17±0.02	11.11±0.04	11.02±0.06	10.94±0.07	10.74±0.07
634	767	0.41	17 25 14.28	-34 16 38.8	19.234±0.009	17.375±0.004	14.88±0.07	13.61±0.03	13.05±0.04	12.40±0.07	12.08±0.10	11.77±0.12	11.06±0.08
635	768	0.26	17 25 15.89	-34 12 07.4	18.949±0.010	16.813±0.003	14.09±0.04	12.73±0.02	12.17±0.03	11.67±0.09	11.62±0.11	...	...
636	770	0.54	17 25 16.80	-34 12 11.7	18.498±0.006	16.802±0.003	...	13.32±0.07	12.59±0.05	11.46±0.10	11.18±0.08	...	...
637	771	0.05	17 25 16.94	-34 14 03.5	20.668±0.075	18.489±0.014	15.45±0.08	13.99±0.12	13.27±0.06	12.56±0.07	12.39±0.12	11.58±0.14	10.43±0.25
638	772	1.46	17 25 18.39	-34 15 38.8	21.997±0.045	19.325±0.030	...	...	...	13.98±0.10	13.64±0.24	...	...
639	773	0.49	17 25 18.81	-34 14 57.3	...	...	6.55±0.02	6.41±0.04	6.39±0.03	6.68±0.05	6.41±0.05	6.35±0.02	6.36±0.02
640	774	0.60	17 25 18.85	-34 11 54.4	20.261±0.032	18.246±0.010	...	14.13±0.14	...	12.72±0.12	...	...	...
641	775	0.80	17 25 19.29	-34 13 57.0	...	...	...	...	...	13.39±0.13	12.60±0.08	11.32±0.11	...
642	777	0.35	17 25 22.24	-34 16 18.6	22.941±0.127	19.827±0.042	...	...	...	15.08±0.17	14.24±0.25	...	...
643	778	0.15	17 25 23.77	-34 17 55.3	16.961±0.001	15.690±0.001	14.29±0.04	13.46±0.07	13.20±0.07	12.75±0.10	12.64±0.14	...	...

4.1.4 Optical spectroscopy

Spectroscopic observations of the Pismis 24 cluster were performed with VIMOS in August 2008. We used a low resolution grism combined with order sorting filter GG475 and a slit width of 1.″0, resulting in an effective spectral resolution of $\lambda/\delta\lambda$=580 and a spectral coverage from 4800Å to 10000Å. The spectroscopic data were reduced with the VIMOS pipeline, which was also used to extract the raw spectra of the individual targets. These were then flux-calibrated using observations of the standard star LTT 6248.

In the following we will describe how we do the spectral classification of our stars using the VIMOS spectra. We have adopted a two-step approach. In step one we estimate the spectral types from our spectra using the IDL package 'Hammer' (Covey et al. 2007). The Hammer code was originally designed to classify spectra of stars in the absence of appreciable extinction. It uses 29 spectral "features" in the classification process, among which two ("BlueColor" and "Color-1") are related to the broad-band spectral continuum slope. The latter cannot be used for stars whose spectra are reddened due to absorption by intervening dust. The remaining 27 diagnostics are "narrow-band" features, and not affected by extinction. In order to make the Hammer code suitable for classifying our young stars, that typically suffer several magnitudes of optical extinction, we removed the BlueColor and Color-1 features from the Hammer code,

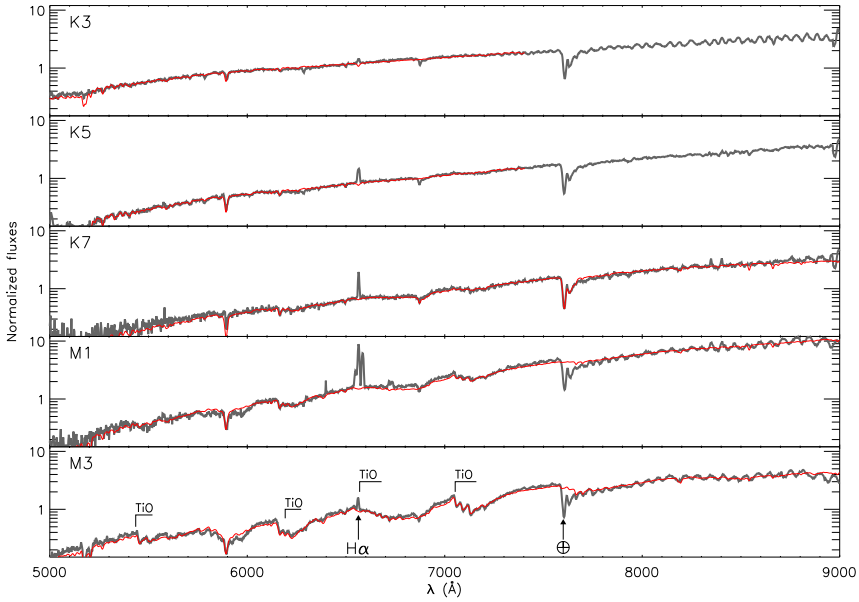

Figure 4.2: Typical spectra (grey thick lines) from our VIMOS observations covering the range of spectral types from K3 to M3. Spectral templates (thin lines) with the same spectral types and spectral resolution are also shown. The templates have been reddened to fit our VIMOS spectra. The prominent Hα emission line and TiO absorption features are indicated. The wiggles on the spectra beyond 7600Å are instrumental artifacts due to the fringing.

keeping the remaining 27 diagnostics. We then ran the code to classify all our spectra, giving initial estimates of the spectral types. In the second step of the classification process we tested the results by fitting spectral templates with spectral types as derived using the Hammer code to the observed VIMOS spectra. The spectral templates are from the 'Hammer' package. We have two free parameters in this fit: the V-band extinction by which the spectral template is reddened using a standard ISM extinction law (Cardelli et al. 1989), and the scaling factor calibrating the spectral template to the observed absolute flux level. The results were then visually inspected for each star to ensure a satisfactory fit to the data was obtained. When the spectral template with initial spectral type from "Hammer" code could not properly fit the observations, the input spectral type was varied by several subclasses until we obtained a good match between the observed spectrum and the spectral template. The spectral type of the best-fitting template was finally adopted as the spectral type of each respective object. In Fig 4.2 we show examples of our VIMOS spectra with a range of spectral types from early K to early M, representing the majority of the young stars in our sample. In each case, we have overplotted the best-fitting spectral template. Over this wavelength range, the changes in the spectral shape are clearly visible, in particular the strength of the TiO absorption bands is a prominent diagnostic for late K to M type stars.

4.1.5 Complementary data sets

A part of the Pismis 24 star cluster has been observed with the Hubble space telescope in the F502N, F656N, F673N, and F850LP bands[1]. We have used these HST images to search for proplyds, i.e. young stars whose circumstellar disks are being photoevaporated by UV photons from nearby massive stars, resulting in a head-tail shaped appearance (see Sect. 4.2.2(4a)).

The 24 μm image of the NGC 6357 complex was taken from the Spitzer MIPSGAL survey (Carey et al. 2009). Parts of the 24 μm Spitzer data were saturated, we fill in those regions using 21.3 μm data from the Midcourse Space Experiment (MSX, Price et al. 2001) survey. We tied the flux scale of the MSX image to that of the MIPSGAL observations using the common unsaturated regions, ignoring the relatively minor differences in the spectral response between both images.

Imaging at 1.2 mm was performed with the SEST Imaging Bolometer Array (Muñoz et al. 2007) and traces the dust continuum emission in high column density regions (Av≥15 mag, Russeil et al. 2010). These data were used to trace the molecular cores in NGC 6357 complex.

4.2 Results

4.2.1 The NGC 6357 complex

In this section, we will present a global view of NGC 6357. We will show the dust emission from mid-infrared to millimeter wavelengths and then investigate the star formation activity throughout the region.

(1) Dust emission in NGC 6357

In Fig. 4.3 we show a three-color composite of the whole NGC 6357 complex (4.5, 8.0, and 24 μm in blue, green, and red, respectively), using data from the GLIMPSE survey at 4.5 and 8.0 μm), and the MIPSGAL surveys at 24 μmwith the saturated regions replaced with the data from MSX survey at 21.3 μm. The emission in the 4.5 μm IRAC band traces mainly the stellar young stars that appear as point sources, with some diffuse emission emitted or scattered by dust, and Brα emission. The 8.0 μm IRAC band shows mainly spatially extended emission consisting of dust continuum radiation and in particular strong emission from Polycyclic Aromatic

[1]We obtained these HST images from http://hla.stsci.edu/hlaview.html.

Hydrocarbons (PAHs) (Povich et al. 2007), beautifully tracing the ionization surfaces where the energetic radiation from the massive stars "eats" its way into the molecular cloud. The 24 μm emission is dominated by continuum dust emission.

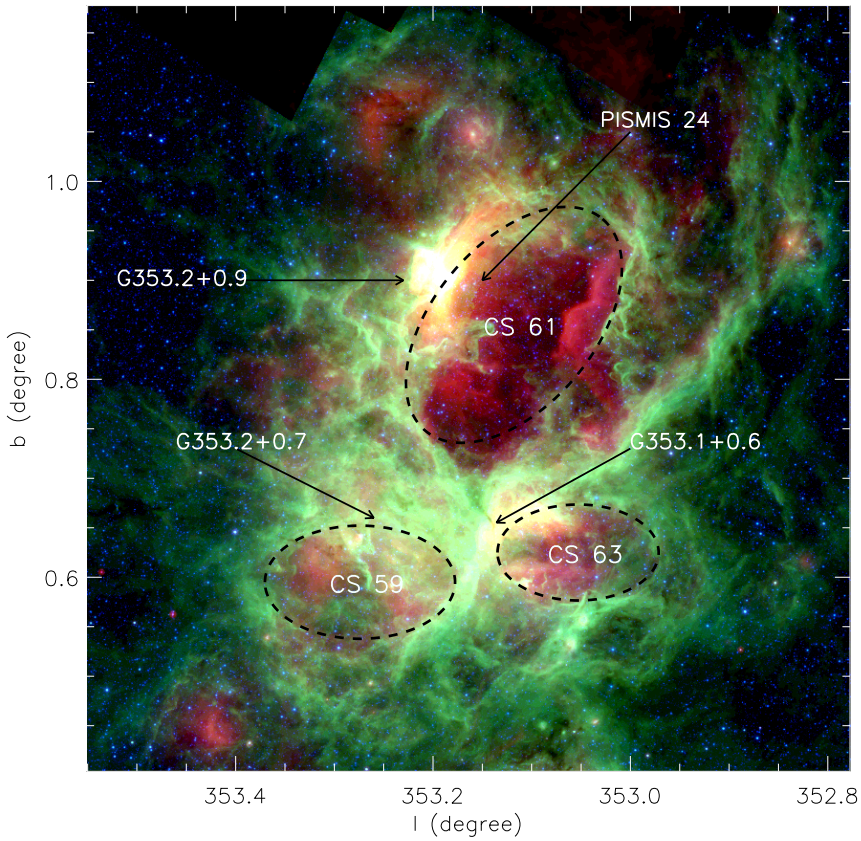

Figure 4.3: Spitzer color image of NGC 6357 complex(red: 24 μm ,green: 8.0 μm , and blue: 4.5 μm). The 4.5 μm and 8.0 μm images are from glimpse GLIMIPSE survey. The 24 μm image is a combination of the images from MIPSGAL and MSX surveys. The three H II regions G353.2+0.9, G353.2+0.7, and G353.1+0.6 are labeled. The position of the Pismis 24 cluster is marked. The dashed lines depict the inner rims of the three bubbles identified by Churchwell et al. (2007).

The most striking aspect of Fig. 4.3 is that the whole region is full of filamentary diffuse emission, with some "bubbles" where 8.0 μm emission is faint or absent and 24 μm emission is dominating. In this field Churchwell et al. (2007) identified three bubbles, named CS 59, CS 61, and CS 63, of which CS 61 is the biggest. The bright H II region G353.2+0.9 lies near bubble CS 61 (Felli et al. 1990). The Pismis 24 cluster appears to be located within CS 61 and the strong UV field and stellar winds from the massive cluster members are likely responsible for creating CS 61. The absence of 8.0 μm emission within CS 61 and the "sharp" edges of the bubble at this wavelength (Fig. 4.3) can be explained by the absence of PAHs within the bubble due to their

destruction by extreme ultraviolet (EUV) photons from massive stars (Voit 1992). Surrounding CS 61 there are high density shells which are traced by the dust continuum emissions at 1.2 mm (see Fig 4.4). Here, the EUV photon fluxes have already been diminished due to absorption by gas and dust within the bubble and PAHs can survive. There are still sufficient amounts of UV photons of lower energy to excite the PAH molecules, which then glow brightly and mark the boundary between the dense cloud material and the cavities carved by the star clusters.

The bubbles CS 59 and CS 63 are much smaller than CS 61. Near these bubbles the H II regions G353.2+0.7 and G353.1+0.6, respectively, are located. Inside bubble CS 63 there are four known OB stars (Neckel 1984), which are ionizing the H II region G353.1+0.6 (Felli et al. 1990) and have likely created this bubble. Inside the bubble CS 59 there are no known massive stars in the literature. Further observations are required to understand the origin of this bubble. In contrast to bubble CS 61, there is weak 8.0 μm emission inside bubbles CS 59 and CS 63, suggesting that their central stars cannot emit sufficient EUV photons to destroy all the PAHs inside the bubbles.

In Fig. 4.4 we show the 1.3 mm dust continuum emission with contours, overplotted on the 5.8 μm IRAC image. The millimeter data trace the high density regions, i.e. the molecular cores, which tend to lie in ring-like structures surrounding the bubbles CS 61, CS 59, and CS 63. Similar structures of molecular gas have been found around many mid-infrared bubbles (Deharveng et al. 2009; Beaumont & Williams 2010). They are thought to arise due to the compression of the molecular clouds by the expanding shock fronts produced by stellar winds or the pressure-driven expansion of the H II regions (Castor et al. 1975; Freyer et al. 2003). Like the 8.0 μm image, the diffuse emission in the 5.8 μm IRAC data is dominated by PAHs (Povich et al. 2007) and likely traces the surface of the molecular clouds.

(2) Star formation in NGC 6357

Using the infrared data from the 2MASS and GLIMPSE surveys we can make an inventory of the disk-bearing young star population in the whole NGC 6357 complex, and thus investigate the global recent star formation activity. The infrared excess emission due to the dusty circumstellar disks causes the infrared colors of stars with disks to be distinctly different from those of diskless objects. Young cluster members that have already lost their disks cannot be robustly distinguished from unrelated field objects based on infrared colors alone. Therefore, contrary to the central regions where we have independent means of identifying diskless young stars (X-rays), we cannot study the whole population of young stars in the NGC 6357 complex on a global scale. We thus restrict ourselves to studying only the disk-bearing stars to trace recent star forming activity. For the central regions where we have X-ray observations and optical spectroscopy we can do a more comprehensive analysis and derive e.g. absolute disk frequencies.

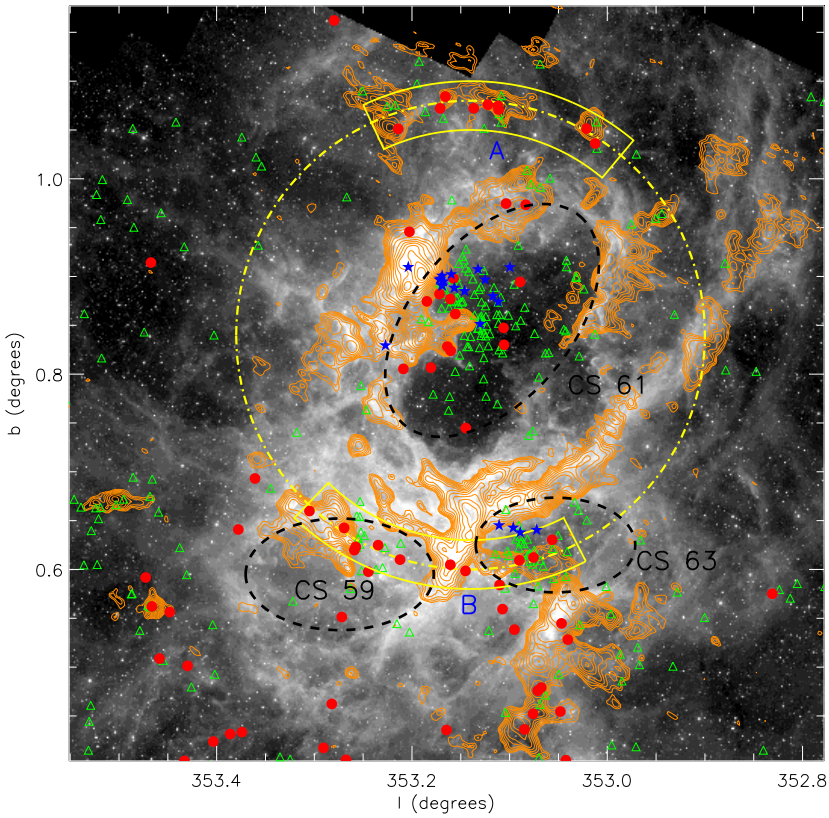

Figure 4.4: 1.3 mm emission (contours) over-plotted on the IRAC [5.8] image of the NGC 6357 complex. The red filled circles mark the Flat/class I objects, and the open triangles mark the class II objects. The asterisks indicate known massive stars. The dashed lines depict the inner rims of the three bubbles identified by Churchwell et al. (2007). In regions A and B, the YSO distribution shows arcs centered on the bubble CS 61.

We use two sets of infrared color-color diagrams to select candidate young disk-bearing stars: (1) [3.6]-[4.5] vs. [4.5]-[8.0] and [3.6]-[4.5] vs. [5.8]-[8.0] color-color diagrams, and (2) H-K_s vs. H-[3.6] and H-K_s vs. H-[4.5] color-color diagrams. The selection criteria are as follows. In the [3.6]-[4.5] vs. [4.5]-[8.0] color-color diagram, objects are marked as YSOs if they meet the following criteria (following Simon et al. 2007): (1) [3.6]-[4.5]>0.6×([4.5]-[8.0])-1.0, (2) [4.5]-[8.0]<2.8, (3) [3.6]-[4.5]<0.6×([4.5]-[8.0])+0.3, and (4) [3.6]-[4.5]>-([4.5]-[8.0])+0.85. On the [3.6]-[4.5] vs. [5.8]-[8.0] color-color diagram, YSOs must obey the criteria: (1) [3.6]-[4.5] ≥0, and [5.8]-[8.0] ≥0.4 (Allen et al. 2004), and (2) [3.6]-[4.5] ≥ 0.67-([5.8]-[8.0])×0.67, where the latter criterion serves to remove the contamination arising from uncertainties in the IRAC photometry. Finally, we clean the thus constructed YSO catalog from contamination by AGNs and galaxies using the criteria of Gutermuth et al. (2008). Based on their IRAC spectral index we divide the YSOs into class I/flat, and class II types (Lada 1987). In Fig. 4.5, we show IRAC

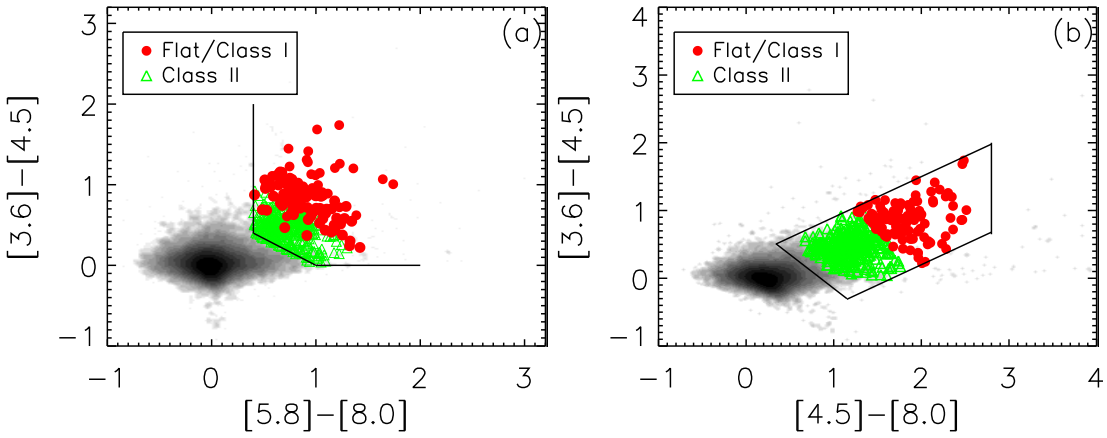

Figure 4.5: (a) Spitzer/IRAC [3.6]-[4.5] vs. [5.8]-[8.0] and (b) [3.6]-[4.5] vs. [4.5]-[8.0] color-color diagrams. YSO candidates are selected using the criteria described in Section 4.2.1(2), and classified as class I, flat-spectrum, or class II objects by their spectral index estimated from four IRAC bands. The filled circles denote class I and flat-spectrum objects, open triangles class II objects.

color-color diagrams of all detected objects, indicating the color boundaries used for the selection of YSOs and showing the class I/flat and class II sources as well as the objects not marked as disk-bearing YSOs with different colors. In total we identify 64 class I/Flat sources and 244 class II sources in the field of Fig. 4.4.

In Fig. 4.4, we show the spatial distribution of the objects identified as young stars with disks in NGC 6357, to which we will in this subsection simply refer to as "YSOs", reminding the reader that the population of young stars *without* disks that is almost certainly also present is not included here. Inside the three bubbles CS 61, CS 59, and CS 63 the number density of YSOs is obviously enhanced, suggesting recent star formation in these regions. In most star-forming regions a strong positional coincidence between young class I/flat YSOs and dense molecular cores is observed (e.g. Chapter 3; Evans et al. 2009). However, in the NGC 6357 complex this correlation is less obvious. The reason for this is currently unclear, possibly the parental molecular clouds of these YSOs have only recently been eroded by nearby massive stars, and star formation is still inactive in the molecular shells surrounding the bubbles.

A closer inspection of Fig. 4.4 reveals an interesting aspect of the spatial distribution of the class I/flat sources: in the regions marked "A" and "B" they appear to form arcs subtending the bubble CS 61. If we approximate the distribution of the sources in regions A and B with a circle we find that the center of the best-fitting circle lies very close to the center of bubble CS 61. This is suggestive of some role of the massive stars in CS 61 in (triggering) the presumably recent formation of the class I/flat sources in regions A and B. Similar configurations, of young stars

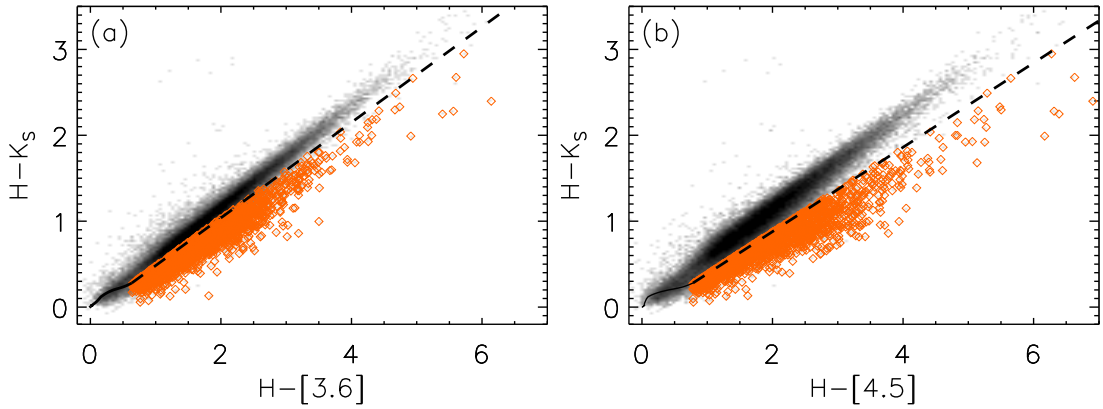

Figure 4.6: (a) H-K_s vs. H-[3.6] and (b) H-K_s vs. H-[4.5] color-color diagrams. The solid lines show the intrinsic colors of diskless stars. The dashed lines and arrows present the extinction laws. The lengths of arrows show a extinction of 2 mag at K band. The open diamonds are the YSO candidates which show excess emission in both [3.6] and [4.5] bands.

forming an arc around an older stellar population, have been found in other star forming regions, e.g., Tr 37, RCW 82, RCW 120 (Sicilia-Aguilar et al. 2005; Pomarès et al. 2009; Deharveng et al. 2009).

The aforementioned criteria for YSO selection require that the stars have been detected in all four IRAC bands. This may cause many low-mass, low luminosity members to be missed due to the limited sensitivity and the strong nebular background in the IRAC [5.8] and [8.0] bands. To probe also the low-mass population, we resort to H-K_s vs. H-[3.6] vs. and H-K_s vs. H-[4.5] color-color diagrams. In Fig. 4.6, we show two color-color diagrams on which the colors of unobscured diskless stars are indicated, together with the reddening vector (Indebetouw et al. 2005). Stars without a clear infrared excess lie in a narrow band on the top-left side of, and roughly parallel to, the reddening vector. Some of these will be cluster members that have already lost their disks, or at least the hot inner parts thereof, but most will be unrelated foreground or background stars. The stars to the bottom-right side of the reddening vector have too red H-[3.6] and H-[4.5] colors to be explained by the reddening of diskless stars, indicating that they have substantial excess emission above the photospheric level at near-infrared wavelengths. Thus, we identify these sources as YSOs if they show excess emissions in both the IRAC [3.6] and [4.5] bands. In the following we will refer to them as “lower-luminosity YSOs”, as opposed the brighter part of the sample that was detected in all four IRAC bands. This distinction, however, is set merely by observational detection limits and the respective stars likely form the fainter and brighter part of the same population.

In Fig. 4.7 we show the distribution of lower-luminosity YSOs selected as described in the previous paragraph and illustrated in Fig. 4.6, together with brighter class I/flat and class II objects

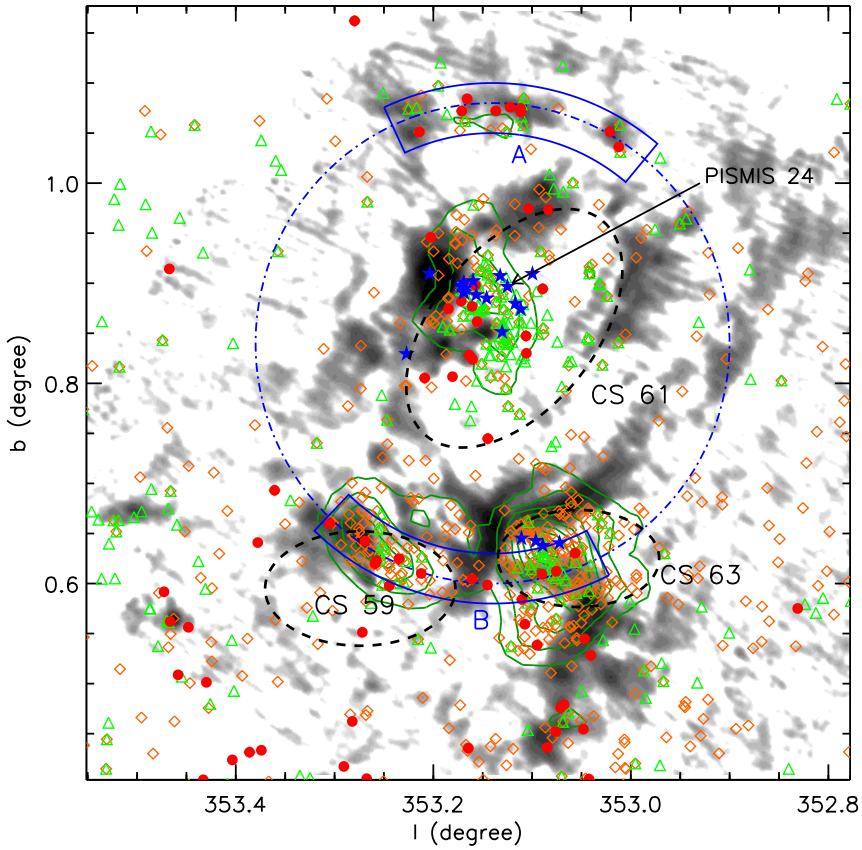

Figure 4.7: 1.3 mm emission map of NGC 6357 complex. Filled circles mark the Flat/class I objects, open triangles mark the class II objects. The filled asterisks show known massive stars in Pismis 24. The open diamonds show the YSO candidates selected from Fig 4.6. The number density of YSO candidates is denoted with contours. Three overdense regions are identified, corresponding to Pismis 24 and two newly found clusters.

that were detected in all IRAC bands. We plot the position of each of the lower-luminosity YSOs and also calculate their surface density, which we plot as contours in Fig. 4.7. In the NGC 6357 complex there are three regions where the distribution of the lower-luminosity YSOs shows an obvious overdensity, which coincide with the concentrations of the higher luminosity YSOs as selected from Fig. 4.5 and shown also in Fig. 4.4. All three coincide with the bubbles discussed earlier. The over-density of low-luminosity YSOs associated with bubble CS 61 is the Pismis 24 cluster, the other two are newly discovered young clusters that are spatially coincident with bubbles CS 59 and CS 63. We will refer to them as the "CS 59 and CS 63 clusters" hereafter. The spatial association of clusters and bubbles in NGC 6357 can be understood since clusters form in dense parts of molecular clouds, whereafter the high UV flux and stellar winds of the massive cluster members create the bubbles.

Contrary to the central regions where we have X-ray and optical data in addition to the Spitzer photometry, the YSO identification in the largest part of the GLIMPSE field relies solely on color-color diagram analysis. This makes the sample more susceptible to contamination by galactic and extra-galactic sources unrelated to the cluster. NGC 6357 is located in the galactic plane looking inward through the Milky Way (l=353°, b=+0.9°) and the galactic extinction in that direction is so high that most extra-galactic sources will be effectively absorbed even at 4.5 μm. Galactic contamination may arise from post-main sequence objects, mostly in the background, and young stars in foreground or background star-forming regions. The number density of the former sources is expected to be low and their distribution uniform, and thus the post-main sequence population should not substantially affect our results in a statistical sense. The contamination from young stars in the foreground and background is more difficult to evaluate. They would mostly be distributed in clusters or loose associations, and to remove them from NGC 6357 would require knowing the distance to each YSO candidate. This can partly be solved by estimating the kinematic distance of the gas that surrounds these YSOs in projection, under the assumption that the YSOs and gas are physically related. The latter assumption appears justified for the vast majority of the field investigated, with e.g. many young objects being spatially coincident with high-density gas, and the young clusters of high-mass stars occupying holes in the gaseous distribution. Russeil et al. (2010) have shown that the molecular gas spatially associated with cluster CS 59 and CS 63 has similar radial velocity to that of NGC 6357, suggesting they are at the same distance. Presently there is no information on the kinematics of the molecular gas in region A, and establishing a physical relation between this region and NGC 6357 requires further observations.

4.2.2 The Pismis 24 cluster

In this section we will zoom in on the Pismis 24 cluster. First we will re-assess the distance to Pismis 24. Then we will investigate the stellar properties of the cluster and derive the stellar masses and ages. Finally we will study the disk properties and frequency of the cluster members and compare them with those of other clusters.

(1) Distance to Pismis 24

There is some discussion in the literature about the distance of Pismis 24, and published estimates range from 1.0 to 3.0 kpc. The most commonly adopted distance of 2.56 kpc was derived by Massey et al. (2001) using observations of six massive stars, adopting their absolute magnitudes and intrinsic colors from the observed spectral types under the assumption that there is a unique absolute magnitude corresponding to each spectral type and luminosity class, and matching these

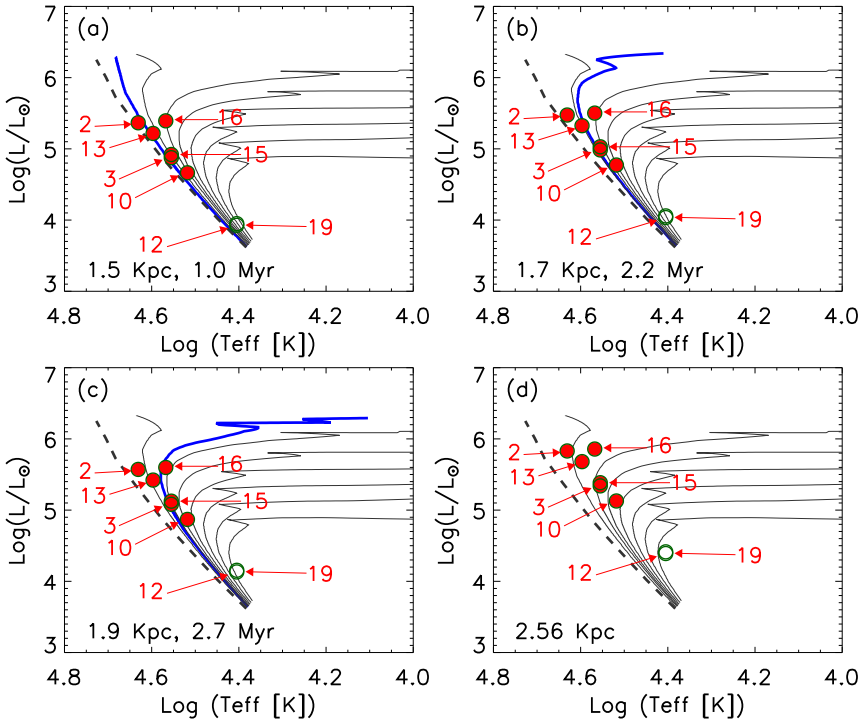

Figure 4.8: HR diagrams for six O-type main-sequence massive stars (Pis 24-2, 13, 16, 3, 15, 10, filled circles), and two B-type main-sequence stars (Pis 24-12, 19, open circles) in Pismis 24. The massive stars are marked with numbers (See Table 4.2). The dashed lines represent the zero-age main sequence locus. The thin solid lines show the isochrones of 2, 3, 4, 5, 6, 8, and 10 Myr. The thick solid lines present the best-fitting isochrones of 1, 2.2, and 2.7 Myr in panels(a)(b)(c), respectively. The evolutionary tracks are from Schaller et al. (1992). The fitting gives a distance of 1.7±0.2 kpc.

to the observed photometry. However, as shown in Fig. 4.8 the spectral types of massive stars do not uniquely constrain their absolute magnitudes without knowledge of their ages. In this work, we use the isochrone-fitting method to estimate the distance to Pismis 24 and the age of the massive stars that are used as distance indicators. Therefore we need to put these stars on the HR diagram, which requires knowledge of the total luminosities and spectral types. We adopted the spectral types and optical photometry in the B and V bands from Massey et al. (2001) and complemented the optical data with photometry in the J, H, and K_s bands from the 2MASS catalog. We then performed SED fitting following the method described in Chapter 3: we take a Kurucz model atmosphere spectrum with a fixed effective temperature corresponding to the observed spectral type, and fit a reddened and scaled version of this model spectrum to the observed photometry. In this fit we thus have only two free parameters: visual extinction A_V and the stellar angular diameter θ. We adopt a standard extinction law (Cardelli et al. 1989) with a total to selective extinction ratio of $R = 3.1$. We used the BVJHK band photometry to

do the SED fitting. We calculated model fluxes by integrating the intensity of the (reddened) model atmospheres over the spectral response curve of the system for each filter. The synthetic photometry was then compared with the observations. By varying the parameters and minimizing the resulting χ^2 we obtain the optimum values for extinction and the angular diameter of each star, from which we can derive the luminosities of the stars assuming a distance.

We used the six O-type main-sequence stars (see Fig. 4.8) to estimated the distance of Pismis 24. By requiring that the six stars are located above the zero-age main sequence locus, we estimated a lower limit on the distance, which is ∼1.4 kpc. We performed isochrone fitting to these six stars, assuming they formed coevally (see Fig. 4.8). Using 1.4 kpc as the lower limit of the distance, we varied the distance and age of the objects and found that the O-stars can be fitted by isochrones with ages of ∼1-2.7 Myr and distances of 1.7±0.2 kpc (see Fig 4.8). This puts NGC 6357 at the same distance as the NGC 6334 cloud (Persi & Tapia 2008), its direct neighbor on the sky, and suggest that both clouds are physically related instead of merely being close in projection. Additional support for this is given by radio observations that show that the average radial velocity of NGC 6357 is similar to that of NGC 6334 (both ~ -4 km s^{-1}), and that there are filamentary structures apparently connecting both complexes (Russeil et al. 2010) .

(2) The heart of Pismis 24

There are 12 known massive stars in the Pismis 24 cluster for which spectral type estimates exist. With the revised distance of 1.7 kpc we estimate their total luminosities, masses, and foreground extinctions. The results are listed in Table 4.2. The median visual extinction of these stars is 5.8 mag with a standard deviation of 0.5 mag. Since these stars have likely already dissipated all their circumstellar material, the observed extinction should be entirely due to absorption by foreground dust.

In Fig. 4.9 we show an HST F850LP image of the center of Pismis 24. In these high-resolution observations Pis 24-18 is resolved into a binary system with a separation of 0.″45, corresponding to a projected distance of ∼765 AU at 1.7 kpc. Wang et al. (2007) detected X-ray emission from Pis 24-18. We find that the secondary component of Pis 24-18 matches the position of the detected X-ray source more closely, and therefore is the more likely counterpart of the X-ray source. In the whole field shown in Fig. 4.9 there are 253 X-ray sources (Wang et al. 2007). Among these, 220 sources have detected optical or infrared counterparts. We used all detected X-ray sources *with* optical/IR counterparts to calculate the surface density of the numbers of stars in the region, and find values of ∼800 pc^{-2} within a projected radius of 0.1 pc from Pis 24-1 and ∼350 pc^{-2} within 0.3 pc from Pis 24-1.

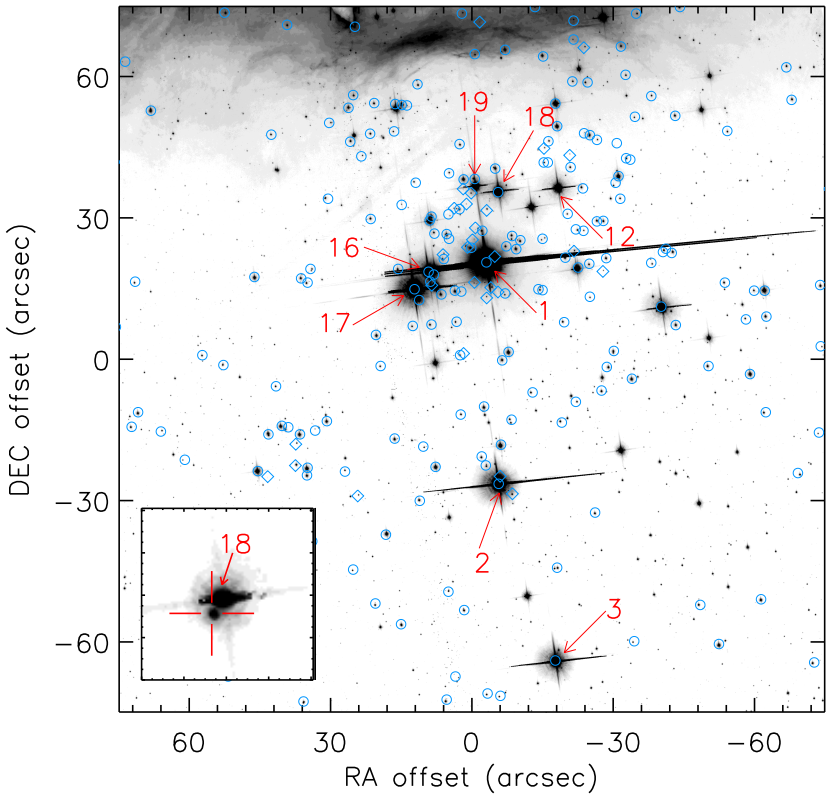

Figure 4.9: HST F850LP image of the center of Pismis 24. The open circles mark the counterparts of X-ray sources previously identified in Wang et al. (2007). The open diamonds represent counterparts of X-ray sources newly identified in the current work. The massive stars in this field are marked with numbers (See Table 4.2). The inset shows the HST F550M image of Pis 24-18, which is resolved into a binary system. The plus sign marks the position of the X-ray emission source detected by Wang et al. (2007).

(3) The low- and intermediate-mass population in Pismis 24

In this section we will inventorize the stellar content of the Pismis 24 star cluster in the low- and intermediate mass range. We will estimate the extinction distribution for the spectroscopy sample, for which we have reliable spectral types from our spectroscopic observations. We will assume that the cluster members without spectroscopy follow the same extinction distribution, in a statistical sense, as the "spectroscopic" sample. We will use an R vs. R-I color-magnitude diagram, in which we de-redden all detected objects according to the derived extinction distribution, to estimate the mass and age distribution of all cluster members by comparison to the theoretical pre-main sequence tracks of Dotter et al. (2008).

(a) Spectral Types and the extinction distribution

Table 4.2: Parameters for massive stars in Pismis 24.

Name	RA (J2000)	DEC (J2000)	Spt[a]	Lum[b] ($L_\odot$)	A_V[c] (mag)	Mass[d] ($M_\odot$)
Pis 24-1NE	17 24 43.497	-34 11 56.86	O3.5 If*	5.89	5.54	74
Pis 24-1SW	17 24 43.481	-34 11 57.21	O4 III	5.81	5.52	66
Pis 24-17	17 24 44.73	-34 12 02.7	O3.5 III	5.93	6.34	78
Pis 24-2	17 24 43.28	-34 12 44.0	O5.5 V(f)	5.47	5.83	43
Pis 24-13	17 24 45.79	-34 09 39.9	O6.5 V((f))	5.33	6.39	35
Pis 24-16	17 24 44.45	-34 11 58.9	O7.5 V	5.50	7.24	38
Pis 24-3	17 24 42.30	-34 13 21.3	O8 V	4.98	5.82	25
Pis 24-15	17 24 28.95	-34 14 50.7	O8 V	5.03	5.47	25
Pis 24-10	17 24 36.04	-34 14 00.5	O9 V	4.77	5.80	20
Pis 24-18	17 24 43.29	-34 11 41.9	B0.5 V	4.47	6.45	15
Pis 24-12	17 24 42.27	-34 11 41.2	B1 V	4.03	5.58	11
Pis 24-19	17 24 43.69	-34 11 40.7	B1 V	4.06	6.09	11

[(a)]Spectral types from Massey et al. (2001) and Maíz Apellániz et al. (2007). [(b)]The total luminosities for Pis 24-1NE and Pis 24-1SW are derived with the absolute V-band magnitudes using the bolometric corrections from Vacca et al. (1996), assuming a distance of 1.7 kpc. The total luminosities for other stars are estimated from SED fittings (see Sect. 4.2.2). [(c)]Besides Pis 24-1NE and Pis 24-1SW, the visual extinction for other stars come from SED fitting (see 4.2.2). The visual extinction for Pis 24-1NE and Pis 24-1SW are from Maíz Apellániz et al. (2007). [(d)] The stellar masses are derived using the evolutionary tracks from Schaller et al. (1992).

In total we have obtained the spectral types of 306 stars in the field of Pismis 24. We have identified 151 of these as cluster members based on positional coincidence with a detected X-ray source. 155 stars in the spectroscopic sample were detected in the X-ray data, and were considered to be unrelated field objects. We did not use the Li I λ6707 absorption line or Hα emission line or as the indicator of youngth properties due to the reasons: (1) the spectral resolution of our spectra is too low to detect the weak Li I λ6707 absorption line; (2) the spectra may suffer from Hα line contamination from the surrounding nebula.

In Fig. 4.10(a) we show the spectral types of all stars in the spectroscopic sample. For the nonmembers the distribution is approximately flat between late K and late M spectral types.

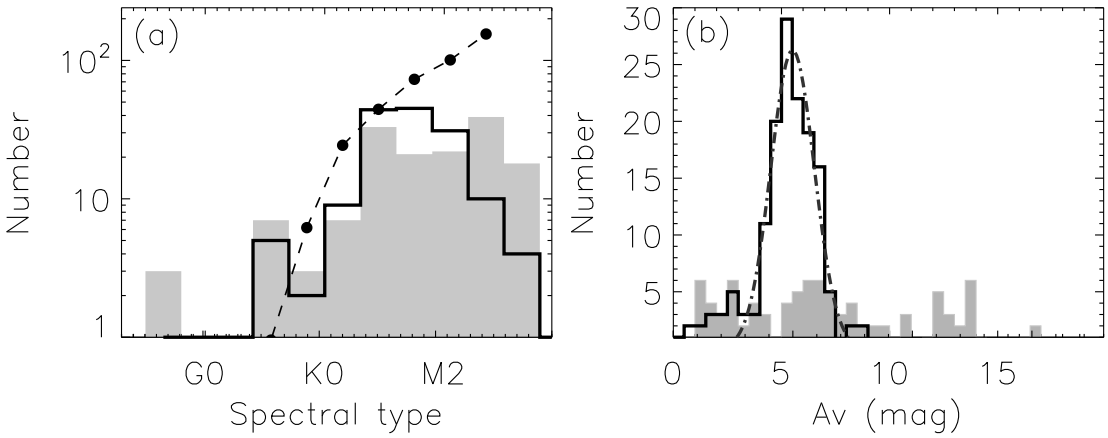

Figure 4.10: (a): the spectral-type distribution of our spectroscopic sample. The filled histogram shows the distribution of stars without X-ray emission. The open histograms display the distribution of X-ray emission stars. The dotted line connecting filled circles show the predicted distribution of spectral type for a 1 Myr cluster with an IMF like that of the Trapezium cluster. The distribution is normalized to the number of K4-K6 stars. (b): the distribution of extinction for the spectroscopic sample. The filled histogram shows the distribution of stars without X-ray emission. The open histogram shows the distribution of X-ray emitting stars. The dash-dotted lines denote Gaussian fits the open histogram, peaking at A_V=5.5 mag with a FWHM of 2.2 mag.

The distribution of the cluster members peaks around K5 and decreases towards later spectral types. In Fig. 4.10(a) we also show a calculated distribution of spectral types for a model cluster with an age of 1 Myr and a mass function as observed in the Trapezium cluster (Muench et al. 2002). Assuming that the Pismis 24 cluster and Trapezium clusters have a similar IMF, we use the model spectral type distribution to evaluate the completeness level for the range of spectral types probed. As shown in Fig. 4.10, the model distribution predicts many more M-type stars than are present in our spectroscopic sample, suggesting that the latter is substantially incomplete for the late spectral types. Assuming a foreground visual extinction of 6 mag and a distance of 1.7 kpc, the R-band magnitude for a PMS stars with a spectral type of M3 and an age of 1 Myr is ~23 mag (Dotter et al. 2008), which is indeed very faint for spectroscopic observations even with the VLT.

We used the observed R-I colors and the intrinsic colors of the stars in the spectroscopic sample to estimate their extinctions, adopting the extinction law of Rieke & Lebofsky (1985). The intrinsic colors corresponding to each spectral type were taken from Bessell et al. (1998). In Fig. 4.10(b) we show the resulting extinction distributions for the cluster members and the unrelated field stars. The two populations show very different extinction distributions. The unrelated field stars show a relatively flat distribution between ~0 and ~15 magnitudes, whereas the cluster members show a strongly peaked distribution centered around 5-6 mag. The median extinction

of the members of Pismis 24 is ~5.3 mag, which is consistent with the extinction estimates of the known massive stars in the cluster (see Sect. 4.2.2(2)). Fitting the observed extinctions with a Gaussian distribution yields a peak value of 5.5 mag and a FWHM of 2.3 mag. In the following we will use the fitted Gaussian distribution of extinctions to derive the probability distribution of masses and ages for each cluster member for which we have only photometric observations but no spectroscopy.

(b) color-magnitude diagrams

In Fig. 4.11(a) we show the R vs R-I color-magnitude diagram for all stars detected in the Pismis 24 field. For comparison we also plot model isochrones of 0.1, 1, 3, and 30 Myr (Dotter et al. 2008). The isochrones have been reddened by the visual extinction of 5.5 mag, the mode of the extinction distribution discussed in Sect. 4.2.2(3a). It can be noted that most of cluster members fall within the 0.1-3 Myr isochrones. In Fig. 4.11(b), we show the dereddened R vs. R-I color-magnitude diagram for our spectroscopic sample, along with the model isochrones of 0.1, 1, 3, and 30 Myr (Dotter et al. 2008).

We estimated the masses and ages of the spectroscopic members of Pismis 24 from the dereddened R vs. R-I color-magnitude diagram (see Fig 4.11(b)) by comparison with the theoretical PMS evolutionary tracks (Dotter et al. 2008). There are several sets of pre-main sequence evolution tracks presented by various authors (e.g. D'Antona & Mazzitelli 1997; Baraffe et al. 1998; Palla & Stahler 1999; Siess et al. 2000; Dotter et al. 2008). In this work, we will adopt the PMS evolution tracks from Dotter et al. (2008), as these have the best resolution in both mass and age. We stress, however, that there are substantial systematic differences between the different sets of tracks (see Hillenbrand & White 2004; Hillenbrand et al. 2008for a detailed discussion of the various sets of PMS evolutionary tracks available in the literature), and our motives for choosing those by Dotter et al. (2008) are pragmatic. Qualitatively, analyses such as ours do not depend on the specific set of tracks chosen, as long as the parameters of every object and every cluster are determined using the same set of theoretical tracks.

The results are listed in Table 4.3. For the cluster members without spectroscopic observations we cannot accurately estimate the mass and age of any individual object since we do not know the foreground extinction towards individual stars. Instead, we derived a mass and age probability function for each object by drawing 2000 random samples from the extinction probability function derived from Fig. 4.10(b). Thus we obtain 2000 "virtual" positions in the R vs. R-I color-magnitude diagram for each observed star, each corresponding to a specific mass and age, and as a whole properly sampling the extinction distribution function. The ensemble of the mass and age estimates of the cluster members yields a good representation of the actual cluster mass and age distributions, which are shown in Fig 4.12.

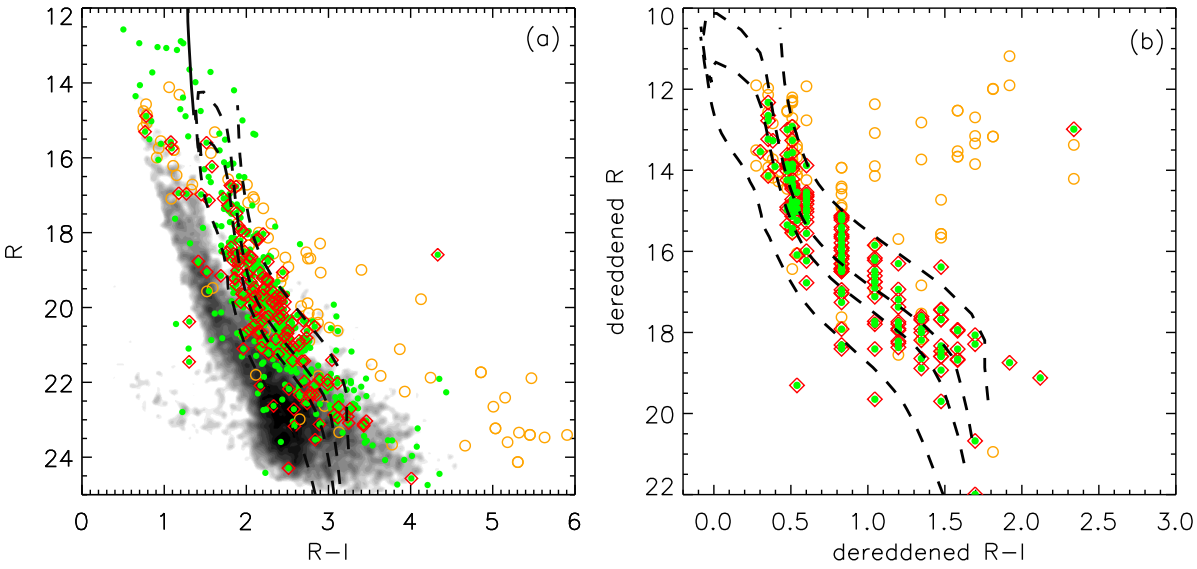

Figure 4.11: (a): R vs R-I color-magnitude diagram for the stars detected on the VIMOS images. The dashed lines are PMS isochrones of 0.1, 1, 3, and 30 Myr (Dotter et al. 2008). The solid line represents the ZAMS (Schaller et al. 1992). The isochrones are reddened by the mode of the extinction distribution of the spectroscopic members of Pismis 24 cluster. The grey density map presents the distribution of all detected sources on the VIMOS images. The filled circles show the counterparts of X-ray sources. The open diamonds mark the X-ray emission stars that have been observed with VIMOS spectroscopy. The open circles present the stars without detected X-ray emissions that have been observed with VIMOS spectroscopy. (b): the dereddened R vs R-I color-magnitude diagram for spectroscopic sample. The extinction for each star is estimated by comparing the observed R-I color with the intrinsic R-I color expected from the spectral type. The symbols are same as in panel (a).

Table 4.3: Stellar parameters for X-ray emissing stars with spectral types in PISMIS 24. Column 2: the identification numbers in Wang et al. (2007)

(1) ID	(2) W07	(3) RA (J2000)	(4) DEC (J2000)	(5) Spt	(6) A_V (mag)	(7) mass ($M_\odot$)	(8) age (Myr)
3	3	17 23 59.16	-34 12 16.9	G5	4.369	2.938	1.4
4	6	17 24 03.22	-34 14 02.2	G5	5.508	2.665	1.9
9	12	17 24 07.66	-34 17 52.4	K5	6.440	0.862	0.6
15	18	17 24 13.60	-34 09 21.3	K2	3.661	1.540	1.1
16	19	17 24 13.60	-34 16 56.7	M9	7.492	...	...
18	21	17 24 13.74	-34 06 57.1	M9	19.531	...	...
19	22	17 24 14.72	-34 10 43.7	F8	1.798	1.664	8.1
25	30	17 24 16.18	-34 13 11.4	K2	2.634	1.475	2.9
29	35	17 24 18.79	-34 12 04.8	K7	4.607	0.666	1.4
30	36	17 24 19.60	-34 15 44.4	K3	5.746	1.271	0.9
31	38	17 24 20.25	-34 13 10.6	K5	6.793	0.834	0.3
35	44	17 24 21.72	-34 13 25.4	M2	4.402	0.408	4.7
36	46	17 24 21.82	-34 12 59.2	M1	4.919	0.428	0.5

Table 4.3: continued.

(1) ID	(2) W07	(3) RA (J2000)	(4) DEC (J2000)	(5) Spt	(6) A_V (mag)	(7) mass ($M_\odot$)	(8) age (Myr)
37	47	17 24 22.05	-34 14 29.7	G5	4.620	2.565	2.1
38	48	17 24 22.95	-34 12 22.0	K5	4.635	0.890	0.9
39	50	17 24 23.47	-34 09 42.3	M3	2.423	0.292	0.1
40	51	17 24 23.95	-34 08 15.8	K3	6.377	1.373	0.2
43	55	17 24 25.40	-34 19 15.8	K3	6.579	1.268	0.7
49	64	17 24 27.30	-34 08 01.0	K5	5.493	0.828	0.3
74	94	17 24 31.35	-34 11 35.2	M0	5.762	0.681	14.0
78	98	17 24 31.66	-34 10 46.7	M4	6.930	...	...
80	101	17 24 32.04	-34 13 05.2	K4	5.131	1.115	1.2
88	110	17 24 32.86	-34 09 02.5	K4	5.216	1.094	0.9
89	112	17 24 33.03	-34 16 54.8	K4	6.238	1.081	0.6
92	115	17 24 33.25	-34 15 15.1	M0	5.095	0.477	0.5
100	124	17 24 33.88	-34 11 55.1	M5	6.513	...	...
101	125	17 24 33.99	-34 05 50.3	K7	7.002	0.514	0.1
108	133	17 24 34.46	-34 12 46.6	K7	4.855	0.655	1.3
110	135	17 24 34.63	-34 08 44.5	K3	5.331	1.269	0.6
113	138	17 24 34.74	-34 15 24.7	M1	4.467	0.512	2.7
127	156	17 24 36.48	-34 12 36.9	G9	4.315	2.031	2.8
129	158	17 24 36.65	-34 15 50.8	K3	4.907	1.283	1.2
134	163	17 24 36.76	-34 11 45.5	K7	5.515	0.533	0.2
135	164	17 24 37.13	-34 12 25.9	K7	5.766	0.547	0.3
142	172	17 24 37.76	-34 12 14.9	M2	6.675	0.400	0.8
144	174	17 24 37.83	-34 12 33.4	M2	5.238	0.417	3.6
151	181	17 24 38.38	-34 11 15.4	M0	4.319	0.548	1.4
154	186	17 24 38.72	-34 12 08.5	K3	5.661	1.294	1.5
157	190	17 24 38.75	-34 17 09.3	K7	5.864	0.550	0.3
160	193	17 24 38.89	-34 14 05.4	K7	4.934	...	...
164	197	17 24 39.03	-34 10 07.8	M7	1.953	...	...
166	199	17 24 39.29	-34 09 39.5	K7	5.629	0.554	0.3
170	203	17 24 39.52	-34 13 18.2	K3	5.249	1.285	0.4
171	204	17 24 39.53	-34 19 40.0	G5	5.153	2.225	3.1
173	206	17 24 39.61	-34 16 33.2	K3	5.140	1.291	4.3
174	207	17 24 39.71	-34 12 19.1	K5	6.064	0.855	0.5
175	208	17 24 39.68	-34 13 47.9	M3	4.920	0.337	1.6
179	212	17 24 39.87	-34 14 11.5	M1	5.166	0.450	0.8
181	214	17 24 40.07	-34 17 12.9	K7	4.852	0.653	1.2
186	219	17 24 40.26	-34 12 10.4	M0	4.407	0.451	0.3
188	221	17 24 40.32	-34 11 54.9	K7	4.759	0.581	0.5
189	223	17 24 40.45	-34 15 03.3	K7	5.164	0.773	4.0
196	230	17 24 40.73	-34 05 34.7	K4	5.100	1.107	1.1
199	233	17 24 40.94	-34 11 04.2	M0	3.737	0.638	4.9
200	234	17 24 40.98	-34 11 26.3	M2	5.576	0.411	1.2
201	235	17 24 40.99	-34 13 17.6	M1	5.663	0.500	2.0
203	238	17 24 41.12	-34 11 34.9	K5	5.718	1.022	3.1
206	241	17 24 41.21	-34 11 11.2	M1	2.754	0.504	2.2
208	243	17 24 41.25	-34 11 38.8	K2	4.997	1.760	0.2
209	244	17 24 41.29	-34 08 59.0	M0	6.250	0.505	0.7
212	247	17 24 41.32	-34 16 11.9	K3	5.025	1.288	1.4
213	248	17 24 41.34	-34 12 16.0	K7	4.201	0.667	1.4
223	258	17 24 41.64	-34 12 50.3	K7	3.876	0.636	1.0
225	260	17 24 41.73	-34 12 04.5	M1	5.452	0.533	4.7
235	272	17 24 41.95	-34 12 26.7	M2	4.999	0.402	0.9
247	285	17 24 42.17	-34 16 23.2	K5	5.275	0.876	0.7
252	291	17 24 42.29	-34 13 01.9	M4	3.031	0.288	0.3
264	309	17 24 42.68	-34 11 02.8	M3	...	...	...
271	318	17 24 43.11	-34 12 30.4	M0	0.977	0.530	87.6
274	321	17 24 43.19	-34 16 42.8	K2	4.850	1.486	2.7
278	326	17 24 43.24	-34 12 17.8	K3	5.185	1.311	2.3
279	328	17 24 43.26	-34 12 35.9	K3	5.142	1.454	0.1

Table 4.3: continued.

(1) ID	(2) W07	(3) RA (J2000)	(4) DEC (J2000)	(5) Spt	(6) A_V (mag)	(7) mass ($M_\odot$)	(8) age (Myr)
283	335	17 24 43.36	-34 11 37.1	K7	4.550	0.521	0.2
288	343	17 24 43.51	-34 09 15.4	K7	4.260	0.791	20.4
306	370	17 24 43.89	-34 13 10.9	K7	4.802	0.609	0.7
312	379	17 24 43.97	-34 11 45.8	K4	6.231	1.114	1.2
321	389	17 24 44.15	-34 13 06.8	M4	2.920	0.267	0.8
323	393	17 24 44.19	-34 13 30.1	K5	6.795	0.840	0.4
327	397	17 24 44.37	-34 12 40.5	K2	4.888	1.602	0.5
328	399	17 24 44.39	-34 10 39.9	K3	5.480	1.286	0.4
339	412	17 24 44.66	-34 12 47.5	M0	5.352	0.427	0.1
344	419	17 24 44.72	-34 08 41.6	K5	6.977	0.845	0.4
348	423	17 24 44.80	-34 17 32.2	K4	5.861	1.152	7.0
349	425	17 24 44.80	-34 16 36.4	K2	8.852	1.566	0.7
351	429	17 24 44.94	-34 11 44.9	M6	15.097	...	...
352	430	17 24 44.95	-34 13 14.0	M8	0.856	...	...
359	439	17 24 45.20	-34 12 54.6	G8	5.626	2.432	1.9
365	447	17 24 45.35	-34 17 48.6	M5	8.695	...	...
367	449	17 24 45.41	-34 13 09.8	K7	6.146	0.618	0.8
370	452	17 24 45.50	-34 11 47.8	M0	5.679	0.447	0.3
373	456	17 24 45.56	-34 15 04.1	K2	6.585	1.378	5.0
375	458	17 24 45.63	-34 11 34.4	M4	6.254	...	...
376	459	17 24 45.69	-34 12 46.5	M5	3.340	...	...
379	462	17 24 45.79	-34 11 21.7	M0	4.165	0.523	1.0
385	469	17 24 45.93	-34 12 41.2	K7	8.118	0.590	0.6
387	471	17 24 46.02	-34 14 07.6	K3	6.168	1.322	0.3
391	475	17 24 46.26	-34 11 43.4	K7	8.320	0.518	0.1
393	477	17 24 46.39	-34 14 16.3	M4	5.592	0.265	0.8
395	480	17 24 46.49	-34 12 56.3	K7	4.286	0.658	1.3
397	482	17 24 46.51	-34 14 42.0	K4	2.869	...	...
401	487	17 24 46.64	-34 13 35.1	M3	5.180	0.342	1.3
404	490	17 24 46.63	-34 13 30.4	M1	5.789	0.384	0.2
408	495	17 24 46.76	-34 12 40.0	K7	4.790	0.606	0.7
414	501	17 24 47.03	-34 13 58.3	M3	5.123	...	...
417	505	17 24 47.13	-34 08 25.0	K7	6.734	0.517	0.1
422	511	17 24 47.33	-34 10 30.3	M0	1.390	0.629	4.3
433	523	17 24 47.77	-34 15 04.1	K5	6.489	0.839	0.4
434	524	17 24 47.82	-34 14 51.0	M1	4.860	0.467	1.1
437	528	17 24 47.94	-34 13 25.2	K7	5.094	0.854	6.7
444	535	17 24 48.16	-34 13 00.6	M1	4.033	0.531	4.4
452	543	17 24 48.74	-34 18 02.3	K5	5.217	0.993	12.4
454	546	17 24 48.95	-34 15 35.9	K7	5.648	0.686	43.2
456	548	17 24 48.96	-34 14 54.1	K7	6.298	0.606	0.7
457	549	17 24 48.96	-34 13 50.9	K3	6.233	1.269	0.8
465	557	17 24 49.26	-34 15 19.2	K7	6.076	0.516	0.1
466	558	17 24 49.31	-34 13 20.2	M0	5.469	0.488	0.6
469	561	17 24 49.46	-34 12 29.1	K3	5.800	1.301	1.8
473	565	17 24 49.66	-34 15 27.9	K3	6.586	1.289	0.4
475	567	17 24 49.79	-34 15 58.9	K3	6.577	1.269	0.8
476	568	17 24 49.79	-34 09 00.4	M2	1.285	0.420	1.9
478	570	17 24 49.85	-34 12 10.9	K7	6.423	0.636	1.0
487	580	17 24 50.41	-34 16 54.7	M3	6.721	0.335	0.4
491	584	17 24 50.73	-34 15 30.1	K7	7.155	0.537	0.2
496	591	17 24 51.35	-34 16 15.0	M2	7.093	0.397	0.8
502	599	17 24 51.96	-34 15 13.2	K5	6.267	0.933	1.4
505	602	17 24 52.17	-34 11 14.3	M1	5.903	...	...
506	603	17 24 52.35	-34 10 23.8	M3	5.008	0.337	1.6
513	611	17 24 53.05	-34 15 38.5	K7	6.817	0.568	0.4
520	619	17 24 53.43	-34 15 51.4	M3	6.144	0.325	0.3
523	622	17 24 53.65	-34 12 22.1	K7	6.798	0.584	0.5
524	623	17 24 53.63	-34 12 15.3	K5	6.924	0.834	0.1

Table 4.3: continued.

(1) ID	(2) W07	(3) RA (J2000)	(4) DEC (J2000)	(5) Spt	(6) A_V (mag)	(7) mass ($M_\odot$)	(8) age (Myr)
525	624	17 24 53.69	-34 16 04.4	K7	5.048	0.706	38.5
526	625	17 24 53.73	-34 16 51.5	K2	5.454	1.570	0.6
537	639	17 24 54.91	-34 11 23.9	M0	6.930	0.504	0.7
546	649	17 24 55.55	-34 16 31.7	K5	5.177	0.833	0.3
562	668	17 24 57.37	-34 16 02.1	M3	7.465	0.326	0.3
565	671	17 24 57.85	-34 10 32.9	M5	3.073	...	...
572	682	17 24 58.94	-34 17 22.7	K7	4.908	0.770	3.9
580	692	17 24 59.75	-34 09 58.8	M1	6.359	0.538	5.5
585	697	17 25 00.30	-34 17 12.7	M2	4.572	...	...
595	711	17 25 02.32	-34 06 26.5	M3	0.160	0.318	2.2
597	714	17 25 02.58	-34 16 28.3	M3	5.690	0.335	0.4
600	718	17 25 03.17	-34 08 49.6	G5	1.557	1.632	7.2
603	722	17 25 03.41	-34 15 52.0	K4	5.786	1.144	1.8
610	730	17 25 05.56	-34 19 19.8	K5	6.209	0.831	0.3
623	752	17 25 09.91	-34 15 51.6	K3	2.146	1.279	0.4
630	760	17 25 11.80	-34 18 36.7	K2	2.314	1.554	0.8
634	767	17 25 14.28	-34 16 38.8	K3	5.076	1.303	3.7
637	771	17 25 16.94	-34 14 03.5	K5	5.927	1.058	4.8
642	777	17 25 22.24	-34 16 18.6	M3	6.163	0.346	1.2
643	778	17 25 23.77	-34 17 55.3	K3	2.863	1.290	1.4

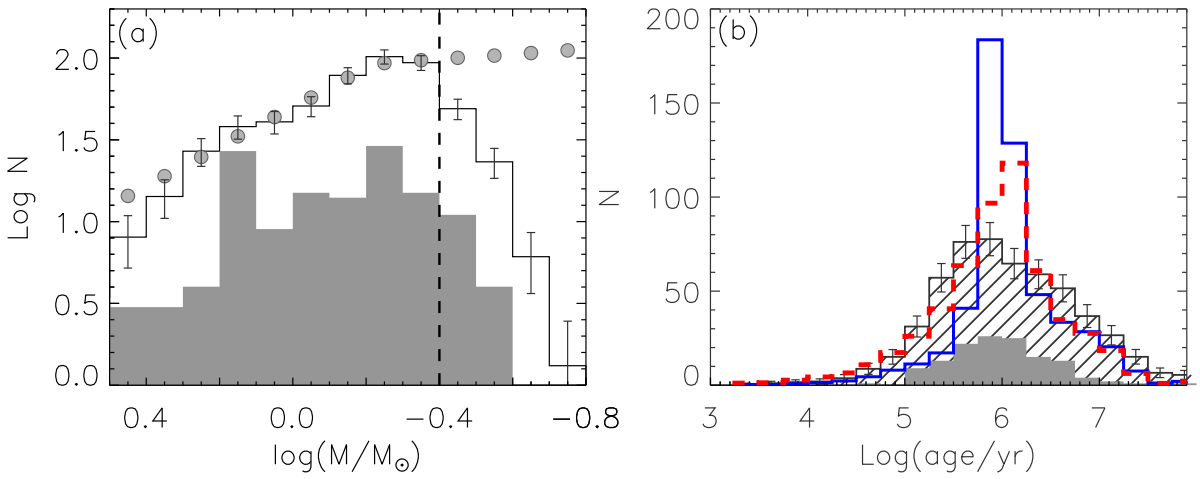

Figure 4.12: (a): The mass distribution of all X-ray emitting stars (open histogram), and X-ray emitting stars with well determined spectral types (filled histogram). The filled circles show the Trapezium IMF, scaled to match the open histogram. The dash line shows the completeness limit of the X-ray observations (~0.4 $M_\odot$). (b): The age distribution of all X-ray emitting stars (line-filled histograms) and X-ray sources with well determined spectral types (filled histograms). Both distributions yield a similar median age of ~1 Myr. The solid-line histograms show the coeval model. The dashed-line histograms represent the model with an age distribution of 0.9±0.9 Myr

In Fig. 4.12(a) we compare the mass distribution of Pismis 24 cluster with the IMF of the Trapez-

ium cluster. The Trapezium IMF and the observed mass function of the Pismis 24 cluster are very similar down to ~0.4 $M_{\odot}$. At masses below 0.4 $M_{\odot}$both distributions are clearly different, with a substantial lack of observed stars in Pismis 24 compared to the Trapezium cluster, which we attribute to incompleteness in the Pismis 24 sample. To further quantify this, we estimate the 10σ detection limits in the VIMOS imaging data in the R and I-bands. These limits vary from region to region due to the highly variable nebular background levels, in particular in the R-band. Here we only give the average 10σ limits, which are 22.5 and 21.1 mag in the R and I bands, respectively. From PMS evolutionary tracks we obtain apparent brightnesses of 22.3 mag in R-band and 19.4 I-band, respectively, for a PMS star with a mass of 0.4 $M_{\odot}$, an age of 1 Myr, and an extinction of $A_{\rm V}$=6 mag (Dotter et al. 2008). This confirms that the relative lack of Pismis 24 members with masses below 0.4 $M_{\odot}$ is at least to a large extent an observational bias due to the limited sensitivity of our VIMOS images.

We also show the mass distribution of the spectroscopic members in Fig. 4.12(a). Compared to the mass function of all known cluster members, the distribution within the spectroscopic sample is much flatter in the mass range between ~1.5 $M_{\odot}$ and ~0.4 $M_{\odot}$, again indicating that a large fraction of the low mass population has not been included in the spectroscopic data.

In Fig. 4.12(b), we show the age distribution of the spectroscopic members and all known members of the Pismis 24 cluster. Both distributions look very similar, though the former sample is very incomplete (see Fig. 4.12(a)). From these distributions, we estimate the median age of Pismis 24. The spectroscopic members give a median age of 0.9 Myr, and all known members give a median age of 1.0 Myr.

As shown in Fig. 4.12(b), the ages of the known members in Pismis 24 show large spread. To investigate the statistical significance of the observed spread in age, we performed a simple Monte Carlo simulation. We first explored the possibility of coeval star formation in Pismis 24. We used Monte Carlo techniques to generate a coeval population of 0.9 Myr old stars at a distance of 1.7 kpc with a mass function of the Trapezium cluster. For each model star, we obtained the magnitude in R and I bands using the evolutionary tracks from Dotter et al. (2008) according to the assumed mass and age. To mimic the observed photometric uncertainties, we varied the model photometry by adding random offsets drawn from a Gaussian distribution with a 1-sigma deviation of 0.1 mag. To simulate the effect of extinction, we reddened the photometry with values drawn at random from the extinction probability function for Pismis 24 (see Fig. 4.10(b)), and included only synthetic stars with R-band magnitudes brighter than 23 mag to well reproduce the observed color-magnitude diagram shown in Fig 4.11(a). In one simulation, we produced a cluster with 1000 stars. We derived the age distribution from the model cluster with the same method that we applied for Pismis 24. We have performed 10 simulations, and obtained an average age distribution from them. The resulting age distribution is shown in Fig 4.12(b). The age spread inferred from the observations is larger than what can be explained by an intrinsically coeval

population with the aforementioned observational uncertainties. Therefore, we explore the possibility of an intrinsic age spread for the members in Pismis 24. We modified the original Monte Carlo simulation by randomly sampling the ages from a uniform distribution between 0-1.8 Myr, and repeating the calculations in an otherwise identical way. The resulting simulated age distribution is shown in Fig. 4.12(b). The simulations assuming an intrinsic age distribution match the observations substantially better than those assuming a coeval population. Still, the modeled peak in the age distribution around ∼1 Myr is somewhat higher than the observed distribution, which may be due to other effects unconsidered in our simulations, e.g., stellar variability, unresolved binary, accretion activity including accretion history and current accretion rates, scattering effect from circumstellar disks (e.g. Burningham et al. 2005; Baraffe et al. 2009; Guarcello et al. 2010). The stellar variability and unresolved binarity can induce the scatter of the apparent luminosity, therefore inducing an apparent spread in ages. Episodic accretion histories has also been proposed to explain the observed spread in HR diagrams by Baraffe et al. (2009). They show that an evolution including short episodes of vigorous accretion followed by longer quiescent phase can reproduce the observed luminosity spread in HR diagrams at ages of a few Myr years in the very low-mass range. Besides the accretion history, current accretion activity can produce excess emission, rendering the colors of young stars bluer and increasing the observed luminosity (Da Rio et al. 2010). Differential accretion rates of young stars can thus disperse young stars on HR diagram. The scattering from circumstellar disks also makes the optical colors of young stars bluer, therefore affecting the derivation of physical parameters, e.g., extinction, and luminosity (Guarcello et al. 2010). All these effects introduce scatter in the distribution of young populations on the HR diagram.

(4) Disk properties in Pismis 24

(a) Photoevaporating disks caught in the act

In Fig. 4.13 we show an interesting object found in Pismis 24 (Hester & Desch 2005), which appears as a bright head with a tail and thus shows the characteristic shape of proplyds. These have been found in many star-forming regions harboring massive stars, e.g. the Orion Nebula (O'dell et al. 1993), NGC 3603 (Brandner et al. 2000), NGC 2244 (Balog et al. 2006), etc. The proplyds are interpreted as the outer disks of young stars that are being photoevaporated by EUV and FUV radiation from nearby massive stars. The energetic photons from neighboring massive stars heat gas in the outer disks to temperatures such that the sound speed exceeds the local escape velocity, allowing the gas to flow away (Hollenbach et al. 2000). This scenario has been reproduced by simulations (see e.g. Richling & Yorke 2000). The tail of proplyd-1 is pointing away from the most massive stellar system in the Pismis 24 cluster, Pis 24-1, suggesting that the

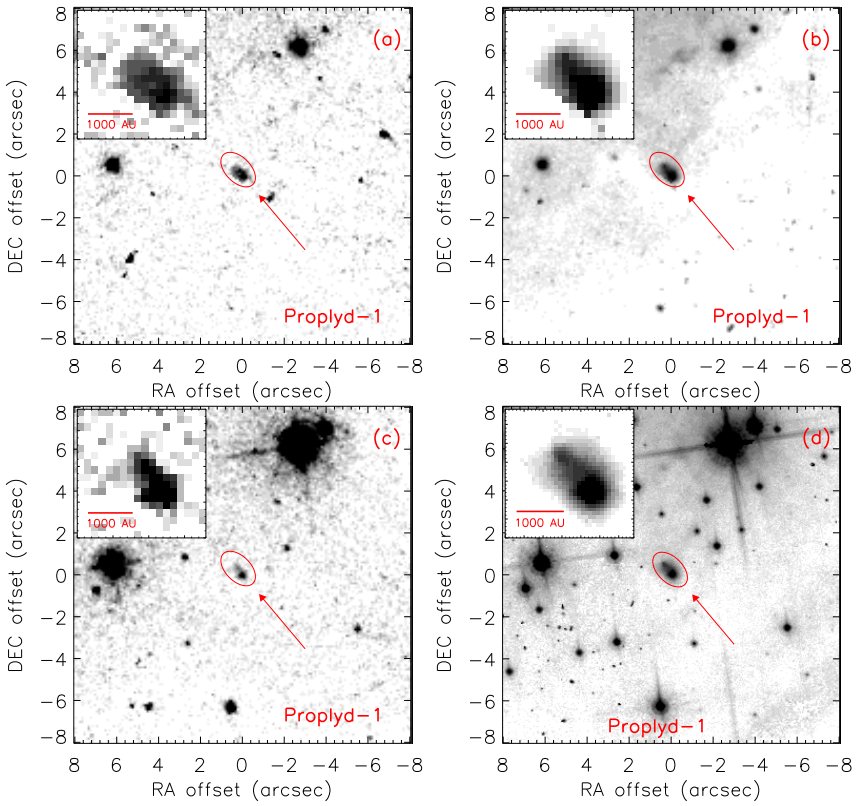

Figure 4.13: A photoevaporating disk candidate in Pismis 24. Panels (a)(b)(c)(d) are centered on RA=17:24:45.26, DEC=-34:11:30.5. Panels (a)(b)(c) are HST images in the F502N, F656N, and F673N bands, which cover [O III], Hα and [S II] respectively. Panel (d) shows the HST image in F850LP band. In each panel, the arrow shows the projected direction of Pis 24-1 relative to the target. The inset in each panel shows a zoom-in of the proplyd in each HST band.

latter is responsible for the creation of proplyd-1. Proplyd-1 is located ~0.″34 from Pis 24-1, corresponding to a projected distance of 0.28 pc.

In Fig. 4.13(a)(b)(c)(d) we show proplyd-1 in the HST F502N, F656N, F673N and 850LP bands, respectively. In all four bands proplyd-1 shows a bright, spatially extended head, but its tail appears different in each band. In the F502N band the tail of proplyd-1 appears more diffuse and extended than in the F656N and F673N bands. The F502N, F656N, and F673N bands cover the [O III]5007, Hα, and [S II] 6717,6731 emission lines, respectively. The different appearance of the tails in the different bands can be attributed to the the abundance of their agent. The Hα and [S II]6717,6731 lines reach their maximum intensity at the hydrogen ionization front (H I-front), whereas the [O III]5007 line attains its maximum outside of the H I-front where EUV photons can still reach the oxygen and ionize O II (Richling & Yorke 2000). In the F850LP band proplyd-1 is firstly presented with a head-tail shape in high resolution (~0.1″). The tail shows a clear cone-

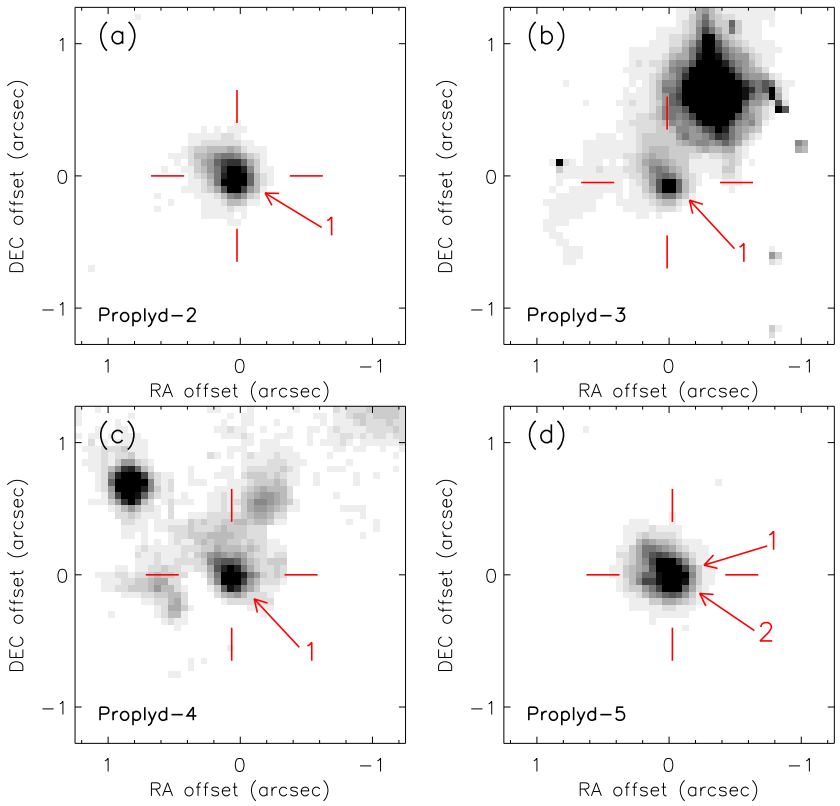

Figure 4.14: Four new photoevaporating disk candidates in Pismis 24. Panels (a)(b)(c)(d) are the images from HST in the F850LP band. Panel (a) is centered on RA=17:24:47.65, DEC=-34:11:25.4; panel (b) is centered on RA=17:24:45.88, DEC=-34:11:24.7; panel (c) is centered on RA=17:24:46.27, DEC=-34:11:19.7; and panel (d) centered on RA=17:24:47.19, DEC=-34:12:10.8. The numbers 1, and 2 on each panel are corresponding to Pis 24-1, and Pis 24-2. The arrow on each panel shows the direction from Pis 24-1 or Pis 24-2 to each proplyd.

like peak shape with extended diffuse emission, similar to the appearance in Hα. We estimate the length from the head to the tail of proplyd-1 in the F850LP band to be $\sim$1.″, corresponding to a projected length of $\sim$ 1700 AU, comparable to the values found in simulations (Richling & Yorke 2000).

Proplyd-1 was also detected in our VIMOS images, with fluxes of 20.02±0.11 mag in R band, and 19.17±0.07 mag in I band. Its R-I color of 0.85 mag is unusually blue compared to that expected for young low-mass star in Pismis 24: for a 1 $M_{\odot}$ star with an age of 1 Myr and behind 5.5 mag of visual extinction we would expect an R-I color of $\sim$2 mag from PMS evolutionary models (Dotter et al. 2008). The comparatively blue R-I color of Proplyd-1 could be due to (1) a dominant contribution of the Hα emission line from the photoevaporating disk to the R-band flux; (2)the scattering effect by the evaporation circumstellar disks. Proplyd-1 is not present

in the 2MASS catalog. In the GLIMPSE catalog it is detected in the [3.6], [4.5], and [5.8] bands, with fluxes of 11.13±0.09 mag, 10.54±0.31 mag, and 9.30±0.10 mag, respectively. These infrared fluxes indicate that proplyd-1 still has an optically thick inner disk.

In addition to the previously known proplyd-1, we find four new proplyd candidates in the F850LP image, hereafter named Proplyd-2, Proplyd-3, Proplyd-4, and Proplyd-5, which are shown in Fig. 4.14. Proplyd-2, 3, 4 show tails pointing away from Pis 24-1, suggesting that the latter is responsible also for these proplyds. Careful inspection of proplyd-5 reveals two tails, a long one pointing away from Pis 24-2 and a shorter tail pointing away from Pis 24-1. This suggests that proplyd-5 is being photoevaporated by two neighboring massive stars simultaneously, with Pis 24-2 dominating in this case. In our VIMOS images we have detected proplyd-2 and proplyd-5. Similar to proplyd-1, they show unusually blue R-I colors (0.51 mag and 0.28 mag, respectively), confirming their proplyd nature. The projected distances from proplyds 2-5 to their ionizing stars are around 0.3-0.5 pc, suggesting that massive stars like Pis 24-1 and Pis 24-2 can directly photoevaporate disks out to distances of at least 0.5 pc.

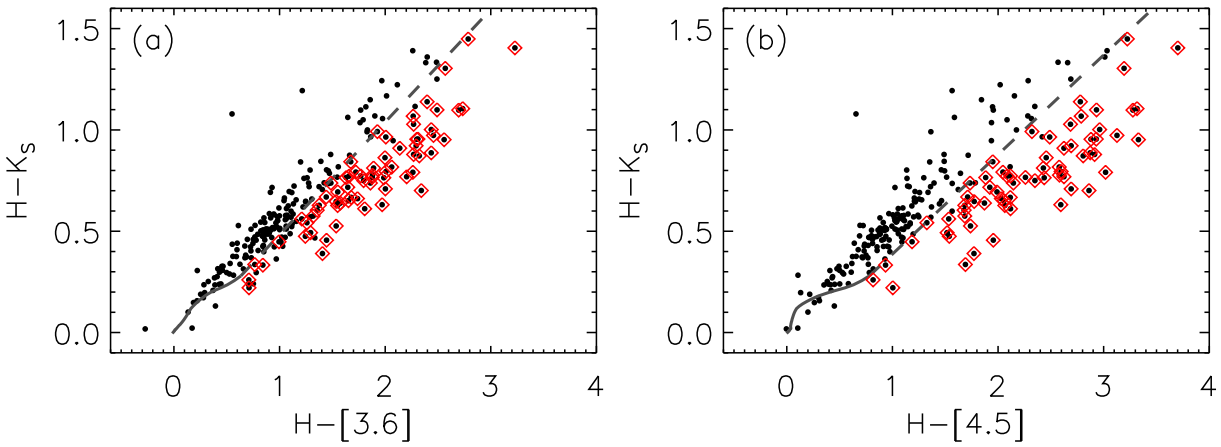

Figure 4.15: (a) H-K_s vs. [H]-[3.6] and (b) H-K_s vs. [H]-[4.5] color-color diagrams for X-ray emitting stars in Pismis 24 cluster. The filled circles represent all the members of Pismis 24 cluster detected in H, K_s, [3.6], and [4.5] bands. The dashed lines and arrows represent the extinction laws. The arrow length denotes one magnitude of extinction in the K band. The open diamonds show the cluster members with inner disks which show excess emission in both [3.6] and [4.5] bands.

(b) The disk frequency in Pismis 24

We will now analyze the "disk frequency" in the Pismis 24 star cluster, i.e. which fraction of cluster members (still) show near-infrared excess emission indicative of optically thick material in the *inner* disk regions. We will use the H-K_s vs. H-[3.6] and H-K_s vs. H-[4.5] color-color

diagrams to identify stars with inner disks. These colors are more suitable than the classical IRAC [3.6]-[4.5] vs. [5.8]-[8.0] color-color diagram in the case of Pismis 24, since requiring objects to be detected in *all* IRAC bands causes the sample to be strongly biased towards relatively luminous sources and sources with disks. By including only the data from the two most sensitive IRAC bands we get a much more representative sample. Exclusion of the 5.8 and 8.0 μm IRAC bands does cause potential transition disk objects, that show infrared excess only in the long wavelength IRAC bands, to be excluded from the disk frequency statistics. In Fig. 4.15 we show the colors of all 279 cluster members that are detected in each of the H, K_s, [3.6], and [4.5] bands. We identify stars as having inner disks if they show excess emission in both the IRAC [3.6] and [4.5] bands. In total, 83 cluster members harbor inner disks, yielding an inner disk frequency of 30±3% in Pismis 24.

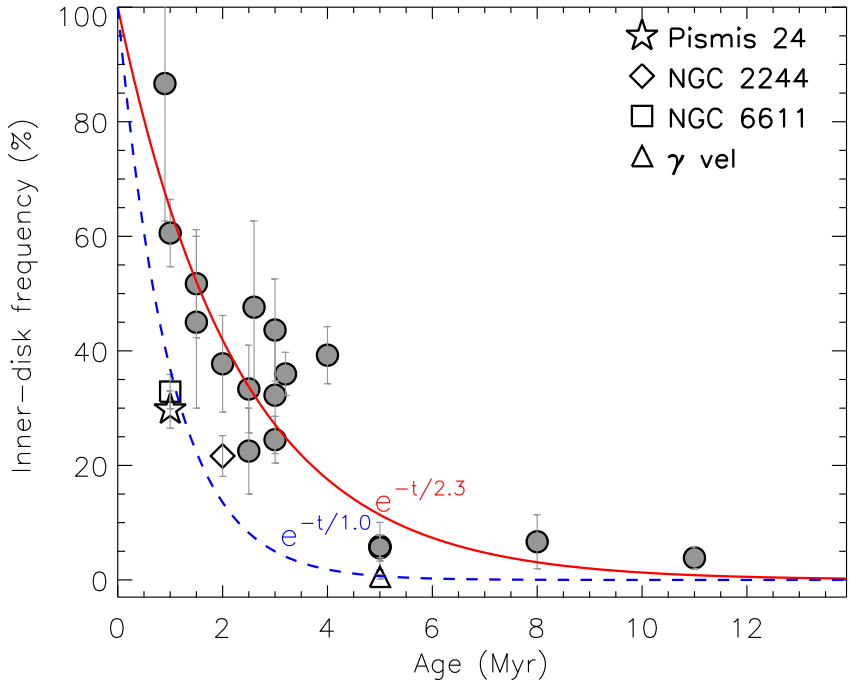

Figure 4.16: The inner disk frequencies (f_{id}) in different star formation regions as a function of age. The frequencies are estimated from H-K_s vs. [K]-[3.6] and H-K_s vs. [K]-[4.5] color-color diagrams. The frequencies are estimated for stars with masses larger than 0.5 $M_{\odot}$, which is the mass completeness limit for Pismis 24 cluster. The dashed line is the fit to inner disk frequencies of the four clusters, Pismis 24, NGC 2244, NGC 6611, and γ vel, which gives f_{id}=$e^{-t/1.0}$, whereas the solid line is the fit to all other star formation regions, which is $f_{id} = e^{-t/2.3}$. Here t is the age in Myr.

For comparison we estimate the inner-disk frequencies of YSOs in other star formation regions (SFRs) using the same diagnostic as employed for the Pismis 24 cluster. A detailed description for each SFR is presented in Appendix 4.4. In order to make a meaningful comparison we should

calculate the disk frequency statistics for YSOs in the same mass range in each region since disk frequencies can depend on stellar mass (e.g. Chapter 3; Lada et al. 2006; Luhman et al. 2008a; Hernández et al. 2007b), especially for YSO populations older than 3 Myr (Kennedy & Kenyon 2009). The lowest mass that we use for selecting YSOs for our comparative disk frequency study is set by the mass completeness limit of the Pismis 24 data. In the latter cluster the mass completeness is mainly limited by the 2MASS H and K_s band data. Given a foreground extinction of Av∼6 mag, the 2MASS H and K_s band magnitude limits of ∼15 and 14.3 mag (10σ), and an age of 1 Myr for Pismis 24, the mass completeness for detection of the photospheric emission in the 2MASS data is approximately ∼0.5 $M_{\odot}$, and we will therefore consider only objects with masses above this limit in our comparative study. The resulting inner-disk frequencies ($f_{\rm id}$) of each SFR as a function of their ages is shown in Fig. 4.16. For comparison we also plot the age-dependency of the *accretor frequency*, which is also proxy for the presence of material in the inner disk, as obtained by Fedele et al. (2010) by fitting an exponential profile to the observed accretor frequencies of a number of star forming regions. In most SFRs the inner disk frequency that we derive matches the accretor frequency behavior derived by Fedele et al. (2010) very well. Four clusters, however, show substantially lower inner disk frequencies: Pismis 24, NGC 2244, NGC6611 and γ vel clusters. These four clusters all harbor extremely massive stars (see Table 4.4).

To see whether the inner disk frequency depends on location within the Pismis 24 cluster we calculated it in four projected distance bins from Pis 24-1 (the dominant UV-photon emitter): ≤0.6 pc, 0.6-1.2 pc, 1.2-1.8 pc, and 1.8-2.4 pc. The result is shown in Fig. 4.17. In the innermost distance bin the disk frequency is ∼19%. In the other three bins it is approximately constant at a substantially higher value of ∼36-38%. The decrease of the disk frequency near Pis 24-1 is a $\sim 2\sigma$ effect in our data. Decreased disk frequencies in the immediate vicinity of massive stars have been found in several massive clusters, e.g. NGC 2244, NGC 6611, and the Arches cluster (Balog et al. 2007; Guarcello et al. 2009; Stolte et al. 2010), suggesting rapid destruction of circumstellar disks in such environments.

In Fig. 4.18, we show the disk frequency as a function of stellar mass in the Pismis 24 cluster. The adopted mass for each star is the median value of its mass probability function (see section 4.2.2(3b)). As shown in Fig. 4.18, the disk frequency increases with decreasing stellar mass in Pismis 24. This is different from the behavior in some small clusters or isolated SFRs at similar ages of ∼1 Myr (e.g. NGC 2068/2071, L1641, and Taurus, Chapter 3; Luhman et al. 2010), but similar to the one in some relative older clusters (e.g. IC 348, Tr 37, and IC 1795, Kennedy & Kenyon 2009Roccatagliata et al. 2010, submitted). Within Pismis 24 we have compared the spatial distribution of cluster members of sub-solar mass with that of members of 1 $M_{\odot}$ or more. The two distributions are not significantly different, and therefore we cannot attribute the lower disk frequency around YSOs with masses above 1 $M_{\odot}$ to comparatively close proximity to the

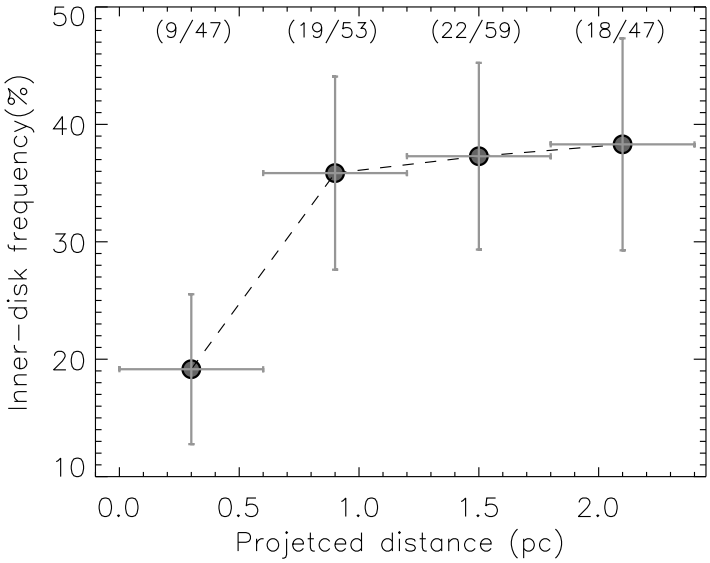

Figure 4.17: The frequencies of inner disk as a function of projected distance from Pismis 24-1, the most massive stellar system in Pismis 24 cluster. Absolute number counts for each bin are given at the top of the panel.

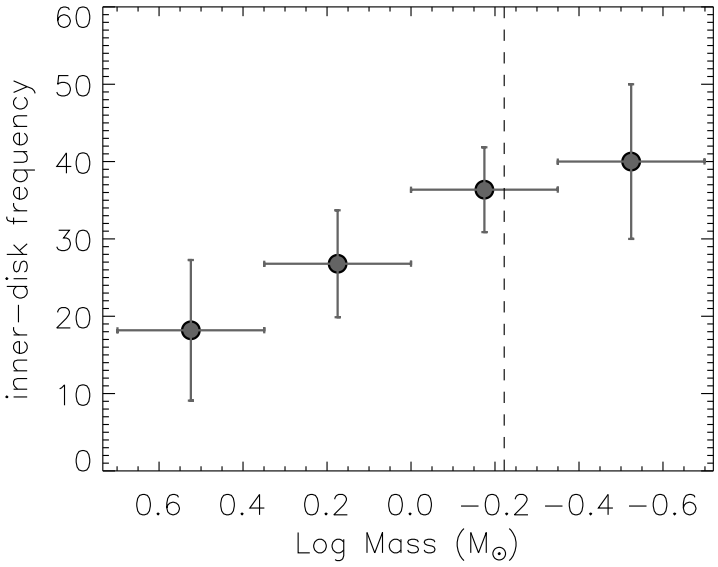

Figure 4.18: The frequencies of inner disk as a function of stellar masses. The dashed line marks the completeness limit of the sample.

massive stars. Our observations suggest that the disks around ∼solar and intermediate mass stars evolve faster than those around lower mass stars in massive clusters like Pismis 24, for reasons that we do not presently understand.

4.3 Discussion

4.3.1 Disk evolution in Pismis 24

As shown in Fig. 4.16 the inner disk frequencies ($f_{\rm id}$) in most SFRs follow the evolutionary function $f_{\rm id} = e^{-t/2.3}$ to good approximation. Clusters in which extremely massive stars are present (Pismis 24, NGC 244, NGC 6611, and γ Vel), however, show a substantially quicker reduction of the inner disk frequency. If we fit the disk frequency as a function of age for the latter four clusters using the same functional shape $f_{\rm id} = e^{-t/\tau_0}$, we find $\tau_0 \sim 1.0$ Myr. Therefore, the average inner disk lifetime in these massive cluster is only half of that in clusters without extremely massive stars, for which we find $\tau_0 \sim 2.3$ Myr. The disks in these massive clusters are evidently rapidly dissipated, but which physical mechanism is driving this development? A range of processes have been proposed to explain disk dissipation, including viscous evolution, gravitational interactions, and photoevaporation by the central star or neighboring massive stars. The latter two mechanisms, stellar encounters and photoevaporation, are potential explanations for the comparatively low disk frequency in massive clusters like Pismis 24.

(1) Stellar encounters

The stellar encounter mechanism involves a circumstellar disk and a nearby passing star. Mutual gravitational interaction can induce a significant loss of mass and angular momentum from the disk (Pfalzner et al. 2006; Olczak et al. 2006; Pfalzner & Olczak 2007; Olczak et al. 2010). Simulations of stellar encounters in a cluster environment like the ONC have shown that stellar encounters are a potentially very important disk dissipation mechanism in the first several Myrs. When the stars involved in the encounters have unequal masses the disks are most affected. Therefore, in dense clusters like the ONC, the massive stars dominate the disk-mass loss (Olczak et al. 2006). The disks around these massive stars are also dissipated more quickly than those around intermediate- and low-mass stars (Pfalzner et al. 2006). Simulations show that, when the disk radii are scaled with the stellar mass, the disk frequencies decrease with increasing stellar masses due to stellar encounters in such cluster environments (Pfalzner et al. 2006). New calculations simulating a range of cluster environments show that the disk mass loss increases with the number density of stars in the cluster, but is not affected by the total number of cluster

members (Olczak et al. 2010). In less dense clusters, i.e. four times sparser than the ONC, the simulations still show substantial disk dissipation due to stellar encounters (Olczak et al. 2010).

We estimated the number density of stars in Pismis 24 from the members selected from the Chandra observations. The X-ray data are complete down to ~0.4 $M_{\odot}$, and the IMF of Pismis 24 closely resembles a standard IMF as that of the Trapezium cluster in the mass range accessible to observations. In order to calculate the total number density of stars with masses larger than 0.08 $M_{\odot}$ (the minimum mass used in the simulations of Olczak et al. 2010), we assumed that the IMF of Pismis 24 follows the standard curve also at masses below 0.4 $M_{\odot}$, where we do not have proper observational constraints. We furthermore assumed the cluster members to be spherically distributed. In this way we derived the number density of stars to be approximately 1.5×10^4 pc^{-3} within 0.1 pc around Pis 24-1, and 2.1×10^3 pc^{-3} within 0.3 pc around Pis 24-1, somewhat lower than those in ONC, where the number density of stars to be approximately 2.4×10^4 pc^{-3} within 0.1 pc around the ONC center, and 3.1×10^3 pc^{-3} within 0.3 pc around the ONC center. Simulations predict that the disk frequency is reduced to approximately 85% of the assumed initial disk frequency of 100% due to the stellar encounters in clusters with such number densities of stars (Olczak et al. 2010). Even though this decrease is substantial, it falls short of explaining the observed inner disk frequency within 0.6 pc around Pis 24-1, which we have shown to be only 19±6%. Therefore, stellar encounters alone can hardly account for the quick dissipation of disks in the Pismis 24 cluster.

(2) Photoevaporation

In a cluster environment like Pismis 24, where dozens of massive stars are present, photoevaporation is another mechanism to dissipate the circumstellar disks around the intermediate- and low-mass cluster members. UV photons from massive stars can heat the gas in the disk surface to temperatures at which the sound speed of the gas exceeds the velocity needed to escape the gravitational potential well of the star, inducing a gas flow away from the disk (Johnstone et al. 1998; Hollenbach et al. 2000). In photoevaporation models a neutral gas flow from the disk surface is driven by non-ionizing FUV photons. EUV photons do not reach the disk surface because they are absorbed by the outflowing material. Further from the disk, where the densities are lower, EUV photons can penetrate and ionize the outflowing gas, forming an ionization front (Johnstone et al. 1998; Störzer & Hollenbach 1999; Richling & Yorke 2000).

The mass-loss rates from photoevaporating disks depend on a number of parameters, in particular on the intensity of the impinging UV field (especially the FUV flux), the disk radii, and the stellar masses. Model calculations predict the mass loss rates from disks due to photoevaporation in the Trapezium cluster to be on the order of 10^{-7} $M_{\odot}$ yr^{-1} up to a projected distance of 0.2 pc away from the ionizing massive star θ^1C Ori, which has a spectral type of O6 (Johnstone et al.

1998; Störzer & Hollenbach 1999; Henney & Arthur 1998). Spectroscopic observations have confirmed these mass-loss rates (Henney & O'Dell 1999). The photoevaporation process effectively dissipates circumstellar disks from the outside inward, up to the gravitation radius (r_g), where the escape velocity equals the sound speed, which in turn is determined by the UV heating (Hollenbach et al. 2000). For a star with a mass of 0.5 $M_\odot$ the gravitation radius is estimated to be ~60 AU, assuming that the disk surface is heated to 1000 K (Adams et al. 2004). Adams et al. (2004) show that when the disk radius is less than r_g the mass loss rates are still considerable down to 0.2 r_g.

In the Pismis 24 cluster there are tens of massive stars and the total FUV photons luminosity is estimated to be ~10 times that of Trapezium cluster. Therefore we expect photoevaporation to be very effective in dissipating the outer disks, down to several tens of AU, around young stars within a distance of 0.6 pc from the center of Pismis 24. The timescale for this dissipation could be less than 0.5 Myr, assuming an initial disk mass of 0.05 $M_\odot$ and mass-loss rates similar to those observed in the Trapezium cluster.

Adams et al. (2004) predict that the photoevaporation-induced mass-loss rates become very low at disk radii below 0.2 r_g. It is almost impossible to photoevaporate disks down to radii $r \leq 0.1 r_g$ if the heating of gas in the disk surface is dominated by FUV photons that heat the gas to ~ 1000 K (Hollenbach & Adams 2004). When also EUV photons can reach the disk surface the gas temperature can reach ~10^4 K. If recombination dominates the opacity to EUV photons the mass-loss rate is given by the following approximate formula:

$$\dot{M} \approx 9 \times 10^{-8} \left(\frac{\Phi}{10^{49}\ \mathrm{s}^{-1}}\right)^{1/2} \left(\frac{d}{10^{17}\mathrm{cm}}\right)^{-1} \left(\frac{r_\mathrm{d}}{30\mathrm{AU}}\right)^{3/2}\ M_\odot yr^{-1} \tag{4.1}$$

where Φ is the EUV photon flux, d is the distance of the circumstellar disk from the ionizing massive star, and r_d is the disk radius (Johnstone et al. 1998; **?**). In the Pismis 24 cluster the EUV fluxes are dominated by the triple system Pis 24-1, from which the EUV photon flux is estimated to be ~10^{50} photons per second. For a circumstellar disk with an initial mass of 0.05 $M_\odot$ an outer radius of 100 AU, and a surface density profile $\Sigma \approx r^{-3/2}$, there will be ~3.5×10^{-3} $M_\odot$ of material within 1 AU, where the hot dust causing the excess emission in the IRAC [3.6] and [4.5] bands resides. To photoevaporate this amount of material at sub-AU radii within a time span of 1 Myr requires a mass-loss rate of ~3.5×10^{-9} $M_\odot$ yr^{-1}induced by EUV photons, which is available only very close to Pis 24-1, within 0.02 pc. Thus, the rapid dissipation of inner disks at radii below ~1 AU around Pismis 24-1 cannot be explained by the direct effect of photoevaporation alone, since most of the cluster members are at distances >> 0.02 pc. Additional physics is required to explain the low inner disk frequency in the Pismis 24 cluster.

Clarke (2007) couples the mass-loss profiles from Adams et al. (2004) with a viscous disk evolution model. In her model, the inner parts of the circumstellar disk are continuously being accreted onto the central star while the outer part is dissipated by the photoevaporation due to UV irradi-

ation from nearby massive stars. Once the outer parts of disk have been stripped of their gas in the photoevaporative flow, the inner disk can no longer be replenished by material from larger radii. The inner disk is then quickly drained by viscous accretion onto the central star. Adopting an accretion rate of 2.5×10^{-8} $M_{\odot}\,\mathrm{yr}^{-1}$, the median accretion rate for ∼solar mass T-Tauri stars in the Taurus star-forming region (Najita et al. 2007), viscous accretion can drain the inner disk within a radius of 30 AU within 1 Myr, given an initial circumstellar disk mass of 0.05 $M_{\odot}$, a disk radius of 100 AU, and a surface density profile $\Sigma \approx r^{-3/2}$. Therefore, the combination of viscous accretion and photoevaporation can effectively dissipate the circumstellar disks of young stars within a radius of ∼0.6 pc from the center of Pismis 24 cluster. The dissipation timescale can be less than 1 Myr, depending on the initial disk masses.

The mass-loss rates from photoevaporation are less sensitive to the intensity of the FUV field than on the disk radius. When the FUV fluxes decrease by a factor of ten the mass-loss rates are reduced only by a factor of 2-3 (Adams et al. 2004). Therefore the mass-loss rate from a circumstellar disk induced by photoevaporation can still be $3\text{-}5\times10^{-8}$ $M_{\odot}\,\mathrm{yr}^{-1}$ at a distance of 2 pc from the massive stars. This is still a substantial mass loss rate and a disk with a mass of 0.05 $M_{\odot}$ can be dissipated on a timescale of ∼1 Myr. For disks that are located at substantially larger distances from the massive stars, direct photoevaporation is likely of minor importance. Still, the radiation from the massive stars substantially increases the local EUV field and can contribute importantly to the ionization of material in the disk surface layers. This may in turn strongly increase the viscosity of the disk material through the magneto-rotational instability, of which occurrence and strength depends on the ionization fraction inside the disk (Stone et al. 2000), and lead to increased accretion rates and reduced disk dissipation timescales.

4.3.2 Hot inner disk evolution and transition disks

The inner disk frequencies (f_{id}) in clusters that do not harbor extremely massive stars (see Sect. 4.2.2(4b) and Fig. 4.16) follow the approximate age dependency $f_{\mathrm{id}} = e^{-t/2.3}$, where t is the cluster age in Myr. The inner disk frequencies are estimated using H-K_s vs. H-[3.6], and H-K_s vs. H-[4.5] color-color diagrams, and thus sources that show infrared excess *only* at wavelengths longer than ∼5 micron are considered to be (inner-) "diskless" in the f_{id} statistic. This means that a substantial fraction of the so-called "transition disks" (TD) are not included in the numerator of the f_{id} statistic as we apply it. If one would include all four IRAC bands in calculating the disk frequency[2], sources without excess emission in the 3.6 and 4.5 μm IRAC channels but

[2]In Pismis 24 this would bias the sample towards comparatively luminous sources or sources with optically thick disks due to the limited sensitivity in the IRAC 5.8 and 8.0 μm bands, and hence we use data from the more sensitive 3.6 and 4.5 μm bands only. In more nearby clusters the long wavelength IRAC channels are sufficiently sensitive to detect "naked" photospheres down to substantially lower stellar masses, and meaningful disk frequencies can be

with infrared excess in the 5.8 or 8.0 μm IRAC band would be counted as having a disk. This approach was chosen by Fedele et al. (2010), who find a decay of the disk frequency with cluster age according to $f_{\rm disk} = e^{-t/2.9}$. Note that here we distinguish between the "inner disk frequency" $f_{\rm id}$, as traced by the data at $\lambda \lesssim 5$ μm, and the "disk frequency" $f_{\rm disk}$ as traced by observations at $\lambda \lesssim 9$ μm[3]. Thus, the disk frequency $f_{\rm id}$ as traced only by the IRAC [3.6] and [4.5] bands decreases more quickly than $f_{\rm disk}$ as calculated including also the [5.8] and [8.0] channels. The difference can be attributed to the presence of transition disks, and from the above-mentioned relations we can easily calculate which fraction of the disk population is made up by the transition disks: $f_{\rm TD} = \frac{e^{-t/2.9} - e^{-t/2.3}}{e^{-t/2.9}}$, where t is in units of Myr. In the following we will compare this function to $f_{\rm TD}$ values given in the literature.

Muzerolle et al. (2010) use spectral indices between photometry in various IRAC and MIPS bands to select TDs in clusters and aggregates in the NGC 1333, L1688, NGC 2068/2071, IC 348, Ori OB1a/25 Ori and OB1b, and η Cha. They use excess emission in the IRAC 5.8 μm and MIPS 24 μm bands to divide the TDs into three subclasses: classical TDs, weak excess TDs, and warm excess TDs. The classical TDs show little or no excess emission in [5.8] band and strong excess emissions in the MIPS [24] band. Weak excess TDs are similar to classical TDs in the IRAC [5.8] band, but are comparatively faint in the MIPS [24] band. The warm excess TDs show obvious excess emission in the IRAC [5.8] band. When comparing the fraction of the disk population that is considered to be a transition disk ($f_{\rm TD}$) we only count the classical and weak excess TDs in the sample of Muzerolle et al. (2010), because warm excess TDs usually show substantial excess emission in the short wavelength IRAC bands and are thus not counted as transition disks in our $f_{\rm TD}$ statistic. In Fig. 4.19 we plot our derived $f_{\rm TD}$ and compare it with the TD fractions in different SFRs from Muzerolle et al. (2010). We find good agreement between $f_{\rm TD}(t)$ curve that we derive from the comparison of $f_{\rm id}(t)$ and $f_{\rm disk}(t)$ and the more direct determination of $f_{\rm TD}(t)$ by Muzerolle et al. (2010).

Among the whole TD sample of Muzerolle et al. (2010) there are 44% classical TDs. By scaling our $f_{\rm TD}$ function by a factor of 0.44, we obtain the fraction of the total disk population constituted by classical transition disks: $f_{\rm CTD} = 0.44\ f_{\rm TD}$. In Fig. 4.19 we also show $f_{\rm CTD}$, which well matches the $f_{\rm CTD}$ observed by Muzerolle et al. (2010).

calculated using data from all four IRAC bands.

[3]In the current discussion we adopt the latter statistic as the *total* disk frequency, thereby ignoring the fact that some objects exist that have no infrared excess at $\lambda \leq 9$ μm but do show excess emission at e.g. 24 μm. Therefore, the $f_{\rm disk}$ statistic gives only a lower limit to the actual frequency of circumstellar disks. This approach is brought about by practical limitations: the availability and sensitivity of longer wavelength (MIPS) data is substantially less favorable than for the IRAC data. Also crowding/confusion is more problematic at long wavelengths, in particular for distant clusters like Pismis 24

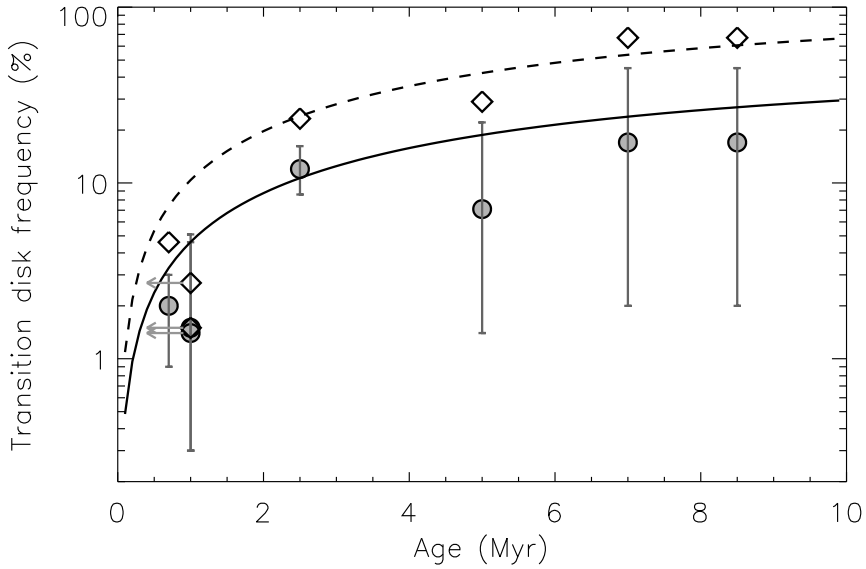

Figure 4.19: The frequencies of TDs (diamonds) and classical TDs (filled circles) among the disk population in different clusters/aggregates, including NGC 1333, L1688, NGC 2068/2071, IC 348, OB1b, η Cha, OB1a/25 Ori. The observational data are obtained from Muzerolle et al. (2010), besides the age of NGC 2068/2071 which is from Chapter 3. The left-pointing arrows indicate that the ages for NGC 1333, and L1688 are up-limits. The TD sample include classical TDs and weak excess TDs from Muzerolle et al. (2010). The dashed line is the predicted frequency ($f_{\rm TD} = \frac{e^{-t/2.9}-e^{-t/2.3}}{e^{-t/2.9}}$) of TDs among all the disk population as a function of age. The solid line is the predicted frequency ($f_{\rm CTD} = 0.44\ f_{\rm TD}$) of classical TDs among all the disk population as a function of age.

4.4 Summary

We have performed a detailed observational study of the massive star-forming region NGC 6357, with a special focus on the central cluster Pismis 24. Our study includes X-ray data from the literature, optical photometry and spectroscopy performed with VLT/VIMOS, HST archival data, infrared data from the literature as well as our own Spitzer imaging of the central cluster, and millimeter data.

Using infrared color-color diagrams we have searched for disk-bearing YSOs in the whole NGC 6357 complex. These are concentrated in three clusters: the known Pismis 24 cluster and two newly discovered clusters that are associated with the known bubbles CS 59 and CS 63.

We have re-assessed the distance to Pismis 24 by fitting model isochrones to six O-type stars in the HR diagram. We find good fits for isochrones of 1 to 2.7 Myr and distances of 1.7±0.2 kpc.

This puts the NGC 6357 complex at the same distance as the NGC 6334 complex, its close neighbor on the sky, suggesting that both clouds are physically related. Other evidence in the literature supports this notion.

Using high resolution HST imaging we find that the massive star Pis 24-18 is a binary system. Positional information suggests that the secondary component is responsible for the X-ray emission detected from this system.

We have performed an optical imaging and spectroscopic survey of Pismis 24, the main cluster in the NGC 6357 region, using X-ray observations to identify the cluster members. Using a combination of optical photometry and spectroscopy we estimate stellar masses, ages, and foreground extinction values of the brighter part of the population (the "spectroscopic sample"). Using the well defined extinction distribution observed in the spectroscopic sample we have derived the mass and age probability function of a much larger sample of young stars for which we have good photometry but that were too faint for spectroscopy. We find that the cluster mass function of Pismis 24 closely resembles the IMF of the Trapezium cluster down to the completeness limit of our data of $\sim$0.4 $M_{\odot}$. The median age of the cluster members is approximately 1 Myr.

We have detected five proplyds in the Pismis 24 cluster, four of which were previously unknown. The massive stellar system Pis 24-1 is the main source responsible for four of the proplyds. The fifth proplyd shows two tails: one pointing away from Pis 24-1 and the other from Pis 24-2, suggesting that this object is being photoevaporated from two directions simultaneously. Adopting a distance of 1.7 kpc for Pismis 24 cluster we estimate the projected distances of these proplyds from their ionizing sources to be $\sim$0.4-0.5 pc.

We employed H-K_s vs. H-[3.6] and H-K_s vs. H-[4.5] color-color diagrams to statistically investigate the disk frequency in the Pismis 24 cluster. We find that the disk frequency in Pismis 24 is much lower than that in clusters of similar age but without extremely massive stars. Three other clusters harboring extremely massive stars also show comparatively low disk frequencies. The dissipation timescale for the inner disks regions in massive clusters like Pismis 24 is only roughly half of the value observed in the clusters/star-forming regions without extremely massive stars.

We also find that the disk frequency depends on the location of objects within the Pismis 24 cluster: within 0.6 pc from the dominant massive stellar system Pis 24-1 the disk frequency is substantially lower than at larger radii. This provides direct observational evidence that extremely massive stars can affect the evolution of disks around intermediate- and low-mass stars in their vicinity. The observed disk frequency increases with decreasing stellar mass.

The disk frequency as traced by excess emission in the IRAC [3.6] and [4.5] bands only decreases more quickly with cluster age than the disk frequency derived when including also the [5.8] and [8.0] bands. The difference is due to the transition disk population that shows no infrared ex-

cess in the short-wavelength IRAC bands but does have excess emission in the long-wavelength bands. From these observations we derive the occurrence of transition disks among the total disk population, as a function of time, which agrees well with previously published statistics.

Appendix

(1) Disk frequencies in different star formation regions

In table 4.4, we list each SFR used in Fig 4.16. In the table, there are 18 SFRs, of which median ages range from ~0.7-11 Myr. To allow a comparative study on disk frequencies of different SFRs, we only select YSOs with masses ≥0.5 $M_{\odot}$in each SFR since the disk frequencies show dependence on stellar masses. To do this in each SFR, we use H-band magnitudes as a measure of YSO masses. For each SFR, we estimate the H-band magnitude for a PMS star with the median age of the SFR from the PMS evolutionary tracks from Dotter et al. (2008), and use this H-band magnitude as lower limit to select YSOs in that SFR. The H-band limit magnitude for each SFR is listed in Table 4.4. We obtain photometry of each YSO in H, Ks, [3.6], and [4.5] bands. The H and Ks band photometry are from 2MASS survey, and the photometry in IRAC [3.6] and [4.5] bands from the literature and our work. The references for that the IRAC [3.6] and [4.5] photometry come from are listed in Table 4.4. For the four SFRs, ONC, OMC 2/3, Mon R2, and NGC 2244, their photometry in IRAC bands come from our work. For these SFRs, we download BCD images from Spitzer archive, mosaiced the images with Mopex software, and performed psf-fitting photometry on the mosaiced images with IDL codes described in Chapter 3. Similar to what we have done for Pismis 24 cluster, we estimate the disk frequency of each SFR using H-Ks vs. H-[3.6], and H-Ks vs. H-[4.5] color-color diagrams. The YSO is considered as having an inner disk if it shows excess emission in [3.6] and [4.5] bands. The resulting disk frequency of each SFR is listed in table 4.4.

Table 4.4: the fractions of YSO with [3.6] and [4.5] band excess emissions in different SFRs. Column 3: the median age of each SFR. Column 4: the references for the median age of SFR. Column 5: the spectral types for the most massive star in each SFR. Column 6: the criteria for YSO selection. X: stars with X-ray emission, IR: stars with excess emission at infrared bands, Hα: Hα photometry, Sp: members confirmed by spectroscopy, PM: photometric members. Column 7: the references for YSO selections. Column 8: the fractions of stars with excess emissions in [3.6] and [4.5] bands. Column 9: H-band magnitude limit. Column 10: the references for Spitzer IRAC data.

(1)	(2)	(3)	(4)	(5)	(6)	(7)	(8)	(9)	(10)
	Dis	Age			YSO		DF	Limit	
Name	(pc)	(Myr)	Ref	Spt	criteria	Ref	(%)	(mag)	IRAC
Taurus	140	1.5	(1)	...	X, IR	(2)	52±9	8.9	(2)
IC 348	315	2.5	(3)	B5 V	X, SP	(3)	23±8	11.0	(3)
NGC 2068/71	450	0.9	(4)	B1.5 V	SP	(5)	87±24	10.8	(4, 5)
ONC	450	1.0	(6)	O6 V	X	(7)	61±6	11.1	(8)
OMC 2/3	450	3.0	(9)	...	X	(10)	44±9	11.4	(8)
Ori 1b	440	5.0	(11, 12)	O9.5 V	SP	(13)	6±2	12.3	(13)
25 Ori	330	8.0	(11, 12)	B1 V	SP	(13)	7±5	12.0	(13)
λ Ori	400	5.0	(14)	O8 III	OP, IR, SP	(14)	6±4	12.1	(14)
NGC 7160	900	11.0	(15)	B1 II-III	SP	(15)	4±2	14.5	(16)
Cep OB 3b	725	2.5	(17)	O7 V	X	(17)	33±8	12.4	(17)
Cep B+S155	725	1.5	(17)	O7 V	X	(17)	45±15	12.8	(17)
NGC 2264	800	2.5	(18)	O7 V	X, Hα, IR, Sp	(19)	36±4	13.0	(19)
NGC 2362	1480	5.0	(20)	O9 Ib	X, IR, SP	(21)	6±2	14.9	(21)
Mon R2	830	2.0	(22)	...	X	(23)	38±8	12.9	(8)
NGC 2244	1400	2.0	(24)	O5 V	X	(25)	22±4	14.0	(8)
NGC 6611	2000	1.0	(26)	O5 V	X	(26)	33±3	14.3	(27)
Cha I	165	2.6	(28)		SP, IR	(29)	48±15	9.6	(29)
σ Ori	440	3.0	(30)	O9.5 V	X, IR, SP, PM	(30, 31)	24±4	11.9	(30)
NGC 7129	1000	3.0	(31)	...	X	(32)	32±10	13.7	(32)
γ vel	350	5.0	(33)	WC	X, PM	(33)	0.5±0.4	11.8	(33)
Tr 37	900	4.0	(15)	O6.5 V	SP, X	(15,34)	39±5	13.5	(16,34)

(1) Briceño et al. (2002); (2) Luhman et al. (2010); (3) Lada et al. (2006); (4) Chapter 3; (5) Flaherty & Muzerolle (2008); (6) Hillenbrand (1997); (7) Getman et al. (2005); (8) this chapter; (9) Peterson (2005); (10) Tsujimoto et al. (2002); (11) Briceño et al. (2005); (12) Briceño et al. (2007); (13) Hernández et al. (2007a); (14) Barrado y Navascués et al. (2007); (15) Sicilia-Aguilar et al. (2005); (16)Sicilia-Aguilar et al. (2006a); (17) Getman et al. (2009); (18) Sung et al. (2004); (19) Sung et al. (2009); (20) Moitinho et al. (2001); (21) Currie et al. (2009); (22) Carpenter et al. (1997); (23) Kohno et al. (2002) (24) Park & Sung (2002); (25) Wang et al. (2008); (26) Guarcello et al. (2007); (27) GLIMPSE archive data; (28) Luhman (2004a, 2007); (29) Luhman et al. (2008a); (30) Luhman et al. (2008b); (31) Hernández et al. (2007b); (32) Stelzer & Scholz (2009); (33) Hernández et al. (2008). (34) Mercer et al. (2009)

Chapter 5

Summary and Future Works

5.1 Summary

The objective of this work is to investigate the properties of young stars and their disks in qualitatively different environments: the sparse stellar association ϵ Cha, L1630N and L1641 regions of clustered and distributed star formation in Orion, and the massive cluster Pismis 24. The main achievements of this study are summarized as follows:

- **Disk evolution in different environments:** We have investigated the disk evolution in different environments, which include isolated star-forming regions, sparse stellar association, medium-size stellar clusters, and massive clusters. We find that the disks are dissipated faster in cluster environments, especially in massive clusters with early O-type massive stars.

- **Accretion rates as a function of stellar mass:** We estimated the accretion rates of a sample of young stars in L1630N and L1641, from Hα, Hβ, and He I λ5876 line luminosities. By analyzing the relationship between accretion rates and stellar masses, we found a dependence of $\dot{M}_{\rm acc} \propto M_*^{\alpha}$, with α ~3.1 in the subsolar mass range. An investigation of a large literature sample of mass accretion rate yields a similar slope of α ~2.8 in the subsolar regime, but a shallower slope of α ~2.0 if the whole mass range of 0.04 $M_{\odot} \leq M_* \leq 5\ M_{\odot}$ is included.

- **Accretion activities of transition disks:** Studies of the accretion rates of young stars in L1630N and L1641 suggest that the fraction of stars with transition disks with significant accretion activity is relatively low compared to stars which still have optically thick disks (26±11% and 57±6%, respectively). However, those transition disks that *do* show significant accretion have the same median accretion rate as normal optically thick disks (3-4$\times 10^{-9}\ M_{\odot}\ {\rm yr}^{-1}$).

- **Age distribution of various populations:** In L1630N and L1641, we find that the ages of CTTSs and WTTSs with disks are statistically indistinguishable. WTTS without disks are substantially older than the CTTSs, while the ages of the transition disk systems and the diskless WTTSs are also impossible to statistically distinguish.

- **Dust properties of protoplanetary disks surrounding cool stars:** We derived the mass-averaged sizes of amorphous silicates grains from the Spitzer IRS spectra of members in ϵ Cha. From the combination of data in ϵ Cha and in the literature for M-type pre-main-sequence stars, we find the mass-averaged sizes of amorphous silicate grains increase with the increasing accretion rates when the accretion rates $\gtrsim 10^{-9} M_{\odot}\,\mathrm{yr}^{-1}$, and become approximate constant while accretion rates $\lesssim 10^{-9} M_{\odot}\,\mathrm{yr}^{-1}$.

5.2 Future projects

In this section, I will describe the projects on which I am going to work in the future. I have obtained the data for some of these projects. I describe each project as follows:

5.2.1 Accretion behaviors of young stellar objects

The process of mass accretion onto stars is key to understanding the evolution and dissipation of circumstellar disks, as well as the process of planet formation. Theoretical and observational investigations of classical T Tauri stars (CTTS) have favored the magnetospheric accretion model for mass transfer from the circumstellar disk onto the young star. In this model, various emission lines, such as the hydrogen Balmer series, He I λ5876, Brγ, etc., are formed in the infalling magnetospheric flow. In addition, optical/ultraviolet excess continuum emission is produced in the accretion shocks. These emission lines and the excess emission can be used to estimate the accretion rates of YSOs, with the help of models or empirical relations between line luminosity and accretion luminosity.

(1) Accretion variation of young stellar objects

Previous studies have shown that the accretion rates of CTTSs with the similar masses and ages commonly scatter by up to 2 orders of magnitude, which can be due to accretion variation or differential disk properties. We have performed a multi-epoch Hα spectroscopic survey of YSOs in L1641, including YSOs with "full" or transition disks using Hectochelle/MMT. In total, we have obtained high-resolution Hα spectra for ~250 targets. Half of them have been observed at two epochs separated by an interval of one month. Further observations are scheduled for

November 2010. We will estimate the accretion rates of these targets by modeling their Hα line profiles (Muzerolle et al. 2001) or using the empirical relation between accretion rate and full width of the Hα line at 10% of the peak intensity (Natta et al. 2004). We wish to extend this study by observing more targets in L1641, as well as young stars in other star formation regions (e.g. L1630N, and IC 348) with Hectochelle/MMT. We have already performed a spectroscopic survey of L1630N before and compiled a large sample of young stars which can be input catalog for observations with Hectochelle/MMT. The cluster IC 348, with an age of 2-3 Myr, is at a very important stage of disk evolution and dissipation. By comparing variations in accretion rate in these clusters, we can investigate how these variations depend on stellar age and disk evolution.

(2) Accretion behavior of YSOs with transition disks and "full" disks

Transitional objects (TOs) have disks that are being dissipated, and may represent the end of the (giant) planet formation phase. The physical mechanism driving the dissipation process is unclear, and the roles of viscous accretion, photo-evaporation and planet formation are being intensely debated. An important diagnostics is the comparison of the accretion rate of matter onto the central star for both transition disks and less evolved classical T Tauri systems. Recent studies of the L1630 and L1641 (see Chapter 3) and Trumpler 37 (Sicilia-Aguilar et al. 2010) star-forming regions suggest that TOs that are actively accretion do so at roughly the same median rate as normal CTTSs. This is inconsistent with what Najita et al. (2007) find in Taurus, namely that the accretion rates of TOs are ~10 times lower than those of normal accreting TTS at the same disk mass. Furthermore, they find approximately the same median accretion rate of ~2-4$\times10^{-9}$ $M_{\odot}$/yr for their TOs as in Chapter 3 and Sicilia-Aguilar et al. (2010), but an accretion rate approximately 10 times higher for normal CTTSs in Taurus compared to those in the three aforementioned clusters. To investigate this apparent discrepancy, we performed a SOFI/NTT K-band spectroscopic survey of YSOs with transition disks and "full" disks in L1630, L1641, σ Ori, and λ Ori. The project was awarded 6 nights, and the observations took place in November 2009. The data are currently under reduction. We will derive the effective temperatures from the full K-band spectra and estimate the accretion rates from the Brγ emission line. With these data complemented with those from Hectochelle/MMT, we will constrain the role of the accretion in the evolution and dissipation of the disk. In addition, according to photoevaporation models, the disk can be dissipated very efficiently when the accretion rates are lower than the mass-loss rates due to photoevaporation. Therefore, studies of the accretion rates of young stars can also be used to evaluate the role of photoevaporation in the disk dissipation. I will extend these studies by applying for new observations with appropriate instruments.

(3) The scaling law of the accretion rate with stellar mass

In previous publications (Muzerolle et al. 2003, 2005; Natta et al. 2006; Garcia Lopez et al.

2006; Herczeg & Hillenbrand 2008; Gatti et al. 2008), an empirical relation has been established between the average accretion rate and the mass of the central star namely $\dot{M}_{\rm acc} \propto M_{\star}^{\alpha}$, with $\alpha \sim 2$. From our study, we have found that the dependency of the accretion rate on stellar mass actually appears to be steeper ($\alpha \sim 3$) in the sub-solar mass regime than that ($\alpha \sim 2$) in the whole mass regime (see Chapter 3). Some possible scenarios to explain this are: 1) a lower-mass disk, in which the entire column is ionized for an active magneto-rotational instability (MRI), and which thus is subject to fully viscous evolution, and gives a dependence of $\alpha \approx 2.5$; and 2) a higher-mass disk, in which thermal ionization by irradiation from the central star is dominant, causing an MRI-active surface layer of column density, which gives a dependence of $\alpha \approx 1$ (Hartmann 2006). I wish to test this scenario by measuring the accretion rates of a large sample of young stars over a range of stellar masses from brown dwarfs to intermediate-mass stars at similar ages, since the accretion rates show a decrease trend with the increasing stellar ages.

5.2.2 Disk evolution in different environments

Circumstellar disks play a key role in the formation of new stars and planetary systems. Through disks, a significant fraction of the stellar mass is accreted, while at the same time the excess angular momentum is transported outward. After the main accretion phase has ended, gas-rich circumstellar disks can survive at low accretion rates until they are dissipated. The disk dissipation process has been constrained observationally by investigating the fraction of young stars that have strong excess emission from disk material at infrared wavelengths, in clusters exhibiting a range of ages. These studies indicate that the lifetime of inner disks is a few Myr. Knowledge of the evolution of circumstellar accretion disks is pivotal to our understanding of star and planet formation; yet, despite intensive theoretical and observational studies, the disk dissipation process is not well understood. A range of processes have been proposed to explain disk dissipation, including viscous evolution, gravitational interactions, and photoevaporation by the central star or neighboring massive stars. The relative importance of these processes is still intensely debated. In some star formation regions, investigations of WTTS with ages of 1-2 Myr show that up to 50% of WTTS no longer possess inner disks. On the other hand, classical T Tauri stars, at similar ages and masses to the WTTS, still have inner disks, indicating that at least some young stars can dissipate their disks at very early ages. Studies of the relation between disks frequencies and stellar mass show that it varies from region to region. In some regions (e.g. NGC 2068/2071, Cha I, and Taurus), the frequencies of disks increase with increasing stellar mass, in other regions (e.g. Pismis 24, IC 348, Tr 37, and Orion OB1bc), the disk frequencies show a decrease trend with increasing stellar mass. The mechanism responsible for the difference is not understood. To address these questions, we need to study a large sample of well-characterized young stars.

As the major subject of my PhD study, I investigated the disk properties in several star-forming regions, including ϵ Cha association, L1630-North, L1641, and the massive cluster Pismis 24, which span a range of stellar environments from isolated star formation (parts of L1641) to the massive cluster (Pismis 24). Though I have gained much knowledge from these studies, many questions in the fields remain unresolved. Therefore, I wish to study more star-forming regions. We plan to combine the infrared data from 2MASS, Spitzer, and Herschel with the optical imaging and spectroscopy from e.g. Hectospec/MMT. We will use the infrared data to characterize the disk properties, e.g. disk masses, flared or flat geometry, the presence of inner hole, and optical imaging and spectroscopy to derive the properties of central stars (stellar masses and ages, accretion rates). Such studies will shed further light on: 1) the main mechanisms responsible for driving disk evolution and dissipation; 2) how disk evolution and dissipation are related to the properties of the central star, and local environments.

5.2.3 The nature of very low luminosity objects: are they proto-brown dwarfs?

An interesting population of very low mass protostars or proto-brown dwarfs, called "very low luminosity objects" (VeLLOs), has been discovered via observations of star-forming regions performed within the Spitzer "c2d" legacy program. Some VeLLOs were found in cores that were previously classified as "starless", based on IRAS and ISO observations. These VeLLOs show SEDs typical of protostars. Detailed radiative transfer models of them indicate that their "internal luminosities" are less than 0.1 $L_{\odot}$, where the internal luminosity is defined as the sum of the contributions of the central quasi-hydrostatic object and the accretion-induced luminosity. The inferred internal luminosities of these protostars are much lower than expected from star formation models: for a protostar with a mass of 0.08 $M_{\odot}$ (the stellar/substellar boundary), a radius of 3 $R_{\odot}$, and a mass accretion rate of $\dot{M}_{\rm acc}$~2×10^{-6} $M_{\odot}$ yr^{-1} (as predicted by the standard Shu model), the accretion luminosity alone contributes ~1.7 $L_{\odot}$. This is much brighter than the typical internal luminosities of VeLLOs, and in some extreme cases even 100 times brighter.

A possible explanation of the VeLLO objects is that the mass accretion in the very early phases of the star formation process is episodic, and that VeLLOs are in a quiescent state, i.e. not actively accreting (Kenyon & Hartmann 1995; Young & Evans 2005). Several mechanisms have been proposed to explain such episodic accretion, such as gravitational instability (Vorobyov & Basu 2005, 2006) and quasi-periodic magnetically driven outflow regulation (Tassis & Mouschovias 2005). Another idea that has been proposed to explain the VeLLO phenomenon is that the masses of the central sources are very low. VeLLOs with the lowest internal luminosity could have masses of only several tens that of Jupiter. Thus, these VeLLOs may be proto-brown dwarf candidates forming in isolation, if the mass in their envelopes is below that required to form

a star. Large surveys at (sub-) millimeter wavelengths have been performed towards the star formation regions in which our VeLLOs are located. From these observations the masses of the envelopes of these VeLLOs can be estimated

We started a project on characterizing the VeLLOs with ISAAC/VLT, for VeLLOs selected from Dunham et al. (2008). All the targets reside in nearby star-forming regions that have been imaged by the Spitzer IRAC and MIPS instruments. The project has been awarded 15 hours. The observations were done during ESO Period 85. We have already obtained low-resolution H-and K-band spectra, and medium-resolution Brγ-line spectra, for ten VeLLOs. We plan to determine the effective temperatures and surface gravity from the H- and K-band spectra, and estimate the accretion rates from the Brγ emission line. By obtaining these fundamental parameters, we can clarify the nature of the hitherto mysterious VeLLOs.

5.2.4 The role of magnetic fields in the cloud formation

With the unprecedented sensitivity of the Herschel space telescope, the filamentary density structure of molecular clouds has been revealed. Studies suggest that dense cores may originate with the fragmentation of filaments. Therefore, understanding the formation of filaments is a crucial step to understanding star formation. There are three leading scenarios of filament formation: (1) anisotropic gravitational contractions due to magnetic fields: the material collapse along the strong magnetic fields and form high-density thin layers perpendicular to fields. Projections of such layers may appear as filamentary structures perpendicular to magnetic fields; (2) anisotropic turbulence due to magnetic fields: magnetic tension can suppress turbulent energy cascade along magnetic field directions and cause turbulent eddies to elongate along magnetic field directions. MHD simulations of molecular clouds show equi-velocity filaments aligned with magnetic fields when the fields are dynamically important compared to turbulence; (3) turbulent shock: in three-dimensional simulations of supersonic turbulence, filaments are formed at the intersection of postshock sheets. Since this kind of filaments are postshock structures, they are commonly found in regions with small flow velocity, at the intersections of high-velocity patches. Both filaments and magnetic fields will be randomly oriented in this scenario.

While the the positions of filaments can be traced from dust emission or extinction maps, the directions of magnetic field lines can be traced by the polarization of dust emission and background star light. We have proposed a K-band polarimetric survey of background star light towards the clouds Aquilla, Ophiuchus, Chamaeleon, and Lupus. Extinction maps toward these molecular clouds all show an intriguing pattern: the filaments with low extinction are parallel with each other, and at the same time perpendicular to filaments with high extinction (Li et al., in preparation). Therefore, some mechanism must play an important role in shaping these filaments. We

will use the K-band polarization of background star light to trace the directions of magnetic fields in the region. The orientation correlation between filamentary clouds and magnetic fields can be used to distinguish the main mechanism responsible for the filament formation.

5.2.5 IMF of embedded young clusters

The initial mass function (IMF) is important in many astrophysical studies, and can be used to model the properties and evolution of stellar systems. Young embedded clusters are excellent laboratories for investigations of the IMF, since there is little or no loss of members due to stellar or dynamical evolution. The most direct way to construct the IMF of a young embedded cluster is to perform a photometric and spectroscopic survey of all the cluster members. One can derive the effective temperatures for all the members from the spectra, and put them on the HR diagram to estimate stellar masses and ages. Though this method is robust, it has the disadvantage that it requires spectra to be observed for a complete sample of cluster members over the entire range of stellar masses, and therefore much telescope time. Another way to derive the IMF of a young cluster is to transfer its luminosity function to a mass function. With the development of sensitive and large-format imaging arrays at near-infrared wavelengths, the near-infrared luminosity function, which span the entire range of stellar/substellar masses, can be readily constructed for many embedded stellar clusters. However, unlike the case of main-sequence stars, these luminosity functions can not be directly converted into mass functions, because the mass-luminosity relation for pre-main sequence stars is a function of time. In addition, the duration of star formation for a young cluster can be comparable to its mean age. Consequently, it is necessary to model the luminosity function with knowledge of both the star formation history (SFH) and the time-dependent PMS mass-luminosity relation in order to constrain the mass function for a young cluster from its luminosity function.

During my master study, I constructed Monte–Carlo codes to constrain the IMF from the luminosity functions of embedded young clusters, similar to the work by Muench et al. (2000). I intend to apply this method to a large sample of embedded young clusters, observed by deep near-infrared imaging surveys (e.g., UKIRT and VISTA). Details of the SFH of a cluster is basic input for the Monte Carlo simulation. In order to obtain the SFH of a young cluster, we will propose a spectroscopic survey of a subsample of cluster members, and derive the SFH from the subsample. Considering the SFH of the subsample as an approximation of the cluster SFH, we can constrain the IMF of the cluster from the Monte–Carlo simulation.

Acknowledgments

When I first came to MPIA as a visitor in June 2007, I were so fascinated with this institute, and dreamed of being a PhD student here. I thank Prof. Thomas Henning for providing me the opportunity to do my PhD research at MPIA. The time has passed so fast. Since I work here as a PhD student, it has been almost three years. During this period, there are a lot of people who have helped me on my research and life. It is a great pleasure to take this opportunity to express my deep gratitude and appreciation of all of them.

I would like to thank Prof. Thomas Henning again for giving me the skillful guidance, many important suggestions and profound comments on my work, and for refereeing my thesis. Prof. Thomas Henning has spent so much time and energy on promoting the communications between Germans and Chinese on Astronomy specifically in the field of star and planet formation, which has benefited Chinese astronomical community to a great extent. Here, I would also like to thank him for all he has done for improving Chinese Astronomy.

In particular, I would like to thank Dr. Roy van Boekel. During my first three-month visiting MPIA in 2007, he provided me the chance to join his excellent project on "Protoplanetary disk evolution in Orion's suburbs", which finally become the main part of this thesis. He also helped me to get a PhD position in MPIA. As one of my supervisors, he has spent so much time on my work. And he is always so earnest and patient to answer every question that I ask. Without his help, it would have been so difficult for me to complete this thesis in three years. Thank you, Roy! I am indebted to you forever!

I would especially like to thank Prof. Dr. Andreas Quirrenbach for being part of my thesis committee and refereeing my thesis.

During preparing this thesis, I have received the helps from Paul Boley for correcting the summary, from Oliver Porth and Boyke Rochau for translating the abstract to the German version, and from Bhargav Vaidya for correcting this acknowledgments. I am very grateful to them.

I thank Dr. Christian Fendt for accepting me as an IMPRS student, and providing me a lot of help during my study. I thank Dr. Henrik Beuther for being my adviser during the IMPRS seminar. I am grateful to Dr. Jeroen Bouwman for providing me the reduced Spitzer IRS spectra, and to Dr. Attila Juhasz for giving me his TLTD codes for analyzing the IRS spectra. Without these data and codes, I would have not been able to complete Chapter 2 of this thesis. Thanks to Dr. Aurora Sicilia-Aguilar for many useful comments on my work and proposals. I thank Prof. Kees Dullemond, Dr. Jinyoung Serena Kim, Dr. Wei Wang, Dr. Huabai Li, Dr. Andrés Carmona, and Dr. Veronica Roccatagliata for their valuable discussions, collaborations and tremendous help on my work.

I am grateful to Xuepeng Chen. When I just came to Heidelberg, he helped me settle down in a completely new environment of this institute, and also helped to find me a place to stay in Heidelberg. I thank Hsiang-Hsu Wang, Javier A. Rodón, Patrick Weise, Bhargav Vaidya, Mario Gennaro, Dading Nugroho, Mauricio Cisternas, Kasper Borello Schmidt, Yuan Wang, Chao Liu, and Xi Kang, for their help on my work and life. And, it is great fun to play table soccer with Javier, Bhargav, Mario, Mauricio, Kasper.

I am especially indebted to my wife, Tingting Li, for her love and wonderful food that she has cooked everyday. I am so sorry for that I have not taken her to travel any places in Europe since she came to Heidelberg. Hope I can make up in the near future.

There are still a lot of other people who have helped me during my study and stay in Heidelberg. To list all of their names can expand this thesis to too big size. So, I would like to thank all of them in whole.

Bibliography

Acke, B. & van den Ancker, M. E. 2006, A&A, 449, 267

Acke, B., van den Ancker, M. E., Dullemond, C. P., van Boekel, R., & Waters, L. B. F. M. 2004, A&A, 422, 621

Acke, B., Verhoelst, T., van den Ancker, M. E., et al. 2008, A&A, 485, 209

Adams, F. C. 2008, Physica Scripta Volume T, 130, 014029

Adams, F. C., Hollenbach, D., Laughlin, G., & Gorti, U. 2004, ApJ, 611, 360

Adams, F. C., Lada, C. J., & Shu, F. H. 1987, ApJ, 312, 788

Akeson, R. L., Boden, A. F., Monnier, J. D., et al. 2005a, ApJ, 635, 1173

Akeson, R. L., Walker, C. H., Wood, K., et al. 2005b, ApJ, 622, 440

Alcalá, J. M., Spezzi, L., Chapman, N., et al. 2008, ApJ, 676, 427

Alexander, R. D., Clarke, C. J., & Pringle, J. E. 2006, MNRAS, 369, 229

Allen, L. E. 1995, PhD thesis, AA(Department of Physics and Astronomy, University of Massachusetts, Amherst)

Allen, L. E., Calvet, N., D'Alessio, P., et al. 2004, ApJS, 154, 363

Alonso-Albi, T., Fuente, A., Bachiller, R., et al. 2009, A&A, 497, 117

Alves, J., Lada, C. J., & Lada, E. A. 1999, ApJ, 515, 265

Ambartsumian, V. A. 1947, in Stellar Evolution and Astrophysics (Erevan: Acad. Sci. Armenian S. S. R.)

Andre, P., Ward-Thompson, D., & Barsony, M. 2000, Protostars and Planets IV, 59

Andrews, S. M. & Williams, J. P. 2005, ApJ, 631, 1134

Anthony-Twarog, B. J. 1982, AJ, 87, 1213

Apai, D., Pascucci, I., Bouwman, J., et al. 2005, Science, 310, 834

Armitage, P. J., Clarke, C. J., & Palla, F. 2003, MNRAS, 342, 1139

Artymowicz, P. & Lubow, S. H. 1994, ApJ, 421, 651

Bally, J., Stark, A. A., Wilson, R. W., & Langer, W. D. 1987, ApJ, 312, L45

Balog, Z., Muzerolle, J., Rieke, G. H., et al. 2007, ApJ, 660, 1532

Balog, Z., Rieke, G. H., Su, K. Y. L., Muzerolle, J., & Young, E. T. 2006, ApJ, 650, L83

Baraffe, I., Chabrier, G., Allard, F., & Hauschildt, P. H. 1998, A&A, 337, 403

Baraffe, I., Chabrier, G., & Gallardo, J. 2009, ApJ, 702, L27

Barrado y Navascués, D., Béjar, V. J. S., Mundt, R., et al. 2003, A&A, 404, 171

Barrado y Navascués, D., Stauffer, J. R., Morales-Calderón, M., et al. 2007, ApJ, 664, 481

Beaumont, C. N. & Williams, J. P. 2010, ApJ, 709, 791

Beckwith, S. V. W., Sargent, A. I., Chini, R. S., & Guesten, R. 1990, AJ, 99, 924

Béjar, V. J. S., Zapatero Osorio, M. R., & Rebolo, R. 1999, ApJ, 521, 671

Benjamin, R. A., Churchwell, E., Babler, B. L., et al. 2003, PASP, 115, 953

Bertout, C., Siess, L., & Cabrit, S. 2007, A&A, 473, L21

Bessell, M. S., Castelli, F., & Plez, B. 1998, A&A, 333, 231

Bouwman, J., de Koter, A., Dominik, C., & Waters, L. B. F. M. 2003, A&A, 401, 577

Bouwman, J., Henning, T., Hillenbrand, L. A., et al. 2008, ApJ, 683, 479

Bouwman, J., Lawson, W. A., Dominik, C., et al. 2006, ApJ, 653, L57

Bouwman, J., Meeus, G., de Koter, A., et al. 2001, A&A, 375, 950

Brandner, W., Grebel, E. K., Chu, Y., et al. 2000, AJ, 119, 292

Briceño, C., Calvet, N., Hernández, J., et al. 2005, AJ, 129, 907

Briceño, C., Hartmann, L., Hernández, J., et al. 2007, ApJ, 661, 1119

Briceño, C., Luhman, K. L., Hartmann, L., Stauffer, J. R., & Kirkpatrick, J. D. 2002, ApJ, 580, 317

Burningham, B., Naylor, T., Littlefair, S. P., & Jeffries, R. D. 2005, MNRAS, 363, 1389

Calvet, N., D'Alessio, P., Watson, D. M., et al. 2005, ApJ, 630, L185

Calvet, N. & Gullbring, E. 1998, ApJ, 509, 802

Calvet, N. & Hartmann, L. 1992, ApJ, 386, 239

Calvet, N., Hartmann, L., & Strom, S. E. 2000, Protostars and Planets IV, 377

Calvet, N., Muzerolle, J., Briceño, C., et al. 2004, AJ, 128, 1294

Cardelli, J. A., Clayton, G. C., & Mathis, J. S. 1989, ApJ, 345, 245

Carey, S. J., Noriega-Crespo, A., Mizuno, D. R., et al. 2009, PASP, 121, 76

Carpenter, J. M., Meyer, M. R., Dougados, C., Strom, S. E., & Hillenbrand, L. A. 1997, AJ, 114, 198

Carpenter, J. M., Wolf, S., Schreyer, K., Launhardt, R., & Henning, T. 2005, AJ, 129, 1049

Castor, J., McCray, R., & Weaver, R. 1975, ApJ, 200, L107

Chabrier, G., Baraffe, I., Allard, F., & Hauschildt, P. 2000, ApJ, 542, 464

Chiang, E. I. & Goldreich, P. 1997, ApJ, 490, 368

Churchwell, E., Watson, D. F., Povich, M. S., et al. 2007, ApJ, 670, 428

Cieza, L. & Baliber, N. 2007, ApJ, 671, 605

Cieza, L., Padgett, D. L., Stapelfeldt, K. R., et al. 2007, ApJ, 667, 308

Cieza, L. A., Swift, J. J., Mathews, G. S., & Williams, J. P. 2008, ApJ, 686, L115

Clarke, C. J. 2007, MNRAS, 376, 1350

Clarke, C. J., Gendrin, A., & Sotomayor, M. 2001, MNRAS, 328, 485

Clarke, C. J. & Pringle, J. E. 1993, MNRAS, 261, 190

Cohen, M. & Witteborn, F. C. 1985, ApJ, 294, 345

Comerón, F., Fernández, M., Baraffe, I., Neuhäuser, R., & Kaas, A. A. 2003, A&A, 406, 1001

Covey, K. R., Ivezić, Ž., Schlegel, D., et al. 2007, AJ, 134, 2398

Currie, T. 2010, ArXiv e-prints

Currie, T. & Kenyon, S. J. 2009, AJ, 138, 703

Currie, T., Lada, C. J., Plavchan, P., et al. 2009, ApJ, 698, 1

Da Rio, N., Robberto, M., Soderblom, D. R., et al. 2010, ArXiv e-prints

Dahm, S. E. 2005, AJ, 130, 1805

Dahm, S. E. 2008, AJ, 136, 521

Dahm, S. E. & Carpenter, J. M. 2009a, AJ, 137, 4024

Dahm, S. E. & Carpenter, J. M. 2009b, ArXiv e-prints

Dahm, S. E. & Hillenbrand, L. A. 2007, AJ, 133, 2072

Dahm, S. E. & Simon, T. 2005, AJ, 129, 829

Dahm, S. E., Simon, T., Proszkow, E. M., & Patten, B. M. 2007, AJ, 134, 999

D'Alessio, P., Hartmann, L., Calvet, N., et al. 2005, ApJ, 621, 461

D'Antona, F. & Mazzitelli, I. 1997, Memorie della Societa Astronomica Italiana, 68, 807

Deharveng, L., Zavagno, A., Schuller, F., et al. 2009, A&A, 496, 177

Diolaiti, E., Bendinelli, O., Bonaccini, D., et al. 2000, A&AS, 147, 335

Dorschner, J., Begemann, B., Henning, T., Jaeger, C., & Mutschke, H. 1995, A&A, 300, 503

Dotter, A., Chaboyer, B., Jevremović, D., et al. 2008, ApJS, 178, 89

Dullemond, C. P. & Dominik, C. 2004, A&A, 417, 159

Dullemond, C. P., Hollenbach, D., Kamp, I., & D'Alessio, P. 2007, Protostars and Planets V, 555

Eisner, J. A., Chiang, E. I., Lane, B. F., & Akeson, R. L. 2007, ApJ, 657, 347

Eisner, J. A., Lane, B. F., Akeson, R. L., Hillenbrand, L. A., & Sargent, A. I. 2003, ApJ, 588, 360

Epchtein, N., de Batz, B., Capoani, L., et al. 1997, The Messenger, 87, 27

Evans, N. J., Dunham, M. M., Jørgensen, J. K., et al. 2009, ApJS, 181, 321

Fazio, G. G., Hora, J. L., Allen, L. E., et al. 2004, ApJS, 154, 10

Fedele, D., van den Ancker, M. E., Acke, B., et al. 2008, A&A, 491, 809

Fedele, D., van den Ancker, M. E., Henning, T., Jayawardhana, R., & Oliveira, J. M. 2010, A&A, 510, A72+

Fedele, D., van den Ancker, M. E., Petr-Gotzens, M. G., & Rafanelli, P. 2007, A&A, 472, 207

Feigelson, E. D., Lawson, W. A., & Garmire, G. P. 2003, ApJ, 599, 1207

Felli, M., Persi, P., Roth, M., et al. 1990, A&A, 232, 477

Finkbeiner, D. P., Padmanabhan, N., Schlegel, D. J., et al. 2004, AJ, 128, 2577

Flaherty, K. M. & Muzerolle, J. 2008, AJ, 135, 966

Freyer, T., Hensler, G., & Yorke, H. W. 2003, ApJ, 594, 888

Furlan, E., Hartmann, L., Calvet, N., et al. 2006, ApJS, 165, 568

Gâlfalk, M. & Olofsson, G. 2008, A&A, 489, 1409

Garcia Lopez, R., Natta, A., Testi, L., & Habart, E. 2006, A&A, 459, 837

Gatti, T., Natta, A., Randich, S., Testi, L., & Sacco, G. 2008, A&A, 481, 423

Gautier, III, T. N., Rebull, L. M., Stapelfeldt, K. R., & Mainzer, A. 2008, ArXiv e-prints, 804

Genzel, R., Reid, M. J., Moran, J. M., & Downes, D. 1981, ApJ, 244, 884

Getman, K. V., Feigelson, E. D., Luhman, K. L., et al. 2009, ApJ, 699, 1454

Getman, K. V., Flaccomio, E., Broos, P. S., et al. 2005, ApJS, 160, 319

Grady, C. A., Woodgate, B., Torres, C. A. O., et al. 2004, ApJ, 608, 809

Guarcello, M. G., Damiani, F., Micela, G., et al. 2010, ArXiv e-prints

Guarcello, M. G., Micela, G., Damiani, F., et al. 2009, A&A, 496, 453

Guarcello, M. G., Prisinzano, L., Micela, G., et al. 2007, A&A, 462, 245

Gullbring, E., Hartmann, L., Briceno, C., & Calvet, N. 1998, ApJ, 492, 323

Gustafsson, B., Edvardsson, B., Eriksson, K., et al. 2008, A&A, 486, 951

Gutermuth, R. A., Megeath, S. T., Muzerolle, J., et al. 2004, ApJS, 154, 374

Gutermuth, R. A., Myers, P. C., Megeath, S. T., et al. 2008, ApJ, 674, 336

Haisch, Jr., K. E., Lada, E. A., & Lada, C. J. 2001, ApJ, 553, L153

Hamann, F. 1994, ApJS, 93, 485

Harris, S., Clegg, P., & Hughes, J. 1988, MNRAS, 235, 441

Hartigan, P., Edwards, S., & Ghandour, L. 1995, ApJ, 452, 736

Hartigan, P. & Kenyon, S. J. 2003, ApJ, 583, 334

Hartigan, P., Kenyon, S. J., Hartmann, L., et al. 1991, ApJ, 382, 617

Hartmann, L. 2001, AJ, 121, 1030

Hartmann, L. 2002, ApJ, 578, 914

Hartmann, L. 2005a, in Astronomical Society of the Pacific Conference Series, Vol. 337, The Nature and Evolution of Disks Around Hot Stars, ed. R. Ignace & K. G. Gayley, 3–+

Hartmann, L. 2005b, in Astronomical Society of the Pacific Conference Series, Vol. 341, Chondrites and the Protoplanetary Disk, ed. A. N. Krot, E. R. D. Scott, & B. Reipurth, 131–+

Hartmann, L., Calvet, N., Gullbring, E., & D'Alessio, P. 1998, ApJ, 495, 385

Hartmann, L., Cassen, P., & Kenyon, S. J. 1997, ApJ, 475, 770

Hartmann, L., D'Alessio, P., Calvet, N., & Muzerolle, J. 2006, ApJ, 648, 484

Hartmann, L., Hewett, R., & Calvet, N. 1994, ApJ, 426, 669

Hartmann, L., Megeath, S. T., Allen, L., et al. 2005, ApJ, 629, 881

Haynes, R. F., Caswell, J. L., & Simons, L. W. J. 1979, Australian Journal of Physics Astrophysical Supplement, 48, 1

Henney, W. J. & Arthur, S. J. 1998, AJ, 116, 322

Henney, W. J. & O'Dell, C. R. 1999, AJ, 118, 2350

Henning, T. 2008, Physica Scripta Volume T, 130, 014019

Henning, T. 2010, ARA&A, 48, 21

Henning, T., Jäger, C., & Mutschke, H. 2004, in Astronomical Society of the Pacific Conference Series, Vol. 309, Astrophysics of Dust, ed. A. N. Witt, G. C. Clayton, & B. T. Draine, 603–+

Henning, T. & Meeus, G. 2009, ArXiv e-prints

Henning, T. & Mutschke, H. 1997, A&A, 327, 743

Herbig, G. H. 1998, ApJ, 497, 736

Herbig, G. H. & Dahm, S. E. 2002, AJ, 123, 304

Herbig, G. H. & Dahm, S. E. 2006, AJ, 131, 1530

Herczeg, G. J. & Hillenbrand, L. A. 2008, ApJ, 681, 594

Hernández, J., Briceño, C., Calvet, N., et al. 2006, ApJ, 652, 472

Hernández, J., Calvet, N., Briceño, C., Hartmann, L., & Berlind, P. 2004, AJ, 127, 1682

Hernández, J., Calvet, N., Briceño, C., et al. 2007a, ApJ, 671, 1784

Hernández, J., Hartmann, L., Calvet, N., et al. 2008, ApJ, 686, 1195

Hernández, J., Hartmann, L., Megeath, T., et al. 2007b, ApJ, 662, 1067

Hester, J. J. & Desch, S. J. 2005, in Astronomical Society of the Pacific Conference Series, Vol. 341, Chondrites and the Protoplanetary Disk, ed. A. N. Krot, E. R. D. Scott, & B. Reipurth, 107–+

Higdon, S. J. U., Devost, D., Higdon, J. L., et al. 2004, PASP, 116, 975

Hillenbrand, L. A. 1997, AJ, 113, 1733

Hillenbrand, L. A. 2002, ArXiv Astrophysics e-prints

Hillenbrand, L. A. 2008, Physica Scripta Volume T, 130, 014024

Hillenbrand, L. A., Bauermeister, A., & White, R. J. 2008, in Astronomical Society of the Pacific Conference Series, Vol. 384, 14th Cambridge Workshop on Cool Stars, Stellar Systems, and the Sun, ed. G. van Belle, 200–+

Hillenbrand, L. A., Strom, S. E., Vrba, F. J., & Keene, J. 1992, ApJ, 397, 613

Hillenbrand, L. A. & White, R. J. 2004, ApJ, 604, 741

Hirota, T., Bushimata, T., Choi, Y. K., et al. 2007, PASJ, 59, 897

Høg, E., Fabricius, C., Makarov, V. V., et al. 2000, A&A, 355, L27

Hollenbach, D. & Adams, F. C. 2004, in Astronomical Society of the Pacific Conference Series, Vol. 323, Star Formation in the Interstellar Medium: In Honor of David Hollenbach, ed. D. Johnstone, F. C. Adams, D. N. C. Lin, D. A. Neufeeld, & E. C. Ostriker , 3–+

Hollenbach, D. J., Yorke, H. W., & Johnstone, D. 2000, Protostars and Planets IV, 401

Houck, J. R., Roellig, T. L., van Cleve, J., et al. 2004, ApJS, 154, 18

Huélamo, N., Figueira, P., Bonfils, X., et al. 2008, A&A, 489, L9

Indebetouw, R., Mathis, J. S., Babler, B. L., et al. 2005, ApJ, 619, 931

Isella, A., Testi, L., & Natta, A. 2006, A&A, 451, 951

Ishihara, D., Onaka, T., Kataza, H., et al. 2010, A&A, 514, A1+

Jaeger, C., Molster, F. J., Dorschner, J., et al. 1998, A&A, 339, 904

Jayawardhana, R., Hartmann, L., Fazio, G., et al. 1999, ApJ, 521, L129

Johnstone, D., Hollenbach, D., & Bally, J. 1998, ApJ, 499, 758

Joy, A. H. 1945, ApJ, 102, 168

Juhász, A., Bouwman, J., Henning, T., et al. 2010, ApJ, 721, 431

Juhász, A., Henning, T., Bouwman, J., et al. 2009, ApJ, 695, 1024

Kemper, F., Vriend, W. J., & Tielens, A. G. G. M. 2004, ApJ, 609, 826

Kennedy, G. M. & Kenyon, S. J. 2009, ApJ, 695, 1210

Kenyon, S. J. & Hartmann, L. 1987, ApJ, 323, 714

Kenyon, S. J. & Hartmann, L. 1995, ApJS, 101, 117

Kessler-Silacci, J., Augereau, J., Dullemond, C. P., et al. 2006, ApJ, 639, 275

Kohno, M., Koyama, K., & Hamaguchi, K. 2002, ApJ, 567, 423

Kramer, C., Alves, J., Lada, C. J., et al. 1999, A&A, 342, 257

Kraus, S., Preibisch, T., & Ohnaka, K. 2008, ApJ, 676, 490

Kurucz, R. 1994, Solar abundance model atmospheres for 0,1,2,4,8 km/s. Kurucz CD-ROM No. 19. Cambridge, Mass.: Smithsonian Astrophysical Observatory, 1994., 19

Kurucz, R. L. 1979, ApJS, 40, 1

Kwan, J. & Tademaru, E. 1995, ApJ, 454, 382

Lada, C. J. 1987, in IAU Symposium, Vol. 115, Star Forming Regions, ed. M. Peimbert & J. Jugaku, 1–17

Lada, C. J., Lada, E. A., Clemens, D. P., & Bally, J. 1994, ApJ, 429, 694

Lada, C. J., Muench, A. A., Luhman, K. L., et al. 2006, AJ, 131, 1574

Lada, E. A., Depoy, D. L., Evans, II, N. J., & Gatley, I. 1991, ApJ, 371, 171

Lahuis, F. & Boogert, A. 2003, in SFChem 2002: Chemistry as a Diagnostic of Star Formation, ed. C. L. Curry & M. Fich, 335–+

Lawson, W. A., Lyo, A., & Bessell, M. S. 2009, MNRAS, 400, L29

LeFevre, O., Saisse, M., Mancini, D., et al. 2003, in Presented at the Society of Photo-Optical Instrumentation Engineers (SPIE) Conference, Vol. 4841, Instrument Design and Performance for Optical/Infrared Ground-based Telescopes. Edited by Iye, Masanori; Moorwood, Alan F. M. Proceedings of the SPIE, Volume 4841, pp. 1670-1681 (2003)., ed. M. Iye & A. F. M. Moorwood, 1670–1681

Leinert, C., van Boekel, R., Waters, L. B. F. M., et al. 2004, A&A, 423, 537

Li, W., Evans, II, N. J., & Lada, E. A. 1997, ApJ, 488, 277

Lin, D. N. C. & Papaloizou, J. C. B. 1993, in Protostars and Planets III, ed. E. H. Levy & J. I. Lunine, 749–835

Lombardi, M., Alves, J., & Lada, C. J. 2006, A&A, 454, 781

Looper, D. L., Bochanski, J. J., Burgasser, A. J., et al. 2010a, ArXiv e-prints

Looper, D. L., Burgasser, A. J., Kirkpatrick, J. D., & Swift, B. J. 2007, ApJ, 669, L97

Looper, D. L., Mohanty, S., Bochanski, J. J., et al. 2010b, ApJ, 714, 45

Luhman, K. L. 2004a, ApJ, 602, 816

Luhman, K. L. 2004b, ApJ, 616, 1033

Luhman, K. L. 2007, ApJS, 173, 104

Luhman, K. L., Allen, L. E., Allen, P. R., et al. 2008a, ApJ, 675, 1375

Luhman, K. L., Allen, P. R., Espaillat, C., Hartmann, L., & Calvet, N. 2010, ApJS, 186, 111

Luhman, K. L., Hernández, J., Downes, J. J., Hartmann, L., & Briceño, C. 2008b, ApJ, 688, 362

Luhman, K. L. & Rieke, G. H. 1999, ApJ, 525, 440

Luhman, K. L., Stauffer, J. R., Muench, A. A., et al. 2003, ApJ, 593, 1093

Luhman, K. L. & Steeghs, D. 2004, ApJ, 609, 917

Lynden-Bell, D. & Pringle, J. E. 1974, MNRAS, 168, 603

Lyo, A., Lawson, W. A., & Bessell, M. S. 2008, MNRAS, 389, 1461

Maddalena, R. J., Morris, M., Moscowitz, J., & Thaddeus, P. 1986, ApJ, 303, 375

Maíz Apellániz, J., Walborn, N. R., Morrell, N. I., Niemela, V. S., & Nelan, E. P. 2007, ApJ, 660, 1480

Mamajek, E. E. 2005, ApJ, 634, 1385

Mamajek, E. E., Lawson, W. A., & Feigelson, E. D. 1999, ApJ, 516, L77

Mamajek, E. E., Meyer, M. R., Hinz, P. M., et al. 2004, ApJ, 612, 496

Massey, P., DeGioia-Eastwood, K., & Waterhouse, E. 2001, AJ, 121, 1050

Massi, F., Brand, J., & Felli, M. 1997, A&A, 320, 972

Meeus, G., Juhász, A., Henning, T., et al. 2009, A&A, 497, 379

Meeus, G., Waters, L. B. F. M., Bouwman, J., et al. 2001, A&A, 365, 476

Megeath, S. T., Flaherty, K. M., Hora, J., et al. 2005a, in IAU Symposium, Vol. 227, Massive Star Birth: A Crossroads of Astrophysics, ed. R. Cesaroni, M. Felli, E. Churchwell, & M. Walmsley, 383–388

Megeath, S. T., Hartmann, L., Luhman, K. L., & Fazio, G. G. 2005b, ApJ, 634, L113

Mendoza, E. E. 1966, ApJ, 143, 1010

Mendoza, E. E. 1968, ApJ, 151, 977

Mercer, E. P., Miller, J. M., Calvet, N., et al. 2009, AJ, 138, 7

Meyer, M. R. & Beckwith, S. V. W. 2000, in Lecture Notes in Physics, Berlin Springer Verlag, Vol. 548, ISO Survey of a Dusty Universe, ed. D. Lemke, M. Stickel, & K. Wilke, 341–+

Miesch, M. S. & Bally, J. 1994, ApJ, 429, 645

Min, M., Waters, L. B. F. M., de Koter, A., et al. 2007, A&A, 462, 667

Mohanty, S., Jayawardhana, R., & Basri, G. 2005, ApJ, 626, 498

Moitinho, A., Alves, J., Huélamo, N., & Lada, C. J. 2001, ApJ, 563, L73

Monnier, J. D., Berger, J.-P., Millan-Gabet, R., et al. 2006, ApJ, 647, 444

Monnier, J. D., Millan-Gabet, R., Billmeier, R., et al. 2005, ApJ, 624, 832

Muñoz, D. J., Mardones, D., Garay, G., et al. 2007, ApJ, 668, 906

Muench, A. A., Lada, E. A., Lada, C. J., & Alves, J. 2002, ApJ, 573, 366

Muzerolle, J. 2008, in http://www.ipac.caltech.edu/spitzer2008/talks/JamesMuzerolle.html

Muzerolle, J., Allen, L. E., Megeath, S. T., Hernández, J., & Gutermuth, R. A. 2010, ApJ, 708, 1107

Muzerolle, J., Calvet, N., & Hartmann, L. 1998a, ApJ, 492, 743

Muzerolle, J., Calvet, N., & Hartmann, L. 2001, ApJ, 550, 944

Muzerolle, J., Hartmann, L., & Calvet, N. 1998b, AJ, 116, 2965

Muzerolle, J., Hillenbrand, L., Calvet, N., Briceño, C., & Hartmann, L. 2003, ApJ, 592, 266

Muzerolle, J., Luhman, K. L., Briceño, C., Hartmann, L., & Calvet, N. 2005, ApJ, 625, 906

Muzerolle, J., Megeath, S. T., Gutermuth, R. A., et al. 2004, ApJS, 154, 379

Najita, J. R., Strom, S. E., & Muzerolle, J. 2007, MNRAS, 378, 369

Natta, A., Grinin, V., & Mannings, V. 2000a, Protostars and Planets IV, 559

Natta, A., Meyer, M. R., & Beckwith, S. V. W. 2000b, ApJ, 534, 838

Natta, A., Testi, L., Muzerolle, J., et al. 2004, A&A, 424, 603

Natta, A., Testi, L., & Randich, S. 2006, A&A, 452, 245

Neckel, T. 1978, A&A, 69, 51

Neckel, T. 1984, A&A, 137, 58

O'dell, C. R., Wen, Z., & Hu, X. 1993, ApJ, 410, 696

Olczak, C., Pfalzner, S., & Eckart, A. 2010, A&A, 509, A63+

Olczak, C., Pfalzner, S., & Spurzem, R. 2006, ApJ, 642, 1140

Osterloh, M. & Beckwith, S. V. W. 1995, ApJ, 439, 288

Palla, F. & Stahler, S. W. 1999, ApJ, 525, 772

Park, B. & Sung, H. 2002, AJ, 123, 892

Pascucci, I., Apai, D., Luhman, K., et al. 2009, ApJ, 696, 143

Persi, P., Ferrari-Toniolo, M., Roth, M., & Tapia, M. 1986, A&A, 170, 97

Persi, P. & Tapia, M. 2008, Star Formation in NGC 6334, ed. Reipurth, B., 456–+

Peterson, D. E. 2005, PhD thesis, The University of Rochester, United States – New York

Pfalzner, S. & Olczak, C. 2007, A&A, 462, 193

Pfalzner, S., Olczak, C., & Eckart, A. 2006, A&A, 454, 811

Pomarès, M., Zavagno, A., Deharveng, L., et al. 2009, A&A, 494, 987

Povich, M. S., Stone, J. M., Churchwell, E., et al. 2007, ApJ, 660, 346

Preibisch, T., Ossenkopf, V., Yorke, H. W., & Henning, T. 1993, A&A, 279, 577

Price, S. D., Egan, M. P., Carey, S. J., Mizuno, D. R., & Kuchar, T. A. 2001, AJ, 121, 2819

Quillen, A. C., Blackman, E. G., Frank, A., & Varnière, P. 2004, ApJ, 612, L137

Reipurth, B., Pedrosa, A., & Lago, M. T. V. T. 1996, A&AS, 120, 229

Riaz, B. & Gizis, J. E. 2008, ApJ, 681, 1584

Rice, W. K. M., Wood, K., Armitage, P. J., Whitney, B. A., & Bjorkman, J. E. 2003, MNRAS, 342, 79

Richling, S. & Yorke, H. W. 2000, ApJ, 539, 258

Rieke, G. H. & Lebofsky, M. J. 1985, ApJ, 288, 618

Rieke, G. H., Young, E. T., Engelbracht, C. W., et al. 2004, ApJS, 154, 25

Rochau, B., Brandner, W., Stolte, A., et al. 2010, ApJ, 716, L90

Roeser, S., Demleitner, M., & Schilbach, E. 2010, AJ, 139, 2440

Román-Zúñiga, C. G., Elston, R., Ferreira, B., & Lada, E. A. 2008, ApJ, 672, 861

Rucinski, S. M. 1985, AJ, 90, 2321

Rucinski, S. M., Matthews, J. M., Kuschnig, R., et al. 2008, MNRAS, 391, 1913

Russeil, D., Zavagno, A., Motte, F., et al. 2010, A&A, 515, A55+

Sacco, G. G., Franciosini, E., Randich, S., & Pallavicini, R. 2008, A&A, 488, 167

Schaller, G., Schaerer, D., Meynet, G., & Maeder, A. 1992, A&AS, 96, 269

Servoin, J. L. & Piriou, B. 1973, phys. stat. sol., 55, 677

Setiawan, J., Henning, T., Launhardt, R., et al. 2008, Nature, 451, 38

Shu, F. H. 1977, ApJ, 214, 488

Shu, F. H., Adams, F. C., & Lizano, S. 1987, ARA&A, 25, 23

Sicilia-Aguilar, A., Bouwman, J., Juhász, A., et al. 2009, ApJ, 701, 1188

Sicilia-Aguilar, A., Hartmann, L., Calvet, N., et al. 2006a, ApJ, 638, 897

Sicilia-Aguilar, A., Hartmann, L. W., Briceño, C., Muzerolle, J., & Calvet, N. 2004, AJ, 128, 805

Sicilia-Aguilar, A., Hartmann, L. W., Fürész, G., et al. 2006b, AJ, 132, 2135

Sicilia-Aguilar, A., Hartmann, L. W., Hernández, J., Briceño, C., & Calvet, N. 2005, AJ, 130, 188

Sicilia-Aguilar, A., Hartmann, L. W., Watson, D., et al. 2007, ApJ, 659, 1637

Sicilia-Aguilar, A., Henning, T., Juhász, A., et al. 2008, ApJ, 687, 1145

Siess, L., Dufour, E., & Forestini, M. 2000, A&A, 358, 593

Siess, L., Forestini, M., & Bertout, C. 1997, A&A, 326, 1001

Simon, J. D., Bolatto, A. D., Whitney, B. A., et al. 2007, ApJ, 669, 327

Skrutskie, M. F., Cutri, R. M., Stiening, R., et al. 2006, AJ, 131, 1163

Spezzi, L., Alcalá, J. M., Covino, E., et al. 2008, ApJ, 680, 1295

Stelzer, B. & Scholz, A. 2009, A&A, 507, 227

Stetson, P. B. 2000, PASP, 112, 925

Stolte, A., Morris, M., Ghez, A., et al. 2010, ArXiv e-prints

Stone, J. M., Gammie, C. F., Balbus, S. A., & Hawley, J. F. 2000, Protostars and Planets IV, 589

Störzer, H. & Hollenbach, D. 1999, ApJ, 515, 669

Strom, K. M., Strom, S. E., Edwards, S., Cabrit, S., & Skrutskie, M. F. 1989, AJ, 97, 1451

Strom, K. M., Strom, S. E., & Merrill, K. M. 1993, ApJ, 412, 233

Sung, H., Bessell, M. S., & Chun, M. 2004, AJ, 128, 1684

Sung, H., Stauffer, J. R., & Bessell, M. S. 2009, AJ, 138, 1116

Torres, C. A. O., Quast, G. R., Melo, C. H. F., & Sterzik, M. F. 2008, Young Nearby Loose Associations, ed. Reipurth, B., 757–+

Tsujimoto, M., Koyama, K., Tsuboi, Y., Goto, M., & Kobayashi, N. 2002, ApJ, 566, 974

Vacca, W. D., Garmany, C. D., & Shull, J. M. 1996, ApJ, 460, 914

Valdes, F., Gupta, R., Rose, J. A., Singh, H. P., & Bell, D. J. 2004, ApJS, 152, 251

van Boekel, R., Min, M., Leinert, C., et al. 2004, Nature, 432, 479

van Boekel, R., Min, M., Waters, L. B. F. M., et al. 2005, A&A, 437, 189

van Boekel, R., Waters, L. B. F. M., Dominik, C., et al. 2003, A&A, 400, L21

van der Plas, G., van den Ancker, M. E., Fedele, D., et al. 2008, A&A, 485, 487

Vinković, D., Ivezić, Ž., Jurkić, T., & Elitzur, M. 2006, ApJ, 636, 348

Vinković, D., Ivezić, Ž., Miroshnichenko, A. S., & Elitzur, M. 2003, MNRAS, 346, 1151

Voit, G. M. 1992, MNRAS, 258, 841

Wang, J., Townsley, L. K., Feigelson, E. D., et al. 2008, ApJ, 675, 464

Wang, J., Townsley, L. K., Feigelson, E. D., et al. 2007, ApJS, 168, 100

Webb, R. A., Zuckerman, B., Platais, I., et al. 1999, ApJ, 512, L63

Weintraub, D. A., Sandell, G., & Duncan, W. D. 1989, ApJ, 340, L69

White, R. J. & Basri, G. 2003, ApJ, 582, 1109

White, R. J. & Hillenbrand, L. A. 2004, ApJ, 616, 998

Wilson, B. A., Dame, T. M., Masheder, M. R. W., & Thaddeus, P. 2005, A&A, 430, 523

Wilson, T. L., Mezger, P. G., Gardner, F. F., & Milne, D. K. 1970, A&A, 6, 364

Winston, E., Megeath, S. T., Wolk, S. J., et al. 2009, ArXiv e-prints

Winston, E., Megeath, S. T., Wolk, S. J., et al. 2007, ApJ, 669, 493

Yamamura, I., Makiuti, S., Ikeda, N., et al. 2010, VizieR Online Data Catalog, 2298, 0

York, D. G., Adelman, J., Anderson, Jr., J. E., et al. 2000, AJ, 120, 1579

Young, E. T., Lada, C. J., Teixeira, P., et al. 2004, ApJS, 154, 428

Zinnecker, H. & Yorke, H. W. 2007, ARA&A, 45, 481